



HAL
open science

Laser-Induced Nucleation in a Coaxial Microfluidic Mixer

Zhengyu Zhang

► **To cite this version:**

Zhengyu Zhang. Laser-Induced Nucleation in a Coaxial Microfluidic Mixer. Other. Université Paris Saclay (COmUE), 2019. English. NNT : 2019SACLN023 . tel-03284318

HAL Id: tel-03284318

<https://theses.hal.science/tel-03284318>

Submitted on 12 Jul 2021

HAL is a multi-disciplinary open access archive for the deposit and dissemination of scientific research documents, whether they are published or not. The documents may come from teaching and research institutions in France or abroad, or from public or private research centers.

L'archive ouverte pluridisciplinaire **HAL**, est destinée au dépôt et à la diffusion de documents scientifiques de niveau recherche, publiés ou non, émanant des établissements d'enseignement et de recherche français ou étrangers, des laboratoires publics ou privés.

Laser-induced Nucleation in a Coaxial Microfluidic Mixer

Thèse de doctorat de l'Université Paris-Saclay
École Normale Supérieure Paris-Saclay

École doctorale n°573 Interfaces : approches interdisciplinaires,
fondements, applications et innovation (Interfaces)
Spécialité de doctorat : Chimie

Thèse présentée et soutenue à Cachan, le 13 Juin 2019, par

Zhengyu Zhang

Composition du Jury :

Alain Ibanez Directeur de recherche, CNRS (– Institut Néel)	Président
Yong Chen Directeur de recherche, Ecole Normale Supérieure (– UMR 8640)	Rapporteur
Stéphane Veesler Directeur de recherche, CNRS (CINaM)	Rapporteur
Sladjana Novakovic Associate Professor, Vinča Institute of Nuclear Sciences	Examineur
David Carrière Directeur de recherche, CEA (– NIMBE)	Examineur
Robert B. Pansu Directeur de recherche, ENS Paris-Saclay (– PPSM)	Examineur
Anne Spasojević - de Biré Professeure, CentraleSupélec (– SPMS)	Directeur de thèse
	Co-Directeur de thèse

Thèse de doctorat

LASER-INDUCED NUCLEATION IN A COAXIAL MICROFLUIDIC MIXER

DISSERTATION

Submitted to the École Doctorale Interfaces of the Université Paris-Saclay

in Partial Fulfilment of the Requirements for the Degree of

DOCTOR OF PHILOSOPHY

in Chemistry

at

École Normale Supérieure Paris-Saclay

by

Zhengyu Zhang

Supervised by

Dr. Robert B. Pansu

Prof. Anne Spasojević - de Biré

Summer 2019

Acknowledgement

More than 8200 kilometres had I flied from Beijing to Paris on September 15, 2015. I can still see that day vividly. My mother saw me off at the Beijing International Airport. It was a long, noisy, and freezing flight. I drank much wine and covered my numb body with my father's coat. Six o'clock in the morning, Director Robert Pansu was waiting at the Aeroport de Charles de Gaulle. That was the first time I took a plane, the first time I stepped on the land of another country, and the first time Director Pansu and I met in person, although we had had video meetings discussing my master study and my forthcoming PhD. He gave me a quick tour of Paris: l'*École Normale Supérieure*, la *Société Chimique de France*..., after which we arrived at l'*ENS-Cachan*. He introduced me to the lab of PPSM and then drove me to the bank, my dorm, and the supermarket. He took care of a new student like a father would. That gave me the first impression of France: warm, kind, and caring. Yet, on the very next day I was hopelessly lost on the RER B (which reflects another aspect of France) for a meeting with Prof. Anne Spasojević - de Biré.

It was Prof. Spasojević - de Biré who recruited me from Beijing, at which time she was the Dean of the *École Centrale de Pékin*, and I was in the last year of my master studies on rapid solidification of laser melting deposited titanium in the same university. Looking for a PhD position, I was fascinated by her research on laser-induced nucleation and the polymorphism control by laser polarisation. She accepted my application and arranged several meetings on our campus. I would not pretend that I was not shocked when I first saw her in a wheelchair but then quickly amused, because she ran faster than I through flocks of students, once even raced joyfully with a food delivery guy. Yet, it was not for her driving skills that she was famous among Centralians in Beijing, but for her strictness in teaching. Indeed, she has always been kind to me, letting me pay attention to the cultural gap between France and China, drag me back to the original research plan, explaining the knowledge that I should have learnt before, and sometimes testing me.

The last three and half years has been a tremendous journey, during which I have been

fortunately blessed by my research supervisors: Robert and Anne. Professionally, they are always ready to help with the experiment, to answer questions, including stupid ones, and to have discussions. Personally, they have been taking good care of me, helping me fit in the lab and the French society. They are not only my research advisors, but more like my family in France.

I am amazed on a daily basis by Robert's scope of knowledge and depth of thinking both in and out our field. From him, I have realised that being a scholar is not only about doing experiment and solving equations, but also a way of behaviour, of manner, of language, and of being professional. This can only be learnt through observations: we have been doing experiment together, analysing data together, solving equations together, having lunch together, and attending conferences together. These have been valuable opportunities for me to observe like what a real scientist should be. I treasure this experience as the most important training from my PhD.

I am also amazed on the same daily basis by Anne's skills, diligence, and strictness. She emphasises on the way of thinking. She has been updating a database of NPLIN related papers filled with the tested compounds, laser types, experimental parameters, results, and proposed mechanisms. She teaches me to rapidly dig pertinent information from literature and to compare with our results. Not only does she work day and night, but also with strictness and efficiency. She urges me to pay attention to details and to timing, for experiments, for writing, and for presentations. She pointed out the smallest flaws in my manuscript, word by word, table to table, figure to figure. I really appreciate that. She is the strongest person I ever know and will always be my inspiration.

I have also benefited much from our engineer Jean-Frédéric Audibert. It was Jeff who spent hours and hours aligning the laser again and again, who answered my questions on the details of the experiment, who repaired the laser when I broke everything down, who maintained all the equipment, who taught me experimental skills from the basics, who came on emergency at any time by a text message, who never said no to requests from a student. Nothing

in this thesis could have been accomplished if there had not been him.

Many different techniques were involved in our research. I must also extend a huge thank to our collaborators, colleagues, fellow and former students who contributed to this work, notably: Valérie Génot developed the microfluidic device and the first *Comsol* model; Director Stéphane Veesler is the parrain de thèse, who travelled from Marseille to Paris to check the progress of the thesis at the midterm and gave me advices; Bi Ran measured the solubility of DBDCS, the mixing properties of the solvents, and anti-solvent focusing of Pastis; Prof. Thomas Rodet extracted the fastest FLIM video from our data; Dr. Wenjing Li taught me how to use the NPLIN setup in SPMS; Prof. Soo Young Park's team synthesised DBDCS and measured its melting point and melting enthalpy; Director Isabelle Leray and Dr. Naresh Kumar synthesised Calix-cousulf; Dr. Javier Perez, Dr. Mehdi Zeghal, Dr. Guillaume Tresset, and Prof. Brigitte Pansu organised a SAXS experiment at the *Synchrotron SOLEIL*; Evgeny Turbin, Dr. Yury Prokazov, and Dr. Werner Zusratter have developed and have been maintaining the FLIM detector; Philippe Scouflaire has built and has been maintaining the NPLIN setup in SPMS; Dr. Vu-Long Tran and Dr. Yuanyuan Liao are the first users of the microfluidic device; Dr. Bertrand Clair and Dr. Aziza IKNI are the first users of the NPLIN setup in SPMS; Nada Bošnjaković-Pavlović is currently doing experiments with the NPLIN setup in SPMS; Arnaud Brosseau is the engineer maintaining the spectroscopy room of PPSM; Jean-Pierre Lefèvre is the engineer for the microfluidic room of IDA; Dr. Rasta Ghasemi is the engineer maintaining the SEM of IDA. Thank you all for your help with our research.

It goes without saying that our research would have gone nowhere without the financial support. I am thankful to the *Laboratoire Photophysique et Photochimie Supramoléculaires et Macromoléculaires (PPSM)*, to the *Laboratoire Structures Propriétés, Modélisation des Solides (SPMS)*, to the *Institut d'ALEMBERT*, to the *ENS Paris-Saclay*, to *CentraleSupélec*, to the *Université Paris-Saclay*, to the *Centre National de la Recherche Scientifique*, to the République française and her warm-hearted people, for supporting my research and for welcoming and hosting me during my research.

I would like to also thank my *alma mater*, *Gansu University of Technology*, for giving me strict engineering training. This year is her centennial anniversary. I wish her a happy birthday. I am equally thankful to *Beijing University of Aeronautics and Astronautics* (BUAA), to Prof. Huaming Wang and Dr. Haibo Tang, and to the *National Engineering Laboratory of Additive Manufacturing for Large Metallic Components*. BUAA opened my door from engineering to academics, from China to France. I have been benefiting day-to-day during my PhD from the training in BUAA: *thermodynamics, physical metallurgy, physical chemistry, mass, heat, and momentum transfer in materials processing, XRD, SEM, DSC, DTA*, and so on.

There are not enough words in my English vocabulary to express how much I am grateful to my parents. Not only did they support me through the ups and downs, but it was their education, which cultivated my interest and belief in science. They came to France to support me when I was overwhelmed by the manuscript while my wife was about to give birth. They have done more than enough.

Some special thanks are given to my DD (dear daughter), Xingxian, for her kicking, laughing, crying, vomiting, hiccupping, and pooping, alongside my writing the manuscript. Considering your nine months in the uterus, you accompanied nearly half of my PhD. Thank you for being a lovable rascal. You have my unconditional love, but you need to work hard to gain my respect. I cannot wait to see you become a strong, brave, independent woman.

My last gratitude is reserved for the most important person, my wife, Weixi, whose love and devotion not only encouraged me throughout my PhD, but also will be the best solace for a short life in a grand universe.

To my wife

Weixi Wang Zhang

who gives me the best accompany and solace

in a grand and dark universe full of mysteries

Abstract

Crystallisation is one of the elementary operations of chemical engineering. Materials are extracted by crystallisation and purified by recrystallisation. But crystal nucleation remains a mystery, and the classical nucleation theory has been undermined by numerous experimental evidences. We have built a microfluidic precipitation device by mixing solvents to produce and continuously observe the birth of a large number of crystals. The molecule chosen for the study is DBDCS, which is fluorescent in solid state (aggregates, crystals, ...), but not in solution. Its nuclei will thus be the first luminous object in the mixture.

We have calculated the thermodynamics of the ternary mixture of water (1)-1,4-dioxane (2)-DBDCS (3) from what is known for the binary mixture of 1-2 and the solubility curve of 3 in 1-2, using a two-body-three-body interaction model. From that we have estimated the diffusion coefficients for *Comsol* simulation. The thermodynamics of the ternary mixtures hypothesised a liquid phase of 3.

A parametric sweep of the microfluidic parameters was carried out. Three types of spontaneous phase transitions from liquid have been recorded: i) nano-particles; ii) droplets; iii) crystals. By plotting the observations as a function of the average composition of the mixture, a working phase diagram of 1-2-3 in the microfluidic system has been established. Droplets prevail on the phase diagram. The volume fraction of the droplets obeys the lever rule of phase separation to a supersaturated solution and a nearly pure liquid phase of DBDCS (3). The liquid-liquid phase separation requires a strong supersaturation following the diffusion of water (1). The study of the solubility of 3 in 1-2 shows that the chemical potential of DBDCS (3) in water (1) is $17.4 RT$ higher than that in 1,4-dioxane (2). The diffusion of 1 in 2 induces the formation of an energy barrier that repels and concentrates 3 towards the flow centre. Numerical simulation shows that the supersaturation ratio at the flow centre where the liquid-liquid phase separation occurs is beyond 50 and reaches up to 10^6 order of magnitude. The product of this liquid-liquid phase separation is a cloud of sub-micrometric droplets. But the chemical potential gradient can, under certain conditions, group these nanodrops into a string of micrometric drops

of the same size.

As the fraction of 2 increases in the anti-solvent, the potential barrier starts to be outweighed by the configurational entropy of mixing. This is shown by the distribution of the fluorescence of the molecules (*yield* $< 10^{-4}$). About five seconds out from the injection nozzle, the formation and growth of crystals is observed. The numerical simulation indicates that for crystallisation the supersaturation ratio does not exceed 3.5. Rapid imaging and fluorescence lifetime imaging allow the crystals to be observed one by one. Three different polymorphs are identifiable by fluorescence lifetime: the green and the blue phases already reported, and a short-lived phase. The growth rates are widely dispersed, making it difficult to locate and to observe spontaneous nucleation.

By focusing a femtosecond infrared laser on the clouds of nanodrops, we observe an optical tweezing effect capable of collecting these drops. By focusing this laser before spontaneous crystallisation is manifesting, we observe a multiplication of the number of crystals formed by a factor of five. This is the laser-induced nucleation of crystals. These crystals have the same growth rate, size distribution, and polymorph distribution as the spontaneous crystals. This laser-induced nucleation is therefore very soft and induces a minimal change in the nucleation mechanism. An optical tweezing effect that locally concentrates the precursors of the nuclei and increases the supersaturation may explain this observation. This laser-induced nucleation makes it possible to locate the nucleation. At the focal point of the femtosecond infrared laser, we observe the accumulation of a phase with a short fluorescence lifetime, which can be an indication for disordered aggregates. The short lifetime disappears after the passage in the laser focal spot while the green phase grows slowly. This may be a direct observation of a two-step nucleation.

Résumé

La cristallisation est une des opérations élémentaires du génie chimique. Les matières produites sont extraites par cristallisation et purifiées par recristallisation. Mais la nucléation du cristal reste un mystère et la théorie classique de la nucléation est battue en brèche par de nombreuses données expérimentales. Nous avons construit un dispositif microfluidique de précipitation par mélange de solvants pour produire de manière continue et observer la formation d'un grand nombre de cristaux. La molécule étudiée est le DBDCS dont les cristaux sont fluorescents mais pas la molécule. Le germe sera ainsi le premier objet lumineux du mélange.

Nous avons calculé la thermodynamique du mélange ternaire DBDCS-1,4-dioxane-eau à partir de ce qui est connu pour le mélange 1,4-dioxane-eau et de la courbe de solubilité du DBDCS dans 1,4-dioxane-eau, dans le cadre du modèle H^3M . Ceci nous a permis de fournir à *Comsol* les valeurs des coefficients de diffusion du mélange ternaire. La thermodynamique des mélanges ternaires postule une phase liquide du DBDCS.

Nous observons cette phase dans une expérience de précipitation après 1ms de mélange. La mesure du volume de cette phase liquide confirme qu'elle est pratiquement pure. L'apparition de cette phase liquide nécessite une forte sursaturation. Celle-ci fait suite à la diffusion de l'eau qui repousse et concentre le DBDCS au centre du dispositif. L'étude du temps mis à atteindre la concentration critique en fonction de la concentration initiale en DBDCS dans le flux central permet d'obtenir une valeur de 50 à 70 fois la saturation pour la concentration critique d'apparition de la phase liquide DBDCS. Le produit de cette décomposition liquide-liquide est un nuage de gouttelettes sub-micrométriques. Mais le gradient de potentiel chimique peut, dans certaines conditions, regrouper ces nano-gouttes en un chapelet de gouttes micrométriques de même taille.

Lorsque l'anti-solvant n'est pas de l'eau pure, mais un mélange 1,4-dioxane-eau, la barrière de potentiel ne l'emporte pas sur l'entropie de la diffusion, ce que montre la répartition

de la fluorescence résiduelle des molécules (rendement $< 10^{-4}$). Sur des temps de l'ordre de 5s, on observe la formation et la croissance de cristaux dans un mélange localement homogène. La simulation numérique indique que dans ces conditions la sursaturation relative ne dépasse pas 3,5. L'imagerie rapide et la fluorescence permettent d'observer les cristaux un par un. Trois polymorphes différents sont identifiables par leur durée de vie : les phases vertes et bleues déjà observées et une phase de courte durée de vie. Ces cristaux présentent une vitesse de croissance moyenne proportionnelle à la concentration locale.

En focalisant un laser sur les nuages de nano-gouttes, on observe un effet de pince optique capable de rassembler ces gouttes. En focalisant ce laser dans la zone de supersaturation maximale dans des conditions de nucléation spontanée, on observe une multiplication du nombre de cristaux formés d'un facteur cinq. Nous sommes en présence d'une nucléation induite par laser. Ces cristaux présentent la même vitesse de croissance, la même distribution en nombre des polymorphes, que les cristaux obtenus spontanément. Cette nucléation induite par laser est donc très douce et induit un changement minimal du mécanisme de la nucléation. Un effet de pince optique qui concentre localement les précurseurs du germe et augment transitoirement la sursaturation pourrait avoir cet effet.

Cette nucléation induite par laser permet de localiser la nucléation. Au point focal du laser NPLIN, nous observons la cumulation d'une phase de durée de vie de fluorescence courte, donc peut être désordonnée. Elle disparaît après le passage dans le laser pendant qu'une phase de grande durée de vie (la phase verte) croit lentement. Ce serait une observation directe d'une nucléation en deux étapes.

Table of contents

Acknowledgement	I
Abstract.....	VI
Résumé	VIII
Table of nomenclatures.....	XIV
List of acronyms and abbreviations	XVIII
Table of physical constants.....	XX
List of figures	XXI
List of tables.....	XXVIII
List of appendixes.....	XXX
General introduction.....	1
Chapter 1. State of art.....	6
1.1. Crystallisation from solution	7
1.1.1. Generalities.....	7
1.1.2. Nucleation theories	8
1.2. Non-photochemical laser-induced nucleation (NPLIN).....	16
1.2.1. Necessity for control nucleation	16
1.2.2. NPLIN: definition and literature	17
1.2.3. NPLIN: characterisation techniques	21
1.3. Microfluidics	22
1.3.1. Two phases microfluidics	22
1.3.2. Crystallisation in microfluidics.....	25
1.4. Fluorescence.....	26
1.4.1. Electronic states.....	26
1.4.2. Jablonski diagram.....	27
1.4.3. Fluorescence yield	28
1.4.4. Fluorescence lifetime.....	29
1.4.5. Solid state fluorescence	30
1.4.6. Video fluorescence lifetime imaging microscopy (FLIM).....	34
1.5. (2Z,2'Z)-2,2'-(1,4-phenylene)bis(3-(4-butoxyphenyl) acrylonitrile) (DBDCS)	35
1.5.1. Synthesis.....	35
1.5.2. Characterisation.....	36
1.5.3. Photoluminescent properties	37
Chapter 2. Experimental: parametric sweep of a coaxial microfluidic mixer for diffusive antisolvent precipitation, coupled with a focused IR laser for NPLIN and a wide-field UV laser for FLIM	45
2.1. A diffusive coaxial microflow antisolvent precipitation system	46
2.1.1. Reactive part of the coaxial microflow mixer	46
2.1.2. Flow control in the microfluidic system	50
2.1.3. Structure of the coaxial microflow	56
2.1.4. Assembling the microfluidic system.....	61
2.2. Laser and microscopy setup for microfluidic NPLIN and FLIM	63
2.3. Microfluidic parametric sweep and NPLIN	67
Chapter conclusion.....	71
Chapter 3. Thermodynamics of water (1)-1,4-dioxane (2)-DBDCS (3) ternary system ..	74
3.1. Molar excess mixing volume, dynamic viscosity, and refractive indices by Redlich-Kister equation	76
3.2. Thermodynamics of antisolvent-solvent-solute ternary mixing	80
3.2.1. Ideal mixing model.....	80
3.2.2. Regular mixing model	83

3.2.3. H ³ M model for real solvent mixing	90
3.2.4. Jouyban-Acree equation for solubility prediction of slightly soluble solute in aqueous-organic mixture with H ³ M model	91
3.3. Applying the H³M model to water (1)-1,4-dioxane (2)-DBDCS (3) irregular ternary system	93
3.3.1. Solubility of DBDCS in water (1)-1,4-dioxane (2) mixture.....	93
3.3.2. Thermodynamic parameters of water (1)-1,4-dioxane (2)-DBDCS (3) ternary system	95
3.4. Brief introduction to thermodynamics of diffusion.....	100
3.4.1. Intrinsic diffusion coefficient.....	100
3.4.2. Mutual diffusion coefficients.....	105
3.5. Diffusion of water (1)-1,4-dioxane (2)-DBDCS (3) mixture.....	107
3.5.1. Estimation of the diffusion coefficients of water (1)-1,4-dioxane (2) binary system with Moggridge equation	107
3.5.2. Estimation of the diffusion coefficient of DBDCS in binary system of water (1)-1,4-dioxane (2)	109
3.6. Thermodynamic stability of water (1)-1,4-dioxane (2)-DBDCS (3) ternary mixture	113
3.6.1. Liquid-liquid phase separation (LLPS).....	113
3.6.2. Crystallisation from antisolvent-solvent mixture	124
Chapter conclusion.....	125
Chapter 4. Comsol simulation.....	128
4.1. Comsol simulation model of the coaxial microflow mixer	129
4.1.1. Model	129
4.1.2. Parameters	132
4.1.3. Studies	133
4.2. Simulation of the inter-diffusion of water (1)-1,4-dioxane (2) binary system without DBDCS	134
4.2.1. Central jet radius.....	134
4.2.2. Flow entrance length	136
4.3. Simulation of the diffusion of DBDCS in a field of solvent composition	140
Chapter conclusion.....	143
Chapter 5. Phase diagram of water (1)-1,4-dioxane (2)-DBDCS (3) system in the coaxial microfluidic mixer. Part I: Non-crystalline phase transition	145
5.1. Phenomena observed in the coaxial microfluidic mixer	147
5.2. Evidences for antisolvent focusing of DBDCS	148
5.3. Phase diagram of water (1)-1,4-dioxane (2)-DBDCS (3) the coaxial microfluidic mixer.....	151
5.4. The soluble region.....	153
5.5. Nano-objects	154
5.5.1. <i>In situ</i> OM observation	154
5.5.2. Nature of the nano-particles.....	157
5.5.3. <i>Post-mortem</i> observation	158
5.6. Liquid-liquid phase separation.....	159
5.6.1. From nanoparticles to droplets	159
5.6.2. Formation mechanism of the droplets.....	161
5.6.3. Abnormally large, backward flowing droplets, inner structure and crystallisation of the droplets caught in flow by Marangoni effect.	163
5.6.4. <i>Post-mortem</i> drying of the droplets	168
5.6.5. Solidification of the droplets in the flow.....	169
5.7. Kinetic characteristics of the coaxial microflow mixer	170
5.7.1. A simple relation to calculate the droplet formation distance and the average focusing velocity.....	172
5.7.2. Dependence of the average focusing velocity on microfluidic parameters	176

5.7.3. Dependence of LLPS and nano-precipitation starting position on microfluidic parameters	185
5.7.4. Quality of the prediction of the chemical potential focusing velocity, distance, the binodal LLPS threshold and the diffusion coefficient of DBDCS in water (1)-1,4-dioxane (2) coaxial microflow.....	189
5.8. Droplet size dependence on microfluidic parameters	192
5.8.1. The total volume fraction of the droplets in the flow	192
5.8.2. The size of the DBDCS droplets.....	196
Chapter conclusion.....	203
Chapter 6. Phase diagram of water (1)-1,4-dioxane (2)-DBDCS (3) system in the coaxial microfluidic mixer. Part II: spontaneous crystallisation	206
6.1. Spontaneous crystallisation from a homogeneous microflow	207
6.2. Crystal habits of DBDCS	208
6.2.1. Spontaneous crystals in the flow.....	208
6.2.2. <i>Post-mortem</i> observation	211
6.2.3. Heterogeneous crystallisation on the wall of the microfluidic channel	212
6.3. FLIM map of spontaneous crystallisation of DBDCS in microflow.....	214
6.4. Counting and identifying flowing fluorescent particles with the fastest FLIM video	224
6.5. Measuring DBDCS crystal size by FLIM	227
6.6. The birth rate and growth rate of spontaneous DBDCS crystals in the microflow of water (1)-1,4-dioxane (2) mixture.....	230
6.6.1. <i>Comsol</i> simulation of the environment	230
6.6.2. Definition of the variables	231
6.6.3. By FLIM.....	233
6.6.4. By OM.....	237
6.7. Summary of all the spontaneous phase transition types observed in the coaxial microfluidic system.....	242
Chapter conclusion.....	244
Chapter 7. Laser-induce nucleation in microfluidics.....	246
7.1. Laser-induced crystals	248
7.1.1. Early stage of laser-induced nucleation	248
7.1.2. Nucleation rate, growth rate and polymorph distribution of laser-induced crystals in microfluidics	252
7.1.3. Impact of laser parameters on laser-induced crystallisation in microfluidics	261
7.1.4. <i>Post-mortem</i> characterisation of NPLIN crystals.....	272
7.2. Laser's effect on LLPS and droplets	273
7.2.1. Laser dragging the central-peripheral flow interface	273
7.2.2. Laser accelerating the phase separation and droplets formation	274
7.2.3. Laser releasing the abnormally large droplets from the “droplet trap”	276
7.2.4. Laser changing the size of the stable droplets	278
7.3. Effect of the focused IR laser of nano-objects	279
7.3.1. Dark line	279
7.3.2. Laser-induced two-step crystallisation: droplets→crystals.....	280
7.3.3. Laser-induced bubbles on nano-precipitates' surface	282
7.3.4. Impact of laser induction position.....	284
7.4. Other observation with the femtosecond IR laser	286
7.4.1. Laser tweezers	286
7.4.2. Bubbles, explosion, laser ablation.	287
7.5. NPLIN working phase diagram.....	288
Chapter conclusion.....	292

General discussion and perspective.....	293
Discussion.....	294
On the experimental device	294
On the thermodynamic calculations and the <i>Comsol</i> simulations.....	295
On the quantitative description of the LLPS.....	295
On the properties of the ternary system water (1)-1,4-dioxane (2)-DBDCS (3) obtained spontaneously in the coaxial microfluidic device.	299
On the properties of the ternary system water (1)-1,4-dioxane (2)-DBDCS (3) laser-induced in the coaxial microfluidic device.....	304
On the polymorphism of DBDCS.....	306
On the different crystallisation techniques.....	309
On the different methods for producing droplets	311
On the NPLIN mechanism	313
On the crystallisation mechanism	313
On the potentiality of our method.....	314
Perspectives.....	316
On a better understanding of DBDCS	316
On the improvements of our experimental device	318
On the improvements of methodologic developments.....	320
Towards the understanding the mechanism of nucleation	321
As a (very) final conclusion.....	322
References	324
Appendix	Appen-1

Table of nomenclatures

Notation	Definition	Unit
Latin letters		
a, b, c	lattice length parameter	m
A	area	m ²
A_m	molar surface area	m ² ·mol ⁻¹
B_x	accumulative crystal birth rate from nozzle to x μm	s ⁻¹
$B_{x_1}^{x_2}$	sectional crystal birth rate during $x_1 \sim x_2$ μm from nozzle	s ⁻¹ ·m ⁻¹
c, p	subscripts “c” and “p” denote central and peripheral flows, respectively	
d	distance	m
d_L	distance from nozzle to the induction laser focal point	m
d_N	distance between two successive nucleation events in microflow	m
d_p	phase transition starting distance from nozzle	m
D	diameter	m
D_i^F	intrinsic diffusion coefficient of species i	m ² ·s ⁻¹
D_{ij}^F	mutual diffusion coefficient of species i and j	m ² ·s ⁻¹
D^∞	diffusion coefficient in infinite dilute solution	m ² ·s ⁻¹
D^*	self-diffusion coefficient	m ² ·s ⁻¹
f	hydrodynamic factor of maximum central flow radius	1
f_{rep}	laser pulse repetition rate	Hz
\mathbf{F}	force	N
g_A	crystal area growth rate	m ² ·s ⁻¹
g_L	crystal linear growth rate	m·s ⁻¹
G_m	molar Gibbs energy	J·mol ⁻¹
G_v^L	volume Gibbs energy of liquid phase	J·m ⁻³
G_v^S	volume Gibbs energy of solid phase	J·m ⁻³
$\Delta_s^L G_v$	volume Gibbs energy change from liquid to solid	J·m ⁻³
ΔG_N	Gibbs energy change of a nucleus	J
ΔG_N^*	nucleation energy barrier	
$\Delta_{\text{melt}} H_v$	volume melting enthalpy	J·m ⁻³
$\Delta_r H_m$	molar enthalpy of a reaction	J·mol ⁻¹
I	optical intensity	W·m ⁻²
\mathbf{I}	identity tensor, matrix	
\mathbf{j}	flux in moving coordinate system	kg·m ⁻² ·s ⁻¹
\mathbf{J}	flux in fixed coordinate system	kg·m ⁻² ·s ⁻¹
k	rate constant	
k_{FRET}	rate constant of the Förster resonant energy transfer	

k_F	fluorescence decay rate constant	
k_{IC}	rate constants of internal conversion	
k_{ISC}	rate constants of intersystem crossing	
k_{ISOM}	rate constants of isomerisation	
K_N	nucleation rate constant	
k_Q	quenching rate constant	
l_c	concentration entrance length	m
l_h	hydrodynamic entrance length	m
L_c	length of a crystal	m
M_i	molar mass of species i	kg·mol ⁻¹
M_n	mean molar mass	kg·mol ⁻¹
n	amount	mol
n_D	refractive index	1
N	number of particles	1
N^*	number of nuclei <i>per</i> unit volume	m ⁻³
N_{ab}	number of photons absorbed	1
N_{em}	number of photons emitted	1
N_H	heterogeneous nucleation rate	m ⁻³ ·s ⁻¹
N_L	Laser-induced nucleation rate	m ⁻³ ·s ⁻¹
N_S	spontaneous nucleation rate	m ⁻³ ·s ⁻¹
p	probability	1
P_{avg}	laser average power	W
Pe	Péclet number	1
P_{peak}	laser peak power	W
Q	flow rate	m ³ ·s ⁻¹
Q_A	activation energy	J·mol ⁻¹
Q_c	central flow rate	m ³ ·s ⁻¹
$\Delta_{mix} Q$	loss of flow rate after mixing of solvents	m ³ ·s ⁻¹
Q_p	peripheral flow rate	m ³ ·s ⁻¹
r	radius	m
r^*	critical radius	m
r_3^*	radius of liquid DBDCS molecules	m
$r_{c,max}$	maximum radius of a jet	m
r_{drop}	radius of droplet	m
r_o	radius of a cylindrical tube before it breaks in to droplets	m
$R_{channel}$	radius of a microfluidic channel	m
Re	Reynolds number	1
R_{FRET}	FRET distance	m

R_m	molar refractivity	$\text{m}^3 \cdot \text{mol}^{-1}$
S	singlet state	
$\Delta_r S_m$	molar entropy change of a reaction	$\text{J} \cdot \text{mol}^{-1} \cdot \text{K}^{-1}$
t	time	s
t_I	induction period	s
t_N	nucleation event time interval	s
T	triplet state	
T	temperature	K
τ	Transpose of a matrix	
T_{melt}	melting point	K
ΔT	supercooling	K
\mathbf{v}	velocity field	$\text{m} \cdot \text{s}^{-1}$
v	advective velocity of a laminar flow	$\text{m} \cdot \text{s}^{-1}$
$v_{\text{effective}}$	effective velocity of a laminar flow	$\text{m} \cdot \text{s}^{-1}$
v_{max}	maximum flow velocity of a laminar flow	$\text{m} \cdot \text{s}^{-1}$
\mathbf{v}^F	diffusive velocity	$\text{m} \cdot \text{s}^{-1}$
$\overline{\mathbf{v}_r^F}$	average antisolvent focusing velocity of a solute	$\text{m} \cdot \text{s}^{-1}$
V	volume	m^3
V_m	molar volume	$\text{m}^3 \cdot \text{mol}^{-1}$
$\Delta_{\text{mix}} V_m$	excess molar mixing volume	$\text{m}^3 \cdot \text{mol}^{-1}$
w	focused laser beam radius	m
x_i	amount fraction of species i	1
x_s	amount fraction solubility	1
x_{ibj}	amount fraction binodal decomposition limit of species i in j	1
x_{isj}	amount fraction solubility of species i in j	1
x_{ispinj}	amount fraction spinodal decomposition limit of species i in j	1
x, y, z	Cartesian coordinates	
x, r, φ	horizontal cylindrical coordinates	
Greek letters		
α, β, γ	lattice angle parameter	$^\circ$
β	supersaturation ratio	1
γ	surface tension	$\text{N} \cdot \text{m}^{-1}, \text{J} \cdot \text{m}^{-2}$
γ_{sL}	interfacial free energy between solid and liquid phase	$\text{N} \cdot \text{m}^{-1}, \text{J} \cdot \text{m}^{-2}$
γ_i	activity coefficient of species i	
∇	Hamiltonian operator	
∇^2	Laplace operator	
η	kinetic viscosity	$\text{m}^2 \cdot \text{s}^{-1}$
λ	wavelength	m

λ	period of in the Plateau–Rayleigh instability	m
λ_{em}	emission wavelength	m
μ	chemical potential	J·mol ⁻¹
$\ddot{\mu}$	dynamic viscosity	Pa·s
ν	frequency	Hz
ρ	mass concentration	kg·m ⁻³
ρ_{D}	mass density	kg·m ⁻³
ρ_{b}	mass concentration binodal decomposition limit	kg·m ⁻³
ρ_{ibj}	mass concentration binodal decomposition of species i in j	kg·m ⁻³
ρ_{s}	solubility in mass concentration	kg·m ⁻³
ρ_{isj}	mass concentration solubility of species i in j	kg·m ⁻³
ρ_{spin}	mass concentration spinodal decomposition limit	kg·m ⁻³
ρ_{ispinj}	mass concentration spinodal decomposition limit of species i in j	kg·m ⁻³
$\Delta\rho$	supersaturation	kg·m ⁻³
\sum	sum	
τ_{F}	fluorescence lifetime	s
τ_{p}	laser pulse width	s
ϕ_i	volume fraction of species i	1
ϕ_i°	volume fraction of species i without considering the solute	1
Φ_{F}	quantum yield	
Other		
\cdot	inner product operator	
\otimes	outer product operator	
\int	integral	
∂	partial derivative	
*	hypothetical liquid state of a solute	

List of acronyms and abbreviations

ABS	acrylonitrile butadiene styrene
ac	alternating current
AIE	aggregation-induced emission
ATR-FTIR	attenuated total reflectance Fourier-transform infrared spectroscopy
BF	bright field
CCD	charge-coupled device
CL	circular left-handed
CMOS	complementary metal–oxide–semiconductor
CNT	classical nucleation theory
CP	crossed polarisers
CR	circular right-handed
CW	continue wavelength
DBDCS	(2Z,2'Z)-2,2'-(1,4-phenylene)bis(3-(4-butoxyphenyl) acrylonitrile)
dc	direct current
DLS	dynamic light scattering
DSC	differential scanning calorimetry
DVP	divinyl benzene
EF	electric field
ENS Paris-Saclay	École Normale Supérieure Paris-Saclay
FBRM	beam reflectance measurement
FEP	fluorinated ethylene propylene
FLIM	fluorescence lifetime imaging microscopy
FRET	Förster resonant energy transfer
fs	femtosecond
HEWL	hen-egg white lysozyme
IC	internal conversion
ID	inside diameter
IR	infrared
ISC	intersystem crossing
ISOM	isomerisation
LLPS	liquid-liquid phase separation
NA	numerical aperture
NIR	near-infrared
NPLIN	non-photochemical laser-induced nucleation
OD	optic density
OD	outside diameter
OM	optical microscopy
PCA	principal component analysis
PDMS	polydimethylsiloxane
PEEK	polyether ether ketone
PNC	pre-nucleation cluster
POTS	1H,1H,2H,2H-perfluorooctyltriethoxysilane
PSPM	Laboratoire de Photophysique et Photochimie Supramoléculaires et Macromoléculaires
PVM	particle vision and measurement
ROI	region of interest
SAXS	small angle X-ray scattering
SEM	scanning electron microscopy
SPMS	Laboratoire Structures Propriétés et Modélisation des Solides
ssNMR	solid-state nuclear magnetic resonance
SVA	solvent vapor annealing
TA	thermal annealing

TEM	transmission electron microscopy
TICT	twisted intramolecular charge transfer
TPE	tetraphenylethylene
TSCSPC	time- and space- correlated single photon counting
TST	two-step nucleation theory
UV	ultraviolet
vr	vibrational relaxation
WF	wide-field
WD	working distance
XRD	X-ray diffraction

Table of physical constants

Quantity	Symbol	Value	Unit
Elementary charge	e	$1.602\,176\,487(40) \times 10^{-19}$	C
Faraday constant $N_A \cdot e$	F	96 485.3399(24)	C·mol ⁻¹
Boltzmann constant R / N_A	k_B	$1.380\,6504(24) \times 10^{-23}$	J·K ⁻¹
Avogadro constant	N_A	$6.022\,141\,79(30) \times 10^{23}$	mol ⁻¹
Molar gas constant	R	8.314 472(15)	J·mol·K ⁻¹

List of figures

Figure 1.1. Chronology of scientists and their contributions towards understanding nucleation. (Adapted from [Kathmann, 2005]).....	8
Figure 1.2. Sketch of the Gibbs energy gain ΔG_N as a function of the crystalline nucleus size r . (Adapted from [Sosso, 2016]).....	12
Figure 1.3. Schematic comparison of the Gibbs energy gain ΔG_N and the structural change in terms of the cluster size r (Adapted from [Sosso, 2016]).....	15
Figure 1.4. Schematic definition of NPLIN used in this manuscript.....	18
Figure 1.5. Growth of the papers on NPLIN according to our extended definition. . .	18
Figure 1.6. Distribution of NPLIN papers according to the compounds studied.	19
Figure 1.7. Some key-figures of NPLIN setups.....	20
Figure 1.8. Schematic representation of NPLIN sample-holders.	21
Figure 1.9. The movement of the flow around a drop of DVB in a gradient of water (channel wall) and ethanol (channel centre). (Adapted from [Hajian, 2015]).....	25
Figure 1.10. Schematic representation of the electron in the ground or excited state.	26
Figure 1.11. Schematic energy levels in atoms, molecules, and semiconductors. (Adapted from [Douglas, 2013]).....	27
Figure 1.12. Simple Jablonski diagram illustrating the primary deactivation processes occurring upon excitation. Electronic levels are represented by heavy lines. (Adapted from [Douglas, 2013]).....	28
Figure 1.13. Effect of defects in a fluorescent crystal.	32
Figure 1.14. Molecular structure of DBDCS.	36
Figure 1.15. Schematic illustration for the preparation of DBDCS using a reactive inkjet printing method. (Adapted from [Jeon, 2015]).....	36
Figure 1.16. IR spectral change in DBDCS film due to the UV irradiation or heating. The asterisk indicates the band of CO ₂ . (Adapted from [Fujimori, 2016]).....	37
Figure 1.17. Photo of DBDCS crystals. (Adapted from [Yoon, 2010]).....	38
Figure 1.18. Fluorescence microscope images of DBDCS spots after 24 h at different temperatures on glass and PDMS films (λ_{ex} 330~385 nm). (Adapted from [Jeon, 2015]).....	38
Figure 1.19. The absorption and fluorescence spectra of DBDCS in CHCl ₃ . (Adapted from [Shi, 2017b]).....	39
Figure 1.20. The fluorescence decay profiles of DBDCS nanoparticles in THF-water mixture (dark green line), Green-phase VD film (green line), and Blue-phase VD film (blue line) under 400 nm excitation. (Adapted from [Yoon, 2010]).....	40
Figure 1.21. The change in the colour of the fluorescence has been rationalised by Yoon, et al as the change in the interaction of dimers. (Adapted from [Yoon, 2010])	40
Figure 1.22. Colour contour map of calculated exciton splitting for a dimer pair at a different displacements (Adapted from [Yoon, 2010]).....	42
Figure 1.23. Experimental lifetimes (ns) of DBDCS as reported in the literature.....	43
Figure 1.24. Photos of the luminescence writing-erasing cycle on a DBDCS-PMMA film. (Adapted from [Yoon, 2010]).....	44
Figure 1.25. RGB fluorescence switching in DBDCS/m-BHDCS bicomponent film (Adapted from [Kim, 2015]).....	44
Figure 2.1. Schematic illustration of the microfluidic NPLIN experiment.....	48
Figure 2.2. Typical procedures of “static” NPLIN (top) and “microfluidic” NPLIN (bottom).....	49
Figure 2.3. Design of the versatile coaxial microflow system.....	51

Figure 2.4. Parameters of the coaxial microfluidic mixer.	53
Figure 2.5. Clogging of the borosilicate syringe after a long time of experiment. A: clogging by caesium acetate in THF-water microflow; B: clogging by DBDCS precipitation in water (1)-1,4-dioxane (2).....	54
Figure 2.6. Loss of flow rate after mixing coflow of water (1)-1,4-dioxane (2) and of water (1)-THF (2) calculated using equation 2.9 in terms of volume fractions.	56
Figure 2.7. Central flow jet shape after injection nozzle.	58
Figure 2.8. Central flow maximum radius as function of central/peripheral flow ratio. Data is well described by equation (2.14).....	59
Figure 2.9. Design from the supporter for the microfluidic capillaries.	62
Figure 2.10. Assembled diffusive coaxial microflow antisolvent precipitation system.	63
Figure 2.11. Schematic illustration of the laser and microscopy setup for microfluidic NPLIN and FLIM	64
Figure 2.12. Laser and microscope setup for microfluidic NPLIN and FLIM mounted with the microfluidic system.....	67
Figure 2.13. Parametric matrix of the experimental inputs and outputs for water (1)-1,4-dioxane (2)-DBDCS (3) system. * denotes supersaturated mother solution.	68
Figure 2.14. Calliper fixed on the microscope stage to measure distance in the microflow.....	69
Figure 2.15. Adjustable microscope stage movement blocker (in the red circle).....	70
Figure 2.16. The microfluidic system mounted on X-ray line SWING of synchrotron Soleil.	71
Figure 3.1. Molar excess mixing volume of water (1)-1,4-dioxane (2) binary mixture at 298.15 K [Aminabhavi, 1995].....	77
Figure 3.2. Estimation and experimental values of the mixing properties of water (1)-1,4-dioxane (2) binary system at 298.15 K.	80
Figure 3.3. Stability of ideal solutions. $\Delta_{\text{mix}} G_m$ of ideal binary (A) and ternary (B) mixtures at 298.15 K are shown. B2 is B1 flattened. Ideal mixtures are always stable.	83
Figure 3.4. Stability of regular solutions.	85
Figure 3.5. Molar mixing free energy change $\Delta_{\text{mix}} G_m$ of ternary regular mixtures with different interaction parameters Ω (values noted on graphes in RT) at 298.15 K.	89
Figure 3.6. DBDCS amount fraction solubility in binary system of water (1)-1,4-dioxane (2) as a function of solvents molar composition (+ to the top axis) and of solvents volume composition (■ to the bottom axis).	94
Figure 3.7. A “log ternary diagram” of water (1)-1,4-dioxane (2)-DBDCS (3) mixture.	96
Figure 3.8. Activity of water (1)-1,4-dioxane (2) binary system at 298.15 K, measured by [Vierk, 1950], fitted with regular solution model and H ³ M model respectively. ...	97
Figure 3.9. Diffusion direction of a regular solution with $\Omega = 3RT$ at 298.15 K.....	103
Figure 3.10. Prediction of mutual and intrinsic diffusion coefficient of water and 1,4-dioxane at 298.15 K.	108
Figure 3.11. Thermodynamic factor of diffusion coefficients of water (1)-1,4-dioxane (2) at 298.15 K	109
Figure 3.12. Estimation of hypothetical tracer diffusion coefficient of DBDCS in water (1)-1,4-dioxane (2) mixture at 298.15 K.	112
Figure 3.13. Thermodynamic stability and diffusion direction of a binary irregular solution at 298.15 K.	114

Figure 3.14. Thermodynamic stability of the binary system of DBDCS and 1,4-dioxane at 298.15 K.	118
Figure 3.15. Thermodynamic stability of the binary system of DBDCS and water at 298.15 K.	120
Figure 3.16. Stability of water (1)-1,4-dioxane (2)-DBDCS (3) ternary mixture.....	122
Figure 3.17. A calculated ternary phase diagram of water (1)-1,4-dioxane (2)-DBDCS (3).....	124
Figure 3.18. Zoom in of the Gibbs energy of DBDCS in water (1)-1,4-dioxane (2) mixture near the soluble domain.....	125
Figure 4.1. Axisymmetric geometry of the simulation domain of the reactive part of the coaxial microflow mixer.	130
Figure 4.2. An example of the parametric sweep simulation: $\rho_{3c} = 0$, $Q_c = 370$ nl/min, $\phi_p = 100\%$, $Q_p = 1$ μ l/min	134
Figure 4.3. Comparison of the OM images and Comsol simulation of the refractive index n_D of a parametric sweep of a central flow of 1,4-dioxane into a peripheral flow of water. The microfluidic parameters are marked on the small OM images.....	135
Figure 4.4. Comparison of the Comsol simulation (■), theoretical calculation (line) and the experimental measurement (▲) of the maximum central jet $r_{c,max}$ as a function of flow ratio.....	136
Figure 4.5. Comsol simulation of the development of a laminar flow of a Poiseuille velocity profile along its radius.....	137
Figure 4.6. Parametric sweep simulation of flow velocity profiles along tube centre (top) and its gradient (bottom) on the flow direction. The hydrodynamic entrance length l_h is 200 μ m.....	138
Figure 4.7. Comsol simulation of the development of a homogeneous concentration.. ..	139
Figure 4.8. Parametric sweep simulation of 1,4-dioxane mass concentration along flow centre (top) and its gradient (bottom) on the flow direction. This reflects the concentration entrance length l_c of the flow.	140
Figure 4.9. Simulation of DBDCS diffusion in a field of solvent composition.....	141
Figure 4.10. Simulation of DBDCS diffusion in a field of solvent composition.	143
Figure 5.1. Typical phenomena observed in the coaxial microfluidic mixer with water (1)-1,4-dioxane (2)-DBDCS (3) system.	147
Figure 5.2. A whole image of the demixing.	149
Figure 5.3. Evidences and simulation for antisolvent focusing of DBDCS.	150
Figure 5.4. Working phase diagram of water (1)-1,4-dioxane (2)-DBDCS (3) phase diagram in the microfluidic mixer measured by a parametric sweep.	152
Figure 5.5. Precipitation of a vague line and its disappearance because the diffusion of solute driven by the anti-solvent composition gradient, frames taken from a video moving along the flow.	154
Figure 5.6. A column of DBDCS nano-particles formed along the flow centre.	156
Figure 5.7. By blocking the microfluidic channel, the flow was temporarily stopped, and the nano-particles were “frozen” in the suspension.	156
Figure 5.8. Precipitation of a dark line later dispersed in to a column of nanoparticles, frames taken from a video along the flow.	157
Figure 5.9. In situ OM transmission image (left) and CP image (right) of the nanoparticles 26980 μ m away from the injection nozzle.	158

Figure 5.10. Drying process of a suspension of DBDCS nano-particles collected on a glass slide.	159
Figure 5.11. A~C: post-mortem SEM image of DBDCS nano-particles collected on copper grid; D~F: bigger objects appeared among nano-particles after 1 month.....	159
Figure 5.12. Nanoparticles gathered to be droplets.	160
Figure 5.13. Droplets along the flow.	161
Figure 5.14. Zoom of formation of droplets. A: droplets appeared from the centre of the microfluidic channel and then grow and merge to a stable size.	162
Figure 5.15. Direct breaking of the centre flow by a Plateau–Rayleigh instability...	163
Figure 5.16. Frames taken from a video of abnormally large droplet in trapped by Marangoni effect with t the elapsed time in the video.....	164
Figure 5.17. A: abnormally large droplet dragged to the tip by the strong Marangoni effect and left remanence on the nozzle; B: abnormally large droplet crystallised and flushed away by the flow.	165
Figure 5.18. Crystallisation of trapped abnormally large crystals observed during a washing.	166
Figure 5.19. Inner structure of the trapped abnormally large droplet.....	167
Figure 5.20. Post-mortem OM observation of the droplets	168
Figure 5.21. Collected dark line of droplets on glass slide. A: suspension in solvents mixture; B: dried.....	169
Figure 5.22. Crystallisation of the liquid DBDCS stacked as a pillar along the flow centre.....	169
Figure 5.23. Two-step crystallisation of caesium acetate in the microfluidic mixer.	170
Figure 5.24. By changing only Q_p , d_p was observed to be fixed at $430 \mu m$	173
Figure 5.25. Schematic illustration of the movement of DBDCS in the antisolvent focusing of the coaxial microfluidic mixer.	174
Figure 5.26. Dependence of average anti-solvent focusing velocity $\overline{v_r^F}$ on microfluidic input parameters.....	178
Figure 5.27. Prediction of slopes as a function of flow ratio.	180
Figure 5.28. Dependence of the average anti-solvent focusing velocity of DBDCS on ρ_{3c} in the coaxial mixer of water (1)-1,4-dioxane (2) flows.....	181
Figure 5.29. Dependence of the average anti-solvent focusing velocity of DBDCS on ϕ_{1p} , $\frac{Q_c}{Q_p}$, and ρ_{3c} in the coaxial mixer of water (1)-1,4-dioxane (2) flows.....	182
Figure 5.30. The chemical potential focusing limit (red) of DBDCS by water (1)-1,4-dioxane (2) in the working phase diagram of water (1)-1,4-dioxane (2)-DBDCS (3) in coaxial microfluidic mixer.....	184
Figure 5.31. LLPS and nano-precipitation starting position's dependence on microfluidic control parameters.....	186
Figure 5.32. Dependence of d_p on ρ_{3c} and ϕ_{1p}	187
Figure 5.33. Droplet formation position as a function of Q_c , ρ_{3c} and ϕ_{1p}	188
Figure 5.34. New prediction of antisolvent focusing velocity and droplet formation distance with equation (5.4) and (5.5) using fitted parameters.....	191
Figure 5.35. Size dependence of droplets on Q_p	192
Figure 5.36. Size dependence of droplets on ϕ_{1p}	193
Figure 5.37. Size dependence of droplets on ρ_{3c}	193
Figure 5.38. Fraction of new phases from the LLPS in the ternary phase diagram of	

water (1)-1,4-dioxane (2)-DBDCS (3).....	195
Figure 5.39. Total droplet volume fraction is linear with DBDCS total concentration. Every millilitre of the droplet phase contains 1.2 g DBDCS.....	196
Figure 5.40. Surface tension of binary mixture of water (1)-1,4-dioxane (2).	199
Figure 5.41. Droplets radius as a function of ϕ_{1p} and r_0	201
Figure 5.42. Droplet radius measurement vs prediction by Plateau-Rayleigh instability model.....	202
Figure 6.1. Spontaneous crystallisation of DBDCS from water-1,4- dioxane mixture in the coaxial microfluidic mixer.....	208
Figure 6.2. Crystal habit of DBDCS spontaneous crystallisation from water (1)-1,4-dioxane (2) in the coaxial mixer	209
Figure 6.3. Crystal habit of DBDCS spontaneous crystallisation from water-(THF20-1,4-dioxane80) in the coaxial mixer.	210
Figure 6.4. Schematic formation mechanism of the “butterfly” twin crystal habit of DBDCS in the microflow.....	211
Figure 6.5. Drying process of the DBDCS butterfly crystals collected at the end of the microfluidic channel.	212
Figure 6.6. Small crystals grow appeared at the “empty” space.....	212
Figure 6.7. Heterogeneous DBDCS crystals on the microfluidic channel wall.....	213
Figure 6.8. FLIM image of three crystals grown on the wall from a flow of water-(THF20dioxane80)-DBDCS mixture.....	214
Figure 6.9. Fluorescence intensity and lifetime treatment of DBDCS spontaneous crystals in the microflow of water (1)-1,4-dioxane (2).....	215
Figure 6.10. A collection of fluorescence decays collected at different position along the spontaneous crystallisation in the flow	217
Figure 6.11. The fluorescence lifetime images collected along the spontaneous crystallisation in the microflow	218
Figure 6.12. Comsol simulation of the volume fraction of water, the solubility, the mass concentration, and supersaturation of DBDCS in the microflow	219
Figure 6.13. The decays collected from different areas on the FLIM map along the spontaneous crystallisation in the flow	220
Figure 6.14. The PCA of the fluorescence decays collected on the FLIM map.	221
Figure 6.15. Contribution from the principal components to the fluorescence intensity in the time trace.....	222
Figure 6.16. Contribution from the “Oligo” DBDCS and the crystals to the fluorescence intensity in the two regions of interests along the microflow.....	223
Figure 6.17. The residuals of the data described by the four components: Microscope, Molecule, “Oligo” and “CPFluctant”.	224
Figure 6.18. The fluorescence intensity (red) and lifetime (blue) signal collected from the flow centre area.....	225
Figure 6.19. Fluorescence intensity and lifetime after the correction of the detection time.	226
Figure 6.20. Frames of the fastest FLIM video.	227
Figure 6.21. The total number of photons counted per DBDCS crystal versus the transit time through a virtual line in the flow.	228
Figure 6.22. Rotation of crystals in the flow of DBDCS crystals in a mixture of water-THF in the coaxial microflow.....	229
Figure 6.23. Comsol simulation of the mass concentration (solid curve) and supersaturation (dashed curve) of DBDCS along the flow centre for different observations discussed in this work.....	231

Figure 6.24. Number distribution of the nucleation event time interval, t_N , measured by FLIM.....	233
Figure 6.25. FLIM measurement of the DBDCS crystal area A_c distribution and accumulative birth rate B_x along the microflow.	234
Figure 6.26. The correlation between the fluorescence lifetime of individual particles and their size for six positions along the flow.	236
Figure 6.27. OM measurement of nucleation rate and growth rate of spontaneous crystallisation versus distant from injection nozzle (bottom axis) and residence time (top distance).....	239
Figure 6.28. OM measurement of nucleation rate and growth rate of spontaneous crystallisation versus distant from injection nozzle (bottom axis) and residence time (top distance).....	241
Figure 6.29. Summary of all the spontaneous phase transition behaviours observed in the coaxial microfluidic system.	243
Figure 7.1. Laser-induced DBDCS crystals from a mixture of water (1)-1,4-dioxane (2) in the coaxial microfluidic mixer.	249
Figure 7.2. FLIM image of the microfluidic NPLIN in Figure 7.1.	250
Figure 7.3. The fluorescence decays of DBDCS molecules with and without the IR femtosecond laser.....	251
Figure 7.4. Spontaneous crystallisation and growth of DBDCS along the coaxial microfluidic mixer without IR laser.....	253
Figure 7.5. Growth process of the laser-induced crystals along the microfluidic channel.	254
Figure 7.6. Growth process of the crystals induced with half the full laser power. .	255
Figure 7.7. Comparison the nucleation rate and the growth rate between laser-induced (red) and spontaneous crystallisation (olive) under the same microfluidic conditions in the coaxial mixer measured by OM.	258
Figure 7.8. Comparison of the FLIM measurement of the laser-induced nucleation (red) and spontaneous nucleation (blue) of DBDCS in the coaxial microflow.	259
Figure 7.9. The fluorescence lifetime distribution (the curve covering the circles plotted vertically at the distance from nozzle) of laser-induced (red) and the spontaneous (blue) DBDCS crystals measured along the coaxial microflow..	261
Figure 7.10. Impact of laser induction position. Laser was turned on at different distance d_L to the nozzle.....	262
Figure 7.11. The impact of the laser induction position d_L on the laser-induced crystal birth-rate B_{10mm}	264
Figure 7.12. Impact of IR laser power P_{avg} on induced crystals. Observed 10100 μm from the nozzle.	265
Figure 7.13. Impact of laser average power P_{avg} on laser-induced crystal the birth rate B_{10mm}	266
Figure 7.14. Size of laser-induced crystals decreased with laser average power P_{avg}	267
Figure 7.15. Impact of laser repetition rate f_{rep} on laser-induced crystals.....	269
Figure 7.16. Cross comparison of the impact of laser average power P_{avg} on laser-induced crystal birth rate B_{10mm} at different repetition rate f_{rep}	270
Figure 7.17. The impact of laser polarisation on the laser-induced DBDCS crystal	

from water (1)-1,4-dioxane (2) mixture.....	271
Figure 7.18. Impact of laser polarisation on the accumulative crystal birth rate $B_{10\text{mm}}$ of DBDCS in the coaxial microflow of water (1)-1,4-dioxane (2).....	272
Figure 7.19. Post-mortem OM image of collected laser-induced crystals on glass slides.	273
Figure 7.20. The effect of the focused femtosecond IR laser on the interface between the central jet of 1,4-dioxane and the peripheral flow of water.	274
Figure 7.21. Impact of focused IR laser on droplet formation.....	275
Figure 7.22. A~B: two examples of laser releasing abnormally large droplets from the droplet trap. C: the process how laser released the trapped droplets..	277
Figure 7.23. By increasing the contrast of the image, it shows laser had induced a dark line before releasing the suspended large droplet..	278
Figure 7.24. Laser's effect on the size of the droplets.	278
Figure 7.25. Laser induced a dark line in the nano-sized precipitation of DBDCS in the microflow.	280
Figure 7.26. OM transmission image and CP image of laser-induced droplet formation from amorphous nano-objects and the crystallisation of the droplets later in the microflow.....	281
Figure 7.27. Laser-induced explosion dependence on laser average power.....	283
Figure 7.28. Laser-induced explosion dependence on flow velocity.....	284
Figure 7.29. Impact of laser induction position on interaction with DBDCS nano-particles.....	285
Figure 7.30. Using the femtosecond IR laser as tweezers to move impurities in pure water.....	287
Figure 7.31. A~C: laser-induced explosion, ablation, and bubbles on surface of absorbing solids; D: capillary wall burnt by long time laser explosion.	288
Figure 7.32. Summary of spontaneous phase transition types and the effect of the focused fs IR laser in the coaxial microfluidic system with some characteristic parameters of interest are marked on the schemes.....	289
Figure 7.33. Microfluidic NPLIN working phase diagram.....	291
Figure D.1. Lifetime decay (ns) of “object” produced in the microfluidic device compared to the literature (black circle).	307
Figure D.2. Experimental SAXS spectra of DBDCS crystals in microfluidic device.	308
Figure D.3. Theoretical powder X-ray diffraction spectra of DBDCS calculated by reciprOgraph	309
Figure D.4. Extraction of Table S2 from [Yoon, 2010]. The Green and the Blue phases in ground powder sate are indicated with a coloured border.	309
Figure D.5. Schematic illustration of a complete full NPLIN experiment in our microfluidic setup and its simulation.....	315
Figure D.6. List of parameters used in a complete full NPLIN experiment in our microfluidic setup and its simulation.....	315

List of tables

Table 2.1. Parameters of mixing volume functions for binary mixtures of water (1)-1,4-dioxane (2) and water-THF [Aminabhavi, 1995].....	55
Table 2.2. Average power of the IR laser on the sample plane of different polarisations (P: parallel to flow; S: vertical to flow; CL: circular left-handed; CR: circular right-handed).....	66
Table 2.3. Laser and microscope configuration and type of experiment.....	66
Table 3.1. Basic physical properties of the materials in this thesis at 298.15 K: dynamic viscosity μ , surface tension γ , molar surface A_m , density ρ_D , refractive index n_D , molar refractivity R_m , molar mass M and molar volume V_m . * denotes calculation of a solute state.	76
Table 3.2. Parameters of mixing functions for binary mixtures of H ₂ O and 1,4-dioxane[Aminabhavi, 1995]	77
Table 3.3. Model constants in the Jouyban-Acree model for water (1)-1,4-dioxane (2) system [Jouyban, 2007]	93
Table 3.4 Recalculation of DBDCS amount fraction solubility, measured by Ran Bi in mass ratio, in binary system of water (1)-1,4-dioxane (2).....	93
Table 3.5 Fitting parameters for estimation of $\Delta_{mix} G_m$ of water (1)-1,4-dioxane (2)-DBDCS (3) ternary mixture.....	97
Table 3.6. Curve fitting parameters in Figure 3.8.....	98
Table 3.7. Curve fitting parameters in Figure 3.6.....	98
Table 3.8 Curve fitting parameters from solubility in pure solvent.....	99
Table 3.9. Measurement of self- [Holz, 2000] and mutual [Leaist, 2000] diffusion coefficients of water and 1,4-dioxane at 298.15 K, with D_{12}^F the mutual diffusion coefficient in the mixture, D_i^* the self-diffusion coefficient of species i , and D_i^∞ the limiting diffusion coefficient of species i in an infinitely diluted solution.....	105
Table 5.1. Comparison of predicted and fitted parameters in equation (5.4) and (5.5):chemical affinity of DBDCS for 1,4-dioxane compared to water, binodal LLPS threshold of DBDCS in 1,4-dioxane and the radius of solute DBDCS	190
Table D.1. List of parameters which can be predicted with our three main equations	296
Table D.2. List of parameters which can be calculated with our model.....	297
Table D.3. Properties of water (1)-1,4-dioxane (2)-DBDCS (3) mixture.....	297
Table D.4. Different outputs of our calculations	298
Table D.5. Different objects observed spontaneously via OM.....	299
Table D.6. Properties of spontaneous droplets as deduced via OM, SEM post-mortem observation. Experiments with IR laser will enhance this assumption (wide supra).	301
Table D.7. Properties of spontaneous crystals as deduced via OM, and fluorescence.	303
Table D.8. Properties of spontaneous and laser induced crystals of DBDCS in the ternary mixture of water (1)-1,4-dioxane (2)-DBDCS (3) as deduced via OM, and fluorescence.	304
Table D.9. Properties of NPLIN crystals of DBDCS in the ternary mixture of water (1)-1,4-dioxane (2)-DBDCS (3) as deduced via OM, and fluorescence.....	305
Table D.10. Different conditions and nucleation methods to obtain crystals from our microfluidic device in the ternary mixture water (1)-1,4-dioxane (2)-DBDCS (3).	

Conditions and Figures are given as examples.	310
Table D.11. Different conditions and nucleation methods to obtain droplets from our microfluidic device in the ternary mixture water (1)-1,4-dioxane (2)-DBDCS (3). Conditions and Figures are given as examples.	311
Table P.1. Examples of experiment to be done on DBDCS solvent-antisolvent mixture.	317

List of appendixes

Appendix A	Appen-1
A.i. Thermodynamic versus kinetic aspect of nucleation	Appen-1
A.ii. Bibliography description of NPLIN experiment	Appen-2
A.iii. Experimental techniques for crystallisation observation	Appen-10
A.iii.i. Classical techniques for crystallisation observation	Appen-10
A.iii.ii. Techniques for pre-nucleation clusters observation.....	Appen-11
A.iv. Bibliography of DBDCS characterisation	Appen-16
A.v. Preliminary test materials	Appen-18
Appendix B	Appen-19
B.i. Technical details of the microfluidics	Appen-19
B.i.i. The microfluidic system holder	Appen-19
B.i.ii. Microfluidic capillaries, connectors, and chambers	Appen-19
B.i.iii. Pumps system, Harvard Apparatus	Appen-20
B.ii. Structure of the coaxial microflow	Appen-20
B.ii.i. Central jet radius.....	Appen-20
B.ii.ii. Flow entrance length	Appen-21
B.iii. Assembling the microfluidic system	Appen-22
B.iii.i. Assembling procedures	Appen-22
B.iv. Problems related with the microfluidic device	Appen-27
B.iv.i. Cleanness of the capillaries.....	Appen-27
B.iv.ii. Temperature control	Appen-28
B.iv.iii. Deformation and degradation of the device	Appen-28
B.iv.iv. Precipitation on the injection nozzle of the central flow	Appen-29
B.iv.v. Working distance of the objective.....	Appen-30
B.iv.vi. Leakage and bubble	Appen-30
B.iv.vii. Influence of gravity	Appen-30
B.iv.viii. Flow expansion by the big capillary	Appen-30
B.v. Technical details of the laser sources and illumination type	Appen-31
B.v.i. Diascopic illumination for bright field (BF) imaging, Köhler illumination typ.....	Appen-31
B.v.ii. Episcopic illumination for wide-field fluorescence (ep-fl) imaging and IR focusing:	Appen-31
B.vi. Technical details of the microscope and optics	Appen-32
B.vi.i. Microscope	Appen-32
B.vi.ii. Objective and filters arrangement.....	Appen-32
B.vii. Technical details of the sensor and detector	Appen-33
B.vii.i. CCD camera Retiga R1, <i>QImaging</i>	Appen-33
B.vii.ii. QA–Fluorescence Life time Imaging (FLIM).....	Appen-33
B.viii. Laser power, repetition rate, and laser focal spot intensity profile	Appen-34
Appendix C	Appen-37
C.i. Thermodynamic activity of water (1)-1,4-dioxane (2) system	Appen-37
C.ii. Limitation of H³M model and Acree-Jouyban equation	Appen-37
C.iii. Estimation of the melting point, the solid-liquid phase change enthalpy and entropy of DBDCS	Appen-42
C.iv. Recent development on the mutual diffusion coefficient of self-associating species	Appen-46
Appendix D	Appen-49
D.i. Global parameters, global variables, and local variables for <i>Comsol</i> simulation	Appen-49

D.ii. Justification of separation of the concentration- and composition- driven diffusion by using the migration in electric field model in <i>Comsol</i>.....	Appen-52
Appendix E	Appen-55
E.i. FLIM measurement of spontaneous precipitation of Calix-Cousulf-Cs⁺² nano-particles.....	Appen-55
Appendix F.....	Appen-57
F.i. SAXS study with swing@soleil experiment.....	Appen-57

General introduction

Nucleation is a frontier of chemistry. The classical nucleation theory postulates that the transition state which is at the maximum of the energy barrier on the way to crystallisation is a small crystal. This explains the control of crystallisation by kinetics, the production of various polymorphs, and the existence of an amorphous phase and supersaturated solutions. But there are evidences that contradict this model for not describing the actual crystallisation routes [Karthika, 2016]. Crystal growth and design is still the domain of a knowhow and art.

The control of crystal polymorphism is important in the metal industry for mechanical properties, in the pharmaceutical industry for solubility and bioavailability properties, and in the semiconductor industry for electronic properties.

Crystallisation mechanism has been mainly studied indirectly *via post-mortem* approaches such as time-resolved X-Ray diffraction [Fleury, 2014], atomic force microscopy [Warzecha, 2017], electron microscopy [Nielsen, 2014, Schubert, 2017], and so forth. Crystallisation remains a rare and random event. To know when and where a crystal will arise is a requirement for spatial and temporal control of nucleation. Non-Photochemical Laser-Induced Nucleation (NPLIN) is an answer [Duffus, 2009]. NPLIN has been firstly observed by Garetz *et al* in 1996 [Garetz, 1996]. By shining a laser (femto- or nano-second, pulsed or continuous waves) on a supersaturated solution, crystallisation is induced [Fang, 2014, Yuyama, 2016, Liu, 2017a]. The Laboratory *Structures Propriétés et Modélisation des Solides (SPMS)* UMR 8580 du *CNRS, CentraleSupélec* has developed a robot for the assessment and quantitative evaluation of the laser-induced crystallisation. They have shown that, for pharmaceutical drugs, depending on the laser power, the number of laser shots, and their polarisation, one can control the number or the polymorph of crystals [Clair, 2014, Ikni, 2014, Li, 2016b]. The optical tweezing effect as one of the explanations for the NPLIN has been proposed first by Masuhara in the case of polymers [Katsura, 1998, Sugiyama, 2012]. The calculation of the optical forces has been done for pulsed laser, including photon pressure, refraction, and trapping effects [Usman, 2013]. It has been shown by Walton et Wynne [Walton, 2018] that molecules can be focused and that the phase transition can be described by including

an electromagnetic term the Gibbs energy.

Recently, the Laboratory *Photophysique & Photochimie Supramoléculaires et Macromoléculaires (PPSM)* UMR 8531 du CNRS, l'ENS Paris-Saclay has developed a microfluidic device for the observation of fluorescent crystals and precipitates [Tran, 2016]. The polymorphs of the fluorescence molecule can be distinguished by their fluorescence lifetimes. The uphill diffusion of the solute by a repulsion by the anti-solvent is a known concept that is included in the fundamental equations of thermodynamic of ternary mixtures [Krishna, 2015]. But this solvent driven segregation has not been put forward as a driving force in microfluidic except for the movement of particles [Hajian, 2015].

The production of nanoparticles has been reviewed [Wang, 2015, Ma, 2017, Tao, 2019] and has produced important synthetic success, for example, the reactive precipitation of magnetic particles in co-flow by Abou-Hassan *et al* [Abou-Hassan, 2009], from whom we have receive the tube microfluidic approach. Other examples are the reactive precipitation of fluorescent perovskite nanoparticle by Lignos *et al* [Lignos, 2016] and the precipitation of nanometric fluorescent polymeric sensor by A.Reisch [Reisch, 2018]. But few papers have been published on the mechanism of the production of nanoparticles in microfluidics by solvent shifting. The formation of microdroplets through the gathering on nano droplets was postulated [Aubry, 2009]. This is in this community that the focusing of droplets by the Marangoni effect has been first observed [Hajian, 2015].

The goal of this PhD is to use a co-flow microfluidic device associated to an *in situ* fluorescence characterisation to follow the nucleation and crystallisation of DBDCS (2Z,2'Z)-2,2'-(1,4-phenylene)bis(3-(4-butoxyphenyl) acrylonitrile), an Aggregation-Induced Emission (AIE) luminogen molecule. To control spatially and temporally the nucleation, an NPLIN experiment is included on the microfluidic device. This idea is the consequence of a small project funding between IDA and CentraleSupélec to support collaboration between researchers of the both institutions.

The manuscript is organised as following:

Chapter 1 summarises the *State of art* concerning nucleation, NPLIN, fluorescence imaging (FLIM), and DBDCS molecule.

Chapter 2 describes in detail the *Experimental coaxial microfluidic mixer for diffusive antisolvent precipitation, coupled with a focused IR Laser for NPLIN and a wide-field UV Laser for FLIM*. This device will allow a *parametric sweep* of the different parameters.

Chapter 3 presents the *Thermodynamics of water (1)-1,4-dioxane (2)-DBDCS (3) ternary system* used in this work. The molar volume, dynamic viscosity, and refractive indices of the mixture will be expressed using the Redlich-Kister type equation. After an Introduction to the thermodynamics of antisolvent-solvent-solute ternary mixtures, the Jouyban-Acree equation and the H3M model will be applied to the ternary system of 1-2-3. The thermodynamics of diffusion and its application to the diffusion of 1-2-3 mixture will be discussed. Finally, the thermodynamic stability of 1-2-3 ternary mixture will be addressed.

Chapter 4 exposes the *Comsol simulation* allowed by the thermodynamic equations developed in the previous chapter. Some preliminary comparisons between predictions and observations are presented.

Chapter 5 exhibits the *Part 1 of the Phase diagram of water (1)-1,4-dioxane (2)-DBDCS (3) system in the coaxial microfluidic mixer: the Non-crystalline phase transition*. After the phenomena observed during the phase transitions by solvent displacement and evidences for antisolvent focusing of DBDCS, a phase diagram of 1-2-3 in the coaxial microfluidic mixer will be established. Then, the soluble region, nano-objects, liquid-liquid phase separation, and kinetic characteristics of the coaxial microflow mixer will be carefully described.

Chapter 6 displays the *Part 2 of the Phase diagram of water (1)-1,4-dioxane (2)-DBDCS (3) system in the coaxial microfluidic mixer: the spontaneous crystallisation*. It focuses on the domain where crystals are produced. It inventories the crystal habits of DBDCS and the

FLIM characterisation of spontaneous crystallisation of DBDCS in microflow: the counting and identifying of flowing fluorescent particles (the crystal size, the birth rate, and the growth rate of spontaneous DBDCS crystals). Finally, a schematic summary of the spontaneous phase transition types observed in the coaxial microfluidic system will be given.

Chapter 7 concerns the *Laser-Induce Nucleation in Microfluidics*. The effects of the focused IR laser on the different objects produced in Chapter 5 (flows, nanodroplets, nanoparticles, and droplets) and Chapter 6 (crystal production) are described. A complete schematic summary of the NPLIN working phase diagram will be drawn.

The last **chapter** contains a *general discussion and conclusion* and emphasises the *perspectives* of this work.

Chapter 1. State of art

1.1. Crystallisation from solution	7
1.1.1. Generalities.....	7
1.1.2. Nucleation theories	8
1.2. Non-photochemical laser-induced nucleation (NPLIN)	16
1.2.1. Necessity for control nucleation	16
1.2.2. NPLIN: definition and literature	17
1.2.3. NPLIN: characterisation techniques	21
1.3. Microfluidics	22
1.3.1. Two phases microfluidics	22
1.3.2. Crystallisation in microfluidics	25
1.4. Fluorescence	26
1.4.1. Electronic states.....	26
1.4.2. Jablonski diagram	27
1.4.3. Fluorescence yield	28
1.4.4. Fluorescence lifetime.....	29
1.4.5. Solid state fluorescence	30
1.4.6. Video fluorescence lifetime imaging microscopy (FLIM).....	34
1.5. (2Z,2'Z)-2,2'-(1,4-phenylene)bis(3-(4-butoxyphenyl) acrylonitrile) (DBDCS)	35
1.5.1. Synthesis.....	35
1.5.2. Characterisation.....	36
1.5.3. Photoluminescent properties.....	37

In this chapter, we will describe some generalities on crystallisation in solution and explore the different theories of nucleation, *wiz.* the classical nucleation theory and the two-step nucleation theory (section 1.1). The special aspect of the thermodynamics versus kinetics is given in Appendix A.i. The non-photochemical laser induced nucleation (NPLIN) technique used in this work is described in section 1.2. More information on the papers dealing with NPLIN is given in Appendix A.ii. The original device in which we would induce nucleation, microfluidic devices are presented in section 1.3. Among the experimental techniques for observation crystallisation detailed in Appendix A.iii, the fluorescence method is outlined in section 1.4. Finally, the main target molecule is described in section 1.5 with its literature on lifetimes in Appendix A.iv, while the three other compounds tested in preliminary experiment are given in Appendix A.v.

1.1. Crystallisation from solution

1.1.1. Generalities

Crystallisation is a ubiquitous phenomenon occurring in nature, technology, and even in biology [Sleutel, 2014], with a large number of textbooks dedicated to such a subject, for examples: [Mullin, 2001, Myerson, 2002, Cöelfen, 2008, Bergfors, 2009, Tung, 2009, Andreea, 2012, Lewis, 2015]. In one classic book on this subject, *Nucleation: Basic Theory with Applications* [Kashchiev, 2000], Kashchiev goes beyond the typical examples of (in)organic [Tung, 2009], protein, and colloidal crystallisation and widens the discussion with examples as diverse as volcano eruptions, the initiation of divers' decompression sickness, and the formation of black holes as stated by Sleutel *et al* [Sleutel, 2014]. For example, it can be encountered in our body as our skeletal support is based on crystalline calcium phosphate [Fratzl, 2004]. Osteoporosis is directly connected to crystallisation [Dorozhkin, 2016]. Crystals are present in both healthy (bones) and ailing humans (formation of kidney and gall stones, uric acid crystals in gout, amyloid fibrils and insoluble plaques, the latter been considered the causative agents in some neurodegenerative diseases, such as Alzheimer's disease and Parkinson's disease) [Nanev, 2017a]. Another well-known example is the great toughness of nacre, if compared to

geological crystals [Currey, 1997], which is based on a sophisticated microstructure of the biogenic composite. Crystallisation is the basis of the structure determination of biological macromolecules [Helliwell, 2017]. It is also essential for the manufacture of products as varied as electronic devices [Liu, 2009, Qu, 2016]. In the pharmaceutical context, a recent special issue of *Drug Delivery Today* edited by Douroumis *et al* [Douroumis, 2017] has stated the importance of crystallisation in this area as also reviewed by Gao *et al* [Gao, 2017].

1.1.2. Nucleation theories

1.1.2.1. Classical nucleation theory (CNT)

Nucleation research has a long history spanning over 280 years (Figure 1.1) [Gibbs, 1879, Kathmann, 2005, Sosso, 2016]. To evoke nucleation, the equilibrated system needs to be supersaturated, *i.e.* it is necessary to change the system energetic status [Nanev, 2017b]. Phase transitions, such as crystallisation, freezing, condensation, and bubble formation are almost always dependent on a nucleation event. Nucleation determines the main properties of the crystal population, including the crystal polymorph, the number of crystals, and the size distribution. It is typically described in terms of classical nucleation theory (CNT).

Year	Scientist(s)	Development
1724	Fahrenheit	Studied freezing and phase equilibria to devise his temperature scale and was the first to supercool water.
1795	Lowitz	Observed that supersaturated solutions seeded with crystals of the new phase caused crystallization but that foreign seeds had no effect.
1806	Laplace	Derived the mathematical condition for mechanical equilibrium of a spherical droplet.
1813	Gay-Lussac	Studied how different chemical systems sustain different supersaturations before crystallizing and also found scratching, shaking, or rubbing could induce crystallization.
1848	Pasteur	Discovered enantiomers via crystallization of sodium ammonium tartrate (SAT).
1866	Gernez	Found that pure (L) or (R) SAT seed crystals did not crystallize a liquid of the opposite chirality.
1876	Gibbs	Established the criterion for phase stability and derived the critical free energy of formation.
1875	Coulier	
1880	Aitken	Found that droplet formation from normal air was sensitive to dust, ions, or other impurities.
1897	Wilson	
1886	Helmholtz	Found that droplet formation from a water vapor jet into air was sensitive to dust, ions, and other chemicals.
1896	Ostwald	Proposed the "Law of Stages" which states that a metastable supersaturated state does not spontaneously transform into the most stable state, but to the next state more stable than itself.
1926	Volmer and Weber	Established a kinetic theory of nucleation and recognized that the metastability of the supersaturated state is a matter of kinetics
1927	Farkas	Proposed a detailed kinetic mechanism whereby clusters grow and decay by addition and loss of single monomers and that the critical cluster constitutes the bottleneck for the phase transformation.
1935	Becker and Döring	
1939	Band	Formulated classical nucleation theory
1939	Frenkel	

Figure 1.1. Chronology of scientists and their contributions towards understanding nucleation. (Adapted from [Kathmann, 2005])

The crystal nuclei in metastable liquid grow continuously if they exceed a critical size

limit and are subsequently stabilised. Based on the CNT [Li, 2016a], nucleation is mainly governed by two factors, that are, the interfacial free energy γ_{sL} and the volume Gibbs energy change between the solid and liquid phases $\Delta_s^L G_v$. For a pure liquid,

$$\begin{aligned}\Delta_s^L G_v &= G_v^L - G_v^s \\ &= \frac{\Delta_{\text{melt}} H_v (T_{\text{melt}} - T)}{T_{\text{melt}}} \\ &= \frac{\Delta_{\text{melt}} H_v \Delta T}{T_{\text{melt}}}\end{aligned}\tag{1.1}$$

with G_v^L and G_v^s the volume Gibbs energy of the liquid and the solid phases respectively, $\Delta_{\text{melt}} H_v$ the volume melting enthalpy, T_{melt} the melting point, and $\Delta T \equiv T_{\text{melt}} - T$ the degree supercooling; as for a solute in solution:

$$\begin{aligned}\Delta_s^L G_v &= G_v^L - G_v^s \\ &= \frac{\mu_L - \mu_s}{V_m} \\ &= \frac{RT \ln a_L - RT \ln a_{\text{solid}}}{V_m} \\ &\approx \frac{RT}{V_m} \ln \frac{x}{x_s} \\ &= \frac{RT}{V_m} \ln \beta\end{aligned}\tag{1.2}$$

with μ_L and μ_s the chemical potential of the solute, V_m its molar volume, R the ideal gas constant, a_L and a_{solid} the thermodynamic activity of the liquid and solid solute respectively,

x the amount fraction of the solute in the liquid, x_s its amount fraction solubility, and $\beta \equiv \frac{x}{x_s}$

the supersaturation ratio. Equation (1.1) and (1.2) show that the degree of supercooling is the driving force for the crystallisation of a pure liquid, and the supersaturation ratio for a solution.

The Gibbs energy change of homogeneous nucleation can be expressed as

$$\begin{aligned}\Delta G_N &= -V\Delta_L^s G_v + A\gamma_{sL} \\ &= -\frac{4}{3}\pi r^3 \Delta_L^s G_v + 4\pi r^2 \gamma_{sL}\end{aligned}\quad (1.3)$$

where V is the volume of the nucleus, A its surface area, and r its radius. $\Delta_L^s G_v$ acts to stabilise the nuclei, and the interfacial free energy γ_{sL} works as an energy barrier preventing the formation of the nuclei. The critical radius r^* of nuclei is given by $\frac{d\Delta G_N}{dr} = 0$, as shown on Figure 1.2 (the maximum of the purple curve):

$$r^* = \frac{2\gamma_{sL}}{\Delta_L^s G_v} \quad (1.4)$$

Clusters smaller than r^* is not stable. The attachment of new molecules on a critical nucleus will decrease its free energy. Yet the free energy of a critical nucleus is still higher than monomers. Therefore, energetic fluctuation of the liquid, besides compositional and structural fluctuations, is needed to overcome the barrier. Substitution of equation (1.1) and (1.2) into (1.4) gives the dependence of r^* on the supercooling for pure liquids and on the supersaturation ratio for solutions, respectively:

$$r^* = \frac{2\gamma_{sL}T_{\text{melt}}}{\Delta_{\text{melt}}H_v\Delta T}, \quad (1.5)$$

and

$$r^* = \frac{2\gamma_{sL}V_m}{RT \ln \beta} \quad (1.6)$$

where ΔT and β are controllable parameters. The larger the supercooling or the supersaturation, the smaller the crystal radius is required, hence the easier the nucleation.

The height of the energy barrier of homogeneous nucleation is given by substituting equation (1.4) to equation (1.3):

$$\begin{aligned}
\Delta G_N^* &= -V^* \cdot \Delta_L^s G_v + A^* \cdot \gamma_{sL} \\
&= -\frac{2}{3} \cdot 16\pi \frac{\gamma_{sL}^3}{\Delta_L^s G_v^2} + 16\pi \frac{\gamma_{sL}^3}{\Delta_L^s G_v^2} \\
&= \frac{16}{3} \pi \frac{\gamma_{sL}^3}{\Delta_L^s G_v^2} \\
&= \frac{A^* \cdot \gamma_{sL}}{3}
\end{aligned} \tag{1.7}$$

with * denoting for properties of critical nuclei. Equation (1.7) shows that for a critical nucleus, the decrease of volume free energy only compensates two third the increase of interfacial free energy. The local energetic fluctuation must be larger than one third the interfacial free energy to overcome the homogeneous nucleation energy barrier.

Homogeneous nucleation was once thought impossible, as foreign impurities in the liquid can catalyse nucleation. If the contact angle of the embryo, say a spherical cap, on a flat catalytic surface in the liquid is θ , the heterogeneous nucleation energy barrier is reduced to

$$\Delta G_{N,het}^* = \frac{(2 + \cos \theta)(1 - \cos \theta)^2}{4} \Delta G_N^* \tag{1.8}$$

If $\theta = \pi$, the solid does not interact with the substrate, homogeneous nucleation will occur away from the impurity. If $\theta = 0$, the solid completely wet the catalyst, and $\Delta G_{N,het}^* = 0$. This means the catalytical impurity has coherent crystalline structure as the crystal, and epitaxial growth of the crystal will start directly on the interface. For $0 < \theta < \pi$, $\Delta G_{N,het}^* < \Delta G_N^*$, although the critical radius for the spherical nucleus is the same as for homogeneous nucleation, the number of molecules in a critical nucleus and the energy barrier is reduced. If the catalytic impurities have hollow surfaces, the reduction can be greater. Therefore, depending upon the shape and the wetting properties of the interface between the solid impurity and the liquid phase, the heterogeneous nucleation energy barrier $\Delta G_{N,het}^*$ can be much smaller than homogeneous nucleation, as shown in Figure 1.2.

If the supercooling or the supersaturation is high enough to reach the spinodal

decomposition limit. The second derivative of the free energy of the system in terms of composition is negative. Any compositional fluctuation will lead to a reduction of free energy. Uphill diffusion towards segregation of a cloud of small droplets will occur, as depicted in Figure 1.2.

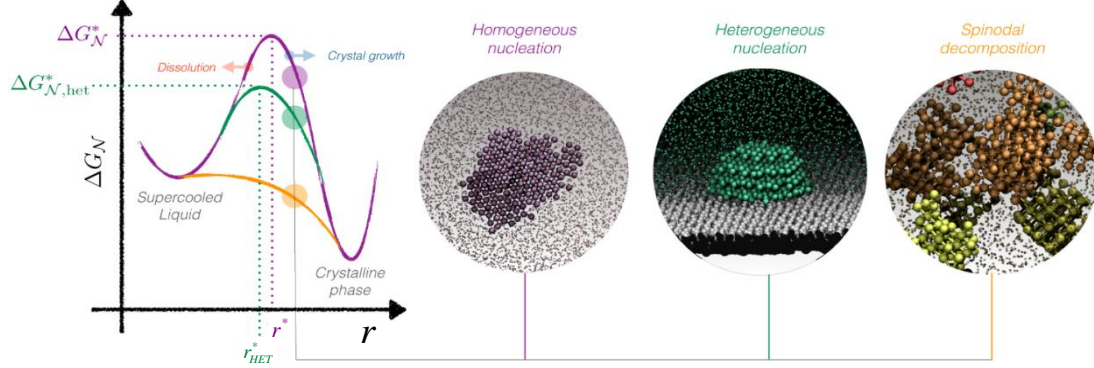


Figure 1.2. Sketch of the Gibbs energy gain ΔG_N as a function of the crystalline nucleus size r , in the cases of homogeneous nucleation (purple), heterogeneous nucleation (green), and spinodal decomposition (orange), with the corresponding energy barriers ΔG_N^* and critical radii r^* . The three snapshots depict the nucleating clusters for each scenario. (Adapted from [Sosso, 2016])

Substitution of equation (1.1) and (1.2) into (1.7) gives

$$\Delta G_N^* = \frac{16}{3} \pi \frac{\gamma_{sL}^3 T_{\text{melt}}^2}{\Delta_{\text{melt}} H_v^2 \Delta T^2} \quad (1.9)$$

and

$$\Delta G_N^* = \frac{16}{3} \pi \frac{\gamma_{sL}^3 V_m^2}{R^2 T^2 \ln^2 \beta} \quad (1.10)$$

for pure liquid and solute in solution, respectively. The nucleation energy barrier decreases with the supercooling ΔT or supersaturation ratio β . These are the controllable parameters. The CNT points out, at given ΔT or β , a ordered cluster must be larger than r^* and be in the locally high energy fluctuation to become a stable nucleus.

Nucleation rate is the number of stable nuclei formed *per* unit time in a unit volume. The nucleation rate of homogeneous nucleation N_s depends upon two factors: the number of clusters larger than r^* *per* unit volume N^* and the number of molecules attached to a nucleus *per* unit time f_o :

$$N_s = N^* f_o \quad (1.11)$$

where N^* can be estimated as the number of molecule groups with an activation energy of ΔG_N^* using the Arrhenius equation:

$$N^* = N_A \cdot c \cdot \exp\left(-\frac{\Delta G_N^*}{k_B T}\right) \quad (1.12)$$

where N_A is the Avogadro number, c the amount concentration, k_B the Boltzmann constant. f_o is related with number of molecules s close to the surface of the nucleus, the vibration frequency of the liquid molecule ν , the diffusion activation energy Q_A , and its probability to be accepted by the nucleus p :

$$f_o = s \cdot \nu \cdot p \cdot \exp\left(-\frac{Q_A}{k_B T}\right) \quad (1.13)$$

Thus, the homogeneous nucleation rate can be expressed as

$$N_s = N_A \cdot c \cdot s \cdot \nu \cdot p \cdot \exp\left(-\frac{Q_A}{k_B T}\right) \cdot \exp\left(-\frac{\Delta G_N^*}{k_B T}\right) \quad (1.14)$$

For a pure liquid, c and s can be treated as constants. Whereas for a solute in a solution, its concentration is a controllable parameter. Neglecting the change in the surface area of the nuclei, the spontaneous nucleation rate of solute crystals from solutions can be written as

$$N_s = K_N \cdot c^2 \cdot \exp\left(-\frac{1}{\ln^2 \beta}\right) \quad (1.15)$$

where K_N is a nucleation rate constant.

1.1.2.2. Two-step nucleation theory (TST)

The CNT has purposely avoided the difficulties in the determination of the structure of the nuclei by assuming the precursor has already the same crystalline structure of the bulk crystal. More and more evidences, including simulation evidences [Gavezzotti, 1999, Soga, 1999, Shore, 2000, Nicolis, 2003], theoretical evidences [Haas, 2000, Pan, 2005, Lutsko, 2006], and experimental evidences [Galkin, 2002, Vekilov, 2004, Filobelo, 2005] are showing the other way around. Hence, the two-step nucleation theory (TST) was proposed [ten Wolde, 1997]. According to the TST, crystallisation occurs in two distinct sequential steps. The first step is the formation of a local region where the solute concentration significantly exceeds the average, but the solute particles stay disordered as in a liquid. Depending on the particular solution, this locally concentrated region can be a solute “droplet”, a metastable disordered solute “cluster”, or simply a relatively strong concentration fluctuation. The second step is the development of spatial order (a crystal nucleus) within the local region of high concentration. Gebauer *et al* [Gebauer, 2014] have concluded that the pre-nucleation clusters (PNCs) comprise five major characteristics: i) PNCs are composed of the constituent atoms, molecules, or ions of a forming solid, but can also contain additional chemical species. ii) PNCs are small, thermodynamically stable solutes, and there is thus formally no phase boundary between the clusters and the surrounding solution. iii) PNCs are molecular precursors to the phase nucleating from solution, and hence participate in the process of phase separation. iv) PNCs are highly dynamic entities and change configuration on timescales typical for molecular rearrangements in solution, *i.e.* within hundreds of picoseconds. v) PNCs can have encoded structural motifs resembling, or relating to, one of the corresponding crystalline polymorphs. (Figure 1.3)

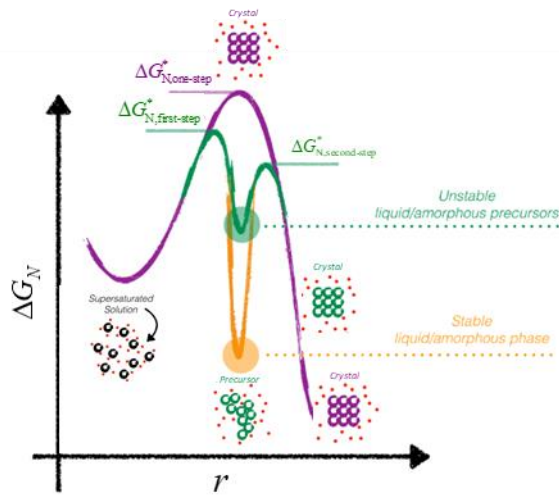


Figure 1.3. Schematic comparison of the Gibbs energy gain ΔG_N and the structural change in terms of the cluster size r of one-step (purple) versus two-step (green for unstable precursor and orange for stable precursor) nucleation for a generic supersaturated solution. (Adapted from [Sosso, 2016])

In Figure 1.3, the one-step mechanism predicted by CNT (purple) is characterised by a single free energy barrier, $\Delta G_{N,one-step}^*$. In contrast, the two-step nucleation requires a free energy barrier, $\Delta G_{N,first-step}^*$, to be overcome through a local density fluctuation of the solution, leading to a dense, but not crystalline-like, precursor. The latter can be unstable (green) or stable (orange) with respect to the liquid phase, being characterised by a higher (green) or lower (orange) free energy basin. Once this dense precursor has been obtained, the second step consists of climbing a second free energy barrier, $\Delta G_{N,second-step}^*$, corresponding to the ordering of the solute molecules within the precursor from a disordered state to the crystalline phase.

The TST mechanisms are now reasonably well established for some proteins [Chevreuil, 2018], and other macromolecular solutes [Vekilov, 2010]. Experimental evidence obtained for several systems also suggests that the first step is relatively fast, and that the second step (spatial ordering) is rate determining [Vekilov, 2011].

1.1.2.3. Aggregational nucleation

A third model has been proposed and observed that differs from both the CNT and TST by the size of the building blocks that gather into a crystal. The classical views, from both CNT and TST, consider the distinct stages of crystallisation to proceed via attachment of monomers, which (depending on the crystal) can be atoms, ions, or molecules. This third model assumes that nanoparticles as building blocks, can aggregate to form mesoscopically structured crystals, abbreviated mesocrystals [Gebauer, 2011]. A recent Faraday discussion has been dedicated to *Nucleation - A Transition State to the Directed Assembly of Materials* leading to three very interesting discussions on the papers included in this issue which give an actual state of art of the different mechanisms [Price, 2015a, Price, 2015b, Zanni, 2015]. More detailed explanations can be found in the paper of Erdemir *et al* [Erdemir, 2009], Vekilov *et al* [Vekilov, 2010], and Sauter *et al* [Sauter, 2015]. Finally, a very complete review on nucleation mechanisms has recently been written by Zhang *et al* [Zhang, 2017a].

1.2. Non-photochemical laser-induced nucleation (NPLIN)

1.2.1. Necessity for control nucleation

Firstly, in the process of forming a solid phase from a supersaturated solution, nucleation is the key step governing the timescale of the transition. Secondly, controlling nucleation is an essential aspect in many crystallisation processes, where distinct crystal polymorphism, size, morphology, and other characteristics are required [Smeets, 2017].

The experimental difficulties in the visualisation of the structure of the critical clusters can be grouped into three categories: i) the constituent atoms or molecules are so small that even if the clusters are detected, their structures cannot be discerned by most microscopic techniques; ii) the PNCs exist for extremely short times after which they either grow to macroscopic crystals or decay; iii) the PNCs are relatively small, and due to Brownian diffusion, they freely move throughout the available volume of the mother phase [Yau, 2001]. Because nucleation is of a stochastic nature, it is necessary to perform a large number of experiments to obtain reliable data [Hammadi, 2015]. These three aspects (necessity of spatial and temporal

nucleation control, difficulties of visualisation, stochastic nature of nucleation) imply that original crystallisation method needs to be developed. Different routes can be followed. Maeki *et al* [Maeki, 2012] have presented an approach for single crystallisation of protein by using droplet-based microfluidics. That approach has been extensively developed by Veessler group [Hammadi, 2015]. They have also use an external electric field to induce nucleation at a desired place [Hammadi, 2009b]. Xue *et al* have shown how nucleating sites number can be controlled in the nanoscale system by chemical etching and the heterogeneous nucleating behaviour presented by the branching growth of nanorods [Xue, 2010].

1.2.2. NPLIN: definition and literature

Hence 1996, Garetz *et al* [Garetz, 1996] has discovered accidentally that a laser can induce nucleation of urea in supersaturated solution. Later on, different groups have explored the nucleation induced by laser. Laser-induced nucleation appears with small organic compounds, inorganic species, or protein macromolecules in supersaturated solutions. This phenomenon was initially called Non-Photochemical Laser-Induced Nucleation (NPLIN), according to the fact that the mechanism stated by Garetz *et al* seems not to involve any photochemical reactions. The laser used was a pulsed nanosecond laser. In 2003, Adachi *et al* [Hiroaki, 2003] used a pulsed femtosecond laser to trigger nucleation of different proteins at the focal point and some years later Sugiyama *et al* [Sugiyama, 2007] has used a continue wavelength (CW) laser for inducing crystallisation of glycine in heavy water. For our best knowledge, until now more than seventy papers (Figure 1.5 and Appendix A.ii) have been dedicated to this subject if we consider that an NPLIN experiment (Figure 1.5) consists in the crystallisation of a specie (small organic molecule, inorganic, and protein) induced by a laser (pulsed or CW, at a pico-, femto-, or nano- second frequency) without any hypothesis upon the mechanism (laser trapping, photon pressure, cavitation, Kerr effect...). The abbreviation NPLIN was extended firstly by Clair *et al* [Clair, 2014] to all laser-induced nucleation from solution without seeding. This extension of the initial NPLIN seems to be accepted now (Figure 1.5 and Figure 1.6). Some key figures of the 54 NPLIN papers published until now (see

Appendix A.ii) are given in Figure 1.7. All these NPLIN experiments have demonstrated that laser induces nucleation (or at least when the laser is turned off) whereas the control solution remains in the metastable state.

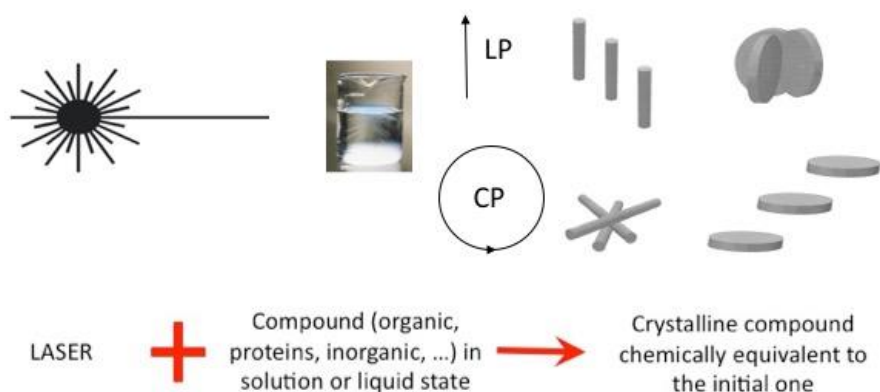


Figure 1.4. Schematic definition of NPLIN used in this manuscript.

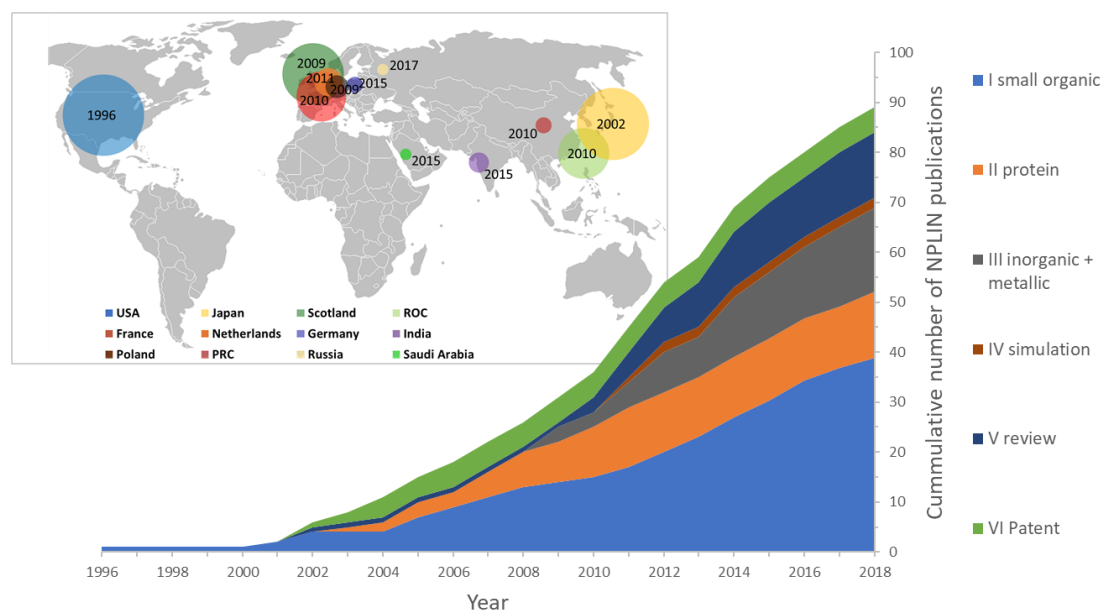


Figure 1.5. Growth of the papers on NPLIN according to our extended definition. The first three groups (I to III) concern papers where new experiments are reported; IV corresponds to paper presenting only simulation of NPLIN mechanism; V corresponds to review or vulgarisation papers; and VI patents. In the insert, the countries where the experimental research have been done. The size of the bullet

corresponds to the number of publications (I to V). The date corresponds to the first paper published in the country. The full list of publications is in Appendix A.ii.

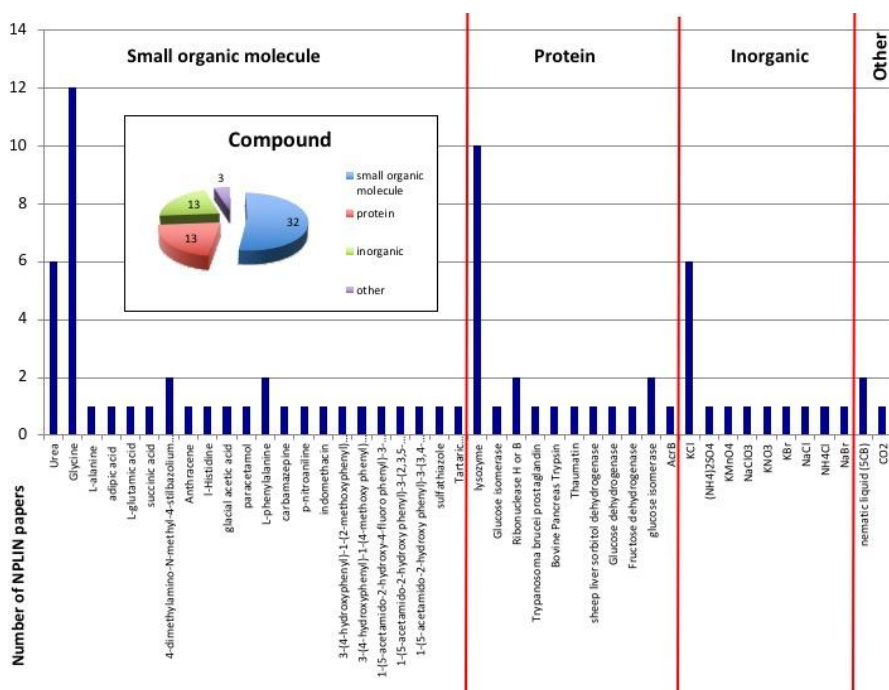


Figure 1.6. Distribution of NPLIN papers according to the compounds studied.

A precise spatial control of the nucleation can be obtained through NPLIN experiments when the laser is focused through a microscope lens; that concerns half of the reported experiments. (Figure 1.7.b). Different wavelengths have been used from 260 nm to 1064 nm (Figure 1.7.d). It has been demonstrated by Garetz group that the wavelength has no influence on the nucleation efficiency for an equal energy density.

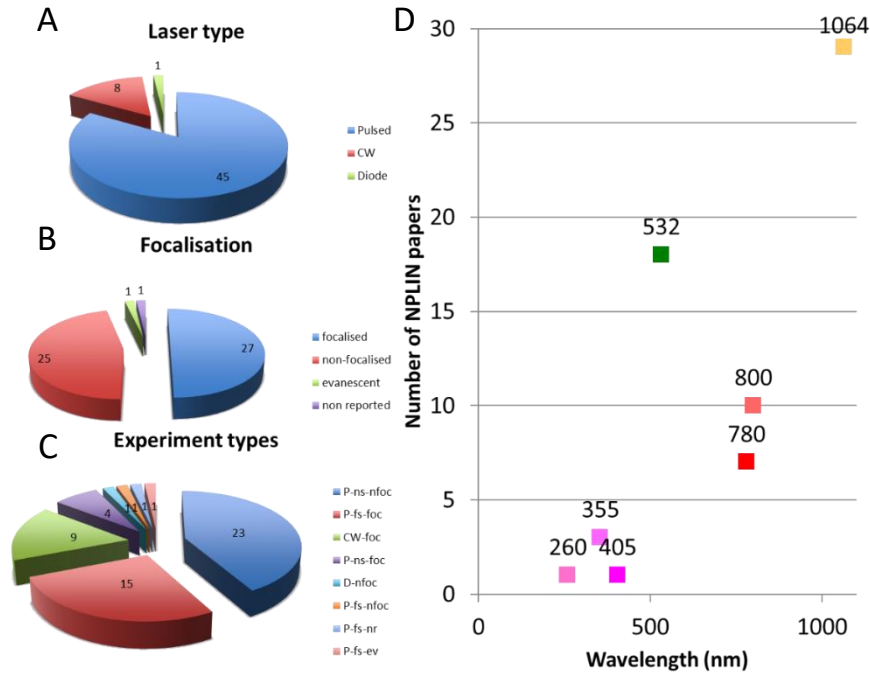


Figure 1.7. Some key-figures of NPLIN setups. A: laser type (*Pulsed (P)*, *continuous waves (CW)*, *laser diode (D)*). B: focalisation (*focalised (foc)*; *non-focalised (non-foc)*; *evanescent (ev)*; *non-reported (nr)*). C: combination of the laser type, the pulse duration *femtosecond (fs)* or *nanosecond (ns)* and the focalisation type; D: wavelength (nm). A paper could be counted more than one time.

The experimental sample holders are categorised in four groups depending on the volume of the sample-holder: 1 – 10 pL (as referred to as **1**), 2 – 500 μ L (as referred to as **2** to **7**), 1 – 10 mL (as referred to as **8** to **14**) and > 500 ml (as referred to as **15**). The sample-holder **16** corresponds to the one developed in this thesis. Sample-holder **1** to **15** corresponds to static NPLIN experiments. All these sample-holder are presented in Figure 1.8.

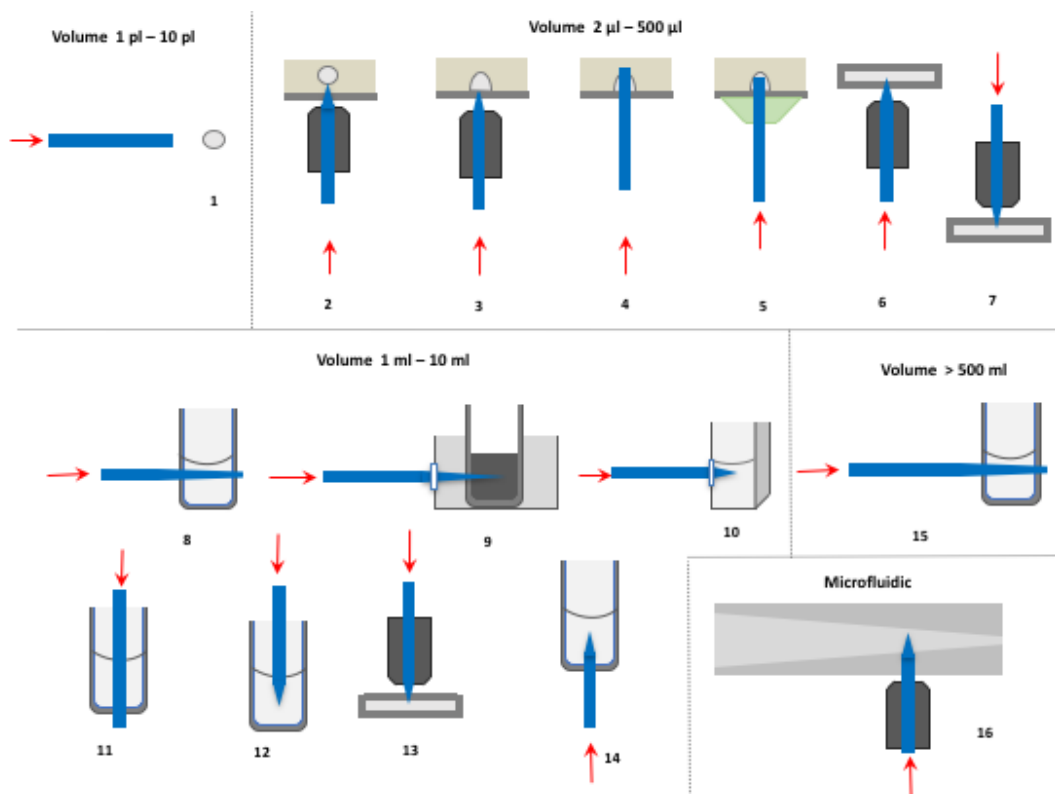


Figure 1.8. Schematic representation of NPLIN sample-holders. The blue line represents the beam whatever the wavelength is. The red arrow the direction of the beam. Shape of the beam indicate if the focused or not. The objective figures in dark.

The bibliographic review of the NPLIN experiments has led to attribute to our NPLIN definition (those stated in Figure 1.4) to 54 experimental papers. The characterisation of these experiments is summarised in Table Appen.A.1 and Table Appen.A.2. A list of NPLIN modelling papers is given in Table Appen.A.3, while the list of review papers is given in Table Appen.A.4.

1.2.3. NPLIN: characterisation techniques

In NPLIN experiments or in crystallisation inside droplets in microfluidic devices, there is still a bottle-neck of observation time. Due to the reasons exposed above the early stage of the nucleation cannot be directly observed, and only hypothesis can be indirectly stated. Only real-time *in situ* observations can provide new insight in understanding nucleation mechanism. Such techniques are rare. Fluorescence spectrometry represents one of the best methods, taking

into account that for some compounds, monomers, dimmers, tetramers, and later on polymorphs can have different fingerprints in the fluorescence spectra. For example, Ye *et al* [Ye, 2015] based on a novel organic chromophore with morphology-dependent fluorescence and judicious design of the observation procedure, has demonstrated the *in situ* and direct observation of the crystallisation process of molecular microparticles. Profiting from the response of the self-fluorescence, the appearance and the interface evolution of the forming crystalline phase inside the particle can be clearly observed. This study presents a realistic picture of the microscopic kinetics of a solid-solid transition. Two papers on NPLIN have already used fluorescence as observation technique [Yoshikawa, 2009, Murai, 2010] on a F-lysozyme protein leading to a demonstration the cavitation mechanism.

1.3. Microfluidics

Microfluidics allow manipulation of very small volume of liquid. This is useful when the reactant is rare or expensive. Microfluidic was popularised by George Whitesides in 1988 in a paper where he describes the production of microdevice from the photolithography of SU8 resins and the moulding of polydimethylsiloxane (PDMS) polymer [Beer, 2008]. But a limitation of PDMS is the swelling by organic solvents and its affinity for hydrophobic dyes. For the formation of droplets, David Weitz laboratory has developed an all glass microfluidic with a self-centring inner capillary using cylindrical and square tubes [Utada, 2005].

1.3.1. Two phases microfluidics

Two phase microfluidics started in the 2002, it has become a leading domain in that field [Anna, 2003]. The formation of droplets of regular sizes of water in perfluorinated oil became the main trend. Each drop is a micro reactor, it is well stirred with a well-defined composition, and can be addressed individually. The crystallisation is confined in the droplets, thus preventing heterogeneous crystallisation on the walls and impurities [Shang, 2017].

The formation process of droplets from two immiscible liquids have been theorised [Guillot, 2007]. It is known since Plateau and Rayleigh that a liquid with a cylindrical shape is

unstable and does break up into droplets. Their major result is that non-viscous cylindrical jets in air are unstable to disturbances of their surface whose wavelength is larger than the jet circumference. According to Guillot *et al* [Guillot, 2007], these surface oscillations can propagate up stream, and after a transient state a permanent regime of drop formation at the nozzle is observed. But at higher flow rates, a cylindrical jet is observed before it breaks into drops. Guillot *et al* have further included in the theory the confinement of the jet into a microfluidic device. The phase diagram of the droplet/jet domains can be predicted.

Since 1990s, a large amount of research effort has been devoted to the microfluidic synthesis of nanoparticles [Ma, 2017]. The market is that of injected drugs. According to Xu *et al* [Xu, 2017] the particle produced by microfluidics are more narrow-size-dispersed than those produced by conventional methods. This allows a steadier release of the active ingredient. Surfactant methods can produce uniformly-sized particles smaller than 800 nm in diameter. Physical methods such as mechanical agitation, high pressure nozzle, microfluidic shearing, and co-flowing produce particles from 10 μ m and larger. Thus, there is a domain around 1 μ m that is a frontier for both approaches. This micrometric size is the one required for intravenous injections. Recently, the co-flow of two miscible solvents has start to gain theoretical interest.

By using miscible solvents in a droplet formation device, it is expected that after the formation of the size monodispersed droplets, the miscible solvent will leave the droplet with a smaller particle. Dripping and jetting of the two miscible liquids are seen. A phase diagram is qualitatively observed even if the surface tension between two miscible phases is difficult to measure.

But in the case of poly-caprolactone ($M = 45,000$ g/mol) dissolved in a mixture of dichloromethane and acetone, the particle formed are big, hollow shells. Precipitation occurs at the surface before full evaporation [Xu, 2017]. In the case of Poly(D,L-lactide-co-glycolide) ($M = 4000 \sim 5000$ g/mol) dissolved in a mixture of dichloromethane-DMSO, nanoparticles formed are smaller than those expected from the drying of the droplets. Xu *et al* assume that

numerous size monodispersed particles are formed inside each drop.

A noticeable exception to the difficulty to produce micrometre sized particles is the Ouzo precipitation that produces an emulsion of anethol by mixing two miscible solvents water and ethanol. These emulsions are size monodisperse and have a typical diameter of 1 μm [Sitnikova, 2005]. Different models have been proposed to explain the size monodispersity of the particles produced the variation of this size with the mixing conditions. All authors agree that the two solvents mix, leaving the solute in a supersaturated state. According to Brick *et al* [Brick, 2003] a spinodal decomposition of the ternary mixture occurs, whereas Vitale *et al* [Vitale, 2003] as well as Aubry *et al* [Aubry, 2009] assume a nucleation and growth of the liquid phase since, based on the overall composition of the mixture, the Ouzo effect does not occur in a region where the spinodal decomposition could occur.

Hajian *et al* [Hajian, 2015] had a better observation of the Ouzo effect by using microfluidics. They studied the injection of ethanol loaded with divinylbenzene into water. They observed the presence of a tube of droplets sticking around the centre of the flow. They postulated that the droplets are made by the nucleation of divinylbenzene in a water rich phase. They estimated that this annulus is not a due to the inertial focusing [Segré, 1961] since a flow of the particles towards the centre is observed. They supposed that the droplets of divinylbenzene formed in the water phase migrate back to the flow centre because of a Marangoni effect.

These droplets move in a region of the flow with a strong gradient of composition, rich in ethanol at the centre rich in water at the periphery [Balasubramaniam, 2000]. The divinyl benzene (DVP) drop has a higher surface energy in water than in ethanol. Thus, it tends to move towards the centre of the flow that minimises the surface energy. But the tube of droplets is hallowed since when the droplets reach the ethanol at centre flow, they can re-dissolve. As the ethanol diffuses away the droplets move close to the centre until the gradient disappears. The Marangoni displacement leads to the focusing of the DVB droplets at the flow centre [Hajian, 2015].

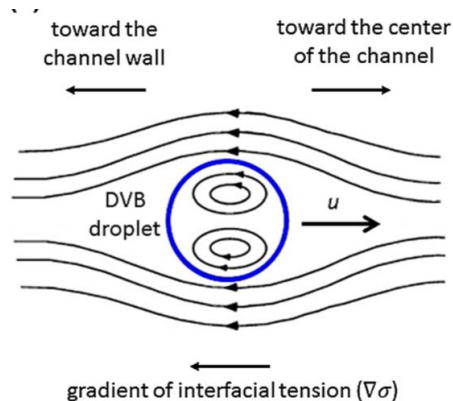


Figure 1.9. The movement of the flow around a drop of DVB in a gradient of water (channel wall) and ethanol (channel centre). (Adapted from [Hajian, 2015])

1.3.2. Crystallisation in microfluidics

Microfluidic system is used in chemistry and biotechnology fields [Haeberle, 2007, Ohno, 2008, Yamaguchi, 2013]. A continuous low in microchannels can be used to create a well-defined and predictable interfacial region among streams. Recently, droplet-based microfluidic systems are studied as an interesting platform [Song, 2006, Leng, 2009, Theberge, 2010, Casadevall i Solvas, 2011]. In contrast to a continuous flow system, droplet system provides isolated microscale reaction chambers, leading to both rapid mixing and low dispersion of the reactants [Song, 2006, Casadevall i Solvas, 2011]. Moreover, a reduced sample volume (nanolitre range) can be useful for high throughput screening systems. Due to these interesting features, many applications using droplet-based microfluidics have been reported, including enzyme assay [Roach, 2005, Han, 2009], chemical and biochemical screening [Chen, 2006], PCR reaction [Beer, 2008, Schaerli, 2009], and cell assay [He, 2005]. In a recent review, Shi *et al* [Shi, 2017a] has described the different geometry used in microfluidic devices, which can be divided into four main categories: continuous flow microfluidics, droplet-based microfluidics, valve-based microfluidics, and digital microfluidics. We have recently optimised a microfluidic platform as described by Tran *et al* [Tran, 2016].

A variety of methods including microfluidics have also been applied to separate nucleation and crystal growth. Microfluidics-based platform has already been reported as a

convenient tool to explore protein crystallisation conditions [Li, 2010]. Furthermore, another application for protein crystallisation, such as *in situ* X-ray diffraction measurement, decoupling of crystal nucleation and growth, and membrane protein crystallisation have been reported [Hansen, 2006, Talreja, 2010].

1.4. Fluorescence

1.4.1. Electronic states

Fluorescence is a manifestation of the quantum nature of materials. It relies on the existence of distinct energy states. The absorption of a photon promotes the molecule to an excited state. Among other pathways, the excited state can return to the ground state by the emission of a second photon. The states can be described by the way electrons are distributed among orbitals. In the ground state, all the electrons are distributed between the orbital with the lowest energy (Figure 1.10).

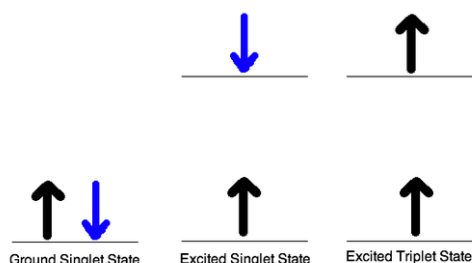


Figure 1.10. Schematic representation of the electron in the ground or excited state.

For the same distribution of electrons among orbitals, different organisation of the electron's spin is possible. For most systems, two cases are possible: singlet and triplet. Due to a quantum effect, the exchange interaction, the triplet will have a smaller energy than the singlet. This singlet-triplet splitting will be smaller if the two electrons have less orbitals in common. The singlet and triplet states will have different energies in the case of small molecules. Whereas for conjugated polymers, twisted molecules, and semi-conductors, the singlet and triplet states have similar energies. Thus, the molecular energy diagram describes well the excited states of systems with wide orbitals (Figure 1.11). The different energy levels of an

excited material are represented in the case of atoms, molecules, and semi-conductors. In Atoms, the same distribution of electrons in excited orbital will provide different energy of the excited states depending on the spin organisation of the electrons. This is not the case for semi-conductors where the energy of the exchange interaction can be neglected.

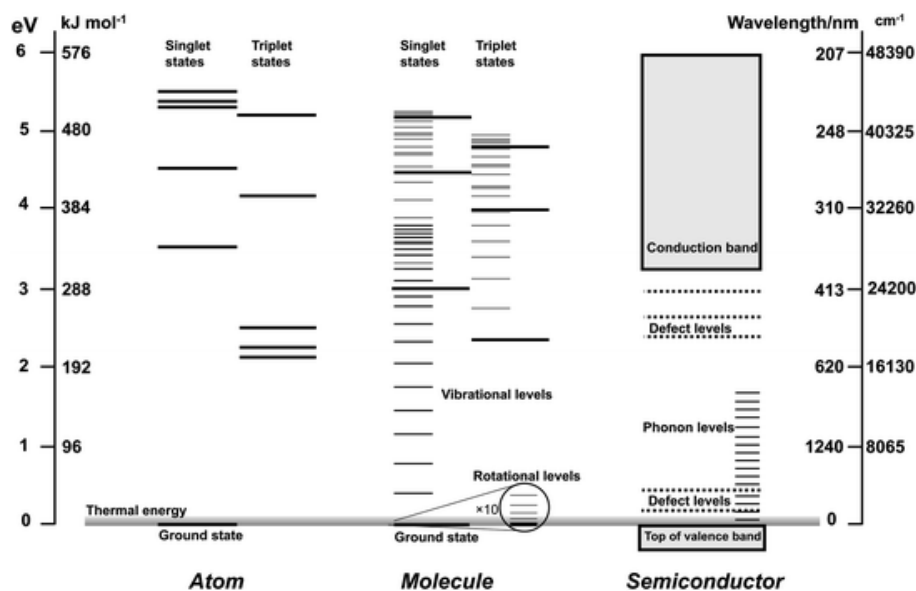


Figure 1.11. Schematic energy levels in atoms, molecules, and semiconductors. The atom has only electronic energy levels (long dark lines). The molecule has: electronic levels (long dark lines); vibrational levels (shorter lines); and rotational levels (magnification $\times 10$). The semiconductor has: valence and conduction bands, intermediate ‘defect’ energy levels, and phonon energy levels, which correspond to a wide variety of low energy and high energy lattice vibrations. Thermal energy at room temperature is shown by the horizontal graded grey band. (Adapted from [Douglas, 2013])

1.4.2. Jablonski diagram

The different exchange (deactivation) pathways between the excited states of a small molecule are summarised in the Jablonski (Perrin) diagram. Electronic levels are represented by heavy lines. Absorption spectra are composed of a few massifs corresponding to $S_0 \rightarrow S_1$,

$S_0 \rightarrow S_2$, $S_0 \rightarrow S_3$. After absorption, the dissipation of the energy passes through the vibrational relaxation (vr) and the internal conversion (IC) within a few picoseconds. The IC can be described as a coupling between the state $S_{n,v=0}$ and $S_{n-1,v=m}$ (S_n stands for electronic energy level and $v = m$ for vibrational level). The rate of IC decreases with m . Due to a larger energy gap from the S_0 state, S_1 state can trap the excitation for a few nanoseconds. There is enough time for fluorescence to occur. The fast relaxation towards the S_1 state simplifies the photophysics and explains that the photophysics and the photochemistry generally does not depend on the excitation wavelength. The fluorescence spectrum is composed of a single massif.

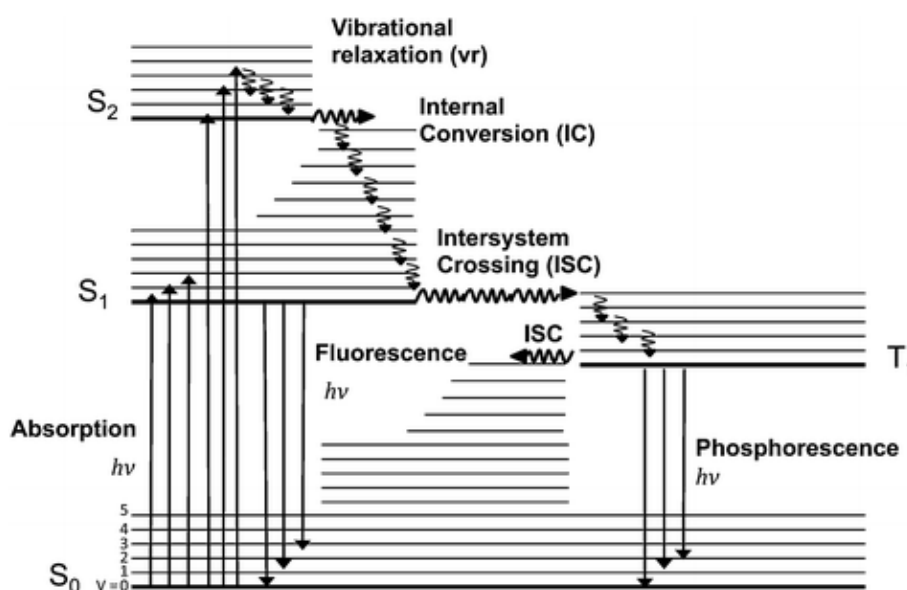


Figure 1.12. Simple Jablonski diagram illustrating the primary deactivation processes occurring upon excitation. Electronic levels are represented by heavy lines.

(Adapted from [Douglas, 2013])

1.4.3. Fluorescence yield

From the first excited state, different processes are possible, such as fluorescence, internal conversion, intersystem crossing, and isomerisation (ISOM) with their corresponding rate constants: k_F , k_{IC} , k_{ISC} and k_{ISOM} .

The fluorescence quantum yield is the probability that a photon is emitted after the

absorption of a photon. It is given by the ratio of the fluorescence rate constant and the sum of all the competing rate constants:

$$\begin{aligned}\Phi_F &= \frac{N_{em}}{N_{ab}} \\ &= \frac{k_F}{k_F + k_{IC} + k_{ISC} + k_{ISOM}} \\ &= \frac{k_F}{\sum k}\end{aligned}\tag{1.16}$$

where N_{em} is the number of photons emitted, and N_{ab} the number of photons absorbed.

1.4.4. Fluorescence lifetime

After excitation by a short laser pulse, the rate at which a population of excited states disappears is the sum of all the deactivation rates:

$$\frac{d[S_1]_t}{dt} = -[S_1]_t \cdot \sum k\tag{1.17}$$

where $[S_1]_t$ is the concentration of excited state molecules at time t . Equation (1.17) predicts an exponential decay

$$[S_1]_t = [S_1]_0 \cdot \exp(-\sum kt)\tag{1.18}$$

with a deactivation constant $\sum k$. Both radiative and non-radiative processes can depopulate the excited state. The fluorescence will decay at the rate by which the excited population deactivates. Therefore, instead of $\frac{1}{k_F}$, the fluorescence lifetime refers to the average time by

which the molecule stays in its excited state before emitting a photon:

$$\tau_F = \frac{1}{\sum k}\tag{1.19}$$

It is not a measure of the fluorescence decay rate constant, but the sum of all radiative and non-radiative deactivation rate rates. A measure of the k_F can be done from the measurement of the

total deactivation rate constant $\sum k$ (equation (1.17)) and the fluorescence quantum yield Φ_F (equation (1.16)).

1.4.5. Solid state fluorescence

In solids, the fluorescent molecules are closely packed. Thus, excited molecules can interact with molecules that have an excited state with a similar energy. This favours the coupling between the excited molecules and the neighbours, which leads to a diffusion of the excitation, a delocalisation of the excitation or a trapping. The coupling can be through the dipole/dipole interaction or the exchange interaction.

1.4.5.1. Förster resonant energy transfer

The Förster resonant energy transfer (FRET) is the coupling of an excited molecule with a neighbour through dipoles. In a classical model, an excited state is produced by the interaction of an electromagnetic wave with a ground state. The excited state is an oscillating dipole. This oscillating dipole behaves as an antenna, emitting a local electric field and exciting in turn the neighbouring molecules. From the classical model, the quantum theory keeps the distance dependence of the effect and the angular dependence. The rate of the energy transfer k_{FRET} between a donor and an acceptor at distance r is given by:[Fleming, 1986]

$$k_{\text{FRET}} = k_F \left(\frac{r}{r_{\text{FRET}}} \right)^6 \quad (1.20)$$

and

$$R_{\text{FRET}}^6 = \frac{9000 \ln 10}{128 \pi^5 N_A} \frac{\kappa^2 \Phi_F}{n_D^4} \int \frac{I_F(\bar{\nu})}{\int I_F(\bar{\nu}) d\bar{\nu}} \frac{\varepsilon_A(\bar{\nu})}{\bar{\nu}^4} d\bar{\nu} \quad (1.21)$$

where Φ_F is the fluorescence quantum yield of the donor, κ^2 the dipole orientation factor, n_D the refractive index of the medium, I_F the fluorescence intensity of the donor, $\bar{\nu}$ the frequency in cm^{-1} , and ε_A the acceptor molar extinction coefficient in $1 \cdot \text{mol}^{-1} \cdot \text{cm}^{-1}$.

In a sample composed of identical molecules, the FRET will result in a diffusion of the excitation among neighbouring molecules. If the solid contains defects or impurities, these impurities can capture the excitation and dissipate it. This leads to a quenching of the fluorescence.

From the distance dependence of the FRET rate constant, we can deduce that the transfer to remote acceptor will be slower than the transfer towards a close acceptor. Compared to liquids, the quenching in solids depends not only on the concentration of quenchers but on their distribution around excited molecules.

1.4.5.2. Frenkel exciton

If the coupling between the excited molecule and its neighbours is stronger, the energy of the excited state starts to change, and a broadening of the excited states energy is observed. If N molecules are involved in the coupling, N excited states are calculated. Their energy spread over $\pm 2\left(1 - \frac{1}{N}\right)J$ around the original energy [McRae, 1958]. Depending on the sign of the coupling term J , the lowest state in energy can be an allowed transition (J aggregates) or a forbidden transition (H aggregates). In the case of a J aggregate, the fluorescent rate k_F of the lowest excited state (the one responsible for the emission) will be accelerated by \sqrt{N} . Thus, the formation of a J aggregates will increase the fluorescence rate and the fluorescence yield. Infinite fluorescent rates are predicted, but at room temperature disorder tends to trap the delocalisation on a smaller number of molecules [Lemaistre, 2004]. These calculations can be extended to real 3D crystals [Liao, 2018].

To the opposite of the fully or partially delocalised model, in some cases the excited state, because of its new dipole moment and the acidity or basicity of its orbitals, can interact with its surroundings. The exciton or an excited dimer can be stabilised and trapped by its neighbourhood. The full quantum mechanics calculation has been done in the case of difluoroboron- β -diketones [Wilbraham, 2018]. This family of molecules forms often

fluorescent molecular solids. The emission is broad, with a good yield and a long fluorescence lifetime.

1.4.5.3. Fluorescence decays in solid state: Perrin model

In solid state, the fluorescence decay is seldomly exponential. Most of the time, this is attributed to the heterogeneity of the solid sample. This heterogeneity has many origins. For an amorphous sample, a random environment will surround each emissive molecule. This environment can influence k_F , and a distribution of k_F can be extracted from the multiexponential decay. Solid samples contain point defects, dislocations, and grain boundaries. These defects are not fluorescent and will dissipate the excitation. By the FRET their neighbours will transfer their energy at a rate that depends on the distance to the defect. This again will create a multiexponential decay.

This has been theorised by Grözel [Millar, 1981] and by us [Hartmann, 2012].

$$\ln\left(\frac{[S]}{[S]_0}\right) = -k_F t - [Q_0] \int_0^t k_Q(u) du \quad (1.22)$$

where k_Q is the quenching rate constant.

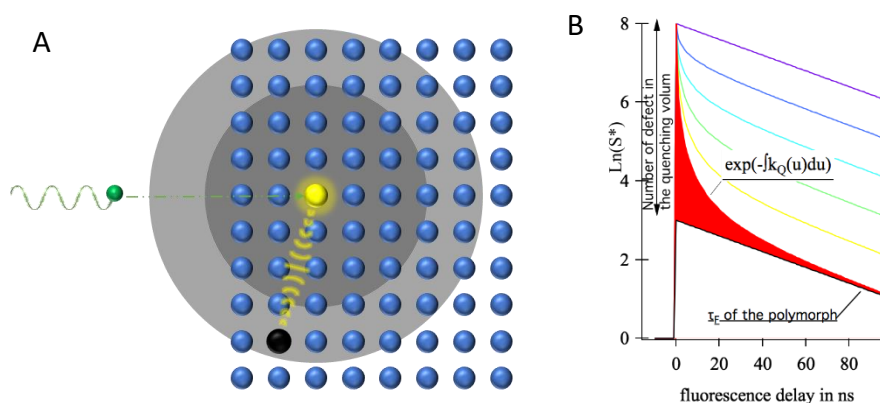


Figure 1.13. Effect of defects in a fluorescent crystal. A: 2-D organisation of the molecules in a fluorescent crystal containing a defect with a short range (1 nm) distance dependent perturbation. The green ball represents an excitation photon. The yellow ball is an excited molecule in the fluorescent crystal. The black ball represents

a defect in a short range of the exciton. Depending on the distance, the defect can quench the fluorescence. B: a typical fluorescence decay of a slightly defective fluorescent crystal (Adapted from [Hartmann, 2012]). The long-life component with an exponential decay (purple) is that of the perfect crystal. The amplitude of the initial drop of the fast component gives the concentration of the defects.

Thus, in the presence of vacancies, only a part of the crystal will emit with the perfect crystal lifetime. Part of it exhibit a shorter lifetime.

1.4.5.4. Aggregation-Induced Emission (AIE)

Many fluorescent molecules are not fluorescent in solid state, such as fluorescein, rhodamine or Bodipy [Vu, 2013]. Among other reasons is the photoredox properties of excited states:



The excited states contain energy that can be used to give or take electrons from their surrounding according to the equation [Rehm, 1970]:

$$E_{S^+/S_1} = E_{S^+/S_0} + \Delta E_{00} + \frac{e^2}{4\pi\epsilon r} \quad (1.24)$$

where E_{S^+/S_1} is the redox potential of the excited state, E_{S^+/S_0} the redox potential of the ground state, ΔE_{00} the energy of the excited state expressed in eV, e the elementary charge, and r the distance between the excited state and its neighbour in the solid.

For some molecules these deactivation processes are less present [Shi, 2017b]. The increase of fluorescence in the solid state can be due to an increase of k_F . This is true in the case of the formation of J aggregates, and this was the first observation of the AIE phenomenon [Wurthner, 2011]. But these solids exhibit short lifetimes are difficult to measure with our set up. The increase of the fluorescence can be due to a reduction of a deactivation process present in solution. This can be a Twisted Intramolecular Charge Transfer (TICT) process [Grabowski,

2003]. Such twisting of the molecule is prevented in the crystal that explains the AIE phenomenon.

1.4.6. Video fluorescence lifetime imaging microscopy (FLIM)

Fluorescence Lifetime Imaging has been developed to characterise the FRET in live cells. Different technical approaches have been proposed to tackle the different challenges: a limited number of photons, the very short fluorescence lifetimes, and the high number of pixels. The most common approach is to add a timing unit behind the photomultiplier of a confocal two-photon microscope [Becker, 2015].

Two-photon microscopes offer the possibility of confocal imaging (to image voxel one by one in 3D), but compared to one photon confocal microscope, only the observed voxel is excited and bleached. Thus, two-photon microscopy is less aggressive for the sample. The cost for that improvement is to buy an expensive pulsed laser (150 k€). For a small added price (25 k€), a time resolved photon counting unit can be added.

The data acquisition rate is limited by the scanning speed of the mirrors through the sample and the photon counting rate. Usual scanning rates range from 200 Hz up to 1000 Hz, which is the number of lines scanned *per* second. A 1024×1024 pixel image will be scanned in 1.24 s. At this rate, the collection time of the photons of one pixel is 1 ms. For most samples higher scanning rates are not desirable because of the limited number of photons emitted by the sample.

Based on confocal scanning, *Beker & Hickl GmbH*[®] [Becker, 2014] reported video FLIM recording of the fluctuations of fluorescence lifetime by scanning chloroplasts in leaves of grass. They record spontaneous fluctuations of the fluorescence along a line of 256 pixels with a time resolution of 60 ms. In addition to spontaneous fluctuations, light triggered fluctuations can be produced and recorded. By the average of 40 excitation cycles, synchronised fluctuations of chloroplast lifetimes have been recorded and averaged with a resolution of 1 ms.

Faster acquisitions rate can be achieved by multiplexing the number of confocal beams,

the detection of the photons with a multi-anode (4×4) photomultiplier tube together with the counting electronics (×8) as propose by *Lavision*[®]. With this instrument [Rinnenthal, 2013], it is possible to achieve the acquisition of 131×131 images every 82 ms.

Gated charge-coupled device (CCD) is the second technical answer to video FLIM. A light amplifier is placed in front of an imaging detector. The light amplifier can be turned on for a very short time: 1 ns. By recording the light intensity at five times delays after the laser excitation, the decay can be quantified as a biexponential decay. The light amplifier does not give more sensitivity to that technique than competitors since under microscope, we are in the regime of single photon detection. In fact, its overall sensitivity is lower than that of single photon counting setups [Rinnenthal, 2013]. But this technique benefits from the imaging capacity of the CCD detectors. The maximum acquisition rate is defined as a fraction of the reading rate of the CCD.

Complementary metal–oxide–semiconductor (CMOS) detectors are silicon detectors where each pixel contains sensitive area and electronics. If each sensitive area is an avalanche photo diode, and the electronics is a timing circuit, an array of single photon counting and timing units can be created. This massive parallelisation allows very fast acquisition rates. This was done by Charbon group [Antolovic, 2016] with an array of 512×128 10k frame *per second* (100 μs acquisition rate) for a 4 bits image (16 grey levels).

1.5. (2Z,2'Z)-2,2'-(1,4-phenylene)bis(3-(4-butoxyphenyl) acrylonitrile)

(DBDCS)

1.5.1. Synthesis

The molecule chosen for our study is (2Z,2'Z)-2,2'-(1,4-phenylene)bis(3-(4-butoxyphenyl) acrylonitrile) (DBDCS, molecular structure in Figure 1.14). It is an AIE luminogen. DBDCS was first synthesised by Yoon *et al* [Yoon, 2010]. Later on, Jeon *et al* [Jeon, 2015] proposed an *in situ* synthesis using a reactive inkjet printing method for producing DBDCS films (Figure 1.15). This compound is also named α -DBDCS in the literature, while

β -DBDCS is another position isomer of the same molecule (depending of the position of the acrylonitrile substituent on the C=C bond).

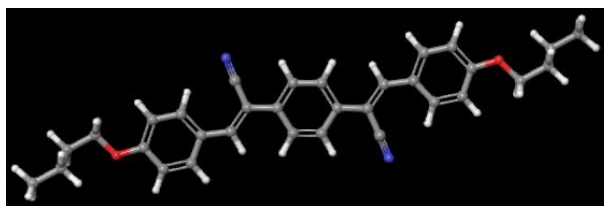


Figure 1.14. Molecular structure of DBDCS.

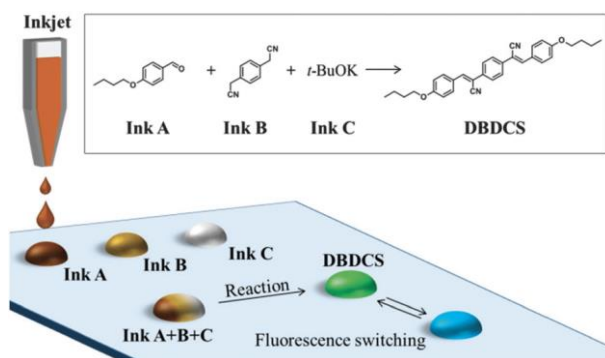


Figure 1.15. Schematic illustration for the preparation of DBDCS using a reactive inkjet printing method. (Adapted from [Jeon, 2015])

1.5.2. Characterisation

Yoon *et al* have characterised two crystalline phases, the G-DBDCS (G for green) and the B-DBDCS (B for blue) phases. The G-DBDCS phase has been recrystallised from ethyl acetate solution. Single crystal X-ray diffraction (XRD) experiment has been performed leading to the determination of the crystal structure at 273 K. The B-DBDCS phase is obtained by annealing powder of G-DBDCS. It has been characterised by powder X-ray diffraction [Yoon, 2010] and later by Kim *et al* [Kim, 2015] (Appendix A.iii).

The infrared (IR) spectra has been recorded by Fujimori *et al* (Figure 1.16) [Fujimori, 2016]. To confirm the change in the molecular structure, Fujimori *et al* measured the IR spectra of the DBDCS film on a ZnSe substrate before and after photoirradiation, concomitant with the microcrystal powder of DBDCS. In the difference spectrum between before and after ultraviolet

(UV) irradiation (sky blue line), positive absorbances were observed at 1593, 1510, 1253, and 1176 cm^{-1} . It is indicated that the positive absorbances become stronger and weaker in oscillator strength of the bands within the molecule by the photoirradiation. The bands of positive absorbance were, respectively, assigned to the stretching band of the two olefins (1593 cm^{-1}), stretching band of the benzene substituents (1510 cm^{-1}), stretching band of the ether groups (1253 cm^{-1}), and stretching vibration of the benzene rings (1176 cm^{-1}) based on vibrational analysis of calculations. Therefore, the spectral change by photoirradiation can be ascribed to the conformational change around the olefin and the ether group. They have established small differences authorizing the characterisation of the two phases. The spectral change by photoirradiation can be ascribed to the conformational change around the olefin and the ether group. An IR spectrum of DBDCS is also reported by Jeon *et al* [Jeon, 2015].

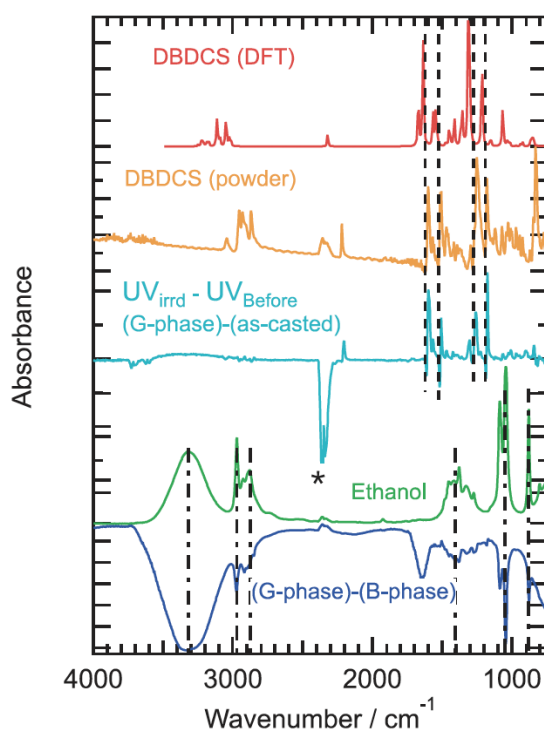


Figure 1.16. IR spectral change in DBDCS film due to the UV irradiation or heating.

The asterisk indicates the band of CO_2 . (Adapted from [Fujimori, 2016])

1.5.3. Photoluminescent properties

Under a UV light, DBDCS emits in green or in blue colour (Figure 1.17 and Figure

1.18).

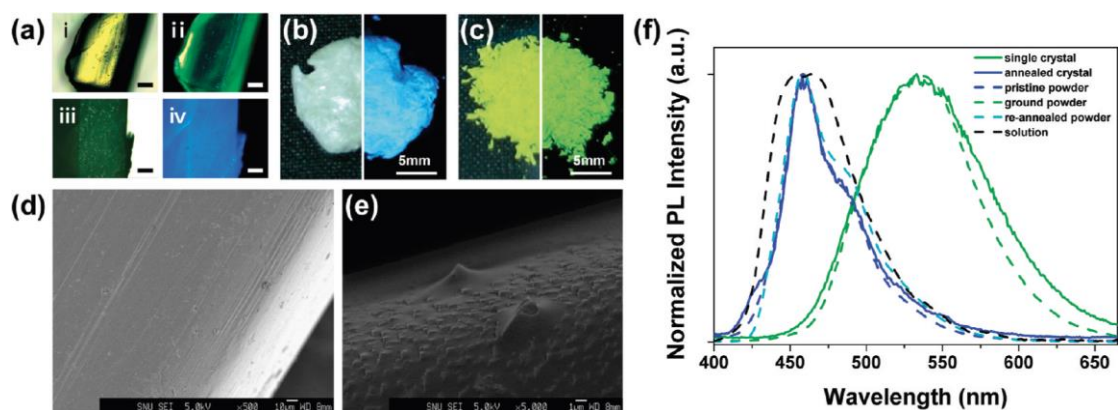


Figure 1.17. (a) Photo of a single crystal: before annealing, under room light (i), and UV light (ii), and after annealing, under room light (iii), and UV light (iv) (scale bar 0.2 mm). (b) Photo of the pristine powder under room (left) and UV light (right). (c) Photo of the ground powder under room light (left) and UV light (right). (d) SEM image of the surface morphology of DBDCS single crystal. (e) SEM images of the surface morphology of DBDCS annealed crystal. (f) Normalised photoluminescence spectra of DBDCS single crystal (green solid line), annealed crystal (blue solid line), pristine powder (blue dashed line), ground powder (green dashed line), reannealed powder (sky-blue dashed line), and solution (black dashed line). (Adapted from

[Yoon, 2010])

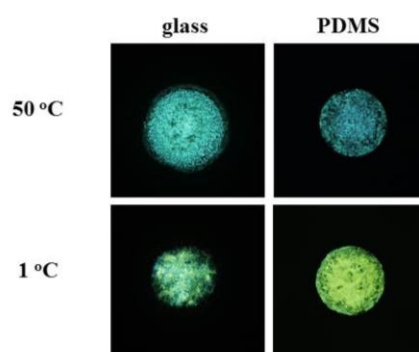


Figure 1.18. Fluorescence microscope images of DBDCS spots after 24 h at different temperatures on glass and PDMS films (λ_{ex} 330~385 nm). (Adapted from [Jeon,

2015])

The absorption spectrum of DBDCS contains two massifs at 372 and 325 nm and one fluorescence massif at 440 nm in CHCl_3 . One vibrational sub-structure can be seen in the fluorescence spectrum in CHCl_3 .

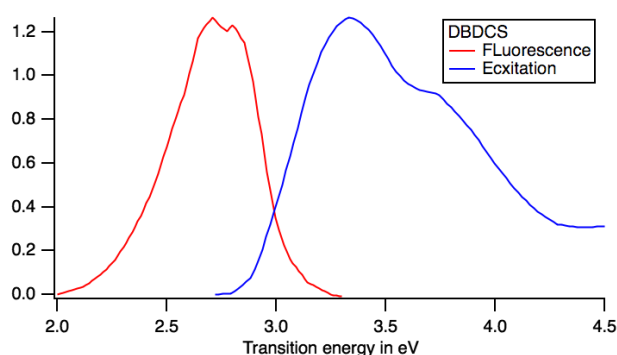


Figure 1.19. The absorption and fluorescence spectra of DBDCS in CHCl_3 . (Adapted from [Shi, 2017b])

DBDCS has a good fluorescence yield. This can be due to the formation of delocalised J aggregates in the solid state as for cyanine. But the emission is broad and has a long lifetime. We suppose that, like for difluoroboron- β -diketones, DBDCS forms localised excitons. Their fluorescence spectrum and lifetime depend strongly on the organisation of the molecules in the crystal. Again, like difluoroboron- β -diketones, this is a small oligomer, typically an excited dimer that is responsible for the emission. This is the conclusion by J. Gierschner [Shi, 2017b].

DBDCS belongs to this second family of AIE molecules where a TICT process kills the fluorescence in solution. In solid state, the isomerisation is blocked allowing the fluorescence. In addition, the formation of localised excimers traps the excitation on a dimer. The trapping prevents the diffusion of the exciton and its destruction by defects. The fluorescence decay of DBDCS crystals remains quite sensitive to vacancies that allows a local movement of DBDCS.

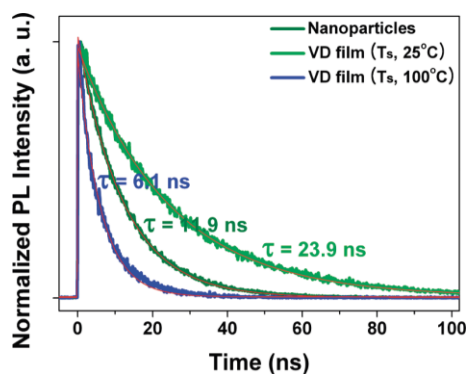


Figure 1.20. The fluorescence decay profiles of DBDCS nanoparticles in THF-water mixture (dark green line), Green-phase VD film (green line), and Blue-phase VD film (blue line) under 400 nm excitation. (Adapted from [Yoon, 2010])

Yoon et al [Yoon, 2010] has assigned the change of emission properties as following. The interlayer distance between the adjacent molecular sheets is 3.7 Å, consistent with other π - π stacking distances reported earlier for substituted DSBs. The driving force for this specific slip-stack formation is the antiparallel coupling between the local dipoles. Since the outer phenyl rings are electron-rich with butoxy-substituents while the central phenyl ring is electron-poor with cyano groups, DBDCS is a D-A-D molecule comprising two local dipoles (Figure 1.23) which add to a zero net dipole moment. Antiparallel dipole coupling places the central ‘A’ ring of the upper sheet just above the ‘D’ ring of the lower sheet, bringing about efficient excitonic and excimeric coupling between DBDCS molecules.

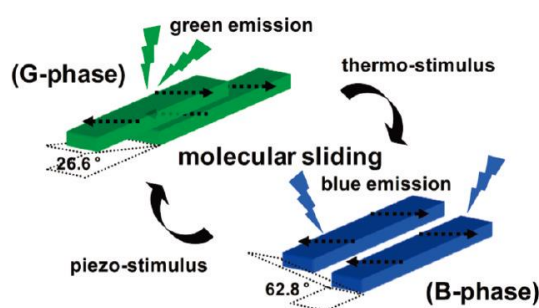


Figure 1.21. The change in the colour of the fluorescence has been rationalised by Yoon, et al as the change in the interaction of dimers. (Adapted from [Yoon, 2010])

Yoon et al [Yoon, 2010] have described as the *H-type aggregation* due to the excitonic

coupling between the transition dipoles of adjacent molecules for nano particles in suspension. The situation is similar in the G-phase crystal, whose spectral features are akin to those of the nanoparticle suspension. In addition, the emission lifetime is quite long (23.9 ns), and clear *H-aggregation* behaviour is observed in the absorption spectrum. On the other hand, the emission spectrum of the Blue-phase gains vibronic structure and shows a pronounced hypsochromic shift, indicating a loss of excited state delocalisation between adjacent molecules by a substantial reduction of π - π overlap. As a result, the emission lifetime becomes also shorter (6.1 ns) than that of the Green-phase. To reduce such overlap, the slip in the Blue-phase must be essentially along the short x-axis, and not like in the Green-phase along y. At this point, Yoon *et al* [Yoon, 2010] have stressed that the phase transition observed here is a quite unique example to study separately exciton and excimer coupling in molecular crystals; while the Green-phase shows rather weak excitonic coupling, excimer formation is favoured by pronounced overlap of the π -systems. In the Blue-phase, excimer formation is diminished, while excitonic interaction substantially increases. The driving force for the phase transition is clearly provided by the local dipoles as introduced through the cyano group. While in the metastable Green-phase antiparallel coupling of the local dipoles kinetically stabilises the structure, a smooth slip of the molecular sheets with a very low activation barrier leads to the formation of the Blue-phase with the energetically favoured formation of a head-to-tail arrangement of the local dipoles (see Figure 1.21). Indeed, as seen in Figure 1.22, an x-slip leads to a substantial increase of excitonic coupling roughly by a factor of 2, in a good agreement with the experimental result.

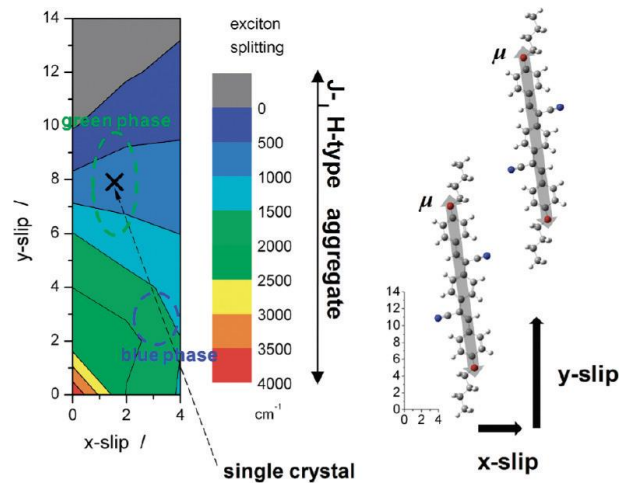


Figure 1.22. Colour contour map of calculated exciton splitting for a dimer pair at a different displacements x, y (in \AA); the separation in z amounts 3.7\AA . A slip of 4\AA (14) corresponds to a translation by half a molecular length in x (y). (Adapted from [Yoon, 2010])

Yoon's theory does apply to DBDCS crystals, but it assumes that crystals have no defects. Some of these defects will contribute to kill the fluorescence and the observed fluorescence decays will be shorter than the one predicted by the theory. This explains the wide distribution of fluorescence decay reported in the literature for the Green and Blue phases. The different characteristics of DBDCS are summarised in Table Appen.A.6, while lifetimes are graphically presented in figure 1.21.

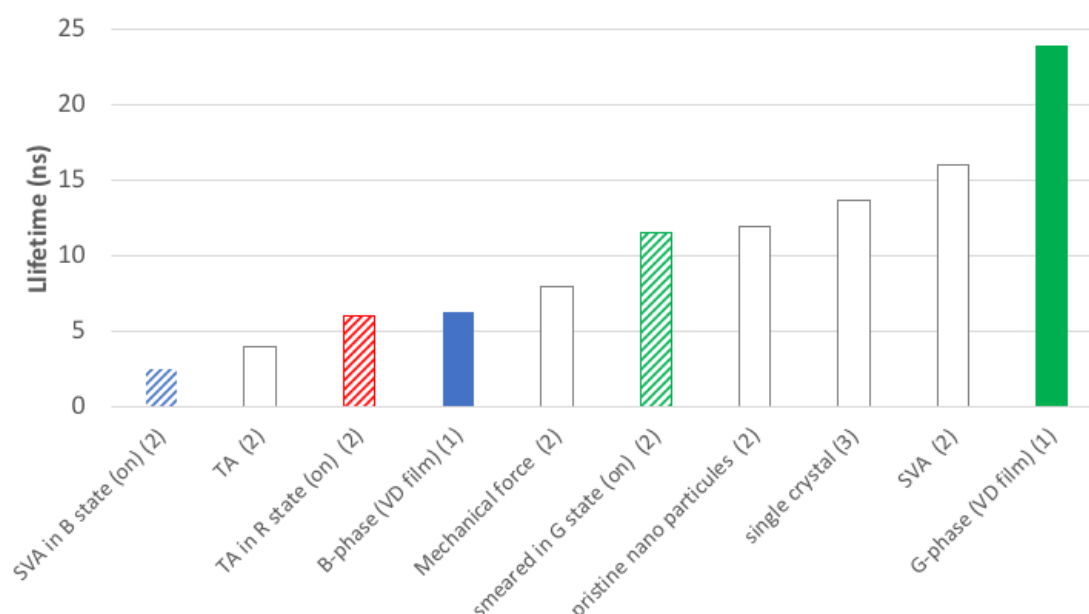


Figure 1.23. Experimental lifetimes (ns) of DBDCS as reported in the literature: (1) [Yoon, 2011], (2)[Kim, 2015], (3)[Shi, 2017b]. The experimental condition of DBDCS preparation in the solid state is given for each value. For compounds for which the phase has been attributed the colour code corresponds to the name of the phase. When the measurement has been done on the emitting solid, it appears as dashed area. White bar figures measurement with no attribution of the phase.

TA=thermal annealing, SVA=solvent-vapor annealing, SM=smearing.

As reported by Yoon *et al* [Yoon, 2010], DBDCS exhibits two distinguishable and reversibly switchable luminescent phases (B and G) in the solid state: i) the green luminescent phase ($\lambda_{em} = 533\text{nm}$, fluorescence quantum yield $\Phi_F = 0.45$) was generated by solvent vapor annealing (SVA) or mechanical force; and ii) the blue emitting phase ($\lambda_{em} = 548\text{nm}$, $\Phi_F = 0.31$) was generated by thermal annealing (TA). Yoon *et al* has established that there is a reversible process (thermo- or piezo- stimulus) between the B- and the G-DBDCS phases (Figure 1.24). When a film is created with two layers (one of DBDCS, one of m-DBDCS (see DBDCS derivatives section)) a polychrome can be obtained (Figure 1.25). [Kim, 2015]

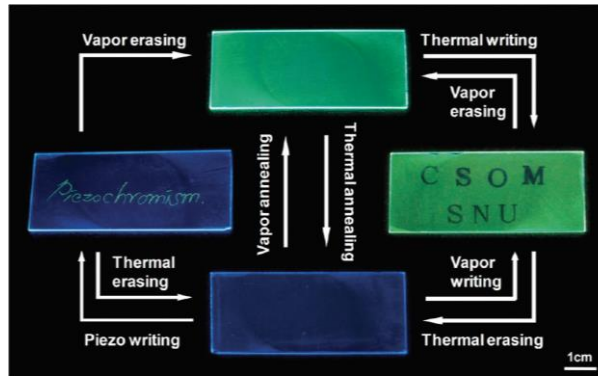


Figure 1.24. Photos of the luminescence writing-erasing cycle on a DBDCS-PMMA film. (Adapted from [Yoon, 2010])

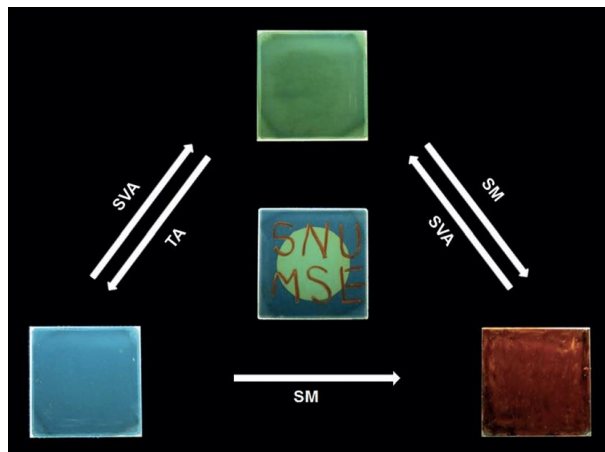


Figure 1.25. RGB fluorescence switching in DBDCS/m-BHDCS bicomponent film: fluorescence changes by various stimuli of solvent vapor annealing (SVA), thermal annealing (TA), and smearing (SM). (Adapted from [Kim, 2015])

Chapter 2. Experimental: parametric sweep of a coaxial microfluidic mixer for diffusive antisolvent precipitation, coupled with a focused IR laser for NPLIN and a wide-field UV laser for FLIM

2.1. A diffusive coaxial microflow antisolvent precipitation system	46
2.1.1. Reactive part of the coaxial microflow mixer	46
2.1.2. Flow control in the microfluidic system	50
2.1.3. Structure of the coaxial microflow	56
2.1.4. Assembling the microfluidic system	61
2.2. Laser and microscopy setup for microfluidic NPLIN and FLIM	63
2.3. Microfluidic parametric sweep and NPLIN	67
Chapter conclusion.....	71

This chapter is the description of the experiment in this thesis. The first step of our research is to build the microfluidic system. The diffusive coaxial microflow antisolvent precipitation system coupled with a wide filed (WF) femtosecond (fs) ultraviolet (UV) laser for fluorescence excitation and a focused infrared (IR) fs laser for inducing nucleation, or with an X-ray beam for *in situ* structural characterisation, is described in section 2.1, with some basic microfluidic parameters. The technical details of the materials for the microfluidic system are listed in Appendix B.i. Numerical descriptions of the structure of the microflow are attached in Appendix B.ii. The detailed process of assembling the microfluidic system and the frequently encountered problems are listed in Appendix B.iii and Appendix B.iv, respectively. The laser and microscopy setups for FLIM and NPLIN are described in section 2.2, with technical details of the laser source, the optics, and the FLIM detector attached in Appendix B.v, Appendix B.vi, and Appendix B.vii, respectively. The experimental procedures of a microfluidic parametric sweep for spontaneous and laser-induced nucleation in the coaxial mixer are described in section 2.3, with some parameters relate to phase transition in the coaxial mixer defined. The measurement and control of the energy of the IR laser reached the sample is described in Appendix B.viii.

2.1. A diffusive coaxial microflow antisolvent precipitation system

2.1.1. Reactive part of the coaxial microflow mixer

In this work, precipitation by antisolvent was studied in a 25 mm long observation window on a diffusive coaxial laminar microflow mixer, as schematically shown in Figure 2.1. The coaxial microflows consisted of two miscible solvents (species 1 and 2) and a solute (species 3). Species 3 was a molecule or compound, insoluble in species 1 (solvent 1, the antisolvent) but soluble in species 2 (solvent 2, the good solvent). A central flow of a mixture of species 2 and 3 was coaxially injected through a small capillary, without surfactant, into a peripheral flow, 210 μm in diameter, of a mixture of species 1 and 2. A jet flow was formed at the injection nozzle. After the momentum exchange and mass transportation between the co-flows, a laminar microflow of a highly supersaturated homogenous single phase developed.

Spontaneous phase transition was observed along the flow. The distance from the injection nozzle to where spontaneous phase transition started to be observed was defined as d_p through optical microscope (detection limit 1 μm). An induction period was defined:

$$t_p \equiv \int_0^{d_p} \frac{1}{v_x(x,0)} dx \approx \frac{d_p}{v_x(d_p,0)} \quad (2.1)$$

with $v_x(x,0)$ the velocity of the flow along the flow centre in a horizontal cylindrical coordinate system (Figure 2.1).

A nucleation event interval was defined as d_N , the distance between two objects successively precipitated. Nucleation event spatial interval along flow centre gives nucleation event temporal interval:

$$\overline{t_N} \equiv \frac{\overline{d_N}}{v_z(d_p,0)}, \quad (2.2)$$

and an accumulative (from the nozzle to x μm) crystal birth rate specifically applied to this cylindrical microfluidic system was defined:

$$B_x \equiv \left\langle \frac{1}{t_N} \right\rangle. \quad (2.3)$$

B_x , with a unit of s^{-1} , is different than the theoretical nucleation rate N with a unit of $\text{s}^{-1} \cdot \text{m}^{-3}$. It means the number of precipitated objects passing through an effective cross-section *per* unit time at x μm , or the number of nuclei produced *per* unit time from the nozzle to x μm away, or the probability for a precipitated object to be observed after d_p . The average nucleation rate on a cross section x μm from the nozzle can be derived from B_x :

$$N = \frac{1}{\pi R_{\text{channel}}^2} \frac{dB_x}{dx} \quad (2.4)$$

with R_{channel} the radius of the microfluidic channel.

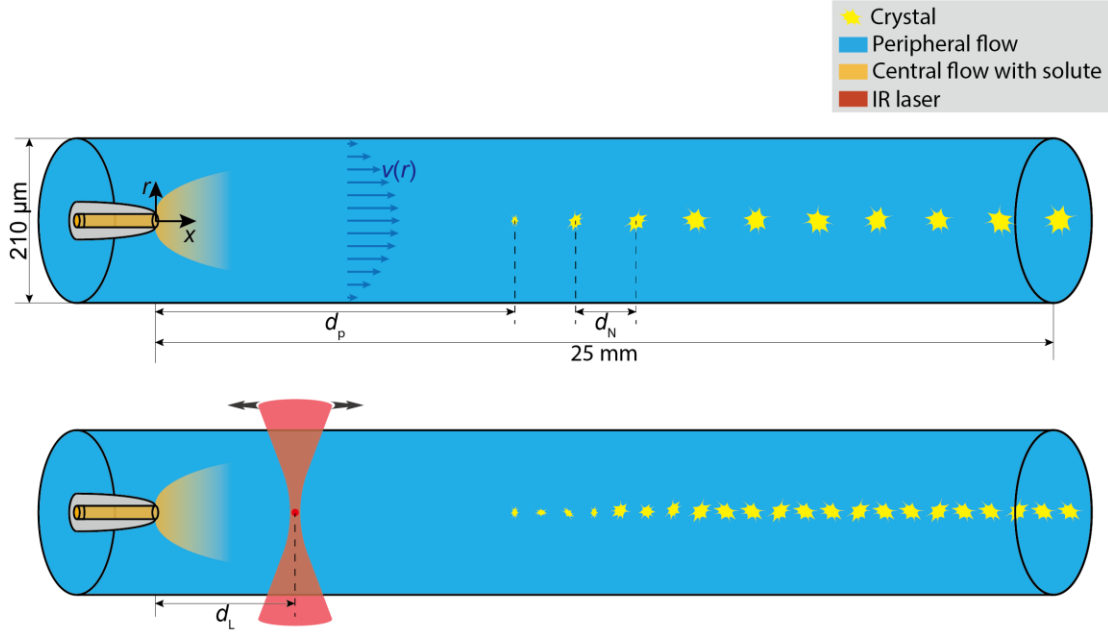


Figure 2.1. Schematic illustration of the microfluidic NPLIN experiment: spontaneous crystallisation (up) controlled by a diffusive co-axial microflow mixer and laser-induced crystallisation in microfluidics (down) by focusing a pulsed infrared laser at flow centre.

Microfluidic NPLIN was conducted by focusing a pulsed femtosecond IR laser ($\lambda = 1030\text{nm}$, $f_{\text{rep}} = 1 \sim 10\text{MHz}$, $\tau_p = 400\text{fs}$, $P_{\text{avg}} = 0 \sim 0.32\text{W}$) at flow centre ($d_L, 0$), $d_L \in (0, d_p)$, with d_L the distance from the injection nozzle to laser focal point. If laser can indeed induce nucleation, a raise of B_x or a decrease of d_p should be observed.

Comparison of classical NPLIN nucleation experiment, as referred in the text as “static” NPLIN, and NPLIN in the microfluidic environment, as referred as “microfluidic” NPLIN, is schematically drawn on figure 2.2. In the microfluidic NPLIN system, instead of temperature control, the supersaturation is achieved by mixing the good and anti-solvents. The nucleation time is reduced from minutes to milliseconds. The microfluidic NPLIN laser is a focused femtosecond IR laser. The blind time for observation after laser irradiation is covered by FLIM

measurement. The growth process can be followed along the flow. It consumes very small amount of fluorescent solute.

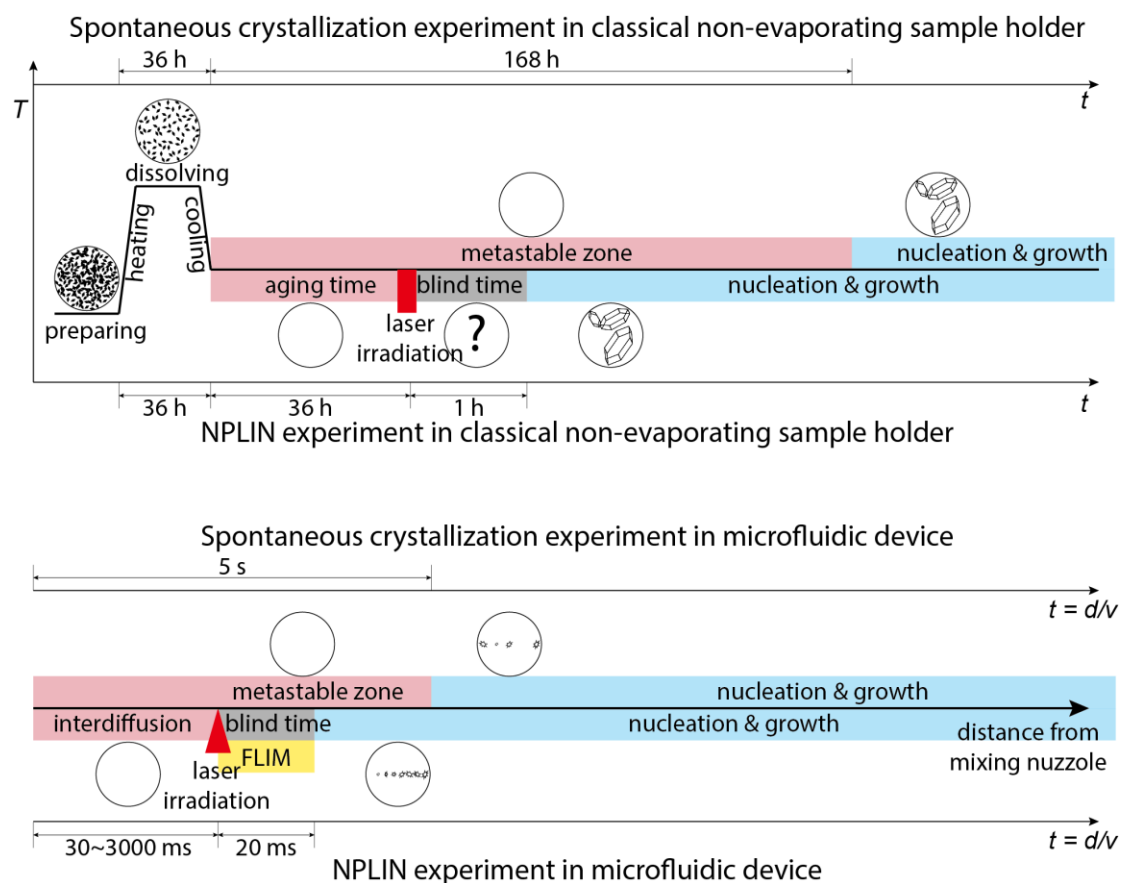


Figure 2.2. Typical procedures of “static” NPLIN (top) and “microfluidic” NPLIN (bottom). The first line of each part represents the spontaneous nucleation, while the second line represent the NPLIN experiment. The time values indicated in the “static” NPLIN are those of glycine (150 % of supersaturation) as described by [Clair, 2014].

In the same simple holder type they are of the same orders. They could vary significantly in other experimental devices.

This thesis is mainly based on water (antisolvent)-1,4-dioxane (good solvent)-DBDCS (solute) ternary system. Preliminary tests were conducted with THF-water-Calix-Cousulf- Cs^{+2} , THF-water-(caesium acetate), THF-water- CsCl , water-THF-DBDCS, water-(THF20-1,4-dioxane80)-DBDCS, and water-acetone-DBDCS systems.

2.1.2. Flow control in the microfluidic system

To achieve the coaxial microflows in Figure 2.1, Génot and Audibert [Tran, 2016] developed a diffusive coaxial microflow mixer and tested with DBDCS at Lab *PPSM, ENS-Cachan*. We have further improved it to make parametric sweep and *in situ* observation of laser-induced nucleation in microfluidics. The detailed design of the microfluidic system is shown in Figure 2.3

Kinetics and thermodynamics of phase transition by antisolvent is governed by supersaturation. For that, 4 microfluidics parameters (Figure 2.4 left) were controlled: ρ_{3c} , mass concentration of species 3 (solute) in the central flow; ϕ_{1p} , volume fraction of solvent 1 (antisolvent) in the peripheral flow; Q_c and Q_p , the flow rates of the central and peripheral flow respectively. Temperature of the observation window was not actively controlled yet.

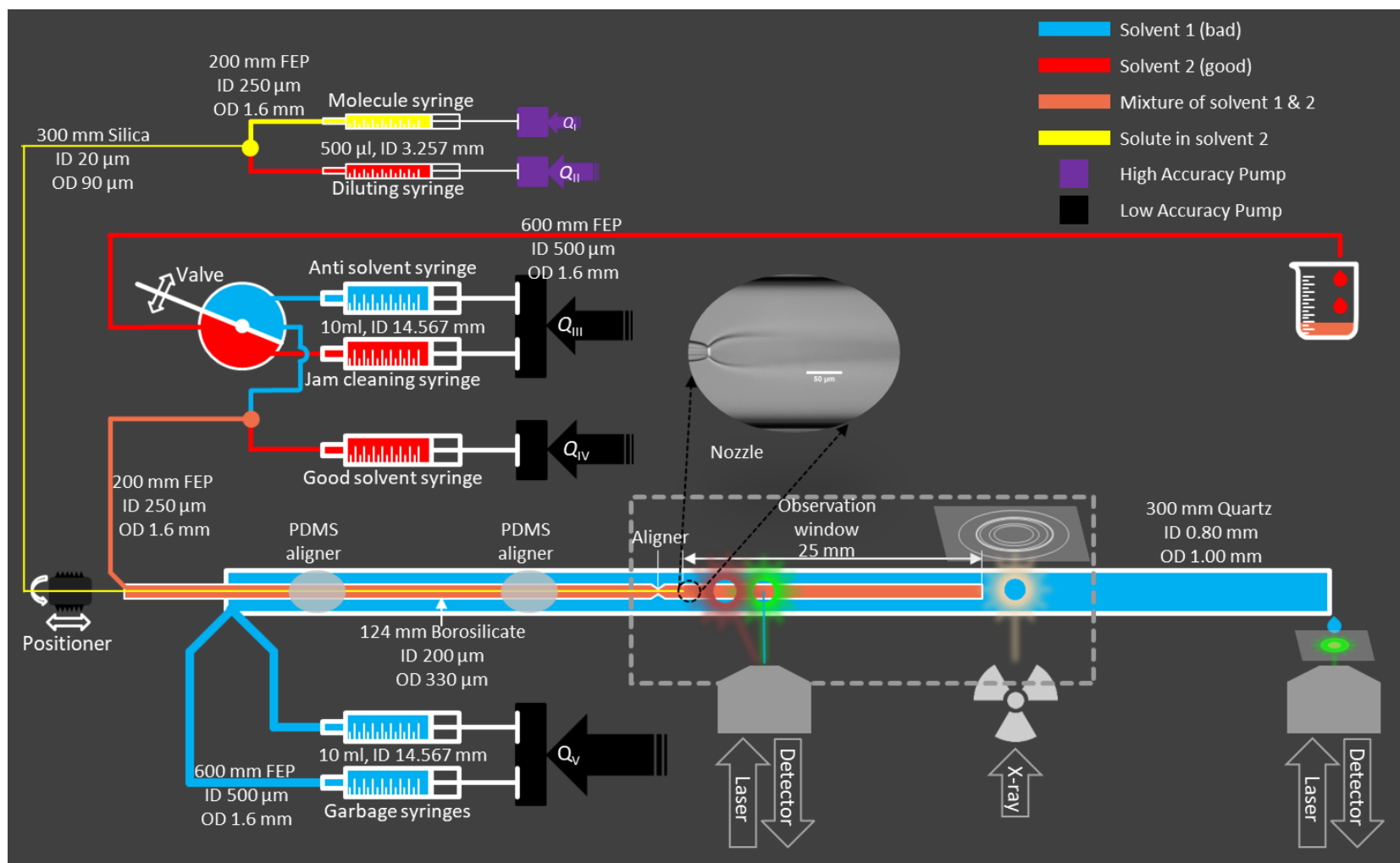


Figure 2.3. Design of the versatile coaxial microflow system.

In Figure 2.3, the central flow was injected into the system through the yellow line, a silica capillary tube (inside diameter (ID) 20 μm , outside diameter (OD) 90 μm , *Polymicro Technologies*) under a 10 μm thick protective polyimide coating. Mass concentration of species 3 in the central flow, ρ_{3c} , was controlled by mixing two independent flows, Q_I and Q_{II} . Q_I was a saturated solution of species 3 in solvent 2 in a gas tight glass syringe (ID = 3.257mm, 500 μl , VWR) pushed by a *Pico Plus Elite Pump 11* syringe pump (*Harvard Apparatus*), and Q_{II} solvent 2 in a same type glass syringe pushed by a *Pico Plus* syringe pump (*Harvard Apparatus*). The central flow rate and the mass concentration of species 3 in it (Figure 2.4 left) was scanned by continuously changing Q_I and Q_{II} :

$$Q_c = Q_I + Q_{II} , \quad (2.5)$$

$$\rho_{3c} = \frac{Q_I}{Q_c} \rho_{3s2} , \quad (2.6)$$

with ρ_{3s2} the solubility of species 3 in solvent 2. In Q_c (or in Q_I), the flow rate of species 3 was estimated as:

$$Q_3 = \frac{\rho_{3s2} N_A V_{m,3} Q_I}{M_3} \quad (2.7)$$

with $V_{m,3}$ the volume of a molecule of species 3 in solution, M_3 its relative molar mass, and N_A the Avogadro constant. The rest of Q_c (or Q_I) would be the flow rate of species 2.

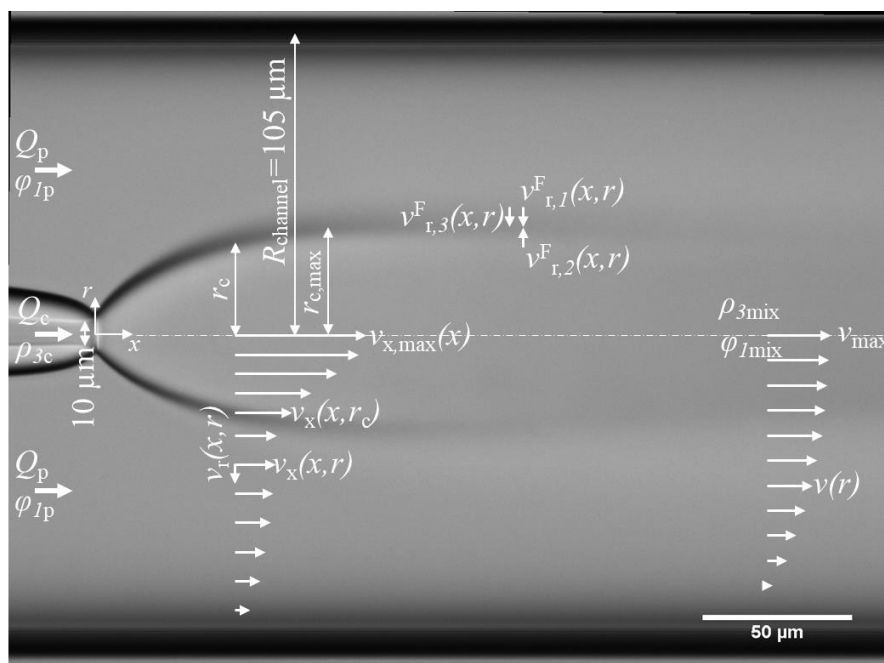


Figure 2.4. Parameters of the coaxial microfluidic mixer.

The peripheral flow was a mixture of two independent flows, solvent 1 in Q_{III} and solvent 2 in Q_{IV} , both in gas tight glass syringes (ID = 14.567mm, 10 ml, VWR) pushed by *PHD 2000 Infusion pumps (Harvard Apparatus)*. Another syringe of solvent 2 was also mounted on Q_{III} next to the syringe of solvent 1, which served as a cleaning module of the microfluidic mixer. The two syringes of solvent 1 and 2 on Q_{III} were connected to an actuated switching valve (*Rheodyne® MXP*), which switched the peripheral flow between a mixture of solvent 1 and 2 and pure solvent 2. This was a practical design, because after a long time of strong precipitation, the microfluidic channel could be clogged with precipitates, as shown in Figure 2.5. By switching the peripheral flow from anti-solvent to pure solvent 2, the blockage was dissolved within tens of seconds, thus the micro channel quickly cleaned, and precipitation conditions restored after switching back to antisolvent.

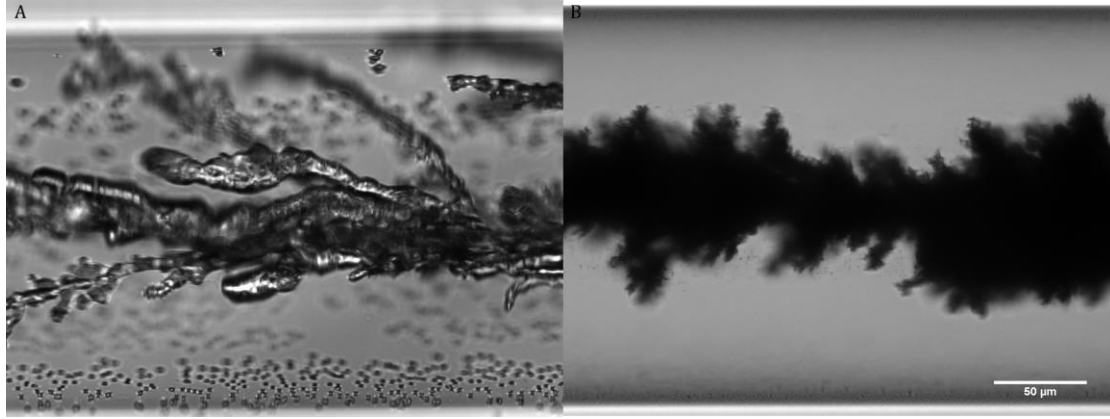


Figure 2.5. Clogging of the borosilicate syringe after a long time of experiment. A: clogging by caesium acetate in THF-water microflow; B: clogging by DBDCS precipitation in water (1)-1,4-dioxane (2).

After the switching valve, the peripheral flow was injected into a round borosilicate glass capillary (ID = 200 μm , OD = 330 μm , *CM Scientific*). The flow rate of the peripheral flow and the volume fraction of antisolvent in it (Figure 2.4 left) was scanned by changing Q_{III} and Q_{IV} continuously:

$$Q_p = Q_{\text{III}} + Q_{\text{IV}} + \Delta Q_p, \quad (2.8)$$

$$\phi_{1p} = \frac{Q_{\text{III}}}{Q_{\text{III}} + Q_{\text{IV}}}, \quad (2.9)$$

where ΔQ is the loss of peripheral flow rate caused by the excess mixing volume of solvent 1 and 2, ϕ_{1p} the volume fraction of solvent 1 in the peripheral flow. $\phi_{2p} = 1 - \phi_{1p}$. The loss of flow rate after mixing flows of solvent 1 and 2 was estimated as:

$$\frac{\Delta_{\text{mix}} Q}{Q_1 + Q_2} = \frac{\phi_1 \phi_2}{V_{m,1} \phi_2 + V_{m,2} \phi_1} \sum_{n=0}^4 A_n \left(\frac{V_{m,1} \phi_2 - V_{m,2} \phi_1}{V_{m,1} \phi_2 + V_{m,2} \phi_1} \right)^n \quad (2.10)$$

with Q_1 and Q_2 the flow rates of solvent 1 and 2, $V_{m,1}$ and $V_{m,2}$ the molar volume of species 1 and 2, A_n the adjustable parameters in the mixing volume function for binary systems. Here for the peripheral flow,

$$\frac{\Delta_{\text{mix}} Q}{Q_{\text{III}} + Q_{\text{IV}}} = \frac{\phi_p \phi_{2p}}{V_{m,1} \phi_{2p} + V_{m,2} \phi_{1p}} \sum_{n=0}^4 A_n \left(\frac{V_{m,1} \phi_{2p} - V_{m,2} \phi_{1p}}{V_{m,1} \phi_{2p} + V_{m,2} \phi_{1p}} \right)^n.$$

Values of A_n in mixing functions of water (1)-1,4-dioxane (2) and water-THF binary systems were taken from [Aminabhavi, 1995]'s measurement, listed in Table 2.1. After mixing the central and peripheral flows, the total flow rate loss

$$\frac{\Delta_{\text{mix}} Q_{\text{total}}}{Q_1 + Q_{\text{II}} + Q_{\text{III}} + Q_{\text{IV}} - Q_3} = \frac{\phi_{1\text{mix}}^o \phi_{2\text{mix}}^o}{V_{m,1} \phi_{2\text{mix}}^o + V_{m,2} \phi_{1\text{mix}}^o} \sum_{n=0}^4 A_n \left(\frac{V_{m,1} \phi_{2\text{mix}}^o - V_{m,2} \phi_{1\text{mix}}^o}{V_{m,1} \phi_{2\text{mix}}^o + V_{m,2} \phi_{1\text{mix}}^o} \right)^n,$$

where $\phi_{1\text{mix}}^o$ and $\phi_{2\text{mix}}^o$ are the volume fractions of component 1 and 2 in the mixture without DBDCS,

$$\phi_{1\text{mix}}^o = \frac{Q_{\text{III}}}{Q_1 + Q_{\text{II}} + Q_{\text{III}} + Q_{\text{IV}} - Q_3} \quad (2.11)$$

and $\phi_{2\text{mix}}^o = 1 - \phi_{1\text{mix}}^o$. The losses of flow rate after mixing flows of water (1)-1,4-dioxane (2) and water-THF were calculated using equation (2.10) and plotted in Figure 2.6. In both systems, nearly 2% peripheral flow rate is lost when the ratio of water and 1,4-dioxane (or water and THF) is around 1:1.

Table 2.1. Parameters of mixing volume functions for binary mixtures of water (1)-1,4-dioxane (2) and water-THF [Aminabhavi, 1995]

System	A_0 /(ml/mol)	A_1 /(ml/mol)	A_2 /(ml/mol)	A_3 /(ml/mol)	A_4 /(ml/mol)
1-2	-2.496	1.756	-0.703	0.204	-0.462
Water-THF	-3.057	1.389	-0.837	1.757	-0.602

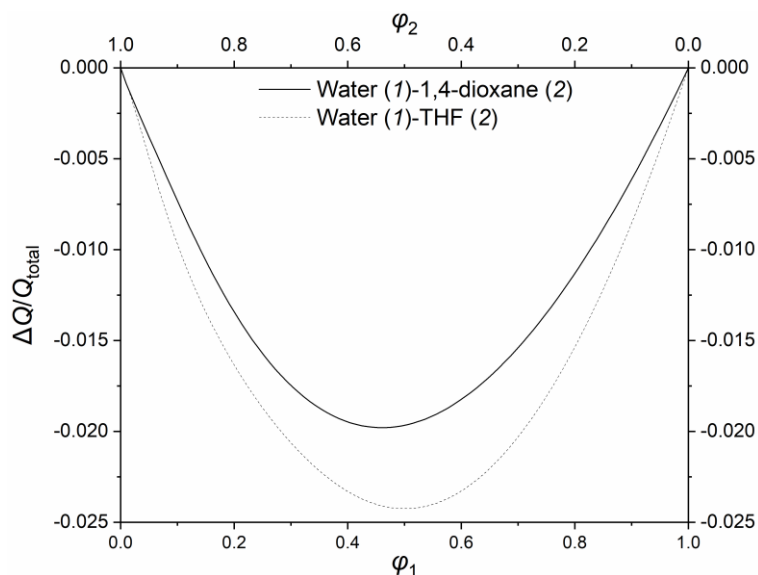


Figure 2.6. Loss of flow rate after mixing coflow of water (1)-1,4-dioxane (2) and of water (1)-THF (2) calculated using equation 2.9 in terms of volume fractions.

The observation window of the coaxial microflow mixer was limited inside the borosilicate glass tube within 25 mm after the injection nozzle along the flow, as this was the reactive part of the system where phase transitions occurred. Outside the borosilicate glass tube, a constant flow, Q_v , of solvent 1 was injected into a round quartz tube (ID = 0.8mm, OD = 1.0mm, *CM Scientific*) from two gas tight glass syringes (ID = 14.567mm, 10 ml, *VWR*) by a *PHD 2000 Infusion* pump (*Harvard Apparatus*). This quartz tube was to expand the flow at the end of the borosilicate tube to match the beam size for X-ray detection of the phase transition. Therefore, the quartz tube and Q_v was removed when X-ray experiment was not conducted. All the solvents were filtered (*FGLP 0.22 μm, Millipore*) at the exits of the syringes' luer tips to remove any impurities. Samples was collected at the end of the borosilicate tube for *post-mortem* examinations.

2.1.3. Structure of the coaxial microflow

The microfluidic parameters are shown in Figure 2.4. Before the injection nozzle, the average velocities of the central and peripheral flows are

$$v_{\text{effective,c}} = \frac{Q_c}{\pi R_{\text{nozzle}}^2}, \quad (2.12)$$

$$v_{\text{effective,p}} = \frac{Q_p}{\pi (R_{\text{channel}}^2 - R_{\text{nozzle}}^2)}. \quad (2.13)$$

with $R_{\text{channel}} = 105\mu\text{m}$ and $R_{\text{nozzle}} = 5\mu\text{m}$. The density and dynamic viscosity of the co-flows were similar. $v_{\text{effective,c}} \gg v_{\text{effective,p}}$. A jet flow was formed at the mixing nozzle. In Figure 2.4, although solvent 1 and 2 were miscible, because of the high Péclet number, an interface between central and peripheral flow was present after the nozzle instead of a single-phase laminar flow.

By expressing the conservation of mass for the central and peripheral flows, the maximum of the jet flow radius $r_{\text{c,max}}$ for immiscible coaxial flows can be estimated by [Guillot, 2007]

$$\begin{aligned} r_{\text{c,max}} &= R_{\text{channel}} \cdot \sqrt{1 - \sqrt{1 - \frac{Q_c}{Q_c + Q_p}}} \\ &= R_{\text{channel}} \cdot \sqrt{1 - \sqrt{\frac{1}{1 + \frac{Q_c}{Q_p}}}}. \end{aligned} \quad (2.14)$$

$r_{\text{c,max}}$ of miscible water (1)-1,4-dioxane (2) in our coaxial mixer was measured for different flow rates and used as a reference to guarantee the flow rates had reached the targets during parametric sweeping, as shown in Figure 2.7 and Appendix B.ii.i. Hereby we define

$$f = \sqrt{1 - \sqrt{\frac{1}{1 + \frac{Q_c}{Q_p}}}} \text{ as the hydrodynamic factor.}$$

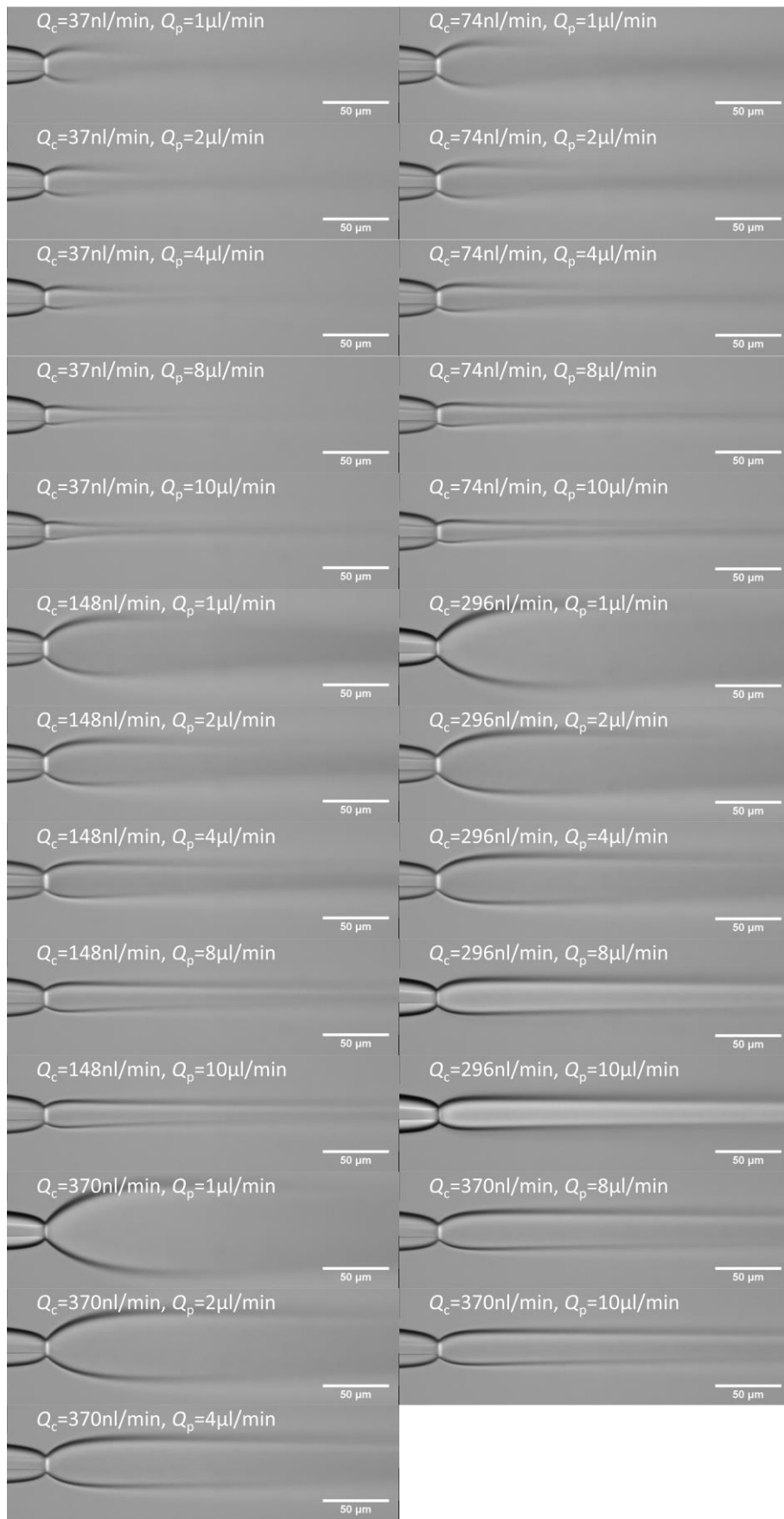


Figure 2.7. Central flow jet shape after injection nozzle. Injection of 1,4-dioxane into

water. The flow rates are indicated on the images. These images represent that the maximum radius of the central jet depends on flow rates. The contrast between the two flows is due to the change in the refractive indices between the two solvents. The progressive dimming of that contrast is due to the inter-diffusion between the two solvents.

Measured $r_{c,max}$ was plotted against the central/peripheral flow ratio in Figure 2.8.

Equation (2.14)

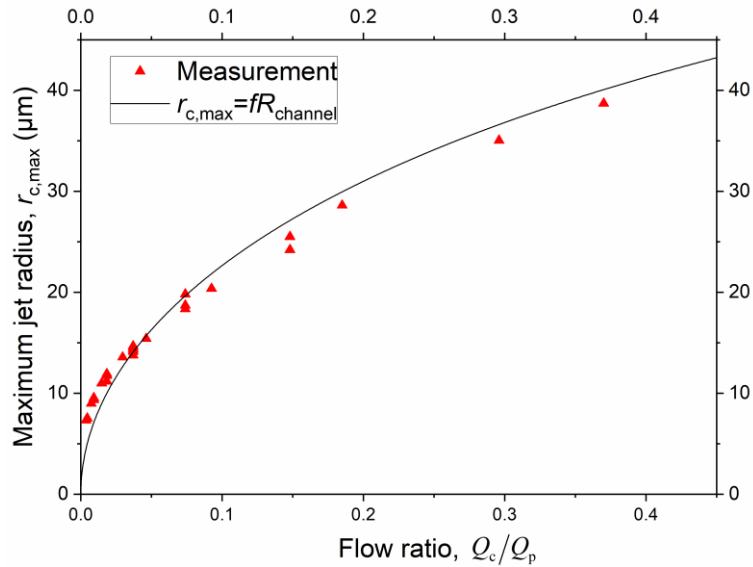


Figure 2.8. Central flow maximum radius as function of central/peripheral flow ratio.

Data is well described by equation (2.14).

After injection, the average velocity of the flow is

$$v_{\text{effective}} = \frac{Q_I + Q_{II} + Q_{III} + Q_{IV} + \Delta Q_{\text{total}}}{\pi \cdot R_{\text{channel}}^2} \quad (2.15)$$

The distance to develop an equilibrium laminar flow velocity profile can be estimated as [Incropera, 2007]:

$$l_h = 0.065 \cdot 2R_{\text{channel}} \cdot Re \quad (2.16)$$

with l_h the hydrodynamic entrance length, Re the Reynolds number. After l_h , a laminar flow was developed.

$$Re = \frac{2R_{\text{channel}} v_{\text{effective}} \rho_D}{\dot{\mu}} \quad (2.17)$$

where ρ_D is the mass density, $\dot{\mu}$ the dynamic viscosity.

We have a Reynolds number around 0.1~1.1. The jet will be finished and the Poiseuille profile will be established after 1~15 μm depending on the flow rates (Appendix B.ii.ii). The larger the flow rates, the longer l_h . The velocity profile over an effective cross-section in the final mixture is the Poiseuille profile (Figure 2.4, right)

$$v(r) = v_{\text{max}} \cdot \left(1 - \frac{r^2}{R_{\text{channel}}^2} \right), \quad (2.18)$$

$$\begin{aligned} v_{\text{max}} &= 2 \cdot v_{\text{effective}} \\ &\approx 2 \cdot \frac{Q_c + Q_p}{\pi \cdot R_{\text{channel}}^2}, \end{aligned} \quad (2.19)$$

with v_{max} the maximum of the speed profile at the laminar flow centre. In this coaxial microflow mixer, the laminar flow velocity profile converts distance from nozzle into reaction time:

$$t \approx \frac{x}{v(r)}. \quad (2.20)$$

After injection, the distance needed for the concentration to reach equilibrium was estimated as [Incropera, 2007]:

$$l_c = 0.05 \cdot 2R_{\text{channel}} \cdot Pe \quad (2.21)$$

with l_c the concentration entrance length, Pe the Péclet number. After l_c , a laminar flow with a homogeneous composition of solvents was developed.

$$Pe = \frac{2R_{\text{channel}} v_{\text{effective}}}{D^F} \quad (2.22)$$

where D^F is the Fick diffusion coefficient.

We have a Péclet number of 100~1000 and an inter-diffusion distance of 1~11 mm depending on the flow rates (see Appendix B.ii.ii). The larger the flow rate, the longer the entrance distance. We have no experimental check for that prediction but finer calculation by *Comsol*.

The mass concentration of the species 3 in the final mixture was (Figure 2.4, right)

$$\rho_{3\text{mix}} = \frac{\rho_{3c}}{Q_I + Q_{II} + Q_{III} + Q_{IV} + \Delta Q} . \quad (2.23)$$

The amount fraction solubility of species 3 in the final mixture of the laminar flow was estimated using the Jouyban-Acree model [Jouyban, 2007] (details see section 3.2.4 and 3.3.1):

$$x_{3\text{smix}} = x_{3s1}^{\phi_1^o} \cdot x_{3s2}^{\phi_2^o} \exp \left(\phi_1^o \phi_2^o \sum_{n=0}^2 \frac{A_n (\phi_2^o - \phi_1^o)^n}{T} \right) \quad (2.24)$$

with x_{3s1} and x_{3s2} the amount fraction solubility of species 3 in solvent 1 and in solvent 2, ϕ_1^o and ϕ_2^o the volume fraction of solvent 1 and solvent 2 neglecting the volume taken by the solute, A_n the solvent-solvent and solute-solvent interaction terms. Thus, the supersaturation in the final mixture

$$\Delta x_3 = x_{3\text{mix}} - x_{3\text{smix}} , \quad (2.25)$$

$$\beta = \frac{x_{3\text{mix}}}{x_{3\text{smix}}} , \quad (2.26)$$

with Δx_3 the amount fraction supersaturation of species 3 in the final mixture and β the supersaturation ratio.

2.1.4. Assembling the microfluidic system

All three capillaries were mounted, coaxially aligned and flow connected through two polyether ether ketone (PEEK) 7-port manifold (*IDEX*) on a microfluidic device. Figure 2.9

shows the design of the supporter for microfluidic capillaries. Two acrylonitrile butadiene styrene (ABS) prototypes were made by a *HP Design Jet* 3D printer. Later, two such supporters were made from aluminium.

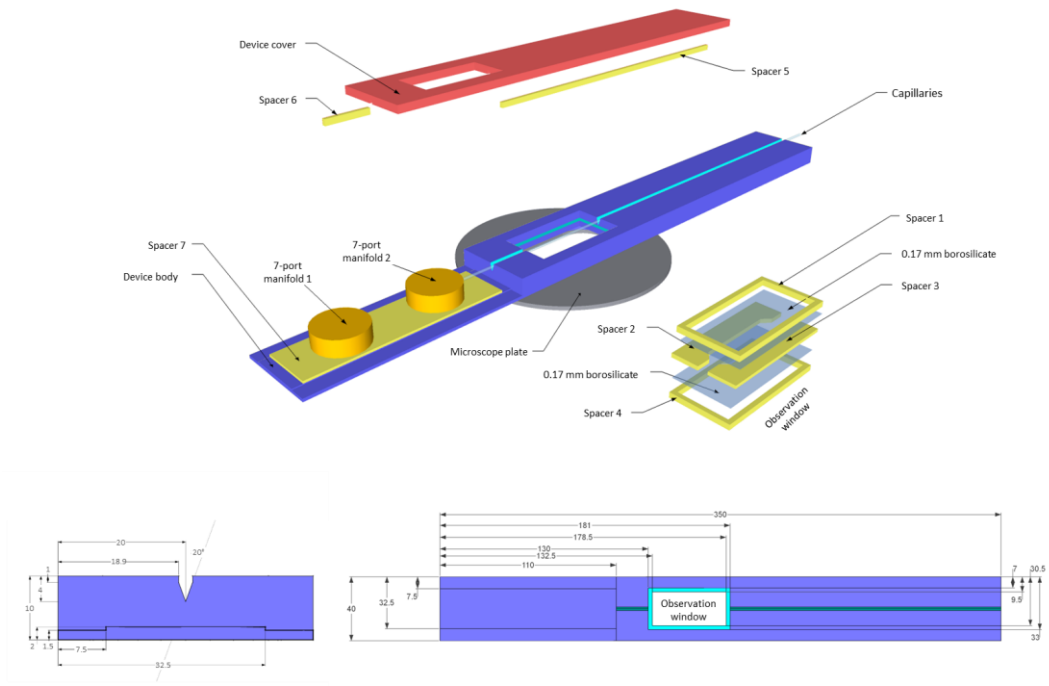


Figure 2.9. Design from the supporter for the microfluidic capillaries.

The detailed procedures and components for assembling the microfluidic system are attached in Appendix B.iii.i, and the frequently encountered problems in Appendix B.iv. The assembled microfluidic system is shown in Figure 2.10.

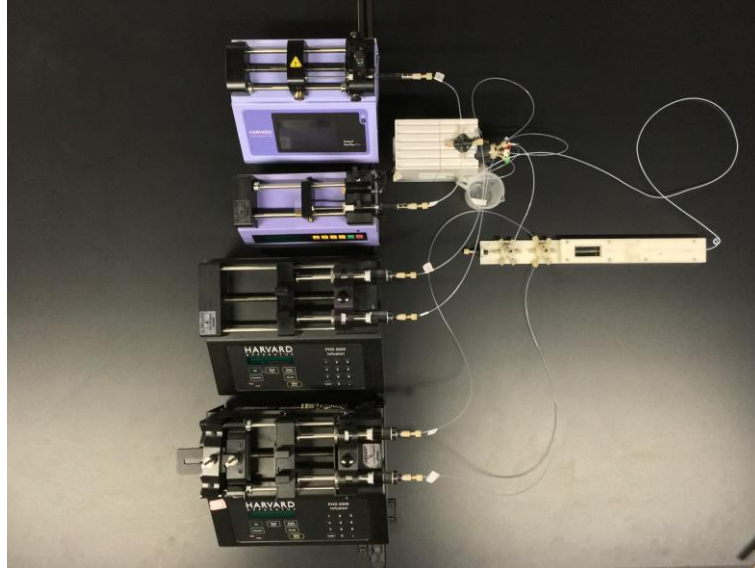


Figure 2.10. Assembled diffusive coaxial microflow antisolvent precipitation system.

The assembled microfluidic system was mounted on an inverted microscope (*Nikon Eclipse*, TE2000-U) for optic observation and FLIM analysis. A pulsed UV laser ($\lambda = 343\text{nm}$, $f_{\text{rep}} = 10\text{MHz}$, $\tau_p = 400\text{fs}$) was sent to the microfluidic channel through the microscope objective in a widefield configuration for fluorescence excitation, and a second pulsed IR laser ($\lambda = 1030\text{nm}$, $f_{\text{rep}} = 1 \sim 10\text{MHz}$, $\tau_p = 400\text{fs}$, $P_{\text{avg}} = 0 \sim 1.2\text{W}$) was focused at flow centre ($d_L, 0$), $d_L \in (0, d_p)$, to induce nucleation. The system was mounted on the X-ray line *SWING* of synchrotron *Soleil* for microfluidic SAXS experiment.

2.2. Laser and microscopy setup for microfluidic NPLIN and FLIM

The scheme of the laser and microscope setup is illustrated in Figure 2.11. Both the pulsed IR laser ($\lambda = 1030\text{nm}$) for nucleation induction and the pulsed UV laser ($\lambda = 343\text{nm}$) for fluorescence excitation came from a T-Pulse 200 self-mode-locked $\text{Yb}^{3+}:\text{KY}(\text{WO}_4)_2$ laser source ($\lambda = 1030\text{nm}$, $f_{\text{rep}} = 10\text{MHz}$, $\tau_p = 400\text{fs}$, $P_{\text{avg}} = 2.9\text{W}$, $\phi = 1.27\text{mm}$, *Amplitude Systemes*).

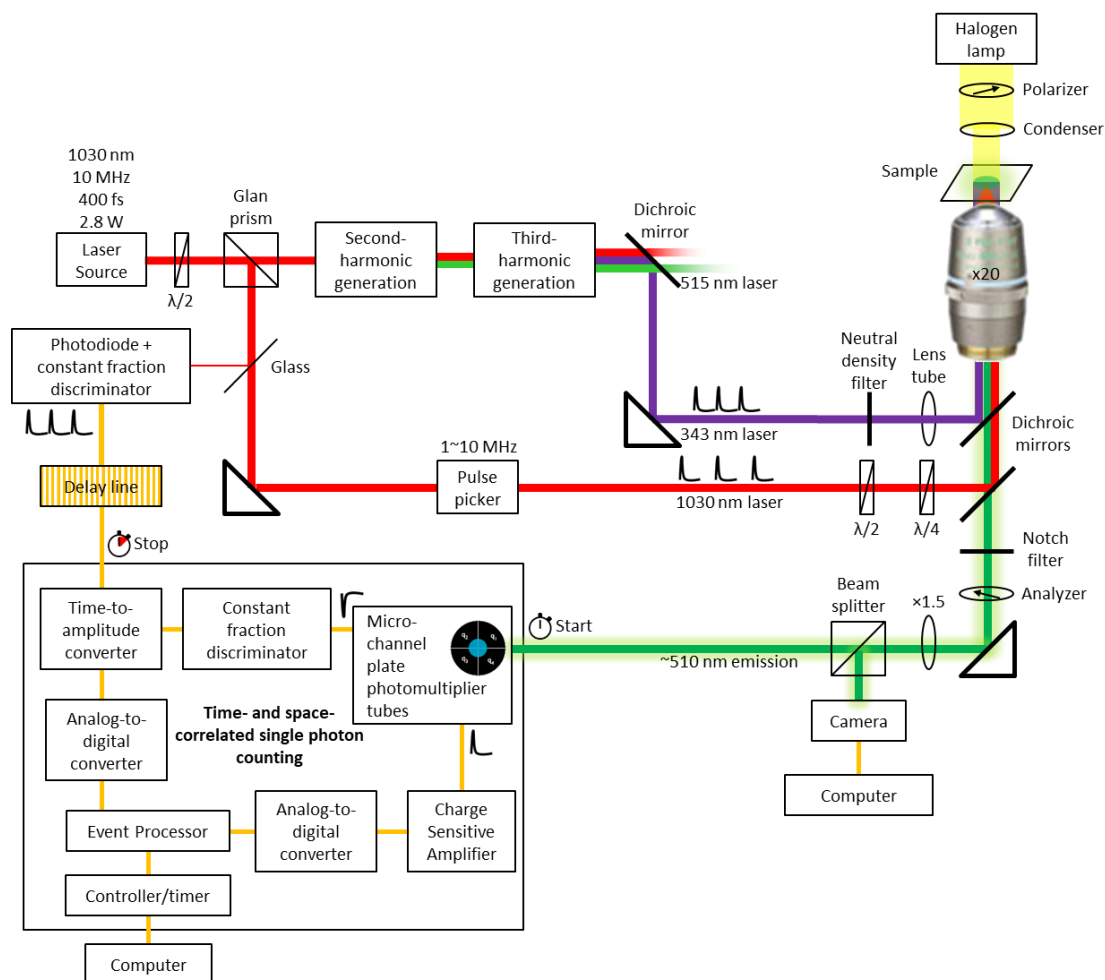


Figure 2.11. Schematic illustration of the laser and microscopy setup for microfluidic NPLIN and FLIM

The original 1030-nm laser beam first went through a half-wave plate, of which the angle θ rotates the linear polarisation of the beam by 2θ . The beam then passed a Glan prism, where s-polarised light was reflected towards the microscope for inducing nucleation and p-polarised light was transmitted to nonlinear optical crystals for generating a UV laser.

The p-polarised light transmitted by the Glan prism was sent to two β -BaB₂O₄ (BBO) non-linear crystals for frequency tripling. The newly generated pulsed 343-nm UV beam was sent to the microscope objective by aluminium mirrors in a widefield configuration, 220 μ m in diameter, to cover the microflow inside of the borosilicate capillary for fluorescence excitation. Its intensity was adjusted by neutral density filters to give the optimised photon count rate for

the Time- and Space-Correlated Single Photon Counting (TSCSPC) detector.

The average power of the IR laser was controlled by turning the half-wave plate, *i.e.* changing the ratio of the IR and UV laser intensities. After the Glan prism, about 5% of the reflected s-polarised light was reflected to a photodiode to generate the stop trigger after a delay line for the TSCSPC system; 95% of that beam entered a pulse picker, which adjusted the repetition rate of the IR laser. The average power of the IR laser after the pulse picker, P_r , was measured with a *SpectraPhysics* optical power meter for different half-wave plate angle θ and then for different repetition rate f_{rep} (see Appendix B.viii). The dependence of P_r on θ was fitted with equation

$$P_r = A \cdot P_o \cdot \cos^2 2\theta \quad (2.27)$$

where P_o is the average power of the laser source, 2.8 W, and A the transmission coefficient of the pulse picker, fitted to be 0.41, which means 60% of the power was lost inside the pulse picker. The dependence of P_r on f_{rep} was not strictly linear (see Appendix B.viii). This might be due to some clippings in the pulse picker.

After the pulse picker, another half-wave plate was mounted to adjust the linear polarisation of the IR laser beam, followed by a quarter-wave plate, to change the polarisation from linear to circular when needed. The IR beam was then reflected into the objective by a dichroic mirror and focused at the microflow centre to induce nucleation. The average power of the IR beam on the sample focal plane of the microscope was measured with an *Ophir* wattmeter for different polarisations with $P_r = 200\text{mW}$, shown in Table 2.2. The size and the intensity profile of the laser focal spot is attached in Appendix B.viii.

To reflect both lasers into the objective (20 \times /0.45, WD 7.4, *Nikon Plan Fluor*) by two dichroic mirrors, an inverted microscope (*Nikon Eclipse*, TE2000-U) had been modified to add a second filter block cassette holder above the original. $\times 1.5$ intermediate magnification was applied before all exit ports of the microscope. A notch filter was put below the dichroic mirrors

to pass only emission from the sample to the microscope exits. Crossed polarisers (CP) were mounted to examine the crystallinity of the phase transitions when necessary.

Table 2.2. Average power of the IR laser on the sample plane of different polarisations (P: parallel to flow; S: vertical to flow; CL: circular left-handed; CR: circular right-handed)

Polarisation	LPS	LPP	CPL	CPR
Power/mW	60	50	55	54
P_r /mW	200	200	200	200
Efficiency η	30%	25%	28%	27%

The dependence of the IR beam line reflection efficiency on polarisation was less than 5%. The average power of the IR laser reached the microflow centre is

$$P_{\text{avg}} = \eta P_r . \quad (2.28)$$

For circular polarisation, $\eta = 0.275$; for linear polarisation vertical to the flow direction, $\eta = 0.3$; and for linear polarisation parallel to the flow direction, $\eta = 0.25$

The configuration of the setup and corresponding experiment types are listed in Table 2.3. For optical microscopy (OM) and crystallinity observation, the signal was sent to a CCD camera (*Retiga R1, Qimaging*). Images and videos (0.01 ms exposure time, 12 frames per second) were taken with *Micro-Manager* and analysed with *ImageJ*.

Table 2.3. Laser and microscope configuration and type of experiment

Configuration	UV	IR+UV	Lamp	IR+lamp	Lamp+CP	IR+lamp+CP
Experiment type	FLIM	NPILN + FLIM	OM	NPLIN + OM	Crystallinity	NPLIN + crystallinity

For FLIM measurement, the emission was sent to the TSCSPC system. The MCP-PM detector (spatial resolution 40 μm , time resolution 60 ps, *Photonscore GmbH*) generated a start trigger and recorded the position of the fluorescence photon. Stop trigger was generated by the next IR pulse through a delay line. The data was collected and processed with *LnTCapture* software in real-time. The recorded fluorescence decays and lifetime images/videos were

analysed with homemade *Igor* macros.



Figure 2.12. Laser and microscope setup for microfluidic NPLIN and FLIM mounted with the microfluidic system.

2.3. Microfluidic parametric sweep and NPLIN

By continuously changing Q_I , Q_{II} , Q_{III} and Q_{IV} , microfluidic parametric sweep of a four dimensional matrix of ρ_{3c} , ϕ_p , Q_c and Q_p was carried out for water (1)-1,4-dioxane (2)-DBDCS (3) system, as shown in Figure 2.13. For $\rho_{3c} = 10\text{g/l}$ and $\rho_{3c} = 16\text{g/l}$, the mother solution, Q_I , was an supersaturated solution dissolved at 60 °C for 24 hours and then kept in syringes at ambient temperature during the experiment.

Efficacy of NPLIN was tested during microfluidic parametric sweep. Impact of the average power P_{avg} , the repetition rate f_{rep} , the distance of focal spot from injection nozzle d_L , and the polarisation of the pulsed IR beam were investigated.

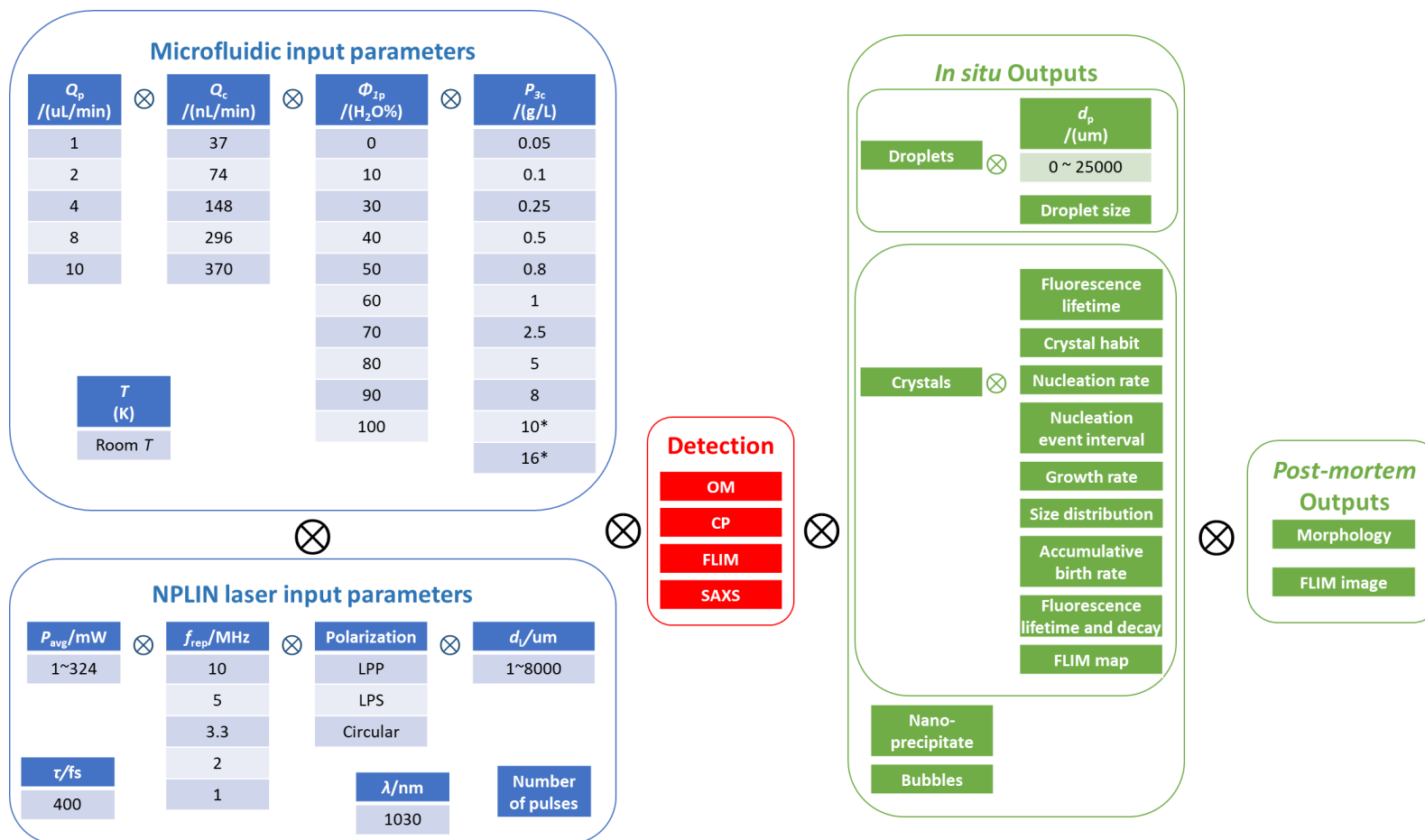


Figure 2.13. Parametric matrix of the experimental inputs and outputs for water (1)-1,4-dioxane (2)-DBDCS (3) system. * denotes supersaturated mother solution.

By OM, direct observation of the morphology and the amount of the precipitate was carried out. The average nucleation event interval $\overline{d_N}$ and the velocity of the centre of the laminar flow v_{\max} were measured. The crystal birth rate, B_x , was derived by equation (2.3). Average size $\overline{A_c}$ (area on image) of the precipitate was measured at different positions along the flow. The value of the distance of each measurement to the injection nozzle x , the precipitation starting position d_p , and the IR laser focus position d_L , were read from a calliper fixed on the microscope stage parallel to the microflow (Figure 2.14).

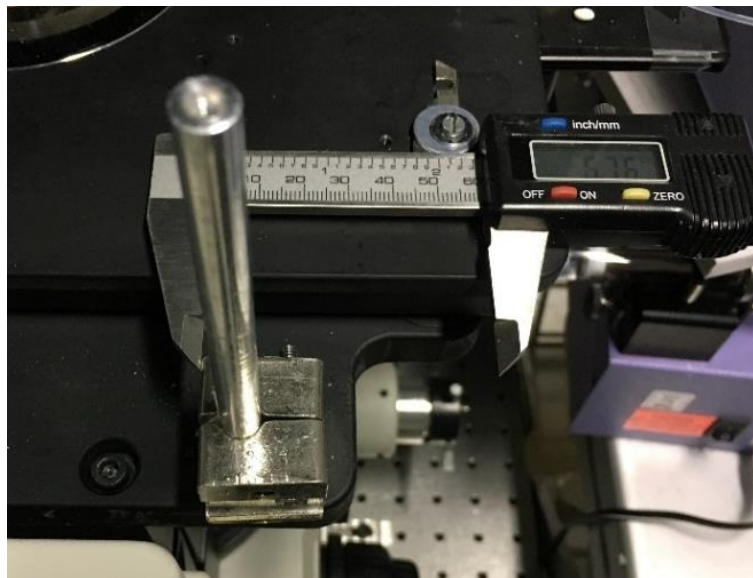


Figure 2.14. Calliper fixed on the microscope stage to measure distance in the microflow.

Because the precipitates were moving alongside the microflow, in many cases, the microscope stage needed to be moved manually to follow the precipitate. The UV laser and IR laser went through the same objective of OM, whereas the growth of the laser-induced nucleation mainly happened outside the field of view of OM. For that we needed to chase the laser-induced precipitates by moving the microscope stage. An adjustable microscope stage movement blocker (Figure 2.15) was installed to limit the distance of each chase. Thus, by turning on the IR laser at the same position, but observing at different distances along the flow,

the laser-induced crystal birth rate B_x (equation (2.3)) and the area growth rate g_A were measured and compared with spontaneous crystallisation.

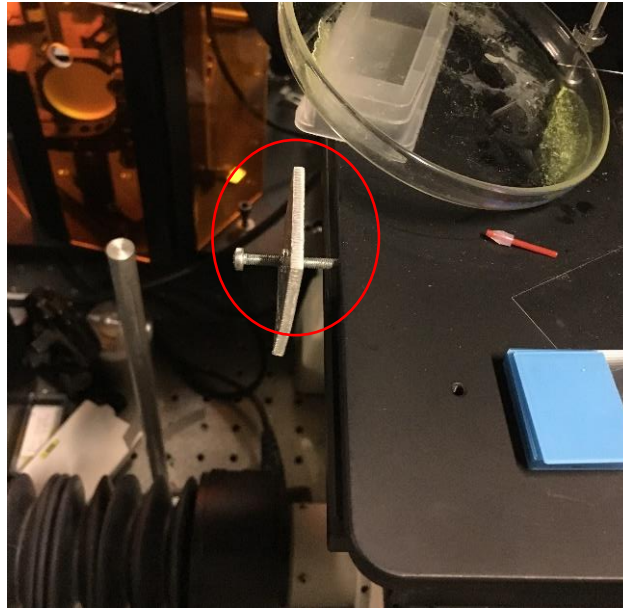
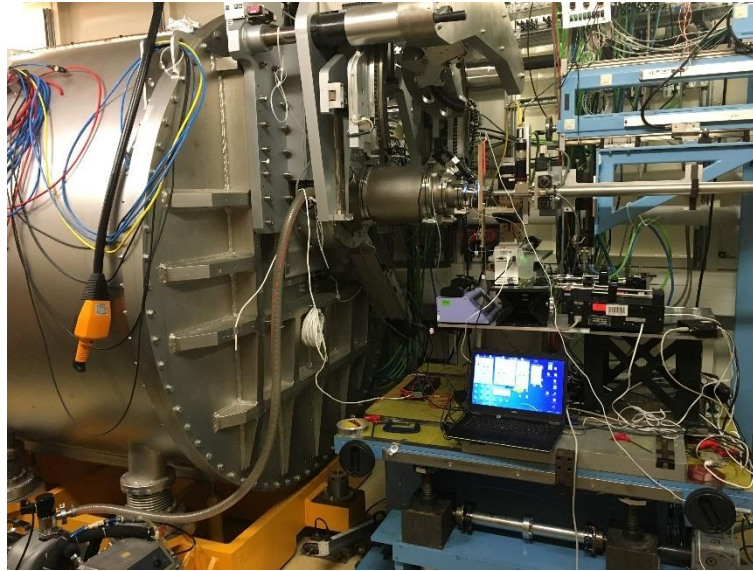


Figure 2.15. Adjustable microscope stage movement blocker (in the red circle).

Preliminary tests of the crystallinity of the precipitates was through CP, as birefringent objects will appear bright in a dark background. The crystalline structure of the precipitate was measured by a microfluidic SAXS at *SWING* line (Figure 2.16) of synchrotron *Soleil* and compared with published data.



*Figure 2.16. The microfluidic system mounted on X-ray line SWING of synchrotron
Soleil.*

The fluorescence decays of the precipitates and the lifetime images of the microflow were taken for typical precipitation conditions along the flow. The species precipitated along the flow were analysed by principal component analysis (PCA) of the fluorescence decays. The maximum velocity of the laminar flow, v_{\max} , was measured by the width of the field of view divided by the time the particles flew across the field of view (residence time) in the flow centre. Knowing v_{\max} , by measuring a second residence time of the particles through a line vertical to the flow, the radius of each particle was taken. A second quantity representing the size of a fluorescent particle is its fluorescence intensity.

Together with experimental inputs and outputs, a multi-dimensional matrix of data was constructed in Excel. From that the precipitation types were plotted against the final mass concentration of species 3, $\rho_{3\text{mix}}$, and the final volume fraction of species 1, $\phi_{1\text{mix}}$, to obtain a phase diagram in the microfluidic system.

Chapter conclusion

A coaxial microfluidic device has been developed. The central jet of the solute in the

good solvent inter-diffuses into a peripheral flow of a mixture of anti- and good solvent. Different supersaturation and flow velocity will be reached, depending on the microfluidic input parameters: the mass concentration of the central flow ρ_{3c} , its flow rate Q_c , the volume fraction of the antisolvent in the peripheral flow ϕ_{1p} , and its flow rate Q_p . The system can be easily cleaned by a solvent switching module in case of clogging.

Some variables that will be used in later chapters has been defined: the spontaneous phase transition starting distance d_p , the position of the NPLIN IR laser d_L , the nucleation event interval t_N in time and d_N in distance, the accumulative crystal birth rate B_x , and the

$$\text{average nucleation rate on a cross section } N = \frac{1}{\pi R_{\text{channel}}^2} \frac{dB_x}{dx} \quad (\text{equation (2.4)}).$$

The more important parameters for the hydrodynamics are the flow ratio Q_c/Q_p and the total flow rate $Q_c + Q_p$, since the maximum central jet radius

$$r_{c,\text{max}} = R_{\text{channel}} \cdot \sqrt{1 - \frac{1}{\sqrt{1 + \frac{Q_c}{Q_p}}}} \quad (\text{equation (2.14)}), \text{ and the flow velocity at the flow centre}$$

$$v_{\text{max}} \approx 2 \cdot \frac{Q_c + Q_p}{\pi \cdot R_{\text{channel}}^2} \quad (\text{equation (2.19)}). \text{ The maximum diameter of the central jet has been}$$

measured and will be used to assure the flow rates reaching the target values.

The more important parameters for the thermodynamics are the overall solute concentration and the total volume fraction of the antisolvent, since the solubility in the mixture is given by Jouyban-Acree model [Jouyban, 2007]

$$x_{3\text{smix}} = x_{3s1}^{\phi_1^o} \cdot x_{3s2}^{\phi_2^o} \exp \left(\phi_1^o \phi_2^o \sum_{n=0}^2 \frac{A_n (\phi_2^o - \phi_1^o)^n}{T} \right) \quad (\text{equation (2.24)}), \text{ the overall}$$

supersaturation $\Delta x_3 = x_{3\text{mix}} - x_{3\text{smix}}$ (equation (2.25)), and the supersaturation ratio

$$\beta = \frac{x_{3\text{mix}}}{x_{3\text{smix}}} \text{ (equation (2.26)).}$$

The microfluidic system is coupled of a focused fs IR laser and a WF fs UV laser for the possibility of laser-induced nucleation and the *in situ* detection of the early stage of nucleation, respectively. As an easily transportable device, it was also mounted on the *SWING* X-ray beamline at the synchrotron *Soleil* for *in situ* SAXS.

To explore the conditions for the spontaneous and the laser-induced nucleation in the microfluidic mixer, a parametric sweep of the microfluidic parameters ρ_{3c} , Q_c , ϕ_{lp} , Q_p , and the laser parameters f_{rep} , P_{avg} , d_L , and its polarisation was planned. The phase transition process can be followed by *in situ* OM, CP, FLIM, and SAXS. The product can also be collected for *post-mortem* characterisation.

Chapter 3. Thermodynamics of water (1)-1,4-dioxane

(2)-DBDCS (3) ternary system

3.1. Molar excess mixing volume, dynamic viscosity, and refractive indices by Redlich-Kister equation	76
3.2. Thermodynamics of antisolvent-solvent-solute ternary mixing	80
3.2.1. Ideal mixing model.....	80
3.2.2. Regular mixing model	83
3.2.3. H ³ M model for real solvent mixing	90
3.2.4. Jouyban-Acree equation for solubility prediction of slightly soluble solute in aqueous-organic mixture with H ³ M model	91
3.3. Applying the H³M model to water (1)-1,4-dioxane (2)-DBDCS (3) irregular ternary system	93
3.3.1. Solubility of DBDCS in water (1)-1,4-dioxane (2) mixture.....	93
3.3.2. Thermodynamic parameters of water (1)-1,4-dioxane (2)-DBDCS (3) ternary system	95
3.4. Brief introduction to thermodynamics of diffusion.....	100
3.4.1. Intrinsic diffusion coefficient.....	100
3.4.2. Mutual diffusion coefficients.....	105
3.5. Diffusion of water (1)-1,4-dioxane (2)-DBDCS (3) mixture.....	107
3.5.1. Estimation of the diffusion coefficients of water (1)-1,4-dioxane (2) binary system with Moggridge equation	107
3.5.2. Estimation of the diffusion coefficient of DBDCS in binary system of water (1)-1,4-dioxane (2)	109
3.6. Thermodynamic stability of water (1)-1,4-dioxane (2)-DBDCS (3) ternary mixture	113
3.6.1. Liquid-liquid phase separation (LLPS).....	113
3.6.2. Crystallisation from antisolvent-solvent mixture	124
Chapter conclusion.....	125

Thermodynamics of the ternary system of the solvent-antisolvent-solute is the foundation for understanding its mixing properties, phase transitions, and computational simulation. DBDCS (3) is a rare molecule, and little of its thermodynamic data has been published, whereas water (1)-1,4-dioxane (2) binary system has been well studied. Since DBDCS (3) in the mixture is less than 0.003 in amount fraction or 16 g/l in mass concentration, we shall treat DBDCS (3) as a solute. In all the sections in this chapter, we shall first examine water (1)-1,4-dioxane (2) binary system and then discuss the ternary system.

This chapter deals with the thermodynamics of water (1)-1,4-dioxane (2)-DBDCS (3). The basic mixing properties of the mixture, including the density, dynamic viscosity, refractivity, and surface energy are estimated in section 3.1 from literatures. Then, we introduce the thermodynamics of ternary mixtures in section 3.2, from ideal solution to irregular solution models. In section 3.3, we extrapolate the interaction parameters from the solubility of DBDCS in water (1)-1,4-dioxane (2) mixture to the ternary system of water (1)-1,4-dioxane (2)-DBDCS (3) using the H³M model and the Acree-Jouyban equation. The thermodynamic activity of water (1)-1,4-dioxane (2) mixture [Vierk, 1950] is attached in Appendix C.i. A discussion on this extrapolation using the H³M model and the Acree-Jouyban equation is included in Appendix C.ii. An estimation of the melting point, the melting enthalpy and entropy is done in Appendix C.iii, and compared with the experimental measurement (Figure Appen.C.4) [Yoon, 2010]. In section 3.4, we briefly introduce the thermodynamics of diffusion, the intrinsic and mutual diffusion coefficients. Some recent development of mutual diffusion coefficient of self-associating species is introduced in Appendix C.iv. Nevertheless, we are looking for a simple but effective prediction for the diffusion velocity and flux. Our estimation of the diffusion coefficients of water (1)-1,4-dioxane (2)-DBDCS (3) is described in section 3.5. Analysis of the stability of water (1)-1,4-dioxane (2)-DBDCS (3) mixture based on free energy and diffusion is detailed in section 3.6. From that a thermodynamic phase diagram of water (1)-1,4-dioxane (2)-DBDCS (3) has been calculated.

3.1. Molar excess mixing volume, dynamic viscosity, and refractive indices by Redlich-Kister equation

The excess molar mixing volume contribute to the non-ideality of the mixture: $\Delta_{\text{mix}} G_m = \Delta_{\text{mix}} H_m - T\Delta S_m = \Delta_{\text{mix}} U_m + p\Delta_{\text{mix}} V_m - T\Delta_{\text{mix}} S_m$. Other mixing properties needed in the calculation part of this thesis include refractive index n_D , dynamic viscosity $\dot{\mu}$, density ρ_D , and surface tension γ .

Some basic physical properties used in this thesis are listed in Table 3.1. The size of DBDCS molecule is 563.74 \AA^3 determined by *CrystalExplorer* based on its structure in the solid state. Assuming its solute state takes 10~15% more volume, *i.e.* $620\sim 648 \text{ \AA}^3$, 635 \AA^3 was taken as the size of DBDCS* molecule, V_{3^*} . Then, its mole volume $V_{m,3^*} = N_A V_{3^*} = 382.40 \text{ ml/mol}$ and its density $\rho_{D,3^*} = \frac{M_3}{V_{m,3^*}} = 1246.35 \text{ g/l}$.

*Table 3.1. Basic physical properties of the materials in this thesis at 298.15 K: dynamic viscosity $\dot{\mu}$, surface tension γ , molar surface A_m , density ρ_D , refractive index n_D , molar refractivity R_m , molar mass M and molar volume V_m . * denotes calculation of a solute state.*

Species number	Species	$\dot{\mu}$ /(mPa·s)	γ /(mN/m)	A_m /(m ² /mol)	ρ_D /(g/l)	n_D	R_m /(cm ³ /mol)	M /(g/mol)	V_m /(ml/mol)
1	Water	0.891	71.98	0.7225E4	997.3	1.3324	3.713	18.015	18.06
2	1,4-Dioxane	1.172	32.8	12.27E4	1028.6	1.4167	21.673	88.11	85.66
3	DBDCS*				1246.35*			476.6	382.40*

The mixing properties of water (1)-1,4-dioxane (2) binary system can be fitted to the Redlich-Kister equation by means of least-squares estimation of nonlinear parameters. The mixing molar volume V_m , dynamic viscosity $\dot{\mu}$, molar refractivity R_m , and refractive index n_D of water (1)-1,4-dioxane (2) binary system at 298.15 K have been measured and fitted to

Redlich-Kister equation by [Aminabhavi, 1995]. They made a mistake on the equation for the mole refractivity. A more recent paper by [Besbes, 2009] on density and dynamic viscosity of water (1)-1,4-dioxane (2) mixture at 298.15 K has made an error with the unit of the fitting parameters by 3 orders of magnitude. The right relation for refractivity of the mixture of water (1)-1,4-dioxane (2) at 297.15 K is given by [Schott, 1961]. Therefore, measurements by Aminabhavi *et al* [Aminabhavi, 1995] was used in this work with the fitting parameters listed in Table 3.2 and the fitting curve plotted in Figure 3.1.

Table 3.2. Parameters of mixing functions for binary mixtures of H₂O and 1,4-dioxane[Aminabhavi, 1995]

Function	A ₀	A ₁	A ₂	A ₃	A ₄
V _m /(ml/mol)	-2.496	1.756	-0.703	0.204	-0.462
$\dot{\mu}$ /(mPa·s)	2.399	-3.769	3.583	-0.723	-1.471

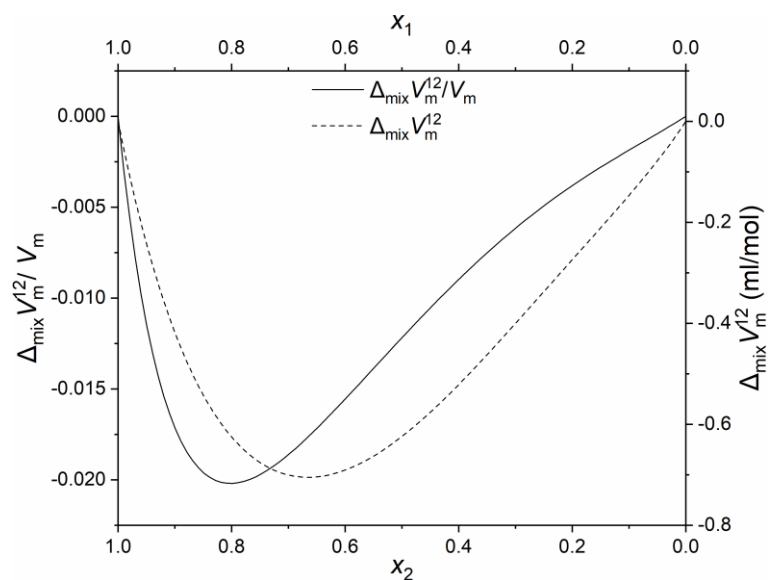


Figure 3.1. Molar excess mixing volume of water (1)-1,4-dioxane (2) binary mixture at 298.15 K [Aminabhavi, 1995].

Figure 3.1 shows that the molar excess mixing volume of water (1)-1,4-dioxane (2) is less than -0.7 ml/mol or -2%. The contribution from the molar excess volume to the molar excess free energy is therefore negligibly, only -0.07 J/mol at maximum.

As for the contribution from DBDCS, the volume of DBDCS in solution can be estimated. Its contributions to the mixture's n_D and $\ddot{\mu}$ are unknown. In this work, the refractive indices are only needed for simulation of water (1)-1,4-dioxane (2). Acree and Jouyban have shown, with the H³M model, that the property of an aqueous-organic-solute mixture can be estimated with the contributions from the solvents, providing a miniscule solute amount fraction. Since the amount fraction of DBDCS (3) is miniscule in the whole solvent composition range, the dynamic viscosity of the ternary mixture is estimated neglecting the contribution from DBDCS (3).

Because the concentration of DBDCS (3) was very diluted and DBDCS (3) molecule is much larger than water and 1,4-xioxane, let us assume that DBDCS has no influence on water (1)-1,4-dioxane (2) interactions with negligible excess mixing volume. Thus, the local mixing volume of the ternary system of water (1)-1,4-dioxane (2)-DBDCS (3) was estimated as (*cf.* equation (2.10))

$$\begin{aligned} V_m &= (x_1 + x_2) \left(\frac{x_1}{x_1 + x_2} V_{m,1} + \frac{x_2}{x_1 + x_2} V_{m,2} + \frac{x_1 x_2}{(x_1 + x_2)^2} \sum_{n=0}^4 A_n \left(\frac{x_2 - x_1}{x_1 + x_2} \right)^n \right) + x_3 V_{m,3} \\ &= x_1 V_{m,1} + x_2 V_{m,2} + \frac{x_1 x_2}{x_1 + x_2} \sum_{n=0}^4 A_n \left(\frac{x_2 - x_1}{x_1 + x_2} \right)^n + x_3 V_{m,3} \end{aligned} \quad (3.1)$$

with the mixing parameters A_n published by [Aminabhavi, 1995] for water (1)-1,4-dioxane (2) binary system ([Aminabhavi, 1995]). The density of the mixture is

$$\rho_D = \frac{x_1 M_1 + x_2 M_2 + x_3 M_3}{V_m} \quad (3.2)$$

The contribution to the dynamic viscosity from the solute state of DBDCS is unknown. Since it was diluted, neglecting the contribution from DBDCS molecules, local dynamic viscosity of the mixture was approximated as the mixing dynamic viscosity of binary system of water (1)-1,4-dioxane (2) [Aminabhavi, 1995]:

$$\ddot{\mu} = \frac{x_1}{x_1 + x_2} \ddot{\mu}_1 + \frac{x_2}{x_1 + x_2} \ddot{\mu}_2 + \frac{x_1 x_2}{(x_1 + x_2)^2} \sum_{n=0}^4 A_n \left(\frac{x_2 - x_1}{x_1 + x_2} \right)^n \quad (3.3)$$

[Aminabhavi, 1995]'s equation for the molar refractivity is wrong, which led to a wrong simulation of the refractive index of the mixture in our *Comsol* simulation. The right relation is given by [Schott, 1961]:

$$R_m = \frac{\phi_1}{\phi_1 + \phi_2} R_{m,1} + \frac{\phi_2}{\phi_1 + \phi_2} R_{m,2} \quad (3.4)$$

with ϕ_1 and ϕ_2 the local volume fraction of water (1) and 1,4-dioxane (2), $R_{m,1}$ and $R_{m,2}$ their molar refractivity. The local refractive indices of the microflow can be calculated from the molar refractivity and a good estimated of the mixing density:

$$n_D = \sqrt{\frac{M_n + 2R_m \rho_D}{M_n - R_m \rho_D}} \quad (3.5)$$

with M_n the local mean molar mass.

The surface tension of a liquid mixture in air can be estimated by

$$\gamma = \frac{\sum \gamma_i A_{m,i} x_i}{\sum A_{m,i} x_i} \quad (3.6)$$

with γ_i the surface tension of species i , $A_{m,i}$ its molar surface area and x_i its amount fraction.

The molar surface areas of water (1) and 1,4-dioxane (2) were measured by [Suarez, 1989] and listed in Table 3.1. The surface tension of water (1)-1,4-dioxane (2) has been reported by [Wohlfarth, 2008].[Suarez, 1989][Suarez, 1989][Suarez, 1989][Suarez, 1989][Suarez, 1989]

Figure 3.2 compares of the experimental values of the mixing properties of water (1)-1,4-dioxane (2) mixture with the equations we shall use.

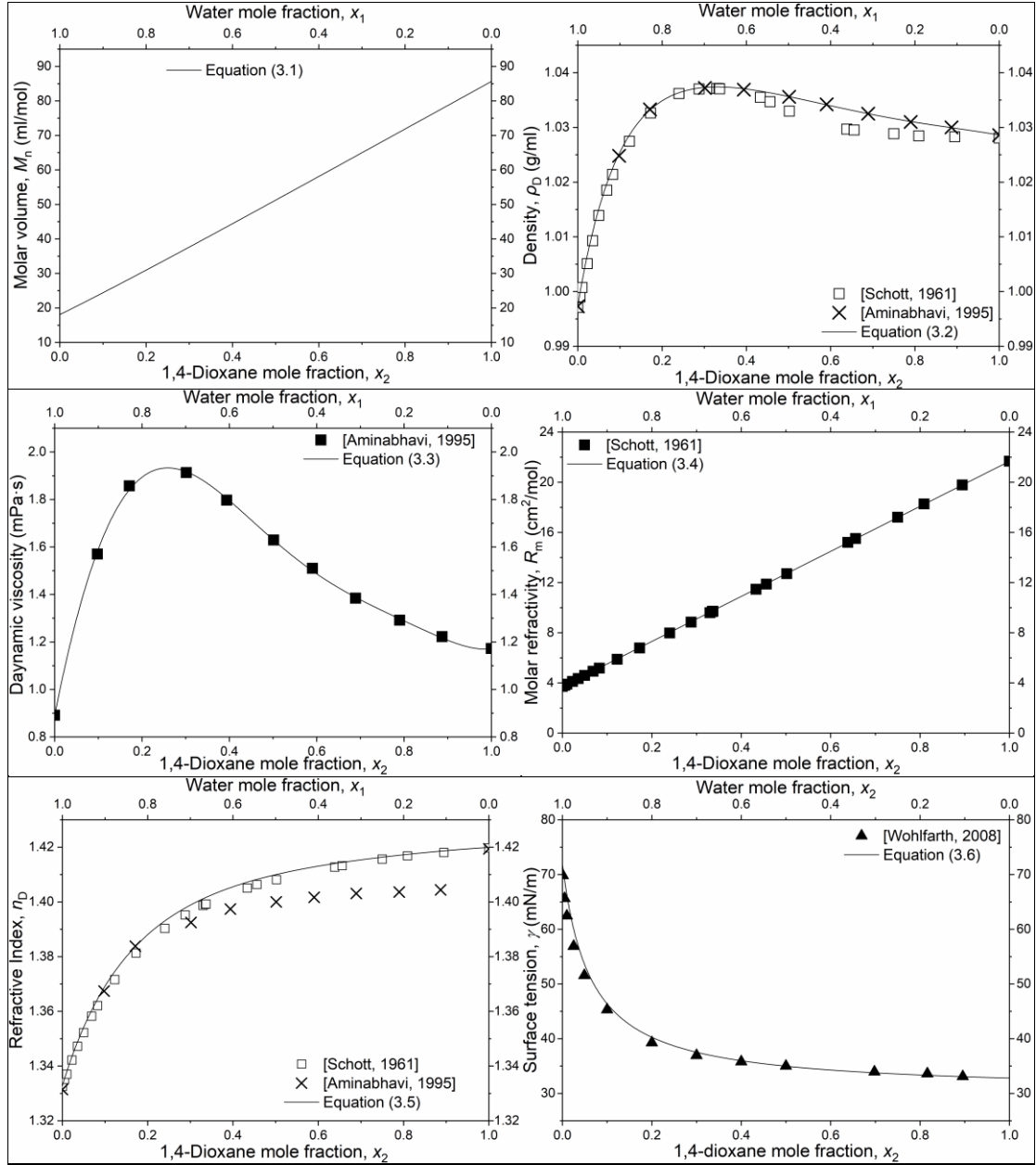


Figure 3.2. Estimation and experimental values of the mixing properties of water (1)-1,4-dioxane (2) binary system at 298.15 K.

3.2. Thermodynamics of antisolvent-solvent-solute ternary mixing

3.2.1. Ideal mixing model

For an ideal mixture, the mixing is fully random and the interaction between species is equivalent or zero. Before mixing, the molar Gibbs energy of the system,

$$G_m^o = x_1 G_{m,1}^o + x_2 G_{m,2}^o + x_3 G_{m,3}^o \quad (3.7)$$

with x_i the amount fraction of species i (1 denotes antisolvent, 2 good solvent, and 3 solute), $G_{m,i}^o$ the molar Gibbs energy the pure substance (chemical potential μ_i^o).

For liquid solvents, $G_{m,i}^o$ is a simple standard reference state of the pure liquid, whereas for a solid solute, the mixing can be regarded as first melting of the solid and then dissolving of the melt by introducing a hypothetical pure liquid state, denoted by *:

$$\begin{aligned} G_{m,3}^* &= G_{m,3}^o + \Delta_{\text{melt}} H_{m,3} \left(1 - \frac{T}{T_{\text{melt},3}^*} \right) \\ &= G_{m,3}^o + T_{\text{melt},3}^* \Delta_{\text{melt}} S_{m,3} \left(\frac{\Delta T}{T_{\text{melt},3}^*} \right) . \\ &= G_{m,3}^o + \Delta_{\text{melt}} S_{m,3} \Delta T \end{aligned} \quad (3.8)$$

with $\Delta_{\text{melt}} H_{m,3}$ its molar hypothetical fusing enthalpy, $T_{\text{melt},3}^*$ the hypothetical melting point, and ΔT the supercooling. Using this hypothetical liquid state as the reference state of the solute, before mixing

$$G_m^{o*} = x_1 G_{m,1}^o + x_2 G_{m,2}^o + x_3 G_{m,3}^* \quad (3.9)$$

and after mixing,

$$G_m = x_1 G_{m,1}^o + x_2 G_{m,2}^o + x_3 G_{m,3}^* + p \Delta_{\text{mix}} V_m + \Delta_{\text{mix}} U_m - \Delta_{\text{mix}} S_m T , \quad (3.10)$$

with p the pressure, ΔV_m the excess mixing molar volume, ΔU_m the molar excess mixing internal energy, ΔS_m the molar mixing entropy, and T the temperature.

The molar mixing configurational entropy of a fully random mixing is given by the Boltzmann equation and the Stirling equation:

$$\begin{aligned} \Delta_{\text{mix}} S_m &= k_B \ln \left(\frac{N_A!}{x_1 N_A! x_2 N_A! x_3 N_A!} \right) . \\ &= -R(x_1 \ln x_1 + x_2 \ln x_2 + x_3 \ln x_3) \end{aligned} \quad (3.11)$$

Whereas ΔV_m and ΔU_m are zero for ideal mixtures. Therefore,

$$G_m = x_1 G_{m,1}^o + x_2 G_{m,2}^o + x_3 G_{m,3}^* + RT (x_1 \ln x_1 + x_2 \ln x_2 + x_3 \ln x_3) . \quad (3.12)$$

Keeping the amount fraction of any species equal to zero will give the equations for ideal mixing of the rest two species.

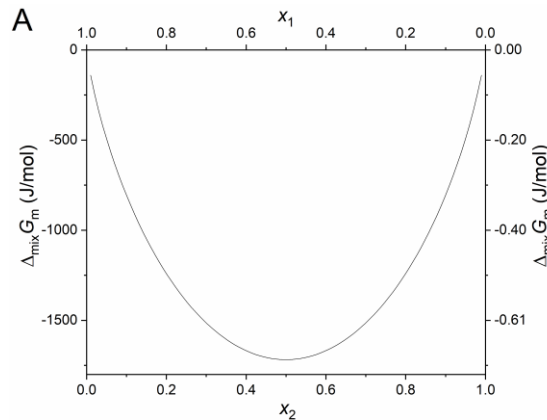
The chemical potential of solvent i in ideal mixture is

$$\begin{aligned} \mu_i &= \frac{\partial G}{\partial n_i} \\ &= \frac{\partial \sum_i n_i G_m}{\partial n_i} \\ &= \mu_i^o + RT \ln x_i \end{aligned} \quad (3.13)$$

with $\mu_i^o = G_{m,i}^o$, and for the solute,

$$\mu_3 = \mu_3^* + RT \ln x_i . \quad (3.14)$$

Figure 3.3 shows $\Delta_{\text{mix}} G_m = G_m - G_m^{o*}$ of binary and ternary systems using pure liquid as reference states. Since the mixing is fully random with no excess enthalpy, $\Delta_{\text{mix}} G_m$ is always negative and symmetric with only one minimum at the geometric centre. By comparing the ternary and binary ideal solution, it is noticeable that as the third component being added, the mixing entropy further increases. $\Delta_{\text{mix}} G_m$ goes down to minimum at the centre of the triangle. With zero or equivalent interaction energies, the species are always miscible.



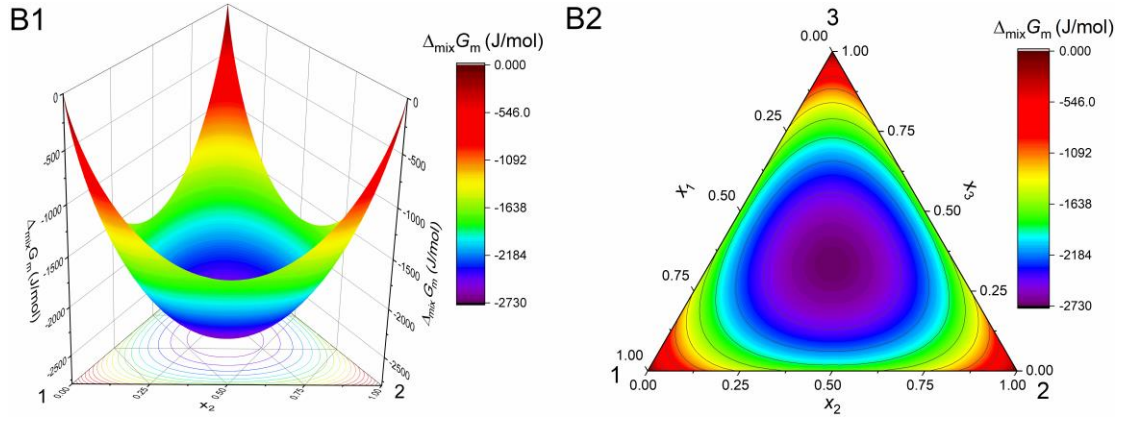


Figure 3.3. Stability of ideal solutions. $\Delta_{\text{mix}}G_m$ of ideal binary (A) and ternary (B) mixtures at 298.15 K are shown. B2 is B1 flattened. Ideal mixtures are always stable.

3.2.2. Regular mixing model

Assuming a hypothetical average coordinate number Z with only two-body interactions in a fully random ternary mixture, neglecting three-body and higher order interactions,

$$U_m^o = \frac{1}{2} x_1 N_A Z \epsilon_{11} + \frac{1}{2} x_2 N_A Z \epsilon_{22} + \frac{1}{2} x_3 N_A Z \epsilon_{33} , \quad (3.15)$$

and

$$U_m = \frac{1}{2} x_1 N_A Z x_1 \epsilon_{11} + \frac{1}{2} x_2 N_A Z x_2 \epsilon_{22} + \frac{1}{2} x_3 N_A Z x_3 \epsilon_{33} + x_1 N_A Z x_2 \epsilon_{12} + x_2 N_A Z x_3 \epsilon_{23} + x_1 N_A Z x_3 \epsilon_{13} \quad (3.16)$$

Therefore

$$\begin{aligned} \Delta_{\text{mix}}U_m &= x_1 x_2 N_A Z \left(\epsilon_{12} - \frac{1}{2} (\epsilon_{11} + \epsilon_{22}) \right) + x_3 x_1 N_A Z \left(\epsilon_{13} - \frac{1}{2} (\epsilon_{11} + \epsilon_{33}) \right) \\ &\quad + x_2 x_3 N_A Z \left(\epsilon_{23} - \frac{1}{2} (\epsilon_{22} + \epsilon_{33}) \right) \\ &= x_1 x_2 \Omega_{12} + x_2 x_3 \Omega_{23} + x_3 x_1 \Omega_{13} \end{aligned} \quad (3.17)$$

with ϵ_{ij} the mole interaction energy of i - j contact and Ω_{ij} the interaction parameter between species i - j . Therefore, the Gibbs energy of the system after mixing,

$$\begin{aligned}
G_m &= x_1 G_{m,1}^o + x_2 G_{m,2}^o + x_3 G_{m,3}^* + p\Delta V_m \\
&+ x_1 x_2 \Omega_{12} + x_2 x_3 \Omega_{23} + x_3 x_1 \Omega_{13} \quad . \\
&+ RT (x_1 \ln x_1 + x_2 \ln x_2 + x_3 \ln x_3)
\end{aligned} \quad (3.18)$$

ΔV_m is usually negligible unless the size of the species is too different, while ΔU_m cannot be treated as insignificant compared to the mixing entropy unless the interaction parameters are minor compared to RT .

The chemical potential of solvent i in regular solution model,

$$\begin{aligned}
\mu_i &= \frac{\partial G}{\partial n_i} \approx \frac{\partial F}{\partial n_i} = \frac{\partial \sum_i n_i F_m}{\partial n_i} \\
&= \mu_i^o + RT \ln x_i + (1 - x_i) (x_j \Omega_{ij} + x_3 \Omega_{i3}) - x_j x_3 \Omega_{j3} \quad .
\end{aligned} \quad (3.19)$$

Its thermodynamic activity a_i and activity coefficient γ_i ,

$$\begin{aligned}
\ln a_i &= \ln \gamma_i x_i \\
&= \ln x_i + \frac{1}{RT} \left((1 - x_i) (x_j \Omega_{ij} + x_3 \Omega_{i3}) - x_j x_3 \Omega_{j3} \right)
\end{aligned} \quad (3.20)$$

In the case of a solute,

$$\begin{aligned}
\mu_3 &= \mu_3^* + RT \ln x_3 + (1 - x_3) (x_1 \Omega_{13} + x_2 \Omega_{23}) - x_1 x_2 \Omega_{12} \\
\ln a_3 &= \ln \gamma_3 x_3 = \ln x_3 + \frac{1}{RT} \left((1 - x_3) (x_1 \Omega_{13} + x_2 \Omega_{23}) - x_1 x_2 \Omega_{12} \right)
\end{aligned} \quad (3.21)$$

Keeping the amount fraction of any species zero gives the binary regular solution model. The hypothetical Gibbs energy change of binary and ternary regular solutions with different interaction parameter Ω using pure liquids as reference states are shown in Figure 3.4 and Figure 3.5 respectively.

Figure 3.4 shows that, when $\Omega_{ij} = N_A Z \left(\epsilon_{ij} - \frac{1}{2} (\epsilon_{ii} + \epsilon_{jj}) \right) < 0$, the mixing is exothermic, the free energy is lower than ideal mixture, and the attraction between different species is larger than that between same species, which means not only the mixing is favourable,

but also the association between different species is likely to happen; with $\Omega_{ij} = N_A Z \left(\epsilon_{ij} - \frac{1}{2}(\epsilon_{ii} + \epsilon_{jj}) \right) = 0$, the solution is an ideal solution; with $0 < \Omega_{ij} = N_A Z \left(\epsilon_{ij} - \frac{1}{2}(\epsilon_{ii} + \epsilon_{jj}) \right) < 2RT$, the mixing is endothermic, the interaction energy between different species is greater than that between the same species, which means the species are slightly repelling each other, yet the mixture is still stable because the mixing entropy overcomes ΔH ; if Ω_{ij} is about $2RT$, the mixture is at its critical point; when $2RT < \Omega_{ij} = N_A Z \left(\epsilon_{ij} - \frac{1}{2}(\epsilon_{ii} + \epsilon_{jj}) \right)$, two minima of $\Delta_{mix} G_m$, a and b, appeared, the fully random arrangement of all the molecules is no longer stable, self-associating and segregation is favoured by thermodynamics, a mechanical mixture of two new phases of x_a and x_b will be more stable than the homogeneous solution. The regular mixture between a and b will decompose to phase a and phase b. x_a and x_b are the mutual solubilities of the two liquids.

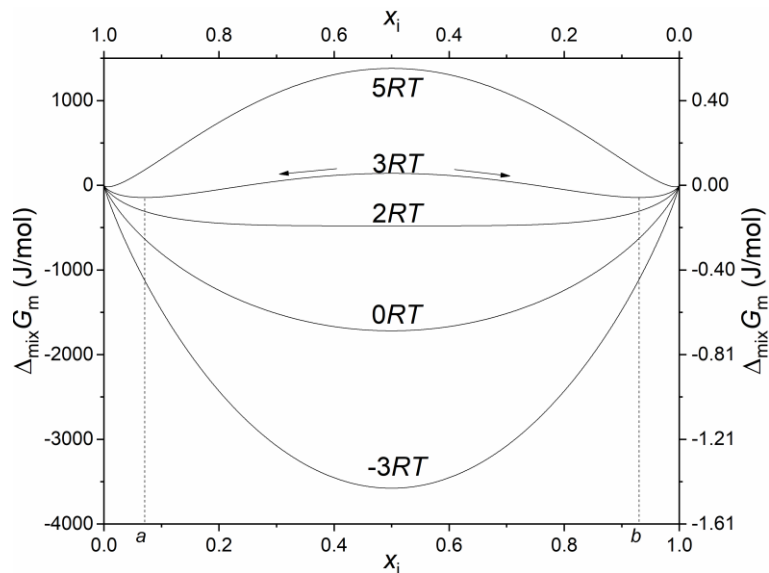
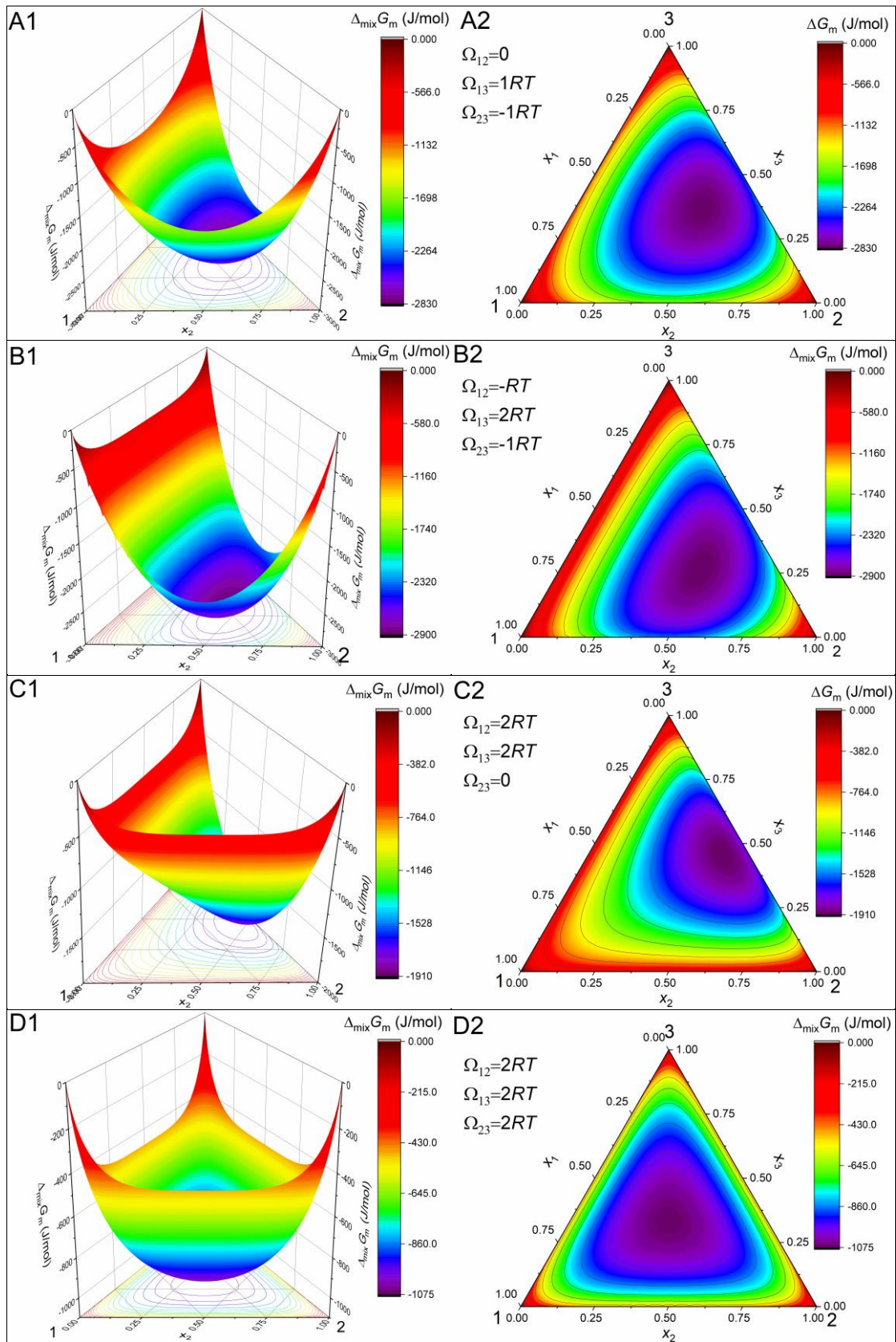
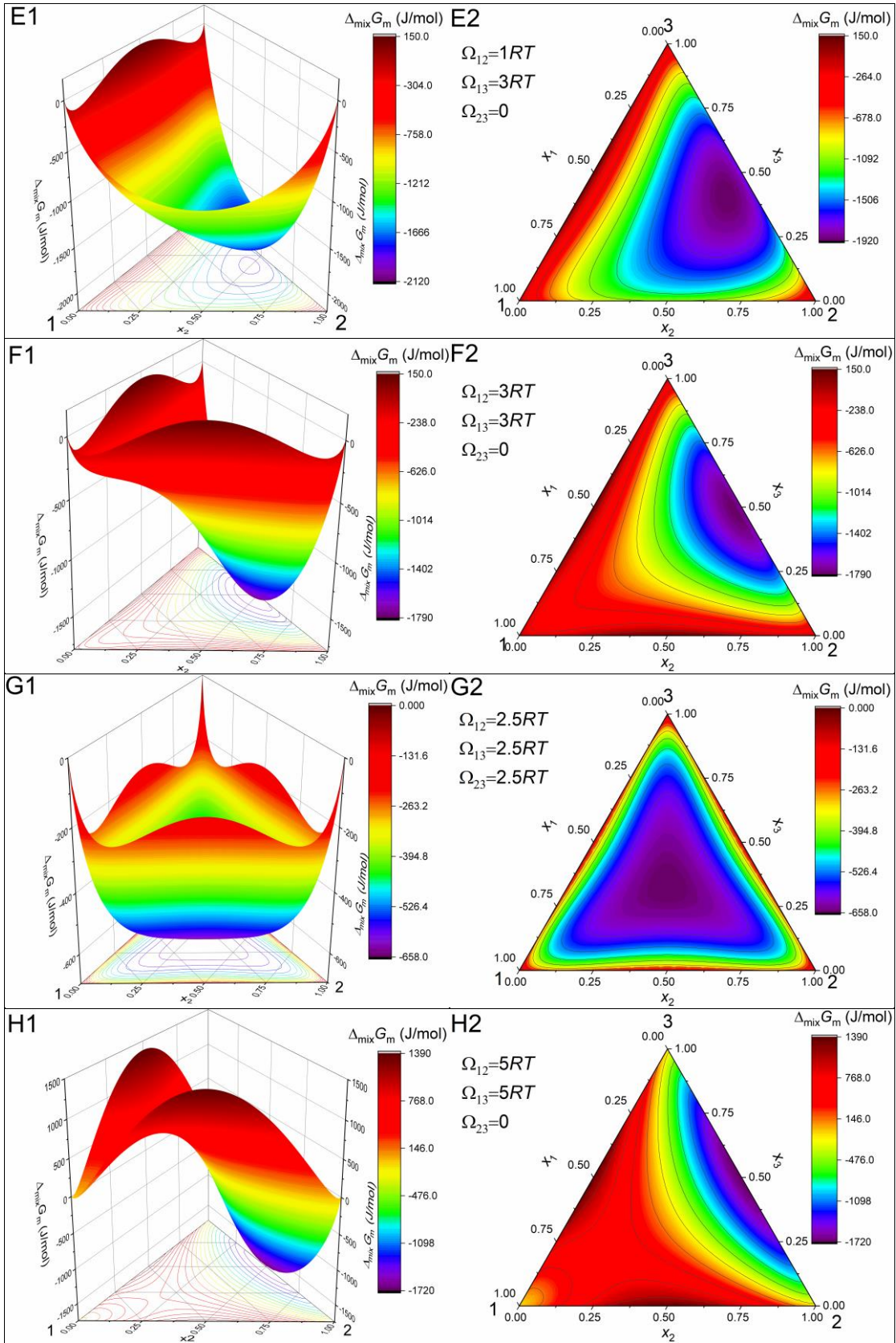


Figure 3.4. Stability of regular solutions. $\Delta_{mix} G_m$ of binary regular solutions with different values of the interaction parameters Ω (labelled above the curves) at 298.15 K are shown. The mutual solubilities of a regular solution with $\Omega = 3RT$ are

given by the points *a* and *b*. They are the minima and the double tangent points of $\Delta_{\text{mix}}G_m$. Regular solution with $\Omega = 3RT$ between *a* and *b* will decompose to phase *a* and phase *b*.

Figure 3.5 gives examples of $\Delta_{\text{mix}}G_m$ of ternary mixtures in regular solution model with different interaction parameters Ω (values noted on graphs in RT). Ternary systems with all binary interaction parameters $\Omega < 2RT$ have one minimum on $\Delta_{\text{mix}}G_m$, as shown in Figure 3.5.A. All species are miscible. Figure 3.5.B~D have one, two, three interaction parameters equal to $2RT$, respectively, and the rest $\Omega < 2RT$. Although binary regular solution with $\Omega = 2RT$ is at its critical point and the mixture starts to be unstable (see Figure 3.4), the addition of a third species dramatically increases entropy, therefore the ternary mixture is stable with one minimum. This holds true for slightly larger Ω . Figure 3.5.E~G have one, two, three binary interaction parameters slightly larger than $2RT$, respectively. The corresponding binary systems are immiscible because of the strong repulsion between the components. Yet entropic contribution caused by the third component overcomes the repulsion between the binary components. The ternary mixture is stable. In Figure 3.5.H and I, with two Ω larger than $3RT$, $\Delta_{\text{mix}}G_m$ is shaped like a saddle with two minima on each side. Demixing of the homogenous solution on the saddle between the two minima into a mechanical mixture of two phases on the common tangent point pairs near the minima of the free energy is favoured. From Figure 3.5.J on, Ω between all components are larger than or equal to $3RT$. $\Delta_{\text{mix}}G_m$ has three minima. Therefore, three stable phases will co-exist in the central region of the phase diagram.





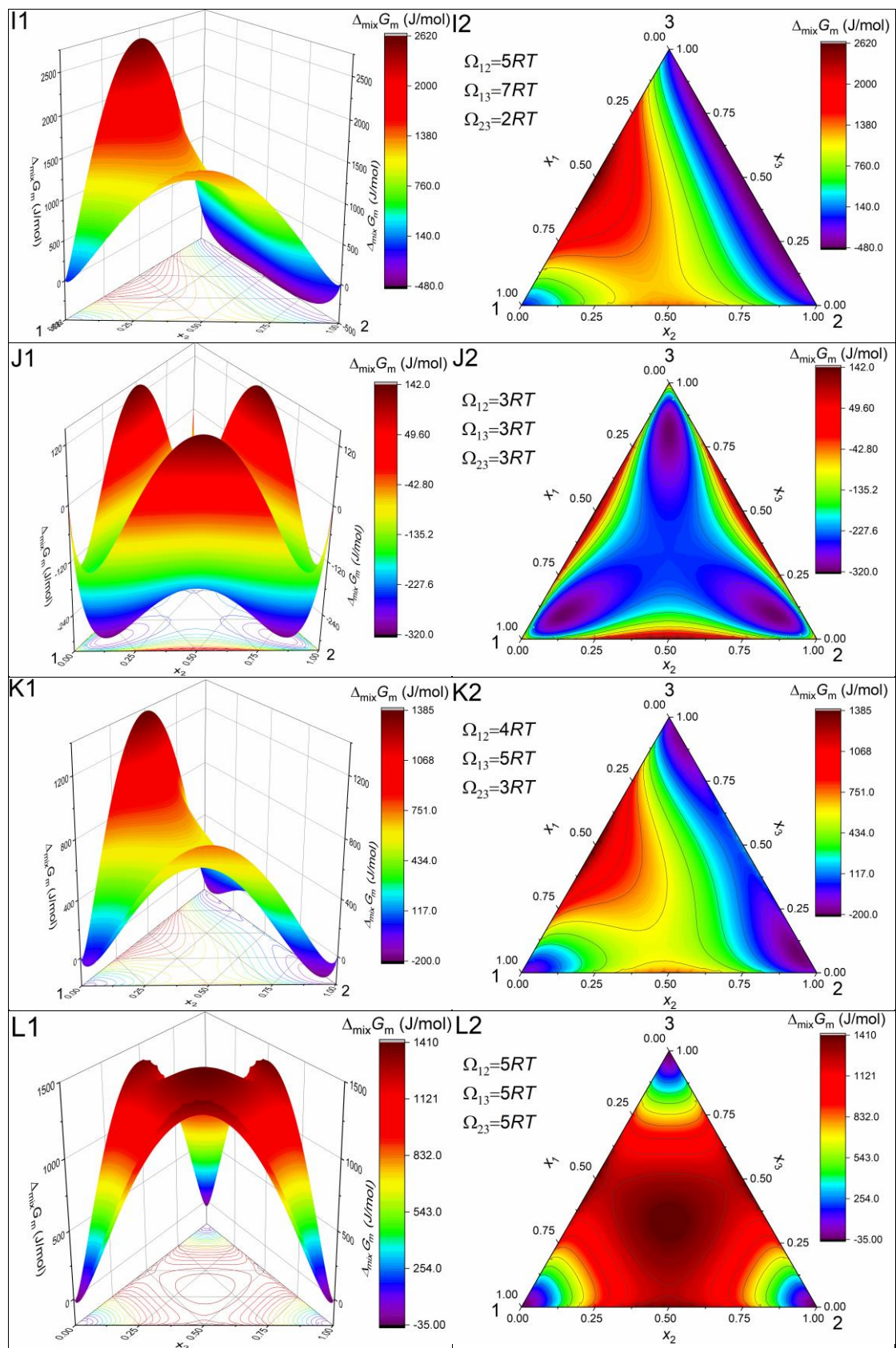


Figure 3.5. Molar mixing free energy change $\Delta_{\text{mix}}G_m$ of ternary regular mixtures with different interaction parameters Ω (values noted on graphs in RT) at 298.15 K.

Figure X2 is X1 flattened.

3.2.3. H³M model for real solvent mixing

As described in the previous section, with $\Omega_{ij} > 0$, the two components tend to repel each other; whereas with $\Omega_{ij} < 0$, the two components tend to attract each other. For regular solutions, $\Delta_{\text{mix}} G_m$ is symmetric over composition. As for real solutions, the mixing will generally not be random, neither the interaction energy $N_A Z \left(\varepsilon_{ij} - \frac{1}{2} (\varepsilon_{ii} + \varepsilon_{jj}) \right)$, because of the segregation. Many models have been proposed to describe the vapor-liquid equilibria of real binary solutions: equations based upon theories [Gierycz, 1986], methods for the description of excess functions [Redlich, 1948], and equations of state [Abbott, 1986]. As for ternary systems [Renon, 1968, Abrams, 1975], it is more difficult because of the complexity of the model and the lack of sufficient multicomponent data. [Hwang, 1991] proposed semi-theoretical relations (H³M model) for the excess functions, taking into account two-body and three-body interactions and self-association, that predict ternary mixture behaviour from binary data with good accuracy. It has been tested with 1,4-dioxane-ethanol-water, acetonitrile-ethanol-water, and acetone-ethanol-water, which are close to our system. Assuming that the entropic contribution to $\Delta_{\text{mix}} G_m$ can be represented by Raoult's law, H³M model gives the molar mixing free energy change of ternary liquid solvent mixture as:

$$\begin{aligned}
 \Delta_{\text{mix}} G_m &\approx \Delta_{\text{mix}} F_m \\
 &= RT (x_1 \ln x_1 + x_2 \ln x_2 + x_3 \ln x_3) \\
 &\quad + x_1 x_2 (\Omega_{12} + a_1^{12} x_1^3 + a_2^{12} x_2^3) + x_2 x_3 (\Omega_{23} + a_2^{23} x_2^3 + a_3^{23} x_3^3) \\
 &\quad + x_1 x_3 (\Omega_{13} + a_1^{13} x_1^3 + a_3^{13} x_3^3)
 \end{aligned} \tag{3.22}$$

with Ω_{ij} two-species interaction parameter, and a_i^{ij} used to describe solvent clustering (a negative a_i^{ij} means strong self-association). With the absence of a_{ijk} term assuming a 3 species interaction in the equation, all parameters can be measured from binary mixtures. The chemical potential of species i in the ternary system is given as:

$$\begin{aligned} \mu_i = \mu_i^o + RT \ln x_i + (1-x_i) & \left(x_j \left(\Omega_{ij} + 4a_i^{ij} x_i^3 \right) + x_k \left(\Omega_{ik} + 4a_i^{ik} x_i^3 \right) \right) \\ & + (1-4x_i) \left(a_j^{ij} x_j^4 + a_k^{ik} x_k^4 \right) - x_j x_k \left(\Omega_{jk} + 4a_j^{jk} x_j^3 + 4a_k^{jk} x_k^3 \right) \end{aligned} \quad (3.23)$$

The binary properties is given by fixing the amount fraction of one species zero in equation (3.22) and (3.23).

H³M model, as far as it has been tested, is sufficiently satisfactory and superior [Hwang, 1991] to the non-random two-liquid model [Renon, 1968] and the UNIQUAC model [Abrams, 1975]. The antisolvent and the solvent used in this thesis are water (1)-1,4-dioxane (2), which have been tested with H³M model. Its description of $\Delta_{\text{mix}} G_m$ of the ternary systems have been optimised. But this model assumes that the mixing is fully random that can be described by Raoult's law. This does not properly describe the entropy of the mixing, as experimentally shown by [Goates, 1958, Christensen, 1982, Suzuki, 2006] (see Appendix C.ii where we have shown that H³M model describes well $\Delta_{\text{mix}} G_m$ but badly $\Delta_{\text{mix}} H_m$ of water (1)-1,4-dioxane (2)). To estimate the diffusion coefficient and the demixing domain of the ternary mixture, we shall work on free energy, thus we shall apply this model to our calculation. H³M has been applied to ternary mixture of well-known solvents. We cannot apply it to DBDCS since data such as the vapor pressure of DBDCS (3) above water (1) or 1,4-dioxane (2) is not known. However, we have recorded the solubility curve of DBDCS in water (1)-1,4-dioxane (2) mixture. We have revisited the theory of the Jouyban-Acree model of the solubility to extract the parameters of the H³M model.

3.2.4. Jouyban-Acree equation for solubility prediction of slightly soluble solute in aqueous-organic mixture with H³M model

Acree [Acree, 1991a, Acree, 1991b] predicted solute solubility in antisolvent-solvent binary mixtures using the solubility in both pure solvents as a function of solvent composition:

$$\ln x_{3s} = x_1^o \ln x_{3s1} + x_2^o \ln x_{3s2} + x_1^o x_2^o \sum_{n=0}^M A_n \left(x_2^o - x_1^o \right)^n \quad (3.24)$$

with x_{3s} the solubility in amount fraction, x_1^o and x_2^o the amount fraction of solvents

neglecting the solute, A_n the curve fitting parameters, and M the degree of the polynomial expansion. The deviation term is a Redlich-Kister kind equation [Redlich, 1948].

Acree then applied the H³M model to the solubility prediction of slightly soluble antisolvent-solvent-solute ternary system [Acree, 1992]. He correlated the interaction energies with the curve fitting parameters in the Redlich-Kister equation. The chemical potential of the solute at saturation in the mixture can be given by equation (3.23) knowing the amount fraction of species 3 is negligible:

$$\begin{aligned} \mu_3^{\text{solid}} \approx & \mu_3^* + RT \ln x_{3s} + x_1 \left(\Omega_{13} + a_1^{13} x_1^3 \right) + x_2 \left(\Omega_{23} + a_2^{23} x_2^3 \right) \\ & - x_1 x_2 \left(\Omega_{12} + 4a_1^{12} x_1^3 + 4a_2^{12} x_2^3 \right), x_{3s} \ll 1 \end{aligned} \quad (3.25)$$

where x_{3s} is the amount fraction solubility of the solute in the mixture. The solubility in pure solvents gives:

$$\begin{aligned} \mu_3^{\text{solid}} \approx & \mu_3^* + RT \ln x_{3s1} + \Omega_{13} + a_1^{13}, x_{3s1} \ll 1 \\ \approx & \mu_3^* + RT \ln x_{3s2} + \Omega_{23} + a_2^{23}, x_{3s2} \ll 1 \end{aligned} \quad (3.26)$$

with x_{3si} is the amount fraction solubility of the solute in solvent i .

Substitution of equation (3.26) into equation (3.25) gives an expression of the solute solubility in binary solvent mixtures as a simple amount fraction average of solubility in pure solvents plus a term of a power series expansion of solvent composition, which is equivalent to the Redlich-Kister equation:

$$\ln x_{3s} = x_1^o \ln x_{3s1} + x_2^o \ln x_{3s2} + \frac{1}{RT} x_1^o x_2^o \left(P_0 + P_1 x_2^o + P_2 x_2^{o2} + P_3 x_2^{o3} \right) \quad (3.27)$$

where

$$\begin{aligned} P_0 &= \Omega_{12} + 4a_1^{12} + a_2^{23} + 3a_1^{13} \\ P_1 &= a_2^{23} - 3a_1^{13} - 12a_1^{12} \\ P_2 &= a_2^{23} + a_1^{13} + 12a_1^{12} \\ P_3 &= 4 \left(a_2^{12} - a_1^{12} \right) \end{aligned} .$$

Here we have corrected some typographic mistakes done by Acree in his final equation.

Jouyban *et al* [Jouyban, 2007] used this model to fit the solubility of 36 drugs in water-dioxane-drug ternary system with the solvent volume fraction average of the solubility in pure solvents:

$$\ln x_{3s} = \phi_1^o \ln x_{3s1} + \phi_2^o \ln x_{3s2} + \phi_1^o \phi_2^o \sum_{n=0}^2 \frac{A_n (\phi_2^o - \phi_1^o)^n}{T} \quad (3.28)$$

with ϕ_1^o and ϕ_2^o the volume fraction of water and 1,4-dioxane regardless of DBDCS. A_n values for solubility function in water (1)-1,4-dioxane (2) system published by Jouyban are listed in Table 3.3.

Table 3.3. Model constants in the Jouyban-Acree model for water (1)-1,4-dioxane (2) system [Jouyban, 2007]

A_0/K	A_1/K	A_2/K
2206.9	1173.1	1997.4

It is easy to correlate Jouyban's version to the "interaction energies", but to this point it has become meaningless. Up to now, Acree-Jouyban equation gives the most satisfactory prediction of solute solubility in aqueous-organic systems [Jouyban, 2006, Dadmand, 2018]. Therefore, Jouyban-Acree equation will be used to fit the solubility of DBDCS; the H³M model will be used to calculate the thermodynamics of water (1)-1,4-dioxane (2)-DBDCS (3) system.

3.3. Applying the H³M model to water (1)-1,4-dioxane (2)-DBDCS (3) irregular ternary system

3.3.1. Solubility of DBDCS in water (1)-1,4-dioxane (2) mixture

The solubility of DBDCS in water (1)-1,4-dioxane (2) mixture in solute/solvent mass ratio was measured by our intern Ran Bi [BI, 2016]. The results were recalculated (Table 3.4 and Figure 3.6) as amount fraction solubility (solute/(solute+solvent)).

Table 3.4 Recalculation of DBDCS amount fraction solubility, measured by Ran Bi in

mass ratio, in binary system of water (1)-1,4-dioxane (2)

ϕ_2	1	0.916259216	0.842431275	0.831882398	0.818106607
x_{3s}	0.001456632	0.000823851	0.000512514	0.000322055	0.000205158
ϕ_2	0.796884019	0.788288668	0.749431892	0.739125625	0.724717933
x_{3s}	0.000138818	9.23852E-05	6.51279E-05	4.70966E-05	3.47032E-05
ϕ_2	0.711153883	0.702421288	0.574463713	0.473290719	0.592943323
x_{3s}	2.58705E-05	1.93651E-05	8.27961E-07	2.07785E-07	2.33051E-06
ϕ_2	0.487316982	0.389159419	0.29146736	0.19387463	0
x_{3s}	5.09162E-07	4.77325E-08	2.46179E-08	1.44464E-08	8.14111E-12 (fitted)

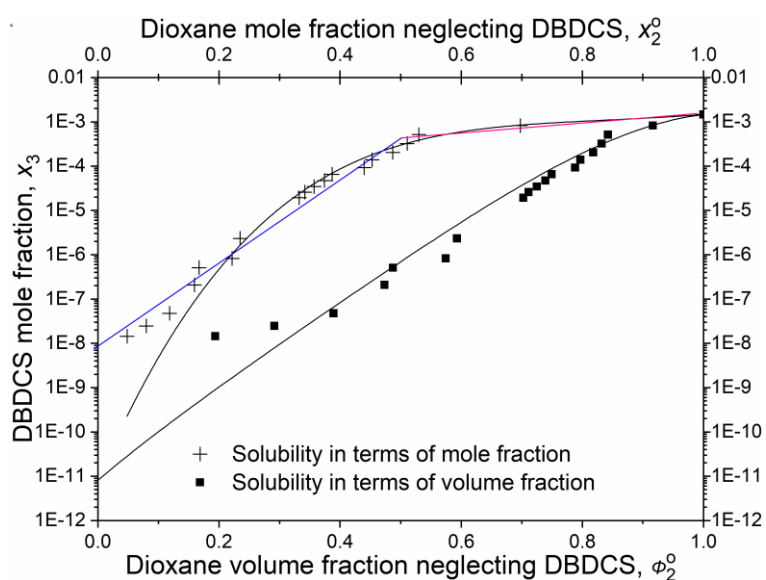


Figure 3.6. DBDCS amount fraction solubility in binary system of water (1)-1,4-dioxane (2) as a function of solvents molar composition (+ to the top axis) and of solvents volume composition (■ to the bottom axis). Originally measured by Ran Bi in mass ratio. The ■ have been fitted by the Jouban-Acree equation (equation (3.27)). The parabola is the fit of the + by the Acree equation (equation (3.28)). The solubility is a measure of the chemical potential of DBDCS molecule in the mixture. The Jouban representation shows that this chemical potential is a linear function of the composition of the solvent expressed in volume fraction.

The solubility of DBDCS in water, x_{3s1} , was too small to be measured. Since the

solubility of DBDCS is miniscule in the whole range of solvent composition, we used the Jouyban-Acree equation (equation (3.28)) to extrapolate the solubility in water to be $8E-12$. Thus, solubility of DBDCS in water (1)-1,4-dioxane (2) mixture can be estimated by equation (3.28) with the measured solubility in 1,4-dioxane and fitted solubility in water, as shown in Figure 3.6.

x_{3s} is also plotted against 1,4-dioxane amount fraction in Figure 3.6, which demonstrates two linear parts: the pink and the blue solid straight line. The blue slope: $0 < x_2 < 0.5$, solubility of DBDCS increases linearly with the number of 1,4-dioxane molecules added into the solution. The pink plateau: $0.5 < x_2$, DBDCS solubility is almost constant in this range, no matter how many more 1,4-dioxane is added, up to pure 1,4-dioxane. Several authors [Hwang, 1991, Acree, 1992, Jouyban, 2007] have attributed the deviation of an amount fraction average of solubility in pure solvents to the non-ideality of mixing enthalpy, or interaction energies. Whereas we know the structure of aqueous-organic mixture is highly organised and complex (see Appendix C.ii). This suggests that the amount of DBDCS molecules soluble in the mixture increases as the size and number of 1,4-dioxane cluster increases in the water network of hydrogen bonds, until most of the hydrogen bonds have been broken by large number of 1,4-dioxane, then water molecules will be trapped in 1,4-dioxane cages, thus DBDCS will hardly “feel” the presence of water molecules. In this range, the amount of DBDCS can be tolerated by the solution will be equivalent to that in pure 1,4-dioxane. This will be more detailed discussed in Appendix C.ii.

3.3.2. Thermodynamic parameters of water (1)-1,4-dioxane (2)-DBDCS (3)

ternary system

Hwang *et al* [Hwang, 1991] demonstrated in their model the curve fitting parameters for ternary aqueous-organic systems can be obtained from binary systems. We have no value on the binary DBDCS (3)-Water (1) and DBDCS (3)-1,4-dioxane (2) along the two edges of the Gibbs triangle. But we have a value of the free enthalpy along the solubility curve of DBDCS. This is shown on Figure 3.7 where the red domains and point on the ternary diagram

show where we have experimental values for $\Delta_{\text{mix}} G_m$. We shall adjust the H³M equation for $\Delta_{\text{mix}} G_m$ to the experimental values over these domains. Because of the very low solubility of DBDCS, we have decided to plot a “log ternary diagram”. Each point on this map represents a composition. The DBDCS amount fraction is read on the log scale. The water and 1,4-dioxane fraction can be read as $x_i = (1 - x_3) \cdot \frac{x_i'}{x_1' + x_2'}$. The only purpose of Figure 3.7 is to demonstrate

from what experimental values we shall extrapolate throughout the Gibbs triangle.

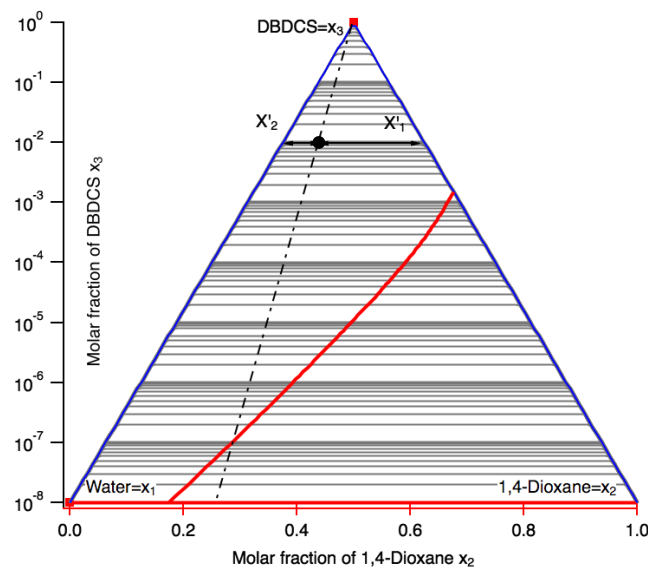


Figure 3.7. A “log ternary diagram” of water (1)-1,4-dioxane (2)-DBDCS (3) mixture. The red lines are assemblies of points where we have experimental values. By adjusting equation (3.27) along the red lines we shall extrapolate the free energy. For the composition of the black dot, as an example, its DBDCS amount fraction is read on the left log scale, and the water and 1,4-dioxane fraction can be read as

$$x_i = (1 - x_3) \cdot \frac{x_i'}{x_1' + x_2'}$$

Table 3.5 summarises the list and the origin of the fitting parameters required by the M³H model.

Table 3.5 Fitting parameters for estimation of $\Delta_{\text{mix}}G_m$ of water (1)-1,4-dioxane (2)-

DBDCS (3) ternary mixture

Species	Ω_{ij}	a_i^{ij}	a_j^{ij}
1,2	From activity of water (1)-1,4-dioxane (2) binary system Suzuki, 2006		
2,3	From solubility of DBDCS (3) in pure solvents	From solubility of DBDCS (3) in water (1)-1,4-dioxane (2)	/
1,3			/

3.3.2.1. Binary parameters of water (1)-1,4-dioxane (2) system from activity using H³M model

Binary aqueous-organic systems, such as water (1)-1,4-dioxane (2), have been extensively studied. We took [Vierk, 1950]'s measurement of the thermodynamic activity by vapor-liquid equilibrium of water (1)-1,4-dioxane (2) system at 298.15 K (Appendix C.i and Figure 3.8), calculated the activity coefficient and fitted the activity with regular model (equation (3.18), dashed lines) and the H³M model (equation (3.22), solid lines), respectively. The curve fitting parameters, or the “interaction energies” are listed in Table 3.6.

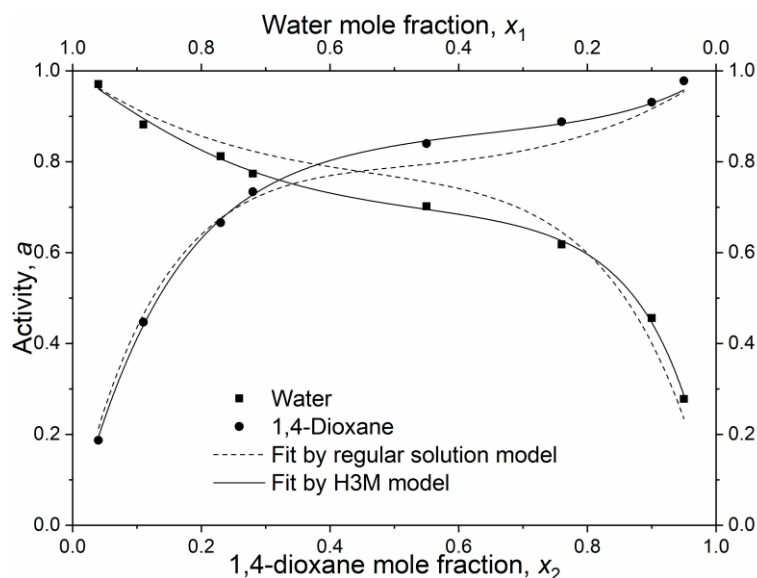


Figure 3.8. Activity of water (1)-1,4-dioxane (2) binary system at 298.15 K, measured

by [Vierk, 1950], fitted with regular solution model and H^3M model respectively.

Table 3.6. Curve fitting parameters in Figure 3.8

Model	Regular	H^3M		
Parameter	Ω_{12} /(J/mol)	Ω_{12} /(J/mol)	a_1^{12} /(J/mol)	a_2^{12} /(J/mol)
From a_1	4245.37732	4152.53535	-1030.71956	876.74493
From a_2	4505.4069	4446.89236	-256.04907	1147.80463
Adopted value		4300 $1.7RT$	-644 $-0.26RT$	1012 $0.4RT$

From the fittings in Figure 3.8, one can see that regular solution model is not capable of well describing water (1)-1,4-dioxane (2) vapor-liquid equilibrium, whereas H^3M model represents a good fit. We have discussed in section 3.2.3 that, although the curve fitting parameters in H^3M model can be used to estimate vapor-liquid equilibrium, the fitted values cannot be treated as “interaction parameters”, but only curve fitting parameters that describe the non-ideality of the mixing free energy. Ω_{12} is positive but smaller than $2RT$, thus, the two solvents are fully miscible. The negative a_1^{12} suggests there is strong self-association of water molecules.

3.3.2.2. Parameters of 1,4-dioxane (2)-DBDCS (3) and water (1)-DBDCS (3)

binary system from solubility

To calculate $\Delta_{mix}G_m$ by equation (3.22), we still need other curve fitting parameters. For that, Acree’s equation (3.27) was used with the three parameters in Table 3.6 to fit the amount fraction solubility of DBDCS over solvent amount fraction to get the unknown curve fitting parameters (Figure 3.6) in Table 3.7.

Table 3.7. Curve fitting parameters in Figure 3.6

Model	Acree	
Parameter	a_1^{13} (J/mol)	a_2^{23} /(J/mol)
Value	46630 $18.8RT$	-4350 $-1.7RT$

To determine the interaction between the solute and both solvents, we shall fit again the solubility of DBDCS using equation (3.25). a_1^{13} and a_2^{23} are fixed as the values in Table 3.7. The difference between the chemical potential of the liquid reference state and the solid state of DBDCS, $u_3^* - \mu_3^{\text{solid}}$, is deduced from the DSC measurement of DBDCS [Kim, 2015] (Figure Appen.C.4 in Appendix C.iii): $T_{\text{melt},3} = 446.85\text{K}$, $\Delta_{\text{fus}}H_{\text{m},3} = 27833.44\text{J/mol}$,

$$\Delta_{\text{fus}}S_{\text{m},3} = \frac{\Delta_{\text{fus}}H_{\text{m},3}}{T_{\text{melt},3}^*} = 62\text{J} \cdot \text{mol}^{-1} \cdot \text{K}^{-1} \quad . \quad \text{Equation (3.8) gives}$$

$$u_3^* - \mu_3^{\text{solid}} = \Delta_{\text{melt}}H_{\text{m},3} \left(1 - \frac{T}{T_{\text{melt},3}^*} \right) = 9262\text{J/mol} = 3.7RT \quad . \quad \text{The solubility of DBDCS in the}$$

mixture is too small to determine its self-association parameters a_3^{13} and a_3^{23} , but we can make approximations by applying the regular solution model on the DBDCS' side. It will not be too far from the reality. At most, the free energy curves will be slightly distorted. Thus, the fitting gives values of the interaction parameters between the solute and the solvents. The results of the fitting are listed in Table 3.8.

Table 3.8 Curve fitting parameters from solubility in pure solvent

Model	H ³ M		Regular	
	Ω_{13}	Ω_{23}	a_3^{13}	a_3^{23}
Parameter	(J/mol)	(J/mol)	(J/mol)	(J/mol)
Value	7410 3.0RT	11280 4.5RT	0	0

$\Omega_{13} = 3RT$, $\Omega_{23} = 4.5RT$. Ω_{13} and Ω_{23} are larger than $2RT$. The liquid phase of DBDCS is only slightly soluble in 1,4-dioxane and non-soluble in water. For a more precise description of the domain rich in DBDCS, we remain with two unknown parameters a_3^{13} and a_3^{23} . They represent non-ideal terms that are important to describe the region rich in DBDCS of the ternary diagram. Due to the limited solubility of DBDCS we have no access to that domain and no way to get them. By applying the regular solution model on the DBDCS side, it

will not be too far from the reality. At most, the free energy curves will be slightly distorted more the DBDCS's side. Therefore, we can nevertheless consult to this calculation. Now with all the curve fitting parameters of water (1)-1,4-dioxane (2)-DBDCS (3) ternary mixture, the mixing Gibbs energy of the mixture and the chemical potential of the solvents and the solute can be estimated. With the free energies, we will be able to estimate the diffusion coefficients of water (1)-1,4-dioxane (2)-DBDCS (3) ternary mixture.

3.4. Brief introduction to thermodynamics of diffusion

3.4.1. Intrinsic diffusion coefficient

Fick's law describes the mass transfer flux directly proportional to the concentration gradient [Fick, 1855]:

$$\mathbf{J}_i = -cD_i^F \nabla x_i \quad (3.29)$$

with D_i^F the Fick diffusion coefficient of species i , x_i its local amount fraction, and c the total local molarity. In very diluted or ideal solutions, D_i^F can be treated as a constant and the diffusion driving force is proportional to x_i .

The driving force of molecular diffusion is the gradient of chemical potential towards a more stable state of a lower free energy [Nernst, 1888, Gibbs, 1906]:

$$\begin{aligned} \mathbf{F}_i &= -\frac{\nabla \mu_i}{N_A} \\ &= -k_B T \nabla \ln a_i \end{aligned} \quad (3.30)$$

with μ_i the chemical potential of species i and N_A the Avogadro constant. The velocity of molecules is proportional to the force applied with respect to the surrounding environment [Stokes, 1851]

$$\mathbf{v}_i = \eta_i \mathbf{F}_i \quad (3.31)$$

with η_i the molecular mobility of species i in the mixture. The molecule mobility of species i can be estimated by Stokes-Einstein equation [Einstein, 1905, Sutherland, 1905]:

$$\eta_i = \frac{1}{6\pi r_i \dot{\mu}} \quad (3.32)$$

with r_i the radius of the molecule and $\dot{\mu}$ the local dynamic viscosity of the environment. The molar diffusion flux with respect to the surrounding environment is given by

$$\begin{aligned} \mathbf{J}_i &= c_i \mathbf{v} \\ &= c_i \eta_i \mathbf{F}_i \\ &= -c_i \eta_i k_B T \nabla \ln a_i, \end{aligned} \quad (3.33)$$

$$\mathbf{J}_i = -c_i \eta_i \left(\frac{\nabla \mu_i^E}{N_A} + k_B T \nabla \ln x_i \right) \quad (3.34)$$

with c_i the local molarity of species i . Equation (3.33) and (3.34) are mathematically equivalent. The former assumes that the non-ideality of the mixing is just a correction of the Fick's law. We shall use the latter because this is the formalism implanted in *Comsol*.

Equation (3.33) can be written in the form of Fick's law by some mathematical rearrangement:

$$\begin{aligned} \mathbf{J}_i &= -c x_i \eta_i k_B T \nabla \ln a_i \\ &= -c \eta_i k_B T \frac{d \ln a_i}{d \ln x_i} \nabla x_i \\ &= -c \eta_i k_B T \frac{x_i da_i}{a_i dx_i} \nabla x_i, \\ &= -c \eta_i k_B T \left(1 + \frac{d \ln \gamma_i}{d \ln x_i} \right) \nabla x_i \end{aligned} \quad (3.35)$$

with γ_i the activity coefficient of species i in amount fraction representation. Therefore, the intrinsic diffusion coefficient of species i

$$\begin{aligned}
D_i^F &= \eta_i k_B T \frac{d \ln a_i}{d \ln x_i} \\
&= \eta_i k_B T \frac{x_i da_i}{a_i dx_i} \quad , \\
&= \eta_i k_B T \left(1 + \frac{d \ln \gamma_i}{d \ln x_i} \right)
\end{aligned} \tag{3.36}$$

with a thermodynamic correction factor $\left(1 + \frac{d \ln \gamma_i}{d \ln x_i} \right)$ [Schreiner, 1922]. Ideal solution and

very diluted species have $\left(1 + \frac{d \ln \gamma_i}{d \ln x_i} \right) = 1$, which means the diffusion coefficient is a constant

related only to the size of the molecule and the dynamic viscosity of the environment; thus, the driving force will be directly the concentration gradient. This is not the case for non-ideal and concentrated solutions. The diffusion driving force is not the concentration gradient, and its direction not necessarily from higher to lower concentration. It is the free energy that is driving molecules to migrate. If the higher concentration has a lower free energy, molecules will tend to climb up the “concentration hill” towards the higher concentration to reduce the free energy of the system. The sign of the thermodynamic factor determines the diffusion direction. For

$\left(1 + \frac{d \ln \gamma_i}{d \ln x_i} \right) > 0$, diffusion is from higher concentration towards lower concentration, thereby

a homogeneous concentration of species i will be developed; whereas for $\left(1 + \frac{d \ln \gamma_i}{d \ln x_i} \right) < 0$,

diffusion is driven from lower concentration towards higher concentration, thereby phase separation should occur. $\left(1 + \frac{d \ln \gamma_i}{d \ln x_i} \right)$ has the same sign as $\frac{d \mu_i}{dx_i}$ and $\frac{d^2 \Delta_{\text{mix}} G_m}{dx_i^2}$. An example

of the diffusion direction’s dependence on free energy in a regular solution with $\Omega = 3RT$ is illustrated in Figure 3.9.

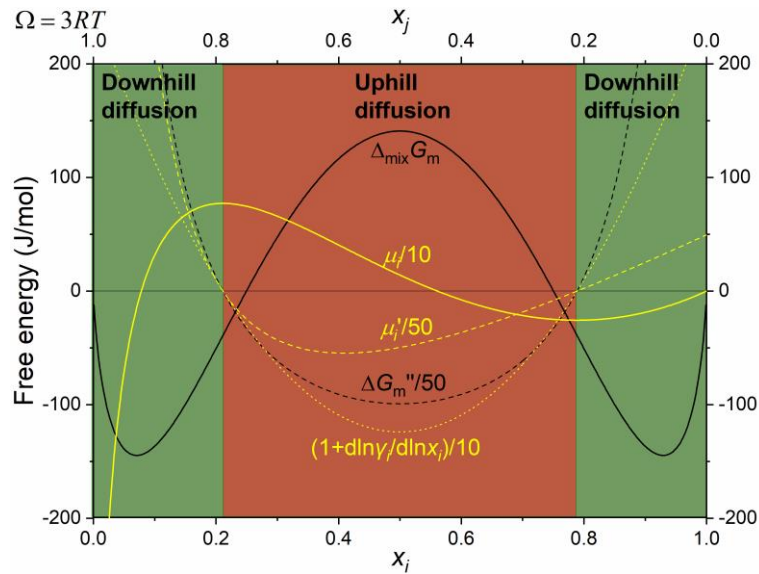


Figure 3.9. Diffusion direction of a regular solution with $\Omega = 3RT$ at 298.15 K. The

sign of the thermodynamic correction factor $\left(1 + \frac{d \ln \gamma_i}{d \ln x_i}\right)$ depends on the second

derivative of $\Delta_{\text{mix}} G_m$, or the derivative of the chemical potential of the species.

Diffusion is downhill towards lower concentration, if the derivative of the chemical potential is positive. This is always true in ideal mixtures. It is uphill towards higher concentration, if the derivative of the chemical potential is negative. In non-ideal solutions, if the mixture composition is in the range where the second derivative of $\Delta_{\text{mix}} G_m$ is negative, diffusion will be towards higher concentration. Green region, downhill diffusion; Cinnamon region, uphill diffusion.

Figure 3.9 shows the relation between diffusion direction and the free energy using a regular solution with $\Omega = 3RT$. The thermodynamic factor of the diffusion coefficient $\left(1 + \frac{d \ln \gamma_i}{d \ln x_i}\right)$ of species i and the derivative of its chemical potential and the second derivative of $\Delta_{\text{mix}} G_m$ change signs simultaneously at the same intercept. In the green region, the chemical potential of species i increases with the amount fraction, hence a downhill diffusion because

the lower concentration has lower free energy. Whereas in the brown zone, the chemical potential of species i decreases with its amount fraction, therefore an uphill diffusion towards higher concentration to reduce the free energy. Uphill diffusion will lead to segregation or separation of the mixture into two phases. The points where diffusion changes direction are the extrema of the μ_i , which is also the inflection points of $\Delta_{\text{mix}} G_m$. This is important for mixture segregation or separation.

For binary systems under giving temperature and pressure, the Duhem-Margules equation gives

$$\begin{aligned} \frac{d \ln a_1}{d \ln x_1} &= \frac{d \ln a_2}{d \ln x_2} \\ 1 + \frac{d \ln \gamma_1}{d \ln x_1} &= 1 + \frac{d \ln \gamma_2}{d \ln x_2} \end{aligned} \quad (3.37)$$

Therefore, the thermodynamic activity of at least one species must be known to estimate the intrinsic diffusion coefficient of the two species. The diffusion direction will be symmetric for both components in binary mixtures.

There are different ways to estimate the effective size of the molecules in solutions. This difficulty can be avoided by using the limiting diffusion coefficients knowing for pure solvents the thermodynamic factor $(1 + \frac{d \ln \gamma_i}{d \ln x_i}) = 1$, therefore

$$D_i^\infty = \frac{1}{6\pi r_i \dot{\mu}_j} k_B T \quad (3.38)$$

with D_i^∞ the infinite dilute diffusion coefficient.

Substituting equation (3.38) into equation (3.36) gives the intrinsic diffusion coefficient without estimating the size of the diffusing molecule:

$$D_1^F = D_1^\infty \frac{\ddot{\mu}_2}{\ddot{\mu}} \left(1 + \frac{d \ln \gamma_1}{d \ln x_1} \right)$$

$$D_2^F = D_2^\infty \frac{\ddot{\mu}_1}{\ddot{\mu}} \left(1 + \frac{d \ln \gamma_2}{d \ln x_2} \right)$$
(3.39)

with measured infinite dilute diffusion coefficients. By doing this, we assume that the hydrodynamic radius of the diffusing molecules does not depend on the composition of the mixture.

3.4.2. Mutual diffusion coefficients

The mutual diffusion coefficients of binary systems is linked with their intrinsic diffusion coefficients by Darken equation [Darken, 1948]:

$$D_{12}^F = x_2 D_1^F + x_1 D_2^F$$
(3.40)

The Self-diffusion coefficients, D_1^* and D_2^* [Holz, 2000], the mutual diffusion coefficient, D_{12}^F and the limiting diffusion coefficients D_i^∞ [Leaist, 2000] of water and 1,4-dioxane are listed in Table 3.9, plotted in Figure 3.10 and fitted with Redlich-Kester equation to the fourth degree of power expansion.

Table 3.9. Measurement of self- [Holz, 2000] and mutual [Leaist, 2000] diffusion coefficients of water and 1,4-dioxane at 298.15 K, with D_{12}^F the mutual diffusion coefficient in the mixture, D_i^ the self-diffusion coefficient of species i , and D_i^∞ the limiting diffusion coefficient of species i in an infinitely diluted solution.*

x_2	$1(D_2^*)$	$0(D_2^\infty)$	0.000180	0.000905	0.00183	0.00508
$D_{12}^F/(10^{-9}\text{m}^2\cdot\text{s}^{-1})$	1.089	1.13	1.10	1.10	1.09	1.06
x_2	0.0222	0.0407	0.0806	0.120	0.170	0.234
$D_{12}^F/(10^{-9}\text{m}^2\cdot\text{s}^{-1})$	0.95	0.82	0.71	0.59	0.52	0.42
x_2	0.323	0.449	0.449	0.644	0.798	0.901
$D_{12}^F/(10^{-9}\text{m}^2\cdot\text{s}^{-1})$	0.34	0.32	0.32	0.47	0.85	1.41
x_2	0.950	0.988	$1(D_1^\infty)$	$0(D_1^*)$		
$D_{12}^F/(10^{-9}\text{m}^2\cdot\text{s}^{-1})$	1.92	2.38	2.53	2.299		

The ratio of the self- and limiting diffusion coefficients of neither water nor 1,4-dioxane follow equation (3.39):

$$\begin{aligned}\frac{\ddot{\mu}_1}{\ddot{\mu}_2} &= \frac{0.891}{1.172} = 0.76 \\ \frac{D_2^*}{D_2^\infty} &= \frac{1.089}{1.13} = 0.96 \neq \frac{\ddot{\mu}_1}{\ddot{\mu}_2} \\ \frac{D_1^\infty}{D_1^*} &= \frac{2.53}{2.299} = 1.10 \neq \frac{\ddot{\mu}_1}{\ddot{\mu}_2}.\end{aligned}$$

The fact that the ratio of the self- and the limiting diffusion coefficients is not equal to the viscosity ratio indicates that the hydrodynamic radius of the diffusing molecule is not the same in pure and in infinitely diluted solutions. This suggests that the diffusion of water and 1,4-dioxane cannot be viewed as free particles moving in an environment of a given dynamic viscosity. 1,4-dioxane molecule moves slower in pure water than theory, and water molecule's mobility in water is even further deviated from the theory than 1,4-dioxane. This could be due to the water molecule hydrogen bond network. There are more hydrogen bonds between water-water than water (1)-1,4-dioxane (2). Since the infinite dilution diffusion coefficients were extrapolated from mutual diffusion coefficients, we have decided to use the limiting diffusion coefficients for calculation, which represents more closely to the environment in the experiment.

The mutual diffusion coefficient D_{12}^F should approach D_1^∞ when x_2 approaches zero and D_2^∞ when x_2 approaches one. Substitution of equation (3.37) and (3.39) into the Darken equation (equation (3.40)) gives:

$$D_{12}^F = \frac{1}{\ddot{\mu}} \left(x_2 \ddot{\mu}_2 D_1^\infty + x_1 \ddot{\mu}_1 D_2^\infty \right) \left(1 + \frac{d \ln \gamma_1}{d \ln x_1} \right), \quad (3.41)$$

Darken equation gives effective prediction of mutual diffusion coefficients in binary metal alloys and nearly ideal liquid mixtures. However, for non-ideal liquid mixtures, it has

been shown that the thermodynamic correction factor has been overestimated [Carman, 1967].

Recently, Moggridge *et al* [D'Agostino, 2011] proposed a correction for the thermodynamic correction factor in cases with no strong correlation between the motion of different molecules:

$$D_{12}^F = \frac{1}{\ddot{\mu}} \left(x_2 \ddot{\mu}_1 D_1^* + x_1 \ddot{\mu}_2 D_2^* \right) \left(1 + \frac{d \ln \gamma_1}{d \ln x_1} \right)^\alpha \quad (3.42)$$

with $\alpha \approx 0.64$ and got effective prediction with fourteen non-ideal liquid mixtures.

3.5. Diffusion of water (1)-1,4-dioxane (2)-DBDCS (3) mixture

3.5.1. Estimation of the diffusion coefficients of water (1)-1,4-dioxane (2) binary system with Moggridge equation

Quantitative theories of diffusion in associated liquid mixtures are still under development. Different approximations of intrinsic and mutual diffusion coefficient of water and 1,4-dioxane was made by different approaches, as shown Figure 3.10 with $\ddot{\mu}$ calculated by equation (3.3) [Aminabhavi, 1995] and chemical potential calculated by equation (3.23). Moggridge's equation (equation (3.42)) gives closer prediction of the mutual diffusion coefficients of water (1)-1,4-dioxane (2) binary system with $\alpha = 0.64$ than Darken equation (equation (3.41)), except small deviation when $0.1 < x_2 < 0.5$. Therefore equation (3.42) is taken to give the mutual diffusion coefficients between water and 1,4-dioxane for the *Comsol* simulation.

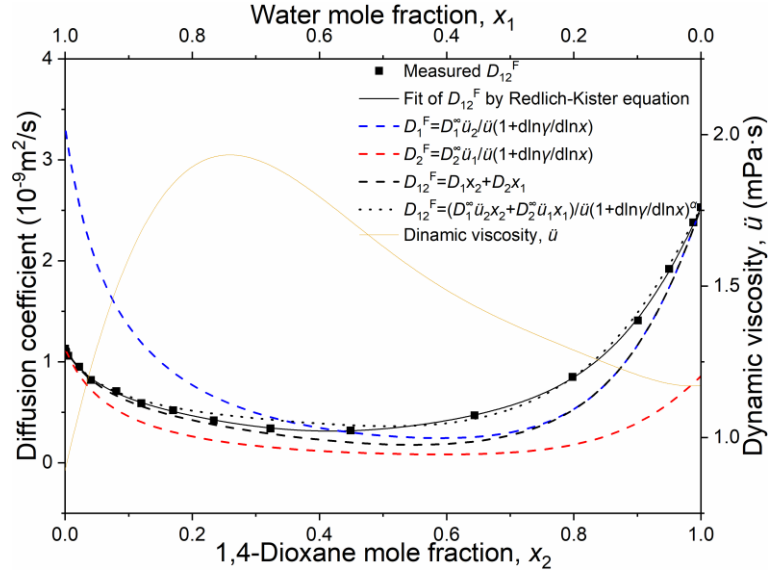


Figure 3.10. Prediction of mutual and intrinsic diffusion coefficient of water and 1,4-dioxane at 298.15 K. Measurement [Leaist, 2000], calculation based on activity measured by [Vierk, 1950] and dynamic viscosity measured by [Aminabhavi, 1995]

Particle mobility is inversely proportional to its size and the viscosity of the environment. This has been reflected in Figure 3.10. The movement of molecules becomes difficult as $\dot{\mu}$ raises to the maximum around $x_2 = 0.6$. Water molecules move twice as fast as 1,4-dioxane because they are much smaller. The thermodynamic correction factor $\left(1 + \frac{d \ln \gamma_i}{d \ln x_i}\right)$ of water (1)-1,4-dioxane (2) binary system is calculated from the activity of water, from the activity of 1,4-dioxane, and from the adopted average value (Table 3.6), respectively, and plotted in Figure 3.11. The three curves are very close, as predicted by the Duhem-Margules equation (equation (3.37)). The thermodynamic correction factor is very close to zero around $x_2 = 0.6$, which means the system is already very close to demix. Under the same concentration gradient, molecules are almost stationary because the driving force is small. If the thermodynamic factor goes to negative, diffusion will be uphill, and the mixture will separate into two phases. With the very large “interaction parameters” between DBDCS and both the solvents, phase separation could be favoured.

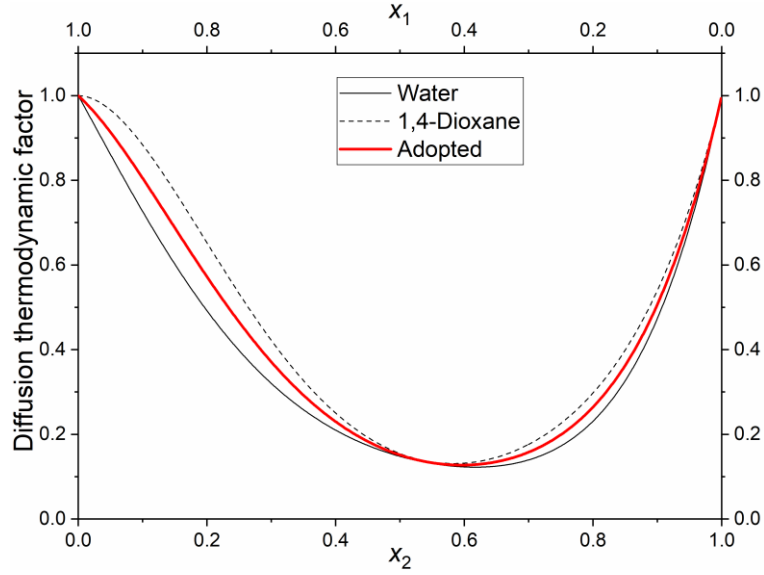


Figure 3.11. Thermodynamic factor of diffusion coefficients of water (1)-1,4-dioxane (2) at 298.15 K calculated with the interaction parameters in Table 3.6. The black solid line is calculated from activity of water in the mixture, the dashed line from the activity of 1,4-dioxane, and the red line from the interaction parameters we adopted for all the calculations and simulations.

3.5.2. Estimation of the diffusion coefficient of DBDCS in binary system of water (1)-1,4-dioxane (2)

Since the concentration of DBDCS is miniscule in the mixture, it is safe to assume that it has no impact on the diffusion between water (1) and 1,4-dioxane (2). Since there is no published measurement of the mobility of DBDCS in water (1)-1,4-dioxane (2), we have used

Stokes-Einstein equation (equation (3.32)) $\eta_3 = \frac{1}{6\pi r_{3^*} \dot{\mu}}$, with r_3 the radius of DBDCS

molecules in fluid estimated as $r_{3^*} = \left(\frac{3}{4\pi} V_{3^*}\right)^{\frac{1}{3}} = 5.33 \text{ \AA}$ with $V_{3^*} = 635 \text{ \AA}^3$ (see section 3.1).

Diffusion is driven by chemical potential gradient. Since the solid solute is in equilibrium with the saturated solution:

$$\begin{aligned}
\mu_3^{\text{solid}} &= \mu_3^* + RT \ln x_{3s} \\
&+ (1 - x_{3s}) \left(x_1^o (\Omega_{13} + 4a_3^{13} x_{3s}^3) + x_2^o (\Omega_{23} + 4a_3^{23} x_{3s}^3) \right) \\
&+ (1 - 4x_{3s}) (a_1^{13} x_1^{o4} + a_2^{23} x_2^{o4}) \\
&- x_1^o x_2^o (\Omega_{12} + 4a_1^{12} x_1^{o3} + 4a_2^{12} x_2^{o3}) \quad , \quad (3.43)
\end{aligned}$$

the chemical potential of DBDCS can be expressed using the solid reference state:

$$\begin{aligned}
\mu_3 &= \mu_3^{\text{solid}} + RT \ln \frac{x_3}{x_{3s}} + (1 - x_3) \left(x_1 (\Omega_{13} + 4a_3^{13} x_3^3) + x_2 (\Omega_{23} + 4a_3^{23} x_3^3) \right) \\
&+ (1 - 4x_3) (a_1^{13} x_1^4 + a_2^{23} x_2^4) - x_1 x_2 (\Omega_{12} + 4a_1^{12} x_1^3 + 4a_2^{12} x_2^3) \\
&- (1 - x_{3s}) \left(x_1^o (\Omega_{13} + 4a_3^{13} x_{3s}^3) + x_2^o (\Omega_{23} + 4a_3^{23} x_{3s}^3) \right) \\
&- (1 - 4x_{3s}) (a_1^{13} x_1^{o4} + a_2^{23} x_2^{o4}) + x_1^o x_2^o (\Omega_{12} + 4a_1^{12} x_1^{o3} + 4a_2^{12} x_2^{o3}) \quad . \quad (3.44)
\end{aligned}$$

Since the amount fraction of DBDCS actually used in this thesis is miniscule, equation (3.44) can be approximated as

$$\mu_3 \approx \mu_3^{\text{solid}} + RT \ln \frac{x_3}{x_{3s}}, \quad x_3 \rightarrow 0, x_{3s} \rightarrow 0 \quad (3.45)$$

The solubility of DBDCS in the mixture can be estimated as (equation (3.28))

$$\ln x_{3s} = \phi_1^o \ln x_{3s1} + \phi_2^o \ln x_{3s2} + \phi_1^o \phi_2^o \sum_{n=0}^2 \frac{A_n (\phi_2^o - \phi_1^o)^n}{T}$$

Equation (3.45) has been used in the *Comsol* simulation, whereas for theoretical descriptions we have neglected the quadratic terms, thereby approximate the chemical potential of DBDCS as

$$\mu_3 \approx \mu_3^{\text{solid}} + RT \ln \frac{x_3}{x_{3s1}^{\phi_1^o} x_{3s2}^{\phi_2^o}} \quad (3.46)$$

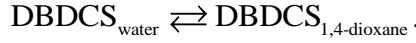
The diffusion driving force of DBDCS molecule is:

$$\begin{aligned}
\mathbf{F} &= -\frac{\nabla \mu_3}{N_A} \\
&= -k_B T (\nabla \ln x_3 - \nabla \ln x_{3s}) \quad , \quad (3.47)
\end{aligned}$$

or

$$\begin{aligned}
\mathbf{F} &= -\frac{\nabla\mu_3}{N_A} \\
&\approx -k_B T \nabla \left(\ln x_3 - \ln \left(x_{3s1}^{\phi_1^0} x_{3s2}^{\phi_2^0} \right) \right) \\
&= -k_B T \nabla \left(\ln x_3 - \phi_1^0 \ln x_{3s1} - (1 - \phi_1^0) \ln x_{3s2} \right) \\
&= -k_B T \left(\nabla \ln x_3 + \ln \left(\frac{x_{3s2}}{x_{3s1}} \right) \nabla \phi_1^0 \right)
\end{aligned} \tag{3.48}$$

with N_A the Avogadro constant and k_B the Boltzmann constant. It contains two terms, $-k_B T \nabla \ln x_3$ for diffusion towards lower concentration of DBDCS and $k_B T \nabla \ln x_{3s}$ or $k_B T \ln(x_{3s2}/x_{3s1}) \nabla \phi_1^0$ for uphill diffusion towards higher fraction of good solvent. In antisolvent-solvent -solute systems, $k_B T \ln(x_{3s2}/x_{3s1})$ is the chemical affinity of DBDCS for 1,4-dioxane compare to water. It is the free energy of the reaction *per* solute molecule $\Delta_r G$:



Thus, the total diffusive flux of DBDCS was estimated as

$$\begin{aligned}
\mathbf{J}_3 &= c_3 \mathbf{v} \\
&= c_3 \eta \mathbf{F} \\
&= -c x_3 \frac{1}{6\pi r_3^* \dot{\mu}} k_B T (\nabla \ln x_3 - \nabla \ln x_{3s}) \\
&= -c \frac{k_B T}{6\pi r_3^* \dot{\mu}} \left(1 - \frac{d \ln x_{3s}}{d \ln x_3} \right) \nabla x_3
\end{aligned} \tag{3.49}$$

or

$$\begin{aligned}
\mathbf{J}_3 &= c_3 \mathbf{v} \\
&= c_3 \eta \mathbf{F} \\
&= -c x_3 \frac{1}{6\pi r_3^* \dot{\mu}} k_B T \left(\nabla \ln x_3 + \ln \left(\frac{x_{3s2}}{x_{3s1}} \right) \nabla \phi_1^0 \right) \\
&= -c \frac{k_B T}{6\pi r_3^* \dot{\mu}} \left(1 + \ln \left(\frac{x_{3s2}}{x_{3s1}} \right) \frac{d \phi_1^0}{d \ln x_3} \right) \nabla x_3
\end{aligned} \tag{3.50}$$

and the total diffusion coefficient of DBDCS

$$D_3^F = \frac{k_B T}{6\pi r_3^* \dot{\mu}} \left(1 - \frac{d \ln x_{3s}}{d \ln x_3} \right) \quad (3.51)$$

or

$$D_3^F = \frac{k_B T}{6\pi r_3^* \dot{\mu}} \left(1 + \ln \left(\frac{x_{3s2}}{x_{3s1}} \right) \frac{d\phi_1^o}{d \ln x_3} \right) \quad (3.52)$$

with a thermal dynamic factor, $\left(1 - \frac{d \ln x_{3s}}{d \ln x_3} \right)$ or $\left(1 + \ln \left(\frac{x_{3s2}}{x_{3s1}} \right) \frac{d\phi_1^o}{d \ln x_3} \right)$. The sign of the thermodynamic factor decides the direction of the diffusion (uphill or downhill). Keep the thermodynamic factor to 1, equation (3.52) gives the tracer diffusion coefficient of DBDCS when treated (Figure 3.12).

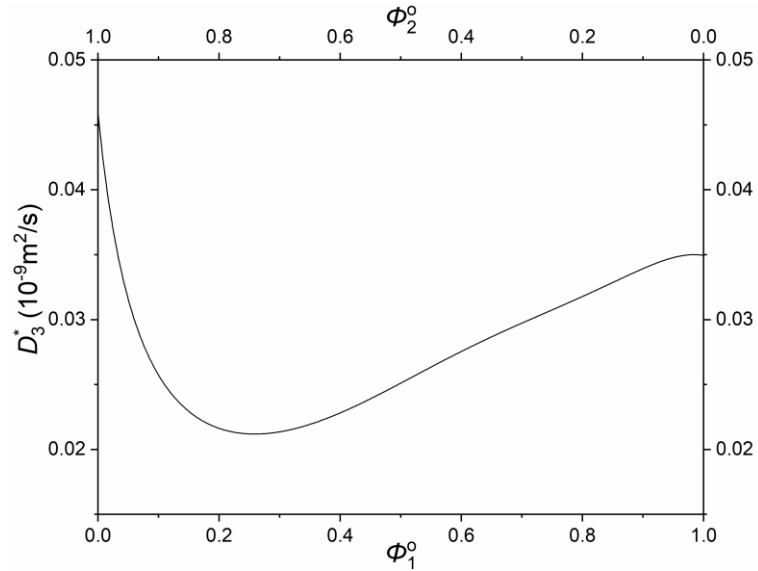


Figure 3.12. Estimation of hypothetical tracer diffusion coefficient of DBDCS in

water (1)-1,4-dioxane (2) mixture at 298.15 K.

3.6. Thermodynamic stability of water (1)-1,4-dioxane (2)-DBDCS (3) ternary mixture

3.6.1. Liquid-liquid phase separation (LLPS)

3.6.1.1. A brief introduction to LLPS

A regular binary mixture with $\Omega > 2RT$ has two minima on $\Delta_{\text{mix}} G_m$ (Figure 3.4). For regular solutions, the decomposition of the solution between the two minima will give a mechanical mixture of two new phases with composition of the minima points. This will not be the case for solutions with interaction energies depend asymmetrically on composition. $\Delta_{\text{mix}} G_m$ of a binary solution with $\Omega = 3RT, a_1^{12} = RT, a_2^{12} = 0$ calculated by H³M model is taken as an example and plotted in Figure 3.13. Although a linear combination of the two minima (the white points in Figure 3.13) on $\Delta_{\text{mix}} G_m$ would be lower than the any point on $\Delta_{\text{mix}} G_m$ between the minima, this combination is not in equilibrium. For a phase transition to occur, not only the new state should have lower free energy, but also the same component must be in equilibrium in all the coexisting phases, *i.e.* the chemical potential of the same component must be equal in all coexisting phases. This requires the composition of coexisting phases to be on the common tangent line of the free energy, as shown in Figure 3.13 (the black points). The composition range between the double tangent points (a and b in Figure 3.13) is the miscibility gap (Cinnamon+Green in Figure 3.13). A homogeneous mixture in the miscibility gap will tend to separate. In the miscibility gap, there are two inflection points of $\Delta_{\text{mix}} G_m$, which are also the extrema of the chemical potential (the yellow line). Between the inflection points (The cinnamon range), $\Delta_{\text{mix}} G_m'' < 0$ (dashed black line in Figure 3.13). When a tiny local compositional fluctuation $x_i + \Delta x$ and $x_i - \Delta x$ occurs, the local Gibbs energy change of the

fluctuation $\frac{1}{2}(\Delta_{\text{mix}} G_m |_{x=x+\Delta x} + \Delta_{\text{mix}} G_m |_{x=x-\Delta x}) - \Delta_{\text{mix}} G_m |_{x=x} < 0$. The system is more stable

after fluctuation. In addition, the chemical potential decreases with concentration in the cinnamon range, therefore diffusion is uphill towards higher concentration. This is the spinodal decomposition limits. Spinodal decomposition is fast, because it is favoured by diffusion. Whereas outside the spinodal limits (Green+Cyan), $\Delta_{\text{mix}} G_m'' > 0$, $\frac{1}{2}(\Delta_{\text{mix}} G_m|_{x=x+\Delta x} + \Delta_{\text{mix}} G_m|_{x=x-\Delta x}) - \Delta_{\text{mix}} G_m|_{x=x} > 0$, therefore, compositional fluctuation is not favoured. The chemical potential increases with concentration, molecular diffusion is downhill towards lower concentration. Although the system is not stable in this range, phase separation is difficult because compositional fluctuation is not favoured both energetically and diffusively. Therefore, in the Green range between the $\Delta_{\text{mix}} G_m$ inflection points and the double tangent points, phase separation goes through a slow nucleation and growth process. Both spinodal and binodal LLPS give the two new phases of the double tangent points a and b. Outside the double tangents pair, the mixture is stable. This is the soluble range.

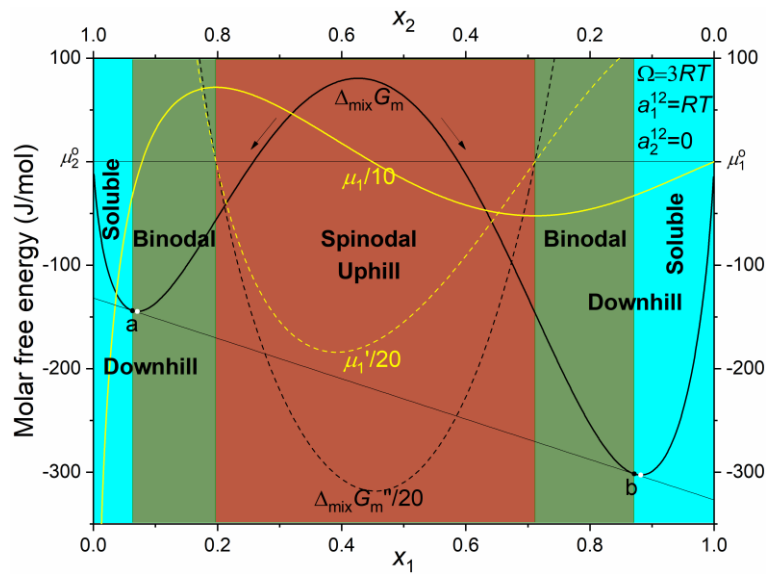


Figure 3.13. Thermodynamic stability and diffusion direction of a binary irregular solution at 298.15 K. The free energies are calculated using H^3M model ($\Omega = 3RT, a_1^{12} = RT, a_2^{12} = 0$). The molar mixing excess free energy $\Delta_{\text{mix}} G_m$, its second derivative $d^2 \Delta_{\text{mix}} G_m / dx_1^2$, the chemical potential μ_1 , and its first derivative $d\mu_1 / dx_1$

are shown. The mixture will decompose into phase a and b (black points). The equilibrium compositions are very near to, but not the minima (white points) of $\Delta_{\text{mix}}G_m$. Cinnamon: spinodal decomposition range; Green: binodal decomposition range. Cinnamon+Green: LLPS range. Cyan: soluble range. Cinnamon: uphill diffusion range. Green+Cyan: downhill diffusion range.

3.6.1.2. Decomposition of solvent-DBDCS binary systems

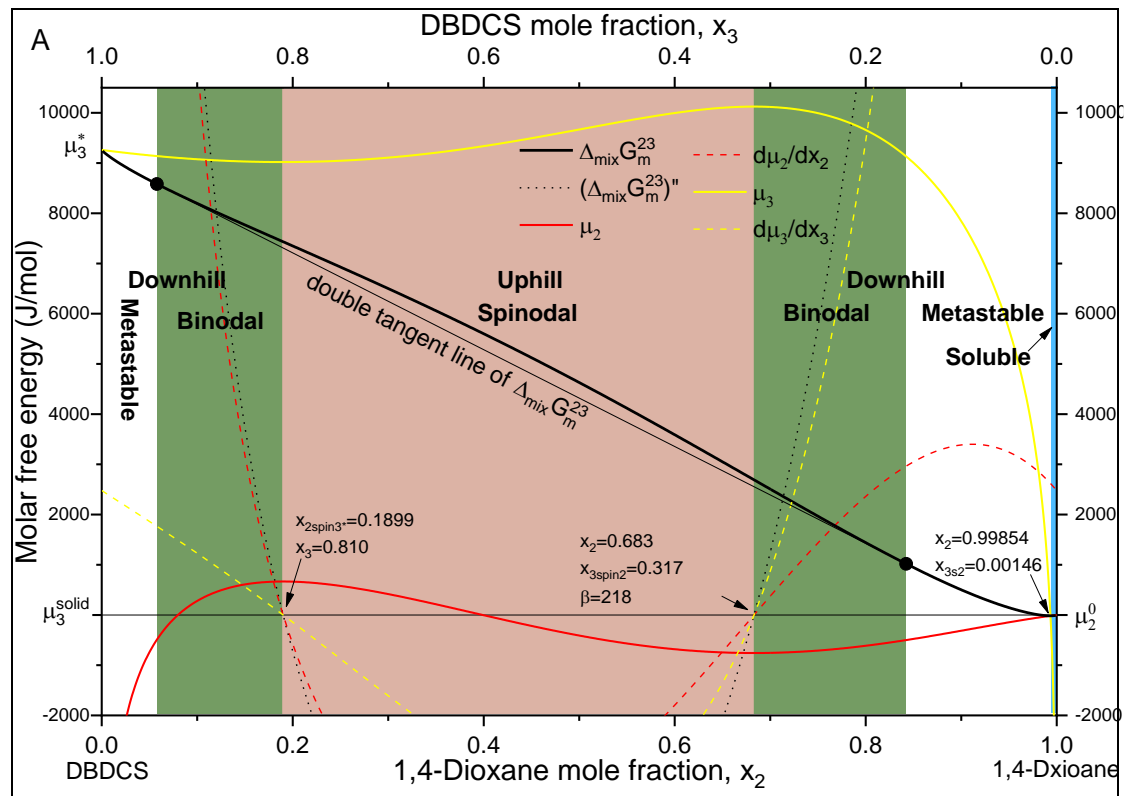
H³M model has provided simple relations to estimate $\Delta_{\text{mix}}G_m$ of ternary liquid solvent mixtures. In the case of a solid solute dissolved in a binary solvent mixture, the model can be extended using the hypothetical liquid solute as the reference state. Previously we have demonstrated the thermodynamic and diffusional condition for a non-ideal mixture to segregate or demix. Let us now, examine the binary systems and then the ternary system of water (1)-1,4-dioxane (2)-DBDCS (3). This is more complex than the decomposition of liquid solvents, since the LLPS is not stable and the liquid-solid phase transition will now be involved.

$\Delta_{\text{mix}}G_m$ of water (1)-1,4-dioxane (2) binary system has been plotted in Figure 3.8. The system is miscible but close to demixing in the middle composition range. The “interaction parameters” of DBDCS with both water and 1,4-dioxane Ω_{13} and Ω_{23} are larger than $2RT$ (see Table 3.8). Therefore, with the presence of higher concentration of DBDCS, demixing of the mixture will occur.

The molar excess mixing free energy $\Delta_{\text{mix}}G_m$, the chemical potentials, the derivative of the chemical potentials, and the second derivative of $\Delta_{\text{mix}}G_m$ of 1,4-dioxane (2)-DBDCS (3) binary system at 298.15 K is calculated with H³M model and plotted in Figure 3.14.A using solid DBDCS as reference state, and in in Figure 3.14.B using liquid DBDCS as reference state. Figure 3.14.A shows that, compared to the solid DBDCS, the liquid mixture is highly unstable. The solubility of the solid DBDCS is given by the intersection of the chemical potential of DBDCS in the mixer with μ_3^{solid} . Above the solubility is the soluble range (the cyan zone on

Figure 3.14). The inflection points of $\Delta_{\text{mix}} G_m^{23}$ give the spinodal limits (the cinnamon region): $x_{2\text{spin}3^*} = 0.1899$ (the amount fraction spinodal decomposition limit of 1,4-dioxane in liquid DBDCS) and $x_{3\text{spin}2} = 0.317$ (the amount fraction spinodal decomposition limit of DBDCS in 1,4-dioxane). Figure 3.14.A and Figure 3.14.B share the same spinodal decomposition limits, as it is determined by the second derivative of $\Delta_{\text{mix}} G_m^{23}$ or the extrema of the chemical potential. If by supercooling or fast mixing, the supersaturation ratio β can go up to 200, spinodal decomposition will happen, as any tiny compositional fluctuation will reduce the free energy (see the sign of $\Delta_{\text{mix}} G_m^{23}$, see Figure 1.3 and section 3.6.1.1) and diffusion will be uphill (see the sign of μ' and section 3.6.1.1). Although the solid DBDCS is the most stable, before going to the solid phase, the system will first reach two metastable compositions of liquids that are in equilibrium: the double tangent points of $\Delta_{\text{mix}} G_m^{23}$. These are the binodal decomposition limits of LLPS of 1,4-dioxane (2)-DBDCS (3): $x_{2\text{b}3^*} = 0.0574$ (the amount fraction binodal LLPS limit of 1,4-dioxane in liquid DBDCS) and $x_{3\text{b}2} = 0.317$ (the amount fraction binodal LLPS limit of DBDCS in 1,4-dioxane). Since the surface tension between the liquid phases should be smaller than between the solid and liquid, the energy barrier of the metastable phase will be smaller than crystallisation (see Figure 1.3). If by supercooling or fast mixing, β can reach up to 100, the binodal decomposition with a smaller energy barrier than crystallisation will occur. Outside the reflection points of $\Delta_{\text{mix}} G_m^{23}$ and inside its double tangent pair, it is the binodal LLPS range (Green on Figure 3.14). Both the spinodal and the binodal LLPS will first give two metastable phases of the binodal LLPS limits. The meta-stable liquid phase rich in DBDCS (the tangent point on the left) will later solidify as its chemical potential is much larger (9 kJ/mol) than the solid reference state (see Figure 3.14.A and Figure 1.3). The remanence liquid rich in solvent (the tangent point on the right) can still crystallise through the slow nucleation and growth process, since the chemical potential of DBDCS in the remanence is nearly equally high as the DBDCS liquid. By conventional crystallisation methods, it is very difficult (or impossible)

to reach such a high supersaturation. That is why the study of spinodal decomposition is difficult. Outside the binodal LLPS limits, the stable DBDCS solid phase will form through the random nucleation of a larger energy barrier. Therefore, in this range, the mixture can stable metastable for a long time before crystallisation is observed. To accelerate the nucleation rate, a large supercooling or supersaturation ratio β is required (see section 1.1.2.1). Formation of nano-sized metastable clusters which later transform or aggerate into bigger crystals is the TSN (section 1.1.2.2) and the aggregational nucleation theory (section 1.1.2.3)



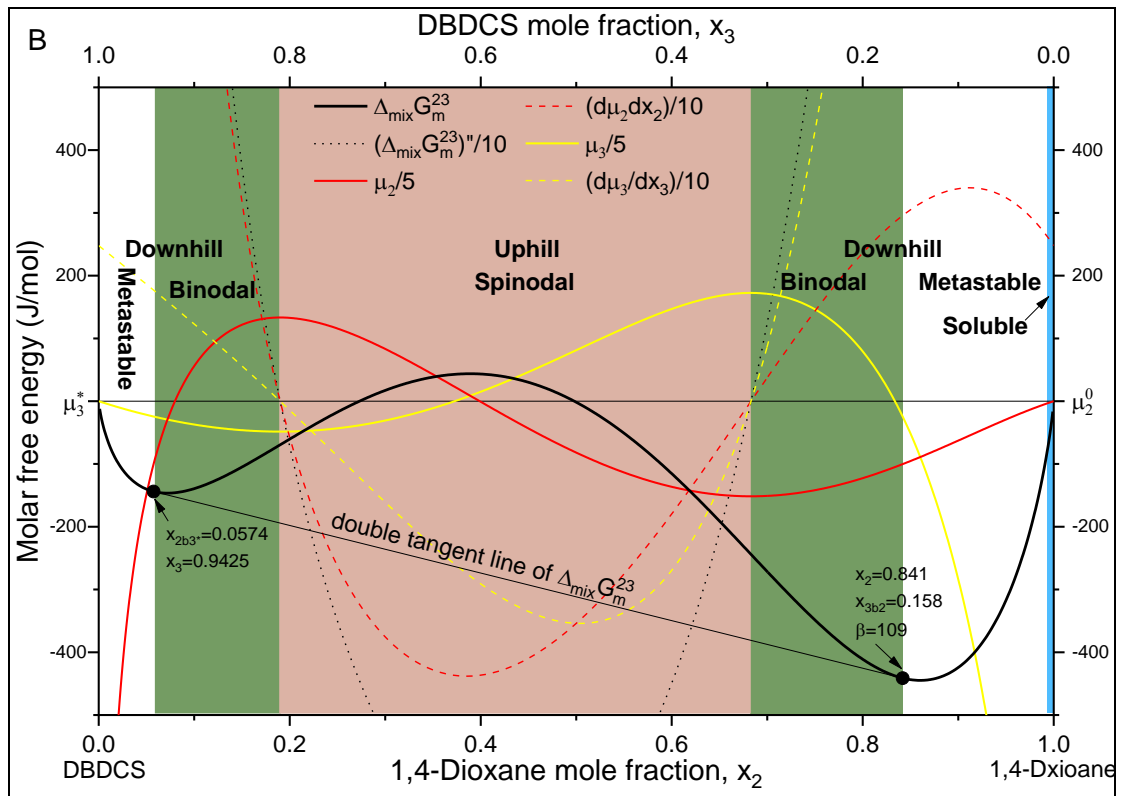
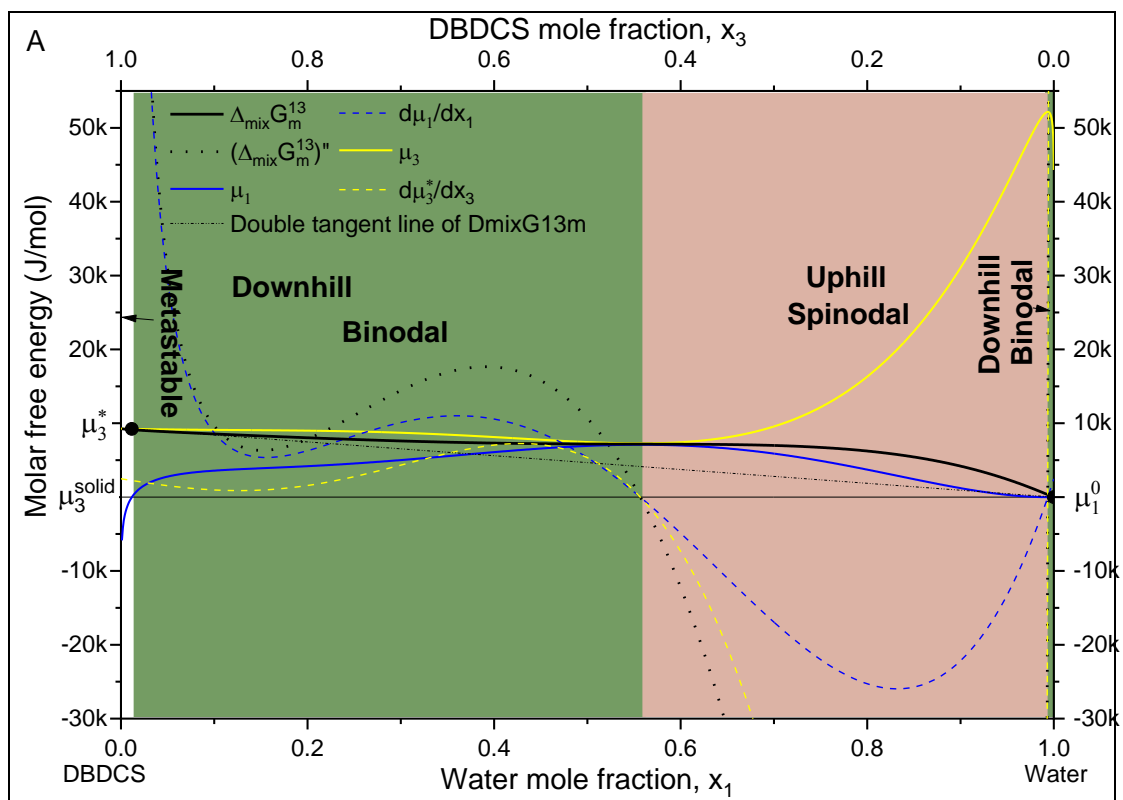


Figure 3.14. Thermodynamic stability of the binary system of DBDCS and 1,4-dioxane at 298.15 K. The molar mixing excess free energy and its second derivative, the chemical potentials and their derivatives are calculated using the H^3M model and the interaction parameters in section 3.3.2, A: using solid DBDCS as reference state. B: using liquid DBDCS as reference state. Cinnamon zone: spinodal decomposition range. Green: binodal LLPS range. Cinnamon+Green: LLPS range. White zone: metastable nucleation and growth range. Blue zone: soluble range. In Green+White+Blue, diffusion is downhill. In Cinnamon zone, diffusion is uphill opposite to Fick's law. The compositions of the limits are marked.

$\Delta_{\text{mix}} G_{\text{m}}^{13}$ of water (1)-DBDCS (3) mixture is plotted in Figure 3.15, as well as the chemical potential and their derivatives. Figure 3.15.A uses solid DBDCS as one of the reference states, and Figure 3.15.B uses liquid DBDCS. Water (1)-DBDCS (3) mixture is highly irregular and more unstable, because of the larger Ω_{13} and a_1^{13} (Table 3.8) than those 1,4-dioxane (2)-DBDCS (3) solution. Therefore, the solubility of DBDCS in water is practically

zero, even difficult to be experimentally measured. The prediction of the solubility given by Jouyban-Acree equation (see section 3.3.1) is $8.14111\text{E-}12$ in amount fraction. This “soluble” range is invisible on Figure 3.15. Both the spinodal and binodal decomposition limits of DBDCS in water are very low in the sense of concentration, but extremely high in terms of superstation ratio ($1\text{E}9$). This means, as difficult as it will be, if there is an unconventional method to fast mix DBDCS in water even to a very low concentration (0.00648 amount fraction), spinodal LLPS will occur. Whereas a slow crystallisation process of DBDCS in water is almost impossible.



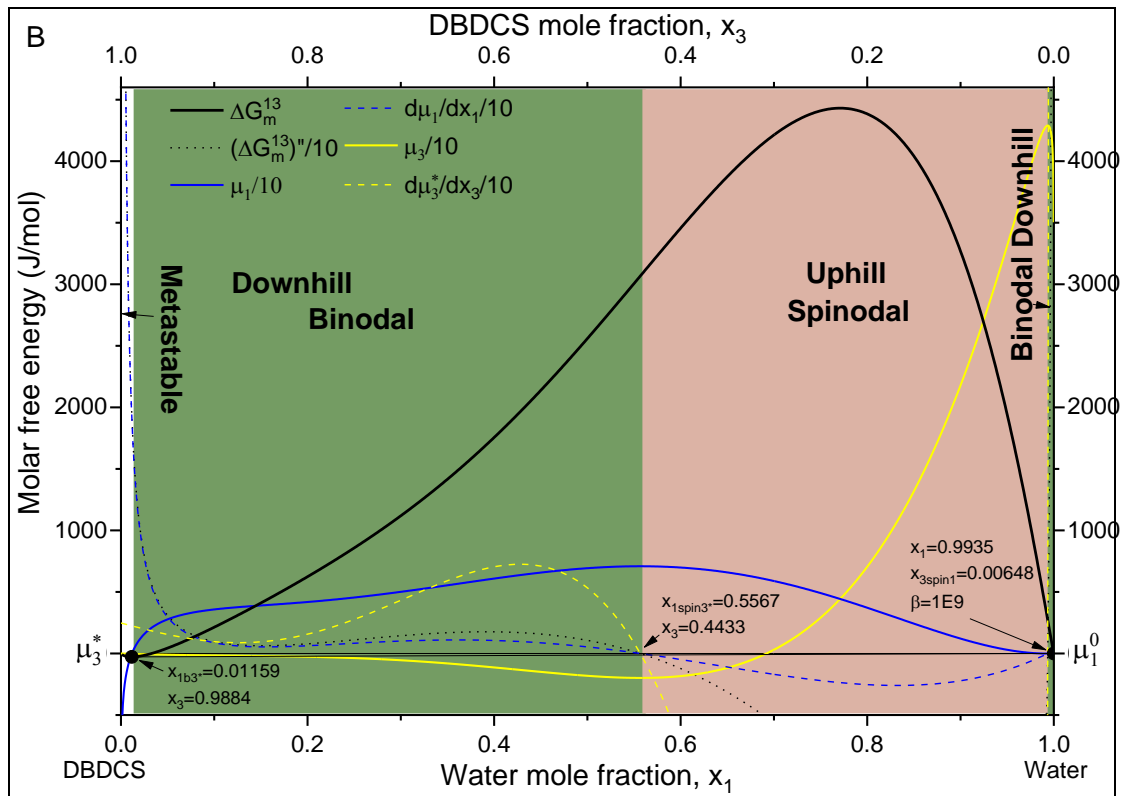


Figure 3.15. Thermodynamic stability of the binary system of DBDCS and water at 298.15 K. The molar mixing excess free energy and its second derivative, the chemical potentials and their derivatives are calculated using the H^3M model and the interaction parameters in section 3.3.2. A: using solid DBDCS as reference state. B: using liquid DBDCS as reference state. Cinnamon zone: spinodal decomposition range. Green zone: binodal LLPS range. White zone: metastable nucleation and growth range. The soluble zone is too miniscule to be seen, or even to be experimentally determined. In Green+White, diffusion is downhill. In Cinnamon zone, diffusion is uphill opposite to the concentration gradient. The compositions of limits are marked.

3.6.1.3. Decomposition of water (1)-1,4-dioxane (2)-DBDCS (3) ternary system of

Section 3.6.1.2 gives the thermodynamic stability, the diffusion direction, and the conditions for spinodal and binodal LLPS in the cases of 1,4-dioxane (2)-DBDCS (3) binary mixture and water (1)-DBDCS (3) binary mixture. These properties are interpolated from the

melting enthalpy of DBDCS and the solubilities of DBDCS in pure solvents. Figure 3.14 and Figure 3.15 make up the two sides of the ternary phase diagram of water (1)-1,4-dioxane (2)-DBDCS (3). With the “interaction parameters” we got from the activities of water (1)-1,4-dioxane (2) binary mixture and the solubility of DBDCS in the mixture, we will be able to further interpolate the rest of the phase diagram using extended H³M model.

The calculated molar excess mixing free energy of water (1)-1,4-dioxane (2)-DBDCS (3) ternary mixture are shown in Figure 3.16.A using liquid DBDCS as reference state, and in Figure 3.16.B using solid DBDCS. The chemical potential of DBDCS in the mixture is plotted in Figure 3.16.C and Figure 3.16.D using liquid and solid DBDCS as reference state, respectively.

Figure 3.16.A shows that, compared to the liquid DBDCS, the ternary mixture is highly unstable with a maximum on the water (1)-DBDCS (3) binary edge, and minima near the corners of 1,4-dioxane and liquid DBDCS. The surface of shaped like a saddle. Composition on the saddle will tend to fall to the two laterals of the saddle. Two metastable liquid phases will be formed: a nearly pure DBDCS liquid and a mixture of water (1)-1,4-dioxane (2) mixture with little DBDCS. Figure 3.16.B shows that after LLPS, the new liquid DBDCS is highly unstable. It will solidify driven by the supercooling degree. The mixture of water (1)-1,4-dioxane (2) with little DBDCS is much more stable. But Figure 3.16.D shows that the chemical potential of DBDCS μ_3 in this remanence is still highly supersaturated. Especially near the corner of water, the chemical potential of DBDCS reaches the maximum, 5 times as high as $\mu_3^* - \mu_3^{\text{solid}}$. That is to say the driving force for DBDCS to precipitate from the mixture rich in water is 5 times as high as that of the pure DBDCS to solidify at 298.15 K, 170 K below the melting point. Even the pure liquid DBDCS can grow into crystals, but in a water rich environment, DBDCS molecules will most likely give amorphous precipitations. Crystal of DBDCS will nucleate and grow from the remanence if a large fraction of 1,4-dioxane is present. The chemical potential of DBDCS is lower than the solid phase only on the edge near pure 1,4-dioxane. That is the soluble region.

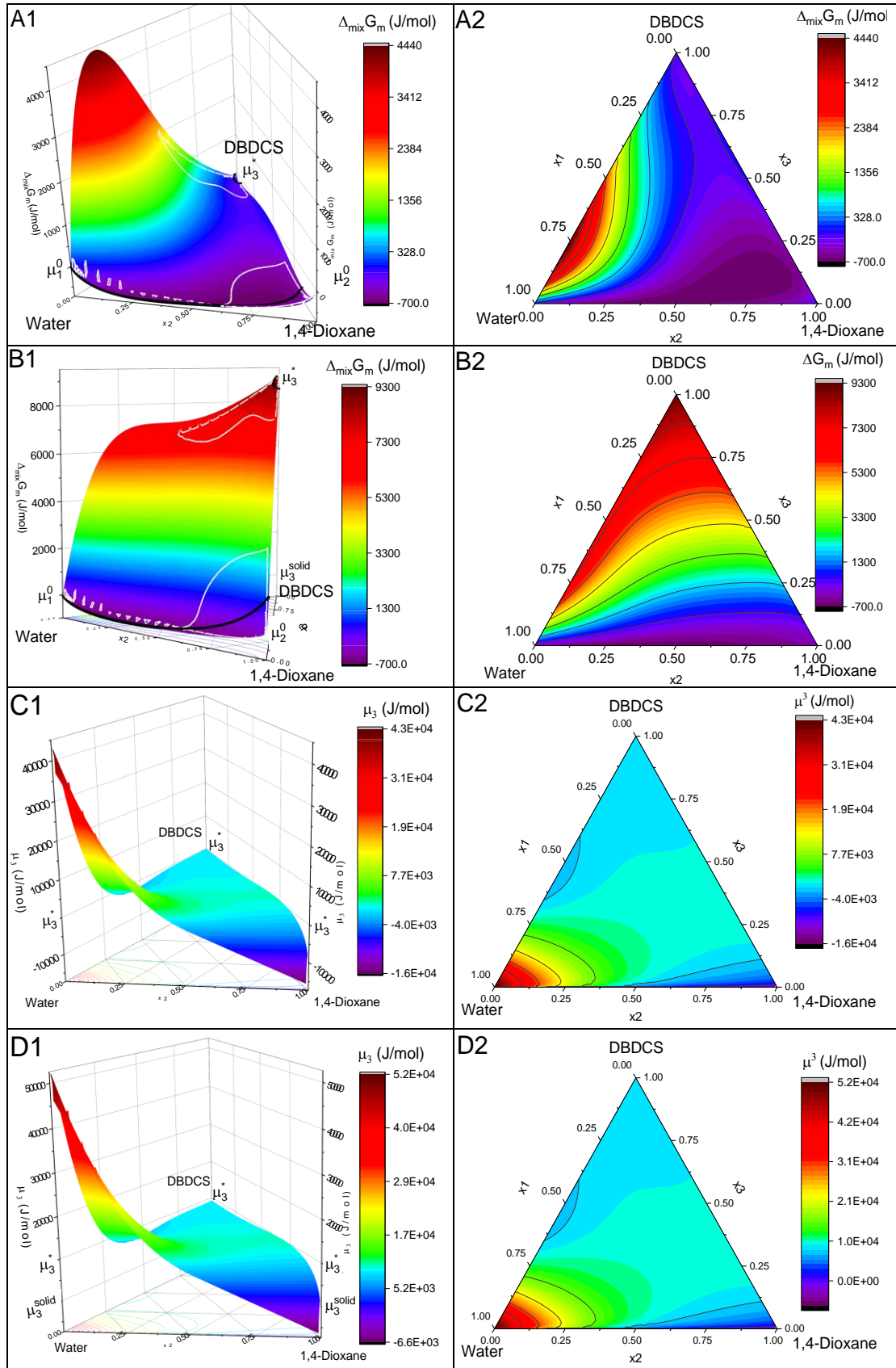


Figure 3.16. Stability of water (1)-1,4-dioxane (2)-DBDCS (3) ternary mixture. A:

$\Delta_{\text{mix}} G_m$ using liquid DBDCS as reference state. B: $\Delta_{\text{mix}} G_m$ using solid DBDCS

reference state μ_3^{solid} . C: μ_3 using liquid DBDCS reference state μ_3^* . D: μ_3 using solid DBDCS reference state μ_3^{solid} . X2 is X1 flattened.

Before reaching the solid DBDCS and a saturated mixture, the compositions on the saddle will firstly reach the two metastable liquids. The composition of the two metastable liquids in equilibrium is given by the common tangent point pairs of $\Delta_{\text{mix}} G_m$. Each common tangent point pair stand for a pair of conjugated, mutually saturated solutions. This is the binodal LLPS curve. Between the binodal LLPS limits, the spinodal zone is the ensemble of composition that will separate into two or three phases through uphill diffusion. Fluctuations of these composition lead to the formation of an enriched and a depleted voxel. In the spinodal domain both voxels are stabilised. Diffusion will be towards higher concentration. Meijering derived the relations which characterise the form of segregation in a ternary regular solution [Meijering, 1950] :

$$\frac{\partial^2 \Delta_{\text{mix}} G_m}{\partial x_1^2} \frac{\partial^2 \Delta_{\text{mix}} G_m}{\partial x_2^2} = \left(\frac{\partial^2 \Delta_{\text{mix}} G_m}{\partial x_1 \partial x_2} \right)^2 \quad (3.53)$$

with $x_3 = 1 - x_1 - x_2$. For such a composition (x_1, x_2, x_3) that satisfies equation (3.53), the curvature of $\Delta_{\text{mix}} G_m$ changes its convexity, and a spinodal decomposition will occur inside the spinodal domain where the surface is not convex. Equation (3.53) holds true for irregular solutions.

The solubility curve, the binodal LLPS limit, and the spinodal decomposition limit are calculated and plotted on Figure 3.17. The mixture inside the spinodal decomposition domain (cinnamon) will fast separate without energy barriers into two metastable phases on the binodal curves (cyan curve). The compositions in the binodal LLPS domain will also segregate into two metastable phases on the binodal curves. The energy barrier of this phase transition is smaller than crystallisation (see Figure 1.2). Both new phases are not stable. Near the DBDCS corner, the new phase is a nearly pure liquid DBDCS. It will solidify driven by a supercooling of 170

K. On the other side, it is metastable mixture of water-1,4-dioxane with little DBDCS. The metastable domain diminishes as the water fraction increases. DBDCS crystals can nucleate and grow from the mixture if a large fraction of 1,4-dioxane is present.

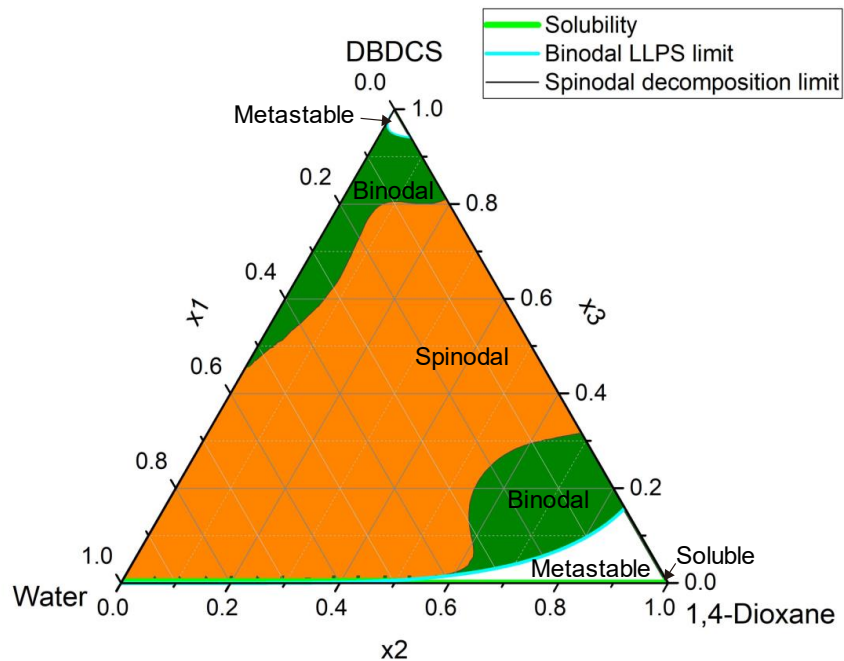


Figure 3.17. A calculated ternary phase diagram of water (1)-1,4-dioxane (2)-DBDCS (3). The soluble region is defined by the intersection of μ_3^* and μ_3^{solid} . The binodal LLPS limit is an assembly of the double tangent points of $\Delta_{\text{mix}} G_m$. The spinodal decomposition limit gives the domain where $\Delta_{\text{mix}} G_m$ is a convex surface.

By normal mixing conditions, it will be extremely difficult for the mixture to enter LLPS domains in a good solvent. However, in our microfluidic device, and because of the fast mixing and anti-solvent driven uphill diffusion, it will be easier to push the mixture into the LLPS domain or even the spinodal decomposition limit.

3.6.2. Crystallisation from antisolvent-solvent mixture

The intersection of μ_3 and μ_3^{solid} on Figure 3.16.D gives the solubility of DBDCS in water (1)-1,4-dioxane (2) mixture. But it is too miniscule to be analysed or even to be seen on

Figure 3.17. Figure 3.18 is a zoom in of the soluble domain on a log scale near the water (1)-1,4-dioxane (2) edge of the ternary phase diagram. The distance from the surface of chemical potential of DBDCS molecules in solution to that of the solid phase is the driving force for crystallisation. When the mixture is mainly composed of 1,4-dioxane, the crystallisation driving force is small, hence a slow crystallisation is possible. As water amount fraction increases, $\Delta G_{m,3}$ raises sharply. In this range, nucleation rate will be very high, size will be very small, even metastable amorphous precipitation or liquid-liquid phase separation is favoured. The solubility in this range is approaching zero, only noticeable with a log scale. The intersection line of the free energy of solid DBDCS and DBDCS in solution is the thermodynamic equilibrium solubility.

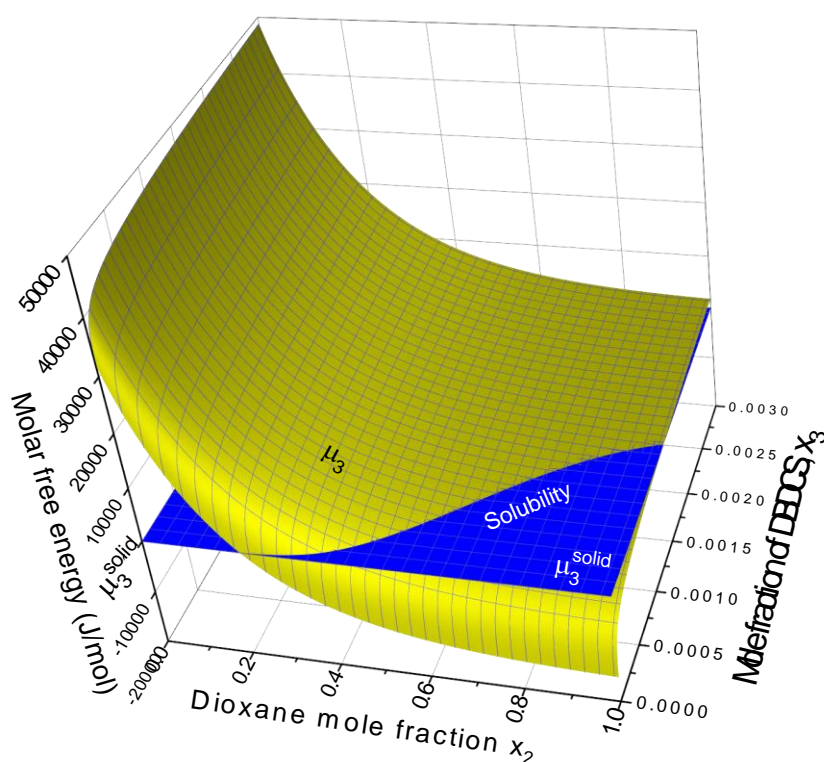


Figure 3.18. Zoom in of the Gibbs energy of DBDCS in water (1)-1,4-dioxane (2) mixture near the soluble domain.

Chapter conclusion

In this chapter, we have collected data on the density, the refractive indices, the

dynamic viscosity, and the surface energy of water (1)-1,4-dioxane (2) binary mixtures. We have estimated the mixing volume of water (1)-1,4-dioxane (2)-DBDCS (3) ternary mixture, assuming DBDCS behaves ideally due to its miniscule concentration. We have no estimation of the contribution of DBDCS to the refractivity and the viscosity of the mixture. But since its concentration is very low, we have decided to neglect its contribution.

To analyse the stability and the diffusion of the mixture, a thermodynamic approach is required. Therefore, we have briefly introduced the ideal mixing model, the regular solution model, and the H³M model for binary and ternary solvent mixtures. H³M model gives good estimation of the properties of non-ideal ternary solvent mixtures using binary interaction parameters. Since we work on non-ideal antisolvent-solvent-solute system, the Jouyban-Acree equation has been introduced to correlate the interaction parameters from solubility of a solute in a mixture of good and bad solvents. H³M model can be extended to systems with a solid solute by considering dissolving as two steps: melting of the pure solute and the mixing of the liquid solute with the solvent. Therefore, the difference in the chemical potential of the liquid and solid solute must be known.

After that, we work to extract the binary interaction parameters to describe the water (1)-1,4-dioxane (2)-DBDCS (3) ternary system. The binary interaction parameters of water (1)-1,4-dioxane (2) was extracted from their thermodynamic activities. From this we have experimental values of $\Delta_{\text{mix}} G_{\text{m}}$ on the binary edge of water (1)-1,4-dioxane (2). The melting temperature and the melting enthalpy has been measured by DSC [Kim, 2015]. Using equation (3.8), the difference of the chemical potential of liquid and crystalline DBDCS has been calculated to be $3.7RT$. This is the apex of pure DBDCS in the ternary phase diagram. Then, we have fitted the solubility of DBDCS in water (1)-1,4-dioxane (2) mixture with the Acree equation (equation (3.27)). These experimental values on one side, on curve in side, and on the apex of the triangle of the ternary phase diagram allows as to interpolate the mixing thermodynamics of the ternary mixture.

After a brief introduction on the thermodynamics of diffusion, the thermodynamic correction factor of water (1)-1,4-dioxane (2) binary system has been estimated. Comparison with experimental values has validated our thermodynamic interaction parameters of water (1)-1,4-dioxane (2).

At the end of this chapter, we have used the interaction parameters to analyse the stability of the binary systems and then the ternary system in the cases of liquid-liquid phase separation (LLPS) and of crystallisation by plotting the mixing free energy and the chemical potentials in ternary phase diagrams. A phase diagram of water (1)-1,4-dioxane (2)-DBDCS (3) has been calculated. It is comprised of a spinodal decomposition domain, two binodal LLPS domains, two metastable domains, and a miniscule soluble domain.

We have shown that $\Delta_{\text{mix}}G_{\text{m}}$ of the ternary diagram of two miscible solvents and a solute can be extrapolated from the solubility curve of the solute in the mixture of the solvent with the approximation of the H³M model and the use of the Jouyban-Acree equation. The same way can and should be used for other systems.

Chapter 4. *Comsol* simulation

4.1. <i>Comsol</i> simulation model of the coaxial microflow mixer	129
4.1.1. Model	129
4.1.2. Parameters	132
4.1.3. Studies	133
4.2. Simulation of the inter-diffusion of water (1)-1,4-dioxane (2) binary system without DBDCS	134
4.2.1. Central jet radius.....	134
4.2.2. Flow entrance length	136
4.3. Simulation of the diffusion of DBDCS in a field of solvent composition	140
Chapter conclusion.....	143

The coaxial microfluidic mixer for antisolvent precipitation has been described in section 2.1, including the flow control, the central jet radius, the flow velocity profile, the hydrodynamic l_h and concentration entrance length l_c . A microfluidic parametric sweep was carried out for water (1)-1,4-dioxane (2)-DBDCS (3). The central flow was 1,4-dioxane saturated with DBDCS. It was injected into a peripheral flow of a mixture of water (1)-1,4-dioxane (2). The thermodynamics of the ternary system was extrapolated from the water (1)-1,4-dioxane (2) binary system and the solubility of DBDCS in the mixture in Chapter 3, including the binary interaction parameters, the chemical potential, the spinodal decomposition limits, the binodal LLPS limits, and the diffusion coefficients. By changing the microfluidic input parameters (the central jet concentration, the antisolvent fraction in the peripheral flow and the flow rates), different flow structure, supersaturation and thus phase transition kinetics will be reached. *Comsol Multiphysics 5.3* is a powerful tool to illustrate the process with numerical results.

In this chapter, we shall use *Comsol* to simulate the mass transportation and the momentum transfer in the microfluidic system, neglecting the heat. Section 4.1 briefly describes the simulation model and studies. The global parameters, global and local variables defined for this model are listed in Appendix D.i. A mathematical justification of our using the *Migration in Electric Field* interface to mimic the movement of DBDCS monomers in a field of chemical potential is attached in Appendix D.ii. Section 4.2 is the simulation of the structure of the coaxial flow of pure solvents without DBDCS, compared with the experimental results, and analytical predictions. Section 4.2 demonstrates two examples of a low supersaturation coflow and a high supersaturation coflow of water (1)-1,4-dioxane (2)-DBDCS (3), respectively.

4.1. *Comsol* simulation model of the coaxial microflow mixer

4.1.1. Model

Only the reactive part of the coaxial microflow mixer was considered in the simulation.

An axisymmetric computational domain was built along the flow centre. It is simply a cylindrical tube with two coaxial round inlets and an outlet on the other end. As shown in Figure 4.1, half of the longitudinal cross-section of the reactive part of the coaxial microflow mixer was defined in an asymmetrical geometry. The small fused silica capillary (inlet c, ID = 10 μ m) was coaxially aligned inside the intermediate borosilicate capillary (inlet p, ID = 210 μ m). The length of simulated domain is 25 mm. Because the system is coaxial, rotating the simulation of the half longitudinal cross-section around the symmetry axis gives the three-dimensional illustration.

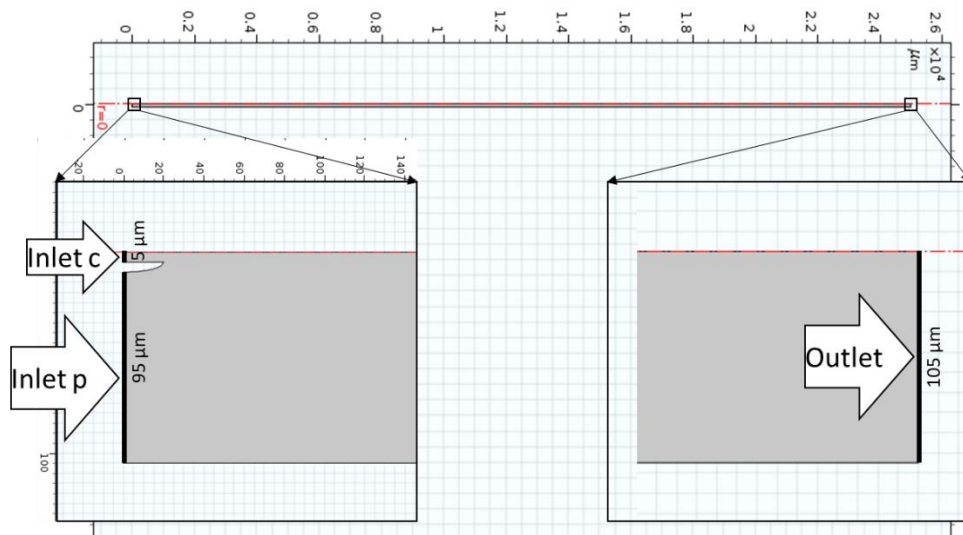


Figure 4.1. Axisymmetric geometry of the simulation domain of the reactive part of the coaxial microflow mixer.

Two *Comsol* physics, *Laminar Flow* and *Transport of Concentrated Species* were coupled. *Laminar Flow* calculates momentum transfer of the coaxial flows in a single phase governed by Navier-Stokes equation:

$$\rho(\mathbf{v} \cdot \nabla) \mathbf{v} = \nabla \cdot \left(-\rho \mathbf{I} + \mu (\nabla \mathbf{v} + (\nabla \mathbf{v})^T) - \frac{2}{3} \mu (\nabla \cdot \mathbf{v}) \mathbf{I} \right) \quad (4.1)$$

and continuity equation:

$$\nabla \cdot (\rho \mathbf{v}) = 0 \quad (4.2)$$

with ρ the density of the mixture, \mathbf{v} its velocity field, μ its local dynamic viscosity and \mathbf{I} an identity tensor. *Transport of Concentrated Species* computes mass transportation by advection-diffusion equation:

$$\nabla \cdot \mathbf{j}_i + \rho(\mathbf{v} \cdot \nabla) w_i = R_i \quad (4.3)$$

with \mathbf{j}_i the diffusive mass flux of species i , w_i its local mass fraction, R_i its net source rate and \mathbf{v} calculated from *Laminar Flow*; and Fick's law:

$$\begin{aligned} \mathbf{j}_i &= -M_i c D_i^F \nabla x_i \\ &= -\rho D_i^F \frac{\nabla x_i}{x_i} \\ &= -\left(\rho D_i^F \nabla w_i + \rho w_i D_i^F \frac{\nabla M_n}{M_n} \right), \end{aligned} \quad (4.4)$$

where M_i denotes the relative molar mass of species i , c the local molar concentration of the mixture, D_i^F the diffusion coefficient of species i in the mixture, x_i its local amount fraction, w_i its local mass fraction and M_n the local mean molar mass of the mixture. The total flux of species i is

$$\mathbf{n}_i = \mathbf{j}_i + \rho \mathbf{v} w_i. \quad (4.5)$$

The capillaries' symmetry axis, inner walls, inlets, and outlets defined the boundaries of the simulation. Boundary conditions for Inlet C was a laminar flow of species 3 and 2 with flow rate Q_c , mass concentration of species 3 ρ_{3c} and zero entrance length. Boundary conditions for Inlet P was a laminar flow of species 1 and 2 with flow rate Q_p , volume fraction ϕ_{1p} and zero entrance length. Boundary conditions for Outlet was a laminar flow with zero exit pressure and zero exit length. Temperature was 298.15 K.

Mesh size of the whole domain was the default normal size calibrated for fluid dynamics. Mesh near the boundaries and the corners were refined to the software predefined

“finer” level. Mesh in 2 rectangles, $(r \in [0\mu\text{m}, 90\mu\text{m}], z \in [0\mu\text{m}, 500\mu\text{m}])$ and $(r \in [0\mu\text{m}, 70\mu\text{m}], z \in [500\mu\text{m}, 5000\mu\text{m}])$ were further refined twice as this was the main area where mass and momentum transfer occurred. To further reduce the size of the mesh will not significantly improve the quality of the simulation but an excess consumption of the computation time.

The initial values of the domain included a laminar flow velocity field $\left(v_x = v_{\max} \left(1 - \frac{r^2}{R^2} \right), v_r = 0 \right)$ (equation (2.18)), zero pressure and a homogeneous composition, $\rho_{3\text{mix}}$ (equation (2.23)) and ϕ_{lmix} (equation (2.11)).

4.1.2. Parameters

The parameters of the materials involved are listed in Table 3.1. The property of DBDCS in solute state is estimated in section 3.1. Its n_D and $\ddot{\mu}$ are unknown. But since its concentration is miniscule, we shall neglect the contribution from DBDCS.

One of the difficulties in this simulation was that the local properties of the simulation domain are not constants but depended on the local composition of water (1)-1,4-dioxane (2)-DBDCS (3). Therefore, the local dynamic viscosity $\ddot{\mu}$ (equation (3.3)), the local mass density ρ_D (equation (3.2)), the local refractive index n_D (equation (3.4) and (3.5)), the local solubility x_{3s} (equation (3.28)) must be defined for the simulation domain.

The *Transport of Concentrated Species* interface requires a diffusion coefficient for each species. We have shown in section 3.4 that diffusion is migration of molecules driven by a field of chemical potential. The driving force is its chemical potential gradient. The chemical potential is a function of the composition of the mixture. For binary systems, there is only one independent component, therefore, the diffusion thermodynamic factor can be easily given as

$\left(1 + \frac{d \ln \gamma_i}{d \ln x_i}\right)$ (equation (3.36)). But for n-component systems, $\ln \gamma_i$ depends on (n-1)

independent variables. It will be easier to simulate the movement of particles of different mobilities in its chemical potential field. Since the concentration of DBDCS is negligible in the system, we can make the approximation that the diffusion of water and 1,4-dioxane is not correlated with DBDCS. Therefore, we can simply use the mutual diffusion coefficients of the binary water (1)-1,4-dioxane (2) system (equation (3.42)). As for DBDCS, it would be easier to simulate particles' movement in a chemical potential field than to give $\left(1 + \frac{d \ln \gamma_i}{d \ln x_i}\right)$.

Therefore, we want to bypass the diffusion coefficient by defining a virtual electric potential field that is equal to the chemical potential of DBDCS in the simulation domain and let every DBDCS molecule carry one virtual elementary charge using the *Migration in Electric Field* interface of *Comsol*. This will be equivalent to a simulation of DBDCS moving in a chemical potential field. The mathematical justification of this bypass is attached in Appendix D.ii.

To make the simulation model versatile and user friendly, we have defined (see Appendix D.i) global parameters (Table Appen.D.1), global variables (Table Appen.D.2) and local variables (Table Appen.D.3). To adapt this simulation model for other systems, one just need to input the corresponding parameters.

4.1.3. Studies

Three types of studies were carried out: (i) time-dependent computation will illustrate the evolution of the system from the initial values to a certain time by a given time step. This is useful to make animations of the flow after the injection until it reaches equilibrium. (ii) Parametric sweep of Q_c and Q_p to simulate the influence of microfluidic input parameters. This allows the flow structure dependence studies, the hydrodynamic velocity profile determination, the hydrodynamic and the concentration entrance length's dependence on a parameter. (iii) Stationary simulation for a converged final equilibrium situation. This takes the shortest simulation time. We will present type (ii) and (iii) in the manuscript.

After each simulation, the velocity field, volume fraction of solvents, mass concentration of DBDCS, uphill and downhill diffusive driving force, velocity and flux of DBDCS, convection flux of DBDCS, refractive index gradient, solubility, supersaturation, supersaturation ratio, expected nucleation rate and growth rate were plotted over different geometric elements (lines, radii, cross-sections...) for a deeper understanding of the coaxial microflow mixer and comparison with the experimental results.

4.2. Simulation of the inter-diffusion of water (1)-1,4-dioxane (2) binary system without DBDCS

4.2.1. Central jet radius

This is a parametric simulation of Q_c of pure 1,4-dioxane and Q_p of pure water (the values are the same than those used for the experiment in Figure 2.7). The simulation gives amount fraction of each species. From that, we can get the volume fraction of a species (for example Figure 4.2.A), n_D of the mixture (Figure 4.2.B) and the gradient of n_D (Figure 4.2.C) in the simulation domain.

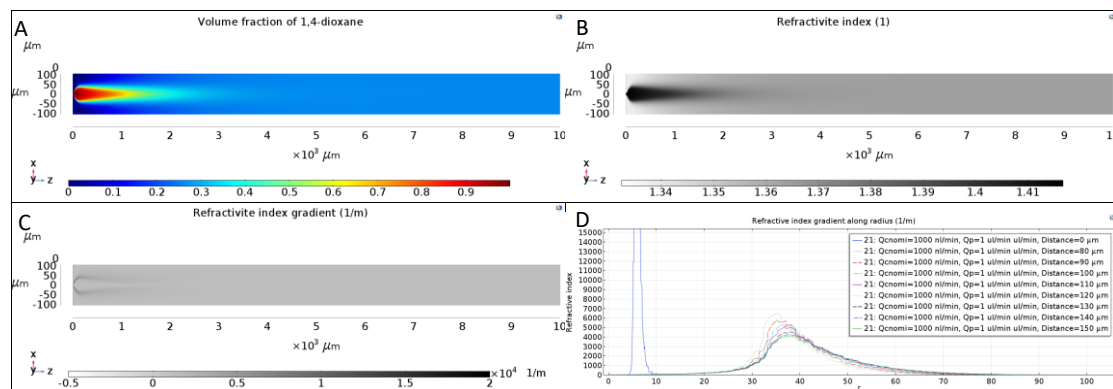


Figure 4.2. An example of the parametric sweep simulation: $\rho_{3c} = 0$, $Q_c = 370 \text{ nl/min}$,

$\phi_{1p} = 100\%$, $Q_p = 1 \mu\text{l/min}$. A: volume fraction of 1,4-dioxane; B: refractive index n_D ; C: gradient of refractive index; D: gradient of refractive index along radius at different distance from nozzle.

In section 2.1.3, we have experimentally shown (see Figure 2.8) that the maximum

central jet radius $r_{c,max} = R_{channel} \cdot \sqrt{1 - \sqrt{1 - \frac{Q_c}{Q_c + Q_p}}}$ (equation (2.14)) from the OM images

(Figure 2.7). The interface between the central jet and the peripheral flow can be seen because of the contrast in the refractive indices. By plotting n_D in the simulation domain, we can compare our simulation with the OM images of the parametric sweep, as shown in Figure 4.3. Our simulation is remarkably close to the experiment for all the parameters tested. This validates our estimation of the diffusion coefficients.

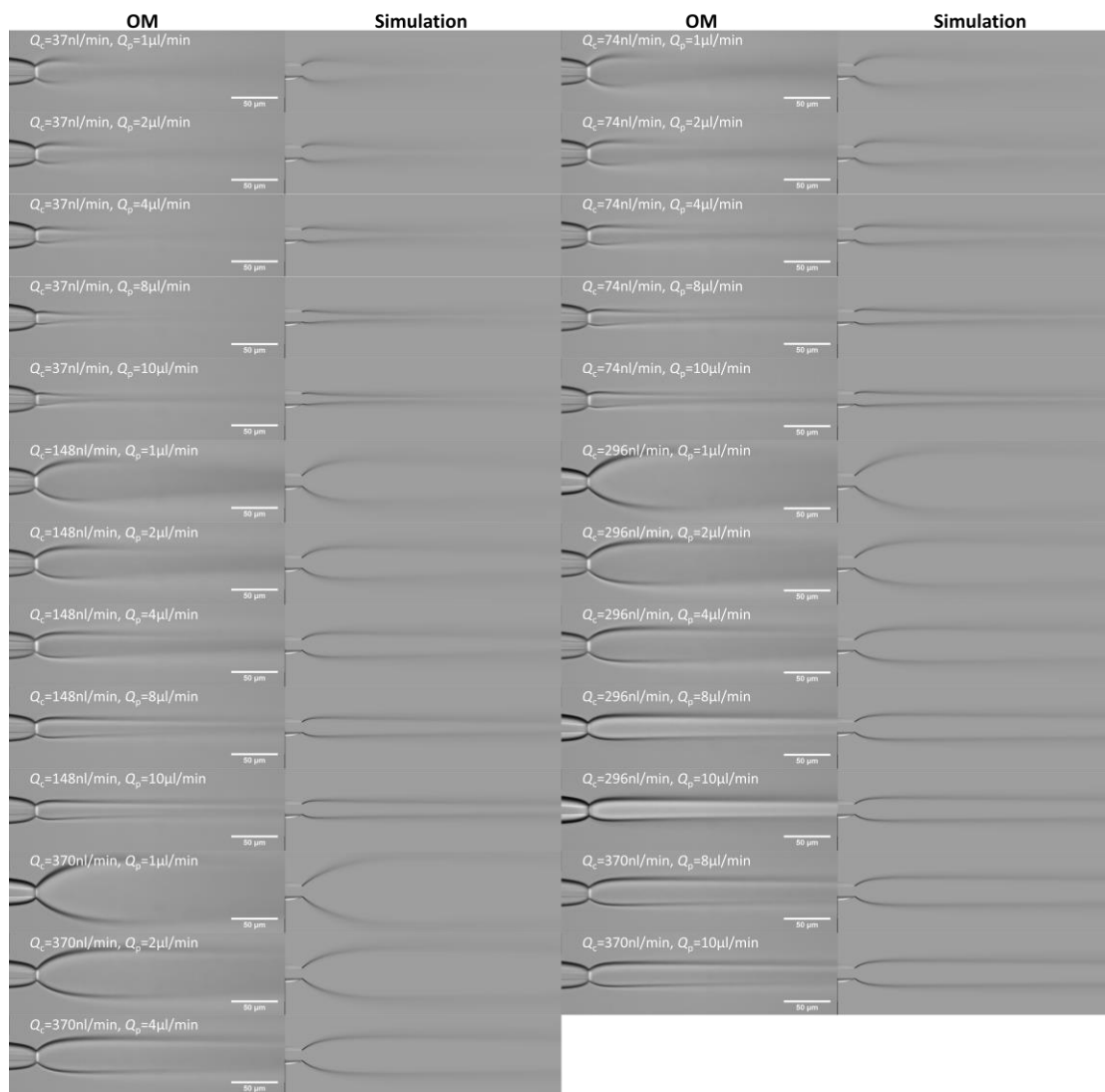


Figure 4.3. Comparison of the OM images and Comsol simulation of the refractive index n_D of a parametric sweep of a central flow of 1,4-dioxane into a peripheral

flow of water. The microfluidic parameters are marked on the small OM images.

We plot the gradient of n_D along the tube radii at different distance from the nozzle (Figure 4.2.D). The maximum of the gradient of n_D is taken as the simulated $r_{c,max}$, then compared with the experimental values in Figure 4.4. The theory (equation (2.14)), the simulation and the experiment match.

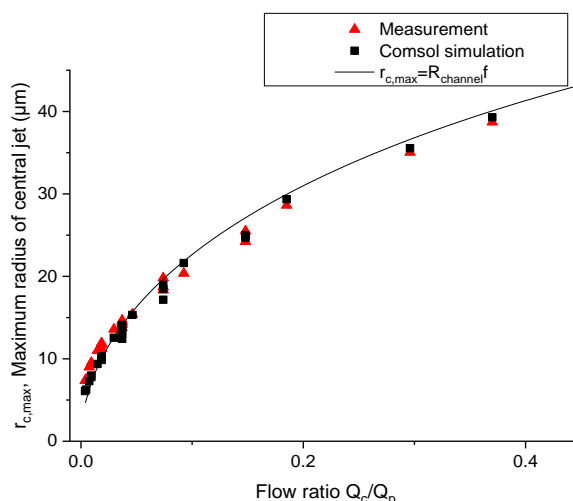


Figure 4.4. Comparison of the Comsol simulation (■), theoretical calculation (line) and the experimental measurement (▲) of the maximum central jet $r_{c,max}$ as a function of flow ratio.

4.2.2. Flow entrance length

In section 2.1.3, we used the Reynolds number Re and the Péclet number Pe to estimate the hydrodynamic entrance length l_h and the concentration entrance length l_c , respectively (see Appendix B.ii.ii). Depending on the flow rates, it takes 1~15 μm to develop a Poiseuille velocity profile and 1~11 mm to reach a homogeneous solvents composition. This is a crude estimation. More precise calculation can be done with *Comsol*.

Figure 4.5 illustrates how a Poiseuille velocity profile along flow radius is developed from the jet to a laminar flow. The microfluidic parameters are

$Q_c = 370 \text{ nl/min}$, $Q_p = 10 \mu\text{l/min}$, $\phi_{1p} = 100\%$, $\rho_{3c} = 0$. At the exit of the injection nozzle, the velocity is much higher than the peripheral flow. Therefore, a central jet is formed after the injection nozzle. A Poiseuille velocity profile along its radius is quickly developed around $100 \mu\text{m}$ from the nozzle.

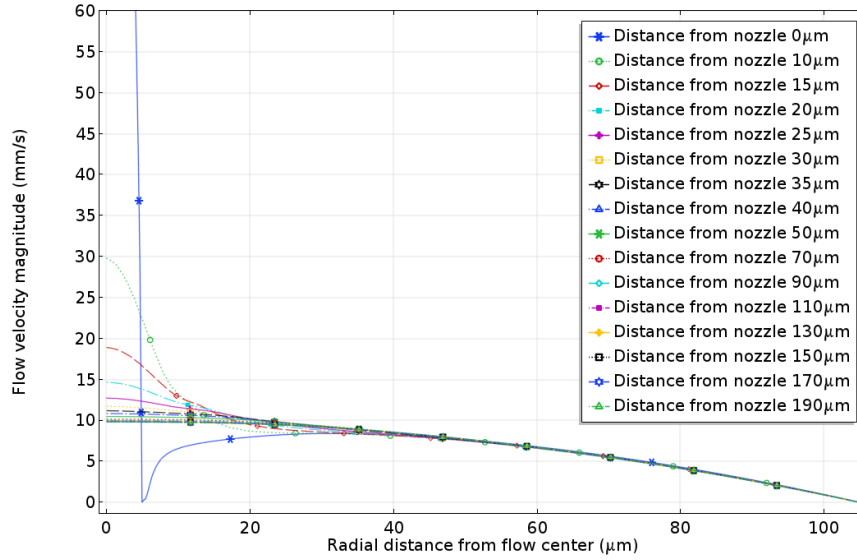


Figure 4.5. Comsol simulation of the development of a laminar flow of a Poiseuille velocity profile along its radius. Microfluidic parameters:

$$\rho_{3c} = 0, Q_c = 370 \text{ nl/min}, \phi_{1p} = 100\%, Q_p = 10 \mu\text{l/min}.$$

l_h is illustrated by the flow velocity at the tube centre v_{\max} . It is plotted in Figure 4.6.

v_{\max} increases from 1 to 10 mm/s as Q_p increases from 1 to 10 $\mu\text{l/min}$. The gradient $\frac{dv_{\max}}{dx}$

goes to zero right before $x=200 \mu\text{m}$ for all tested parameters.

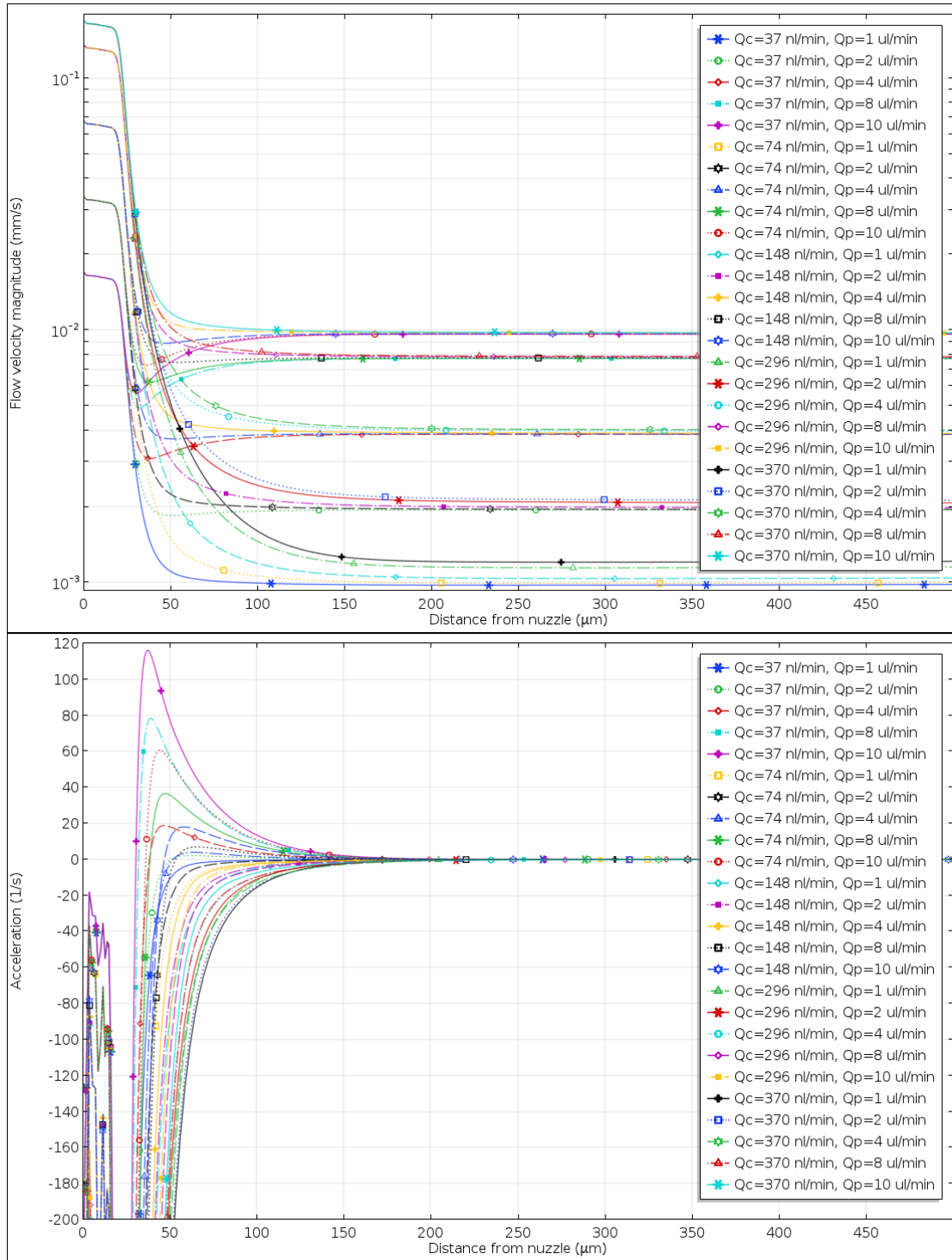


Figure 4.6. Parametric sweep simulation of flow velocity profiles along tube centre (top) and its gradient (bottom) on the flow direction. The hydrodynamic entrance length l_h is $200 \mu\text{m}$.

The evolution of the mass concentration profile of 1,4-dioxane along radius is plotted in Figure 4.7. This is one of the parametric sweep combinations:

$Q_c = 370 \text{ nl/min}$, $Q_p = 10 \mu\text{l/min}$, $\phi_{1p} = 100\%$, $\rho_{3c} = 0$. At the exit of the injection nozzle, it is pure 1,4-dioxane inside and pure water outside. After the injection nozzle, 1,4-dioxane started to diffuse outward and water inward. The mass concentration of 1,4-dioxane near the flow centre decreases as the distance increases, while its concentration on the periphery increases. At distance shorter than $70 \mu\text{m}$, the hydrodynamic expansion of the central flow is seen. From 70 to $650 \mu\text{m}$, is the time it takes for the first water to reach the centre, this comes with a change of the concentration profile. Beyond $650 \mu\text{m}$, the concentration profile is stable with a gaussian profile. 1,4-Dioxane is escaping into the water. A homogeneous concentration is reached around $5000 \mu\text{m}$ from the injection nozzle.

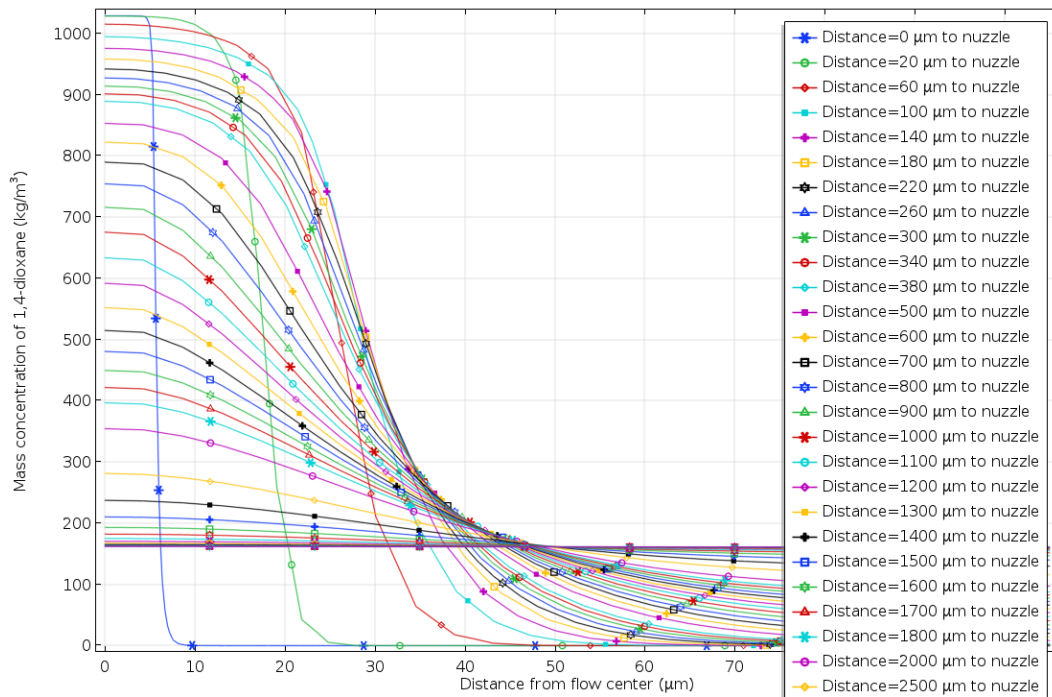


Figure 4.7. Comsol simulation of the development of a homogeneous concentration.

Microfluidic parameters: $\rho_{3c} = 0$, $Q_c = 370 \text{ nl/min}$, $\phi_{1p} = 100\%$, $Q_p = 2 \mu\text{l/min}$.

l_c can be read from the concentration profile along flow centre. Figure 4.8 shows the mass concentration of 1,4-dioxane along the flow centre and its gradient on the flow direction given by *Comsol*. The simulation shows that l_c is between $2\sim 10 \text{ mm}$.

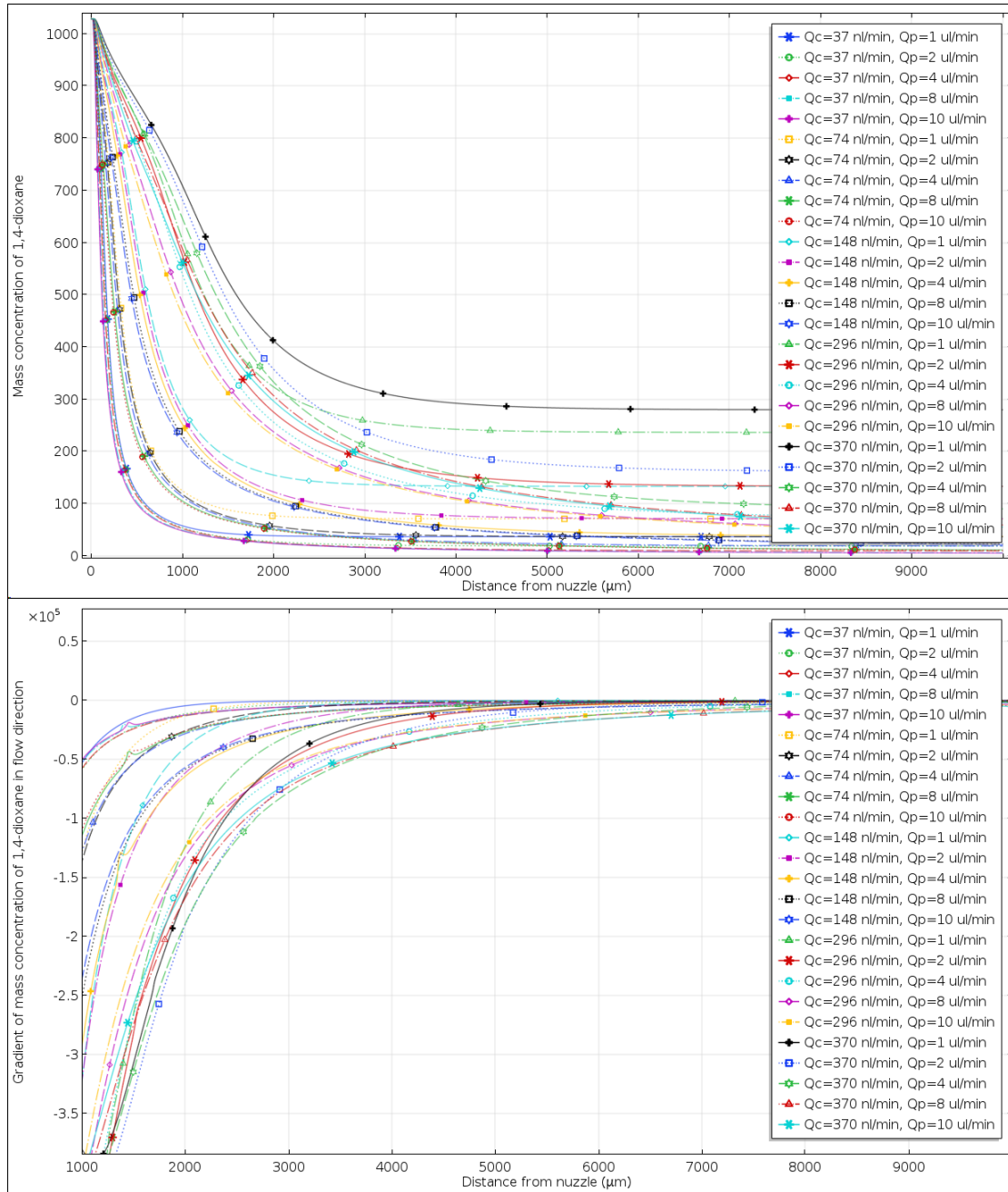


Figure 4.8. Parametric sweep simulation of 1,4-dioxane mass concentration along flow centre (top) and its gradient (bottom) on the flow direction. This reflects the concentration entrance length l_c of the flow.

4.3. Simulation of the diffusion of DBDCS in a field of solvent composition

An example of simulation of the diffusion of DBDCS in a field of composition of water (1)-1,4-dioxane (2) mixture ($\rho_{3c} = 10\text{g/l}$, $Q_c = 148\text{nl/min}$, $\phi_{lp} = 50\%$, $Q_p = 1\mu\text{l/min}$) is

shown in Figure 4.9. These conditions are optimal for the observation of the spontaneous crystallisation (see Chapter 6). Simulation illustrates that after 3 mm, the solvents composition appears homogeneous (Figure 4.9.A). The solubility is a function of solvents fraction. DBDCS is confined in the good solvent. Its concentration increased slightly before 1 mm and then reduces slowly to almost zero after 3 mm. The supersaturation reaches a maximum of 3.5 along the flow centre around 2 mm from the nozzle.

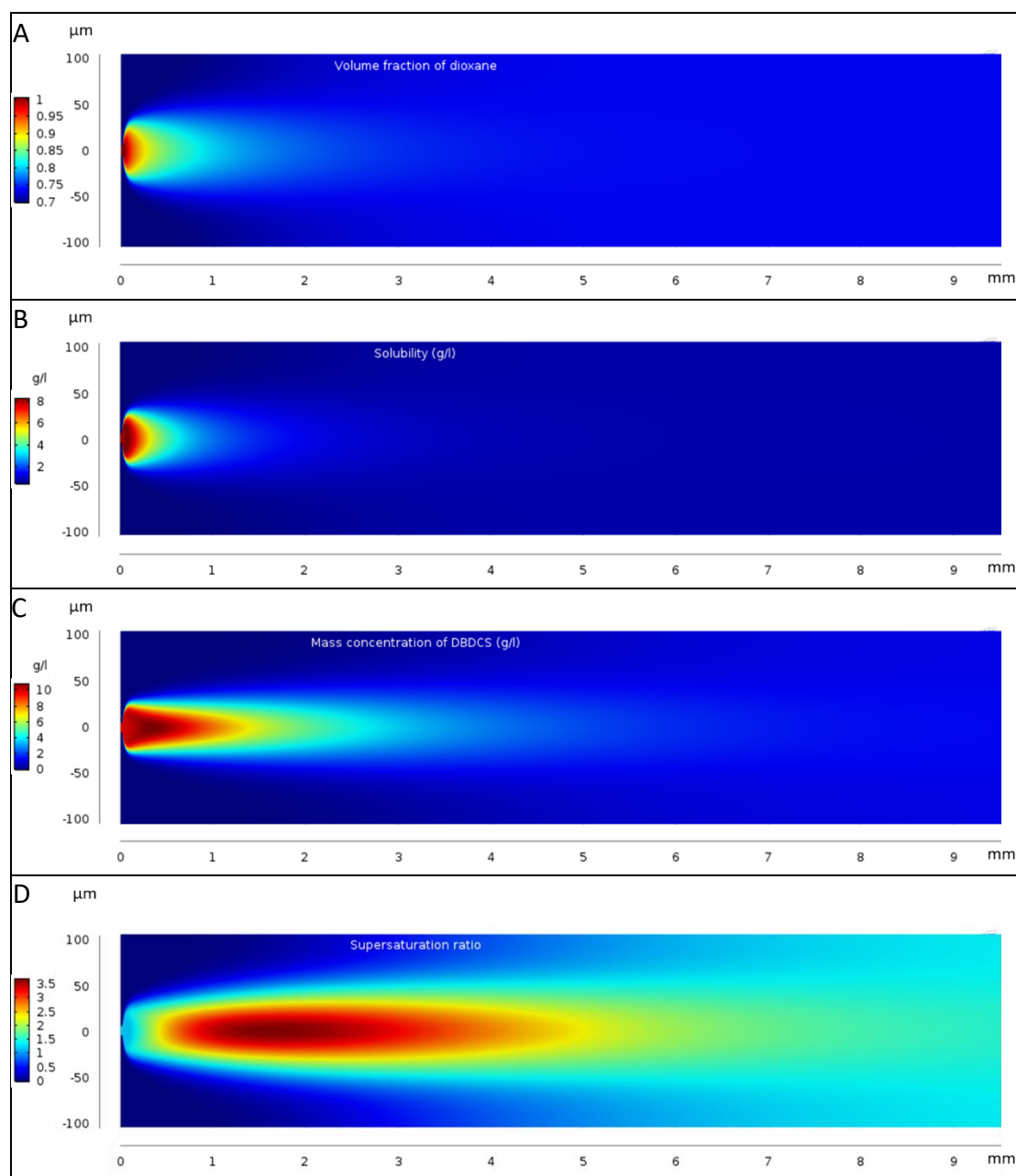


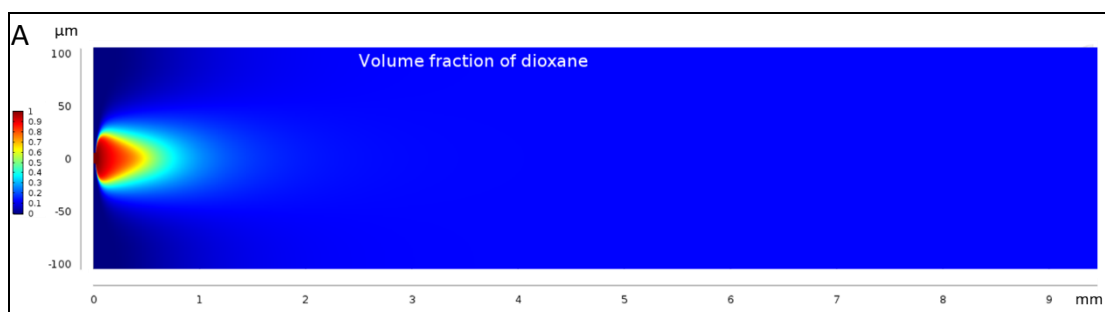
Figure 4.9. Simulation of DBDCS diffusion in a field of solvent composition.

$\rho_{3c} = 10\text{g/l}$, $Q_c = 148\text{nl/min}$, $\phi_{1p} = 30\%$, $Q_p = 1\mu\text{l/min}$. A: volume fraction of 1,4-

dioxane neglecting DBDCS; B: solubility of DBDCS; C: mass concentration of DBDCS; D: supersaturation of DBDCS.

In section 1.1.2.1, we have demonstrated that the nucleation rate of a solute in a solution $N_s = K_N \cdot c^2 \cdot \exp\left(-\frac{1}{\ln^2 \beta}\right)$ (equation (1.15)), with c the molar concentration of the solute and β the supersaturation ratio. One can assume from this simulation, that spontaneous nucleation will start along the flow centre around 2 mm from the injection nozzle. The growth velocity of the crystals would be fast after nucleation and before 3 mm. Then the crystals will grow at a low and almost constant rate.

If we switch the peripheral flow to pure water. The chemical potential gradient of DBDCS will be so high, that it will be strongly repelled to the flow centre where is rich in 1,4-dioxane. This is simulated in Figure 4.10 with other parameters same as Figure 4.9. The computation shows that the DBDCS molecule are strongly pushed towards the flow centre by the anti-solvent. Its concentration reaches 120 g/l. Consequently, the supersaturation is extremely high. Under such an unstable condition, ultra-fast precipitation or LLPS will be possible. This is one of the conditions for “droplet traps”, an extreme scenario of liquid-liquid phase separation, that we will explore in Chapter 5. It must be noticed that this simulation model is not taking phase transition into account. It only simulates the hydrodynamics and the molecular diffusion without phase transition. Therefore, the simulation before the phase transition starting distance d_p will be close to reality, whereas once transition has started, the simulation after d_p will not be different than reality.



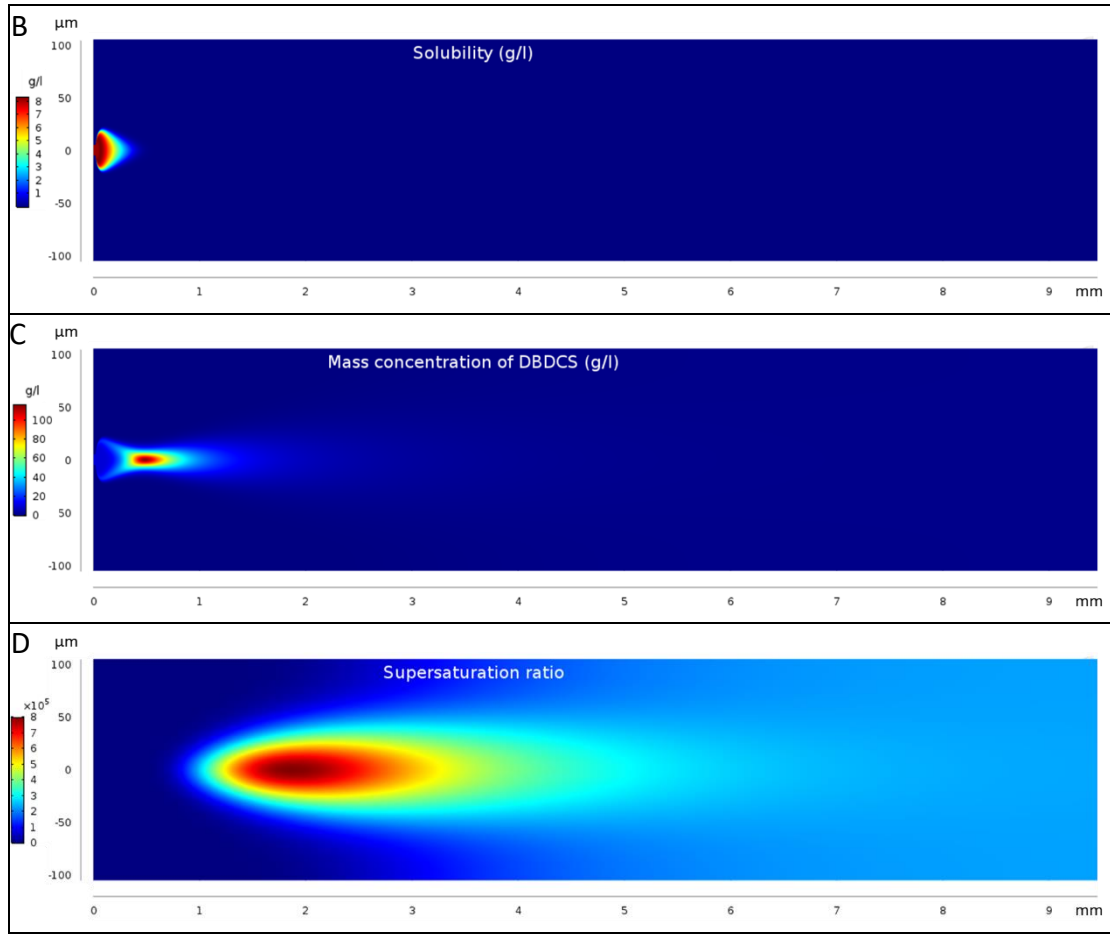


Figure 4.10. Simulation of DBDCS diffusion in a field of solvent composition.

Microfluidic parameters: $Q_c = 148$ nl/min, $Q_p = 1$ μ l/min, $\phi_{1p} = 100\%$, $\rho_{3c} = 10$ g/l. A: volume fraction of 1,4-dioxane neglecting DBDCS; B: solubility of DBDCS; C: mass concentration of DBDCS; D: supersaturation of DBDCS.

Chapter conclusion

The *Comsol* simulation model and parameters for the coaxial microfluidic mixing process of water (1)-1,4-dioxane (2)-DBDCS (3) have been introduced in this chapter with some examples. The phase transition and the mixing heat have not been taken into account in this model. We use this model to simulate the momentum exchange between of coaxial flows and the mass transportation among the species.

A parametric sweep of Q_c and Q_p using pure solvents illustrates excellent agreement between the experiment, the simulation, and the theory of the maximum central jet radius r_{\max} .

The simulation of the refractive index gradient shows excellent agreement with the OM images. The simulation gives detailed illustration of the expansion of the central jet and the evolution of the concentration profile.

Two examples of simulation maps of DBDCS concentration ρ_3 , solubility ρ_{3s} , supersaturation ratio β of the flow are given: one a large fraction of the good solvent, the other with a large fraction of the anti-solvent. Simulation shows that β can be different by 4 order of magnitude.

Chapter 5. Phase diagram of water (1)-1,4-dioxane

(2)-DBDCS (3) system in the coaxial microfluidic

mixer. Part I: Non-crystalline phase transition

5.1. Phenomena observed in the coaxial microfluidic mixer	147
5.2. Evidences for antisolvent focusing of DBDCS	148
5.3. Phase diagram of water (1)-1,4-dioxane (2)-DBDCS (3) the coaxial microfluidic mixer.....	151
5.4. The soluble region.....	153
5.5. Nano-objects	154
5.5.1. <i>In situ</i> OM observation	154
5.5.2. Nature of the nano-particles.....	157
5.5.3. <i>Post-mortem</i> observation	158
5.6. Liquid-liquid phase separation.....	159
5.6.1. From nanoparticles to droplets	159
5.6.2. Formation mechanism of the droplets.....	161
5.6.3. Abnormally large, backward flowing droplets, inner structure and crystallisation of the droplets caught in flow by Marangoni effect.	163
5.6.4. <i>Post-mortem</i> drying of the droplets	168
5.6.5. Solidification of the droplets in the flow.....	169
5.7. Kinetic characteristics of the coaxial microflow mixer	170
5.7.1. A simple relation to calculate the droplet formation distance and the average focusing velocity.....	172
5.7.2. Dependence of the average focusing velocity on microfluidic parameters	176
5.7.3. Dependence of LLPS and nano-precipitation starting position on microfluidic parameters	185
5.7.4. Quality of the prediction of the chemical potential focusing velocity, distance, the binodal LLPS threshold and the diffusion coefficient of DBDCS in water (1)-1,4-dioxane (2) coaxial microflow.....	189
5.8. Droplet size dependence on microfluidic parameters	192
5.8.1. The total volume fraction of the droplets in the flow	192
5.8.2. The size of the DBDCS droplets.....	196
Chapter conclusion.....	203

During the preliminary test of the coaxial microflow mixer with THF-water-(Calix-Cousulf-Cs²⁺), THF-water-(caesium acetate), THF-water-CsCl, water-THF-DBDCS, water-(THF20-1,4-dioxane80)-DBDCS, and water-acetone-DBDCS systems, unexpected phase transitions, such as liquid-liquid phase separation of the miscible solvent-antisolvent systems, metastable solid phases, and two-step crystallisation, had been recorded. To explore the microfluidic conditions whereby the different types of phase transitions occur, a microfluidic parametric sweep was carried out with water (1)-1,4-dioxane (2)-DBDCS (3). The microfluidic system allows us to explore four input parameters: the central jet concentration ρ_{3c} , the antisolvent volume fraction in the peripheral flow ϕ_{1p} and the flow rates of the coflow. The type of phase transition, the kinetics of the phase transition, the number and the size of the new phase, and polymorphs through the fluorescence lifetimes were characterised by OM and FLIM, for both spontaneous and laser-induced phase transitions. The OM and FLIM videos, and table of the phase transition type and distance of the more than 2000 measurements are available on the server *Patrick* of PPSM. These results are organised into the next three parts. We shall present the result of non-crystalline spontaneous precipitation and liquid-liquid phase separation (LLPS) in Chapter 5, the spontaneous crystallisation in Chapter 6, and the laser-induced nucleation in Chapter 7.

In this chapter, section 5.1 briefly introduces the different types of spontaneous phase transition and the typical mass and momentum transportation processes observed in the microfluidic coaxial mixer with water (1)-1,4-dioxane (2)-DBDCS (3). In section 5.3, we present the focusing of the solute towards the flow centre by the gradient of the antisolvent and correlate it with *Comsol* simulation. In section 5.3, the types of the spontaneous phase transitions are plotted in a phase diagram of the overall composition of the mixture. Section 5.4 is about the soluble region of the phase diagram. Section 5.5 describes the *in situ* and *post-mortem* nano-objects precipitated spontaneously. An experiment of nano-particle precipitation of Calix-Cousulf-Cs²⁺ is attached in Appendix E with its FLIM map. Section 5.6 is the observation of LLPS followed by droplets formation at the flow centre. In section 5.7, we shall

propose a semi-theoretical analysis of the kinetics (the antisolvent focusing speed of the solute, the LLPS starting distance, and the antisolvent focusing limit) of the LLPS. Section 5.8 is a study on the size dependence of the droplets on microfluidic parameters.

5.1. Phenomena observed in the coaxial microfluidic mixer

To explore the microfluidic conditions for the different phase transitions, a parametric sweep was designed (see section 2.3 and Figure 2.13). Four microfluidic input parameters can be explored with our set up: ϕ_{lp} (the volume fraction of water in the peripheral flow. We have never put DBDCS in the peripheral flow), ρ_{3c} (the mass concentration of DBDCS in the central flow), Q_c and Q_p , the flow rates of the central and the peripheral flow, respectively.

The different types of spontaneous phase transitions, obtained during the microfluidic parametric sweep for water (1)-1,4-dioxane (2)-DBDCS (3) mixture in the coaxial microflow, are listed in Figure 5.1. These phenomena were observed under different microfluidic parameters.

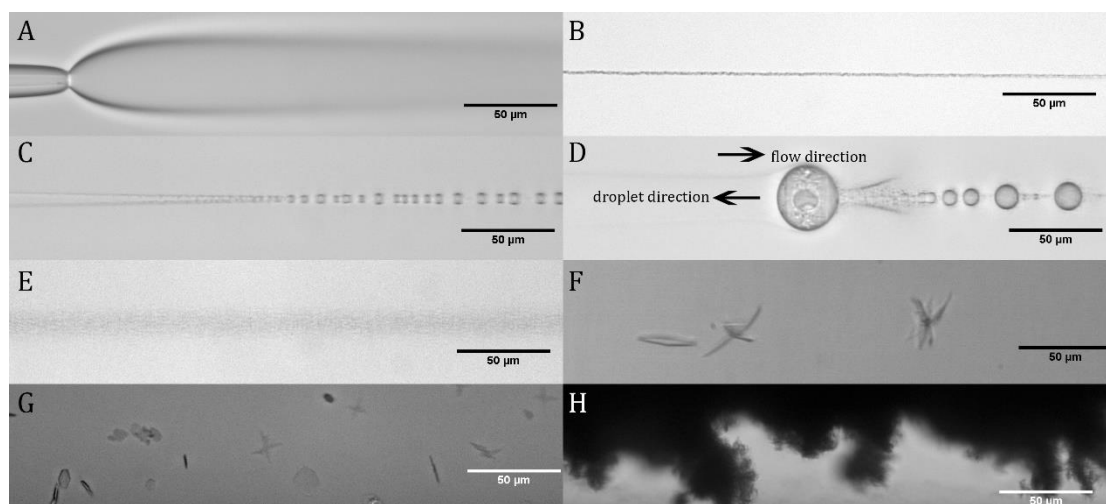


Figure 5.1. Typical phenomena observed in the coaxial microfluidic mixer with water (1)-1,4-dioxane (2)-DBDCS (3) system. A: no phase transition, only inter-diffusion of the central and peripheral flows, microfluidic parameters

$\rho_{3c} = 5 \text{ g/l}$, $Q_c = 74 \text{ nl/min}$, $\phi_{lp} = 20\%$, $Q_p = 1 \mu\text{l/min}$. B: a line of precipitation along

the flow centre, $\rho_{3c} = 0.5 \text{ g/l}$, $Q_c = 148 \text{ nl/min}$, $\phi_{Ip} = 100\%$, $Q_p = 2 \mu\text{l/min}$. C: LLPS

followed by droplets formation,

$\rho_{3c} = 8 \text{ g/l}$, $Q_c = 370 \text{ nl/min}$, $\phi_{Ip} = 80\%$, $Q_p = 10 \mu\text{l/min}$. D: abnormally large droplets

trapped in space or moving to the opposite direction of the flow,

$\rho_{3c} = 5 \text{ g/l}$, $Q_c = 370 \text{ nl/min}$, $\phi_{Ip} = 90\%$, $Q_p = 2 \mu\text{l/min}$. E: a column of nano-sized

objects flowing along the flow centre,

$\rho_{3c} = 16 \text{ g/l}$, $Q_c = 148 \text{ nl/min}$, $\phi_{Ip} = 32\%$, $Q_p = 1 \mu\text{l/min}$. F: spontaneous crystallisation,

$\rho_{3c} = 10 \text{ g/l}$, $Q_c = 111 \text{ nl/min}$, $\phi_{Ip} = 30\%$, $Q_p = 1 \mu\text{l/min}$. G: heterogeneous

crystallisation on the wall, $\rho_{3c} = 10 \text{ g/l}$, $Q_c = 185 \text{ nl/min}$, $\phi_{Ip} = 30\%$, $Q_p = 1 \mu\text{l/min}$. H:

blockage of the microfluidic channel by a large amount of product,

$\rho_{3c} = 1 \text{ g/l}$, $Q_c = 74 \text{ nl/min}$, $\phi_{Ip} = 20\%$, $Q_p = 1 \mu\text{l/min}$.

5.2. Evidences for antisolvent focusing of DBDCS

The formation of droplets, an LLPS, was the dominant observation. This LLPS resulted from the interplay of different processes, as shown in Figure 5.2:

A) Hydrodynamic expansion: the initial expansion or squeezing of the central jet by the peripheral flow. It can be seen by transmission microscopy because of the contrast in the refractive indices of the two flows. It has been described by [Lee, 2001].

B) Solvent inter-diffusion: the dimming of the interface between the central and peripheral coflows, as water and 1,4-dioxane are miscible.

C) Focusing of the solute by the antisolvent: as water and 1,4-dioxane inter-diffuses, DBDCS molecules will be driven by its chemical potential gradient in the field of solvent composition (see section 3.4.1 and 3.5.2). The diffusion coefficient of DBDCS can be derived from its chemical potential. The diffusion of DBDCS will be monitored by fluorescence imaging.

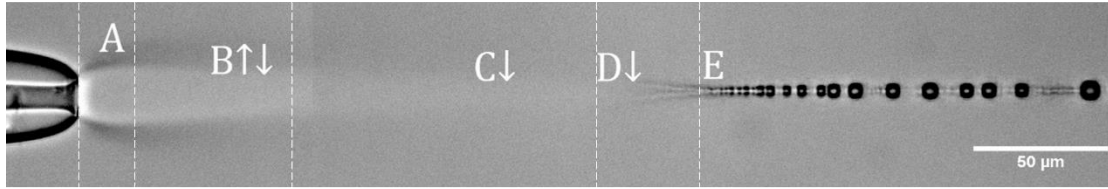


Figure 5.2. A whole image of the demixing. A: hydrodynamic expansion; B: solvents inter-diffusion; C: anti-solvent focusing of the solute; D: droplet focusing; E: stable droplet formation. Microfluidic parameters:

$$\rho_{3c} = 5 \text{ g/l}, Q_c = 30 \text{ nl/min}, \phi_{lp} = 50\%, Q_p = 1 \mu\text{l/min}.$$

D.1) Nano-droplet formation. The appearing of the new liquid phase is indicated by the new contrast between the mother solution and the new phase. The demixing of a solution can be binodal for low supersaturation ($\beta=100$) and spinodal for high supersaturation ($\beta=200$ for DBDCS, see section 3.3.2.1). Spinodal demixing is a faster process than a binodal demixing that requires a nucleation step. Binodal and spinodal LLPS will produce the same thermodynamically meta-stable phase: the almost pure dense DBDCS phase predicted by the thermodynamics (section 3.3.2.2).

D.2) Droplet solvent focusing (Marangoni effect): droplets in a mixture where a gradient of composition is present, move towards the phase with the lower surface tension. One can expect the surface tension is lower in the phase of higher solubility [Hajian, 2015]. DBDCS droplets move towards 1,4-dioxane rich phase. in the case of the injection of divinylbenzene-ethanol into Water observed by microfluidic.

E) Droplet formation: the focusing of DBDCS molecules and nano-droplets lead to the formation of concentrated cylinder of DBDCS. The formation of a regular necklace of droplets is observed. This is where d_p is taken.

The solvent focusing of the solute by the anti-solvent can be observed experimentally by imaging the fluorescence of DBDCS. On Figure 5.3, the DBDCS fluorescence intensity (B) is plotted together with the OM image (A) and *Comsol* simulation (C and D). The fluorescence

intensity of DBDCS is represented using a red-yellow scale. Before the injection nozzle, DBDCS was confined in the capillary. After the injection nozzle, DBDCS expanded due with the central jet. But the comparison with the transmission image, the expansion of the DBDCS flux was limited and reversed by the repulsion from the anti-solvent. OM shows droplet formation around 300 μm from nozzle. This focusing was further accelerated when droplets of a dense liquid phase of DBDCS were formed. These droplets were more efficiently repelled through a Marangoni effect. *Comsol* simulation shows the mass concentration of DBDCS had increased from 5 g/l to 10 g/l at the droplet formation position d_p . As 1,4-dioxane kept escaping and water coming in, β had reached 60 shortly after d_p . This agrees with our thermodynamic calculation of the LLPS of water (1)-1,4-dioxane (2)-DBDCS (3) mixture in section 3.6.

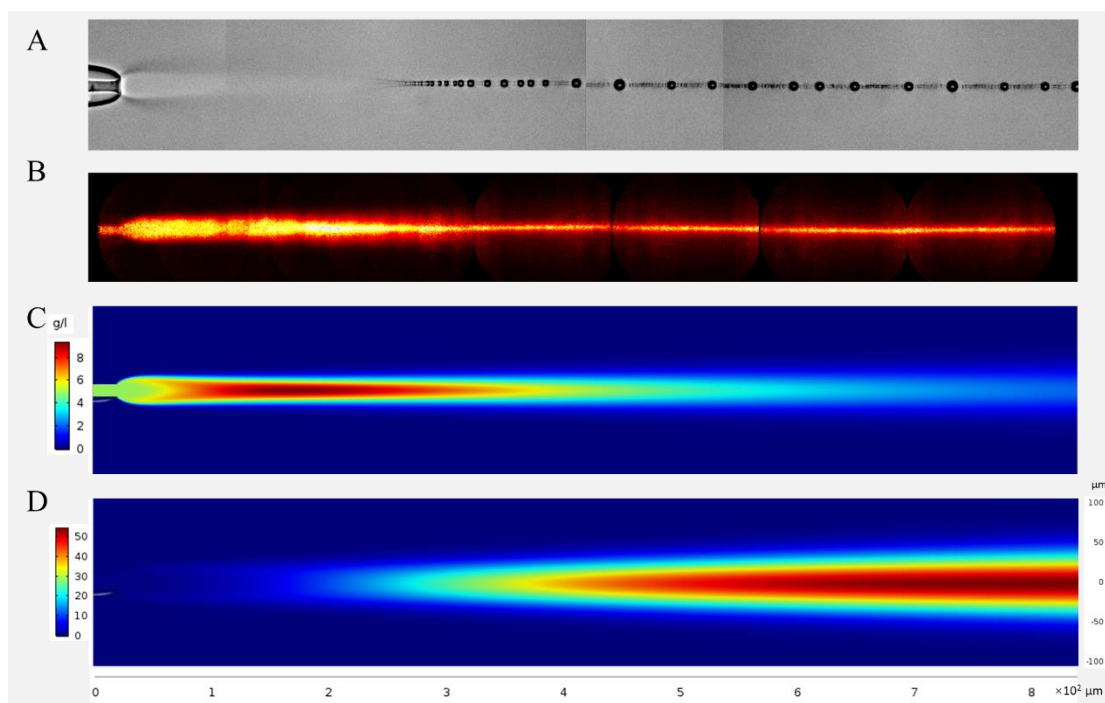


Figure 5.3. Evidences and simulation for antisolvent focusing of DBDCS. A: transmission image of droplet formation; B: fluorescence intensity of DBDCS; C: Comsol simulation of the mass concentration of DBDCS; D: Comsol simulation of the supersaturation ratio β . Microfluidic parameter:

$$\rho_{3c} = 5 \text{ g/l}, Q_c = 30 \text{ nl/min}, \phi_{1p} = 50\%, Q_p = 1 \mu\text{l/min}.$$

5.3. Phase diagram of water (1)-1,4-dioxane (2)-DBDCS (3) the coaxial microfluidic mixer

To examine the dependence of the phase transition behaviour on the input microfluidic parameters, it requires a four- or five-dimensional space. An easier way is to examine the overall composition of the mixture. This is neglecting the kinetics but only considering the thermodynamics. But it is more comprehensible for the user to quickly master the device. Therefore, by plotting and colour coding the observed phase transition types against the overall mixture composition, $\rho_{3\text{mix}}$ and $\phi_{2\text{mix}}$, of the microflow, a working phase diagram of water (1)-1,4-dioxane (2)-DBDCS (3) in the microfluidic mixer has been built, as shown in Figure 5.4. The solubility in Figure 3.6 was recalculated and plotted in the working phase diagram (the green line). The solubility of DBDCS in water (1)-1,4-dioxane (2) mixture measured in solution coincided with the frontier between the liquid region and the phase transition regions in the working phase diagram. The binodal LLPS limit is plotted on in Figure 3.6 as a black line. It is the lower limit for LLPS. The production domains of the other products seem also to be organised in closed domains. Nano-particles, droplets, crystals formation is correlated with $\rho_{3\text{mix}}$ and $\phi_{1\text{mix}}$. The droplet trap is a counter example: the pink points have a large and diffuse dispersion in the thermodynamic diagram.

The hydrodynamic entrance length l_h and concentration entrance length l_c have been introduced in section 2.1.3 and compared with *Comsol* simulation for the microfluidic sweep without DBDCS in section 4.2.2 and Appendix B.ii.ii. For a miscible system, the overall composition will be developed over the concentration entrance length. But our antisolvent-solvent-solute system is not stable. Therefore, it must be noticed that, unless it is in the soluble region, the overall composition of the input will not be reached in the microfluidic channel. There are two reasons: i) the antisolvent gradient can prohibit the diffusion of the solute towards a homogeneous concentration; ii) phase transition will consume the solute from the liquid.

Therefore, the overall concentration does not represent the environment for the phase transition to occur.

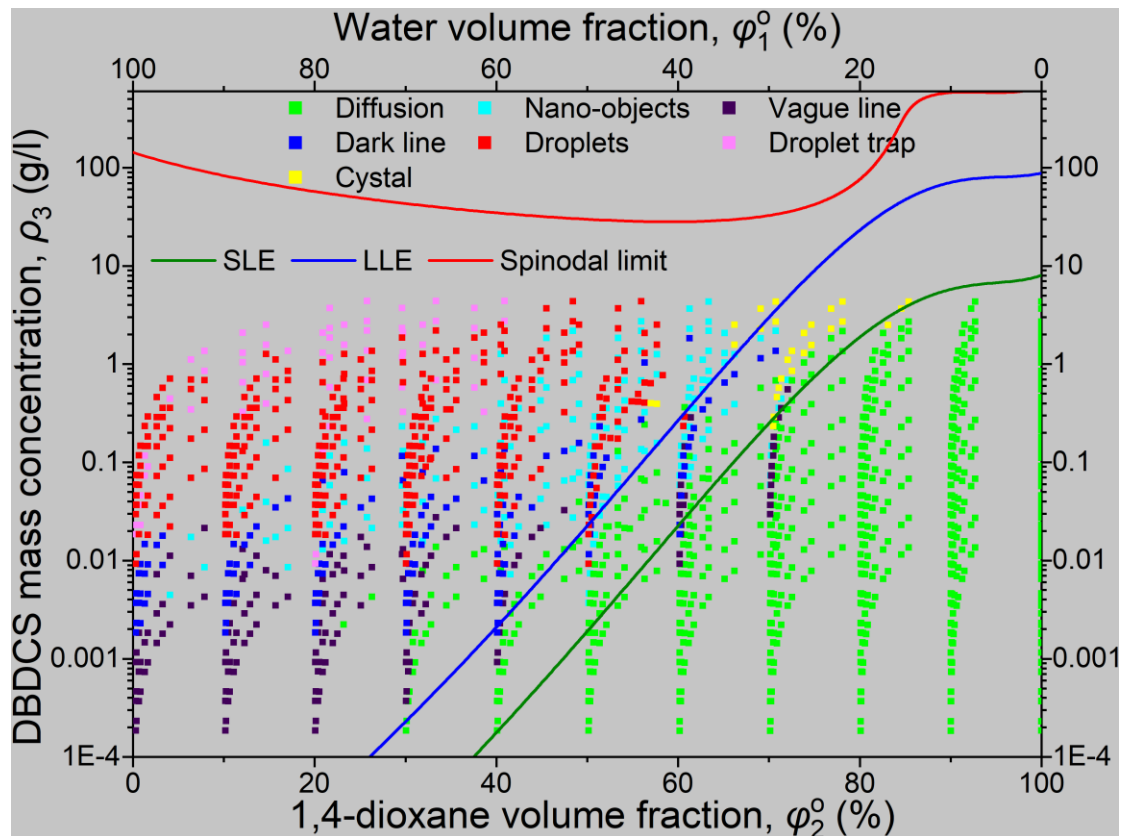


Figure 5.4. Working phase diagram of water (1)-1,4-dioxane (2)-DBDCS (3) phase diagram in the microfluidic mixer measured by a parametric sweep. The types of the experimental observation are indicated by a colour code at the corresponding overall composition of the mixture. The green curve is the solubility measured in solution.

The black curve is the binodal LLPS limit from thermodynamic calculation.

Although it is easier to describe the phase transition types in this 2-D phase diagram, based on $\rho_{3\text{mix}}$ and $\phi_{1\text{mix}}$, than in a 4 dimensional space of the operational microfluidic parameters, ϕ_{1p} , ρ_{3c} , Q_c , and Q_p , this could be confusing because the liquid went through a fast mixing, which was controlled directly by the operational parameters instead of the overall composition. Moreover, different combination of operational parameters can reach the same overall composition. Let us keep this in mind during this chapter. More detailed discussion will

be found in the microfluidic kinetics (section 5.7) and *Comsol* simulation.

5.4. The soluble region

The green points in the phase diagram made up the soluble region. During the experiment of these points, after inter-diffusion of the two coaxial flows, no phase transition was observed by OM in the observation window but only single-phase flow. The mixing of the central jet and the coaxial peripheral flow has been described in the experimental section (section 2.1) and in the simulation section (section 4.2). Although the solute underwent fast mixing and uphill diffusion, the frontier between the soluble region and the region of phase transitions matched with the solubility curve measured in solution very well. Additionally, there is a second surprise that, on the phase diagram, crystals were rare, whereas droplets were everywhere.

Independently of the solution mixing conditions of different compositions mixed at different flow ratio, the thermodynamic prevails. The system finds a way to the equilibrium. This way may be the high supersaturation that is achieved by the anti-solvent focusing of DBDCS. The supersaturation can overcome the nucleation barrier of droplets in the binodal LLPS range more easily than that of crystallisation, or even reach the spinodal decomposition domain. This was surprising at first, since the overall composition of the total flow were not purposely designed beforehand nor controlled directly, but the result of a parametric sweep after some blindly preliminary trials with confusing results. Moreover, the microfluidic experiment and the solubility in solution measurement was conducted independently with the same batch of DBDCS and solvents. Later these over 2000 microfluidic measurements and the solution solubility measurement added up in the phase diagram. This strongly supports our observation and shows that both our flow control and the solubility measurement were precise and with good repeatability.

5.5. Nano-objects

5.5.1. *In situ* OM observation

During the parametric sweep, it was found that if ρ_{3c} was low, some distance (d_p) from the nozzle after the formation of a single phase flow by inter-diffusion of the coflows, the microflow started to precipitate as ϕ_{lp} increased. The precipitation appeared as a very vague line along the flow centre almost undistinguishable, as shown in Figure 5.5, even by our fast camera with the minimum exposure time. The overall composition of the total mixture that gave this kind of vague lines comprised the purple points in the phase diagram.

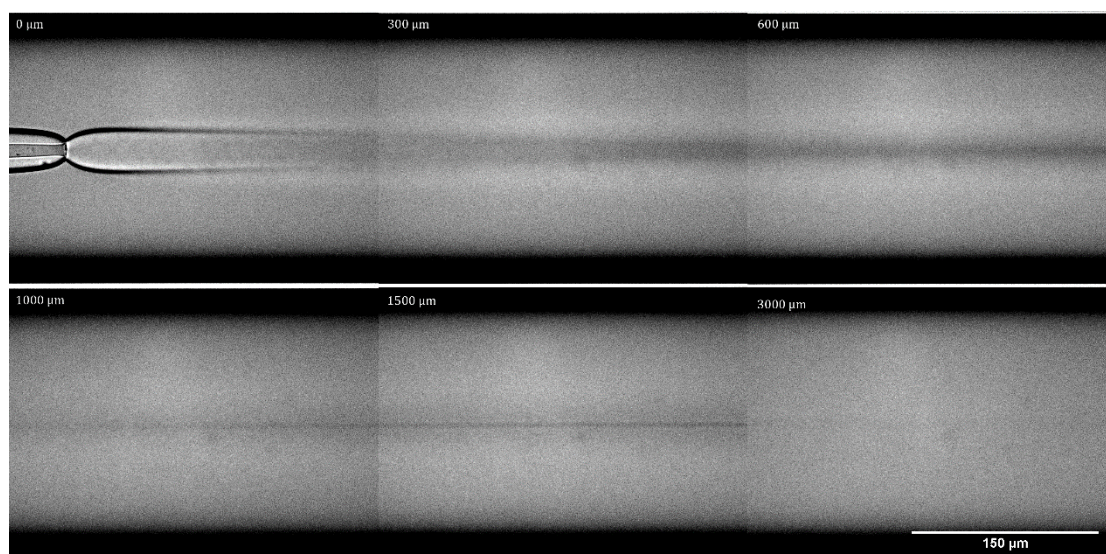


Figure 5.5. Precipitation of a vague line and its disappearance because the diffusion of solute driven by the anti-solvent composition gradient, frames taken from a video moving along the flow. Microfluidic parameters:

$$\rho_{3c} = 0.25 \text{ g/l}, Q_c = 370 \text{ nl/min}, \phi_{lp} = 100\%, Q_p = 4 \mu\text{l/min}.$$

Figure 5.5 contains 6 frames from a video taken along the microfluidic channel. In the video, we can see the central jet flow after the injection nozzle. In the second frame, from the change in the refractive index n_D caused by the inter-diffusion of the solvents, we see 1,4-dioxane diffused outward and water diffused inward. In frame 4, the inter-diffusion of the

solvents has finished, yet a vague line of precipitation started to appear at the centre of the flow. This indicates that DBDCS was pushed towards the flow centre by the anti-solvent gradient as its free energy is lower in the good solvent. Frame 5 (1500 μm) shows the line, 2 μm in width, of DBDCS precipitation. Our camera was not able to capture the objects inside the dark line even with its minimum integration time 0.01ms. Frame 6 is far away from the injection nozzle, where there was no more solvent compositional gradient, DBDCS precipitation re-dissolved and diffused away. The precipitation was a vague line because it was the beginning of the precipitation region. This has been observed on the phase diagram, when $\rho_{3\text{mix}} > 0.01\text{g/l}$, the number of purple points diminished.

As ρ_{3c} increased, precipitation became stronger. On Figure 5.6, a column of submicron-particles appeared at the flow centre. With a lower ϕ_{Ip} , these particles were not pushed towards the flow centre to form a line, but stayed in a larger column, because the focusing force that was the gradient of the antisolvent in the peripheral flow has disappeared 4500 μm after the nozzle. These are the purple point in the phase diagram. There are very limited number of such points. They are located near the solubility curve, because if the ϕ_{Ip} was low, the mixture would stay in the soluble region; whereas if ϕ_{Ip} was high, DBDCS would be pushed towards the flow centre by the antisolvent.

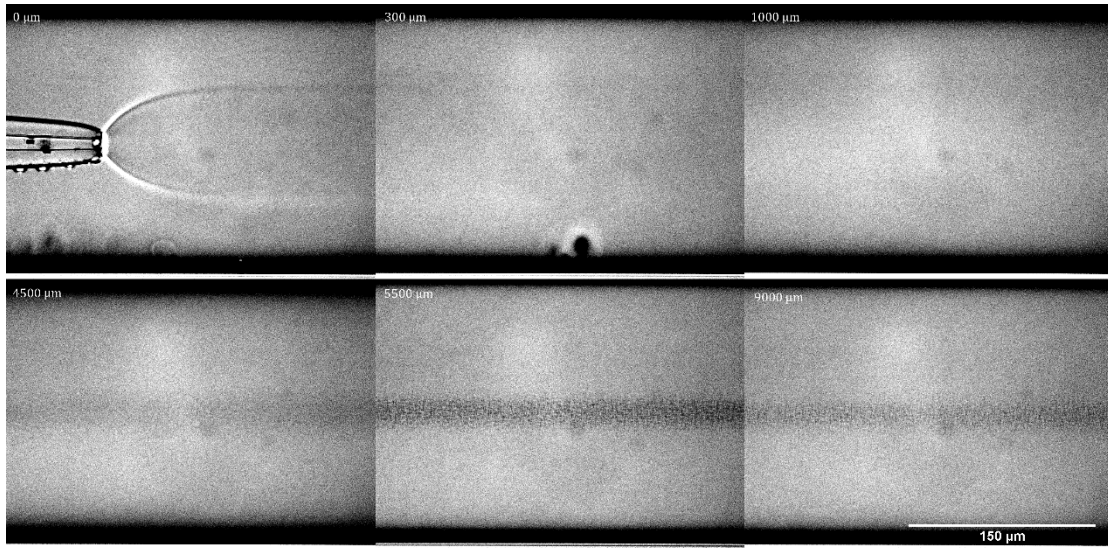


Figure 5.6. A column of DBDCS nano-particles formed along the flow centre.

Microfluidic parameters: $\rho_{3c} = 8 \text{ g/l}$, $Q_c = 555 \text{ nl/min}$, $\phi_{1p} = 40\%$, $Q_p = 1 \mu\text{l/min}$

By blocking the flow channel, the size of each nano-particles could be estimated in a first approximation, to $2 \mu\text{m}$ (in the channel) \times $1 \mu\text{m}$ (perpendicular to the channel) as shown on Figure 5.7.

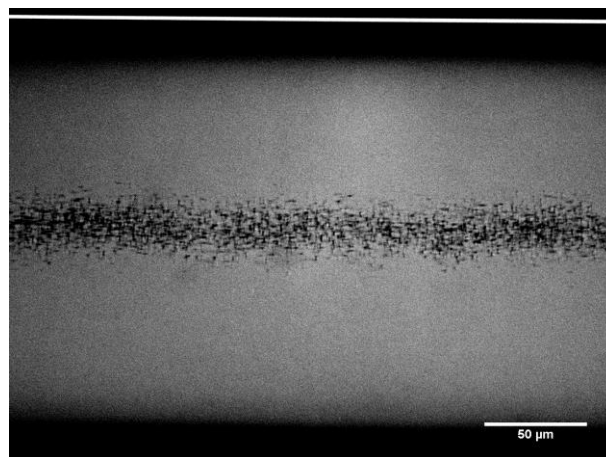


Figure 5.7. By blocking the microfluidic channel, the flow was temporarily stopped, and the nano-particles were “frozen” in the suspension. Brownian motion of the nano-particles was seen.

With a larger ϕ_{1p} , as in Figure 5.8, DBDCS molecules were pushed towards the flow

centre by the antisolvent driven uphill diffusion, the strong precipitation appeared in a line again, yet much darker and thicker than that on Figure 5.5. These points were marked dark blue in the phase diagram of the overall composition. In the phase diagram, the purple, dark and light blue points were overlapping, because the observational difference was dominated by operational parameters, not reflected by the overall composition of the mixture.

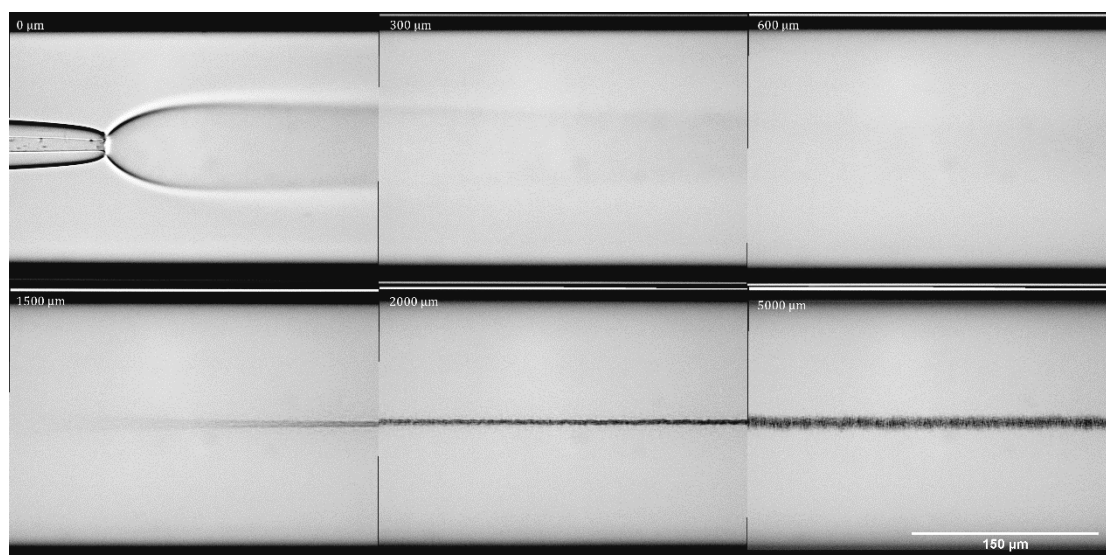


Figure 5.8. Precipitation of a dark line later dispersed in to a column of nanoparticles, frames taken from a video along the flow. Microfluidic parameters:

$$\rho_{3c} = 0.5 \text{ g/l}, Q_c = 370 \text{ nl/min}, \phi_p = 80\%, Q_p = 1 \mu\text{l/min}$$

As the anti-solvent focusing driving force, *i.e.* the solvent composition gradient, had disappeared, the particles started to dissipate away slowly from the flow centre.

Similar behaviour was observed during the preliminary tests with THF-water-(Calix-Cousulf-Cs⁺₂), THF-water-(caesium acetate), THF-water-CsCl, water-THF-DBDCS, water-(THF20-1,4-dioxane80)-DBDCS, and water-acetone-DBDCS systems, but only systematically investigated with water (1)-1,4-dioxane (2)-DBDCS (3).

5.5.2. Nature of the nano-particles

The nano-particles were below the diffraction limit of OM. The nanoparticles were not distinguishable from the background in the flow through crossed polarisers (CP) (Figure 5.9).

This means when the nanoparticles were formed in the microflow, they had an amorphous nature. They were not detectable by SAXS also.

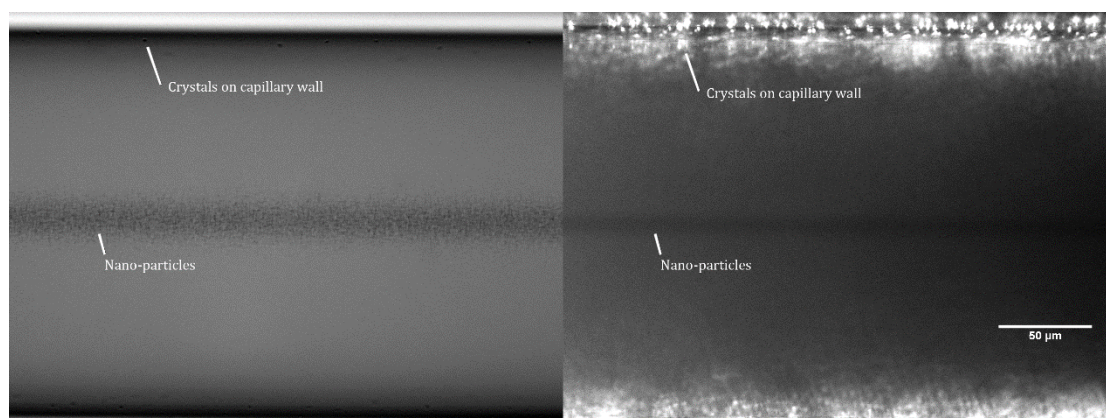


Figure 5.9. In situ OM transmission image (left) and CP image (right) of the nanoparticles 26980 μm away from the injection nozzle. The nano-particles appeared dark under CP (in the flow centre) while the crystals on the wall of the microfluidic channel appeared bright. Microfluidic parameters:

$$\rho_{3c} = 0.5 \text{ g/l}, Q_c = 370 \text{ nl/min}, \phi_{1p} = 70\%, Q_p = 1 \mu\text{l/min}.$$

5.5.3. Post-mortem observation

The nano-particles were collected on glass slide for OM and on silicon wafer for SEM observation. Photos and videos of the sample were taken right after collection, 30 minutes and 1 month after by OM, as shown in Figure 5.10. Figure 5.10.A represents a suspension with nano-particles moving inside by Brownian motion and Marangoni effect. In Figure 5.10.B, the solvent had evaporated, and C, crystals started to appear among the nano-particles. SEM photo revealed the average size of the nano-particles is around 20 nm and they gathered (Figure 5.11). Some bigger objects started to grow from the nano-particles.

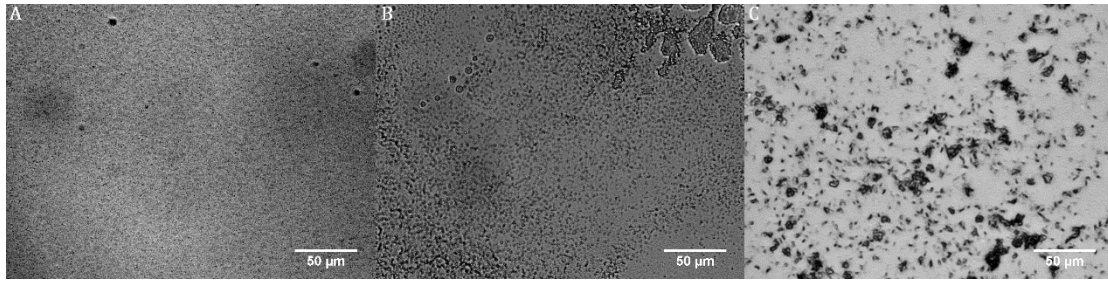


Figure 5.10. Drying process of a suspension of DBDCS nano-particles collected on a glass slide: A. a dispersion in liquid right after collection; B. dried after 30 minutes; C. one month after collection.

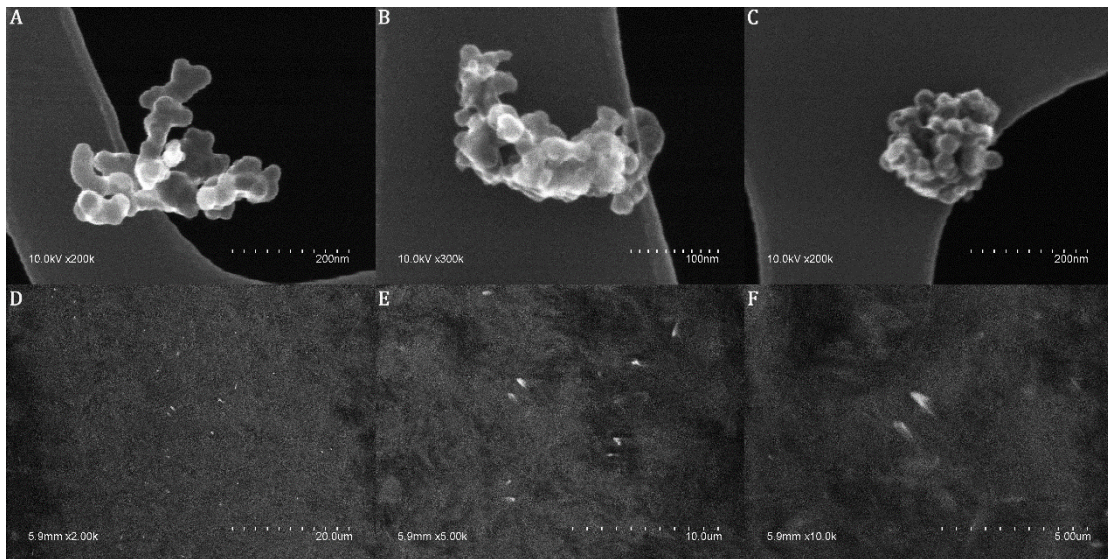


Figure 5.11. A~C: post-mortem SEM image of DBDCS nano-particles collected on copper grid; D~F: bigger objects appeared among nano-particles after 1 month.

5.6. Liquid-liquid phase separation

5.6.1. From nanoparticles to droplets

When $\rho_{3\text{mix}} > 0.04 \text{ g/l}$, red points start to prevail the two-phase region of the phase diagram. These are the conditions where LLPS followed by droplet formation was observed. Once ϕ_{1p} got higher, anti-solvent gradient would dominate solute gradient to push DBDCS towards flow centre, like what the IR laser did, the dark line of DBDCS start to make droplets. This had been observed not only in water (1)-1,4-dioxane (2)-DBDCS (3) system, but first

discovered in the preliminary tests with THF-water-(Calix-Cousulf-Cs⁺₂), THF-water-(caesium acetate), THF-water-CsCl, water-THF-DBDCS, water-(THF20-1,4-dioxane80)-DBDCS, and water-acetone-DBDCS systems.

On Figure 5.12, DBDCS was concentrated in the microflow centre, but this time, in addition to nano-particles, droplets emerged among them, also at the flow centre. The droplets merged and grew for some distance, reaching a stable size and then accompanied the nano-particles until then end of the microfluidic channel.

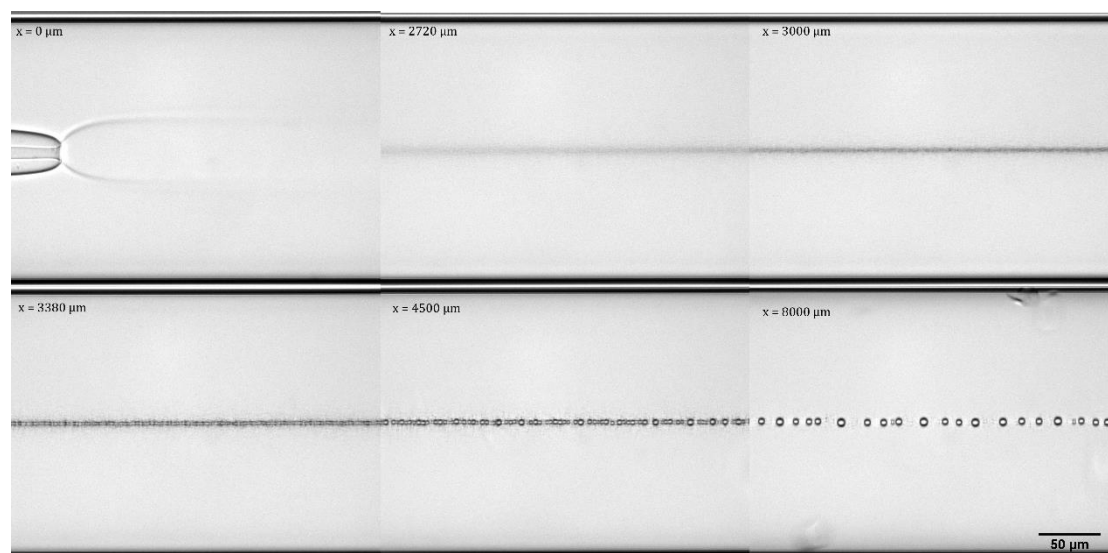


Figure 5.12. Nanoparticles gathered to be droplets. Microfluidic parameters:

$$\rho_{3c} = 5 \text{ g/l}, Q_c = 296 \text{ nl/min}, \phi_{1p} = 40\%, Q_p = 2 \mu\text{l/min}$$

Figure 5.13 shows the stable formation of droplets at a fixed d_p . It followed the standard procedure: hydrodynamic expansion, solvents inter-diffusion, antisolvent focusing of solute molecules, Marangoni and finally the formation of mono-size dispersed droplets. These droplets were stable all through the visible part of the microfluidic channel (residence time about 20s).

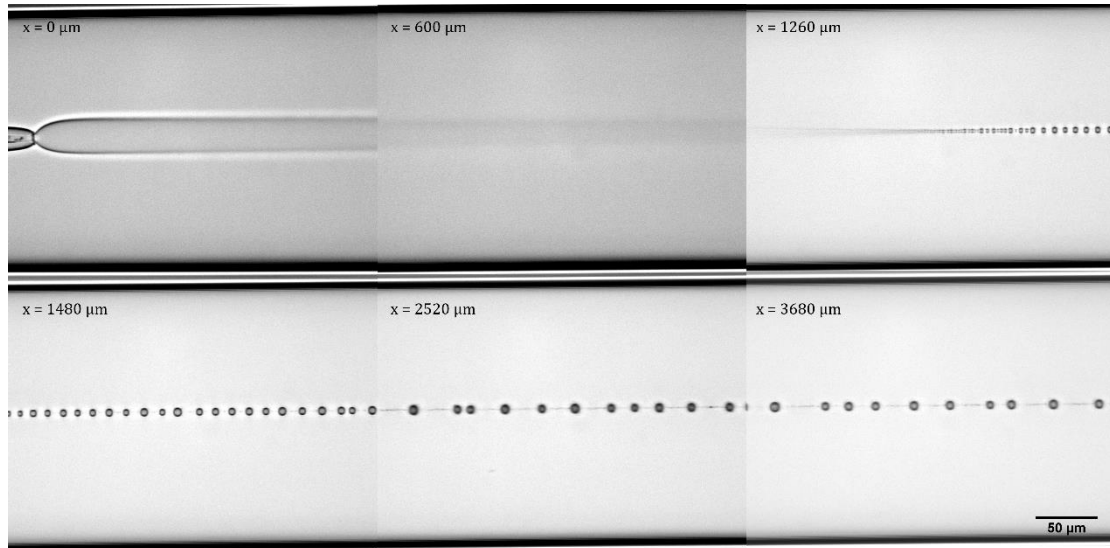


Figure 5.13. Droplets along the flow. Microfluidic parameters:

$$\rho_{3c} = 5 \text{ g/l}, Q_c = 370 \text{ nl/min}, \phi_{lp} = 60\%, Q_p = 10 \mu\text{l/min}$$

5.6.2. Formation mechanism of the droplets

By increasing the size of the droplets, we were able to observe their formation mechanism with OM, as shown in Figure 5.14. an interface between the central and peripheral flow appeared first, where countless sub-micron sized objects appeared simultaneously. Then they were pushed towards the flow centre by the Marangoni effect, and next merged into bigger droplets. The merging of the nano-droplets gives spheres that fuse into bigger ones. From this, we guessed the nano-objects to be a liquid phase. The two images in Figure 5.14 illustrate the variety of the formation mechanism of the droplets. In A the liquid phase appears at the centre of the flow and is fed by the Marangoni focusing of nano objects. In B the droplets are formed at the periphery and merge during their Marangoni focusing.

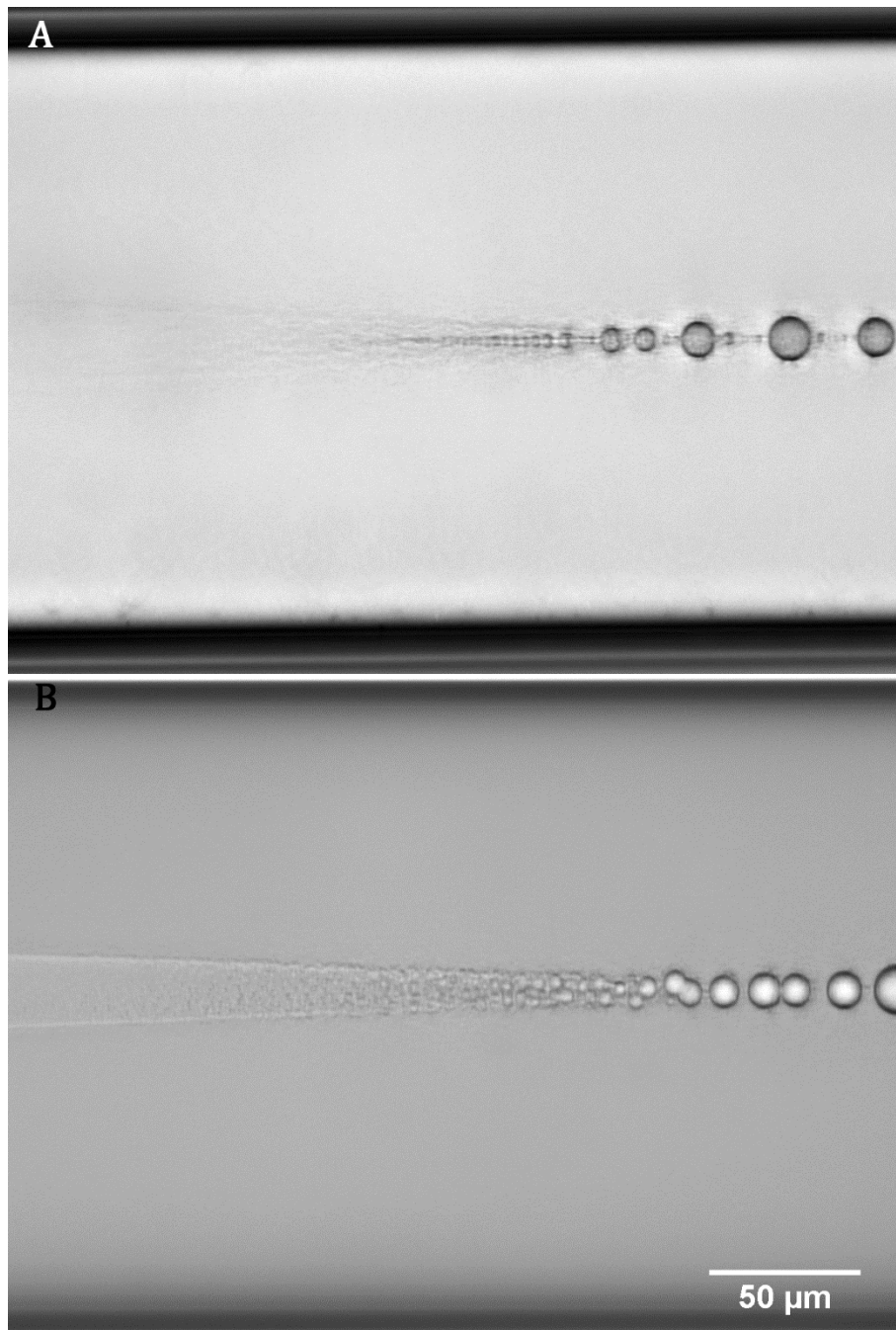


Figure 5.14. Zoom of formation of droplets. A: droplets appeared from the centre of the microfluidic channel and then grow and merge to a stable size. Microfluidic parameters: $\rho_{3c} = 5 \text{ g/l}$, $Q_c = 370 \text{ nl/min}$, $\phi_{lp} = 80\%$, $Q_p = 1 \mu\text{l/min}$, $d_p = 1080 \mu\text{m}$. B: countless sub-micron droplets appeared simultaneously and migrated towards the flow centre, merged into bigger droplets, accompanied by those escaped from the merging. Microfluidic parameters:

$$\rho_{3c} = 8 \text{ g/l}, Q_c = 370 \text{ nl/min}, \phi_{1p} = 80\%, Q_p = 1 \mu\text{l/min}, d_p = 1080 \mu\text{m}$$

The direct breaking of the central flow into droplets by a Plateau-Rayleigh instability has also been observed in our preliminary test (Figure 5.15).

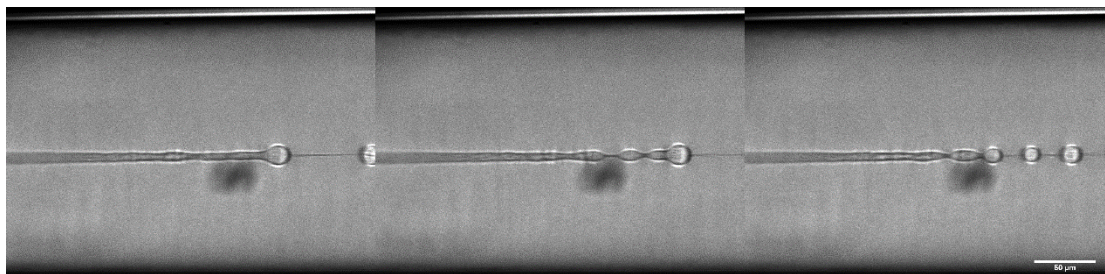


Figure 5.15. Direct breaking of the centre flow by a Plateau-Rayleigh instability. The antisolvent-solvent-solute system was THF-water-(Calix-Cousulf- Cs^+_2). Microfluidic

parameters: $Q_c = 37 \text{ nl/min}$, $\phi_{\text{THF,p}} = 100\%$, $Q_p = 5 \mu\text{l/min}$.

5.6.3. Abnormally large, backward flowing droplets, inner structure and crystallisation of the droplets caught in flow by Marangoni effect.

With a small total flow rate, droplets were not only produced, but also “caught” at their birth place by strong antisolvent focusing, and then merged with newly generated droplets, rendering the size abnormally large, as shown in Figure 5.16. Such a situation is named a “droplet trap” and marked pink in the phase diagram. They can be found overlapping with the red points everywhere, because the presence of a “droplet trap” was dominated by the operational parameters.

In Figure 5.16, big droplets were trapped in the centre. From the left, the incoming central flow of 1,4-dioxane collided on the drop of DBDCS. The collision mixed up water and 1,4-dioxane. From the right, smaller droplets were flowing to the opposite direction than the flow, back towards the nozzle, and merging into the big droplet. These were the circumstances when the anti-solvent focusing was too strong so that the hydrodynamic drag force on the droplets was overcome.

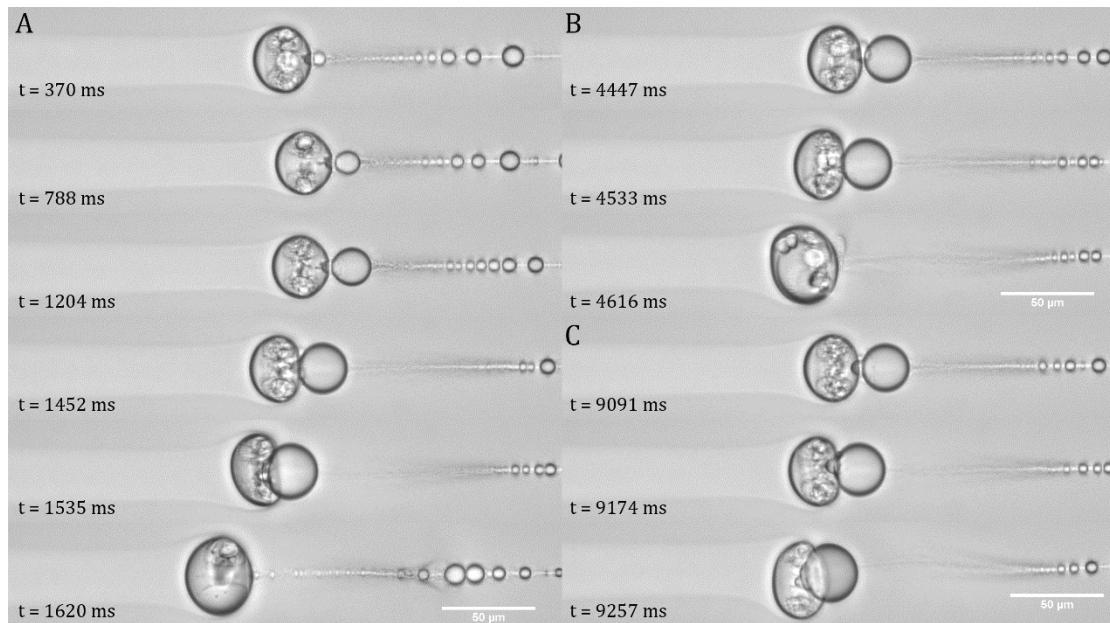


Figure 5.16. Frames taken from a video of abnormally large droplet in trapped by Marangoni effect with t the elapsed time in the video. A: abnormally large droplet trapped at its birth place and how new droplet was trapped behind it, grew, and merged with the already trapped one. B~C: new cycles of droplet trapping and merging continued.

$$\rho_{3c} = 5 \text{ g/l}, Q_c = 296 \text{ nl/min}, \phi_{lp} = 90\%, Q_p = 2 \text{ } \mu\text{l/min}, d_p = 500 \mu\text{m}.$$

These abnormally large droplets were not stable in the microflow, they could end up in three ways (Figure 5.17). In most cases (Figure 5.17.A) they would be dragged backwards until reaching the injection nozzle, thus a new life circle of an abnormally large droplet started. But sometimes an equilibrium of the hydrodynamic force and the Marangoni force could be reached (Figure 5.16), the abnormally large droplet could stay at its birth place so long as the flow was stable (parameter unchanged, microfluidic channel not blocked). In other scenarios (Figure 5.17.B and C), the abnormally large droplet would be trapped at its birth place for a long time and start to crystallise, then flushed away as it grew too large, and thus a new life circle started.

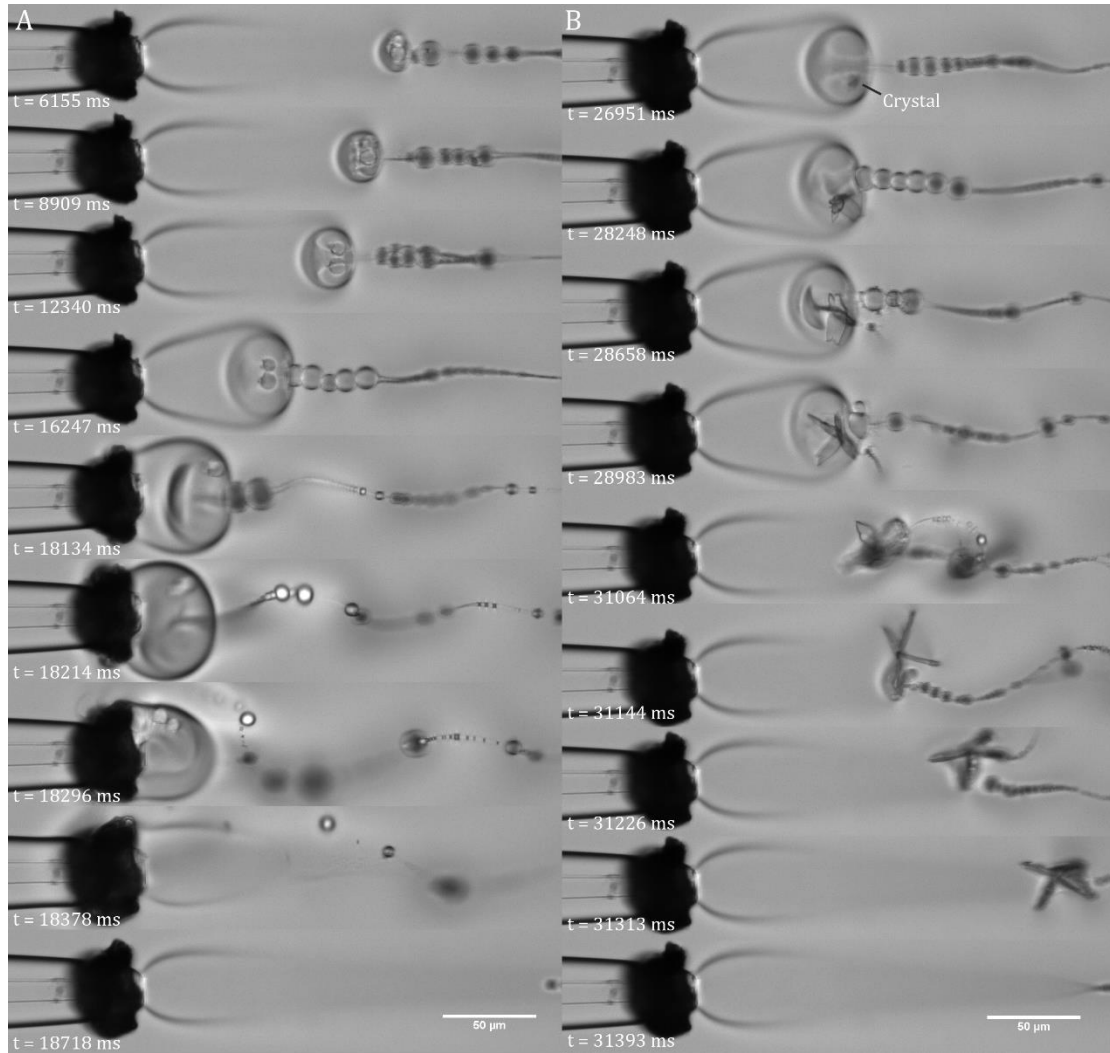


Figure 5.17. A: abnormally large droplet dragged to the tip by the strong Marangoni effect and left remanence on the nozzle; B: abnormally large droplet crystallised and flushed away by the flow. Afterwards, new cycles of abnormally large droplet trapping. Microfluidic parameters:

$$\rho_{3c} = 1\text{g/l}, Q_c = 74\text{nl/min}, \phi_{lp} = 100\%, Q_p = 1\mu\text{l/min}, d_p = 100\mu\text{m}.$$

More than one crystal can form inside one trapped droplet. Figure 5.18.A shows two plate crystals formed in on droplet and then pressed together by the confined volume some seconds later. Figure 5.18.B illustrates that many layers of plat crystals can be attached on a common axis while swirling inside one droplet.

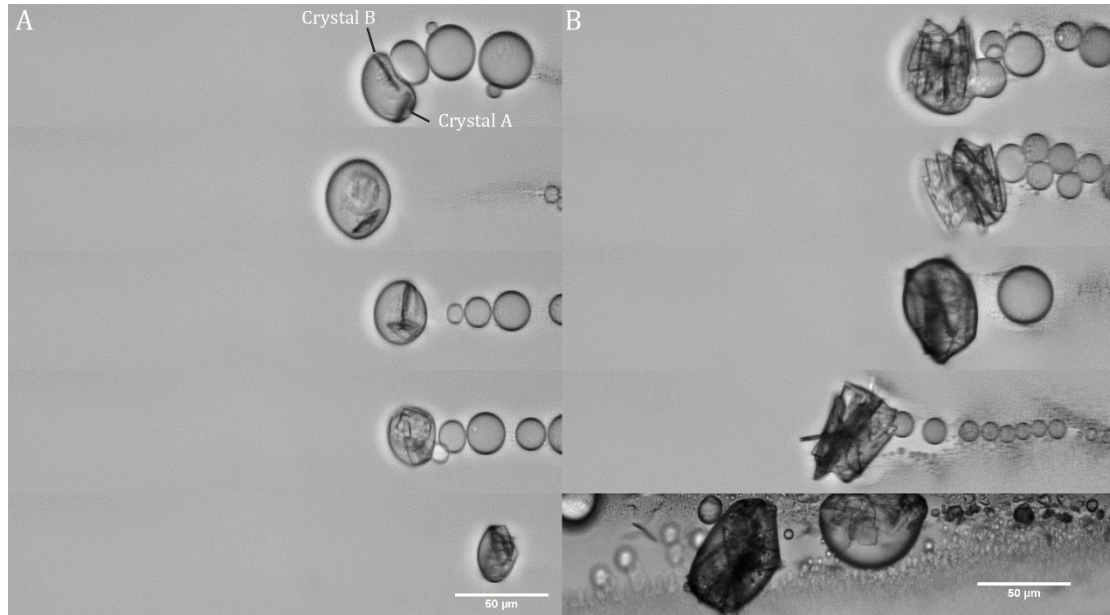


Figure 5.18. Crystallisation of trapped abnormally large crystals observed during a washing. A: two crystals confined in the one droplet; B: a crystal with many extending wings in one large droplet. Microfluidic parameters:

$$\rho_{3c} = 2.5 \text{ g/l}, Q_c = 74 \text{ nl/min}, \phi_{lp} = 70\%, Q_p = 4 \mu\text{l/min} .$$

These trapped abnormally large droplets offer a new way to observe the nucleation and growth of crystals. The nucleation occurs in a small (tens of micrometres) volume; thus, it will be possible to observe the early steps of the nucleation. This confined volume is suspended by a gradient of solvent composition; thus, nucleation and growth occur without contact with solid surfaces. The volume inside the trapped droplet is well agitated by the merging droplets and the Marangoni effect, therefore the crystal growth is fast and not diffusion limited. It is a convenient way to observe the nucleation and growth of micro crystal in a suspended, confined, highly concentrated and well agitated volume repeatedly. Droplets volume could be estimated to a few pl (4 pl for those observed in Figure 5.17). Crystallisation in such confined volume has been already observed and discussed (see for example the work of Veessler group[Grossier, 2011, Rodriguez-Ruiz, 2013]).

We can also benefit from their appearance to get additional information, such as the

inner structure of the droplets and the crystallisation of the droplets in the flow, as shown on Figure 5.19. We can see the Marangoni effect inside the droplet. The inside of the droplet was highly agitated, similar to Figure 1.9.

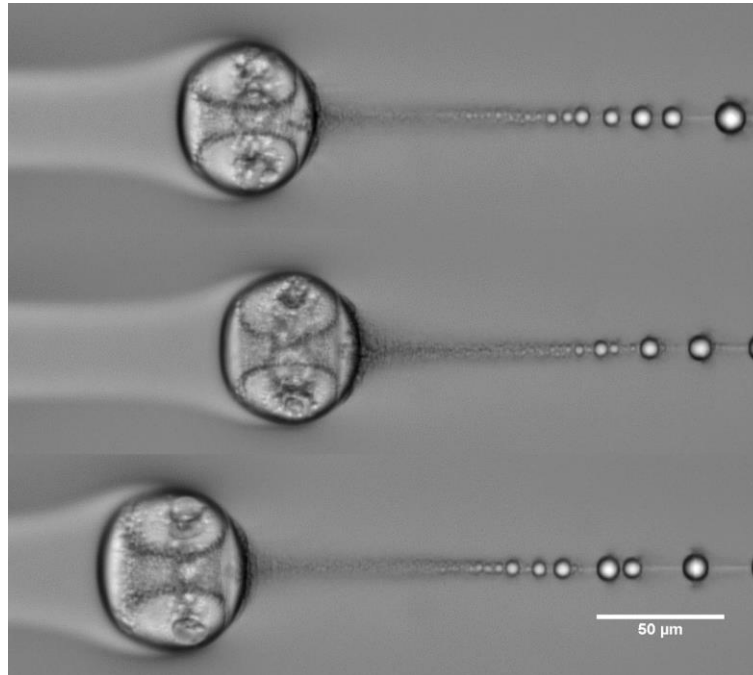


Figure 5.19. Inner structure of the trapped abnormally large droplet. Microfluidic parameter: $\rho_{3c} = 8 \text{ g/l}$, $Q_c = 148 \text{ nl/min}$, $\phi_{lp} = 80\%$, $Q_p = 1 \mu\text{l/min}$, $d_p = 200 \mu\text{m}$.

The backward flowing, abnormally large droplets were periodically encountered in our parametric sweep. It was not confined in a specific sub area of the droplet region, but overlapping with the normal droplet formation points, this is because, again, it was dominated by the operational parameters. It was most likely to appear when there was: i). a high ρ_{3c} ; ii) a high ϕ_{lp} (the higher these two, the stronger the Marangoni driving force); iii) a low flow rate (the lower the hydrodynamic velocity, the easier the droplet would be caught by Marangoni effect).

These abnormal droplets were not stable outside the microfluidic system, they disappeared after been collected at the exit of the microfluidic channel on glass slide, with only nano-particles remaining.

5.6.4. Post-mortem drying of the droplets

Droplets were collected at the end of microfluidic channel on glass slides for *post-mortem* analysis. Figure 5.20 shows the drying process of the collected droplets. Figure 5.20.A is the dispersion of the droplets in the microflow liquid, in the background of which floated some droplets out of focus. In Figure 5.20.B, the liquid has evaporated. D.1 and D.2 shows inside the drying droplet, flower shaped crystals appeared. This is similar to the crystal habit of the abnormally large droplets trapped by Marangoni effect and the spontaneous crystallisation from the flow. In Figure 5.20.C, the droplets have deformed as crystals formed both inside and outside them after one month. D.3 show inside of a dried droplet filled with crystals.

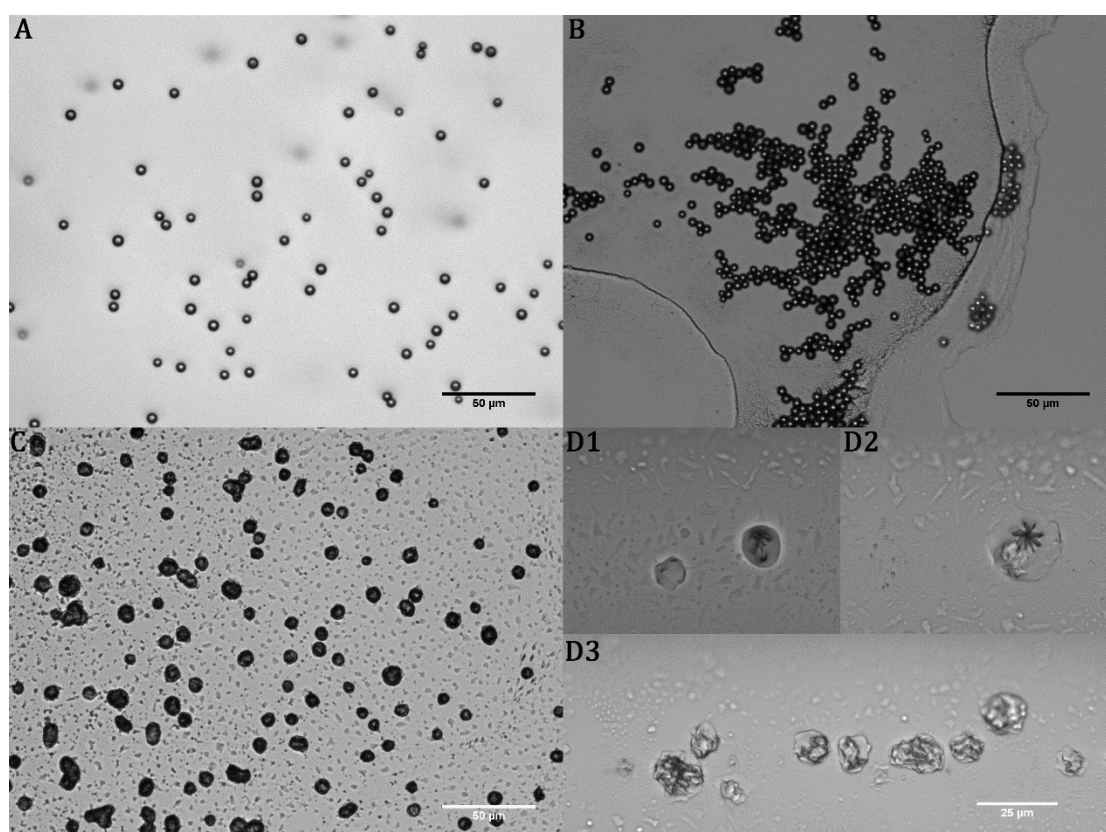


Figure 5.20. Post-mortem OM observation of the droplets: A. dispersion in the flow liquid; B. 30 minutes after collection; C. one month after collection; D. inside droplets: D1~D2 drying, D3 dried.

Post-mortem observation of the collected dark line (Figure 5.21) shows that the dark line of precipitation along the flow centre is actually small droplets. For these conditions, the

size and amount were small and the flow velocity fast so that they appear as a dark line even if the smallest acquisition time of the camera was used.

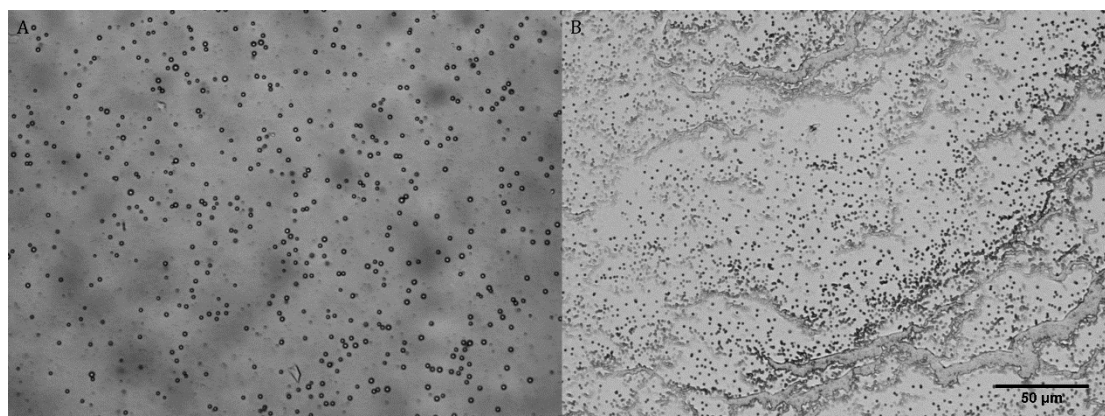


Figure 5.21. Collected dark line of droplets on glass slide. A: suspension in solvents mixture; B: dried.

5.6.5. Solidification of the droplets in the flow

After a long time of non-stopping experiment, the microfluidic channel could be clogged by the strong phase transition product. Figure 5.22 shows that tree accumulated by the droplets was growing backwards along the flow. The coming droplets from the left were being attached to the finger-shaped head of the tree. The head of the tree was still liquid with a smooth surface. Several hundred micron away from the head, its body solidified into dendrites.

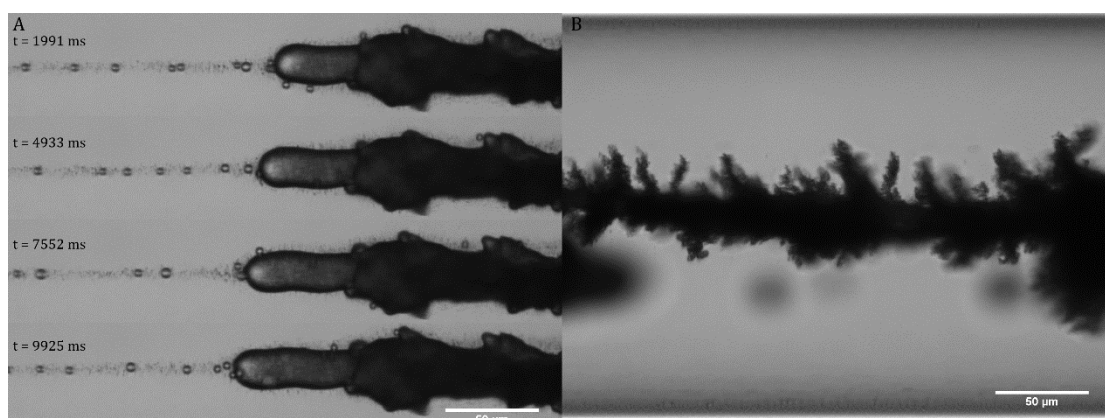


Figure 5.22. Crystallisation of the liquid DBDCS stacked as a pillar along the flow centre. A: the finger-shaped head of the pillar. It was growing because more droplets

were merging into it. B: the solidified body of the column. Microfluidic parameters:

$$\rho_{3c} = 1 \text{ g/l}, Q_c = 74 \text{ nl/min}, \phi_{lp} = 80\%, Q_p = 1 \mu\text{l/min}.$$

Crystallisation of the droplets in the flow has been observed in the preliminary tests using other antisolvent-solvent-solute systems. Figure 5.23 shows the droplet formation and crystallisation along the flow of caesium acetate in a mixture of THF (antisolvent) and water (good solvent). It shows that after the interface of the central jet disappeared, spherical droplets formed 1 mm away from the nozzle. The droplets were stable for about 1 mm and then started to shrink. Around 3 mm, the droplets were no longer seen. At 3.5 mm, dark objects appeared at the flow centre where the droplets used to be. The shape of the dark objects was irregular and the population same as the droplets. The dark objects grow gradually along the flow. This suggests that the droplet is a transient unstable phase. The difference between the chemical potential of the liquid and solid solute was explained in section 3.2.1 and Appendix C.iii. This is a special two-step crystallisation from solution. A highly condensed pure liquid solute separated from the mother solution firstly. Then this unstable liquid solute solidified.

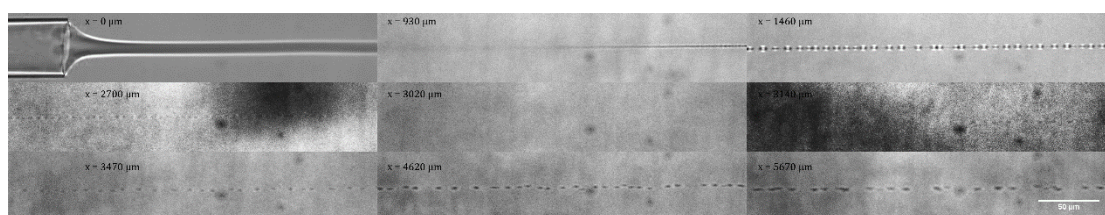


Figure 5.23. Two-step crystallisation of caesium acetate in the microfluidic mixer. Along the microfluidic channel, droplets formed at the flow centre and disappeared. Then, dark objects appeared at the flow centre where the droplets used to be.

Microfluidic parameters:

$$Q_c = 37 \text{ nl/min}, \phi_{\text{THF+dioxane,p}} = 100\%, Q_p = 10 \mu\text{l/min}, d_p = 1000 \mu\text{m}.$$

5.7. Kinetic characteristics of the coaxial microflow mixer

The focusing of DBDCS towards the flow centre and formation of droplets in the coaxial microfluidic mixer was described in section 5.6. *Vice versa*, when injecting large

proportion of good solvent in the periphery, slow crystallisation of solute from a nearly homogeneous flow was observed. To define the limit between these behaviours, the focusing distance and an average focusing speed was measured during the microfluidic parametric sweep. The focusing distance d_p is defined in section 2.1.1. It is the distance from the injection nozzle to where spontaneous phase transitions started to be observed through optical microscope.

d_p was measured during the microfluidic parametric sweep for each condition as a measure of the kinetics of the reaction in the microfluidic system. In a small range of radius near the flow centre, the laminar flow velocity profile could be approximated as uniform. The time for the molecules to reach the LLPS starting position was t_p (equation (2.1)). In the meantime, molecules of species 3 were pushed from $r_{c,max}$ (Figure 2.4, equation (2.14)) towards flow centre by the diffusion of the antisolvent. The uphill radial migrating distance is $r_{c,max}$, assuming LLPS started to be observed by OM around the maximum concentration of species 3, thus the average diffusion velocity magnitude of species 3 towards flow centre until LLPS started was approximated as

$$\begin{aligned} v_{r,up}^F &\approx \frac{r_{c,max}}{t_p} \\ &\approx \frac{r_{c,max} v_{max}}{d_p} \end{aligned} \quad (5.1)$$

When the uphill diffusion driving force, *i.e.* the gradient of solvent 1 fraction, could no longer overcome the downhill diffusion driving force, the concentration gradient of solvent 3, downhill diffusion of species 3 towards the capillary wall started to dominate. Assuming phase transition on the wall started to be observed from d_w , the downhill diffusion velocity of species 3 magnitude was approximated as

$$v_{r,down}^F \approx \frac{R - r_{c,max}}{d_w - d_p} v_{max} \quad (5.2)$$

After d_w , due to the increasing number of the crystals on the capillary wall, FLIM could be carried out anymore.

Analysis of d_p and $v_{r,up}^F$ revealed some unexpected kinetical characteristics of the coaxial microfluidic mixer. This section is dedicated to the kinetics of the momentum and mass transfer between the central and peripheral flows. These relations are important because they will be the fundamentals for all miscible coaxial antisolvent phase transition microfluidic systems.

5.7.1. A simple relation to calculate the droplet formation distance and the average focusing velocity.

In Figure 5.24, the observation distance from the injection nozzle and all operational microfluidic parameters were fixed ($\rho_{3c} = 8 \text{ g/l}$, $Q_c = 148 \text{ nl/min}$, $\phi_{1p} = 80\%$) except for Q_p (increasing from 1 to $80 \mu\text{l/min}$). For all Q_p values, d_p was around $430 \mu\text{m}$. The size of the droplets changed from abnormally large to small, yet the position where these droplets were formed is independent with Q_p , even though the flow velocity was increased by 5640% when the peripheral flow rate increased by 7900%.

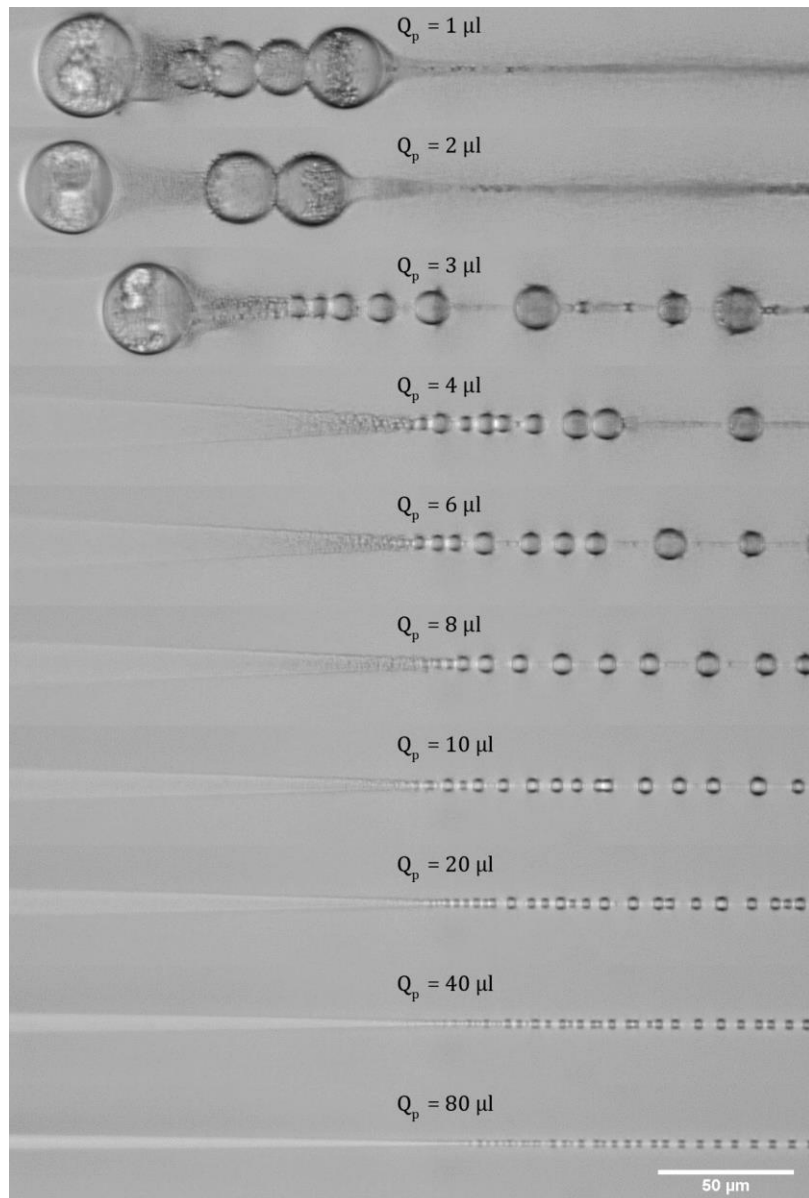


Figure 5.24. By changing only Q_p , d_p was observed to be fixed at 430 μm , regardless the influence of the flow velocity, which had increased by 5640%. Only the droplet size was changing with Q_p . Microfluidic parameters:

$$\rho_{3c} = 8 \text{ g/l}, Q_c = 148 \text{ nl/min}, \phi_{1p} = 30\%, Q_p = 1 \sim 80 \mu\text{l/min}.$$

There are four independent microfluidic input parameters (ρ_{3c} , ϕ_{1p} , Q_c and Q_p) that can influence the behaviour of the system. To analyse the cross influence of each parameter is overwhelming and requires at least a 5-dimensional space.

Figure 5.25 is a schematic illustration of the movement of DBDCS in the antisolvent focusing in the coaxial microfluidic mixer. Taking DBDCS molecules on the periphery of the central flow jet, before t_p (the time when phase transition starts, see 2.1.1), it will have moved d_p on the longitudinal direction and $r_{c,max}$ on the radial direction. As a result, DBDCS molecules will be focused at the droplet formation point. Its longitudinal velocity can be approximated as the laminar flow velocity near the centre of the microfluidic channel, $v_z \approx v_{max} = 2 \frac{Q_c + Q_p}{\pi R_{channel}^2}$ (equation (2.19)). Thus, t_p is given by equation (2.1): $t_p \approx \frac{d_p}{v_{max}}$. The

average focusing velocity was measured by the central flow jet radius $r_{c,max}$ and d_p using equation (5.1): $\overline{v_r^F} \approx \frac{v_{max} r_{c,max}}{d_p}$. $r_{c,max}$ was measured for different flow ratios, because it is

actually a function of flow ratio: $r_{c,max} = R_{channel} \sqrt{1 - \sqrt{1 - \frac{Q_c}{Q_c + Q_p}}}$ (equation (2.14)).

$\sqrt{1 - \sqrt{1 - \frac{Q_c}{Q_c + Q_p}}}$ has been defined as the hydrodynamic factor f of the flow size in section

2.1.2.

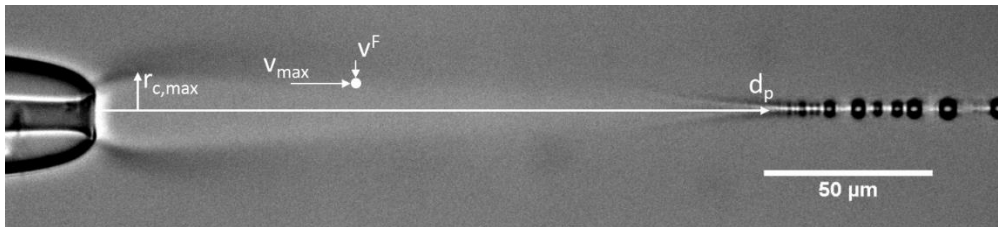


Figure 5.25. Schematic illustration of the movement of DBDCS in the antisolvent focusing of the coaxial microfluidic mixer.

The thermodynamic driving force for the radial migration of DBDCS molecule is the chemical potential gradient: $\mathbf{F} \approx -k_B T \left(\nabla \ln x_3 + \ln \left(\frac{x_{3s2}}{x_{3s1}} \right) \nabla \phi_1^o \right)$ (equation (3.48)).

Thermodynamic calculation (section 3.6.1, Figure 3.14) shows that the LLPS limit of DBDCS

in 1,4-dioxane is $\rho_{3sb2} = 568 \text{ g/l}$ (0.158 in amount fraction). This means that if the concentration of DBDCS in 1,4-dioxane reaches $\rho_{3sb2} = 568 \text{ g/l}$ (supersaturation ratio β of 100) by nonconventional methods, the mixture will separate into two metastable liquid phases, one rich on DBDCS, the other rich in 1,4-dioxane. This LLPS has a smaller energy barrier than crystallisation if β is smaller than 200. In the case of β greater than 200, spinodal decomposition will occur. The new meta-stable liquid phase rich in DBDCS will solidify because its chemical potential is 9 kJ/mol greater than the solid phase. Crystals of DBDCS will nucleate and grow from the remanence liquid phase rich in solvent, since β is still high. Let us assume that the coaxial flow antisolvent focusing has increased the mass concentration of DBDCS up to 568 g/l at d_p . Then, if we make a crude estimation, by the average gradient over $r_{c,max}$ and d_p , the radial component of the chemical potential gradient of DBDCS can be given:

$$\begin{aligned} \mathbf{F}_r &\approx - \frac{k_B T \left(\ln \frac{\rho_{3sb2}}{\rho_{3c}} + \ln \left(\frac{\rho_{3s2}}{\rho_{3s1}} \right) (0 - \phi_{1p}) \right)}{r_{c,max}} \\ &= \frac{k_B T \left(\ln \frac{\rho_{3c}}{\rho_{3sb2}} + \phi_{1p} \ln \frac{\rho_{3s2}}{\rho_{3s1}} \right)}{R_{channel} f} \end{aligned} \quad (5.3)$$

Therefore, the average focusing velocity of DBDCS by the gradient of chemical potential can be estimated by equation (3.31) and (3.32) with the effective diffusional radius of DBDCS r_3^* :

$$\begin{aligned} \overline{\mathbf{v}}_r^F &= \eta \overline{\mathbf{F}}_r \\ &= \frac{k_B T}{6\pi r_3^* \dot{\mu} R_{channel}} \frac{\ln \frac{\rho_{3c}}{\rho_{3sb2}} + \phi_{1p} \ln \frac{\rho_{3s2}}{\rho_{3s1}}}{f} \end{aligned} \quad (5.4)$$

r_3^* can be treated as a constant for the majority part of the focusing before strong self-association starts near d_p . The dynamic viscosity of the environment $\dot{\mu}$ can vary by a factor of two at maximum (see Figure 3.10), which can be treated as a constant by the average value.

Thus, the LLPS starting distance can be given by:

$$\begin{aligned}
d_p &\approx v_{\max} \frac{r_{c,\max}}{v_r^F} \\
&= \frac{2(Q_c + Q_p)}{\pi R_{\text{channel}}^2} \frac{R_{\text{channel}} f}{\frac{k_B T}{6\pi r_3^* \bar{\mu} R_{\text{channel}}} \frac{\ln \frac{\rho_{3c}}{\rho_{3sb2}} + \phi_{1p} \ln \frac{\rho_{3s2}}{\rho_{3s1}}}{f}} \\
&= \frac{12r_3^* \bar{\mu}}{k_B T} \frac{f^2 (Q_c + Q_p)}{\ln \frac{\rho_{3c}}{\rho_{3sb2}} + \phi_{1p} \ln \frac{\rho_{3s2}}{\rho_{3s1}}} \\
&\approx \frac{6r_3^* \bar{\mu}}{k_B T} \frac{Q_c}{\ln \frac{\rho_{3c}}{\rho_{3sb2}} + \phi_{1p} \ln \frac{\rho_{3s2}}{\rho_{3s1}}}, Q_c < Q_p
\end{aligned} \tag{5.5}$$

Equation (5.5) shows that d_p is linear with the central flow rate Q_c and inversely proportional

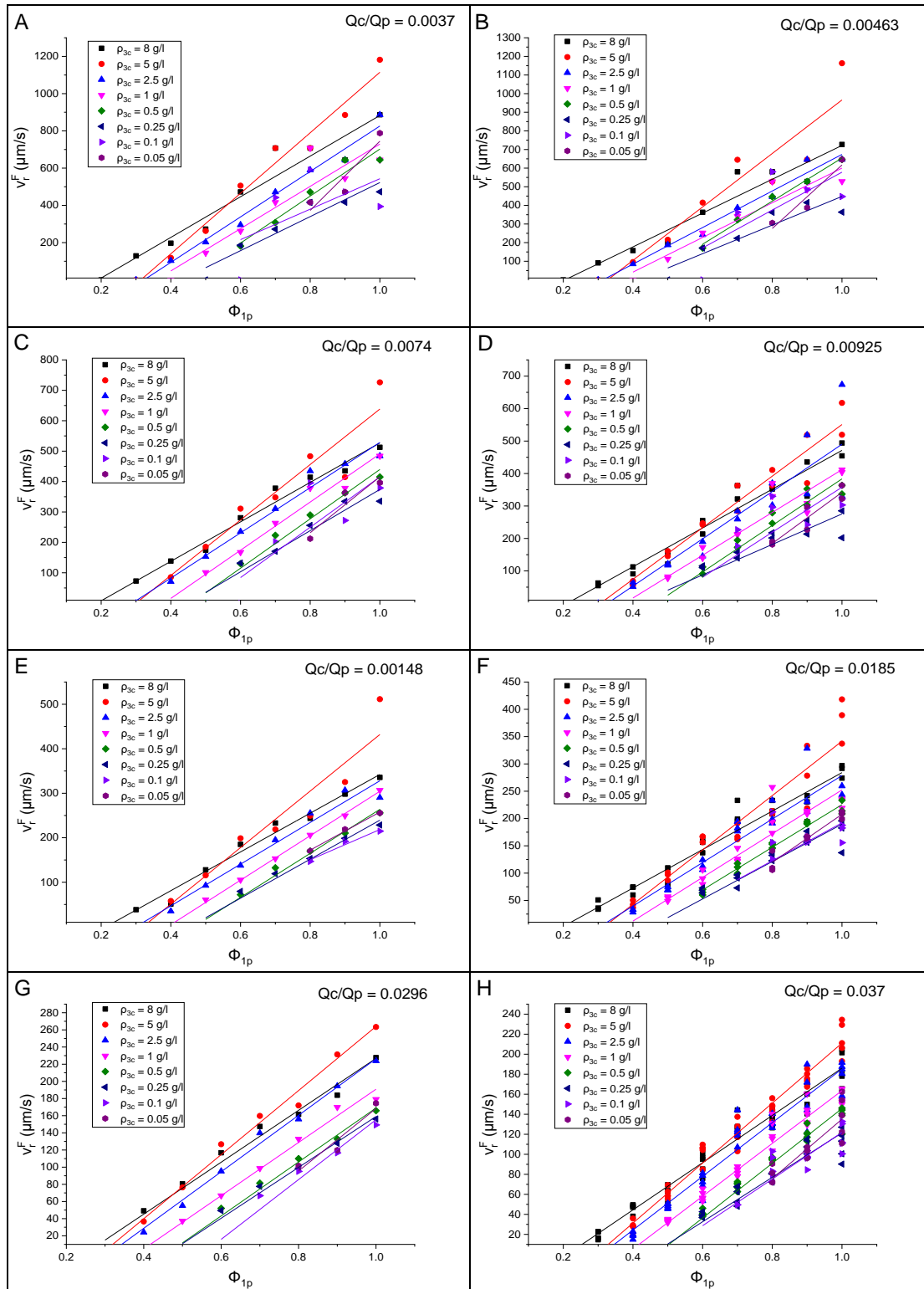
to $\left(\ln \frac{\rho_{3c}}{\rho_{3sb2}} + \phi_{1p} \ln \frac{\rho_{3s2}}{\rho_{3s1}} \right)$. It is independent with Q_p , as observed in Figure 5.24.

In equation (5.4) and (5.5), ρ_{3c} , ϕ_{1p} and $f = \sqrt{1 - \sqrt{1 - \frac{Q_c}{Q_c + Q_p}}}$ are independent microfluidic control parameters. They contain four adjustable parameters: the LLPS threshold ρ_{3sb2} estimated to be 568g/l (section 3.6.1), the chemical affinity of DBDCS for 1,4-dioxane compared to water $\ln \frac{\rho_{3s2}}{\rho_{3s1}} = 17.4$ (section 3.3.1), $r_3^* = 5.33\text{\AA}$ (estimated in section 3.5.2) and $\bar{\mu} \approx 1.5\text{mPa}\cdot\text{s}$. These adjustable parameters are intrinsic to the physical chemistry of the antisolvent-solvent-solute system. The rest are physical constants.

5.7.2. Dependence of the average focusing velocity on microfluidic parameters

The average focusing velocity of DBDCS $\overline{v_r^F}$ was measured for the microfluidic parametric sweep and plotted in Figure 5.26. The parametric sweep measurement was grouped by flow ratio Q_c/Q_p into small figures. The same flow ratio can be reached by different flow

rates of different order of magnitudes. From A to O, flow ratio Q_c/Q_p increased from 0.0037 to 0.37. On each small figure, \overline{v}_r^F increases linearly with water volume fraction in the peripheral flow ϕ_{1p} by the same slope with different offsets related to central flow concentration ρ_{3c} .



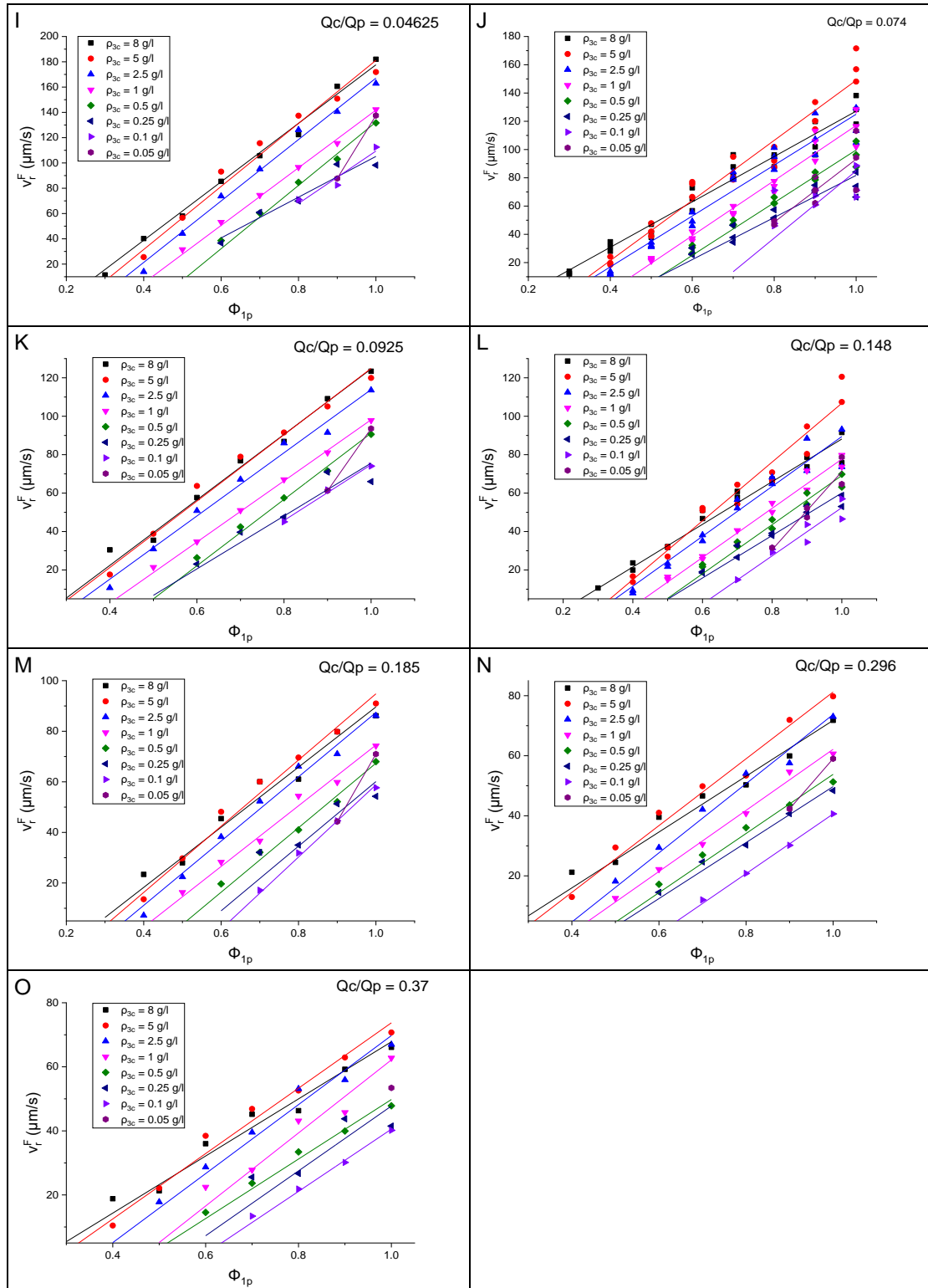


Figure 5.26. Dependence of average anti-solvent focusing velocity \overline{v}_F^F on microfluidic input parameters. Measurements from a parametric sweep are categorised into sub figures by flow ratio Q_c/Q_p . From A to O, flow ratio Q_c/Q_p increased from 0.0037

to 0.37. On each small figure, $\overline{v_r^F}$ increases linearly with water volume fraction in the peripheral flow ϕ_{1p} by the same slope with different offsets related to central flow concentration ρ_{3c} .

Figure 5.26 shows that $\overline{v_r^F}$ increases linearly with ϕ_{1p} by slopes related with Q_c/Q_p and offsets related with ρ_{3c} . Equation (5.4) gives a simple prediction of the focusing velocity by estimating the average radial component of the chemical potential gradient of DBDCS:

$$\overline{v_r^F} = \frac{k_B T}{6\pi r_3^* \dot{\mu} R_{\text{channel}}} \frac{\left(\ln \frac{\rho_{3c}}{568 \text{g/l}} + 17.4 \phi_{1p} \right)}{F_r}. \text{ Taking } r_3^* = 5.33 \text{\AA} \text{ (see section 3.5.2) and the}$$

average $\dot{\mu} \approx 1.5 \text{mPa} \cdot \text{s}^{-1}$ (see Figure 3.10), the linear dependence of $\overline{v_r^F}$ on ϕ_{1p} in Figure 5.26

can be estimated as $\text{slope} = \frac{17.4 k_B T}{6\pi r_3^* \dot{\mu} R_{\text{channel}}} \frac{1}{F_r} = 45.24 \cdot \frac{1}{F_r} \mu\text{m} \cdot \text{s}^{-1}$. The slopes of Figure 5.26

are plotted in Figure 5.27 over the prediction. The prediction is reasonably close to the experimental values. The average ratio between the prediction and the experimental values is 1.17.

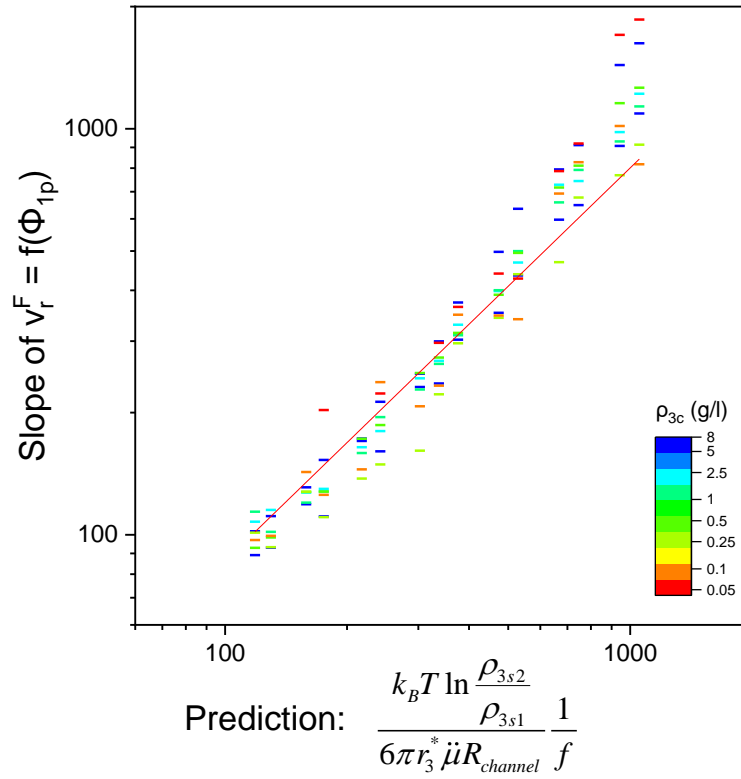


Figure 5.27. Prediction of slopes as a function of flow ratio. In the prediction

$$\text{equation, } f = \sqrt{1 - \sqrt{1 - \frac{Q_c}{Q_c + Q_p}}}, \quad r_3^* = 5.33 \text{ \AA}, \quad \dot{\mu} = 1.5 \text{ mPa} \cdot \text{s}^{-1}, \quad \ln \frac{\rho_{3s2}}{\rho_{3s1}} = 17.4 \text{ and}$$

$$\rho_{3sb2} = 568 \text{ g/l} .$$

Equation (5.4) predicts the x -intercepts of Figure 5.26 to be

$$-\frac{1}{\ln \frac{\rho_{3s2}}{\rho_{3s1}}} \ln \frac{\rho_{3c}}{\rho_{3sb2}} = -\frac{1}{17.4} \ln \frac{\rho_{3c}}{568 \text{ g/l}} .$$

The x -intercepts of $\overline{v_r^F} - \phi_{1p}$ relation is plotted *versus*

the prediction in Figure 5.28. The average ratio of the experimental values to the predictions is

1.125.

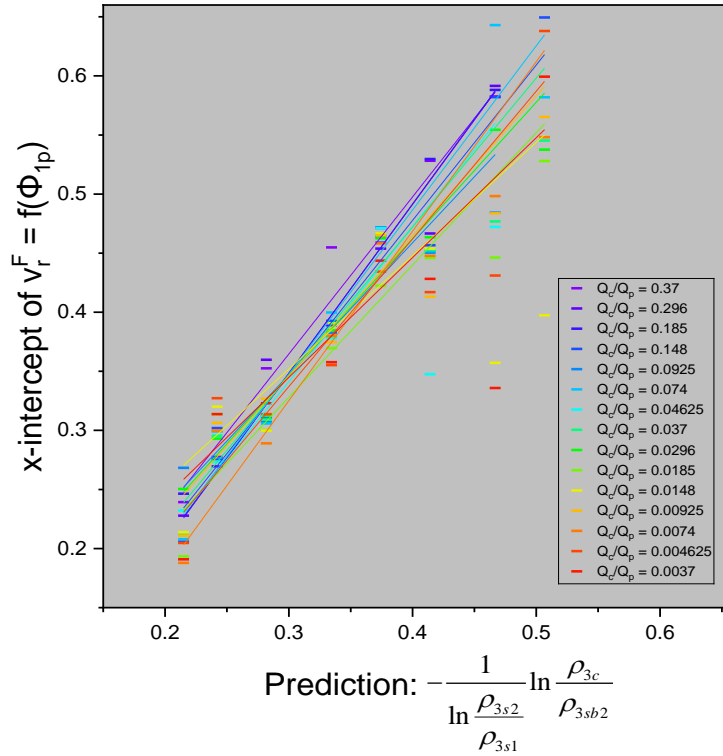


Figure 5.28. Dependence of the average anti-solvent focusing velocity of DBDCS on ρ_{3c} in the coaxial mixer of water (1)-1,4-dioxane (2) flows. In the prediction

$$\text{equation, } \ln \frac{\rho_{3s2}}{\rho_{3s1}} = 17.4 \text{ and } \rho_{3sb2} = 568 \text{ g/l.}$$

On Figure 5.26~Figure 5.28, the dependence of $\overline{v_r^F}$ on ϕ_{1p} , $\frac{Q_c}{Q_p}$, and ρ_{3c} was examined individually by the parametric sweep points. All of them proves the validity of the prediction. Therefore, $\overline{v_r^F}$ should be well predicted by equation (5.4). Hence, 1091 points of $\overline{v_r^F}$ from individual measurements are plotted over the prediction in Figure 5.29. Equation (5.4) gives satisfying prediction of $\overline{v_r^F}$ as a function of ϕ_{1p} , $\frac{Q_c}{Q_p}$, and ρ_{3c} . The average ratio between the prediction to the experiment is 1.37. This proves the prediction describes the mass transfer of the solute in the coaxial mixer very well.

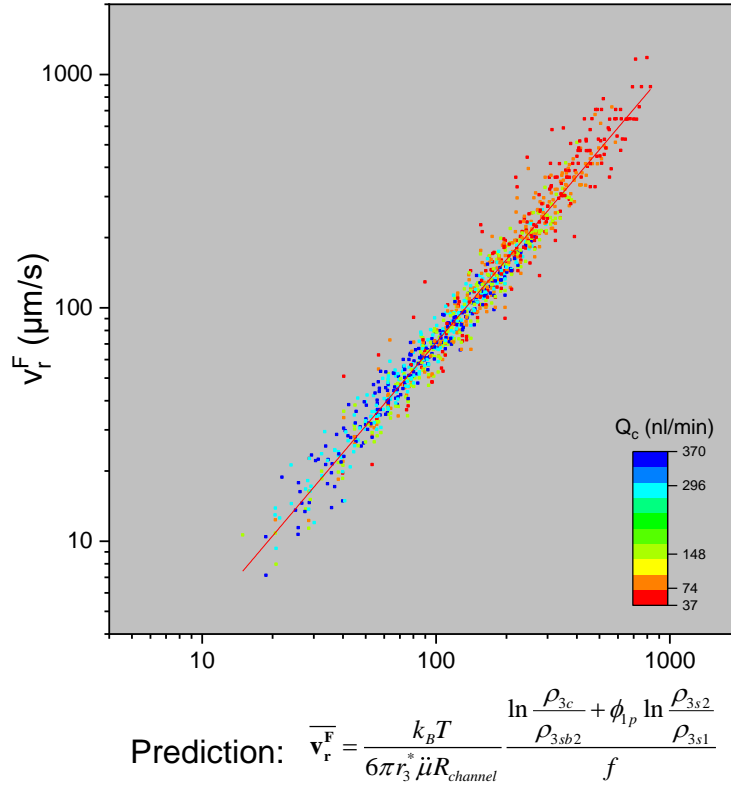


Figure 5.29. Dependence of the average anti-solvent focusing velocity of DBDCS on

ϕ_{1p} , $\frac{Q_c}{Q_p}$, and ρ_{3c} in the coaxial mixer of water (1)-1,4-dioxane (2) flows. In the

prediction equation, $r_3^* = 5.33\text{\AA}$, $\dot{\mu} = 1.5\text{mPa} \cdot \text{s}^{-1}$, $\ln \frac{\rho_{3s2}}{\rho_{3s1}} = 17.4$ and $\rho_{3sb2} = 568\text{g/l}$.

Hereby, we have demonstrated the focusing speed can be predicted by equation (5.4):

$$\begin{aligned} \bar{v}_r^F &= \frac{k_B T}{6\pi r_3^* \dot{\mu} R_{channel}} \frac{\ln \frac{\rho_{3c}}{\rho_{3sb2}} + \phi_{1p} \ln \frac{\rho_{3s2}}{\rho_{3s1}}}{f} \\ &= \frac{1}{6\pi r_3^* \dot{\mu} R_{channel}} \frac{k_B T \ln \frac{\rho_{3c}}{\rho_{3sb2}} + \phi_{1p} \Delta_r G}{f} \end{aligned}$$

where ρ_{3sb2} is the binodal LLPS threshold of DBDCS in 1,4-dioxane and $\Delta_r G$ the free energy of the reaction $\text{DBDCS}_{\text{water}} \rightleftharpoons \text{DBDCS}_{1,4\text{-dioxane}}$, which can be measured from the solubility

in pure solvents: $\Delta_r G = k_B T \ln \frac{\rho_{3c2}}{\rho_{3c1}}$. These parameters are intrinsic to the physical chemistry of the water (1)-1,4-dioxane (2)-DBDCS (3) system, whereas f , ρ_{3c} , and ϕ_{1p} are control parameters of the coaxial mixer.

Out of more than 2000 experiments, only 1091 points of $\overline{v_r^F}$ was measured. This is because for the rest of the experiment, the anti-solvent gradient was not steep enough to overcome the solute concentration gradient. Therefore, in those experiments, DBDCS was not focused towards the flow centre. Instead of droplet formation, these are either the crystallisation or the soluble points in the phase diagram (Figure 5.4).

Equation (5.4) also predicts the limit between the droplet formation region and the crystallisation region. When $\ln \frac{\rho_{3c}}{568\text{g/l}} + 17.4\phi_{1p} > 0$, DBDCS is pushed towards the flow centre by the chemical potential gradient, the concentration reaches the LLPS limit, droplets are formed. When $\ln \frac{\rho_{3c}}{568\text{g/l}} + 17.4\phi_{1p} \approx 0$, DBDCS molecules are kept in a column near the centre of the flow, nano-particles are formed in the column. When $\ln \frac{\rho_{3c}}{568\text{g/l}} + 17.4\phi_{1p} < 0$, depending on the over saturation ratio it will be either a slow nucleation and growth from a nearly homogeneous solution or soluble. The predicted chemical potential focusing limit of DBDCS is plotted in Figure 5.30 (red line).

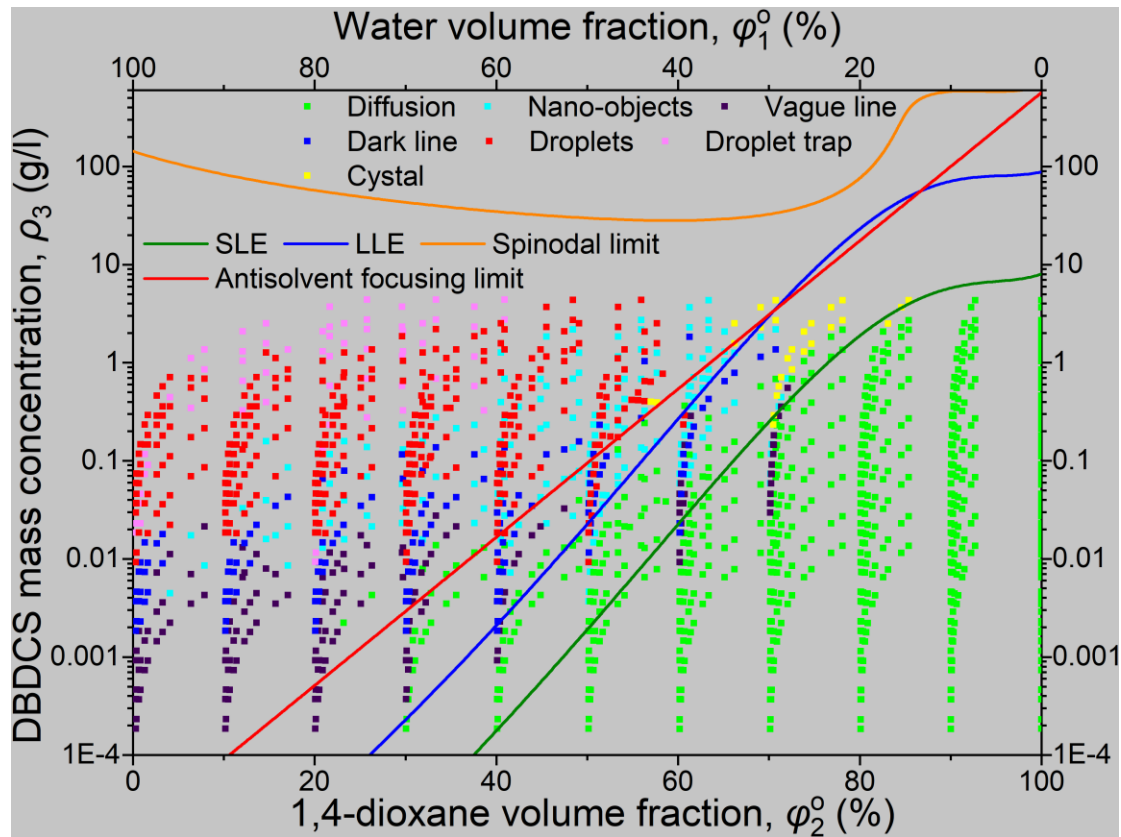


Figure 5.30. The chemical potential focusing limit (red) of DBDCS by water (1)-1,4-dioxane (2) in the working phase diagram of water (1)-1,4-dioxane (2)-DBDCS (3) in coaxial microfluidic mixer, predicted by equation(5.4): $\ln \frac{\rho_{3c}}{\rho_{3sb2}} + \phi_p \ln \frac{\rho_{3s2}}{\rho_{3s1}} = 0$ with

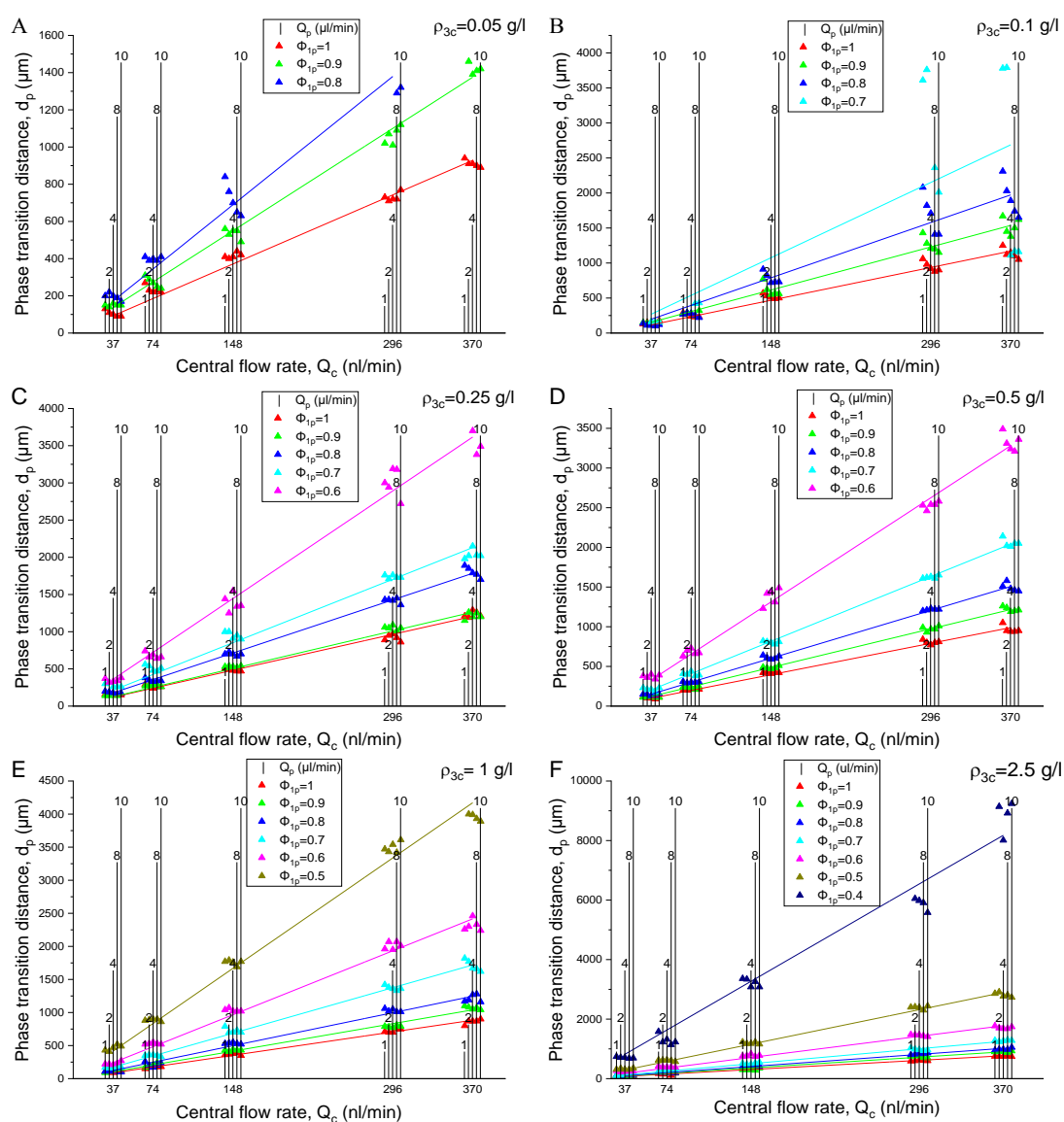
$$\ln \frac{\rho_{3s2}}{\rho_{3s1}} = 17.4 \text{ and } \rho_{3sb2} = 568 \text{ g/l} . \text{The green line on the phase diagram is the solubility predicted by Jouyban-Acree equation. The black curve is the binodal LLPS limit from thermodynamic calculation in section 3.6.1.3.}$$

In Figure 5.30, the antisolvent focusing limit fits well with the experiment observation, lying between the droplet formation points (red) and the crystallisation (yellow) or nanoparticle points (light blue) parallel to the solubility curve. For the lower part of the phase diagram, the concentration of DBDCS was so low that it was not able to form micro-droplets but a line along the flow centre. The antisolvent focusing limit is parallel to the binodal LLPS limit with a small offset. This offset is due to the fact that the antisolvent focusing of the solute makes the

supersaturation ratio at the flow centre higher than the overall supersaturation ratio.

5.7.3. Dependence of LLPS and nano-precipitation starting position on microfluidic parameters

d_p was systematically measured during the microfluidic parametric sweep for droplet formation and nanoparticle precipitation and plotted in Figure 5.31. For points in the soluble region of the phase diagram, d_p was infinite, and for the crystallisation points, d_p was not clearly determined.



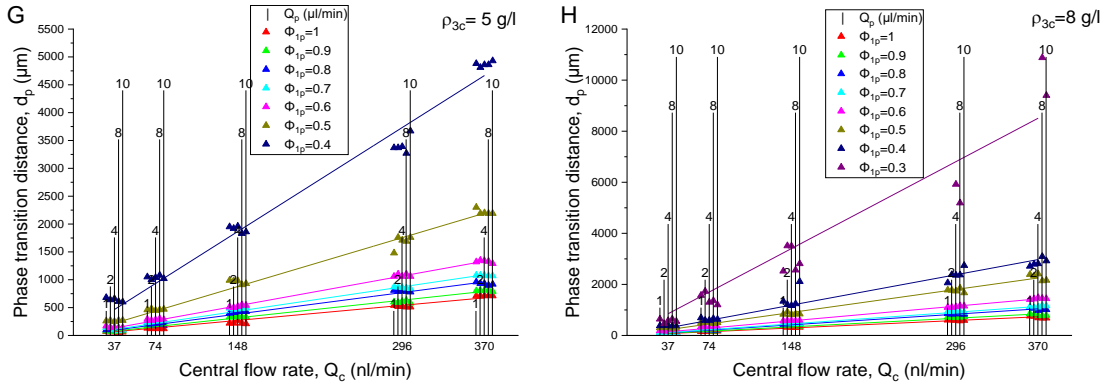


Figure 5.31. LLPS and nano-precipitation starting position's dependence on microfluidic control parameters. Points are grouped into small figures by central flow concentration ρ_{3c} . On each small figure, d_p is plotted against central flow rate Q_c . For each Q_c , five measurements with Q_p increasing from 1 to 10 was plotted close together. The corresponding Q_p was plotted on the corresponding position as a vertical straight line. The length represents Q_p values.

Each point in Figure 5.31 is a different combination of microfluidic input parameters. Each small figure corresponds to a ρ_{3c} value. d_p is plotted against Q_c . For each Q_c , five Q_p was taken, increasing from 1 to 10 $\mu\text{l}/\text{min}$. The five points of five different Q_p but the same Q_c were plotted close together. The corresponding Q_p was plotted on the corresponding position as a vertical straight line. The height represents Q_p values. It illustrates d_p increase linearly with Q_c , despite that the flow velocity was increased almost linearly by Q_p .

Equation (5.5) predicts: $d_p \approx \frac{12r_3^* \ddot{\mu}}{k_B T} \frac{f^2(Q_c + Q_p)}{\ln \frac{\rho_{3c}}{\rho_{3s2}} + \phi_{1p} \ln \frac{\rho_{3s2}}{\rho_{3s1}}}$. It points out d_p is linear

with $f^2(Q_c + Q_p)$. When $Q_c < Q_p$, $f^2(Q_c + Q_p) \approx \frac{1}{2} Q_c$. Therefore, d_p is linear to Q_c unless a very large flow ratio Q_c/Q_p is used.

In Figure 5.31, the slopes of $d_p - Q_c$ dependence depends on both ϕ_{1p} and ρ_{3c} .

Equation (5.5) gives $d_p \approx \frac{6r_3^* \ddot{\mu}}{k_B T} \frac{Q_c}{\ln \frac{\rho_{3c}}{\rho_{3sb2}} + \phi_{1p} \ln \frac{\rho_{3s2}}{\rho_{3s1}}}$. We have estimated in Chapter 3 that

$\ln \frac{\rho_{3s2}}{\rho_{3s1}} = 17.4$, $\rho_{3sb2} = 568 \text{ g/l}$ and $r_3^* = 5.33 \text{ \AA}$. Therefore, we predict the slopes to be

$\frac{6r_3^* \ddot{\mu}}{k_B T} \frac{1}{\left(\ln \frac{\rho_{3c}}{568 \text{ g/l}} + 17.4 \phi_{1p} \right)}$. Taking $\ddot{\mu}$ by the average of $1.5 \text{ mPa} \cdot \text{s}$ (see Figure 3.10), the

slopes of $d_p - Q_c$ dependence in Figure 5.31 were plotted in Figure 5.32 against the prediction.

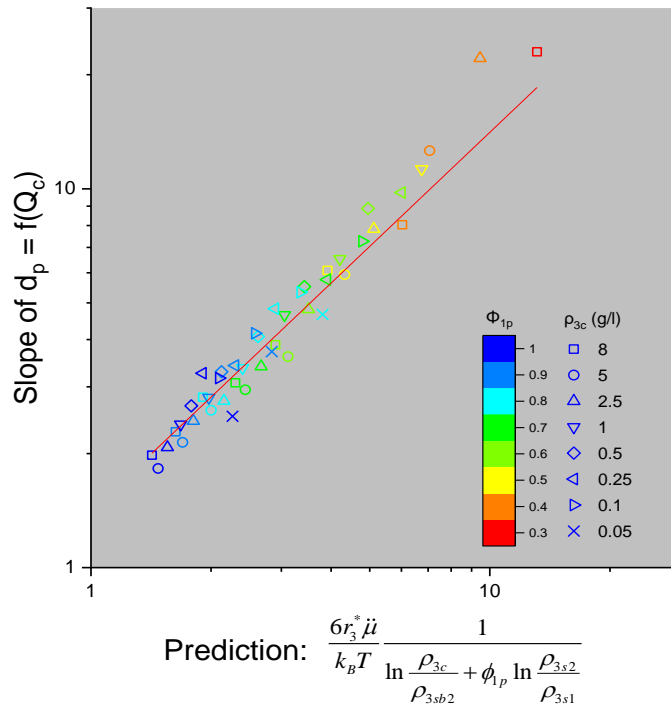


Figure 5.32. Dependence of d_p on ρ_{3c} and ϕ_{1p} . The slope of the linear dependence of

d_p on Q_c is a function of ρ_{3c} and ϕ_{1p} . In the prediction formula, $r_3^* = 5.33 \text{ \AA}$,

$$\ddot{\mu} = 1.5 \text{ mPa} \cdot \text{s}^{-1}, \ln \frac{\rho_{3s2}}{\rho_{3s1}} = 17.4, \text{ and } \rho_{3sb2} = 568 \text{ g/l}.$$

Figure 5.32 illustrates the slope of the linear dependence of d_p on Q_c is a function of ρ_{3c} and ϕ_{1p} . The solubility ratio of solvent/antisolvent and the LLPS threshold must also be

given or they can be fitted from the relation. In our case, the solubility of DBDCS in water was fitted using Acree model (section 3.3.1) and the LLPS threshold calculated from H3M model (section 3.6.1.1). Equation (5.5) gives close prediction of the slopes of the linear relation of d_p and Q_c .

Hereby we have examined the influence of the microfluidic control parameters on the distance where droplets are formed. Figure 5.31 and Figure 5.32 validate our model. Therefore, we can predict d_p using equation (5.5). The parametric measurement of over 1000 d_p values are plotted in Figure 5.33 against our prediction. The average ratio of the prediction to the experimental values is 0.69.

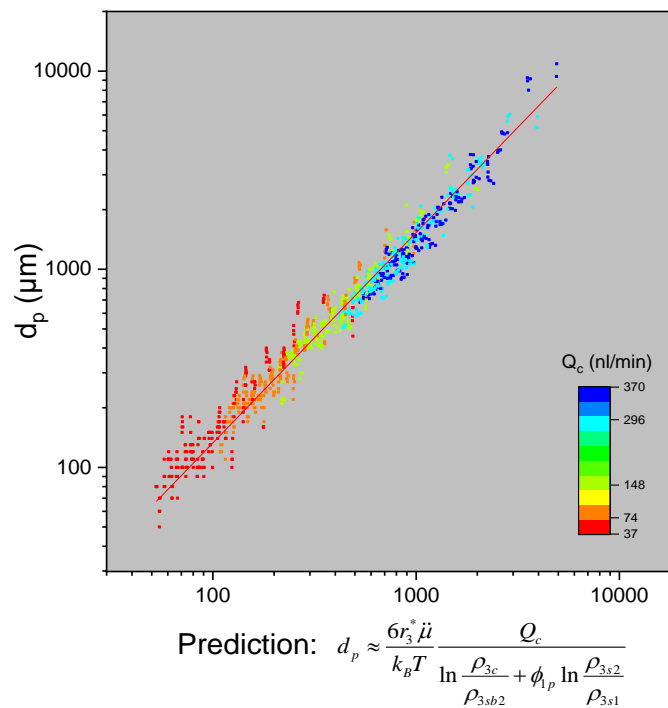


Figure 5.33. Droplet formation position as a function of Q_c , ρ_{3c} and ϕ_{1p} . The binodal LLPS limit and solubility ratio of solvent/antisolvent must be given. $\dot{\mu}$ was treated as a constant for the simplicity. In the prediction formula, $r_3^* = 5.33\text{\AA}$, $\dot{\mu} = 1.5\text{mPa} \cdot \text{s}^{-1}$,

$$\ln \frac{\rho_{3s2}}{\rho_{3s1}} = 17.4, \text{ and } \rho_{3sb2} = 568 \text{ g/l.}$$

Figure 5.33 shows the LLPS and nano-precipitation starting position in the coaxial

mixer can be predicted by equation (5.5): $d_p \approx \frac{6r_3^* \ddot{\mu}}{k_B T} \frac{Q_c}{\ln \frac{\rho_{3c}}{\rho_{3sb2}} + \phi_{1p} \ln \frac{\rho_{3s2}}{\rho_{3s1}}}, Q_c < Q_p$. It

increases linearly with Q_c , and decreases as ϕ_{1p} or ρ_{3c} increases.

Figure 5.29, Figure 5.30 and Figure 5.33 prove, firstly, that our equation for the solute focusing by the antisolvent gradient in the coaxial mixer gives good prediction of i) the solute diffusion velocity, ii) the phase separation position and the limit between the LLPS region, iii) the slow nucleation and growth region in the phase diagram. Secondly, the fact that the points in Figure 5.32 and Figure 5.33 cannot be a simple linear relation if the LLPS limit is changed to another value proves that the droplet formation is LLPS and our calculation of the binodal LLPS limit is good. Thirdly, this model can be extended to other antisolvent-solvent-solute coaxial microfluidic systems. Knowing the solubility ratio of solvent/antisolvent and the binodal LLPS limit, one can make predictions of the behaviour of the coaxial flow. By measuring the droplet formation distance, one can deduce the diffusion coefficient and fit for the solubility and binodal LLPS limit as adjustable parameters in equation (5.4) and (5.5).

5.7.4. Quality of the prediction of the chemical potential focusing velocity, distance, the binodal LLPS threshold and the diffusion coefficient of DBDCS in water (1)-1,4-dioxane (2) coaxial microflow

In the previous sections, we proposed equation (5.4) and (5.5) based on that the driving

force of diffusion is the chemical potential gradient: $\mathbf{F} \approx \frac{k_B T \left(\ln \frac{\rho_{3c}}{\rho_{3sb2}} + \phi_{1p} \ln \frac{\rho_{3s2}}{\rho_{3s1}} \right)}{R_{\text{channel}} f}$ and that

the diffusion velocity is linear with the driving force: $\overline{\mathbf{v}}_r^F = \eta \overline{\mathbf{F}}_r$, to predict the antisolvent

focusing velocity and droplet formation position. In these equations, f , ρ_{3c} , and ϕ_{1p} are control parameters of the coaxial mixer. Three adjustable parameters are intrinsic to the physical chemistry of the antisolvent-solvent-solute system: the difference of the affinity of DBDCS with 1,4-dioxane and with water $\ln \frac{\rho_{3s2}}{\rho_{3s1}}$ (section 3.5.2), the binodal LLPS threshold ρ_{3sb2} (section 3.6.1) and the mobility $\eta = \frac{1}{6\pi r_3^* \dot{\mu}}$ of DBDCS monomers in water (1)-1,4-dioxane (2) mixture (section 3.5.2). The solubility of DBDCS in 1,4-dioxane ρ_{3s2} was measured, yet that in water ρ_{3s1} was too miniscule to be experimentally measured. ρ_{3s1} was fitted using Jouyban-Acree equation (equation (3.28)). The LLPS threshold of DBDCS in 1,4-dioxane was difficult to be reached by conventional mixing method, it was estimated by finding inflection points of ΔG_m calculated with H³M model (equation (3.22)). For η , the average $\dot{\mu}$ of water (1)-1,4-dioxane (2) mixture in the composition range of interest was taken (Figure 3.10). r_3^* the radius of DBDCS solute monomer was estimated in section 3.1. The predicted values are listed in Table 5.1.

Table 5.1. Comparison of predicted and fitted parameters in equation (5.4) and (5.5): chemical affinity of DBDCS for 1,4-dioxane compared to water, binodal LLPS threshold of DBDCS in 1,4-dioxane and the radius of solute DBDCS

Parameter	$\ln \frac{\rho_{3s2}}{\rho_{3s1}}$	ρ_{3sb2} / (g/l)	r_3^* / m
Predicted	17.4	568	5.33
Fitted from d_p	14.4 ± 0.1	277 ± 8	5.4 ± 0.1
Fitted from $\overline{v_r^F}$	17.1 ± 0.6	400 ± 110	5.5 ± 0.2

With the predicted parameters, we have shown in the previous sections the validity of equation (5.4) and (5.5) in predicting $\overline{v_r^F}$ and d_p . With these equations, the dependence of $\overline{v_r^F}$

and d_p on the microfluidic parameters was revealed. *Vice versa*, without knowing the parameters, one can measure d_p systematically to fit for the solute solubility in antisolvent, the binodal LLPS threshold and the hydrodynamic radius of the solute monomer. Therefore, a 4-dimensional fitting of $\overline{v_r^F}$ and d_p , respectively, using microfluidic control parameters as independent variables was conducted for the three predicted parameters: ρ_{3s1} , ρ_{3sb2} and r_3^* . The fitting was successful. The fitted values are listed in Table 5.1. The values from both fittings are within 20% from the predicted values. The experimental measurement of $\overline{v_r^F}$ and d_p are again plotted against equation (5.4) and (5.5) using their own fitted parameters in Figure 5.34. No significant difference can be seen from Figure 5.26 and Figure 5.31.

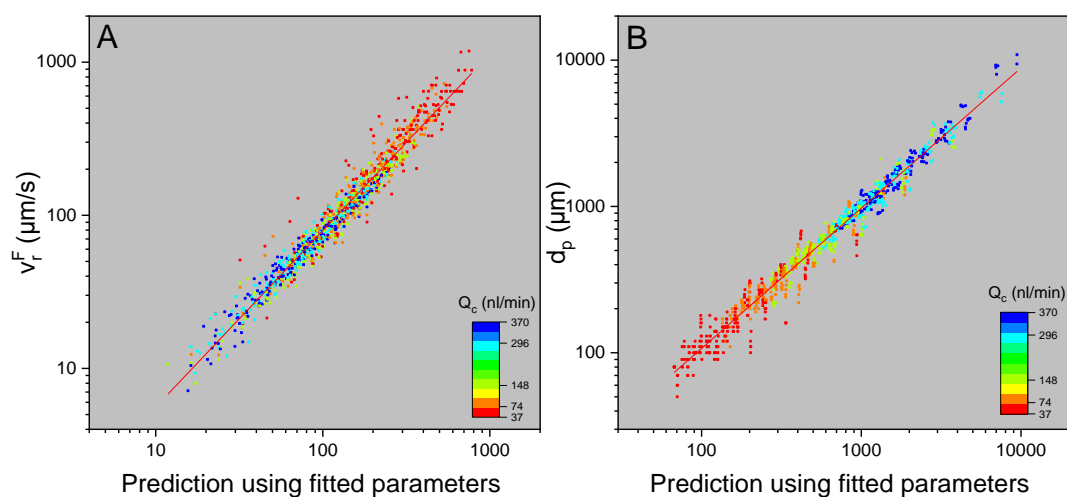


Figure 5.34. New prediction of antisolvent focusing velocity and droplet formation distance with equation (5.4) and (5.5) using fitted parameters.

This supports our calculation in Chapter 3 and our observation that the droplets resulted from a LLPS. This confirms again, that knowing solubility, LLPS limit and size of the solute, $\overline{v_r^F}$ and d_p can be predicted by equation (5.4) and (5.5). *Vice versa*, from systematical measurement of $\overline{v_r^F}$ and d_p in a coaxial mixer, the chemical affinity of the solute for the solvent compared to the antisolvent, the LLPS threshold and the diffusion coefficient can be

deduced.

5.8. Droplet size dependence on microfluidic parameters

5.8.1. The total volume fraction of the droplets in the flow

Figure 5.24 shows that d_p was constant while Q_p was increasing from 1 to 80. It contains two additional pieces of information. At very low Q_p , abnormally large droplets trapped by the gradient of antisolvent appear. The average size of the droplets decreases with Q_p . This was noticed and systematically measured for combinations of different microfluidic parameters.

One of the measurements of the droplet size dependence on peripheral flow rate is shown in Figure 5.35. Fixing the other three operational parameters, the size of the droplets decreased as the peripheral flow increased.

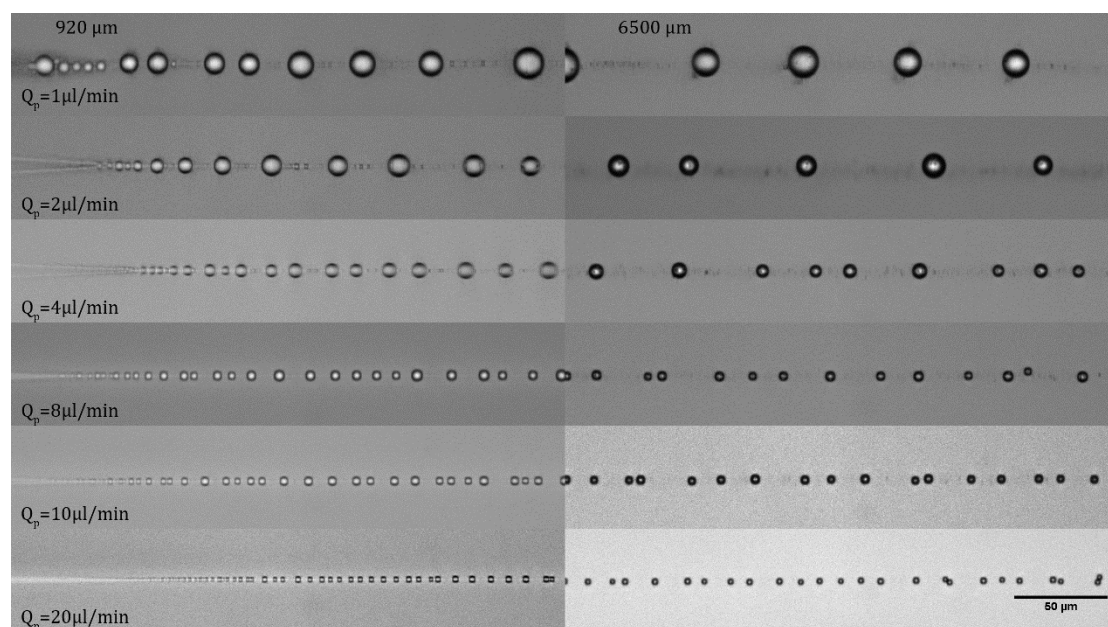


Figure 5.35. Size dependence of droplets on Q_p . The OM image of droplets taken at their birth place (left) and at $x=6500 \mu\text{m}$ (right). Microfluidic parameters:

$$\rho_{3c} = 2.5 \text{ g/l}, Q_c = 370 \text{ nl/min}, \phi_{1p} = 90\% .$$

Figure 5.36 illustrates the size dependence of the droplets on the water volume fraction

in the peripheral flow, ϕ_{1p} . With other three operational parameters fixed, the more antisolvent in the peripheral flow, the larger the driving force for the uphill diffusion, thus the more concentrated DBDCS was at the flow centre, the larger number of droplets required to contain the DBDCS molecules. Therefore, the size of the droplets increased with ϕ_{1p} .

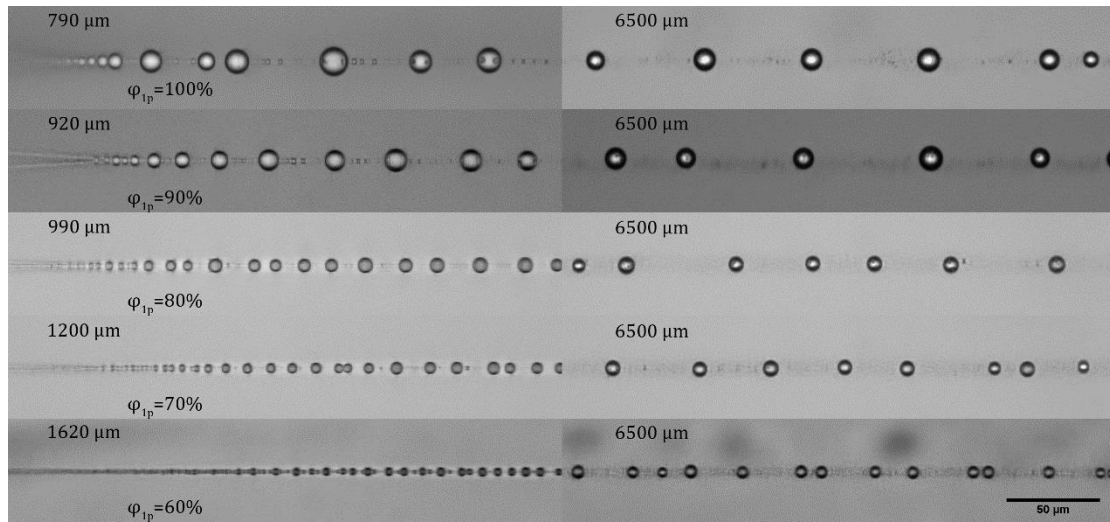


Figure 5.36. Size dependence of droplets on ϕ_{1p} . The OM image of droplets taken at their birth place (left) and at $x=6500 \mu\text{m}$ (right). Microfluidic parameters:

$$\rho_{3c} = 2.5 \text{ g/l}, Q_c = 370 \text{ nl/min}, Q_p = 2 \mu\text{l/min}.$$

In Figure 5.37, the size dependence of the droplets on concentration of DBDCS in the central flow was shown. With other three operational parameters fixed, the size of the droplets increased with the DBDCS concentration.

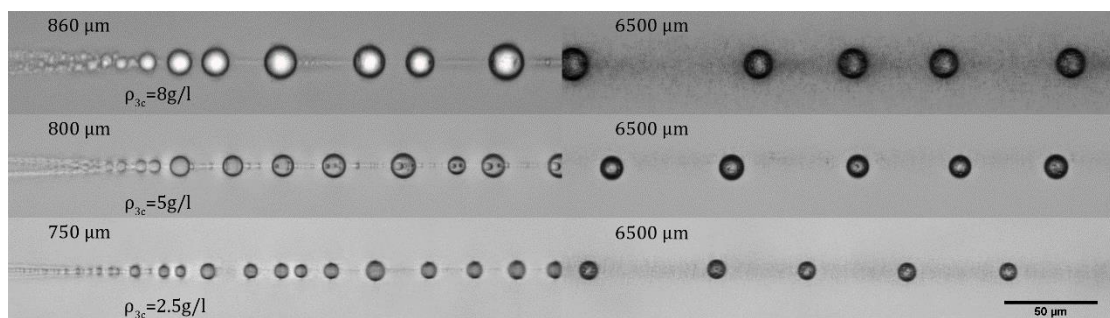


Figure 5.37. Size dependence of droplets on ρ_{3c} . OM image taken at droplets birth

place (left) and at $x=6500 \mu\text{m}$ (right). Microfluidic parameters:

$$Q_c = 370 \text{ nl/min}, Q_p = 1 \mu\text{l/min}, \phi_{lp} = 80\% .$$

Similarly, one was already able to predict that the higher the central flow rate, the bigger the droplets. The effect of increasing the central flow rate is equivalent to decrease the peripheral flow rate. Indeed, fixing ρ_{3c} and ϕ_{lp} , what is important is the flow ratio, Q_c/Q_p . To analyse the dependence on each parameter requires at least 4 dimensions.

From Chapter 3 we have calculated a phase diagram of water (1)-1,4-dioxane (2)-DBDCS (3) by thermodynamics (Figure 3.17 and Figure 5.38). It is comprised of a spinodal decomposition domain (cinnamon), two binodal LLPS domains (green), two metastable domains (white), and a miniscule soluble domain. Mixtures x (see Figure 5.38) in the spinodal decomposition domain and the two binodal LLPS domains will fast separate into two new phases (a and b on Figure 5.38) on the binodal curve (cyan). The new liquid DBDCS (upper white) will solidify and the DBDCS molecule in the lower metastable domain will also crystallise from the liquid. The fraction of the meta-stable liquid DBDCS and the meta-stable remanence is given by the lever rule: $(x_3 - b_3):(a_3 - x_3)$. In our case, the LLPS domain is almost the triangle of the ternary phase diagram itself: $b_3 \approx 0, a_3 \approx 1$. Therefore, the liquid DBDCS formed from LLPS is proportional to the fraction of DBDCS in the mixture:

$$\frac{x_3 - b_3}{a_3 - b_3} = x_3 .$$

The mass density of both phases is around 1 g/l. Therefore, the volume fraction

of the droplets, that is the total volume of the droplets divided by the total volume of the mixture, will be proportional to the total DBDCS fraction.

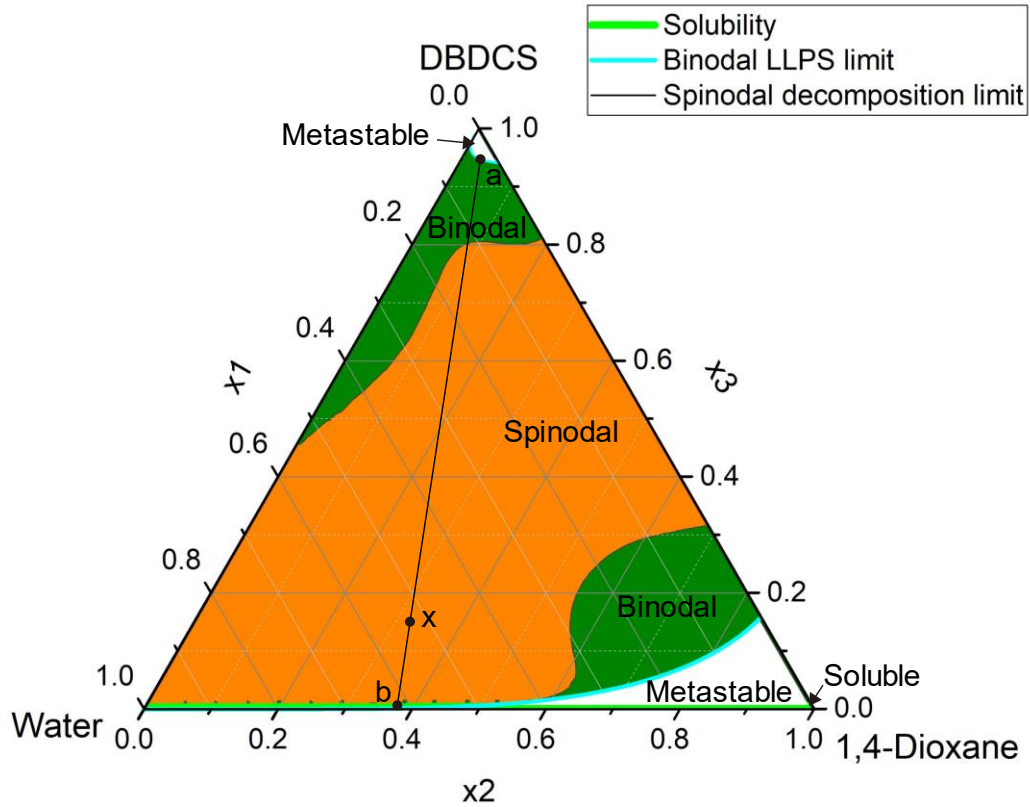


Figure 5.38. Fraction of new phases from the LLPS in the ternary phase diagram of water (1)-1,4-dioxane (2)-DBDCS (3).

Volume of the droplets is something we can measure. The total droplet volume fraction in the microfluidic channel is plotted in Figure 5.39. It illustrates the total droplet volume fraction in the mixture is proportional to the DBDCS concentration. From the slope we can deduce the mass concentration of DBDCS in the droplets is around 1.2 g/ml. In 3.1 the density of the hypothetical liquid DBDCS was estimated to be $\rho_{D3^*} = \frac{M_3}{V_{m,3^*}} = 1246.35 \text{ g/l}$. This suggests the droplets is a transient pure liquid phase of the solute. This was also suggested by the volume change of the droplets after drying. Instead of giving a small crystal from a solution, the crystals from the droplets take almost the same volume as the droplets.

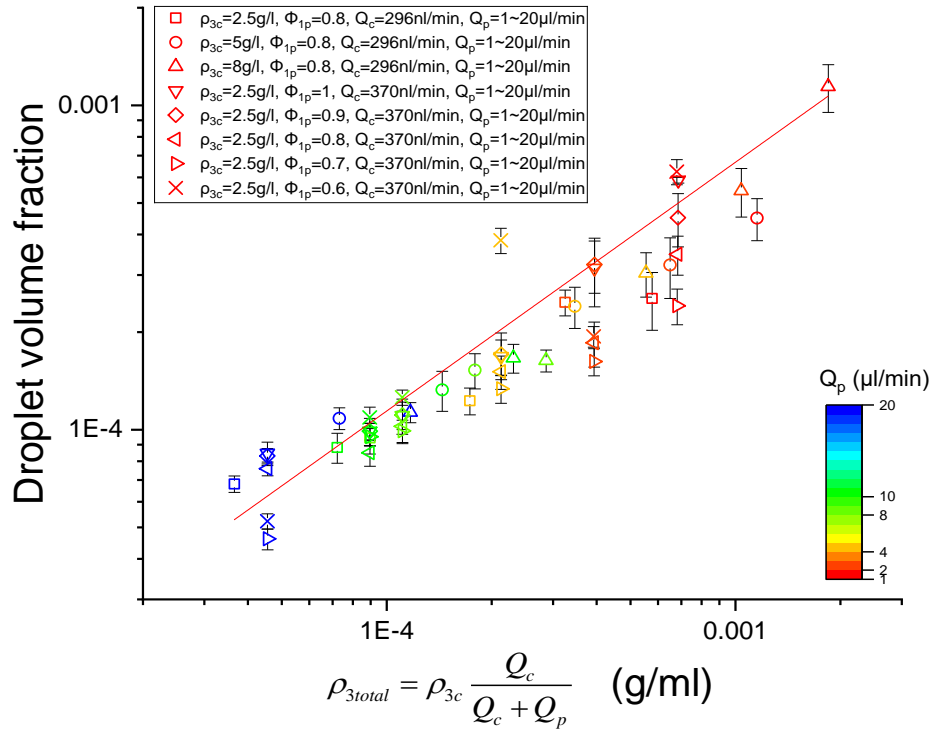


Figure 5.39. Total droplet volume fraction is linear with DBDCS total concentration. Every millilitre of the droplet phase contains 1.2 g DBDCS. It is almost pure liquid DBDCS.

Since $\rho_{3total} = \rho_{3c} \frac{Q_c}{Q_c + Q_p}$, Figure 5.39 also reveals the total droplet volume

fraction's relation with the four input parameters. It is linear with the central flow rate and concentration, inversely proportional to the total flow rate.

5.8.2. The size of the DBDCS droplets

The formation of the droplets can be describes in 3 steps: first, focusing of the solute by the gradient of antisolvent; second, liquid phase separation after the concentration reaches at least the binodal LLPS threshold near d_p ; third, Marangoni focusing and merging of the nano-droplets at d_p . Then different cases were observed: microdroplets merge into a big one that escapes with a constant periodicity, or nano or micro droplets merge into a liquid cylinder

that later breaks into droplets of constant size with a constant periodicity. The last case is similar to the Plateau-Rayleigh instability, the breaking of a viscous liquid cylinder into droplets of a large radius to minimise the surface tension. At the focal point of the antisolvent focusing, the newly emerged liquid phase can be considered at a transient liquid cylinder that shortly breaks into droplets. Neither the nano-droplets nor the cylinder is stable. There is a certain stable size that is related with microfluidic parameters.

Rayleigh [Plateau, 1873, Rayleigh, 1997, Rayleigh, 2010] obtained a dispersion equation describing the instability as a function of the distance between droplets (the wavelength of the instability), the radius of cylinder, the mass density, the surface tension and the viscosity of the liquid. Hundreds of authors referred to his work, but they used only the asymptotic solutions of his equation for zero or infinitely large viscosities. The result is a liquid

cylinder of original radius r_0 will most likely break into droplets sized $r_{\text{drop}} = \sqrt[3]{\frac{3}{2}\sqrt{2\pi}} \cdot r_0$

with a natural instability period $\lambda = 2\sqrt{2}\pi r_0$. [Garin, 2017] We know this cannot describe our data, because the droplet size dependence on ϕ_p is not in the equation. In the equation, the droplet size is only related with the initial cylinder radius. Chandrasekhar [Chandrasekhar, 2013] also considered the stability of a viscous cylindrical jet and obtained his dispersion equation. As the same case of Rayleigh's equation, other works use only the asymptotic solution of Chandrasekhar's equation when the viscosity is very large. Recently, L. Pekker [Pekker, 2017] demonstrated that Chandrasekhar's equation is equivalent to Rayleigh's equation and presented a numerical solution:

$$\lambda = 6.9345\sqrt{\frac{\mu}{\gamma\rho_D}}\sqrt{\frac{r_0}{\gamma\rho_D}} + 9.1174r_0. \quad (5.6)$$

with μ the viscosity of the liquid cylinder, γ the surface tension and ρ_D its mass density.

Thereby, the droplet size can be estimated:

$$r_{\text{drop}} = \sqrt[3]{\frac{3}{4} r_o^2 \left(6.9345 \dot{\mu} \sqrt{\frac{r_o}{\gamma \rho_D}} + 9.1174 r_o \right)} \quad (5.7)$$

In our case, since the total volume of the new liquid phase is equivalent to the total DBDCS input, the radius of the initial cylinder can be estimated as:

$$\begin{aligned} r_o &= R_{\text{channel}} f \\ &= R_{\text{channel}} \sqrt{1 - \sqrt{1 - \frac{\rho_{3c}}{\rho_{D3^*}} \frac{Q_c}{Q_c + Q_p}}} \end{aligned} \quad (5.8)$$

The mass density of liquid DBDCS ρ_{D3^*} was estimated in 3.1 to be 1250 g/l, yet the viscosity of the liquid DBDCS and the surface tension of the liquid to water (1)-1,4-dioxane (2) mixture remains unknown.

The surface tension of a liquid mixture can be estimated by equation (3.6)

$$\gamma = \frac{\sum \gamma_i A_{m,i} x_i}{\sum A_{m,i} x_i}, \text{ with } \gamma_i \text{ the surface tension of species } i, A_{m,i} \text{ its molar surface area, and } x_i$$

its amount fraction. The surface tension of water (1)-1,4-dioxane (2) with air estimated by equation (3.6) with the molar surface areas measured by [Suarez, 1989] is plotted in Figure 5.40 and compared with the experimental data [Wohlfarth, 2008]. Equation (3.6) gives good prediction of the surface tension between water (1)-1,4-dioxane (2) and air. Therefore, if we can estimate the surface tension between liquid DBDCS with water and 1,4-dioxane individually and the viscosity of liquid DBDCS, the size and interval of the DBDCS droplets is given by:

$$\begin{aligned}
r_{\text{drop}} &= \sqrt[3]{\frac{3}{4} r_o^2 \left(6.9345 \ddot{\mu} \sqrt{\frac{r_o}{\gamma \rho_{D3^*}}} + 9.1174 r_o \right)} \\
\lambda &= 6.9345 \ddot{\mu} \sqrt{\frac{r_o}{\gamma \rho_{D3^*}}} + 9.1174 r_o \\
r_o &= R_{\text{channel}} \sqrt{1 - \sqrt{1 - \frac{\rho_{3c}}{\rho_{D3^*}} \frac{Q_c}{Q_c + Q_p}}} \\
\gamma &= \frac{\gamma_{13} A_{m,1} x_1 + \gamma_{23} A_{m,2} x_2}{A_{m,1} x_1 + A_{m,2} x_2}
\end{aligned} \tag{5.9}$$

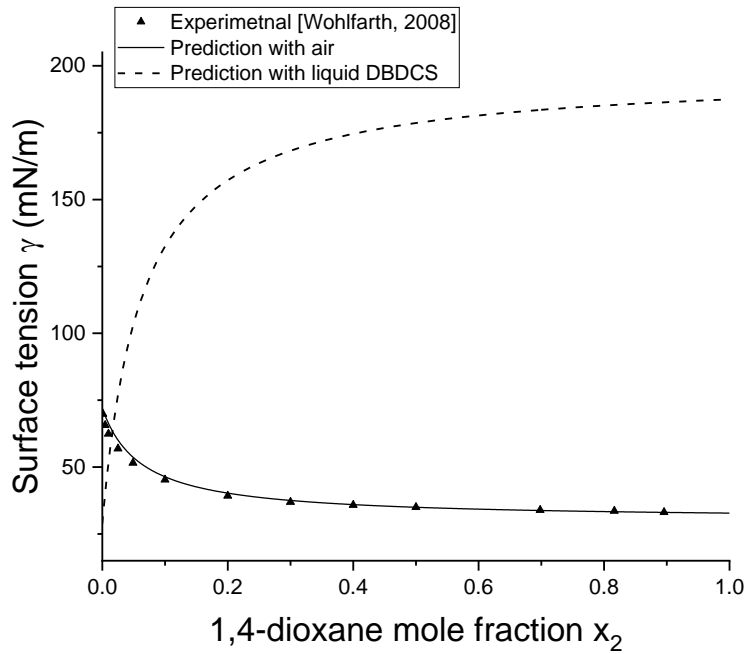


Figure 5.40. Surface tension of binary mixture of water (1)-1,4-dioxane (2). Equation (3.6) gives good estimation for the surface tension between water (1)-1,4-dioxane (2) mixture with air. We shall use this equation to predict the surface tension free energy with solid DBDCS.

Realizing that miscibility and interfacial tension reflect the same intermolecular forces, Dohahue and Bartell [Donahue, 1952] discovered that plotting the interfacial tension of liquid pairs *versus* the log of the sum the mutual solubilities yielded a linear relationship [Demand,

2002]:

$$\gamma_{ow} = a - b \ln(x_{wso} + x_{osw}) \quad (5.10)$$

with $a = -3.33$ and $b = 7.21$ [Lyman, 1982] for organic liquid-water systems at 20~25 °C , $S_{o(w)}$ and $S_{w(o)}$ the mutual amount fraction solubilities. The mutual amount fraction solubility of water and DBDCS was calculated in 3.6.1.2: $x_{3s1} = 8.14E - 12$ and $x_{1s3} = 0.01159$. Therefore, the surface tension between water and DBDCS can be estimated by equation (5.10): $\gamma_{13} = 28.8 \text{ mN/m}$. Hereby, γ_{23} and $\dot{\mu}$ remains unknown, but we can fit them from the data (Figure 5.41). The droplet size measured under various conditions is plotted in Figure 5.41 against ϕ_{1p} and r_o , and fitted with equation (5.9). $\gamma_{23} = 187 \text{ mN/m}$ and $\dot{\mu} = 64.7 \text{ mPa} \cdot \text{s}$. The liquid DBDCS is a very viscous liquid, and its surface tension with water is smaller than with 1,4-dioxane. The predicted surface tension between liquid DBDCS and water (1)-1,4-dioxane (2) by equation (3.6) is plotted in Figure 5.40. Figure 5.41 reveals the droplet size dependence on microfluidic input parameters. r_{drop} increases linearly with r_o . It increases with ρ_{3c} and Q_c . It decreases with the total flow rate. It increases slightly with ϕ_{1p} when ϕ_{1p} is smaller than 0.9 then more rapidly between 0.9~1.

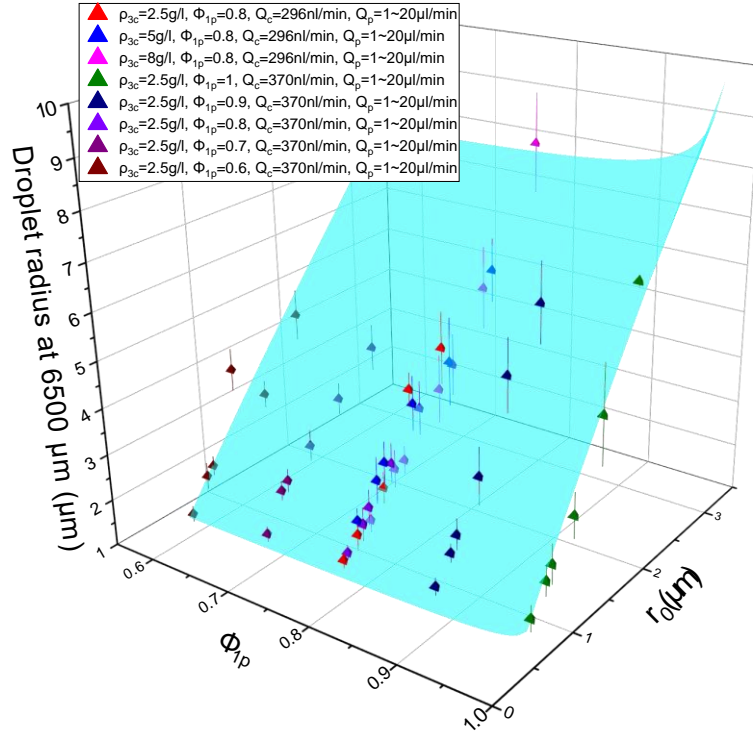


Figure 5.41. Droplets radius as a function of ϕ_p and r_0 .

$$r_o = R_{\text{channel}} \sqrt{1 - \sqrt{1 - \frac{\rho_{3c}}{\rho_{D3^*}} \frac{Q_c}{Q_c + Q_p}}}. \text{ Fitted with equation (5.9).}$$

With the fitting parameters from Figure 5.41 prediction of the droplets by equation (5.9) with is possible. The experimental values *versus* prediction is plotted in Figure 5.42. Since we are using the fitted parameters from the data to predict the same data, it is normal that the equation gives good prediction. It must be noticed that the fitting gives strange surface tension between the liquid DBDCS and 1,4-dioxane, since one can expect the surface tension is lower in the phase of higher solubility [Hajian, 2015].

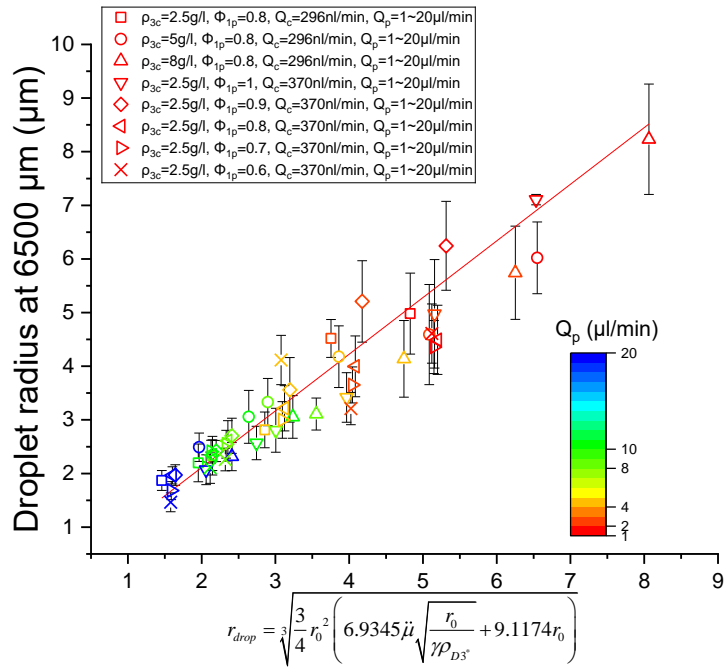


Figure 5.42. Droplet radius measurement vs prediction by Plateau-Rayleigh instability model.

Equation (5.7) use to describe the droplet size has been derived from the Plateau-Rayleigh instability model. But it applies also in the case where no liquid cylinder of DBDCS exists. In most antisolvent-solvent-solute systems, the liquid solute is highly unstable. It is thus difficult to measure the surface tension and viscosity. The asymptotic solutions of Plateau's equation for zero or infinitely large viscosities,

$$r_{\text{drop}} = \sqrt[3]{\frac{3}{2} \sqrt{2\pi} \cdot R_{\text{channel}} \sqrt{1 - \sqrt{1 - \frac{\rho_{3c}}{\rho_{D3^*}} \frac{Q_c}{Q_c + Q_p}}}},$$

is capable to give a good trend of the droplet dependence on central flow concentrate, central flow rate and the total flow rate. However, the anti-solvent fraction also influences the size, since the surface tension between the liquid solute and the antisolvent-solvent mixture depends on the solvents fraction. This term cannot be neglected unless the antisolvent-solvent have very similar properties, which is in contrary to the roles as "antisolvent" and "solvent". Therefore, it can only be applied in the case of a liquid tube breaks in an environment with a constant surface tension.

Chapter conclusion

Eight types of observation have been recorded by OM in the microfluidic device: i) no phase transition, only inter-diffusion of the central and peripheral flows; ii) a line of precipitation along the flow centre; iii) LLPS at the flow centre followed by droplet formation; iv) abnormally large droplets that were trapped in space or moving to the opposite direction of the flow; v) a column of nano-sized objects along the flow centre; vi) spontaneous crystallisation; vii) heterogeneous crystallisation on the wall; viii) blockage of the microfluidic channel by strong phase transitions.

Five zones have been defined in the case of LLPS: i) hydrodynamic expansion of the central jet; ii) solvents inter-diffusion; iii) anti-solvent focusing of the solute; iv) nano-droplet formation and droplet focusing (Marangoni effect); v) stable droplet formation.

A working phase diagram of spontaneous phase transitions of water (1)-1,4-dioxane (2)-DBDCS (3) in the coaxial mixer has been built on the overall composition of the mixture. The solubility curve measured in solution matches with the boundary of the soluble region. The non-crystalline (nano-objects and droplets) phase transitions are dominating the phase diagram.

The droplets were stable during its residence time of the microfluidic channel and crystallised after collection. This transient phase is highly concentrated (1 ± 0.5 amount fraction) DBDCS formed through LLPS caused by anti-solvent focusing. LLPS followed by droplet formation has been observed for other systems also, such as THF-water-(Calix-Cousulf- Cs^+_2), THF-water-(caesium acetate), THF-water-CsCl, water-THF-DBDCS, water-(THF20-1,4-dioxane80)-DBDCS. and water-acetone-DBDCS. For caesium acetate droplet emerged from THF-water mixer, the two-step crystallisation can be observed within the microfluidic channel.

We have noticed that d_p is linear with Q_c , not related with Q_p , by a slope related with ρ_{3c} and ϕ_{1p} . From that, we have proposed semi-theoretical relations (equation (5.3) and equation (5.4)) to predict $\overline{\mathbf{v}_r^F}$ and d_p in the case of spontaneous non-crystalline phase

transitions. Therefore, the droplet formation position can be predicted (equation (5.5)). The prediction of d_p and $\overline{v_r^F}$ of the non-crystalline phase transition (LLPS and fast precipitation of nano-objects) matched the experimental values excellently.

Equation (5.4) also predicts the limit between the fast LLPS region and the slow crystallisation region in the phase diagram. When $\ln \frac{\rho_{3c}}{568\text{g/l}} + 17.4\phi_{1p} > 0$, DBDCS is pushed towards the flow centre by the chemical potential gradient, the concentration reaches the binodal LLPS limit, droplets are formed. When $\ln \frac{\rho_{3c}}{568\text{g/l}} + 17.4\phi_{1p} \approx 0$, DBDCS molecules are kept in a column near the centre of the flow, nano-particles are formed in the column. When $\ln \frac{\rho_{3c}}{568\text{g/l}} + 17.4\phi_{1p} < 0$, depending on the over saturation ratio it will be either a slow nucleation and growth from a nearly homogeneous solution or soluble. The predicted chemical potential focusing limit of DBDCS is plotted in Figure 5.30 (red line).

In these equations, f , ρ_{3c} , and ϕ_{1p} are control parameters of the coaxial mixer. Three adjustable parameters are intrinsic to the physical chemistry of the antisolvent-solvent-solute system: the chemical affinity of the transfer of DBDCS from 1,4-dioxane to water $\ln \frac{\rho_{3s2}}{\rho_{3s1}}$ (section 3.5.2), the LLPS threshold ρ_{3b2} (section 3.6.1) and the mobility $\eta = \frac{1}{6\pi r_3^* \dot{\mu}}$ of DBDCS monomers in water (1)-1,4-dioxane (2) mixture (section 3.5.2). By a systematic measurement of $\overline{v_r^F}$ or d_p in a coaxial microfluidic mixer, the chemical affinity of the solute for the solvent compared to the antisolvent, the LLPS threshold and the diffusion coefficient can be deduced. These equations can be applied to and are the fundamental of other diffusional antisolvent precipitation systems.

The total volume fraction of the droplets in the flow is linearly proportional to the overall concentration of DBDCS. This is the lever rule for the two-phase region, of a pure solute

and a mixture of solvents, in ternary phase diagrams. The dependence of the droplet size r_{drop} on the microfluidic parameters has also been studied. r_{drop} increases with the concentration of the solute, the flow ratio, and the fraction of the antisolvent. We use a recent numerical solution of the Plateau-Rayleigh instability model to estimate this dependence (equation (5.9)), despite it is not breaking of a liquid cylinder into droplets. To use this equation, the surface tension between the pure liquid solute and the mixture of solvents must be given.

With a strong anti-solvent gradient in a slow flow, small droplets were trapped in space or moving to the opposite direction than the flow. Thus, abnormally large droplets emerged from the merging of the backwards flowing droplets. Crystallisation of the transient liquid state of DBDCS can be observed in the trapped abnormally large droplets, confined in a highly agitated small volume (4 pl) and without contact with a solid container. The trapped droplets could be release, firstly, when the size is big enough for the hydrodynamic drag to overcome the trap, secondly, if the trapped droplet crystallises. Droplet trap exists with i). a high ρ_{3c} ; ii) a high ϕ_p ; iii) a low flow rate.

Chapter 6. Phase diagram of water (1)-1,4-dioxane

(2)-DBDCS (3) system in the coaxial microfluidic

mixer. Part II: spontaneous crystallisation

6.1. Spontaneous crystallisation from a homogeneous microflow	207
6.2. Crystal habits of DBDCS	208
6.2.1. Spontaneous crystals in the flow.....	208
6.2.2. <i>Post-mortem</i> observation	211
6.2.3. Heterogeneous crystallisation on the wall of the microfluidic channel	212
6.3. FLIM map of spontaneous crystallisation of DBDCS in microflow.....	214
6.4. Counting and identifying flowing fluorescent particles with the fastest FLIM video	224
6.5. Measuring DBDCS crystal size by FLIM	227
6.6. The birth rate and growth rate of spontaneous DBDCS crystals in the microflow of water (1)-1,4-dioxane (2) mixture.....	230
6.6.1. <i>Comsol</i> simulation of the environment	230
6.6.2. Definition of the variables	231
6.6.3. By FLIM.....	233
6.6.4. By OM.....	237
6.7. Summary of all the spontaneous phase transition types observed in the coaxial microfluidic system.....	242
Chapter conclusion.....	244

This chapter will focus on spontaneous crystallisation. Section 6.1 quickly introduces the overall image of the spontaneous crystallisation of DBDCS in a nearly homogeneous flow of water (1)-1,4-dioxane (2). The special crystal habits of DBDCS in the microflow is illustrated in section 6.2. In section 6.3, we show the process to build a FLIM map along the flow and the extraction of the fluorescence decay and lifetime of different species and their contributions at different regions along the FLIM map by principal component analysis. Section 6.4 explains a second analysis of the same FLIM files to extract the fastest FLIM video of flowing objects and to count and identified these fluorescent crystals using their fluorescence intensity and lifetime signals. Section 6.5 demonstrates that the fluorescence intensity of the fluorescent crystals is also a measure of their size. Section 6.6 shows the size distribution, polymorphism distribution, the nucleation event interval, and the crystal birth rate B_x measured by FLIM and OM along the flow and correlates the results with *Comsol* simulation. Finally, all the spontaneous phase transition phenomenon observed during the parametric sweep of water (1)-1,4-dioxane (2)-DBDCS (3) in the coaxial mixer is summarised, and then presented again on the phase diagram with the solubility curve and antisolvent focusing limit, in section 6.7. The report of the *in situ* SAXS of water-(THF20-1,4-dioxane80)-DBDCS in the coaxial mixer is attached in Appendix F.

6.1. Spontaneous crystallisation from a homogeneous microflow

For the yellow points in the upright corner of the phase diagram (Figure 5.4), spontaneous crystallisation of DBDCS along the microflow was observed after the inter-diffusion of the coaxial flows. This is because, for crystallisation, which is a relatively slow process, a high supersaturation must be achieved but lower than that of the binodal LLPS. Two conditions were necessary: a high DBDCS concentration ρ_{3mix} and a low water fraction in the peripheral flow ϕ_{1p} .

Figure 6.1 shows that, under such conditions, spontaneous crystallisation occurred around 3 mm away from the nozzle at the flow centre and the spontaneous crystals shaped like

butterflies grew along the flow.

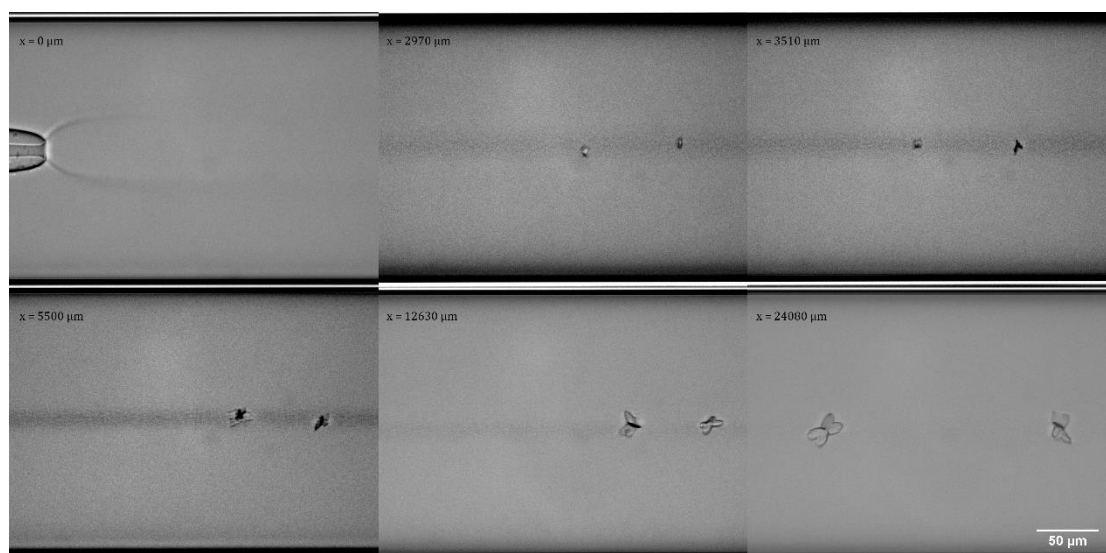


Figure 6.1. Spontaneous crystallisation of DBDCS from water-1,4- dioxane mixture in the coaxial microfluidic mixer. Microfluidic parameters:

$$\rho_{3c} = 16 \text{ g/l}, Q_c = 148 \text{ nl/min}, \phi_p = 30\%, Q_p = 1 \mu\text{l/min}.$$

6.2. Crystal habits of DBDCS

6.2.1. Spontaneous crystals in the flow

Several crystal habits of DBDCS has been observed. Figure 6.2 shows the crystal habit of DBDCS in water (1)-1,4-dioxane (2) mixture: Figure 6.2.A shows crystals shaped like butterflies with four wings in the same plane or more wings in different planes; Figure 6.2B shows more complex crystal habit looked like stack of butterflies.

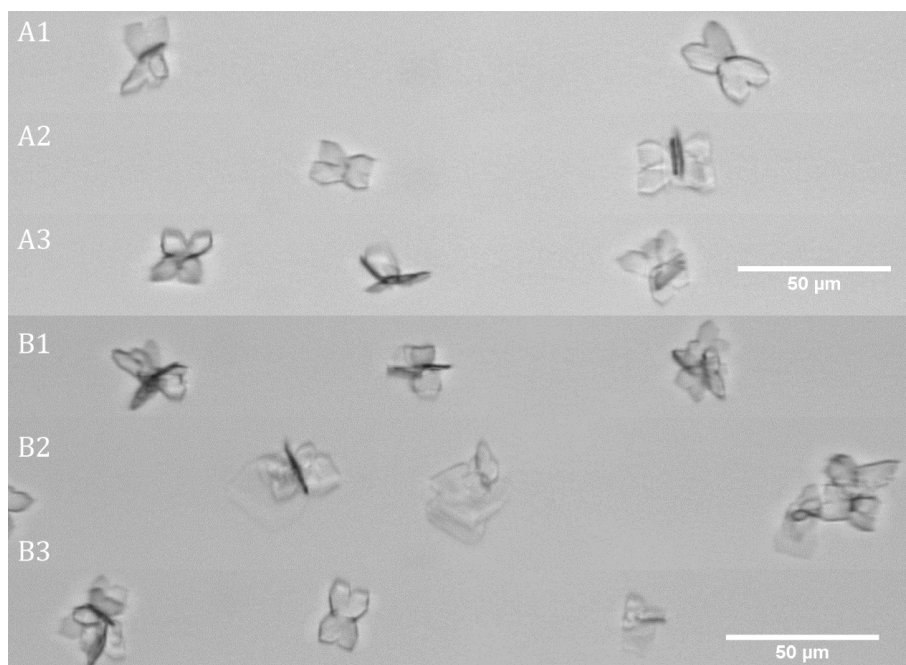


Figure 6.2. Crystal habit of DBDCS spontaneous crystallisation from water (1)-1,4-dioxane (2) in the coaxial mixer: A: butterfly shaped crystals, Microfluidic parameters $\rho_{3c} = 16 \text{ g/l}$, $Q_c = 148 \text{ nl/min}$, $\phi_{1p} = 30\%$, $Q_p = 2 \mu\text{l/min}$; B: multilayer stack of butterfly shaped crystals,

$$\rho_{3c} = 16 \text{ g/l}, Q_c = 148 \text{ nl/min}, \phi_{1p} = 30\%, Q_p = 1 \mu\text{l/min} .$$

Figure 6.3.A shows the rhombus crystal habit observed in water-(THF20-dioxane80)-DBDCS system. Figure 6.3.B shows that a change in nature of the solvent led to a change in the crystal habit. The single crystals were rhombus shaped and the twin crystals consisted of elongated wings, shaped like stars. This could be due to the change in the surface tension between the crystal and the liquid.

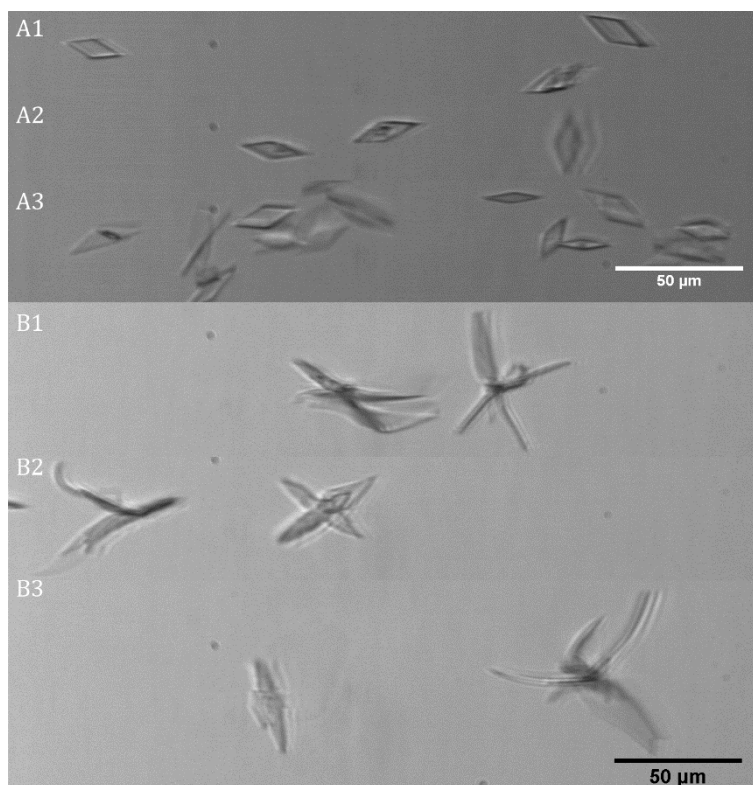


Figure 6.3. Crystal habit of DBDCS spontaneous crystallisation from water-(THF20-1,4-dioxane80) in the coaxial mixer. A: single layer of rhombus habit of DBDCS

crystals in the microflow. Microfluidic parameters:

$\rho_{3c} = 10 \text{ g/l}, Q_c = 185 \text{ nl/min}, \phi_{tp} = 30\%, Q_p = 1 \mu\text{l/min}$; *B: 3D multilayer of rhombus*

habit of DBDCS crystals in the microflow. Microfluidic parameters:

$\rho_{3c} = 10 \text{ g/l}, Q_c = 74 \text{ nl/min}, \phi_{tp} = 30\%, Q_p = 0.5 \mu\text{l/min}$.

The “butterfly” non-classical crystallographic habit could be explained with the formation of twinned crystals (Figure 6.4). Two rhombus crystals (the habit observes with a fraction of THF), grow sharing a twin mirror. This specie could also grow sharing a second twin mirror. Figure 6.4 is a simple representation in 2D, it could be therefore difficult to “see” the organisation in the space. However, the use of a real model and the observation in different directions of the constructed object was in good agreement with the OM of the “butterfly” crystals (Figure 6.2 and Figure 6.3). To observe the birth of the twin, Figure 6.4.D is a zoom of Figure 5.17.B. It is clear that the growth of the crystal, even in the confined volume of the

abnormal droplet is of a twin manner.

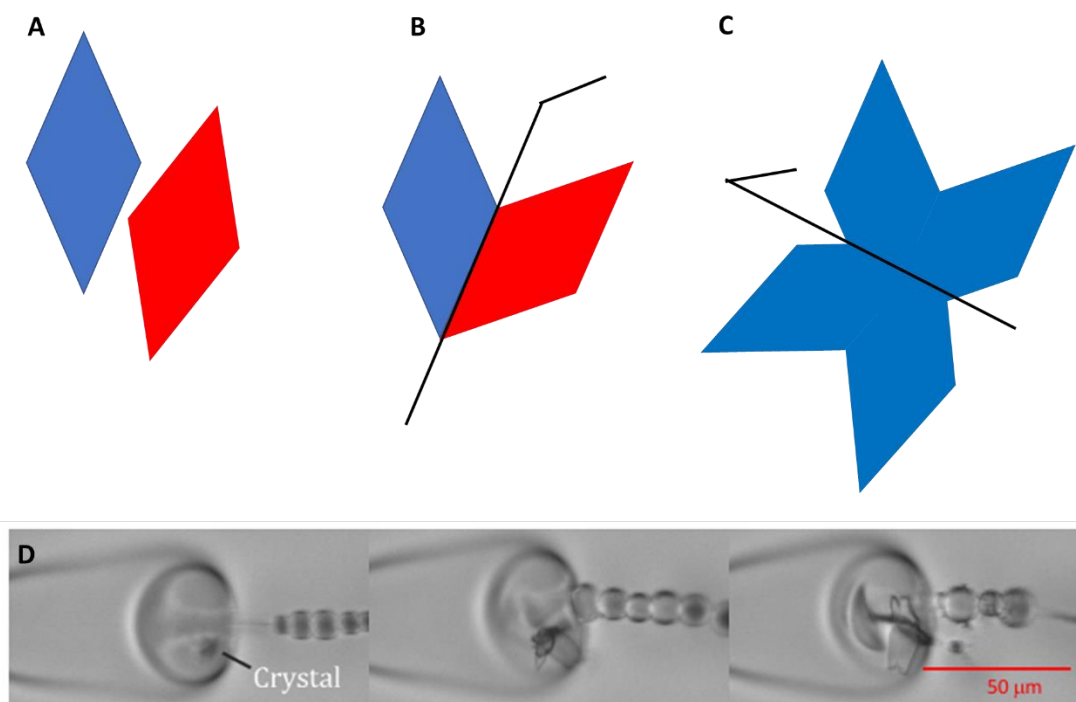


Figure 6.4. Schematic formation mechanism of the “butterfly” twin crystal habit of DBDCS in the microflow. A: two single crystals of DBDCS in rhombus habit. B: first twin law, a mirror. The two crystals share the same face. C: second twin law, is used to modelised the butterfly. D: zoom of the first three images of Figure 5.17.B. Second image after 1291 ms and third image after 410 ms.

6.2.2. Post-mortem observation

The spontaneous crystals of DBDCS were collected on glass slides at the end of the microfluidic tube and observed with OM during the drying process of the solvents, as shown in Figure 6.5. We were never able to observe the three-dimensional butterflies on the collected samples, but only plate-like crystals of DBDCS. The average size of the collected crystals was not significantly different from those observed in the flow 20 mm from the injection nozzle. This means the growth process had finished before the end of the tube.

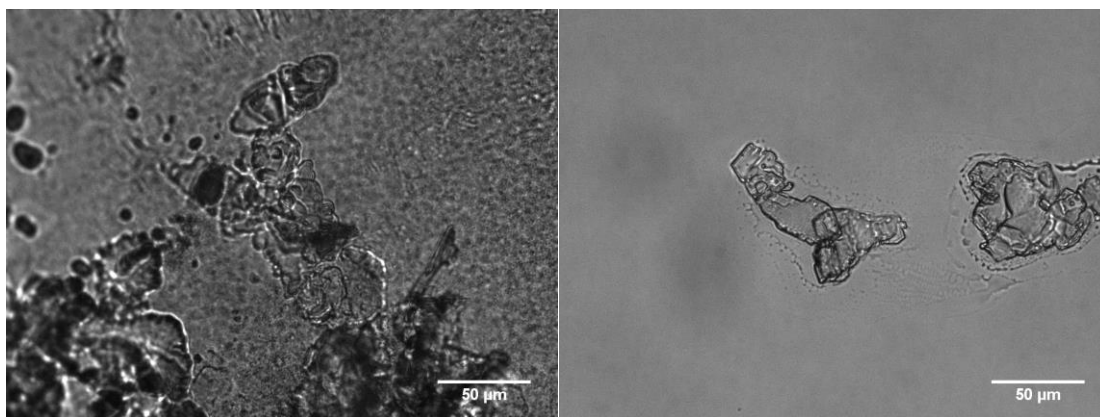


Figure 6.5. Drying process of the DBDCS butterfly crystals collected at the end of the microfluidic channel. Left: crystals suspended in liquid, surrounded by nanoparticles. Right: the liquid had evaporated, leaving only the crystals. The 3D shape of butterfly became 2D plates.

Observation one week after collection showed that countless small crystals filled the “empty” space between the spontaneous “butterfly” crystals formed in the microfluidic system and observed as 2D plate-like. This is shown in Figure 6.6

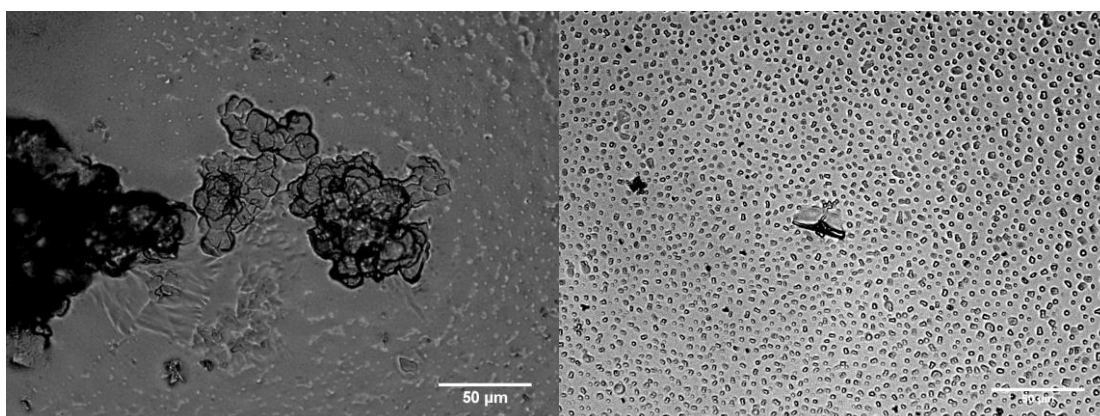


Figure 6.6. Small crystals grow appeared at the “empty” space.

6.2.3. Heterogeneous crystallisation on the wall of the microfluidic channel

Without a high ϕ_{lp} (below the red line of the antisolvent focusing limit in the phase diagram, see Figure 5.30), no strong chemical potential driven focusing of the solute was observed by FLIM. Therefore, the whole volume of the microfluidic channel was permeated by

DBDCS molecules after d_w (equation (5.2)). After this position, DBDCS molecules were in contact with the wall of the microfluidic channel, in addition, the hydrodynamic velocity in the boundary layer is close to zero. Heterogeneous nucleation was favoured in the boundary layer of the microflow. Crystals appeared on the wall of the microfluidic channel sometime during the experiment, even with the surface treatment by perfluorooctyltriethoxysilane (POTS). The heterogeneous crystals on the wall kept growing so long as the experiment continued. Since its appearance, it would immediately, as a background, disturb the FLIM measurement of the flowing objects. After a long time of non-stopping experiment, the heterogeneous crystals grew into excessively large size and started to stack on and even to release from the wall. By that point, the experiment had to stop for a washing procedure (see section 2.1.2). Figure 6.7 shows some examples of different heterogeneous crystal habits of DBDCS on the microfluidic channel wall. It is very interesting that both twinned and untwinned crystals can be produced by heterogeneous nucleation. That is understandable because the wall surface could prevent the possibility of growth through the mirror twin law. At least Figure 6.7 gives the best beautiful images of DBDCS rhombus habit. In fact, these bigger crystals present a 2D distorted hexagonal habit (ratio of the longest side over the shortest = 2.7).

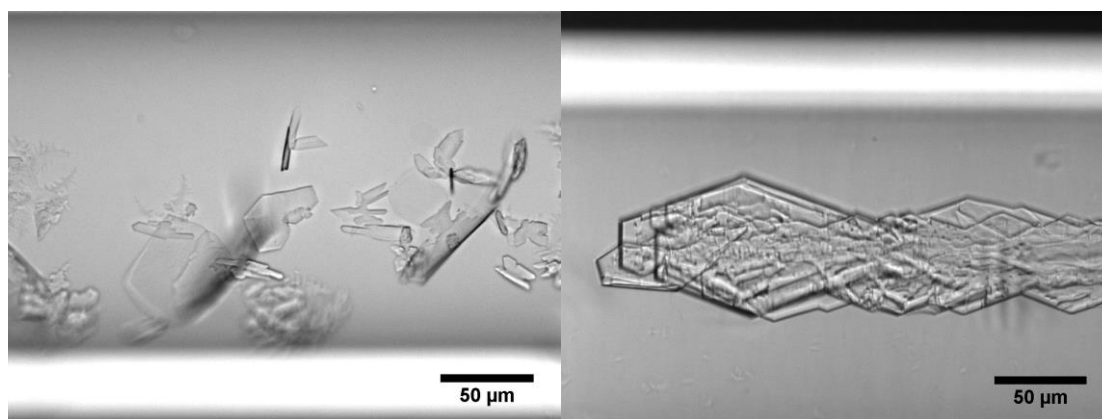


Figure 6.7. Heterogeneous DBDCS crystals on the microfluidic channel wall. Left: obtained from water (1)-1,4-dioxane (2) mixture. Right: obtained from water-

(THF20-dioxane80) mixture.

6.3. FLIM map of spontaneous crystallisation of DBDCS in microflow

OM observation of the DBDCS crystal habit can only provide information on the shape and size. In the case of polymorphs for which the crystal habit is different, OM would be sufficient for polymorphism characterisation (see for example the case of carbamazepine [Ikni, 2014]). For most of the compounds, there is no concrete link between polymorphism and crystal habit, there other methods are needed. Being an AIE molecule, DBDCS' fluorescence lifetime depends on the organisation of molecules in the crystal (see section 1.4.5.4). Our microfluidic device can be coupled with a UV excitation laser, and the fluorescence signal sent to a time- and space- correlated single photon counting detector (see section 2.2). This is the FLIM detector, which can detect DBDCS molecules (see Figure 5.3), its crystal polymorphs (Figure 6.8) and phase transitions. It must be noticed that the crystals with longest lifetime (blues colour on figure 6.8.B) have a rhombus habit. In the next chapter we will need to attribute the different phases observed to the different polymorphs via their lifetimes. Therefore, each crystal will be named with reference to the figures.

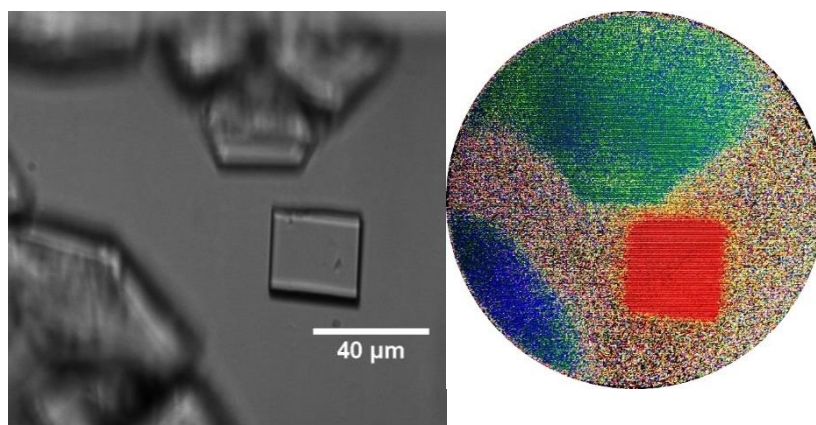


Figure 6.8. FLIM image of three crystals grown on the wall from a flow of water-(THF20dioxane80)-DBDCS mixture. Left: OM image. Right: fluorescence lifetime image. The colour represents fluorescence lifetime: crystal_6.8_THF_red = 4 ns;

crystal_6.8_THF_green = 11 ns; crystal_6.8_THF_blue = 23 ns

DBDCS was chosen in this work to study the aggregation process, because, as an AIE molecule, its crystalline state is fluorescent but not the molecule in solution. Yet, on Figure 6.9.A, the crude FLIM image of a phase transition process in the flow shows a low contrast between the crystals in the flow centre and the molecules in the environment. On the fluorescent intensity signal (red in Figure 6.9.B), small peaks stick over a high background. Only the strong fluctuation of the fluorescence lifetime signal (blue in Figure 6.9.B) suggests the passing of long-lived objects passing through a short-lived environment. This can be explained by a high concentration regime (Figure 6.9.C). The molecules in the flow were absorbing most of the excitation light and few photons reach the crystals. Based on the beer Lambert law, only 1% of the excitation light reaches the centre of the capillary. Even if the fluorescence yield of DBDCS in solution had been low, it absorbed most of the excitation power and the molecule signal dominated. Therefore, the presence of flowing crystals is seen on the intensity trace as small spikes over a high constant background. The presence of the crystal is better seen in the spikes of the lifetime trace.

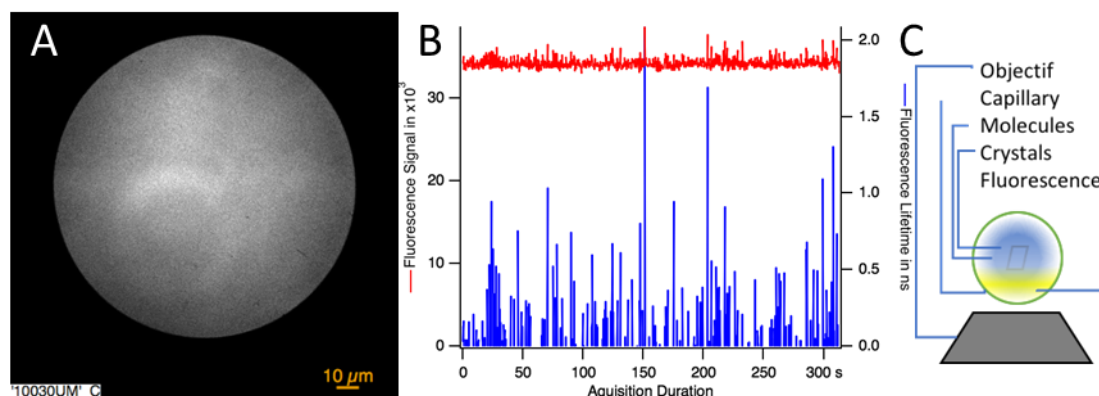


Figure 6.9. Fluorescence intensity and lifetime treatment of DBDCS spontaneous crystals in the microflow of water (1)-1,4-dioxane (2). A: the fluorescence intensity image of spontaneous crystals flowing along the microflow centre integrated over 320 s. B: on the fluorescence signal (red), small peaks are guessed over a high background. Only the strong fluctuation of the lifetime signal trace (blue) suggests

that long-lived object might be passing through a short-lived background. C:
Schematic illustration of the FLIM detection of the spontaneous crystals in the flow.
The crystals are flowing along the flow centre as bright objects in a non-fluorescent
background. But the high concentration of molecules has absorbed most of the
excitation beam. Microfluidic parameters:

$\rho_{3c} = 16 \text{ g/l}, Q_c = 148 \text{ nl/min}, \phi_{lp} = 30\%, Q_p = 1 \mu\text{l/min}$. *FLIM laser parameter:*

$$\tau = 400\text{fs}, \lambda = 343\text{nm}, f_{\text{rep}} = 10\text{MHz}.$$

We have nevertheless succeeded extracting the signal coming from the crystal using two characteristics of the crystal fluorescence confirmed by OM: crystals were in the flow centre and appeared as separated objects in the time scale (see Figure 6.1).

Figure 6.10 is the collection of fluorescence decays measured along the microflow of water (1)-1,4-dioxane (2)-DBDCS (3) mixture with spontaneous crystals flowing in the centre. As the distance to the nozzle increases from 0 μm to 24750 μm , the rise of a population with a long fluorescence lifetime is seen. Lifetime decays are different depending of the position along the device. That means that DBDCS is not anymore under a monomer. These decays are produced by mixtures of DBDCS in different organisations. We shall perform a PCA analysis to count them and to attribute decays to these different states (species) of DBDCS. In some cases, the direct reading of the lifetime from the decays can be done. The peak at 0 ns is the fluorescence of the molecules. The intensity collected at zero delay is a measure of the concentration. This recording shows that molecules are always present in a large excess. From 10030 μm on, the contribution from a long component became more apparent, so that the fluorescence lifetime can be extracted directly: a component with a long lifetime of 23 ns (named as `crystal_6.10_15090-24750_cd_1 = 23 ns`). The species related with the long component in the decays must be DBDCS crystals.

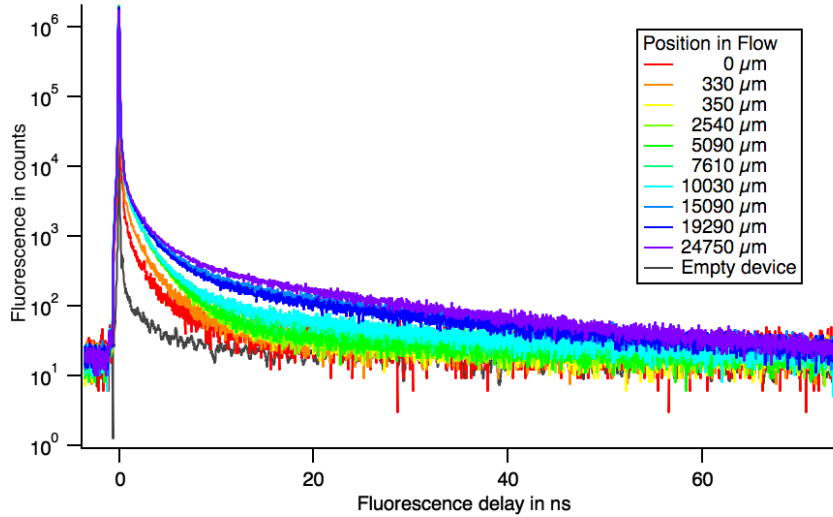


Figure 6.10. A collection of fluorescence decays collected at different position along the spontaneous crystallisation in the flow of water (1)-1,4-dioxane (2)-DBDCS (3). The peak at zero delay can be attributed to the molecules in solution. The long 23 ns component ($crystal_6.10_15090-24750_cd_1 = 23\text{ ns}$) rises with distance, which must be the crystals. It is named as $crystal_6.10_15090-24750_cd_1 = 23\text{ ns}$. Microfluidic parameters: $\rho_{3c} = 16\text{ g/l}$, $Q_c = 148\text{ nl/min}$, $\phi_{lp} = 30\%$, $Q_p = 1\mu\text{l/min}$. FLIM laser parameter: $\tau = 400\text{ fs}$, $\lambda = 343\text{ nm}$, $f_{rep} = 10\text{ MHz}$.

Figure 6.11 is a FLIM map of the spontaneous crystallisation of the same experiment than Figure 6.1 of DBDCS spontaneous crystallisation from a mixture of water (1)-1,4-dioxane (2) in the coaxial microflow. On each FLIM image, the colour of a pixel codes for its average fluorescence time and the brightness scales for its fluorescence intensity. At 0 μm from the injection nozzle, the hydrodynamic expansion of the central jet of 1,4-dioxane and DBDCS is seen from the fluorescence of DBDCS molecules (red). The hydrodynamic expansion finished after 350 μm . After that, the expansion of the fluorescent area was due to the diffusion of DBDCS molecules. At 1350 μm , DBDCS had diffused over the 100 μm of the field of view. At 5090 μm , a faint blue ribbon appeared at the centre of the flow. Nucleation had occurred, and growth was occurring. The density of the blue colour deepened on the following images since the volume of the crystal phase was increasing. The nucleation occurred in a tube 20 μm

in diameter, where the DBDCS concentration is the highest and not at the periphery of the flow where the water fraction is the highest, in agreement with the supersaturation profile calculated with *Comsol* (Figure 6.12). The change in the colour between position 0 μm and 2540 μm , may be due to a change in the aggregation state of the molecules even if fast OM imaging does not show flowing nanoparticles.

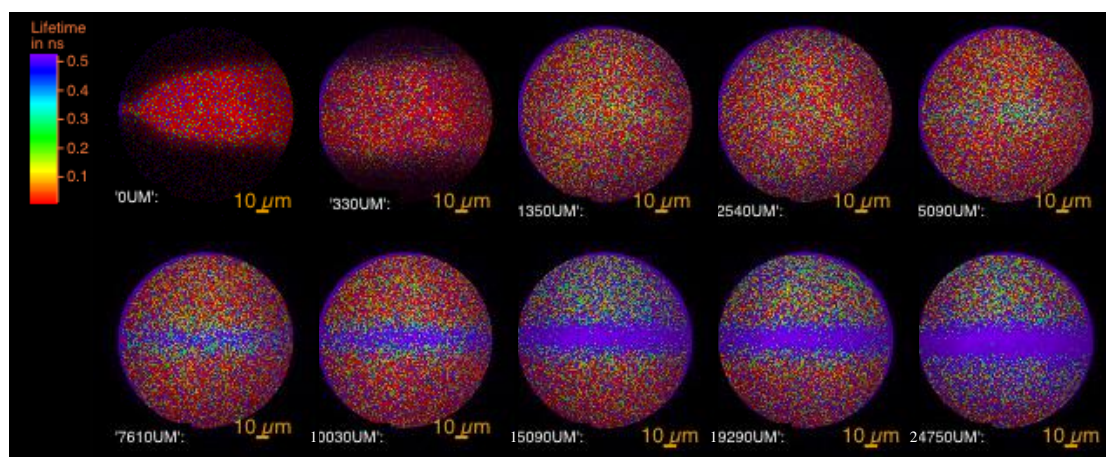


Figure 6.11. The fluorescence lifetime images collected along the spontaneous crystallisation in the microflow of water (1)-1,4-dioxane (2)-DBDCS (3) mixture with spontaneous crystals flowing in the centre. From the nozzle to 1350 μm away, the flow of DBDCS molecules expanded (red) with the central jet. From 5090 μm to the end, the formation of crystals in the centre of the flow is shown by the appearance of a long-lived area. The average lifetime increases as the amount of the crystalline phase increases. Microfluidic parameters:

$$\rho_{3c} = 16 \text{ g/l}, Q_c = 148 \text{ nl/min}, \phi_p = 30\%, Q_p = 1 \mu\text{l/min} . \text{ FLIM laser parameter:}$$

$$\tau = 400\text{fs}, \lambda = 343\text{nm}, f_{\text{rep}} = 10\text{MHz}.$$

Figure 6.12 illustrates the *Comsol* simulation of spontaneous crystallisation conditions in Figure 6.11. It shows that DBDCS molecules were not strongly pushed towards the flow centre, but slowly diffusing away, because the water fraction and gradient was small. The supersaturation ratio β had only reached over 5, which led to a slow crystallisation process.

The highest supersaturated region is within 20 μm in diameter in the flow centre, and between 1 and 3 mm away from the nozzle. The position of the FLIM measurements are marked as black triangles at the bottom, and the dimension of the FLIM observation window and region of interest (ROI).

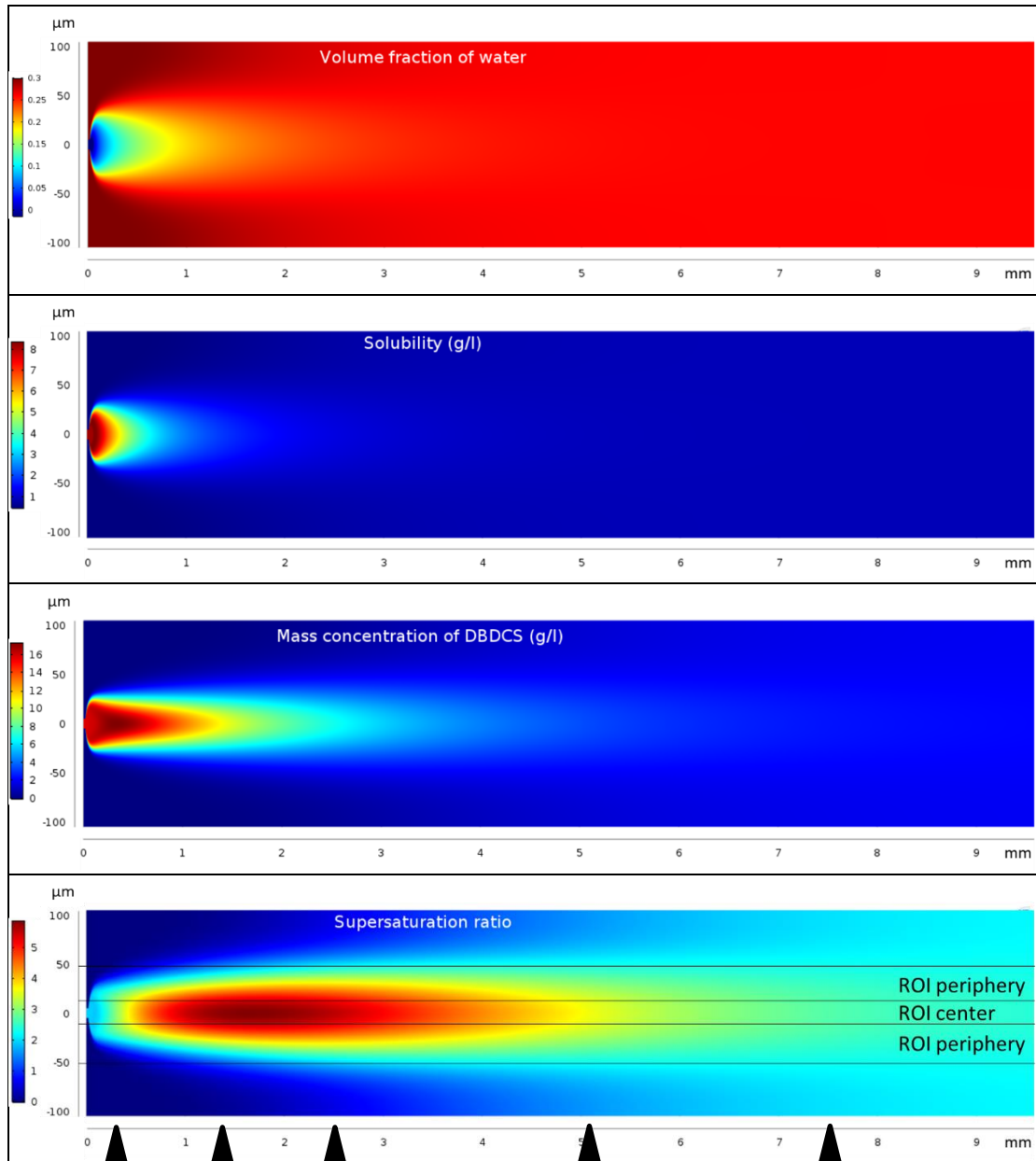


Figure 6.12. Comsol simulation of the volume fraction of water, the solubility, the mass concentration, and supersaturation of DBDCS in the microflow of water (1)-1,4-dioxane (2). The position where the FLIM images presented in Figure 6.11 were recorded is indicated with a black triangle. The ROI of the FLIM analysis is shown as

black lines on the simulation of supersaturation. ROI flow centre plus two ROI periphery gives the diameter of the field of view of the FLIM measurement. the Microfluidic parameters: $\rho_{3c} = 16 \text{ g/l}$, $Q_c = 148 \text{ nl/min}$, $\phi_{1p} = 30\%$, $Q_p = 1 \mu\text{l/min}$.

Based on the FLIM map, we have identified two ROI on the FLIM map corresponding to the presence of different species: flow centre for crystals and flow periphery for molecules (the ROI are schematically illustrated on Figure 6.12). To identify the species, the decays from the two ROIs are collected in Figure 6.13 and analysed on Figure 6.14 using principal component analysis (PCA). Figure 6.13.A confirms that there is a rise of a population mainly with 23 ns lifetime. Figure 6.13.B also illustrates an increase in the fluorescence lifetime in the ROI periphery, even without crystals.

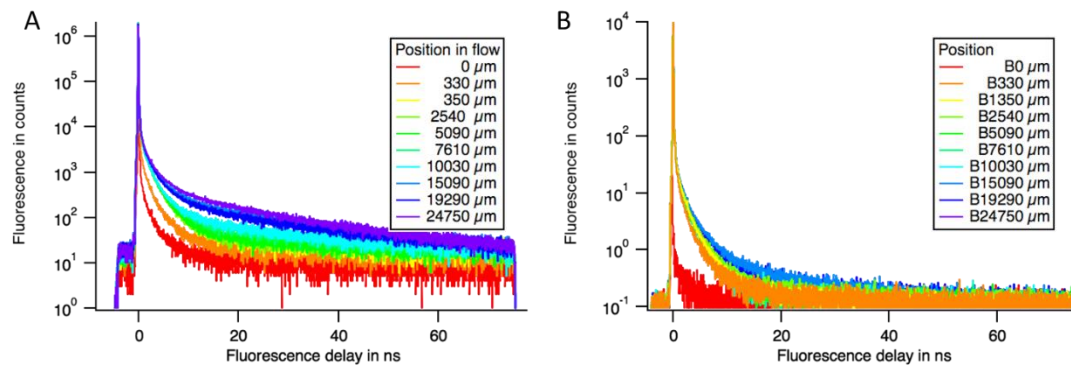


Figure 6.13. The decays collected from different areas on the FLIM map along the spontaneous crystallisation in the flow of water (1)-1,4-dioxane (2)-DBDCS (3). A: from the centre of the flow (see ROI centre in Figure 6.12); B: on the periphery of the flow (see ROI periphery Figure 6.12). They confirm the rise of a population with a 23 ns lifetime (center_6.13_molecule_cd_1 = 23 ns) in the centre and the lengthening of the molecular decay in the water (1)-1,4-dioxane (2) domain. Microfluidic parameters: $\rho_{3c} = 16 \text{ g/l}$, $Q_c = 148 \text{ nl/min}$, $\phi_{1p} = 30\%$, $Q_p = 1 \mu\text{l/min}$. FLIM laser

parameter: $\tau = 400\text{fs}$, $\lambda = 343\text{nm}$, $f_{\text{rep}} = 10\text{MHz}$.

In Figure 6.14, the PCA shows that more than 99,99% of this data set can be describe

by the mean of 4 orthogonal components. We can assume that the contribution of the rest the components describes the noise. We have constructed the four principal decays required to describe the data in the following way:

(i) “Microscope”: the fluorescence of the microscope and dark current of our detector that was measured in the dark area of the 0 μm image.

(ii) “Molecule”: the fluorescence that was measured in the bright area of the 0 μm image. The removal of the detector dark noise from the “Molecule” decay revealed an exponential decay with a lifetime of 1.4 ns ($\text{crystal_6.14_molecule_cd_1} = 1,4$ ns).

(iii) “Oligo”: the decay that was collected from the ROI periphery of the 15090 μm image where it was supersaturated but without crystals. The removal of the detector dark noise “Microscope” from “Oligo” decay revealed an exponential decay with a lifetime of 2 ns ($\text{crystal_6.14_oligo_cd_1} = 2$ ns). The change of lifetime between “Molecule” and “Oligo” might be due to aggregation of monomers, or the change in the environment from pure 1,4-dioxane to a mixture of water (1)-1,4-dioxane (2).

(iv) “CPFlucluant”: the decay that comes with the crystals. CPFlucluant has a long component with a lifetime of 23 ± 2 ns ($\text{crystal_6.14_CPFlucluant_comp_2_cd_1} = 23 \pm 2$ ns) and a short component of 4 ± 2 ns ($\text{crystal_6.14_CPFlucluant_comp_1_cd_1} = 4 \pm 2$ ns).

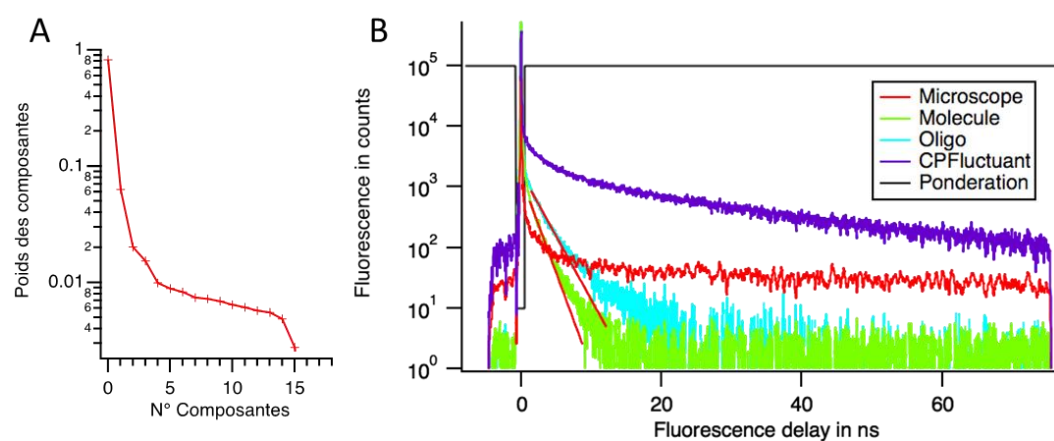


Figure 6.14. The PCA of the fluorescence decays collected on the FLIM map. A: 4

components are required to describe the decay curve space, contributing 80%, 7%, 2%, and 1.5% of the data, respectively. B: construction of the 4 principal component

decays and the noise. Microfluidic parameters:

$$\rho_{3c} = 16 \text{ g/l}, Q_c = 148 \text{ nl/min}, \phi_{lp} = 30\%, Q_p = 1 \mu\text{l/min} . \text{ FLIM laser parameter:}$$

$$\tau = 400\text{fs}, \lambda = 343\text{nm}, f_{\text{rep}} = 10\text{MHz} .$$

Figure 6.15 shows that the contribution of CPFluctuant describes completely and selectively the rise in intensity when a crystal was flow through. The contribution of the other components was constant. That means that each purple peak corresponds to a crystal passing in front of the detector.

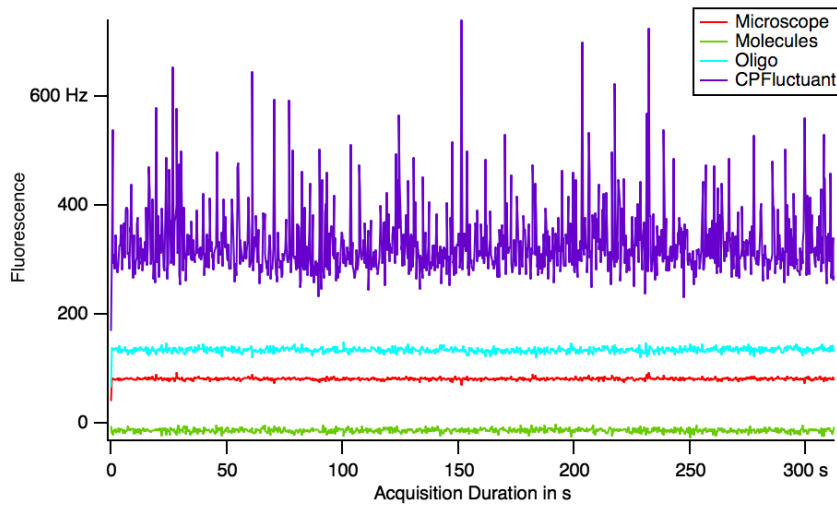


Figure 6.15. Contribution from the principal components to the fluorescence intensity in the time trace. Only the contribution of CPFluctuant (purple) fluctuated. Thus, all the photons emitted by the crystals were described by CPFluctuant. The other components are produced by the PCA analysis. Only one is positive and is close to the

decay of the microscope. Microfluidic parameters:

$$\rho_{3c} = 16 \text{ g/l}, Q_c = 148 \text{ nl/min}, \phi_{lp} = 30\%, Q_p = 1 \mu\text{l/min} . \text{ FLIM laser parameter:}$$

$$\tau = 400\text{fs}, \lambda = 343\text{nm}, f_{\text{rep}} = 10\text{MHz}.$$

From these attributions, we can check some properties of the system. The contribution from the “Oligo” DBDCS and the crystals to the fluorescence intensity in the two regions of interests along the microflow are plotted in Figure 6.16. The contribution of the crystal in the central flow increases along the flow. Whereas the contribution of “Oligo” is high and constant in the ROI of periphery. The Oligo contribution remains significant even far from the nozzle. That means that, even though an oligomer could be consider as a precursor, not every precursor gives a nucleus.

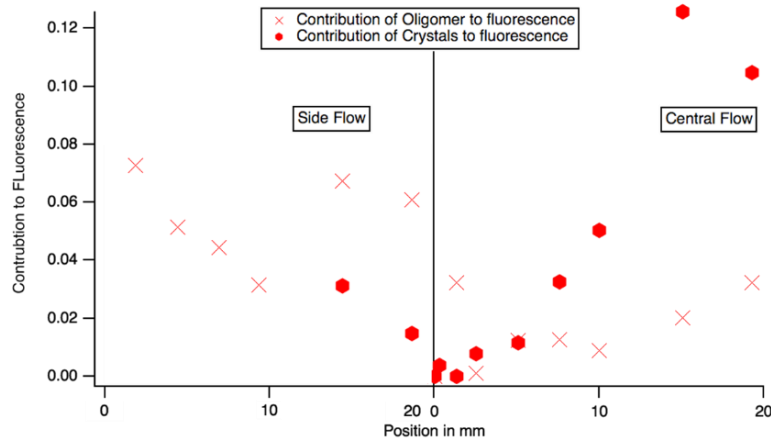


Figure 6.16. Contribution from the “Oligo” DBDCS and the crystals to the fluorescence intensity in the two regions of interests along the microflow. Left: in the ROI of periphery; Right: in the ROI of flow centre. Contribution of “CPFluctuant” in the flow centre increases with the residence time in the device with few crystals in the flow periphery. Microfluidic parameters:

$$\rho_{3c} = 16\text{g/l}, Q_c = 148\text{nl/min}, \phi_{lp} = 30\%, Q_p = 1\mu\text{l/min}.$$

$$\tau = 400\text{fs}, \lambda = 343\text{nm}, f_{\text{rep}} = 10\text{MHz}.$$

The residual of the description of all the fluorescence decays collected in the FLIM map of spontaneous crystallisation by the four principal components are plotted in Figure 6.17. The sign and the amplitude of the residual is random everywhere except in the -718~504 ps

range, which is mostly the fluctuations of our instrument response function. This means that we have a good description of the data by the four proposed components.

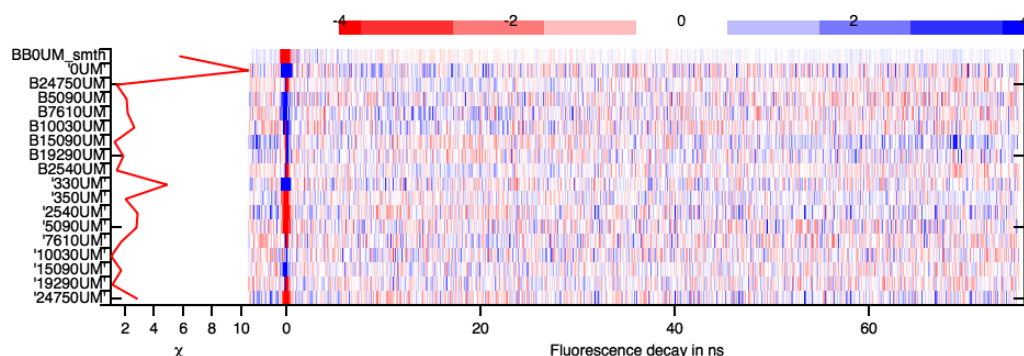


Figure 6.17. The residuals of the data described by the four components: Microscope, Molecule, “Oligo” and “CPFluctant”. These residuals are weighted by their expected amplitude based on a Poisson distribution of the counted photons. The random sign and the amplitude of the residuals everywhere except in the -718 ps and 504ps range show that we have a good description of the data. Microfluidic parameters: $\rho_{3c} = 16 \text{ g/l}$, $Q_c = 148 \text{ nl/min}$, $\phi_{lp} = 30\%$, $Q_p = 1 \mu\text{l/min}$. FLIM laser parameter: $\tau = 400\text{fs}$, $\lambda = 343\text{nm}$, $f_{\text{rep}} = 10\text{MHz}$.

6.4. Counting and identifying flowing fluorescent particles with the fastest FLIM video

In the previous section, we have extracted the decay of the flowing particles. It is composed of two components: $\text{crystal_6.14_CPFluctant_comp_2_cd_1} = 23 \pm 2 \text{ ns}$ and $\text{crystal_6.14_CPFluctant_comp_1_cd_1} = 4 \pm 2 \text{ ns}$. At that stage, the second component can be due to the presence of defects in the crystals or the presence of a second phase.

Figure 6.18 illustrates how the fluorescence of the crystals can be isolated for further analysis. The late photons (those that arrive 504 ps after the laser excitation) coming from the flow centre have been isolated. Their intensity (red) fluctuates in time. A bunch of photons was observed every time a fluorescent object flew through the field of view during 90 ms. The 90

ms can be calculated from the flow velocity of 1.165 mm/s and the size of the field of view. After a discussion with Prof. Thomas Rodet de *l'ENS-Paris Saclay*, we could gather the photons emitted by the particle late in the flow with those collected when the particle passes through a reference line in the image by correcting their collection time by:

$$t_{\text{col}} = t_{\text{detect}} - \frac{x_{\text{detect}} - x_{\text{ref}}}{v_{\text{max}}} \quad (6.1)$$

with x_{detect} the position of the crystal when the photon is detected, v_{max} the laminar flow velocity at the flow centre.

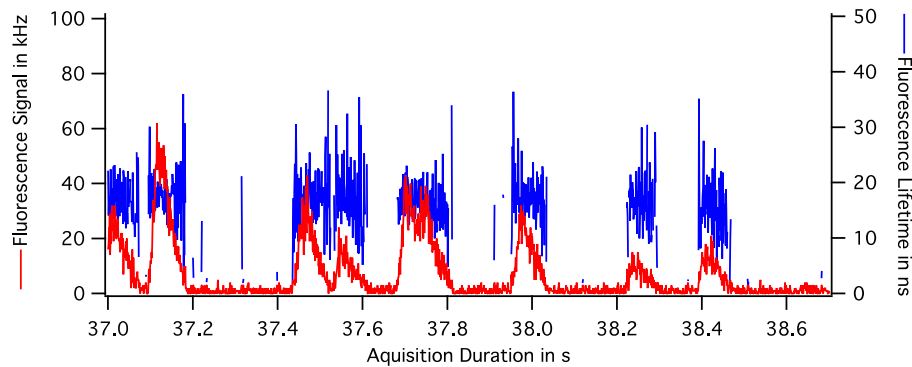


Figure 6.18. The fluorescence intensity (red) and lifetime (blue) signal collected from the flow centre area. The pulses in the fluorescence intensity indicates the crossing of the crystals. The width of the pulses, 90 ms, is the transit time of the particle in the detector field of view. The shape of the pulse is probably related to the shining profile of the UV laser over the sample. Microfluidic parameters:

$$\rho_{3c} = 10 \text{ g/l}, Q_c = 74 \text{ nl/min}, \phi_{lp} = 35\%, Q_p = 2 \mu\text{l/min}. \text{ FLIM laser parameter:}$$

$$\tau = 400\text{fs}, \lambda = 343\text{nm}, f_{\text{rep}} = 10\text{MHz}.$$

This correction for the movement of the crystals allows a better resolution of the different crystals. A better signal to noise ratio of obtained. We have chosen a threshold of 10 photons *per* burst to discriminate burst from noise. The total number of photons varies a lot from crystal to crystal. This can be due to the variation of size of the crystals. According to the

Beer-Lambert law, knowing the molar extinction coefficient of DBDCS at the wavelength of the excitation laser, all the excitation light is absorbed over 0.5 μm . Thus, we expect that the fluorescence intensity will be proportional to the area of the crystal exposed to the laser. The residual width of the photon bursts can also be measured. It will be proportional to the width of the crystal along the flow direction. Indeed, if two photons are emitted at the same time from the two extremities of the crystal, their transit corrected time will be different by a delay of:

$$\Delta t = \frac{\Delta x}{v_{\max}} \quad (6.2)$$

with Δx the crystal's length in the flow direction, v_{\max} the laminar flow velocity at the flow centre.

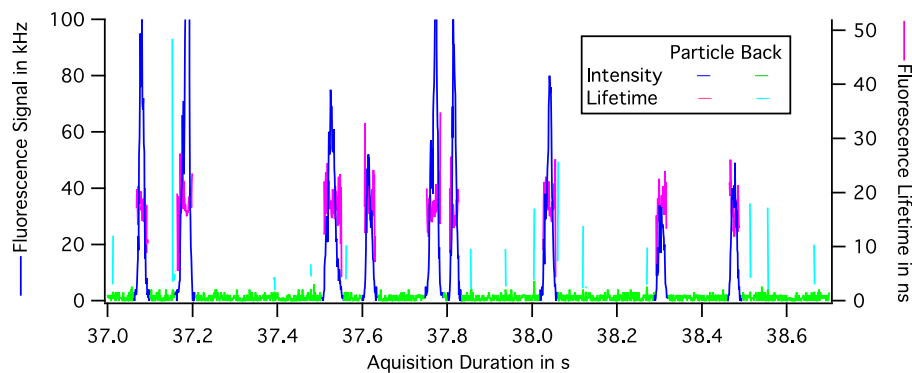


Figure 6.19. Fluorescence intensity and lifetime after the correction of the detection time. We obtained peaks with a better contrast. The area of the pulse is the total fluorescence collected per particle. The remaining pulse width is the time it takes for a particle to flow through a virtual line perpendicular to the flow. This figure is used to check the proper identification of the light pulse by the software. The blue points of the intensity curve are attributed to a particle, and the green points to the background. The fluorescence lifetime of the crystal is measured every 10 ms and attributed to a particle (magenta) or the background (cyan). Microfluidic parameters:

$$\rho_{3c} = 10 \text{ g/l}, Q_c = 74 \text{ nl/min}, \phi_{ip} = 35\%, Q_p = 2 \mu\text{l/min}. \text{ FLIM laser parameter:}$$

$$\tau = 400\text{fs}, \lambda = 343\text{nm}, f_{\text{rep}} = 10\text{MHz} .$$

By an appropriate binning of the pixel, it is even possible to make an image of these individual objects and their environment, gathering the photons emitted during the 90 ms duration of their transit time. This compares with the acquisition rate of the competitive video FLIM acquisition set up by fast confocal scanning [Rinnenthal, 2013].

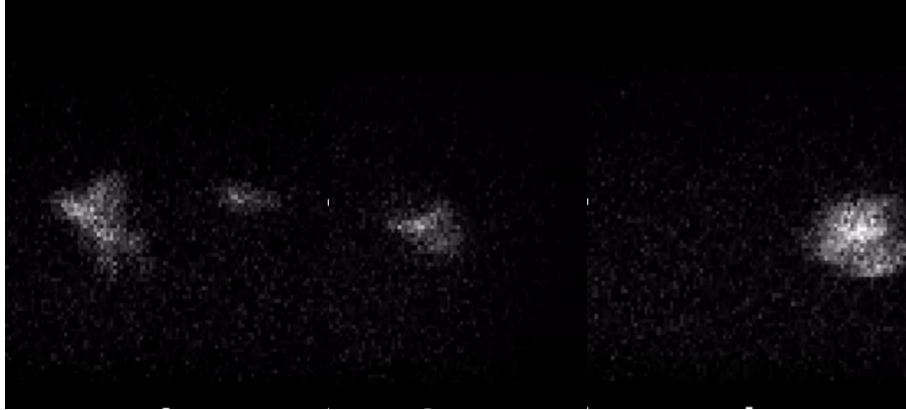


Figure 6.20. Frames of the fastest FLIM video. By gathering all the photon collected during a transit and adding them on the right pixel of the crystal, Prof. Thomas Rodet succeed in reconstructed the FLIM image of the crystals. It confirms the “butterfly” shape of the crystals shown by the transmission movie. Microfluidic parameters:

$\rho_{3c} = 10\text{g/l}, Q_c = 74\text{nl/min}, \phi_{tp} = 35\%, Q_p = 2\mu\text{l/min} .$ FLIM laser parameter:

$$\tau = 400\text{fs}, \lambda = 343\text{nm}, f_{\text{rep}} = 10\text{MHz} .$$

6.5. Measuring DBDCS crystal size by FLIM

We have thus two ways to estimate the size of the crystals and we can compare them. This is what has been done on Figure 6.21 where the fluorescence intensity of individual crystals is plotted as a function of their transit time through a reference fictive line. A quadratic dependence is observed as expected.

The cloud of points representing the intensity of each crystal has been coloured according to their fluorescence lifetime as well. Different polymorphs have different lifetime

and could have different fluorescence quantum yields. The peak amplitude is sensitive to the fluorescence yield, the peak width is not. We see no difference between the distribution of the points with respect to the fitting curve that does correlates with their fluorescence lifetime. This shows that the different polymorphs have the same fluorescence yield. The crystals with the longest lifetime gather on the right part of the figure. They are, on average, larger than those with a short lifetime. They also emit more light, not because of a better fluorescence yield, but a bigger size.

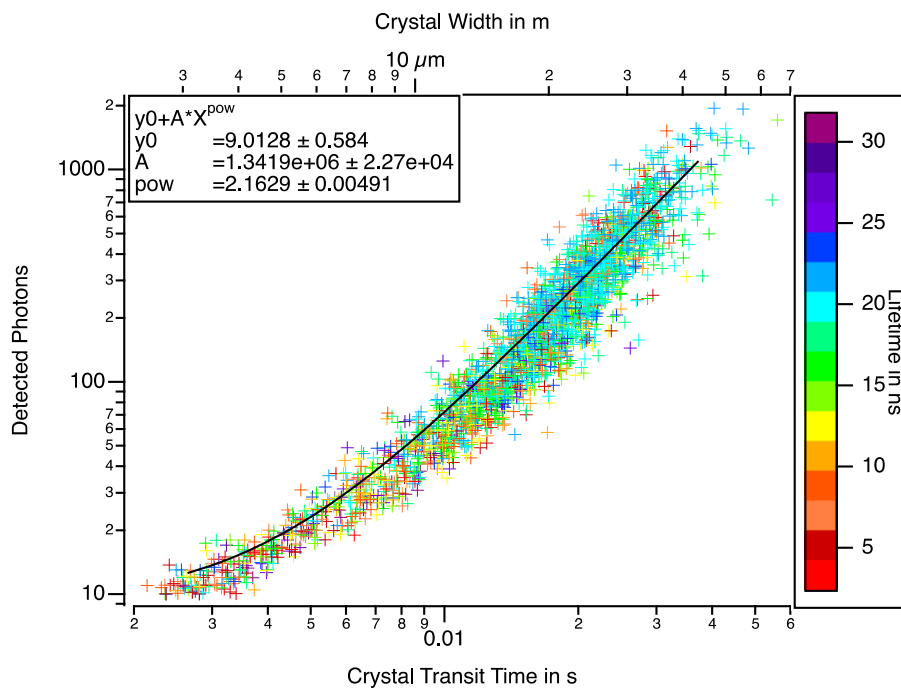


Figure 6.21. The total number of photons counted per DBDCS crystal versus the transit time through a virtual line in the flow. Crystals measured at different position along the flow have been gathered. The number of photons counted spread from 10 (a threshold in the analysis program) to 2000. The transit times spread from 1 ms (the pooling time chosen in the program) to 60 ms. The quadratic dependence between the fluorescence signal and a characteristic size shows that the fluorescence intensity is proportional to crystal area as expected for highly absorbing objects. Particles with longer lifetimes are bigger than those with shorter lifetimes. But for a given width, the number of photons counted depends on the nature of the phase within a factor of two.

They have the same fluorescence yield. Microfluidic parameters:

$\rho_{3c} = 16 \text{ g/l}, Q_c = 148 \text{ nl/min}, \phi_{lp} = 30\%, Q_p = 1 \mu\text{l/min}$. FLIM laser parameter:

$$\tau = 400\text{fs}, \lambda = 343\text{nm}, f_{\text{rep}} = 10\text{MHz}.$$

The distribution of the point around the mean curve is broad. There is a factor of 3 between the less intense particles and the more intense ones for a given size. This is related to the orientation of the crystal (see Figure 6.22) with respect to the excitation light. The crystals were rotating along the flow, therefore the size of their silhouettes on the OM image or the fluorescence intensity depends on, besides its actual size, its orientation with respect to the middle plane. Figure 6.22.A shows the rotation of a rhombus DBDCS crystal rotating while flowing from the left to the right, and Figure 6.22.B a star crystal tracked by the camera flowing along the flow while rotating. The emitted light will depend on the orientation of the crystal transition dipole with respect to the polarisation of the laser light. It is also a matter of shape and orientation of that shape in the field of view. Simulations shows that the transit time of the crystal that is related to its length along the flow is a better estimation of the size than the intensity.

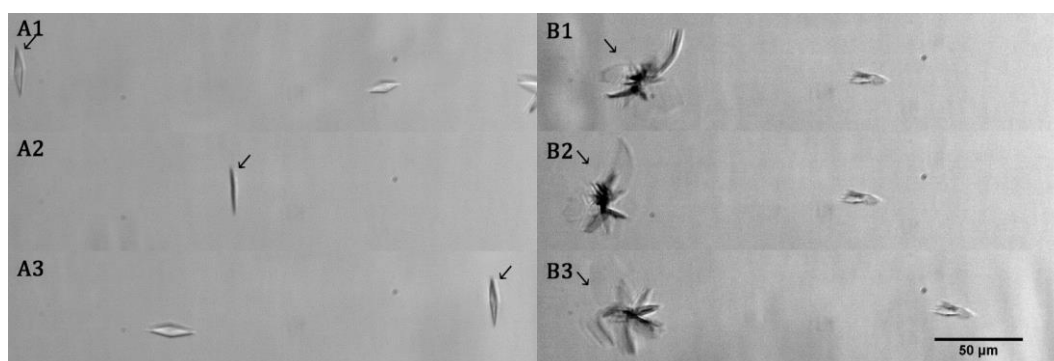


Figure 6.22. Rotation of crystals in the flow of DBDCS crystals in a mixture of water-THF in the coaxial microflow. A: rotation of rhombus crystal while flowing across the fixed field of view; microfluidic parameters:

$\rho_{3c} = 10 \text{ g/l}, Q_c = 185 \text{ nl/min}, \phi_{lp} = 30\%, Q_p = 1 \mu\text{l/min}$; B: rotation of a star crystal of

DBDCS while flowing along the channel and tracked by a moving field of view,

microfluidic parameters: $\rho_{3c} = 10 \text{ g/l}$, $Q_c = 37 \text{ nl/min}$, $\phi_{tp} = 30\%$, $Q_p = 2 \mu\text{l/min}$.

6.6. The birth rate and growth rate of spontaneous DBDCS crystals in the microflow of water (1)-1,4-dioxane (2) mixture

6.6.1. Comsol simulation of the environment

The birth rate and the growth rate depend on the local concentration of the DBDCS. *Comsol* simulation of the mass concentration and supersaturation of DBDCS along the flow centre have been plotted in Figure 6.23 for some typical observations. It shows that with a large fraction of water in the peripheral flow, there is an antisolvent focusing of the solute shortly after the injection nozzle. Whereas with a low fraction of antisolvent, the solute molecules escape from flow centre towards lower concentrations more easily. In the case of abnormally droplets trapped in the flow (section 5.6.3), simulation shows that the concentration at the flow centre can reach as high as 100 g/l, an extremely high supersaturation ratio β of $7 \cdot 10^5$. In the case of stable droplet following a LLPS (section 5.6.2), the concentration in the flow centre is not necessarily high, but β of 60 is high enough to reach the LLPS limit. Combination of a high concentration and a low supersaturation lower than 6 gives slow crystallisation followed by a growth in a constant environment.

The maxima of the antisolvent focusing of the solute concentrations are reached before 3 mm for these simulations. After the concentration maximum, the gradient of the antisolvent was no longer able to confine the solute. DBDCS molecules started to diffuse away. Yet the inter-diffusion between water and 1,4-dioxane was not finished. The solubility is function of solvents composition (see section 3.2.4). It dropped more rapidly than the concentration. Therefore, β reaches the maximum later at 1.6 mm from the nozzle. Then, as the profile of all species became homogeneous, the supersaturation and the concentration both decrease. This simulation suggests, firstly, that nucleation is most likely to happen around 2 mm away from the nozzle. Secondly, once there is a nucleus, the growth rate is already the most rapid that it will ever be. The growth rate can only be smaller afterwards until reaching a constant minimum

at 4 mm away from the nozzle.

It should be noticed that this simulation has not taken into account phase transition yet. Therefore, it is close to reality before d_p . Whereas after d_p , the model does not know the consumption of the solute by phase transition. Should β reach the spinodal limit, the model does not simulate the diffusion direction towards higher concentrations.

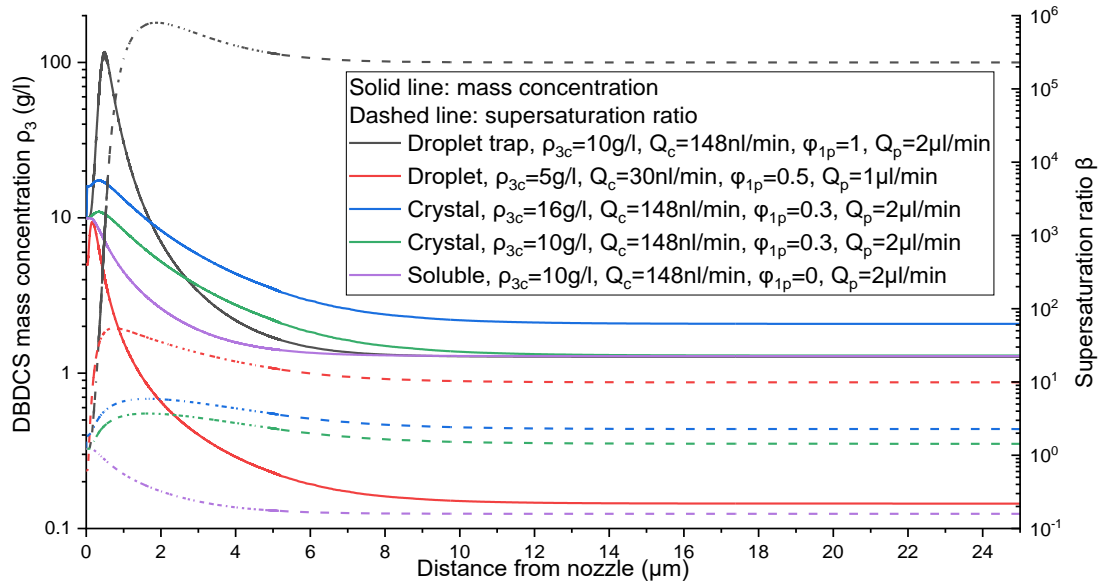


Figure 6.23. Comsol simulation of the mass concentration (solid curve) and supersaturation (dashed curve) of DBDCS along the flow centre for different observations discussed in this work (with the microfluidic parameters in the legend).

6.6.2. Definition of the variables

To measure the accumulative crystals birth rate B_x , we count the number of flowing crystals. We might be wrong if we miss crystals because they are below the detection limit of the OM or of the FLIM. The few crystals that are seen by OM are significantly bigger than the detection limit. This is true on Figure 6.1, and Figure 7.4~Figure 7.6.

B_x was defined in section 2.1 by equation (2.3). It is the frequency by which the crystals were observed at x μm after the injection nozzle, in the unit of s^{-1} . It represents the

number of crystals created during $0 \sim x \mu\text{m}$ in the flow *per* unit time. Thus, we can define a sectional crystal birth rate

$$\begin{aligned} B_{x1}^{x2} &= \frac{B_{x2} - B_{x1}}{x2 - x1} \\ &= \frac{\Delta B_x}{\Delta x} \end{aligned} \quad (6.3)$$

B_{x1}^{x2} is the probability of a crystal to be born during a unit length between $x1 \sim x2 \mu\text{m}$ *per* unit time. This is an easy measure of the nucleation rate of the solute crystals along the microflow.

As a matter of fact, when $\Delta x \rightarrow 0$, the derivative $\frac{1}{\pi R_{\text{channel}}^2} \frac{dB_x}{dx}$ (equation (2.4)) gives the

average nucleation rate N_s over a cross-section at $x \mu\text{m}$.

Spontaneous crystallisation occurs in a stable microflow, wherein the liquid composition and velocity refresh constantly as a function of spatial coordinates. A second characteristic of the spontaneous nucleation in the microflow is the average value and the distribution of the nucleation event interval $t_N = \frac{d_N}{v_{\text{max}}}$ (see equation (2.2)). It is the characteristic time between two random events with a constant probability.

The size distribution and growth rate are also of interest. From the size of crystals on the videos taken at different positions along the flow, the average crystal size A_c , the size distribution and the area growth rate g_A can be measured. From the width of the crystals L_c , we can also measure the average and distribution of L_c and the one dimensional growth velocity g_L .

From the OM and FLIM videos taken at different places along the microfluid channel, the accumulative crystal birth rate B_x , the average nucleation event interval t_N and its distribution, the sectional crystal birth rate B_{x1}^{x2} and the deduced spontaneous nucleation rate

N_s , the average crystal silhouette area A_c and its distribution were measured along the flow.

6.6.3. By FLIM

The apparent nucleation is a rare event that occurs at a rate B_x defined as the number of crystals detected *per* second observed at x μm (see section 2.1.1). FLIM measurement of the distribution of the time between two crystals (nucleation event time interval, t_N (equation (2.2))) is represented on Figure 6.24. In agreement with the theory of Poisson point processes, the distribution of t_N is an exponential of slope $B_x = 1.38 \pm 0.02 \text{ s}^{-1}$. Indeed, B_x can be more simply measured as the crystal count rate at x μm . But this graph shows that the nucleation is random. In a regime of competition for monomers between nuclei, we are expecting a drop of the exponential at short time. In the regime that we have observed of a periodic droplet production, a peak is expected on such histogram.

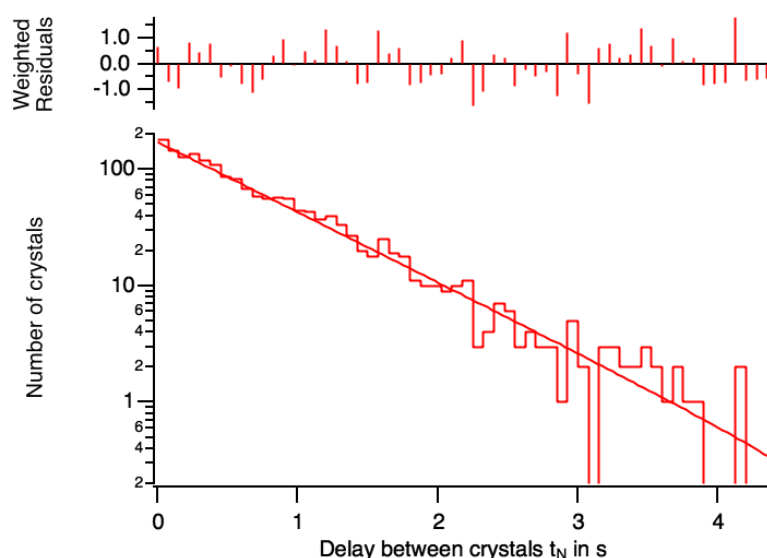


Figure 6.24. Number distribution of the nucleation event time interval, t_N , measured by FLIM. For a nucleation process occurring with a constant probability, we expect an exponential distribution of the number of crystals observed as a function of the time between two nucleation. The width of single bin in the histogram is 74 ms, i.e. 81 μm . Note the absence of deviation from the exponential at short time. Therefore, the

presence of a nucleus does not interfere with the birth of another $81 \mu\text{m}$ away.

Microfluidic parameters: $\rho_{3c} = 16 \text{ g/l}$, $Q_c = 148 \text{ nl/min}$, $\phi_{1p} = 30\%$, $Q_p = 1 \mu\text{l/min}$. FLIM

laser parameter: $\tau = 400\text{fs}$, $\lambda = 343\text{nm}$, $f_{\text{rep}} = 10\text{MHz}$.

We can compare the crystal as they grow along the flow. The accumulative birth rate B_x of spontaneous crystals (grey bar) is displayed on the top of Figure 6.25. B_x started to rise from 2.5 mm from the nozzle, and reached a plateau at 7.5 mm. After that, no increase of crystal population has been observed. The area of each crystal (red circle), measured by fluorescence intensity, is plotted vertically at the corresponding position of the measurement. The size distribution is represented by the black spindle covering the red circles, and the average size by the green square. The average size of the spontaneous crystals increased linearly with time, as well as the sizes distribution.

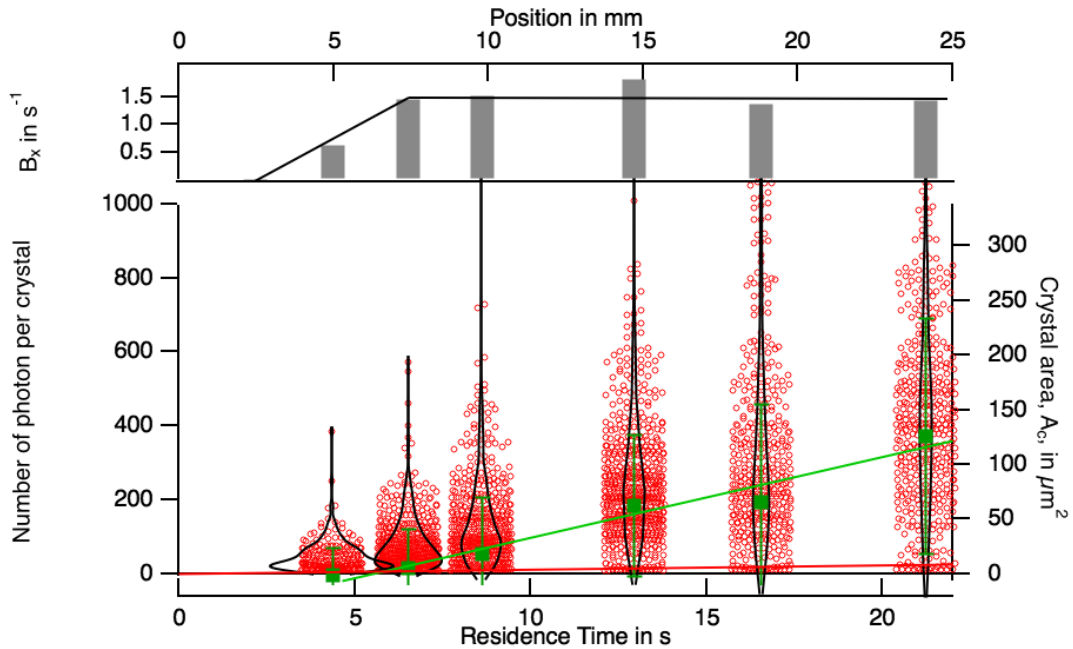


Figure 6.25. FLIM measurement of the DBDCS crystal area A_c distribution and accumulative birth rate B_x along the microflow. The area of each particle measured by fluorescence is represented as a hollow red circle. The distance from the nozzle (bottom axis) was translated into residence time (top axis) knowing the hydrodynamic

velocity at the flow centre. No particle was detected before 4 s of growth. The number of particles detected during 5 min experiment at each position is plotted in the top frame. We measure B_x of 1.3 crystal/s. The average size is represented as green solid squares. The vertical black spindle and the density of the red circles illustrates the size distribution at each position in the flow. Microfluidic parameters:

$\rho_{3c} = 16 \text{ g/l}, Q_c = 148 \text{ nl/min}, \phi_{1p} = 30\%, Q_p = 1 \mu\text{l/min}$. FLIM laser parameter:

$$\tau = 400\text{fs}, \lambda = 343\text{nm}, f_{\text{rep}} = 10\text{MHz}.$$

The growth rate of a crystal depends on the growth mechanism. If we assume a well agitated environment and an excess of DBDCS in solution compared to the crystal phase the growth rate can be related to a growth constant by:

$$-\frac{d[\text{DBDCS}]}{dt} = \frac{dL_c^3}{dt} = k_{\text{Grow}} L_c^n [\text{DBDCS}] \quad (6.4)$$

where L_c^3 is the volume of the crystal, n the dimension of the defect that allows the growth. $n = 0$ if the growth is through corners, $n = 1$ if the growth is through edge, $n = 2$ if the growth is through surface.

The growth is then given by:

$$L_c^{3-n} = k_{\text{Grow}} [\text{DBDCS}] \frac{n-3}{3} \Delta t \quad (6.5)$$

The *Comsol* simulation shows that the DBDCS concentration reaches a plateau after a fast drop during the first 4mm after the nozzle with a value of 2 g/l. We observe a constant rate for the growth of the area of the crystals. This indicates that the DBDCS molecules join the crystal along lines, typically the edges of the crystal. We measure a constant growth rate of the area of $6.6 \mu\text{m}^2/\text{s}$ and a growth rate constant of $3.3 (\mu\text{m}^2/\text{s})/(\text{g/l})$.

In Figure 6.26, the lifetime of each particle has been plotted as a function of its width, for measurement at different positions along the flow. This figure shows that two populations

with distinct lifetimes at 5 ns ($\text{crystal_6.26_1_cd_1} = 5 \text{ ns}$) and 18 ns ($\text{crystal_6.26_2_cd_1} = 18 \text{ ns}$) are present.

The two populations were present in a constant ratio of 20/80 during the first 25 s of the crystallisation. Thus, the two polymorphs were produced and grow independently. The constant lifetime of the 18ns population indicates that scenarios such as the growth of a crystalline phase over an amorphous core or the growth of a crystalline phase covered by a disordered surface are not seen.

The two polymorphs have similar sizes and growth rate. The dispersion of the estimated lifetime decreases with the size of the crystals. The narrowing of the lifetime distribution is due to the improvement of the quality of the lifetime estimation as the number of photons collected *per object* increases from 10 to 2000.

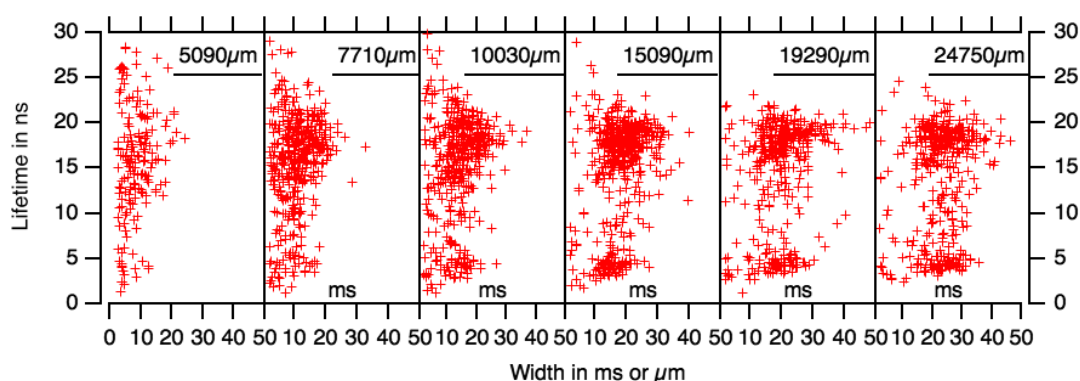


Figure 6.26. The correlation between the fluorescence lifetime of individual particles and their size for six positions along the flow. Two populations with distinct lifetimes at 5 ns ($\text{crystal_6.26_1_cd_1} = 5 \text{ ns}$) and 18 ns ($\text{crystal_6.26_2_cd_1} = 18 \text{ ns}$) are present.

Microfluidic parameters:

$$\rho_{3c} = 16 \text{ g/l}, Q_c = 148 \text{ nl/min}, \phi_{ip} = 30\%, Q_p = 1 \mu\text{l/min} . \text{ FLIM laser parameter:}$$

$$\tau = 400 \text{ fs}, \lambda = 343 \text{ nm}, f_{\text{rep}} = 10 \text{ MHz} .$$

The PCA and the individual particle analysis disagree on one point: PCA extracts a population with a short and a long lifetime associated with the fluctuation of the intensity of

the late photons. (Figure 6.15) Whereas the individual particle analysis shows two distinct populations. We shall favour the idea of two populations. Indeed, the PCA is looking for the minimal number of components to describe the data. By using a sum of the decays of the two populations, we can describe most of the fluctuation leaving the contribution of the difference of the two decays in the residuals of the intensity data (no shown in Figure 6.15). Therefore, we can conclude that the two polymorphs have the following lifetime 18 and 5 ns, in the spontaneous crystallisation of DBDCS in water (1)-1,4-dioxane (2) microflow.

6.6.4. By OM

The accumulative crystal birth rate B_x , the average nucleation event interval t_N and its distribution, the sectional average crystal birth rate B_{x1}^{x2} and the deduced spontaneous nucleation rate N_s , the average crystal silhouette area A_c and its distribution were measured from OM videos taken at different positions along the flow and plotted over the distance from the injection nozzle in Figure 6.27 and Figure 6.28 for two different central flow concentrations respectively.

The water volume fraction in the peripheral flow of Figure 6.27 is below the antisolvent focusing limit. Under this condition, there is little antisolvent focusing of the solute. DBDCS was not focused towards the flow centre, but slowly diffusing towards the periphery. Its concentration is higher at the flow centre. Therefore, crystallisation occurred at the flow centre. On the upper half of Figure 6.27, the crystal birth rate B_x (the open triangles) accumulated from the injection nozzle to x is plotted against the distance x (bottom axis) and the residence time (top axis). Before 2 mm, no crystals were seen. From 3 to 5 mm, the crystal count increased from 0.5 to 3.5 s^{-1} . Then it reaches a plateau throughout the whole microfluidic channel. This means in the volume of the microflow from the injection nozzle to 24 mm away, 6 crystals were born *per* second. They were all born between 2 and 5 mm.

The nucleation time interval t_N (black circle) is also plotted on Figure 6.27 top (to the

right). It is the time between two successive nucleation events, *i.e.* the distance between two successive crystals divided by the flow velocity. The histogram (brown hatched bar) of t_N with its distribution (the covering curve on the histograms) measured at each position is plotted vertically along a vertical line at the corresponding x . t_N decreases as B_x increases. Its distribution is an exponential decay, as expected for a random event occurring with a constant probability.

The sectional average crystal birth rate $B_{x1}^{x2} = \frac{B_{x2} - B_{x1}}{x2 - x1}$ (dashed line) is plotted (to the right) on the middle of Figure 6.27. It is the probability of a crystal to be born during a unit length between $x1 \sim x2$ μm *per* unit time. From this we deduced the homogeneous nucleation rate $N_s = \frac{1}{\pi R_{\text{channel}}^2} \frac{dB_x}{dx}$ (solid curve). The nucleation rate was about $50/(\text{s}\cdot\text{mm}^3)$ at distance 3 mm, then rapidly decreased to practically zero at 5 mm.

On the bottom of Figure 6.27 plotted the measurement of the area of the crystals' silhouettes A_c from the OM videos. A_c increases linearly with x , and its distribution broadens. The fitted area growth rate $g_A = 9.8 \mu\text{m}^2/\text{s}$, and an area growth rate constant of $4.75 (\mu\text{m}^2/\text{s})/(\text{g/l})$. It differs from the rate measured by fluorescence by a factor of two. We shall prefer the values obtained by OM since they are more direct.

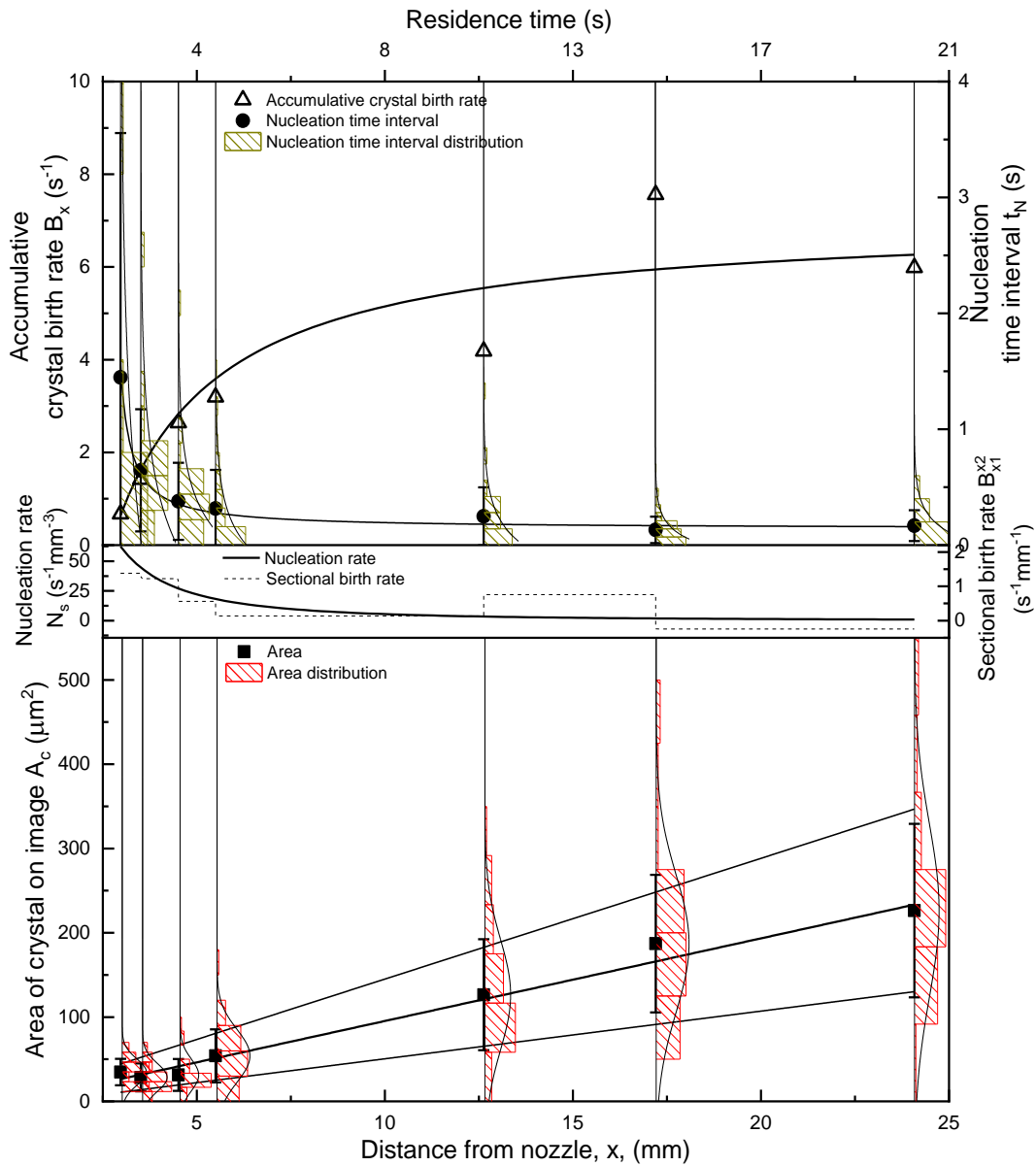


Figure 6.27. OM measurement of nucleation rate and growth rate of spontaneous crystallisation versus distant from injection nozzle (bottom axis) and residence time (top distance). Top: the accumulative (from nozzle to x) crystal birth rate B_x (open triangle), the average nucleation event interval t_N (black circle), histogram of t_N (vertically plotted brown hatched bar) and distribution of t_N (curve covering the histogram). Middle: the sectional crystal birth rate B_{x1}^{x2} (dashed line) and the deduced spontaneous nucleation rate N_s (solid curve). Bottom: the average crystal

silhouette area A_c (black square), histogram of A_c (red hatched bar plotted vertically)

and its distribution (curve on the histogram). Microfluidic parameters:

$$\rho_{3c} = 16 \text{ g/l}, Q_c = 148 \text{ nl/min}, \phi_{1p} = 30\%, Q_p = 1 \mu\text{l/min}.$$

The central jet DBDCS concentration of Figure 6.28 (10 g/l) is two thirds of Figure 6.27 (16 g/l). A lower concentration of DBDCS is diffusing in the same field of composition of the water (1)-1,4-dioxane (2) mixture. The crystal birth rate is half of Figure 6.27 with a larger $g_A = 14 \mu\text{m}^2/\text{s}$ and a growth rate constant $k = 6.8 (\mu\text{m}^2/\text{s})/(\text{g/l})$.

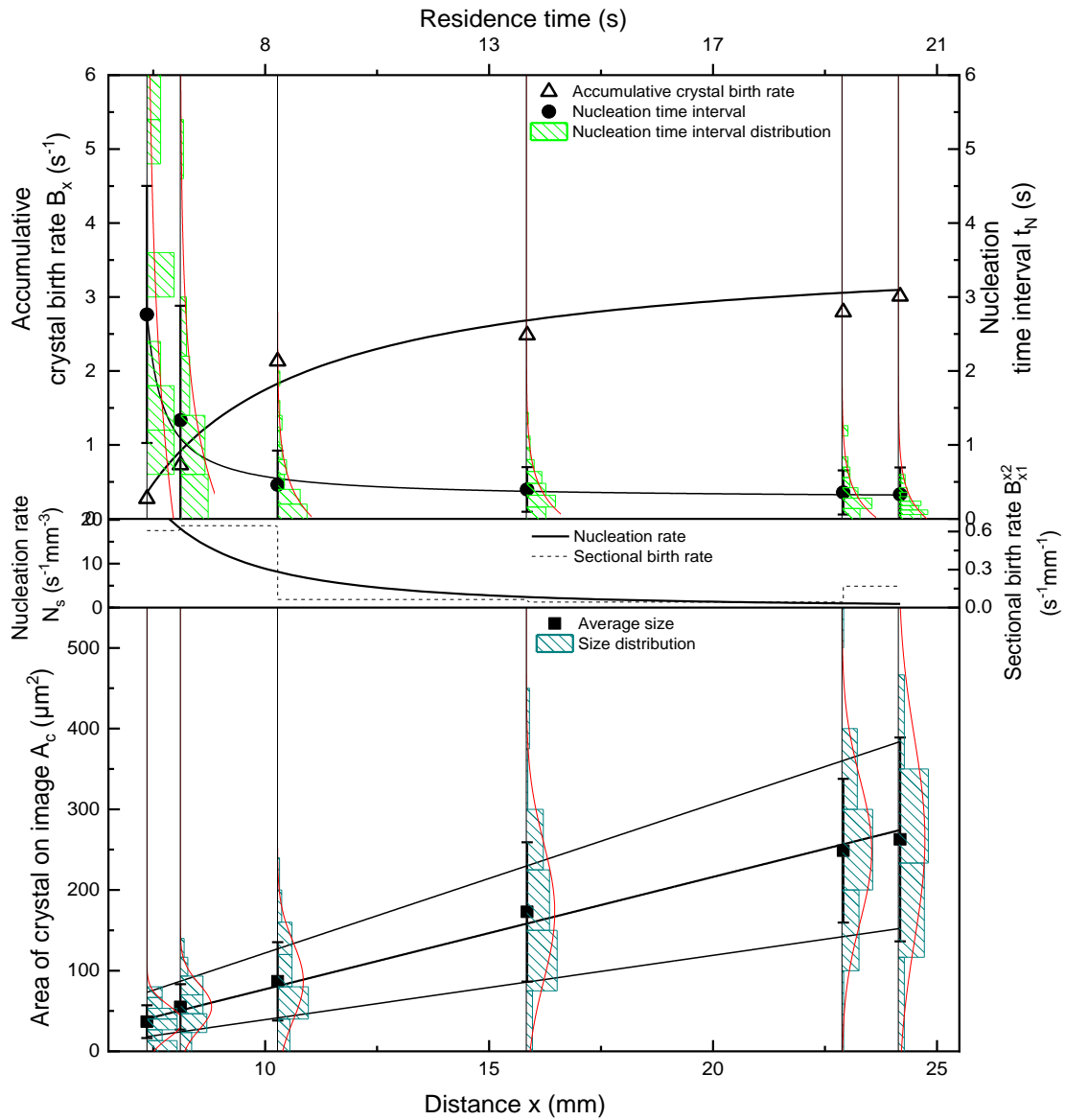


Figure 6.28. OM measurement of nucleation rate and growth rate of spontaneous crystallisation versus distant from injection nozzle (bottom axis) and residence time (top distance). Top: the accumulative crystal birth rate B_x (open triangle), the average nucleation event interval t_N (black circle), histogram of t_N (vertically plotted green hatched bar) and distribution of t_N (red curve covering the histogram).

Middle: the sectional crystal birth rate B_{x1}^{x2} (dashed line) and the deduced spontaneous nucleation rate N_s (solid curve). Bottom: the average crystal silhouette

area A_c (black square), histogram of A_c (blue hatched bar plotted vertically) and its distribution (red curve on the histogram). Microfluidic parameters:

$$\rho_{3c} = 10 \text{ g/l}, Q_c = 148 \text{ nl/min}, \phi_{1p} = 30\%, Q_p = 1 \mu\text{l/min}.$$

6.7. Summary of all the spontaneous phase transition types observed in the coaxial microfluidic system

Figure 6.29 summarises all the spontaneous phase transitions we have observed in the coaxial microfluidic system and described in Chapter 5 and Chapter 6. They are colour coded on the phase diagram. The green line on the phase diagram is the solubility predicted by Jouyban-Acree equation. It is where the free energy of the solid and that of the monomer intersect. The red line is the antisolvent focusing limit predicted by our equation (5.4). It is where the gradient of the anti-solvent is strong enough to push the solute towards the flow centre, *i.e.* the second derivative of the chemical potential of the solute start to be negative. It is noticeable, firstly, that the non-crystalline phase transitions were dominating, with dozens of points of crystallisation among more than 2000 points; secondly, that right above, or sometimes even below the solidus, spontaneous phase transition occurred. This is because the observations are plotted on the overall composition of the mixture, whereas the supersaturation at the flow centre can be extremely high when there was anti-solvent focusing, which depended on the microfluidic input parameters.

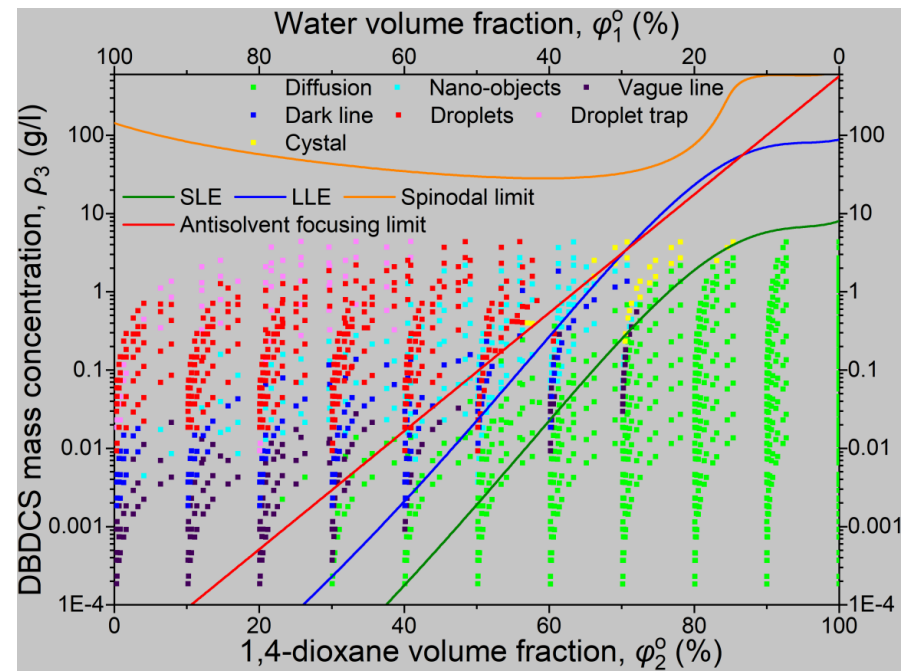
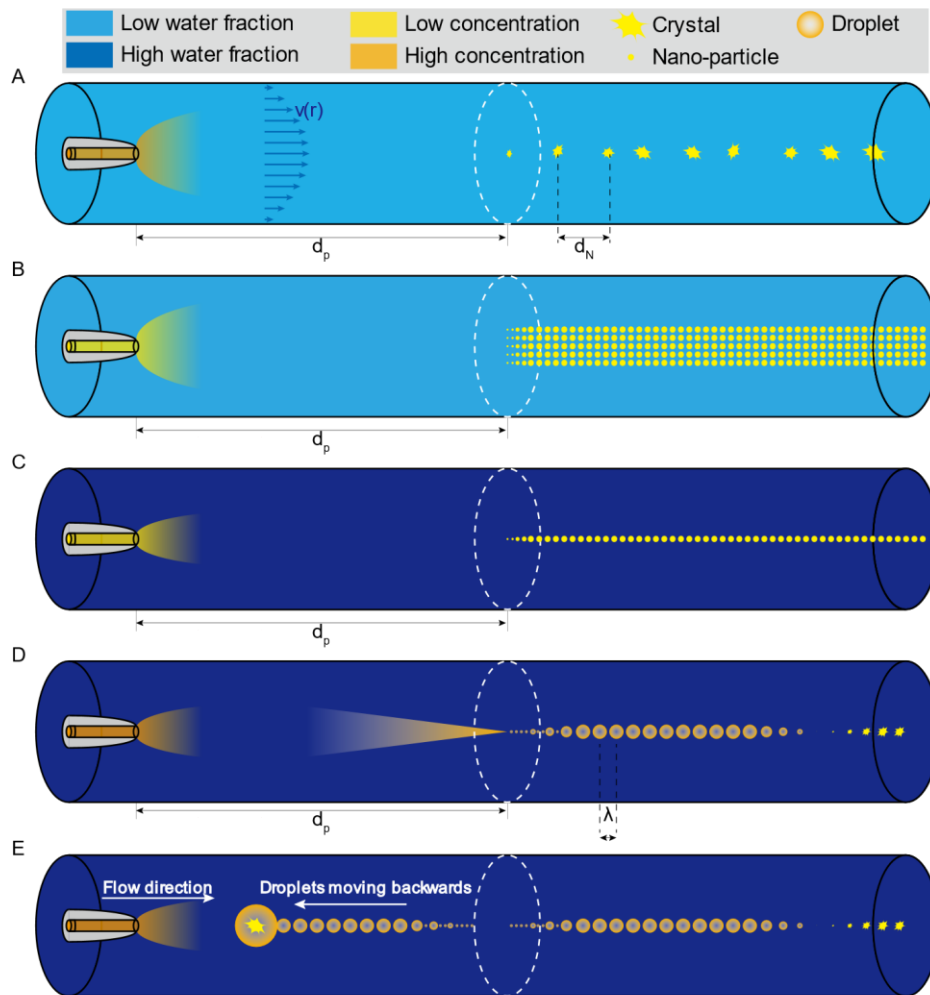


Figure 6.29. Summary of all the spontaneous phase transition behaviours observed in the coaxial microfluidic system. A: homogeneous crystallisation from solution with a high central jet concentration ρ_{3c} and a low antisolvent fraction ϕ_{1p} ; B: precipitation of a column of nano-objects dispersed in the flow

centre with a small ρ_{3c} and a low ϕ_{1p} ; C: a line of precipitation in the flow centre with a low ρ_{3c} and a high ϕ_{1p} ; D: LLPS followed by droplet formation with a high ρ_{3c} and high ϕ_{1p} , which later crystallised; E: abnormally large droplets trapped (or even flowing backwards) in the flow with a high ρ_{3c} , high ϕ_{1p} and small total flow rate, which can have a crystal confined in this small volume. They are colour coded on the phase diagram. The green line on the phase diagram is the solubility predicted by Jouyban-Acree equation. The red line is the antisolvent focusing limit predicted by our equation (5.4). The black curve is the binodal LLPS limit from thermodynamic calculation in section 3.6.1.3.

Chapter conclusion

This chapter was dedicated on the spontaneous crystallisation of DBDCS in a mixture of water (1)-1,4-dioxane (2) in the microfluidic system. Detailed information on the polymorphs, the crystal habit, the number, and size has been recorded by OM and FLIM videos. We have observed two different crystal habit a rhombus and a “butterfly” one. The “butterfly” habit is in fact a twin crystal grew *via* two mirror twin laws. From the individual particle analysis, we have extracted the accumulative crystal birth rate, sectional crystal birth rate, nucleation rate, nucleation time interval, crystal size distribution and a growth rate. We have observed the simultaneous nucleation of two solid phases that grow independently at the same rate from their fluorescence lifetimes. From the PCA analysis, we conclude that in addition to the two phases forming crystals, there are two others that are dispersed in the flow, in particular a 2 ns phase that is present in the water rich phase. This can be an indication of the formation of oligomers in the supersaturated region. *Comsol* simulation of the solute concentration and supersaturation ratio for some typical conditions (droplet following LLPS, abnormal droplet trap, crystals, and no phase transition) have been correlated with the experimental results. Together with the other points from the microfluidic parametric sweep described in Chapter 5,

a phase diagram of water (1)-1,4-dioxane (2)-DBDCS (3) based on the overall composition of the mixture has been developed.

Chapter 7. Laser- induce nucleation in microfluidics

7.1. Laser-induced crystals	248
7.1.1. Early stage of laser-induced nucleation	248
7.1.2. Nucleation rate, growth rate and polymorph distribution of laser-induced crystals in microfluidics	252
7.1.3. Impact of laser parameters on laser-induced crystallisation in microfluidics	261
7.1.4. <i>Post-mortem</i> characterisation of NPLIN crystals	272
7.2. Laser’s effect on LLPS and droplets	273
7.2.1. Laser dragging the central-peripheral flow interface	273
7.2.2. Laser accelerating the phase separation and droplets formation	274
7.2.3. Laser releasing the abnormally large droplets from the “droplet trap”	276
7.2.4. Laser changing the size of the stable droplets	278
7.3. Effect of the focused IR laser of nano-objects	279
7.3.1. Dark line	279
7.3.2. Laser-induced two-step crystallisation: droplets→crystals	280
7.3.3. Laser-induced bubbles on nano-precipitates’ surface	282
7.3.4. Impact of laser induction position	284
7.4. Other observation with the femtosecond IR laser	286
7.4.1. Laser tweezers	286
7.4.2. Bubbles, explosion, laser ablation.	287
7.5. NPLIN working phase diagram	288
Chapter conclusion	292

Static NPLIN has shown that laser is able to shorten the crystallisation induction period of supersaturated solutions from days to minutes and that its polarisation has an impact on the induced polymorphs [Clair, 2014, Ikni, 2014, Li, 2016b]. The advantage of microfluidics is, firstly, the experimental condition will be constantly refreshing so long as the flow is stable; secondly, with a small amount of solute, it can explore a wide range of supersaturations; thirdly, *in situ* observation can be conducted along the flow. Therefore, it is interesting to test the effect of a non-absorbed laser on the solute molecules in the microfluidic system.

During the microfluidic parametric sweep, a fs IR laser was focused at different distances from the injection nozzle along the flow under different microfluidic conditions. OM, crossed polarisers (CP), and FLIM were used to observe the effect of the femtosecond IR laser on supersaturated DBDCS in water (1)-1,4-dioxane (2) system in the coaxial microfluidic mixer.

This chapter focuses on the different effects of the fs laser on water (1)-1,4-dioxane (2)-DBDCS (3) observed in the coaxial mixer. In section 7.1, we shall present the laser-induced crystals, including the early stage of the laser-induced nucleation in 7.1.1, the comparison between the spontaneous and the laser-induced crystal size distribution, polymorphism, nucleation time interval, birth-rate, nucleation rate, and growth rate in 7.1.2, the impact of the laser induction position along the flow, the laser average power, the repetition rate, and the polarisation in 7.1.3, and the *post-mortem* observation in 7.1.4. Section 7.2 describes the effect of the laser on LLPS and droplet formation. In section 7.3, the effect of the laser on the nano-objects is described. Some other observations related with the laser in the microflow, such as laser tweezers, explosions, and laser ablation, are illustrated in section 7.4. Section 7.5 categorises the spontaneous phase transitions of water (1)-1,4-dioxane (2)-DBDCS (3) in the coaxial microflow with the effect of the fs IR laser, from that a new phase diagram of microfluidic NPLIN will be built.

7.1. Laser-induced crystals

7.1.1. Early stage of laser-induced nucleation

For the microfluidic conditions (light blue points on Figure 6.29) just above the solubility curve on the phase diagram, without laser, spontaneous precipitation produced a column of nano-particles. No spontaneous crystals were observed. The antisolvent gradient focusing of the solute is close to zero, DBDCS molecules were confined in a cylinder near the flow centre. The solubility is very low; therefore, fast nucleation of nano-particles was favoured over slow crystallisation. When the femtosecond IR laser was focused at the flow centre 100~200 μm before the formation position of nano-particles, laser-induced crystals were observed for the first time in a microfluidic system, as shown in Figure 7.1. With the laser off, spontaneous crystallisation was not observed in the field of view, whereas with the laser focused at the flow centre, dark objects appeared 100 μm after the laser spot along the flow direction. The induced objects were examined under CP for its crystallinity. In the crossed polariser OM video, the image was dark with no laser. With the IR laser on, bright objects appeared after approximately the same distance as in the transmission OM video. This has proven, firstly, that the IR laser had induced a new phase from a supersaturated microflow of DBDCS in water (1)-1,4-dioxane (2); secondly, these objects had crystalline structure around 41 ms or 100 μm after its birth (taking into account the OM detection limit), knowing that the flow centre velocity was 2.2 $\mu\text{m}/\text{ms}$.

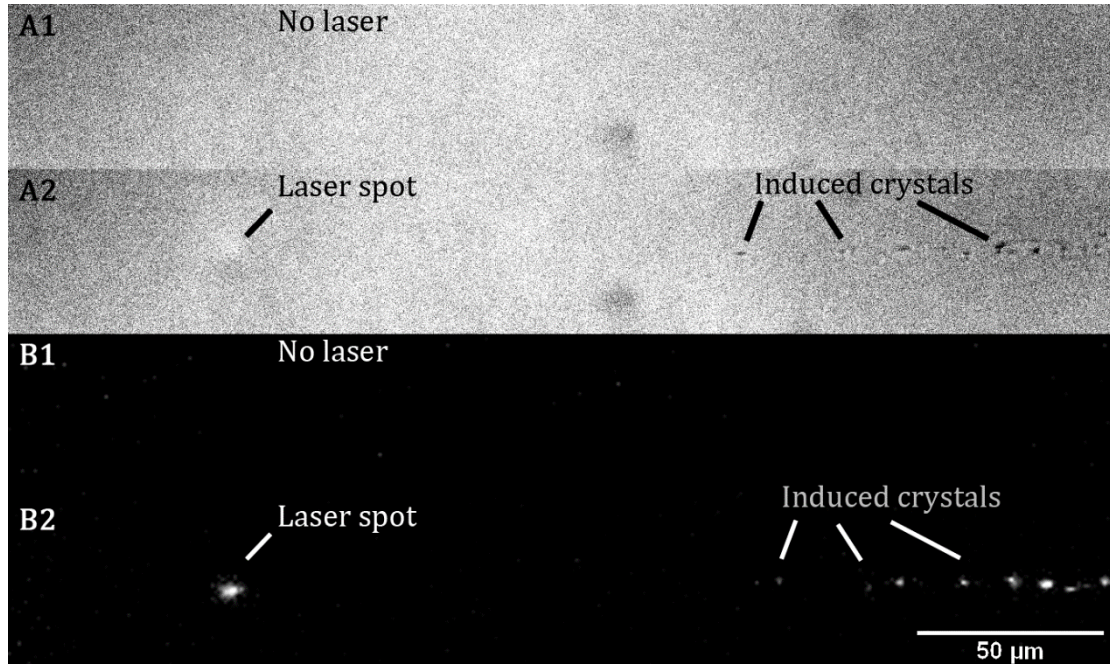


Figure 7.1. Laser-induced DBDCS crystals from a mixture of water (1)-1,4-dioxane (2) in the coaxial microfluidic mixer. A: OM transmission images; A1: with the laser off, spontaneous crystallisation was not observed in the field of view; A2: with the laser on, dark objects were seen 100 μm after the laser spot along the flow; B: CP images; B1: without laser, the field of view was black; B2: the laser-induced objects appeared bright in a dark background, proving these are crystals. Frames taken from videos. Microfluidic parameters:

$$\rho_{3c} = 3.5 \text{ g/l}, Q_c = 285 \text{ nl/min}, \phi_{lp} = 50\%, Q_p = 2 \mu\text{l/min}. \text{ Laser parameters:}$$

$$\tau = 400\text{fs}, \lambda = 1030\text{nm}, f_{\text{rep}} = 5\text{MHz}, P_{\text{avg}} = 120\text{mW}, d_L = 1900\mu\text{m}, \text{ linear } s$$

$$\text{polarisation}(LPS).$$

The earlier stages of nucleation were below the diffraction limit of the OM. As for the spontaneous nucleation (section 6.3), the fluorescence lifetime of DBDCS will be used to study the organisation of the molecules. To probe the change in the organisation of the solute molecule caused by the IR NPLIN laser, our system can send a UV laser ($\lambda = 343\text{nm}$, $f_{\text{rep}} = 10\text{MHz}$, $\tau_p = 400\text{fs}$) as the excitation beam for FLIM and collect the signal with a

time- and space- correlated single photon counting detector. Figure 7.2 is the FLIM image of the laser-induced nucleation, the central red colour (ROI B) shown the flow of DBDCS molecules. DBDCS molecules were moderately confined in a column 65 μm in diameter. The blue polar caps (ROI A) with an apparently lifetime larger than 5 ns, were due to the absence of fluorescence from the sample. This is the lifetime of the background. The blue area on the left (ROI C) is the fluorescence coming from the three-photon excitation by the IR femtosecond laser. The NPLIN IR laser is focused just outside the observation window to reduce the saturation of the FLIM detector. The fluorescence induced by the IR laser appeared as a long-lived fluorescence since the NPLIN laser arrives 3ns after the FLIM laser. ROI A white line (ROI D) in centre of the flow that became stronger to the right was due to the increasing contribution of a long-lived population. It is due to the formation of growing long-lived crystals.

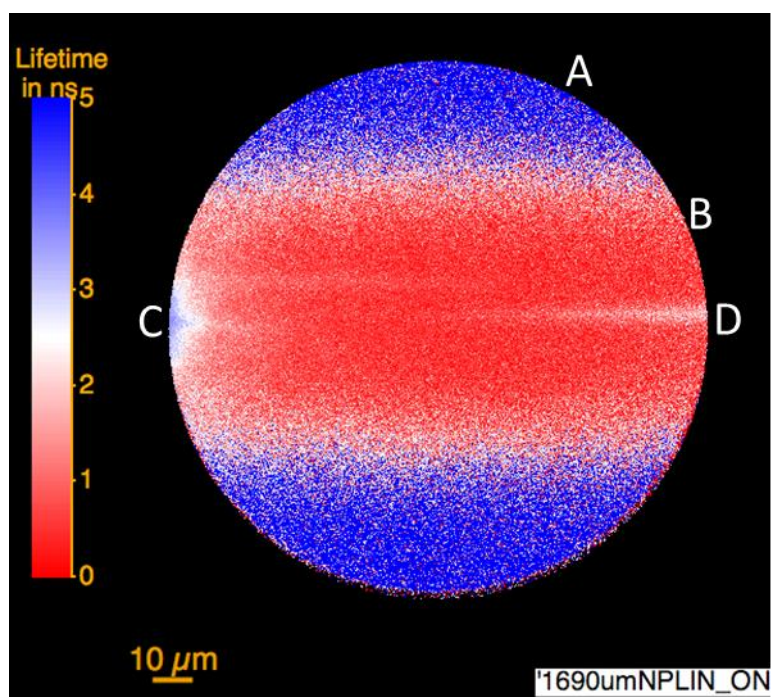


Figure 7.2. FLIM image of the microfluidic NPLIN in Figure 7.1. The DBDCS molecules were within a 65 μm wide cylinder (ROI B). The blue polar caps (ROI A) show the lifetime of the background. The nucleation and growth of a long-lived population in the center of the flow appeared a growing white line on the right of the image (ROI D). The blue spot on the left edge (ROI C) was the fluorescence induced by

a 3 photon excitation of DBDCS by the IR NPLIN laser that is focused out of the field of view. Microfluidic parameters:

$\rho_{3c} = 3.5 \text{ g/l}$, $Q_c = 285 \text{ nl/min}$, $\phi_{lp} = 50\%$, $Q_p = 2 \mu\text{l/min}$. NPLIN laser parameter:

$\tau = 400\text{fs}$, $\lambda = 1030\text{nm}$, $f_{\text{rep}} = 5\text{MHz}$, $P_{\text{avg}} = 120\text{mW}$, $d_L = 1900\mu\text{m}$, LPS. FLIM laser

parameter: $\tau = 400\text{fs}$, $\lambda = 343\text{nm}$, $f_{\text{rep}} = 10\text{MHz}$.

The fluorescence decays from ROI C (very nearby the IR focal point) and ROI D on the FLIM image were collected and compared on Figure 7.3. The decay of DBDCS molecules was recorded in the flow with no NPLIN laser. The decay induced by the NPLIN laser (ROI C) was moved to the left by 3 ns nanosecond for comparison. A population with a lifetime of 4.5 ns (object_7.3_C_cd_3 = 4.5 ns) was present. This signal came from a population that was accumulated by the train of NPLIN pulses. The decay collected from ROI D had a small contribution of a 11 ns long lifetime (object_7.3_D_cd_3 = 11 ns). The absence of the 4.5 ns contribution in the flow a few milliseconds after the exposure to the NPLIN laser suggests that most of the object_7.3_C_cd_3 = 4.5 ns clusters that were created in the laser spot had re-dissolved. A minority of object_7.3_C_cd_3 = 4.5 ns clusters continued to grow into a phase with a 11 ns lifetime (object_7.3_D_cd_3 = 11 ns).

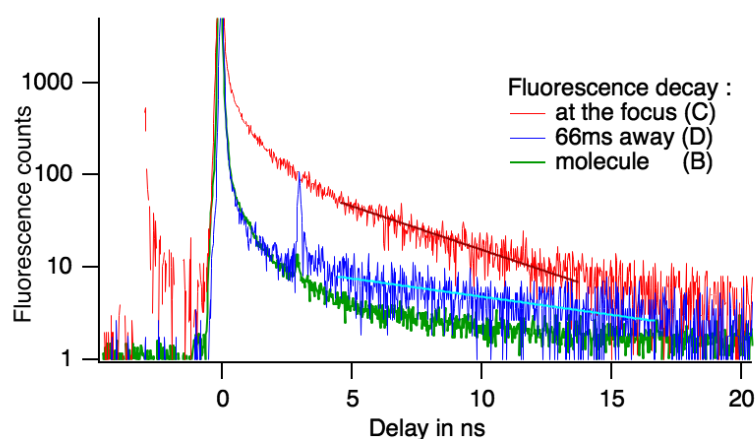


Figure 7.3. The fluorescence decays of DBDCS molecules with and without the IR femtosecond laser. The green decay is of the DBDCS molecules in the flow when

there was no NPLIN laser. The Red decay (containing a component with a fluorescence lifetime: $object_7.3_C_cd_3 = 4.5\text{ ns}$) was collected in ROI C on Figure 7.2. The fluorescence was produced by the IR femtosecond laser and it was shifted by 3 ns for comparison. The blue decay (containing a component with lifetime: $object_7.3_D_cd_3 = 11\text{ ns}$) was collected on the right of the FLIM image (ROI D on Figure 7.2). The blue peak 3 ns after the FLIM laser was due to the scattering of the NPLIN laser-induced fluorescence in the microscope. The green decay was collected in ROI B on Figure 7.2. Microfluidic parameters:

$\rho_{3c} = 3.5\text{ g/l}$, $Q_c = 285\text{ nl/min}$, $\phi_{tp} = 50\%$, $Q_p = 2\text{ }\mu\text{l/min}$. NPLIN laser parameters:

$\tau = 400\text{ fs}$, $\lambda = 1030\text{ nm}$, $f_{rep} = 5\text{ MHz}$, $P_{avg} = 120\text{ mW}$, $d_L = 1900\text{ }\mu\text{m}$, LPS. FLIM laser

parameter: $\tau = 400\text{ fs}$, $\lambda = 343\text{ nm}$, $f_{rep} = 10\text{ MHz}$.

7.1.2. Nucleation rate, growth rate and polymorph distribution of laser-induced crystals in microfluidics

The region of small supersaturation and rich in DBDCS is the domain of spontaneous nucleation without laser. These are the yellow points in the phase diagram. The water fraction in the peripheral flow is small, therefore there was no antisolvent focusing. DBDCS diffused away from higher concentration towards lower concentration until reaching the capillary wall. An almost homogenous laminar flow of a supersaturated solution was developed (see section 4.2.2). Slow nucleation and crystal growth occurred along the flow. Figure 7.4. shows the spontaneous crystals started to be observed around 2~3 mm away from the injection nozzle. After that, the crystals grew into butterflies along the microfluidic channel. This has been characterised in Chapter 6.

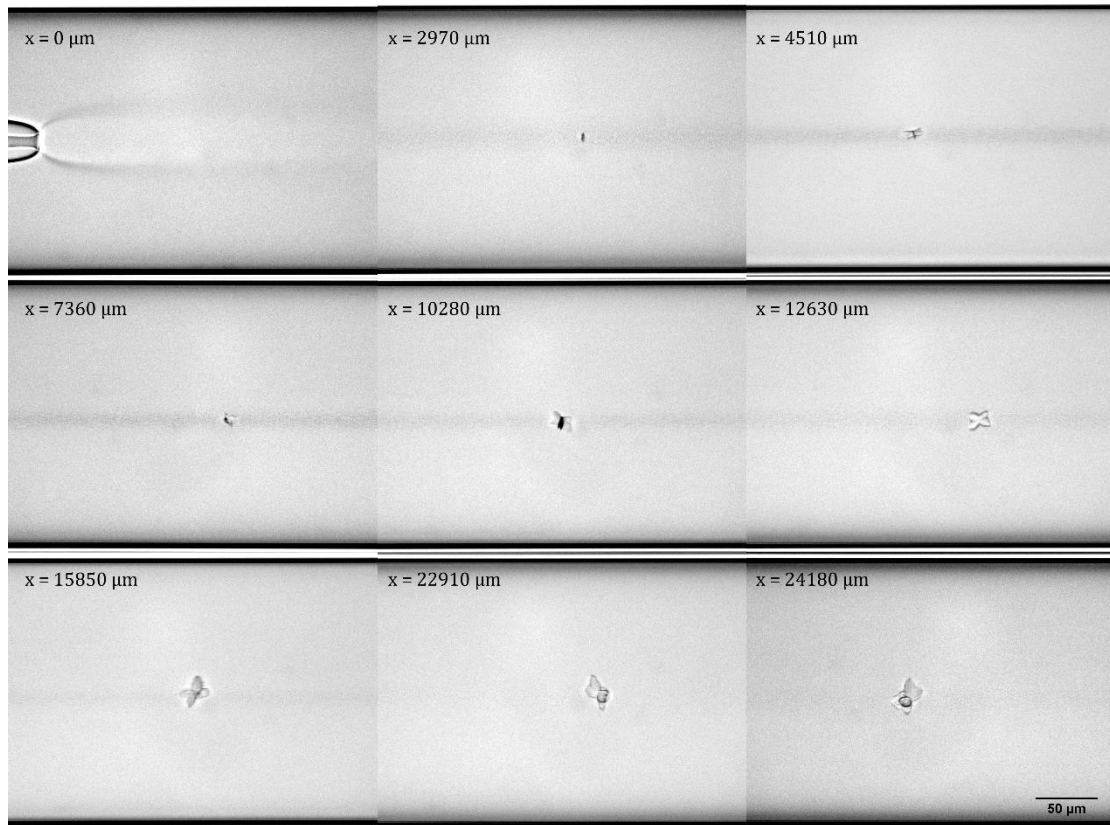


Figure 7.4. Spontaneous crystallisation and growth of DBDCS along the coaxial microfluidic mixer without IR laser. Microfluidic parameters:

$$\rho_{3c} = 16 \text{ g/l}, Q_c = 148 \text{ nl/min}, \phi_{lp} = 30\%, Q_p = 1 \mu\text{l/min}$$

On Figure 7.5, under the same microfluidic conditions than Figure 7.4, with the IR femtosecond laser turned on, a large number of crystals were observed along the microfluidic channel. To induce crystals, the femtosecond IR laser was focused 30 μm away from the injection nozzle and turned on for about 3 seconds (Figure 7.5). Since the crystals were carried by the flow, the growth process occurs along the flow far from the laser induction position. To observe the growth of the laser-induced crystals, the microfluidic device was moved faster than the flow velocity immediately after shutting off the NPLIN laser and stopped at pre-set distances by the microscope stage blocker (see Figure 2.15). Thus, the laser-induced crystals were “intercepted” at positions of interest along the microfluidic channel. One can distinguish the laser-induced crystals thanks to their much higher count rate. In this way, crystals induced at the same position by the same laser under the same microfluidic parameters were observed

by OM or FLIM at different distances, *i.e.* different age after their birth, along the microfluidic channel, repeatedly. Videos were taken at these pre-set observation distances for the laser-induced crystals and then, after the laser-induced crystals had flown away, for the spontaneous crystals.

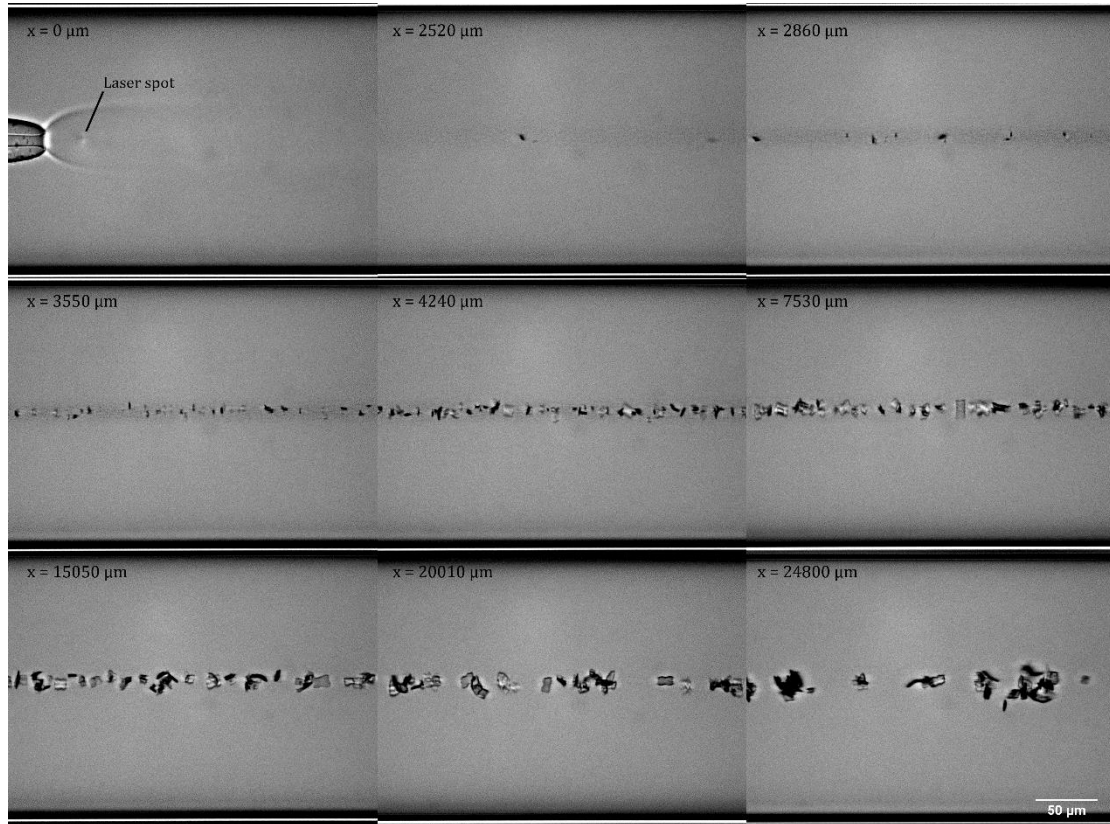


Figure 7.5. Growth process of the laser-induced crystals along the microfluidic channel. Frames taken from videos of nine measurements. The observation distances from the injection nozzle are noted on the up-left corner of each frame. Microfluidic parameters: $\rho_{3c} = 16 \text{ g/l}$, $Q_c = 148 \text{ nl/min}$, $\phi_p = 30\%$, $Q_p = 1 \mu\text{l/min}$, NPLIN laser parameters: $\tau = 400\text{fs}$, $\lambda = 1030\text{nm}$, $f_{\text{rep}} = 10\text{MHz}$, $P_{\text{avg}} = 330\text{mW}$, LPS, $d_L = 30\mu\text{m}$

The measurement was first done with full power of the laser. But the nucleation rate by the full power laser was too high so that crystals were overlapping, rendering the crystal size measurement difficult and inaccurate. Therefore, the experiment was repeated with half the full laser power, as shown in Figure 7.6. At this p_{avg} , most induced crystals were flowing one by

one, instead of overlapping, while the laser's effect was still strong.

From Figure 7.5 and Figure 7.6, one can qualitatively see that laser-induced crystals started to be seen around 2.5 mm and the propagation of its population stopped around 3.5 mm. After 3.5 mm, the increasing of crystal population density had almost finished. Growth of the same population density of crystals was seen along the flow from 4 mm to 25 mm. Near the end of the observation window, the crystals did not grow much but started to gather and overlap.

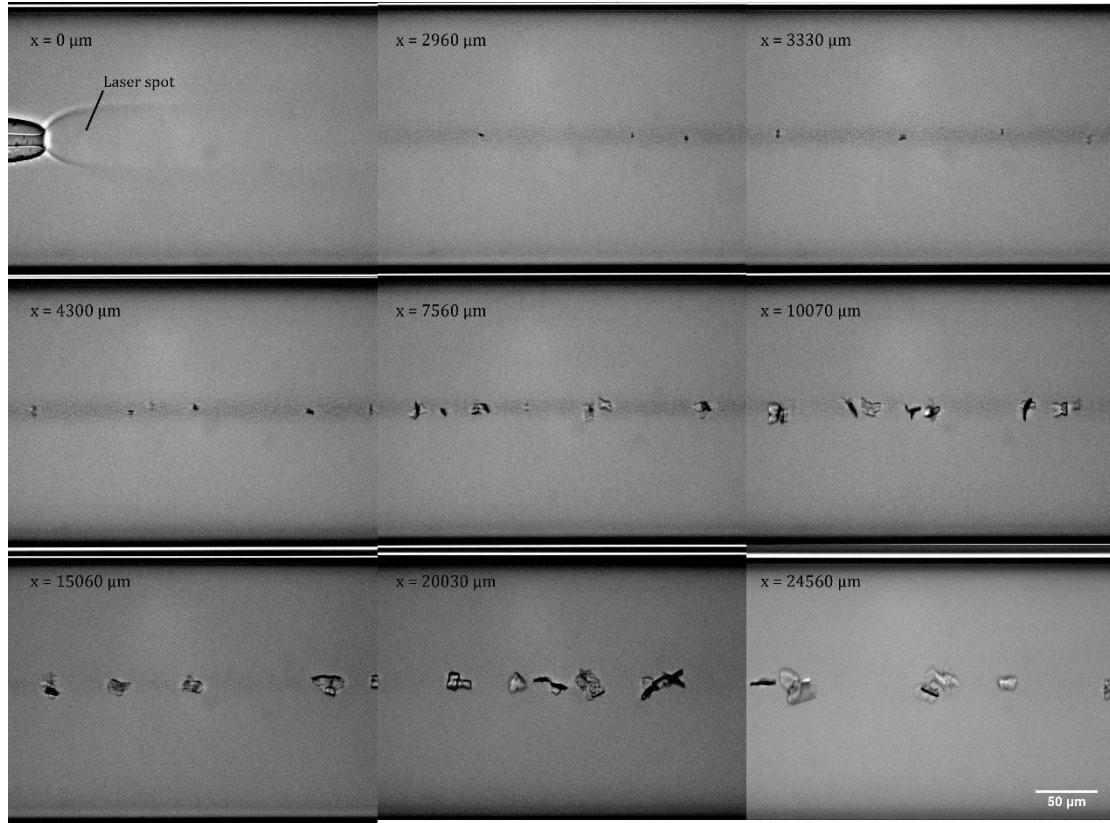


Figure 7.6. Growth process of the crystals induced with half the full laser power. Frames taken from videos of nine measurements. The observational distance from the injection nozzle is noted on the up-left corner of each frame. Microfluidic parameters:

$$\rho_{3c} = 16 \text{ g/l}, Q_c = 400 \text{ nl/min}, \phi_{lp} = 30\%, Q_p = 1 \mu\text{l/min}, \text{ laser parameters:}$$

$$\tau = 400 \text{ fs}, \lambda = 1030 \text{ nm}, f_{\text{rep}} = 10 \text{ MHz}, P_{\text{avg}} = 140 \text{ mW}, \text{LPS}, d_L = 30 \mu\text{m}.$$

The accumulative crystal birth rate B_x has been defined in section 2.1 by equation

(2.3). It is the count rate of crystals at distance x μm , in the unit of s^{-1} . It represents the number of crystals created during $0 \sim x$ μm in the flow *per* unit time. The sectional crystal birth rate

$B_{x1}^{x2} = \frac{B_{x2} - B_{x1}}{x2 - x1}$ (equation (6.3)) is the probability of a crystal to be born during a unit length

between $x1 \sim x2$ μm *per* unit time. This is an easy measure of the nucleation rate of the solute crystals along the microflow. The average nucleation rate on a cross section x μm away from

the nozzle can be calculated as $N = \frac{1}{\pi R_{\text{channel}}^2} \frac{dB_x}{dx}$ (equation (2.4)).

The size distribution and growth rate are also of interest. From the size of crystals' silhouettes on the videos taken at different positions along the flow, the average crystal area size A_c , the size distribution and the area growth rate g_A can be measured. From the width of the crystals L_c , we can also measure the average and distribution of L_c and the one dimensional growth velocity g_L .

From the OM videos taken at different distances along the flow, A_c and its distribution, the nucleation interval t_N and its distribution, and the accumulative crystal birth-rate B_x observed along the flow have been measured using *ImageJ* and plotted in Figure 7.7 for laser-induced and spontaneous crystallisation in the coaxial mixer under the same microfluidic parameters. B_x (open triangle on the upper part of the figure) from both laser-induced (red) and the spontaneous crystals (olive) rose from 0 at $x = 2$ mm and reached a plateau after $x = 5$ mm, of 20 s^{-1} for the laser induced and of 4 s^{-1} for the spontaneous. The range of distance for nucleation is the same, but the laser-induced B_x increased dramatically between 2~3 mm and reached 4 to 5 times as large. This is accompanied by a deeper drop of the average nucleation event interval t_N (dot on the upper part of the figure, red for the laser-induced and olive for the spontaneous). The distribution (hatched bars plotted over vertical lines at the corresponding distance) of the nucleation intervals for each position is an exponential decay (curve covering the histogram on the upper part of the figure), as expected for a random event occurring with a

constant probability. The sectional crystal birth rate B_{x1}^{x2} (dashed sectional lines) and the deduced nucleation rate N (solid curves) are plotted on the middle part of Figure 7.7. The spontaneous nucleation rate (olive solid curve on the middle part) is practically zero compared with the laser-induced (red solid curve on the middle part). The laser-induced nucleation rate also declined to nearly zero after $x = 6$ mm. The nucleation rate before 2 mm is not defined. The IR laser was focused 30 μm from the nozzle, nevertheless crystals were not observed until 2 mm away. This suggests that the fs IR laser was able to induce pre-clusters that survived and aggerated later. After 2 mm, the growth of crystals started to be seen. More crystals were observed at 3 mm. *Comsol* simulation of the mass concentration and of the supersaturation (Figure 6.23) shows that there is an antisolvent focusing of the solute shortly after the injection nozzle. The concentration reaches maximum around $x = 300$ μm from the nozzle with a supersaturation ratio β of 6. Our fs IR NPLIN laser was focused before this point at $x = 30$ μm , during the process of the rise of the concentration. Simulation also shows that the concentration will decline to minimum with β of 2.3 after 6 mm. After that, the environment becomes constant. On Figure 7.7, the average area of crystals (square on the bottom part) of both spontaneous (olive) and laser-induced (red) crystals grew linearly with distance and the size distribution (vertically plotted red hatched bar with a covering curve) became increasingly broad. The fitted area growth rate of laser induced crystals $g_A = 9.17 \mu\text{m}^2/\text{s}$ with a growth rate constant $k = 4.45 (\mu\text{m}^2/\text{s})/(\text{g/l})$. It is not different from g_A of spontaneously born crystals ($g_A = 9.8 \mu\text{m}^2/\text{s}$, $k = 4.75 (\mu\text{m}^2/\text{s})/(\text{g/l})$, see Figure 6.27). The distance d_p where they started to be observed and the rate g_A they grew was not significantly different. This, again, suggests that laser created pre-clusters that behaved as the spontaneous ones. The major difference is the birth rate.

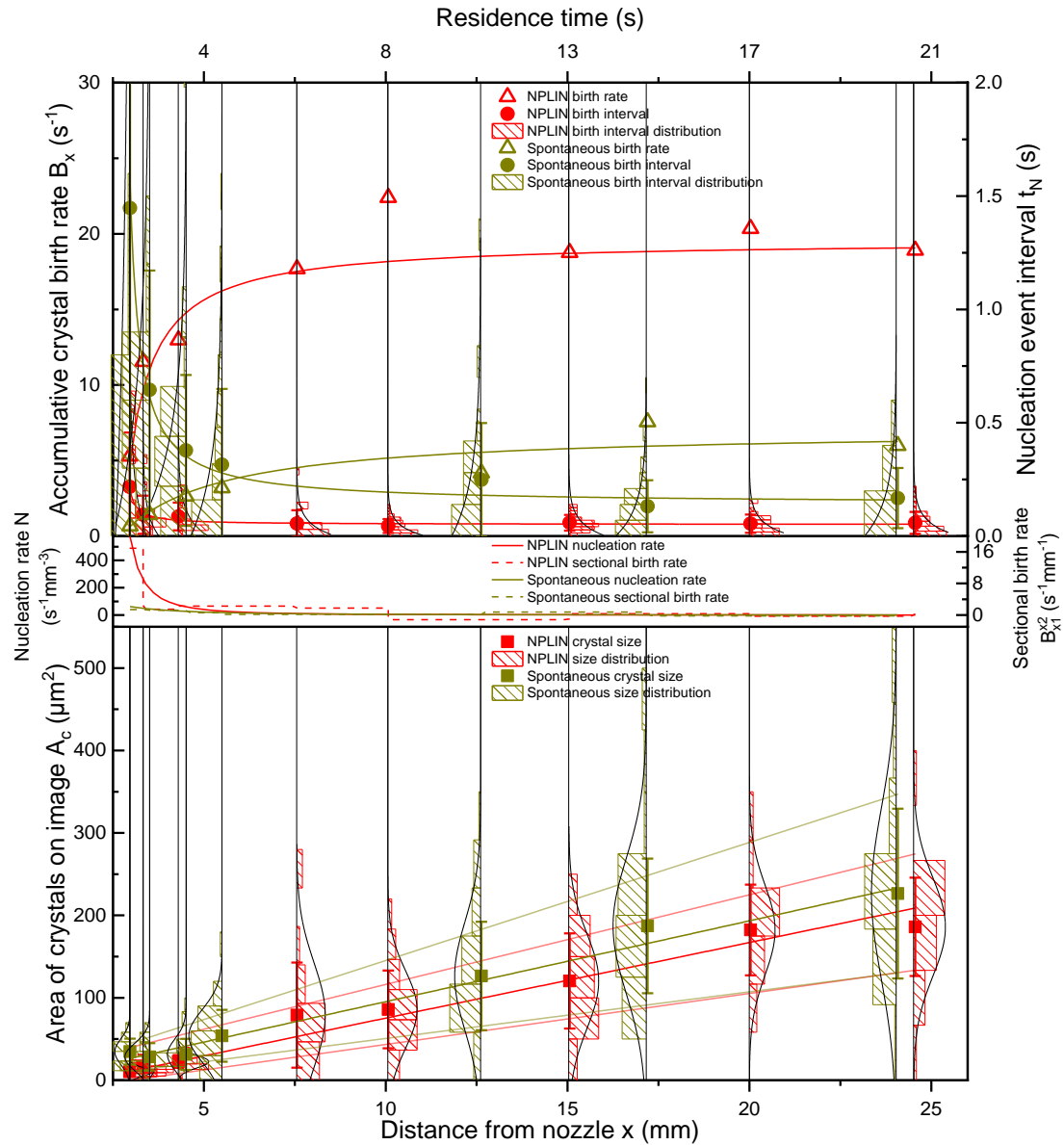


Figure 7.7. Comparison the nucleation rate and the growth rate between laser-induced (red) and spontaneous crystallisation (olive) under the same microfluidic conditions in the coaxial mixer measured by OM. Top: the accumulative (from nozzle to x) crystal birth rate B_x (open triangle), the average nucleation event interval t_N (circle), histogram of t_N (vertically plotted hatched bar) and distribution of t_N (curve covering the histogram). Middle: the sectional crystal birth rate B_{x1}^2 (dashed line) and the deduced spontaneous nucleation rate N (solid curve). Bottom: the average

crystal silhouette area A_c (square), histogram of A_c (hatched bar plotted vertically)

and its distribution (curve covering the histogram). Microfluidic parameters:

$$\rho_{3c} = 16 \text{ g/l}, Q_c = 148 \text{ nl/min}, \phi_{lp} = 30\%, Q_p = 1 \mu\text{l/min}, \text{ laser parameters:}$$

$$\tau = 400\text{fs}, \lambda = 1030\text{nm}, f_{\text{rep}} = 10\text{MHz}, P_{\text{avg}} = 140\text{mW, LPS}, d_L = 30\mu\text{m}.$$

OM can only give the size, number, velocity, and shape of the crystals. Also, it is limited by the diffraction limit. But FLIM can provide additional information as the change in the organisation of the AIE molecules will be reflected on their fluorescence lifetimes. Therefore, the same microfluidic NPLIN experiment was measured by FLIM (Figure 7.8). It gave the lifetime distribution of the crystals (Figure 7.9). By the comparison of the fluorescence lifetime distribution, the impact of laser on the polymorphism can be investigated. In addition, its signal analysis for the particle detection and size measurement can be done with less human time.

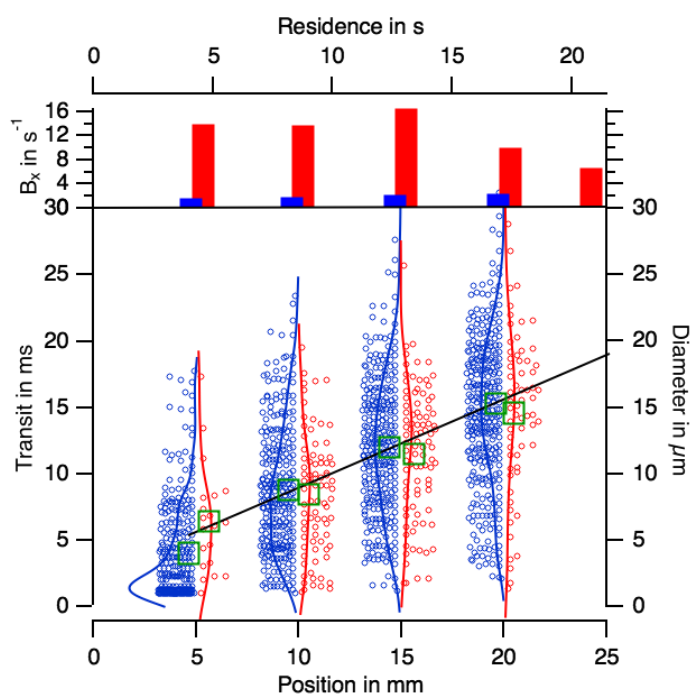


Figure 7.8. Comparison of the FLIM measurement of the laser-induced nucleation (red) and spontaneous nucleation (blue) of DBDCS in the coaxial microflow of water (1)-1,4-dioxane (2). Top: The accumulative (from nozzle to x) crystal birth rate B_x .

Bottom: The diameter (empty circles) of the crystals was measured for each crystal at different positions along the flow. The average size (empty green square), the growth rate and the size distribution (solid curve covering the circles) are the same for both type of crystals. Only the birth rate B_x of crystals has been multiplied by 8.

Microfluidic parameters: $\rho_{3c} = 16 \text{ g/l}$, $Q_c = 148 \text{ nl/min}$, $\phi_{lp} = 30\%$, $Q_p = 1 \mu\text{l/min}$,

NPLIN laser parameters:

$\tau = 400\text{fs}$, $\lambda = 1030\text{nm}$, $f_{\text{rep}} = 10\text{MHz}$, $P_{\text{avg}} = 140\text{mW}$, LPS, $d_L = 30\mu\text{m}$. FLIM laser

parameter: $\tau = 400\text{fs}$, $\lambda = 343\text{nm}$, $f_{\text{rep}} = 10\text{MHz}$.

Figure 7.8 confirms the OM observation. The laser-induced B_x is 1 order of magnitude higher than the spontaneous. The size distribution and growth rate for both laser-induced and spontaneous crystals are not significantly different.

Figure 7.9 provides additional information on the polymorphs by the lifetime distribution of both laser-induced (in red) and spontaneous (in blue) crystals observed along the flow. The lifetime of each crystal was analysed and then plotted (empty circles) vertically at the corresponding distance of measurement. In both cases, there are three polymorphs: crystal_7.10_1_cd_1_NPLIN = 20 ns, crystal_7.10_2_cd_1_NPLIN = 10 ns, crsytal_7.10_3_cd_1_NPLIN = 5 ns, for NPLIN; crystal_7.10_1_cd_1 = 20 ns, crystal_7.10_2_cd_1 = 10 ns, and crystal_7.10_3_cd_1 = 5 ns, for the spontaneous. The majority had a lifetime of 20 ns. Secondly condensed was the lifetime of 5 ns. There were a few particles with a lifetime of 10 ns. No significant difference in the lifetime of DBDCS crystals was observed with and without laser. No impact of the laser on the polymorphism was observed. It must be noticed that, due to the short residence time of each crystals in front of the detector, the determination of the lifetime presents a large discrepancy, especially when the crystals are small i.e. at short distance from the nozzle.

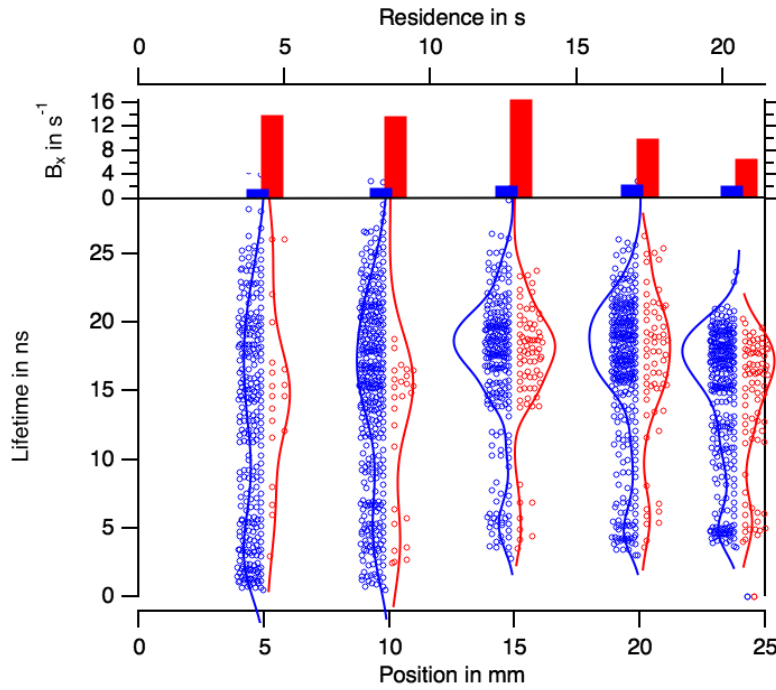


Figure 7.9. The fluorescence lifetime distribution (the curve covering the circles plotted vertically at the distance from nozzle) of laser-induced (red) and the spontaneous (blue) DBDCS crystals measured along the coaxial microflow of water (1)-1,4-dioxane (2). Three polymorphs at 20ns, 5ns and some crystals at 10 ns were formed in the same proportions for both spontaneous and NPLIN crystals.

Microfluidic parameters: $\rho_{3c} = 16 \text{ g/l}$, $Q_c = 148 \text{ nl/min}$, $\phi_{lp} = 30\%$, $Q_p = 1 \mu\text{l/min}$,

NPLIN laser parameters:

$\tau = 400\text{fs}$, $\lambda = 1030\text{nm}$, $f_{\text{rep}} = 10\text{MHz}$, $P_{\text{avg}} = 140\text{mW}$, LPS, $d_L = 30\mu\text{m}$. FLIM laser

parameter: $\tau = 400\text{fs}$, $\lambda = 343\text{nm}$, $f_{\text{rep}} = 10\text{MHz}$.

7.1.3. Impact of laser parameters on laser-induced crystallisation in microfluidics

7.1.3.1. Impact of laser induction position along the flow

Comsol simulation (Figure 6.23) shows that both concentration and supersaturation ratio β of DBDCS at the flow centre rises to a maximum and then decreases to a constant. The

change is dramatically large. This suggests that, with the same microfluidic parameters, if the same laser is sent to different distances from the injection nozzle d_L , the effect could be different.

To investigate the impact of d_L , the IR laser ($f_{\text{rep}} = 10\text{MHz}$ and $p_{\text{avg}} = 135\text{mW}$) was focused at different distances, and the induced crystals were observed at the same position $x = 10050\mu\text{m}$ by OM videos (Figure 7.10). The average power was low on purpose, firstly to avoid the production of too many crystals, secondly to avoid bubble. From the videos, the number of crystals *per* frame increased with d_L (marked on figures) between 30~3000 μm , reached maximum near the spontaneous nucleation position (see section 6.6.4 and 7.1.2). After that, it decreased dramatically to zero, at which point the induced objects changed from crystals to a line of small amorphous phase.

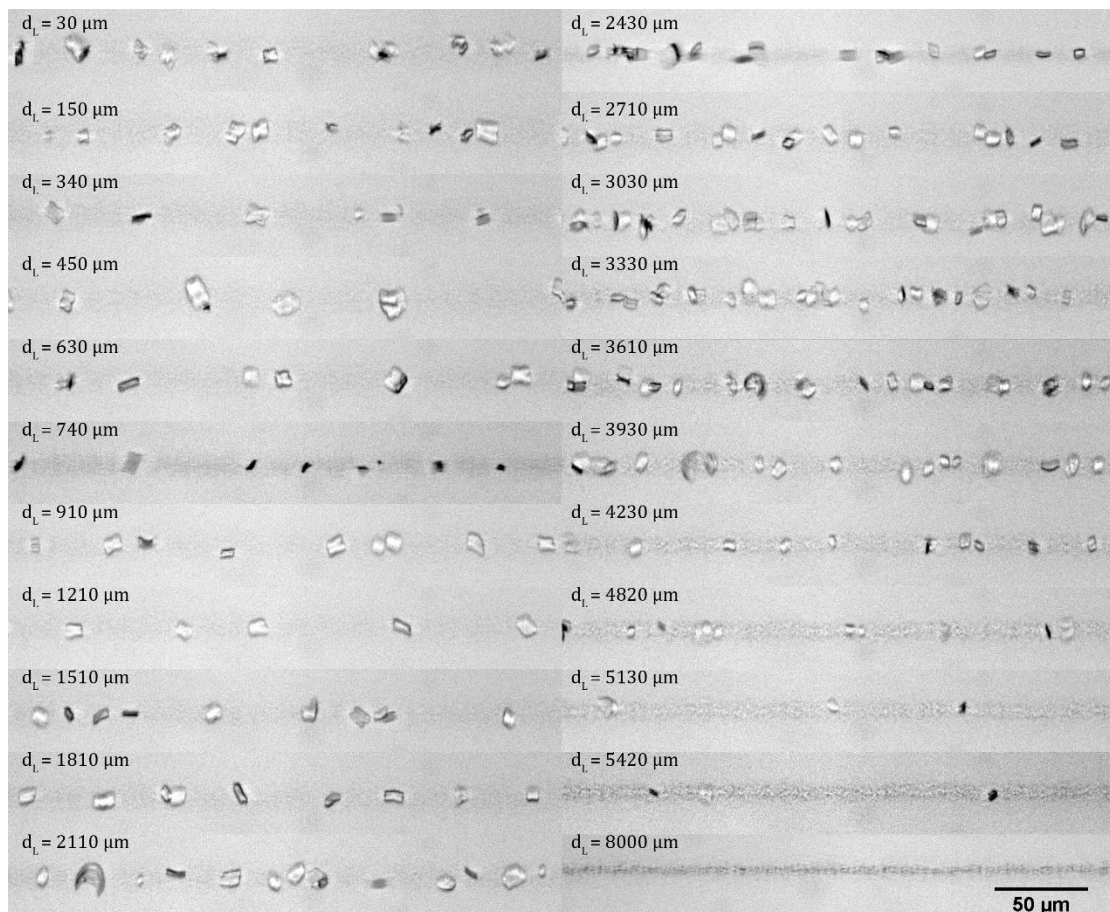


Figure 7.10. Impact of laser induction position. Laser was turned on at different

distance d_L to the nozzle. The videos of laser-induced crystals were taken at 10050 μm . The effect of laser increased with d_L (marked on figures), reached its maximum near the spontaneous nucleation position, and then decreased dramatically. The induced objects changed from crystals to small amorphous phase. Microfluidic parameters: $\rho_{3c} = 16 \text{ g/l}$, $Q_c = 148 \text{ nl/min}$, $\phi_{fp} = 30\%$, $Q_p = 1 \mu\text{l/min}$. Laser

parameters:

$$\tau = 400\text{fs}, \lambda = 1030\text{nm}, f_{\text{rep}} = 10\text{MHz}, P_{\text{avg}} = 135\text{mW}, \text{LPS}, d_L = 30\sim 8000\mu\text{m}.$$

The laser-induced $B_{10\text{mm}}$ were measured from the videos and plotted against the induction distance d_L on Figure 7.11 together with the *Comsol* simulation of the mass concentration and supersaturation ratio of DBDCS at the flow centre. $B_{10\text{mm}}$ rose to maximum around $d_L = 3330\mu\text{m}$ and then declined to almost zero within 2000 μm . The spontaneous $B_{10\text{mm}}$ is 4 s^{-1} and reported in green on Figure 7.11. The place where the first spontaneous crystals are detected (2000 microns) is indicated (dashed line). One can distinguish 3 values: i) for $30\mu\text{m} \leq d_L \leq 2000\mu\text{m}$, $\overline{B_{10\text{mm}}} = 23\text{s}^{-1}$; ii) the maximum $B_{10\text{mm}} = 69\text{s}^{-1}$ when $d_L = 3330\mu\text{m}$; iii) the minimum $B_{10\text{mm}} = 1.3\text{s}^{-1}$ when $d_L = 8000\mu\text{m}$.

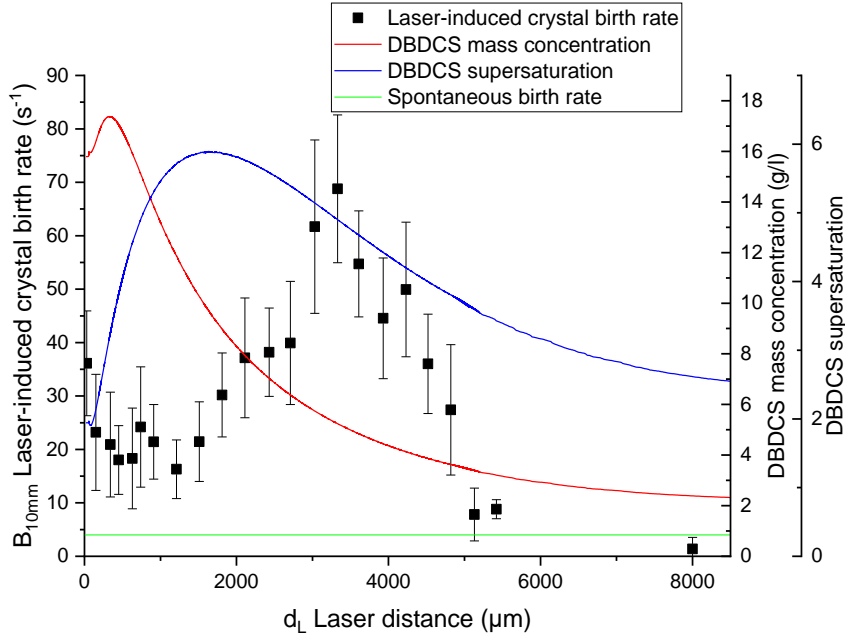


Figure 7.11. The impact of the laser induction position d_L on the laser-induced crystal birth-rate $B_{10\text{mm}}$. The spontaneous crystal birth rate accumulated at 10 mm is reported as the green line for comparison. The red line is the Comsol simulation of the DBDCS mass concentration along the flow centre and the blue line its supersaturation. Microfluidic parameters:

$$\rho_{3c} = 16 \text{ g/l}, Q_c = 148 \text{ nl/min}, \phi_{lp} = 30\%, Q_p = 1 \mu\text{l/min} . \text{ Laser parameters:}$$

$$\tau = 400\text{fs}, \lambda = 1030\text{nm}, f_{\text{rep}} = 10\text{MHz}, P_{\text{avg}} = 135\text{mW}, \text{LPS}, d_L = 30\sim 8000\mu\text{m} .$$

7.1.3.2. Impact of laser power

The Impact of the average power P_{avg} of the femtosecond IR laser that reached the flow centre on the number of induced crystals was investigated by turning the half-wave plate from 0° to 45° with steps of 5° (see section 2.2). The laser power P_r was measured at the exit of the pulse picker and then calculated by equation (2.28) for the energy reached the focal point in the flow. The laser was turned on for around 3 seconds at the flow centre $30 \mu\text{m}$ away from the injection nozzle. Videos for each measurement was recorded by moving the field of view immediately to $10100 \mu\text{m}$ away from the injection nozzle. The laser-induced crystals can be

distinguished from the spontaneous crystals by the birth rate $B_{10\text{mm}}$.

Figure 7.12 shows frames taken from videos of DBDCS crystals induced by different laser power. The number of laser-induced DBDCS crystal *per* frame declined with the IR laser power, whereas the average size slightly increased. When $P_{\text{avg}} \leq 50\text{mW}$, the laser-induced crystals were no longer distinguishable from the spontaneous by the count rate.

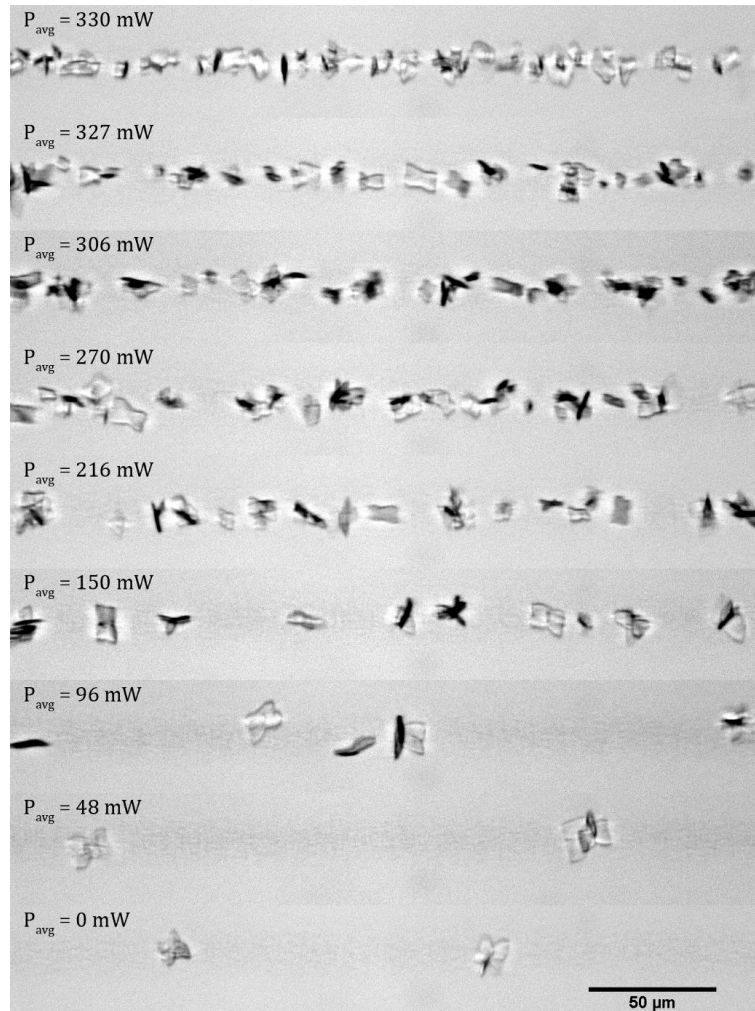


Figure 7.12. Impact of IR laser power P_{avg} on induced crystals. Observed 10100 μm

from the nozzle. Microfluidic parameters:

$\rho_{3c} = 16\text{g/l}$, $Q_c = 148\text{nl/min}$, $\phi_{1p} = 30\%$, $Q_p = 1\mu\text{l/min}$. Laser parameters:

$$\tau = 400\text{fs}, \lambda = 1030\text{nm}, f_{\text{rep}} = 10\text{MHz}, \text{LPS}, d_L = 30\mu\text{m}.$$

The average laser-induced $B_{10\text{mm}}$ of each P_{avg} was measured from the videos and plotted on Figure 7.13. $B_{10\text{mm}}$ increases linearly with P_{avg} with a threshold ($P_{\text{avg}} < 50\text{mW}$). This agrees with almost all static NPLIN papers where the impact of the laser power has been studied: the higher the laser power is, the higher the nucleation efficiency is. Furthermore, the authors ([Ikni, 2014, Li, 2016b]) have established that there is a threshold (a value under which there is no nucleation) and a plateau (nucleation does not any more increase).

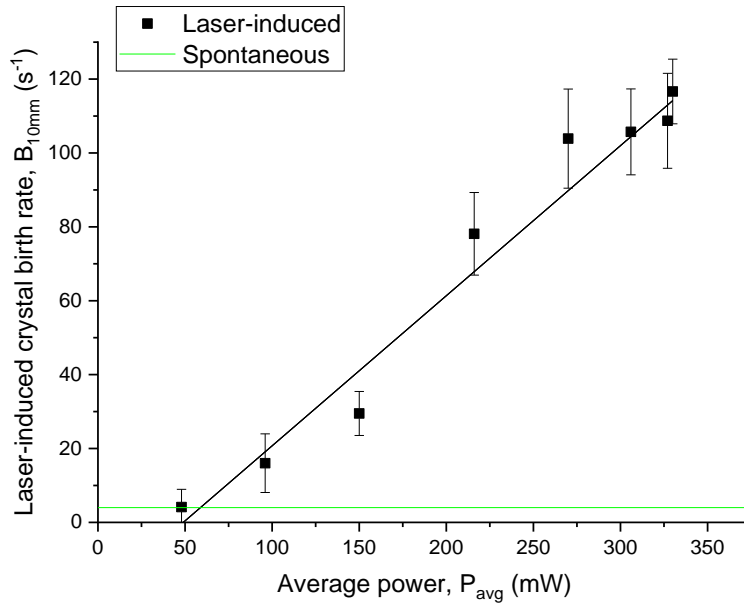


Figure 7.13. Impact of laser average power P_{avg} on laser-induced crystal the birth rate $B_{10\text{mm}}$. The spontaneous crystal birth rate accumulated at 10 mm is reported as

the green line for comparison. Microfluidic parameters:

$$\rho_{3c} = 16\text{g/l}, Q_c = 148\text{nl/min}, \phi_{lp} = 30\%, Q_p = 1\mu\text{l/min}. \text{ Laser parameters:}$$

$$\tau = 400\text{fs}, \lambda = 1030\text{nm}, f_{\text{rep}} = 10\text{MHz}, \text{LPS}, d_L = 30\mu\text{m}.$$

Figure 7.14 qualitatively shows the size of crystals formed from the same microfluidic parameters at the same distance from the injection nozzle and under different P_{avg} .

Spontaneous nucleation produced the smallest number of crystals, which had grown to the biggest size. Whereas with full IR laser power, a large number of crystals was induced at the flow centre, but with a smaller size. This is a competition between thermodynamic and kinetics, for example the growth of a large number of crystals consumes faster the solute concentration. This behaviour has also observed in static NPLIN on sulfathiazole [Li, 2016b] by changing the exposition time (smaller size and more crystals at low exposition time i.e. at less pulse number).

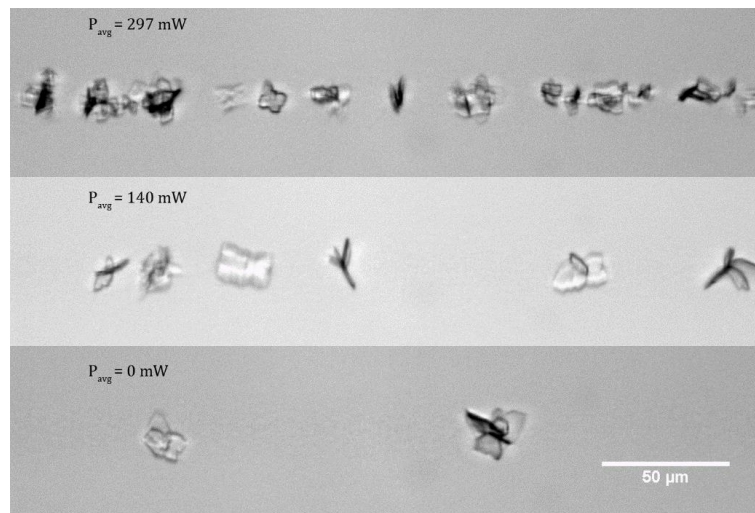


Figure 7.14. Size of laser-induced crystals decreased with laser average power P_{avg} .

Microfluidic parameters: $\rho_{3c} = 16 \text{ g/l}$, $Q_c = 148 \text{ nl/min}$, $\phi_{lp} = 30\%$, $Q_p = 1 \mu\text{l/min}$.

Laser parameters: $\tau = 400\text{fs}$, $\lambda = 1030\text{nm}$, $f_{rep} = 10\text{MHz}$, LPS, $d_L = 30\mu\text{m}$.

7.1.3.3. Impact of laser repetition rate

The impact of the repetition rate of the IR laser was measured by OM in the similar way than the NPLIN growth rate study by chasing (moving the microscope stage faster than the flow along the flow direction to a pre-set distance and then intercept the flow crystals with the camera or detector) the crystals after laser induction. The repetition rate f_{rep} change from 10 to 1 MHz. Laser was focused $30 \mu\text{m}$ away from the injection nozzle at the flow centre for around 3 seconds. After the laser was turned off, the field of view was moved quickly to $10100 \mu\text{m}$ from the nozzle to wait for the induced crystals. The half-wave plate was optimised to 11°

($P_{\text{avg}} = 0.123 \cdot P_o \cdot \cos^2 2\theta$, see section 2.2 and Appendix B.viii) lest the nucleation rate be too high and induced crystals overlap together. In this comparison, the energy of each pulse was the same, yet the number of pulses received by the flow was different. The average power P_{avg} decreased from 315 to 20 mW, accordingly. Frames taken from the OM videos are displayed in Figure 7.15. It qualitatively illustrates that the nucleation rate decreased with f_{rep} , meanwhile the size increased. When $f_{\text{rep}} \leq 2\text{MHz}$, laser-induced nucleation rate was so low that it was no longer distinguishable from the spontaneous crystallisation. Therefore, repetition rates lower than 1MHz were not recorded. That means that we have determined a threshold value under which the NPLIN nucleation efficiency is zero.

The repetition rate was changed from 10 to 1 MHz. The average power P_{avg} decreased from 315 to 20 mW, accordingly, because of the reduction of the number of laser pulses. The peak power of the laser pulses was constant. The laser-induced $B_{10\text{mm}}$ was measured for each repetition rate and plotted against the laser average power P_{avg} in Figure 7.16. The points obtained at reduced repetition rates overlap with those obtained with the same power at 10 MHz. The change in the power fully describes the effect of the change in the laser repetition rate. Therefore, we can finally conclude that the laser repetition rate has no visible effect on the nucleation rate.

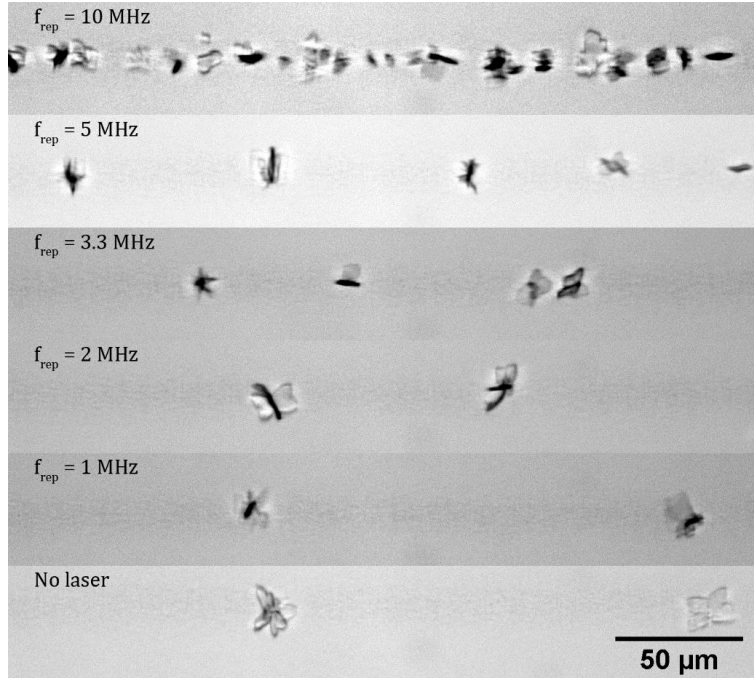


Figure 7.15. Impact of laser repetition rate f_{rep} on laser-induced crystals. Frames

from OM videos taken 10100 μm from the nozzle. Microfluidic parameters:

$\rho_{3c} = 16 \text{ g/l}, Q_c = 148 \text{ nl/min}, \phi_{lp} = 30\%, Q_p = 1 \mu\text{l/min}$. Laser parameters:

$\tau = 400\text{fs}, \lambda = 1030\text{nm}, f_{\text{rep}} = 1\sim 10\text{MHz}, P_{\text{avg}} = 315\sim 20\text{mW}, \text{LPS}, d_L = 30\mu\text{m}$.

We have gathered all the microfluidic NPLIN experiment with the same microfluidic parameters ($\rho_{3c} = 16 \text{ g/l}, Q_c = 148 \text{ nl/min}, \phi_{lp} = 30\%, Q_p = 1 \mu\text{l/min}$) induced at $d_L = 30\mu\text{m}$ by different repetition rate f_{rep} with the same polarisation LPS. The laser-induced $B_{10\text{mm}}$ of these measurements were plotted against the laser average power P_{avg} in Figure 7.16. Below 50mW, the laser-induced $B_{10\text{mm}}$ was practically zero and could not be distinguished from the spontaneous. From 50 mW to 350 mW, $B_{10\text{mm}}$ increased linearly with P_{avg} .

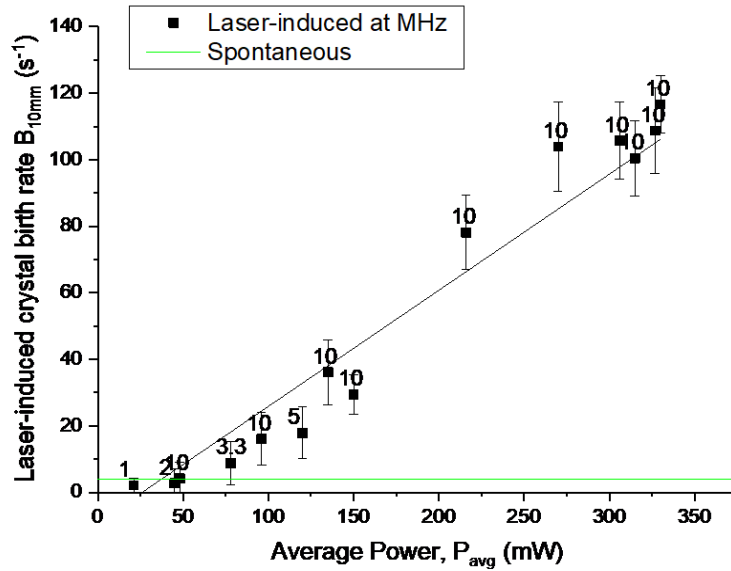


Figure 7.16. Cross comparison of the impact of laser average power P_{avg} on laser-induced crystal birth rate B_{10mm} at different repetition rate f_{rep} (labelled next to the points). The spontaneous crystal birth rate accumulated at 10 mm is reported as the green line for comparison. Microfluidic parameters:

$$\rho_{3c} = 16 \text{ g/l}, Q_c = 148 \text{ nl/min}, \phi_p = 30\%, Q_p = 1 \mu\text{l/min}. \text{ Laser parameters:}$$

$$\tau = 400\text{fs}, \lambda = 1030\text{nm}, f_{rep} = 1\sim 10\text{MHz}, P_{avg} = 315\sim 20\text{mW}, LPS, d_L = 30\mu\text{m}.$$

7.1.3.4. Impact of laser polarisation

Static NPLIN has shown that laser is able to shorten the crystallisation induction period of supersaturated solutions from days to minutes and its polarisation has an impact on the induced polymorphs (see for example [Clair, 2014, Ikni, 2014, Li, 2016b]). Three sets of microfluidic NPLIN experiment was conducted to examine the impact of the polarisation of the IR laser on the induced DBDCS crystals. The first set NPLIN was conducted at $d_L = 3300\mu\text{m}$ (the maximum NPLIN nucleation rate induction position) with full power and repetition rate ($P_{avg} = 297\text{mW}$, $f_{rep} = 10\text{MHz}$). The second set was induced at $d_L = 30\mu\text{m}$ with maximum P_{avg} and f_{rep} , and the third set also at $d_L = 30\mu\text{m}$ with full f_{rep} but P_{avg}

(135mW). OM transmission videos of the induced crystals were taken at $x = 10100\mu\text{m}$. For each set, the measurement was repeated with linear polarisation perpendicular to the flow direction (LPS), linear polarisation parallel to the flow direction (LPP) and circular polarisation (CP) respectively.

Frames of the videos are shown in Figure 7.17. No significant difference in the laser-induced nucleation rate was observed by changing the laser polarisation, in all three conditions. Yet it is still true that the higher the average power, the higher the nucleation rate, and thus the earlier they competed for the limited number of DBDCS molecules. Therefore, the final average crystal size of a higher nucleation rate was smaller than that of a smaller nucleation rate.

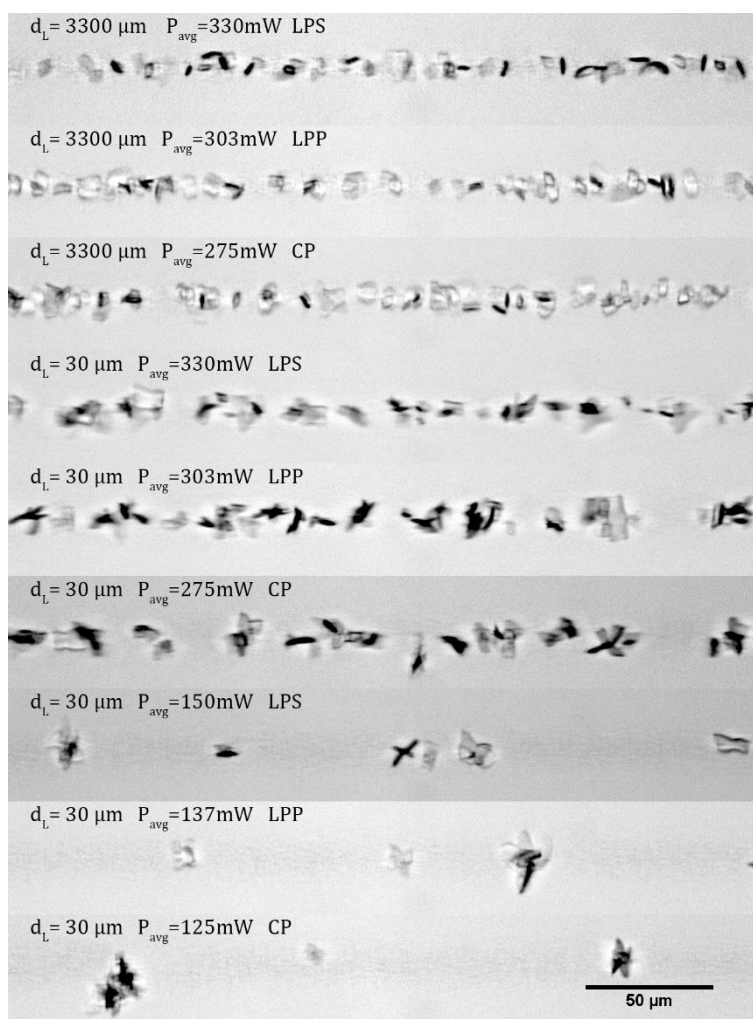


Figure 7.17. The impact of laser polarisation on the laser-induced DBDCS crystal from water (1)-1,4-dioxane (2) mixture. Microfluidic parameters:

$\rho_{3c} = 16 \text{ g/l}, Q_c = 148 \text{ nl/min}, \phi_{lp} = 30\%, Q_p = 1 \mu\text{l/min}$. Laser parameters:

$$\tau = 400\text{fs}, \lambda = 1030\text{nm}, f_{\text{rep}} = 10\text{MHz}.$$

$B_{10\text{mm}}$ was calculated from the videos and plotted against laser parameters in Figure 7.18. No significant impact of laser polarisation could be determined from the result. Furthermore, the crystal habit (butterfly) remains the same. We have not studied the impact of laser polarisation by fluorescence, so we cannot have an idea of the laser impact at the birth of the crystal (in the first few ms).

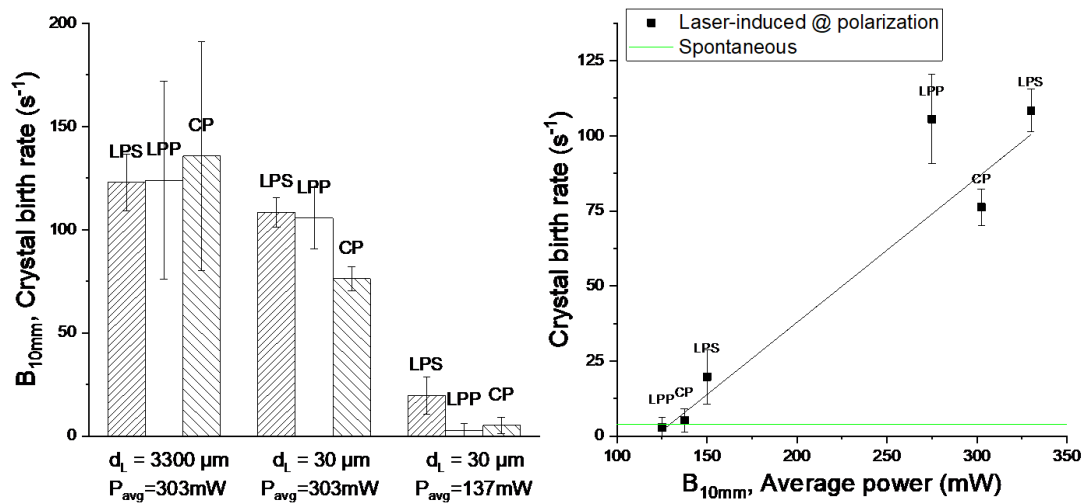


Figure 7.18. Impact of laser polarisation on the accumulative crystal birth rate $B_{10\text{mm}}$ of DBDCS in the coaxial microflow of water (1)-1,4-dioxane (2). The spontaneous crystal birth rate accumulated at 10 mm is reported as the green line for comparison.

Microfluidic parameters: $\rho_{3c} = 16 \text{ g/l}, Q_c = 148 \text{ nl/min}, \phi_{lp} = 30\%, Q_p = 1 \mu\text{l/min}$.

Laser parameters: $\tau = 400\text{fs}, \lambda = 1030\text{nm}, f_{\text{rep}} = 10\text{MHz}$.

7.1.4. Post-mortem characterisation of NPLIN crystals

Laser-induced crystals were collected on glass slides at the exit of the microfluidic channel. The three-dimensional crystal habit of the “butterfly” DBDCS crystals were not observed outside the microfluidic system. Only piles of plate-like DBDCS crystals were seen.

As expected, the number of crystals were much larger than spontaneous crystals. This is the same situation than for the spontaneous nucleation (section 6.2.2).

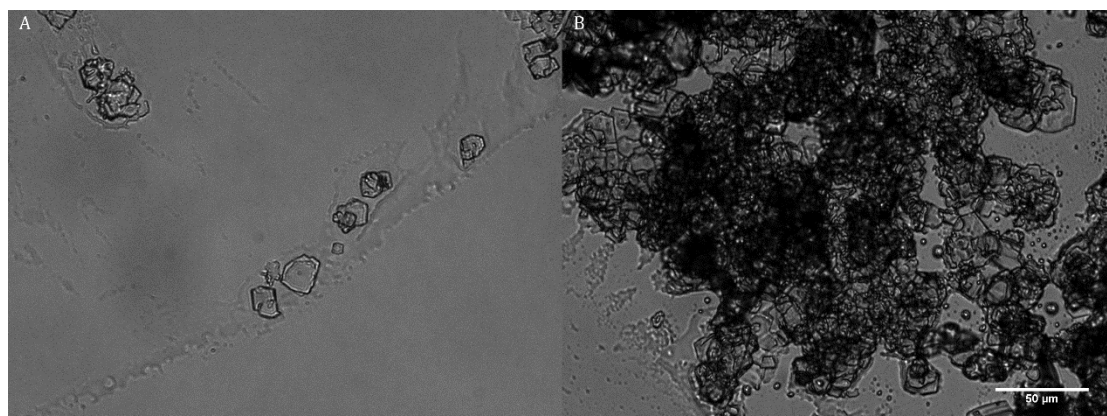


Figure 7.19. Post-mortem OM image of collected laser-induced crystals on glass slides.

7.2. Laser's effect on LLPS and droplets

7.2.1. Laser dragging the central-peripheral flow interface

As described in 2.1.1, the interface between the central flow jet and the peripheral flow was seen after the injection nozzle. The effect of our femtosecond laser on this liquid interface was tested. In Figure 7.20A the central jet diameter was narrowed by the laser and in Figure 7.20B the laser spot dragged the interface away from its original place towards the water's side. These were tested with and without DBDCS. This suggests that our focused femtosecond IR laser was able to interact with solvent molecules without absorption. It is noticeable that the interface is always dragged away from the centre towards the water's side. This agrees with the fact that optical tweezers drag to phases with the higher refractive indices towards the focal point.

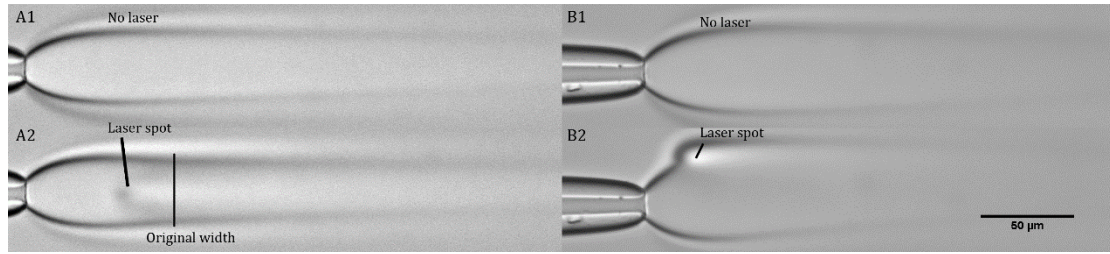


Figure 7.20. The effect of the focused femtosecond IR laser on the interface between the central jet of 1,4-dioxane and the peripheral flow of water. A: focused femtosecond IR laser narrowed the diameter of the central jet flow; B: the laser focus spot dragged the coaxial flow interface away from the original position. No DBDCS was in the flow, only 1,4-dioxane in the centre and water in the periphery.

Parameters: (A) $\rho_{3c} = 0 \text{ g/l}$, $Q_c = 185 \text{ nl/min}$, $\phi_{lp} = 100\%$, $Q_p = 2 \mu\text{l/min}$; (B)

$\rho_{3c} = 0 \text{ g/l}$, $Q_c = 185 \text{ nl/min}$, $\phi_{lp} = 100\%$, $Q_p = 1 \mu\text{l/min}$. Laser parameters:

$$\tau = 400\text{fs}, \lambda = 1030\text{nm}, f_{\text{rep}} = 10\text{MHz}, P_{\text{avg}} = 357\text{mW}, \text{LPS}.$$

7.2.2. Laser accelerating the phase separation and droplets formation

Phase separation of water (1)-1,4-dioxane (2) or water-THF binary systems was not observed without presence of the solute (we have tested DBDCS, caesium acetate, CsCl, Calix-Cousulf-Cs⁺₂) only inter-diffusion and then a single-phase flow. By increasing the concentration of the solute in the ternary system by non-conventional method, such as microfluidics, LLPS followed by droplet formation was observed in the coaxial microfluidic mixer, as described in section 5.6. We have shown in Figure 7.20 that laser was able to drag the transient central-peripheral flow interface without presence of the solute and droplets. What would happen in the case of phase separation and droplet formation? For that, the femtosecond IR laser was focused before the droplet formation position. Its effect is shown in Figure 7.21.

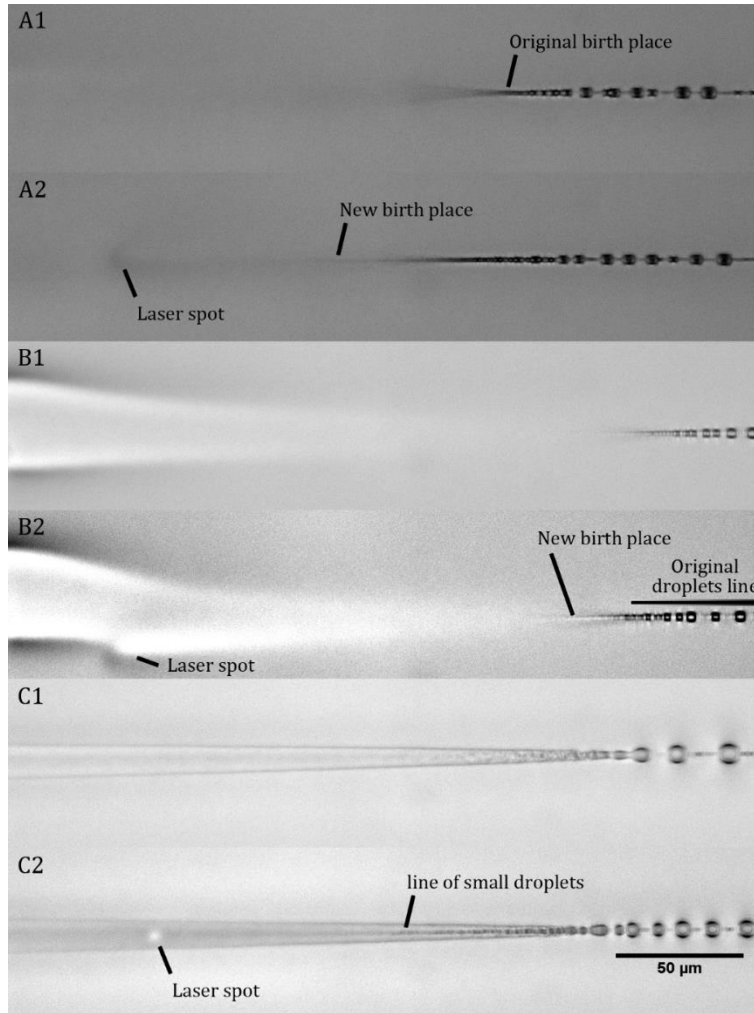


Figure 7.21. Impact of focused IR laser on droplet formation. A: laser brought the droplet formation earlier than the original distance; B: in addition to assisting droplet formation, laser was able to drag the central flow away from the flow centre along with the droplets; C: Laser induced a line of smaller droplets before the original droplet formation position. Parameters: (A)

$$\rho_{3c} = 1 \text{ g/l}, Q_c = 148 \text{ nl/min}, \phi_{lp} = 90\%, Q_p = 2 \mu\text{l/min},$$

$$\lambda = 1030 \text{ nm}, f_{\text{rep}} = 10 \text{ MHz}, \tau = 400 \text{ fs}, P_{\text{avg}} = 357 \text{ mW}, \text{LPS}, d_L = 410 \mu\text{m}; (B)$$

$$\rho_{3c} = 1 \text{ g/l}, Q_c = 74 \text{ nl/min}, \phi_{lp} = 80\%, Q_p = 1 \mu\text{l/min},$$

$$\lambda = 1030 \text{ nm}, f_{\text{rep}} = 10 \text{ MHz}, \tau = 400 \text{ fs}, P_{\text{avg}} = 357 \text{ mW}, \text{LPS}, d_L = 260 \mu\text{m}; (C)$$

$$\rho_{3c} = 5 \text{ g/l}, Q_c = 370 \text{ nl/min}, \phi_{lp} = 100\%, Q_p = 10 \mu\text{l/min},$$

$$\lambda = 1030\text{nm}, f_{\text{rep}} = 10\text{MHz}, \tau = 400\text{fs}, P_{\text{avg}} = 330\text{mW, LPS}, d_L = 610\mu\text{m}.$$

Figure 7.21.A shows laser accelerated droplets formation with a reduced d_p . We have seen laser focusing the 1,4-dioxane flow in Figure 7.20. Therefore, the focusing of 1,4-dioxane increased the focusing of DBDCS by the antisolvent gradient. In fact, d_p was shortened by more than $50\mu\text{m}$ in Figure 7.21.A. DBDCS is an aromatic molecule with a higher n_D than 1,4-dioxane and water. It could contribute to the laser focusing. In Figure 7.21.B, laser was focused at the edge of the central flow jet, in this scenario, not only was the droplet formation distance shortened, it was also shifted laterally. In Figure 7.21.C, the laser induced a line of growing droplets in the flow centre visible by OM around $100\mu\text{m}$ earlier than the original position. This experiment where the LLPS is obtained by a laser tweezer effect can be compared with effect observed in a static mixture by Walton *et al* [Walton, 2018]. They describe the laser effect on the phase transition by adding an electromagnetic energy term in the Gibbs energy. We have illustrated the relation of d_p and v_r^F on microfluidic control parameters (equation (5.4) and

$$(5.5)). d_p \approx \frac{6r_3^* \dot{\mu}}{k_B T} \frac{Q_c}{\ln \frac{\rho_{3c}}{\rho_{3\text{spin}2}} + \phi_{1p} \ln \frac{\rho_{3s2}}{\rho_{3s1}}}. \text{ The fact that laser can shorten } d_p \text{ means suggests}$$

laser was accelerating DBDCS' diffusion towards the flow centre.

7.2.3. Laser releasing the abnormally large droplets from the “droplet trap”

In section 5.6.3, we have shown that a large proportion of antisolvent in the peripheral flow and a slow flow velocity can produce a “droplet trap”. Instead of being carried by the flow, the droplet was suspended or even moved backwards. Crystallisation of the suspended large droplets were observed. Laser was found able to release the abnormally large droplets from the “droplet trap”. Figure 7.22.A and B are two instances where the IR laser released the suspended droplet from the gradient of the antisolvent. Figure 7.22.C shows in steps the process. Without laser, because of the steep anti-solvent gradient and the slow flow velocity, droplets were trapped and flowing backwards after creation. They merge into an abnormally large droplet.

This large droplet was suspended in the flow. This suspension can be stable so long as the flow was not disturbed. When the laser was turned on and focused before the abnormally large droplet, the abnormally large droplet resisted for about 800 ms, during which it crystallised and then was flushed away by the hydrodynamic force. So long as the laser was on, no droplets were flowing back anymore. Therefore, the droplet trap was released by the laser. Yet once the laser was off, a droplet trap reappeared.

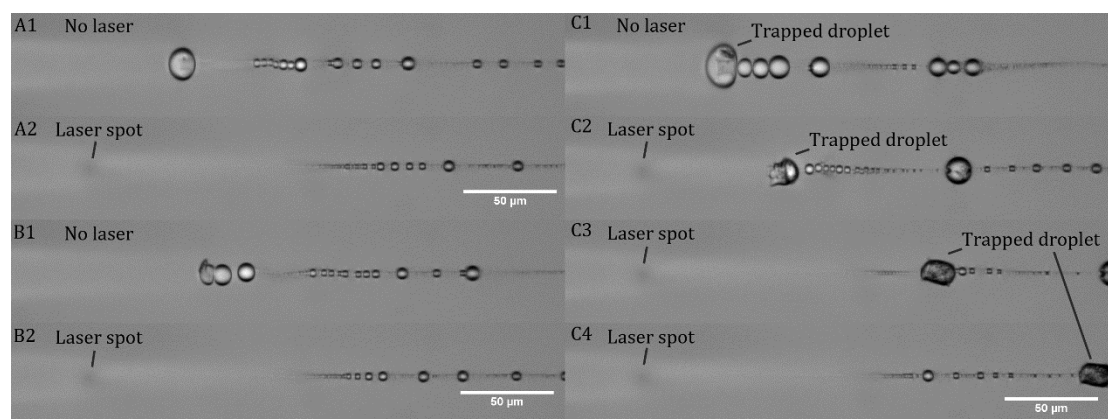


Figure 7.22. A~B: two examples of laser releasing abnormally large droplets from the droplet trap. C: the process how laser released the trapped droplets. C1: with no laser, droplets were flowing to the opposite direction of the flow. An abnormally large droplet was suspended in on the left by the strong anti-solvent gradient. Smaller droplets were merging into it. C2: when the IR laser was focused before the position where the abnormally large droplet was suspended, the trapped droplet started to crystallise. C3: the crystallised droplet was flushed away by the flow. C4: 800 ms later with the laser turned on, no droplets were flow backwards anymore. The droplet trap was therefore released. Microfluidic parameters:

$$\rho_{3c} = 1\text{g/l}, Q_c = 148\text{nl/min}, \phi_{tp} = 90\%, Q_p = 1\mu\text{l/min}, \text{ laser parameters:}$$

$$\tau = 400\text{fs}, \lambda = 1030\text{nm}, f_{\text{rep}} = 10\text{MHz}, P_{\text{avg}} = 330\text{mW}, \text{LPS}, d_L = 150\mu\text{m}.$$

By increasing the contrast of the image, we can see that the IR femtosecond laser has induced a dark line of nano-particles before stabilizing the droplet formation, as shown in

Figure 7.23. It also shows that if the laser spot was moved away from the flow centre, the induced dark line followed the movement of the laser. This proves that the formation of the dark line was correlated with the laser spot. But since the dark line was not in the flow centre, it was pushed towards the flow centre by the anti-solvent focusing. Thus, during the up-down movement of the laser spot, a dark line was observed to swaying after the laser spot.

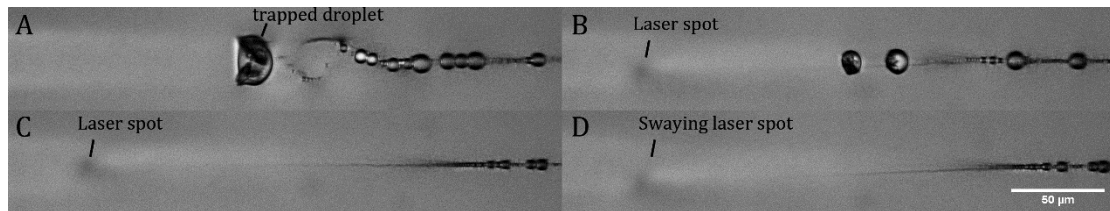


Figure 7.23. By increasing the contrast of the image, it shows laser had induced a dark line before releasing the suspended large droplet. The laser-induced line follows the laser focal spot if we sway the laser up and down. But it was pushed towards the

flow centre by Marangoni effect after 200 μm. Microfluidic parameters:

$\rho_{3c} = 1 \text{ g/l}, Q_c = 148 \text{ nl/min}, \phi_{1p} = 90\%, Q_p = 2 \mu\text{l/min}$, laser parameters:

$\tau = 400\text{fs}, \lambda = 1030\text{nm}, f_{\text{rep}} = 10\text{MHz}, P_{\text{avg}} = 330\text{mW}, \text{LPS}, d_L = 150\mu\text{m}$.

7.2.4. Laser changing the size of the stable droplets

In addition to a reduction of d_p , the femtosecond IR laser was observed to also change the size of the droplets. This is illustrated qualitatively in Figure 7.24. The IR was focused before d_p , the size of the laser assisted droplets was bigger than the spontaneous ones.

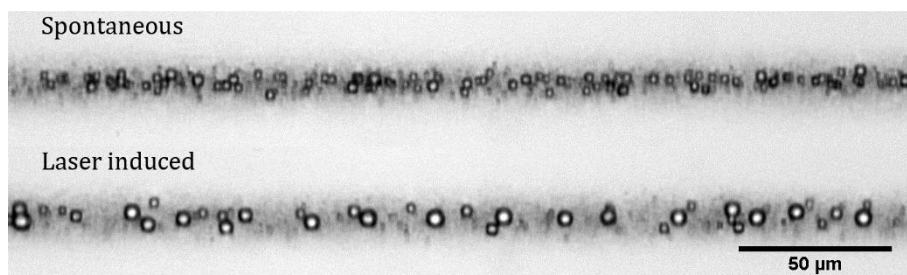


Figure 7.24. Laser's effect on the size of the droplets. The laser assisted droplets were

bigger than the original droplets without laser, yet the population was fewer.

Microfluidic parameters: $\rho_{3c} = 8 \text{ g/l}$, $Q_c = 185 \text{ nl/min}$, $\phi_{1p} = 50\%$, $Q_p = 2 \mu\text{l/min}$. Laser parameters: $\tau = 400\text{fs}$, $\lambda = 1030\text{nm}$, $f_{\text{rep}} = 10\text{MHz}$, $P_{\text{avg}} = 340\text{mW}$, LPS, $d_L = 1050\mu\text{m}$.

7.3. Effect of the focused IR laser of nano-objects

7.3.1. Dark line

In the previous sections, the femtosecond IR laser was focused before the precipitation starting position ($d_L < d_p$). Evidences suggests that the laser is able to focus 1,4-dioxane (2)-DBDCS (3) molecules towards its focal point. We suppose that molecules with larger refractive indices will be focused by the laser. After d_p , spontaneous precipitation started. In this section, we will investigate the effect of the femtosecond IR laser focal spot on the spontaneous precipitation of DBDCS nano-particles in the microflow.

The microfluidic condition of Figure 7.25 is the nanodroplet formation. Without laser, a cylinder of nano-particles of DBDCS was flowing at the flow centre. With the NPILN IR laser focused right after d_p , a dark line was at once formed after the laser spot, whereas the concentration of the nano-objects was reduced outside the dark line. This proves the focused IR laser was able to gather nano-particles towards its centre.

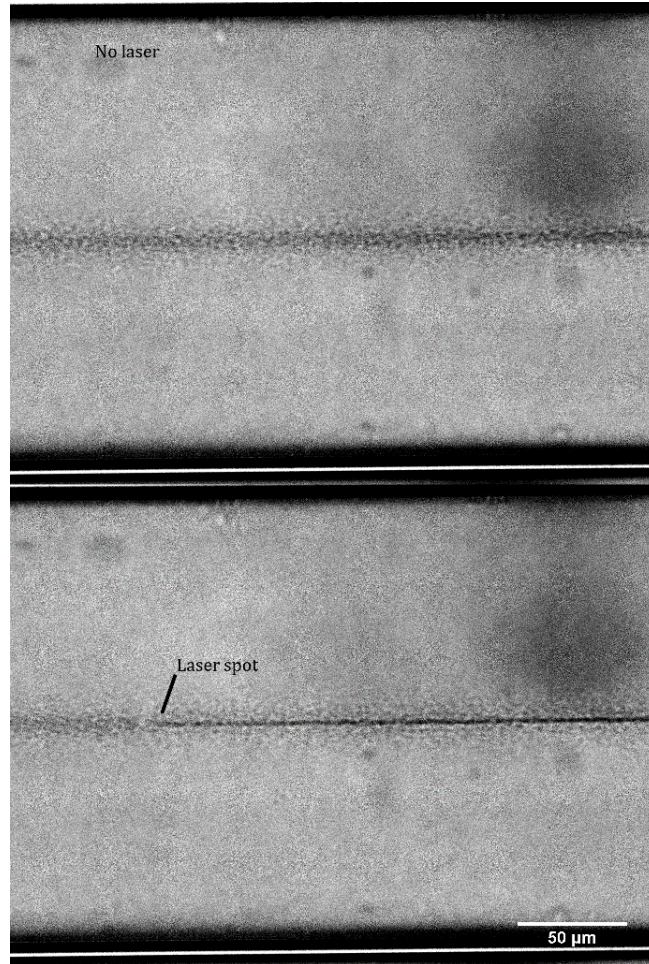


Figure 7.25. Laser induced a dark line in the nano-sized precipitation of DBDCS in the microflow. Microfluidic parameters:

$$\rho_{3c} = 2.3 \text{ g/l}, Q_c = 366 \text{ nl/min}, \phi_{lp} = 50\%, Q_p = 2 \mu\text{l/min}. \text{ Laser parameters:}$$

$$\tau = 400\text{fs}, \lambda = 1030\text{nm}, f_{\text{rep}} = 10\text{MHz}, P_{\text{avg}} = 340\text{mW}, \text{LPS}, d_L = 2000\mu\text{m}$$

7.3.2. Laser-induced two-step crystallisation: droplets→crystals

In Figure 7.26, the concentration of nano-particles was much higher than Figure 7.25, because a higher ρ_{3c} was used. This can be seen on the grey scale of the cylinder of the nano-particles at the flow centre. These nano-objects were amorphous as they appeared dark under CP. 20 mm later, the cylinder of nano-particles became broader, but still consisted of amorphous objects below the diffraction limit of the OM. In this very condensed nano-particle column, the IR laser was focused right after d_p at its full power. A thick dark line appeared

after the laser focal spot. This is the nano-particles gathered by the laser. This time, we were able to illustrate that the dark line gather by the laser is an amorphous liquid phase. It is liquid because it breaks into droplets by Plateau-Rayleigh instability. Some of the droplets became solids after some distances. It is amorphous because it appeared dark under CP. Whereas 10 seconds later, the dried droplets appeared as bright crystals. They had crystallised along the flow. This is a laser-induced two-step nucleation.[Erdemir, 2009]

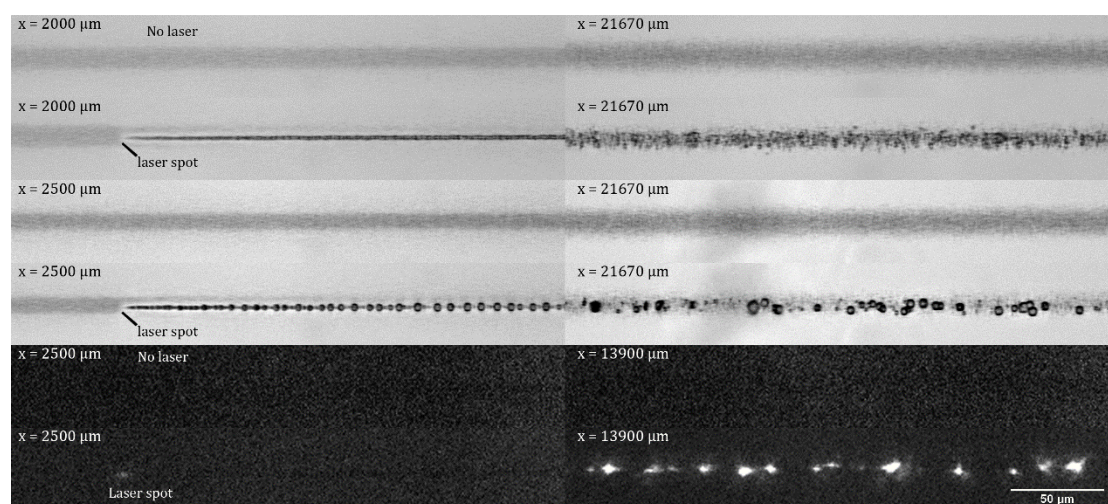


Figure 7.26. OM transmission image and CP image of laser-induced droplet formation from amorphous nano-objects and the crystallisation of the droplets later in the microflow. Without laser, the spontaneous precipitation was a column of nano-objects. These particles are amorphous because they are dark under CP. With the femtosecond IR laser focused at the column of amorphous nano-objects, the nano-objects were gathered to the thick line. This thick line of gathered nano-objects was liquid, because it quickly broke into droplets after the focal spot. These droplets appeared dark under CP shortly after their creation but became bright objects 10 seconds later in the flow. Microfluidic parameter:

$\rho_{3c} = 16 \text{ g/l}, Q_c = 185 \text{ nl/min}, \phi_{1p} = 35\%, Q_p = 0.8 \mu\text{l/min}$. Laser parameters:

$$\tau = 400\text{fs}, \lambda = 1030\text{nm}, f_{\text{rep}} = 10\text{MHz}, P_{\text{avg}} = 340\text{mW}, \text{LPS}.$$

The IR laser focal spot was able to gather nano-particles into a liquid cylinder. This liquid cylinder broke into droplets to reduce the surface tension through Plateau-Rayleigh instability. The droplets crystallised within a few seconds. Two mechanisms can contribute to the observation of the faster development of a crystal phase in bigger droplets. Firstly, if the nanoparticle is smaller than the size of the nucleus, crystallisation will never occur in that particle [Hammadi, 2013]. Secondly, if nevertheless the nucleation does occur in the particle, the crystal size will be limited to the size of the nanoparticle and might be too small to be detected through crossed polarisers. By merging nano-droplets into bigger droplets, the laser favoured the transition from amorphous to the crystalline phase.

7.3.3. Laser-induced bubbles on nano-precipitates' surface

The formation of bubble by focusing a laser in a supersaturated solution has been propose as an NPLIN mechanism.[Nakamura, 2007, Knott, 2011b, Sugiyama, 2011, Yoshikawa, 2014] After the formation of the bubble, heterogeneous nucleation occurs. We have indeed observed bubble formation by laser in the coaxial microflow.

In Figure 7.25 and Figure 7.26, the IR laser was focused on the nano-precipitation. We have noticed that there was a limit d_{bubble} . If $d_p < d_L < d_{\text{bubble}}$, the nano-precipitation will be gathered by the laser. Whereas if $d_L > d_{\text{bubble}}$, bubbles or explosions were generated on the precipitation.

Figure 7.27 shows the dependence of the size and number of bubbles on P_{avg} . Since DBDCS is not absorbing IR, this is through multi-photon absorption. The heat produced is expected to increase with P_{avg} . When P_{avg} is very large, explosion occurred at the focal spot that was disturbing the flow of bubbles.

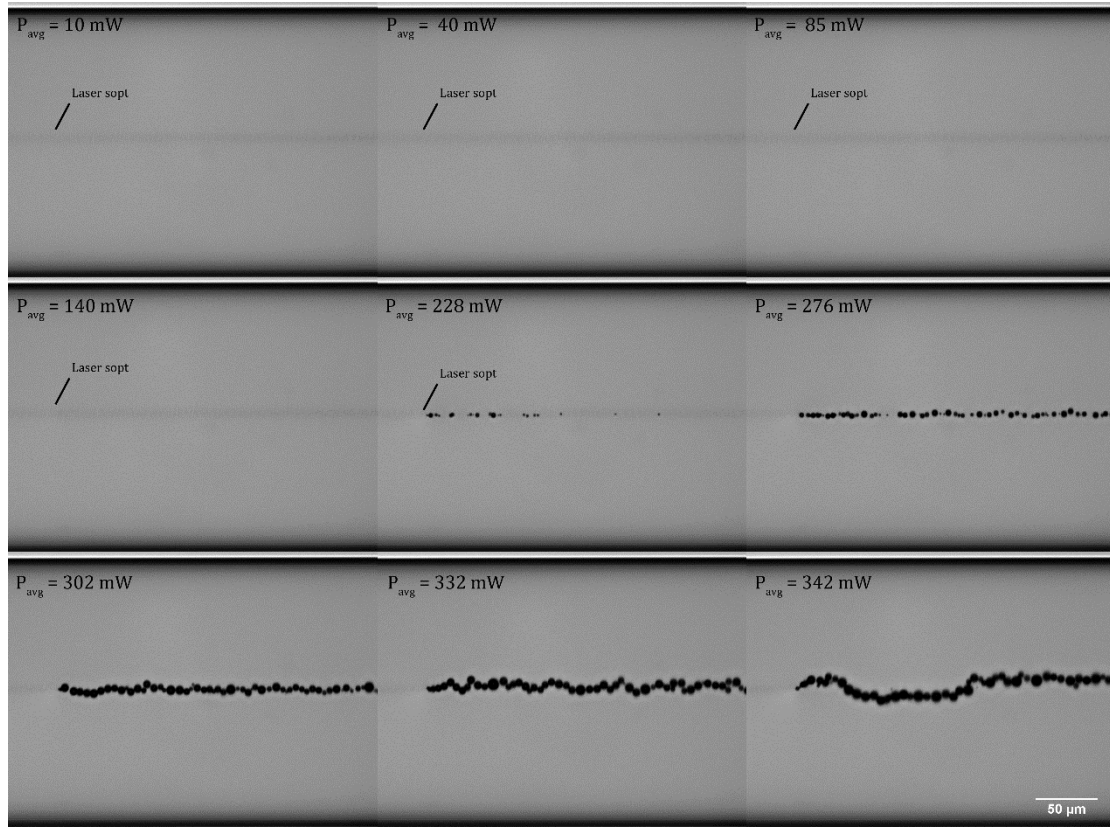


Figure 7.27. Laser-induced explosion dependence on laser average power P_{avg} .

Microfluidic parameter: $\rho_{3c} = 1 \text{ g/l}$, $Q_c = 92 \text{ nl/min}$, $\phi_{Ip} = 50\%$, $Q_p = 1 \mu\text{l/min}$. Laser parameters: $\tau = 400\text{fs}$, $\lambda = 1030\text{nm}$, $f_{rep} = 10\text{MHz}$, LPS, $d_L = 1990\mu\text{m}$.

Since the moving objects were carried by a flow, the effect of the laser-material interaction is not only a matter of the laser parameters, but also the flow parameters. The residence time in the laser spot $t_{residence} \approx \frac{\lambda}{v_{max}}$. The larger the flow rate, the less heat will be absorbed by moving particles. Figure 7.28 shows the impact of flow velocity on laser-induced bubbles. From top to bottom, velocity at the laminar flow centre v_{max} (calculated by equation (2.15)) decreased from 6 mm/s to 2 mm/s, with nano-particles flowing at the centre. Laser was focused on the nano-particles after d_{bubble} . No effect of laser was visible with $v_{max} > 5 \text{ mm/s}$. This is a threshold. The effect of bubble generation increased as v_{max} decreased. With a small v_{max} , the flow of bubble was disturbed by the explosion.

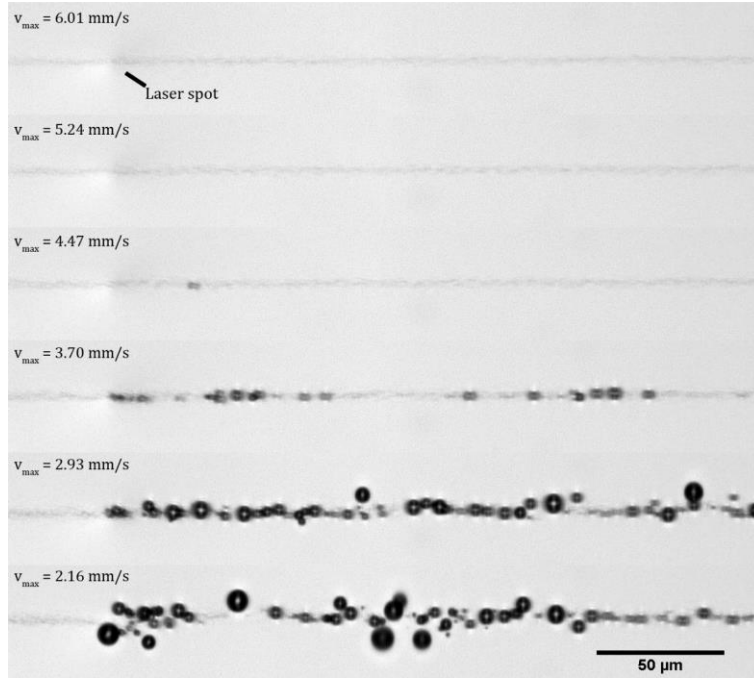


Figure 7.28. Laser-induced explosion dependence on flow velocity. Frames taken from videos. The velocity of the laminar flow centre is marked for each video.

Microfluidic parameters: $\rho_{3c} = 1 \text{ g/l}$, $Q_c = 92 \text{ nl/min}$, $\phi_{ip} = 50\%$, $Q_p = 6 \sim 2 \mu\text{l/min}$.

Laser parameters:

$$\tau = 400\text{fs}, \lambda = 1030\text{nm}, f_{\text{rep}} = 10\text{MHz}, P_{\text{avg}} = 310\text{mW}, \text{LPS}, d_L = 4500\mu\text{m}.$$

In Figure 7.27 and Figure 7.28, the residence time of the moving particles in the IR laser focal spot $0.16\text{ms} < t_{\text{residence}} < 1\text{ms}$. During this time, the energy density in the focal spot

$$U \approx \frac{P_{\text{avg}} t_{\text{residence}}}{\pi 0.25 \lambda^2}.$$

From that, the energy density threshold bubble generation by the IR

femtosecond laser can be estimated. By holding the flow velocity while changing the laser pulse energy, Figure 7.27 gives a threshold of 22 kJ/cm^2 , and by changing the flow velocity while holding the laser power, Figure 7.28 gives 11 kJ/cm^2 by changing flow velocity.

7.3.4. Impact of laser induction position

The impact of the NPLIN laser position d_L on its effect on nano-objects was examined qualitatively in Figure 7.29. Within $250 \mu\text{m}$ of the laser focal spot, when it was far away from

precipitation starting position. Thanks d_p , no laser-induced precipitation was visible. As d_L approaches d_p , a dark line of nano-particles gathered by the laser spot started appeared in the field of view. When d_L exceeds d_p by some distance, gas bubbles were generated at the focal spot. For the same microfluidic and laser parameters, laser's effect on nano-particles is changes from gathering to bubble generation. This suggests some organisational change was still going on about 0.5 s after d_p . After this transition, strong multi-photon absorption will occur.

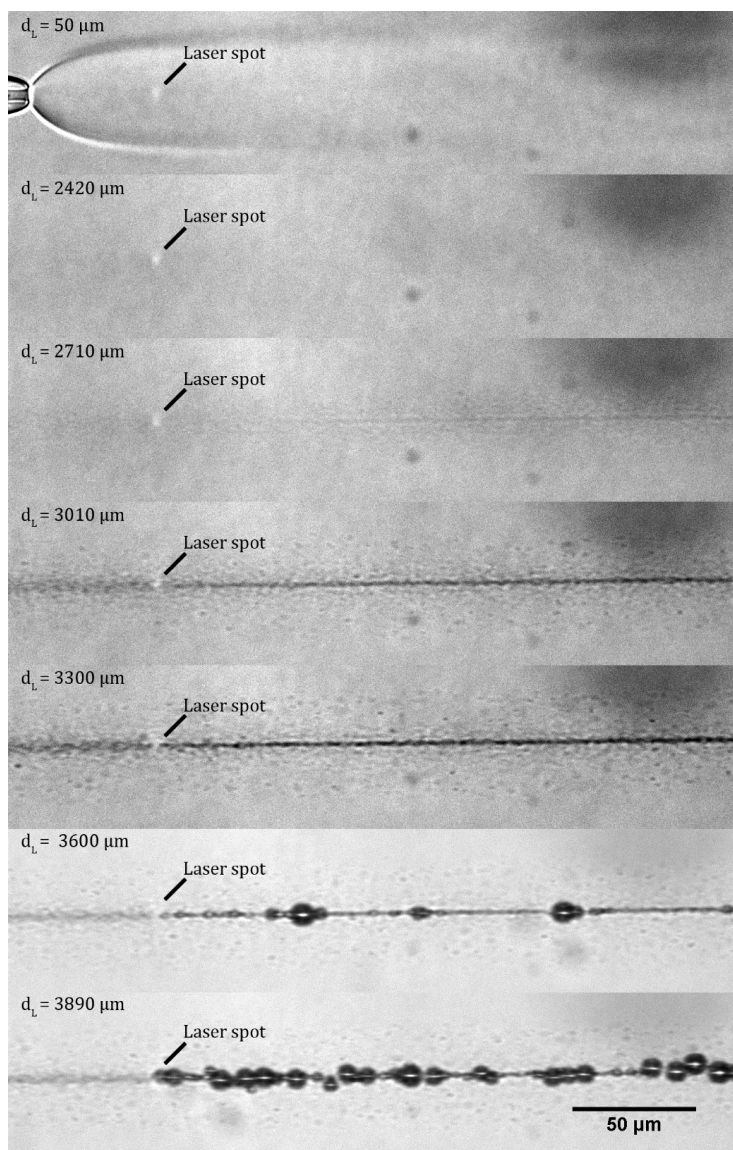


Figure 7.29. Impact of laser induction position on interaction with DBDCS nano-particles. Microfluidic parameters:

$\rho_{3c} = 1.8 \text{ g/l}, Q_c = 311 \text{ nl/min}, \phi_{Tp} = 50\%, Q_p = 4 \mu\text{l/min}$. *Laser parameters:*

$\tau = 400\text{fs}, \lambda = 1030\text{nm}, f_{\text{rep}} = 10\text{MHz}, P_{\text{avg}} = 340\text{mW}, \text{LPS}$.

Figure 7.29 illustrates that, between d_p and d_{bubble} , the laser spot can gather nano-particles without strong multi-photon absorption and bubble generation. The nano-particles were amorphous (Figure 7.26). They underwent some organisational transition between d_p and d_{bubble} . The Oswald ripening of the amorphous nanoparticles is slow (see Figure 5.10). After the organisational transition between d_p and d_{bubble} , strong multi-photon absorption of the IR laser does generate bubbles. During the organisational transition between d_p and d_{bubble} , the nano-objects were gathered by the IR laser focal spot into liquid droplets without bubbles. We think this organisational transition is the solidification of nano-droplets.

7.4. Other observation with the femtosecond IR laser

7.4.1. Laser tweezers

To avoid bubbles generated by the IR laser on absorbing impurities on the capillary wall, impurities on the wall were burned beforehand with the IR laser. During the cleaning process, we noticed the NPLIN IR laser was able to move small impurities in the microfluidic system, as shown in Figure 7.30. Figure 7.30.A is a particle trapped by the laser and moved from bottom to the upper edge of the screen and Figure 7.30.B illustrates an impurity moved from centre to the right. The focal spot of the IR laser in Figure 7.30 was not seen because P_{avg} was small lest the impurity be evaporated. The system was filled with pure water (*milli-Q*), because we notice with 1,4-dioxane bubbles will lead to burning of the capillary (see Figure 7.31).

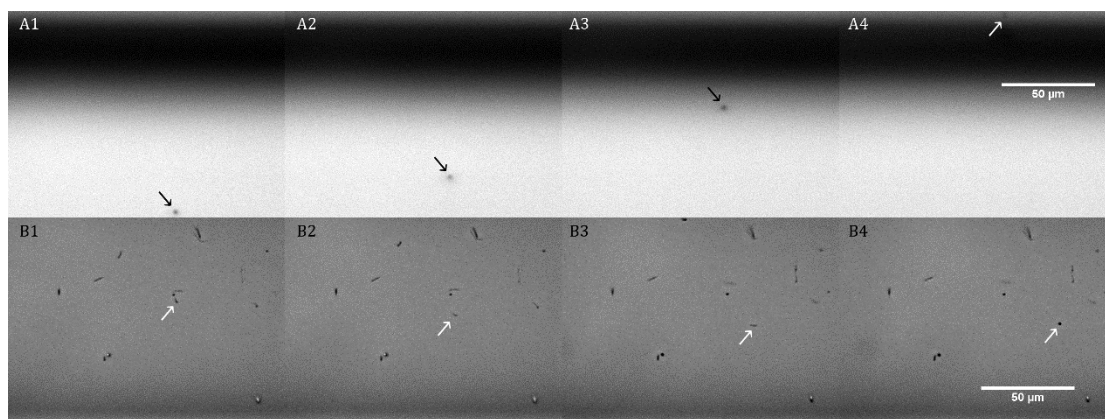


Figure 7.30. Using the femtosecond IR laser as tweezers to move impurities in pure water.

7.4.2. Bubbles, explosion, laser ablation.

Laser ablation on the surface of a mother solid phase can induce heterogeneous nucleation by the bubbles and debris of the explosion [Yoshikawa, 2014]. Yoshikawa proposed that laser-induced nucleation was due to explosion. These effects were also observed in our microfluidic mixer, as shown in Figure 7.31. Figure 7.31A shows the femtosecond IR laser was focused on a strong precipitation of DBDCS nanoparticles after d_{bubble} , explosion occurred at the focal spot and bubbles were generated; in Figure 7.31.B, the full power IR laser was focused on a impurity on the inner surface of the microfluidic channel, laser ablation of the impurity was observed with generation of nano-debris and bubbles; in Figure 7.31.C, the IR laser was focused on an impurity inside the injection nozzle of the small silica capillary filled with DBDCS in 1,4-dioxane, strong explosion was occurred; Figure 7.31.D shows a burning mark on the borosilicate capillary after fusing by the laser. It was noticeable that strong explosion only occurred when there was organic solvent in the flow, evaporation of the absorbing substance was observed without explosion when there was only pure water. If the object was not absorbing, laser had no effect. This means the capillaries must be carefully removed of any impurities on the wall in pure water before starting the laser experiment. And the solvents must be filtered lest any absorbing impurity happen to flow through the focal spot of the IR laser.

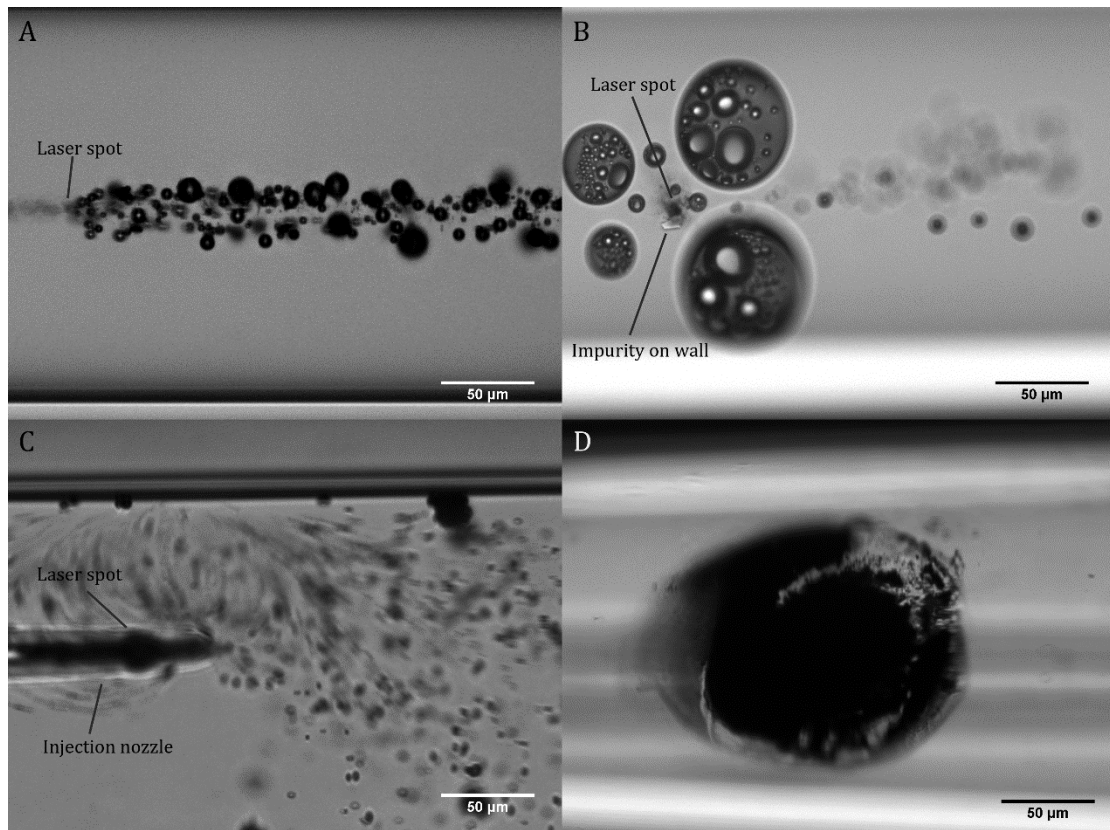


Figure 7.31. A~C: laser-induced explosion, ablation, and bubbles on surface of absorbing solids; D: capillary wall burnt by long time laser explosion. Parameters,

A: $\rho_{3c} = 1 \text{ g/l}$, $Q_c = 185 \text{ nl/min}$, $\phi_{lp} = 70\%$, $Q_p = 1 \mu\text{l/min}$. Laser parameters:

$\tau = 400\text{fs}$, $\lambda = 1030\text{nm}$, $f_{\text{rep}} = 10\text{MHz}$, $P_{\text{avg}} = 340\text{mW}$, LPS, $d_L = 24810\mu\text{m}$.

7.5. NPLIN working phase diagram

Up to now, we have finished describing all the noticeable phase transition behaviours of water (1)-1,4-dioxane (2)-DBDCS (3) in the coaxial microfluidic mixer with and without the femtosecond IR laser. Figure 7.32 is a summary of this thesis. It is a comparison between all the spontaneous phase transition types and the corresponding interaction with the focused IR laser. All the laser-induced and spontaneous phase transition types are colour coded and plotted against the overall composition of the mixture in the phase diagrams in Figure 7.33.

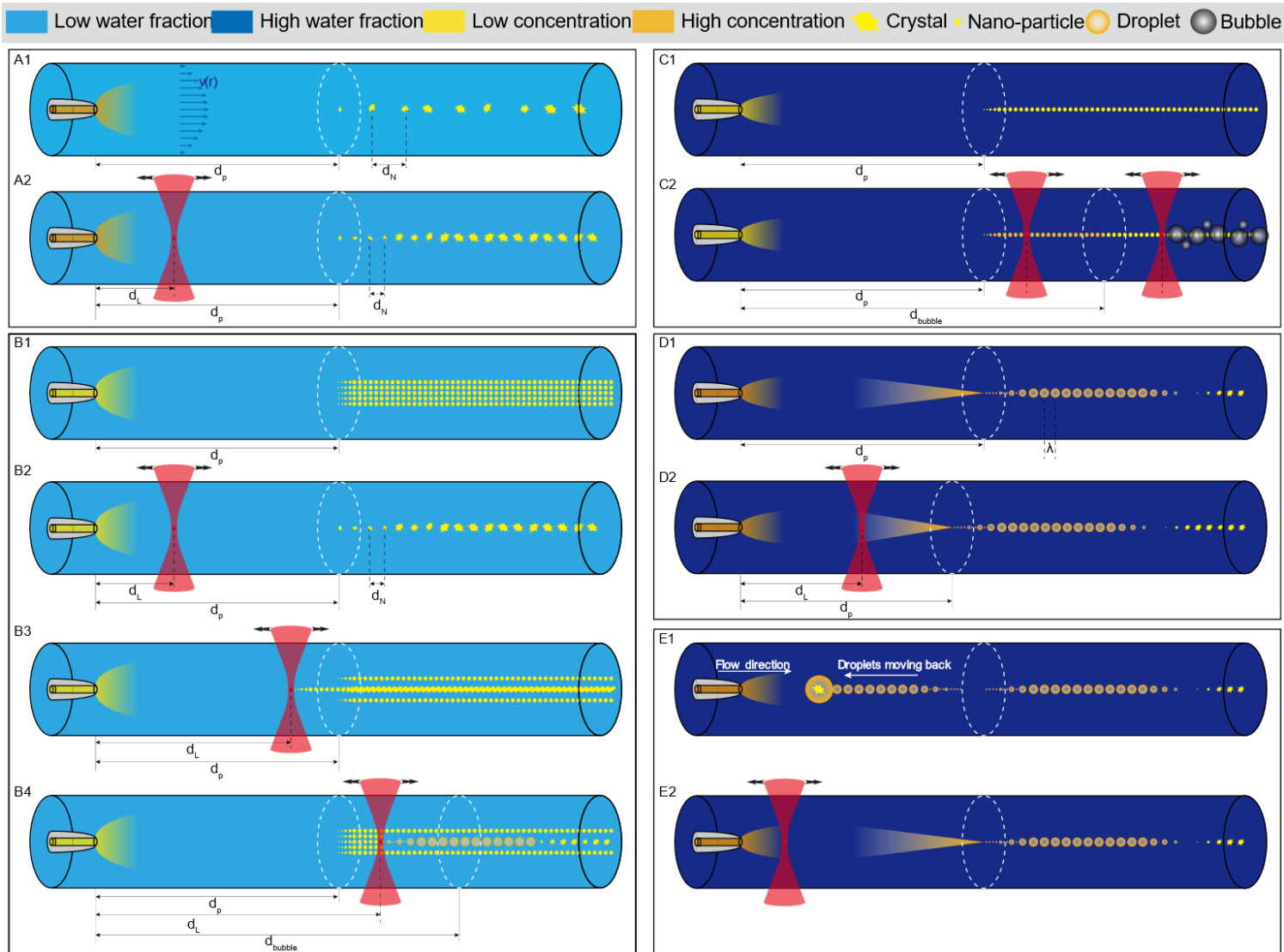


Figure 7.32. Summary of spontaneous phase transition types and the effect of the focused fs IR laser in the coaxial microfluidic system with some characteristic parameters of interest are marked on the schemes.

A1: Spontaneous crystallization with a low water fraction and a high central jet concentration ρ_{3c} . A2: Laser-induced crystallization with the

same microfluidic parameters than A1. An increase in the crystal birth rate B_x and a decrease in the nucleation time interval t_N were observed. B1: Spontaneous precipitation of a column of nano-particles in the flow centre with a small ρ_{3c} and a low ϕ_{lp} ; B2: $d_p - d_L > 200\mu\text{m}$, laser induced crystals with the same parameters than B1; B3: $d_p - d_L < 100\mu\text{m}$, laser induced a dark line of precipitation. B4: $d_p < d_L < d_{\text{bubble}}$, laser gathered nano-particles and induced droplets. The laser-induced droplets crystallised after some distance. C1: With a high ϕ_{lp} and a low ρ_{3c} , a line of precipitation appeared at the flow centre. C2: Focusing the IR laser after d_{bubble} , bubbles were generated, and not before d_{bubble} . D1: With a high ϕ_{lp} and a high ρ_{3c} , spontaneous droplet formation occurred after antisolvent focusing of the solute induced phase separation. These droplets later crystallised. D2: laser accelerated the droplet formation, i.e. d_p decrease with the use of the laser. E1: With a high ϕ_{lp} , a high ρ_{3c} and a total flow rate, abnormally large droplets were trapped by the gradient of the antisolvent. They can be fixed in the flow for a long time and crystallise. They can also flow to the opposite direction of the flow, depending on the parameters. E2: With the NPLIN laser focused before the droplet trap, the trap was released, and the abnormally large droplets flew away.

In Figure 7.33.B, the points that have been tested and analysed for the NPLIN response are displayed. The colour of the point is that of the nature of the objects before NPLIN (same colour code as Figure 7.33.A). The points gave laser-induced crystals are marked as diamonds. The laser-induced lines are marked as a short line. Laser induced droplets are marked by solid circles. Those abnormally large droplet traps that were eliminated by the laser are marked as circle with a cross. Bubbles generated by laser focusing on precipitations are marked as empty circles.

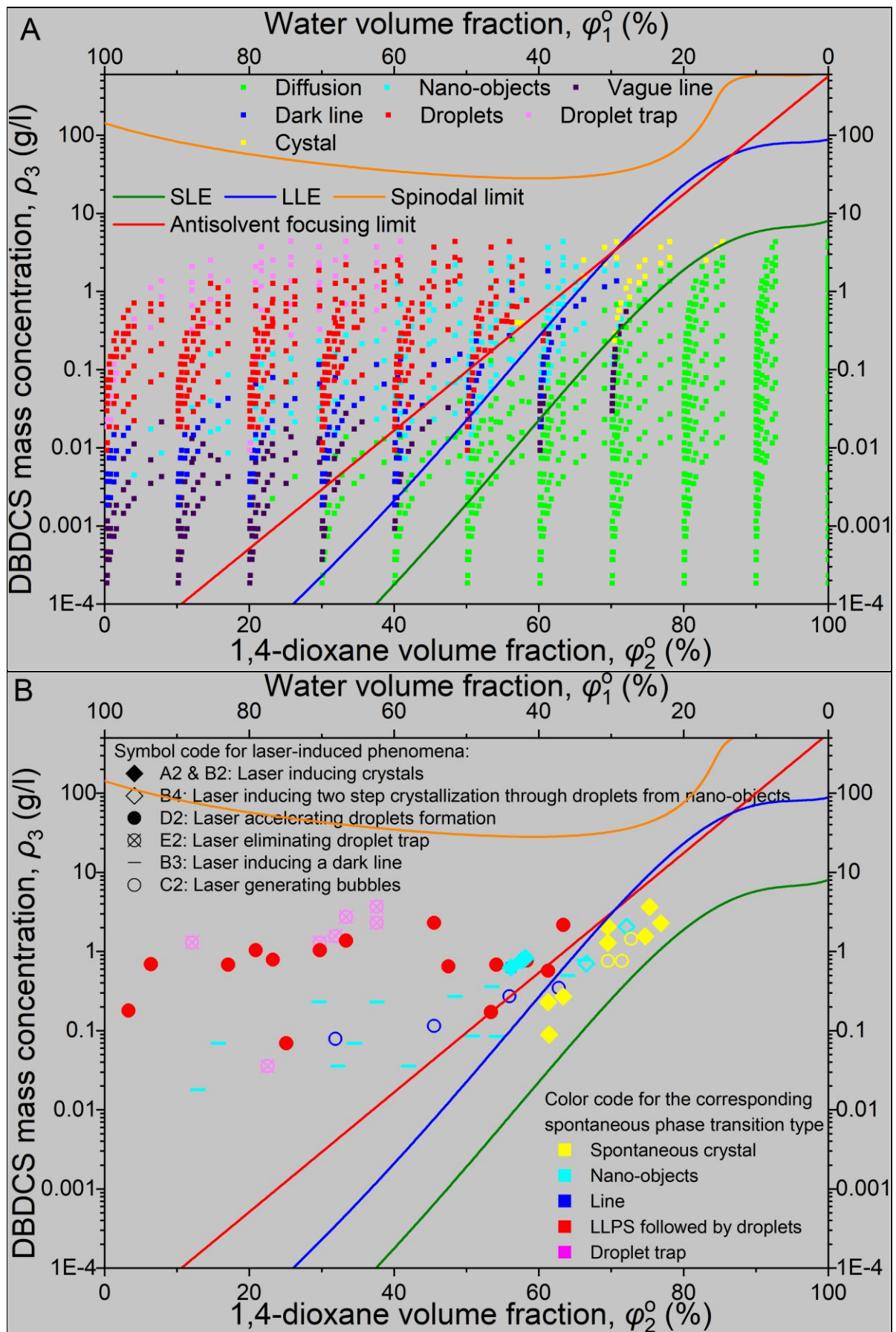


Figure 7.33. Microfluidic NPLIN working phase diagram. The types of observation are

plotted versus the overall mixture composition. A: spontaneous phase transitions without the NPLIN laser; B: laser-induced phenomena. The spontaneous phase transition types are colour coded. The laser-induced phenomena are coded by the symbol shapes. The green line on the phase diagram is the solubility predicted by Jouyban-Acree equation. The red line is the antisolvent focusing limit predicted by our equation (5.4). The black curve is the binodal LLPS limit from thermodynamic calculation in section 3.6.1.3.

Chapter conclusion

The fs IR laser focal spot can gather liquid and molecules of high refractive index towards its centre. The effectiveness increases linearly with the average power but decreases with the flow velocity. It can cause LLPS. It can gather nano-droplets into bigger ones. It can accelerate the nucleation rate by an order of magnitude. The crystal growth rate is not significantly change by the laser, neither the distribution of the polymorphs. The crystal habit remains the same (butterfly). No significant impact of the laser polarisation has been recorded by OM. This very soft NPLIN can be explained by a laser-induced transient supersaturation that will accelerate the nucleation with no change in its intrinsic mechanism. This opens the way to the time resolved study of the nucleation with a spectroscopic identification of the intermediate as it has been initiated in section 7.1.1 (Figure 7.2).

General discussion and perspective

This final part of the thesis will be divided into two main parts: a general discussion and conclusion section and a perspective section. In the discussion, we will address different points (the experimental device, the thermodynamic calculations and *Comsol* simulations, the quantitative description of the LLPS, the properties of the ternary system water (1)-1,4-dioxane (2)-DBDCS (3) obtained spontaneously in the coaxial microfluidic device or are laser-induced, the different crystallisation techniques, the different methods for producing droplets) and finally give some insight into the NPLIN or crystallisation mechanism.

Discussion

On the experimental device

One of the goals of this work was to design and validate an experimental setup able to produce different phase transformation (LLPS, amorphous phase, nucleation, and crystallisation) and to characterise them as soon as possible: in fact, a system which would authorise us to “see the birth” of the crystal.

We have been able to produce such a system. It has been carefully described in **Chapter 2** (Figure 2.3) and in Appendix B. The careful utilisation of the microfluidic device using for example a cleaning process and the impurities treatment *via* the IR laser has allowed us to use its main characteristic: the possibility of a large parameter sweep (Figure 2.4). The *in situ* characterisation system coupling OM, FLIM and cross-polarisation has let us push back the limit of the detection of the object produced: 1 μm by OM, by cross-polarisation or by fluorescence. The limit of detection is disappointing by fluorescence since the molecules in the flow absorb the excitation light and mask the crystals. The resolution of the optical imaging is limited by the objective and its numerical aperture of $\text{NA} = 0.45$ to a value of 1 μm . For a typical speed of the central flow of 1 mm/s we obtain a time resolution of 1 ms. We can distinguish two states of the growth process if they are separated by 1 ms in time or 1 μm in the flow. On Figure 7.2, we have captured the birth of the crystals. But we see that the light of NPLIN laser is saturating the detection and masking the first 20 millisecond of the growth; this can be improved in further experiments.

Our device is transportable and has been used in the Lab and at Swing@soleil.

On the thermodynamic calculations and the *Comsol* simulations

Thermodynamics of the ternary system of the solvent- antisolvent-solute system is the foundation for understanding its mixing properties, phase transition behaviour and computational simulation. We have established that the free energy of mixing of the ternary diagram of two miscible solvents and a solute can be extrapolated from the solubility curve of the solute in the mixture of the solvent with the approximation of the H3M model and the use of the Jouyban-Acree equation.

We have calculated a thermodynamic phase diagram (Figure 3.17) of water (1)-1,4-dioxane (2)-DBDCS (3). It is comprised of a spinodal decomposition domain, two binodal LLPS domains, two metastable domains, and a miniscule soluble domain. Mixtures in the spinodal decomposition domain and the two binodal LLPS domains will first fast separate in to two metastable liquid phases on the binodal curves. One is nearly pure liquid DBDCS, the other is supersaturated mixture of water (1)-1,4-dioxane (2) with DBDCS. The pure liquid DBDCS will solidify. DBDCS Crystal will grow from the romance liquid if a large fraction of DBDCS is present. Crystallisation from a mixture rich in water is almost impossible since the chemical potential of DBDCS in such environment is 5 times as high as the melting enthalpy.

We have proved experimentally the validity of this model using i) a comparison of the OM images and *Comsol* simulation of the refractive index n_D of a parametric sweep of a central flow of 1,4-dioxane into a peripheral flow of water (Figure 4.3 and Figure 4.4); ii) a comparison of the OM, the FLIM image and the *Comsol* simulation (Figure 5.3). We have calculated the expected OM image done by the microscope of the microfluidic tube.

It is important to notice that the simulations are valid until the phase transformation appears (crystal nucleation or LLPS) i.e. before the d_p .

On the quantitative description of the LLPS

The two main equations we have been able to establish, predict (table D.1):

- the antisolvent focusing velocity (equation (5.4)),

- and the droplet radius (equation (5.7)) which was derived from the Plateau-Rayleigh instability model.

The excellent agreement with the experimental values has been shown in Figure 5.34 for antisolvent focusing velocity and droplet formation distance, and in Figure 5.41 for the droplet radius determination.

Table D.1. List of parameters which can be predicted with our three main equations

antisolvent focusing velocity	$\overline{\mathbf{v}}_r^F = \frac{k_B T}{6\pi r_3^* \ddot{\mu} R_{\text{channel}}} \frac{\ln \frac{\rho_{3c}}{\rho_{3b2}} + \phi_{1p} \ln \frac{\rho_{3s2}}{\rho_{3s1}}}{f}$ $= \frac{1}{6\pi r_3^* \ddot{\mu} R_{\text{channel}}} \frac{k_B T \ln \frac{\rho_{3c}}{\rho_{3b2}} + \phi_{1p} \Delta_r G}{f}$	Equation (5.4)
LLPS starting distance	$d_p \approx \frac{6r_3^* \ddot{\mu}}{k_B T} \frac{Q_c}{\ln \frac{\rho_{3c}}{\rho_{3sb2}} + \phi_{1p} \ln \frac{\rho_{3s2}}{\rho_{3s1}}}, Q_c < Q_p$	Equation (5.5)

The model assumes that the driving force of diffusion is the chemical potential gradient:

$$\mathbf{F} \approx \frac{k_B T \left(\ln \frac{\rho_{3c}}{\rho_{3spin2}} + \phi_{1p} \ln \frac{\rho_{3s2}}{\rho_{3s1}} \right)}{R_{\text{channel}} f} \quad \text{Equation (5.3)}$$

and that the diffusion velocity is linear with the driving force:

$$\overline{\mathbf{v}}_r^F = \eta \overline{\mathbf{F}}_r \quad \text{Equation (3.31)}$$

The experiments show that the key parameter is the chemical potential gradient and not the difference in chemical potential as expected. Thus, a theoretical description that assumes a local equilibrium of the solute among the different positions in the solution will not succeed. The next step in complexity is to assume a constant escape flux of solute from the solvent trap. This flux will be a balance between the chemical potential gradient that focuses the solute and Fick diffusion that spreads the solute.

In these equations, f , ρ_{3c} and ϕ_{1p} are control parameters of the coaxial mixer. Two parameters are fixed by the physical chemistry of the antisolvent-solvent-solute system (section 3.5.2): i) the chemical affinity of the transfer of the solute from solvent to antisolvent (section 3.5.2), and ii) the mobility of solute molecules in antisolvent-solvent mixture (table D.2).

Table D.2. List of parameters which can be calculated with our model

chemical affinity	$\ln \frac{\rho_{3s2}}{\rho_{3s1}}$	Equation (3.50)
mobility	$\eta = \frac{1}{6\pi r_3^* \dot{\mu}}$	Equation (3.32)

The LLPS ρ_{3b2} threshold (section 3.6.1) is difficult to predict and measure by other means since it is a highly unstable state. By measuring the droplet formation distance, one can deduce the diffusion coefficient and fit for the solubility and LLPS limit as adjustable parameters in equation 5.4 and 5.5. This supports our calculation in Chapter 3 and our observation that the droplets resulted from LLPS.

One of the outputs of this type of studies will be the determination the LLPS decomposition threshold, by a systematic measurement of $\overline{v_r^F}$ or d_p in a coaxial microfluidic mixer.

In our ternary system the predicted values are:

Table D.3. Properties of water (1)-1,4-dioxane (2)-DBDCS (3) mixture

chemical affinity	LLPS limit	Diffusional radius
$\ln \frac{\rho_{3s2}}{\rho_{3s1}}$	ρ_{3b2}	r_3^*
17.4	568 g/l	5.33 Å

These equations (equation 5.3 and 5.4) can be applied to and are the fundamental of other diffusional antisolvent precipitation systems.

Moreover, the table D.4 summarises the other achievements concerning the thermodynamic work.

Table D.4. Different outputs of our calculations

• Dynamic viscosity $\bar{\mu}$ m determined for the ternary system according to [Aminabhavi, 1995]
• Refractive index and local refractive index determined
• Volume and density of the ternary solution determined [Aminabhavi, 1995]
• Situation of an ideal ternary system is stated
• Determination of $\Delta_{\text{mix}} G_m$ according to different “interaction parameters”
• Jouyban-Acree equation will be used to fit the solubility of DBDCS
• H3M model to calculate the thermodynamics of water (1)-1,4-dioxane (2)-DBDCS (3) system
• Application of H3M model to water (1)-1,4-dioxane (2)-DBDCS (3) real ternary system
• DBDCS amount fraction solubility in binary system of water (1)-1,4-dioxane (2) as a function of solvents molar composition determined experimentally and calculated
• The hydrodynamic radius of the diffusing molecules does not depend on the composition of the mixture
• Thermodynamics of LLPS of DBDCS and 1,4-dioxane graph determined.
• Thermodynamics of LLPS of DBDCS and water determined
• Calculation of $\Delta_{\text{mix}} G_m$ with H3M model of LLPS of water (1)-1,4-dioxane (2)-DBDCS (3)
• Calculation of a thermodynamic phase diagram of water (1)-1,4-dioxane (2)-DBDCS (3) comprised of comprised of a spinodal decomposition domain, two binodal LLPS domains, two metastable domains, and a miniscule soluble domain.
• Binodal LLPS limit of water (1)-1,4-dioxane (2)-DBDCS (3) system
• Spinodal decomposition limit water (1)-1,4-dioxane (2)-DBDCS (3)
• Collection of data on the volume of mixing, the viscosity and refractive index of the mixtures.
• Estimation of the diffusion coefficients requires a thermodynamic approach of the chemical potential of the constituents in the continuous phase of the ternary diagram.




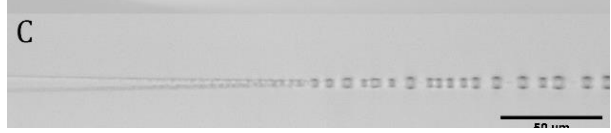
Finally, the work developed in thermodynamics and its implementation in *Comsol* give a

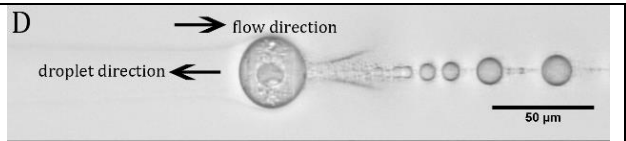



pertinent tool to simulate the mixing of a ternary mixture solute-solvent-anti-solvent if we know: i) the solubility of the solute in the mixture of solvents, and ii) the free energy of the mixing of the two solvents. The simulation precisely describes the inter-diffusion of the two solvents. It reproduces qualitatively the focusing the DBDCS that depends on the composition of the anti-solvent leading either to a LLPS of liquid DBDCS or the nucleation and growth of DBDCS crystals.

On the properties of the ternary system water (1)-1,4-dioxane (2)-DBDCS (3) obtained spontaneously in the coaxial microfluidic device.

After different preliminary tests (more than 200 experiments not presented in this manuscript with different conditions), we have been able to record 2253 points which have been presented in a 2-D working diagram with the final composition (1,4-dioxane volume fraction ϕ_2 , DBDCS mass concentration ρ_3) (Figure 6.29). This diagram has summarised the different observations of the spontaneously produced objects. We will summarise and discuss the properties of these objects in the following section according to three main parts i) the solution state, ii) the LLPS and iii) the nucleation of a solid state. Eight types of objects have been observed by OM in the microfluidic device and are summarised in Table D.5.

Table D.5. Different objects observed spontaneously via OM

Solution state	inter-diffusion of the central and peripheral flows	A 
Non-crystalline phase transitions	a column of nano-sized objects along the flow centre	E 
	a line of precipitation along the flow centre	B 
	liquid-liquid phase separation (LLPS) followed by droplets	C 

	formation abnormally large droplets that flow to the opposite direction of the flow	D 
crystallisation	spontaneous crystallisation	F 
Extrinsic	heterogeneous crystallisation on the wall	G 
	blockage of the microfluidic channel by the strong precipitation	H 

The undersaturated state

When phase transitions are not possible along the 25 mm length of our microfluidic device, one observes only three zones: i) hydrodynamic expansion; ii): solvents inter-diffusion. The solubility curved (measured in solution) agrees with OM observation (Figure 5.4).

The liquid-liquid phase separation

The main phenomenon concerns the solvent focusing i.e. the gathering of the DBDCS molecules at the centre of the flow by the water. This can be explained by the difference of chemical affinity of

DBDCS for 1,4-dioxane compared to water which can be expressed by $\ln \frac{\rho_{3s2}}{\rho_{3s1}} = 17.4$.

The LLPS is observed after the solvent focusing of the solute. The focusing time is in a range from 1 ms to 9000 ms. We have shown that this time is inversely proportional to:

$$\mathbf{F} \approx \frac{k_B T \left(\ln \frac{\rho_{3c}}{\rho_{3sp2}} + \phi_{1p} \ln \frac{\rho_{3s2}}{\rho_{3s1}} \right)}{R_{\text{channel}} f} \quad \text{Equation (5.3)}$$

where ϕ_{1p} is the amount fraction in water of the peripheral flow; $R_{\text{channel}} f$ the radius of the inner flow; ρ_{3c} the DBDCS concentration in the central flow. The term \mathbf{F} can be interpreted as the focusing strength

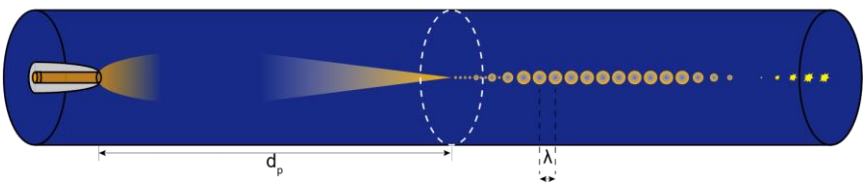
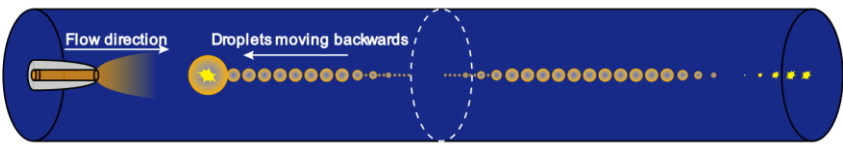
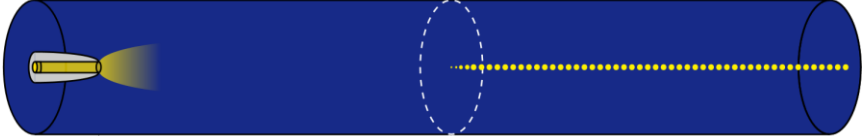
equal to the gradient of the chemical potential of DBDCS between to 1,4-dioxane phase and the focusing phase. DBDCS is not trapped at the centre of the presence by water but attracted towards the centre by 1,4-dioxane.

If the concentration of DBDCS in 1,4-dioxane reaches $\rho_{3b2} = 568 \text{ g/l}$ (supersaturation ratio of 100) by our nonconventional method, the formation of liquid DBDCS droplets will occur with a smaller barrier than crystallisation. This is the LLPS limit. When $\ln \frac{\rho_{3c}}{568 \text{ g/l}} + 17.4\phi_p > 0$, DBDCS is pushed towards the flow centre by the chemical potential gradient, the concentration reaches the LLPS limit, droplets are formed.

Table D.6 Summarises the properties of the LLPS transition which dominates the work diagram of the device.

Table D.6. Properties of spontaneous droplets as deduced via OM, SEM post-mortem observation. Experiments with IR laser will enhance this assumption (wide supra)

Size of droplets	With other three operational parameters fixed, the size of the droplets decreased as the peripheral flow ϕ_p increased.
	With other three operational parameters fixed, the size of the droplets increased as the DBDCS concentration increased.
Number of droplets	With other three operational parameters fixed, the more antisolvent in the peripheral flow, the larger the driving force for the uphill diffusion, thus the more concentrated DBDCS was at the flow centre, the larger number of droplets required to contain the DBDCS molecules.
Total droplet volume fraction	The total droplet volume is equal to the volume of the injected DBDCS.
Nature of droplets	The droplets are a transient pure liquid phase of the solute.
	We measure a 1 ± 0.5 amount fraction of DBDCS in this phase.
Mechanism of droplet formation and evolution	Droplet are created by binodal (low DBDCS supersaturation) or spinodal decomposition (high DBDCS supersaturation $\beta \geq 100$).
	3 steps: - first, focusing of the solute by the gradient of antisolvent; - second, liquid phase separation after the concentration reaches LLPS threshold

	<p>near d_p ;</p> <p>- third, Marangoni focusing and merging of the nano-droplets at d_p .</p>
	<p>D</p> 
	<p>Microdroplets merge into a big one that escapes with a constant periodicity, or nano or micro droplets merge into a liquid cylinder that later breaks into droplets of constant size with a constant periodicity.</p>
	<p>The last case is similar to the Plateau-Rayleigh instability, the breaking of a viscous liquid cylinder into droplets of a large radius to minimise the surface tension.</p>
	<p>At the focal point of the antisolvent focusing, the newly emerged liquid phase can be considered at a transient liquid cylinder that shortly breaks into droplets. Neither the nano-droplets nor the cylinder is stable. There is a certain stable size that is related with microfluidic parameters.</p>
Droplet trap	<p>Droplet trap exists with i) a high ρ_{3c} ; ii) a high ϕ_{lp} (the higher these two, the stronger the Marangoni driving force); iii) a low flow rate (the lower the hydrodynamic velocity, the easier the droplet would be caught by Marangoni effect).</p>
	<p>E</p> 
	<p>Droplet trap size: 4 pl (a confined media)</p>
Line	<p>Post-mortem observation of dark line elucidates their nature: droplets</p>
	<p>C</p> 

The nanoparticles

When $\ln \frac{\rho_{3c}}{568\text{g/l}} + 17.4\phi_{lp} \approx 0$, DBDCS molecules are spread in a column near the centre of

the flow, nano-particles are formed in the column. Nano-particles (purple points on Figure 5.4) are

amorphous. SEM photo revealed the average size of the nano-particles is around 20 nm

The solid state (crystalline)

When $\ln \frac{\rho_{3c}}{568\text{g/l}} + 17.4\phi_{1p} > 0$, depending on the over saturation ratio it will be either a slow

nucleation and growth from a nearly homogeneous solution or soluble. Crystallisation (yellow points on Figure 5.4) occurs with a high DBDCS concentration and a low water fraction in the peripheral flow.

Table D.7 summarised the crystal properties which are independent of the condition used in the microfluidic device.

Table D.7. Properties of spontaneous crystals as deduced via OM, and fluorescence.

crystal habits	- butterfly (in the flow) and rhombus (on the wall) from water-1,4- dioxane in the coaxial mixer - stars (in the flow) and rhombus (in the flow) from THF 30 % -1,4- dioxane 70 %.
localisation of the crystallisation	the hydrodynamic expansion finished after 350 μm .
	the diameter of the crystal flow = 20 μm .
	different areas corresponding to the presence of different species: flow centre for crystals and flow periphery for molecules

Table D.8 summarises the properties of the crystal which depends on the conditions. The main differences we can point this table are:

- accumulative crystal birth rate $B_{>5\text{ mm}}$ is 2 times greater for condition 1 and condition 2 as determined by OM;
- nucleation rate N_S is 1.5 times greater for condition 1 and condition 2 as determined by OM at $x = 3\text{ mm}$, but is equal when the nucleation is finished (at $x = 5\text{ mm}$);
- fitted area growth rate g_A and area growth rate constant are 0.7 times smaller for condition 1 and condition 2 as determined by OM;
- accumulative crystal birth rate $B_{>5\text{ mm}}$ is 4 times greater for condition 1 as determined by OM than the FLIM determination;
- fitted area growth rate g_A and area growth rate constant are 1.5 times greater for condition 1 as determined by OM than the FLIM determination.

Table D.8. Properties of spontaneous and laser induced crystals of DBDCS in the ternary mixture of water (1)-1,4-dioxane (2)-DBDCS (3) as deduced via OM, and fluorescence.

Condition 1: $\rho_{3c} = 16 \text{ g/l}$, $Q_c = 148 \text{ nl/min}$, $\phi_{lp} = 30\%$, $Q_p = 1 \mu\text{l/min}$; Condition 2:

$\rho_{3c} = 10 \text{ g/l}$, $Q_c = 148 \text{ nl/min}$, $\phi_{lp} = 30\%$, $Q_p = 1 \mu\text{l/min}$; Condition 3 :

$\rho_{3c} = 3.5 \text{ g/l}$, $Q_c = 285 \text{ nl/min}$, $\phi_{lp} = 50\%$, $Q_p = 2 \mu\text{l/min}$

Variable	Name	Comment	Condition 1 16g/l		Condition 2 10g/l		Condition 3 3.5g/l	
			OM	FLIM	OM	FLIM	OM	FLIM
B_x	Accumulative crystal birth rate	$x < 2 \text{ mm}$	No crystal	No crystal	No crystal	Data have been recorded but not treated	Data have been recorded but not treated	Data not recorded
		$3 < x < 5 \text{ mm}$	Growth 0.6 to 3 s ⁻¹	0 to 0.6 s ⁻¹	Growth 0.3 to 2 s ⁻¹			
		$x > 5 \text{ mm}$	Plateau at 6 s ⁻¹	Plateau at 1.5 s ⁻¹	Plateau at 3 s ⁻¹			
t_N	nucleation time interval		Its distribution is an exponential decay	Its distribution is an exponential decay	Its distribution is an exponential decay	Data have been recorded but not treated	Data have been recorded but not treated	Data not recorded
		$x < 2 \text{ mm}$						
		$3 < x < 5 \text{ mm}$	1.5 ~ 0.3 s					
		$x > 5 \text{ mm}$	0.3 s	0.6 s				
N	nucleation rate	$x = 3 \text{ mm}$	61 s ⁻¹ mm ⁻³		40 s ⁻¹ mm ⁻³	Data have been recorded but not treated	Data have been recorded but not treated	Data not recorded
		$x = 5 \text{ mm}$	22 s ⁻¹ mm ⁻³		20 s ⁻¹ mm ⁻³			
g_A	fitted area growth rate		9.8 μm ² s ⁻¹	6.6 μm ² s ⁻¹	14 μm ² s ⁻¹	Data have been recorded but not treated	Data have been recorded but not treated	Data not recorded
k	area growth rate constant		4.75 μm ² s ⁻¹ g ⁻¹ l	3.3 μm ² s ⁻¹ g ⁻¹ l	6.8 μm ² s ⁻¹ g ⁻¹ l			

On the properties of the ternary system water (1)-1,4-dioxane (2)-DBDCS (3) laser-induced in the coaxial microfluidic device.

The undersaturated state

In some NPLIN paper [Rungsimanon, 2010] NPLIN nucleation of unsaturated glycine solution has been possible. Unfortunately, we have not been able to induce nucleation under the solubility curve (the green point of the spontaneous working diagram) due to the time that we have had no time to precisely shine the laser just under the solubility curve.

However, we have been able to show (Figure 7.21) suggests that our focused femtosecond IR laser was able to interact with solvent molecules without absorption. It is noticeable that the interface is

always dragged away from the centre towards the water's side. This agrees with the fact that optical tweezers drag to phases with the higher refractive indices towards the focal point.

The liquid-liquid phase separation

As described in section 7.2, we have been able to demonstrate that laser accelerates the phase separation, gather nanodroplets, releases the abnormally large droplets from the “droplet trap” and changes the size of the stable droplets.

The solid state (crystalline)

General properties of crystals produced by NPLIN have similar properties that those spontaneously nucleated. Therefore Table D.7 remains true in the case of NPLIN. However, some quantitative characteristics are different and are summarised in Table D.9. The quantitative differences between OM and FLIM measurements put in evidence from table D.9 and D.10 is due to the mask effect of the molecular DBDCS that hinder the crystals excitation for the FLIM detection. Therefore, the OM values are actually the most reliable values. We will use them to compare the NPLIN and the spontaneous quantitative parameters.

- NPLIN accumulative crystal birth rate $B_{>5\text{ mm}}$ is 3 times greater than the spontaneous one for condition 1 as determined by OM;
- NPLIN nucleation time interval $N_{S > 5\text{ mm}}$ is 0.2 times smaller than the spontaneous one for condition 1 as determined by OM;
- NPLIN nucleation rate N_S is 1.8 times greater than the spontaneous one for condition 1 as determined by OM at $x = 5\text{ mm}$);
- NPLIN fitted area growth rate g_A and area growth rate constant are 0.9 times smaller than the spontaneous one for condition 1 as determined by OM.

Table D.9. Properties of NPLIN crystals of DBDCS in the ternary mixture of water (1)-1,4-dioxane (2)-DBDCS (3) as deduced via OM, and fluorescence.

Variable	Name	Comment	Condition 1 16g/l	
			OM	FLIM
	accumulative crystal birth rate	$x < 2\text{ mm}$		
		$3 < x < 5\text{ mm}$	5~15 s ⁻¹	14 s ⁻¹
		$x > 5\text{ mm}$	15~20 s ⁻¹	14~16 s ⁻¹
	nucleation time interval	$x < 2\text{ mm}$		
		$3 < x < 5\text{ mm}$	0.06~0.24 s	0.07 s
		$x > 5\text{ mm}$	0.07~0.04 s	0.07~0.06 s
N_S	nucleation rate	$x = 3\text{ mm}$	520 s ⁻¹ ·mm ⁻³	

		$x = 5 \text{ mm}$	$40 \text{ s}^{-1} \cdot \text{mm}^{-3}$	
g_A	fitted area growth rate		$9.2 \text{ } \mu\text{m}^2/\text{s}$	$17.6 \text{ } \mu\text{m}^2/\text{s}$
k	area growth rate constant		$4.5 \text{ } (\mu\text{m}^2/\text{s})/(\text{g/l})$	$8.5 \text{ } (\mu\text{m}^2/\text{s})/(\text{g/l})$

On the polymorphism of DBDCS

Characterisation by fluorescence lifetime decay

Spontaneous crystallisation or laser-induced nucleation have given different “object” for which the lifetime has been recorded. Figure D.1 reports these different lifetimes, compared to those already reported in the literature (with a black point over the corresponding column). To attribute the different lifetime decay to the different phases, we have grouped our experimental values in four groups which are attributed to four situations:

- Group I, lifetime decay = $20 \pm 2,5 \text{ ns}$,
- Group II, lifetime decay = $12 \pm 2 \text{ ns}$,
- Group III, lifetime decay = $5 \pm 1 \text{ ns}$,
- Group IV, lifetime decay = $2 \pm 0,5 \text{ ns}$,

According to the literature, I is the green phase and III the blue phase both in solid state. We have assigned IV to oligomer in solution state. II corresponds to a decay which have already been observed in the literature but not described. We will call it the new phase. In fact, the actual discrimination between the phase (green and blue) has been done through the luminescent properties of the “object”. We have not tried to measure the luminescent properties of the crystal we have produced in our microfluidic device. From a structural point of view, Yoon et al [Yoon, 2010] have demonstrated based on theoretical calculations and single X-ray diffraction that the structural differences between the green and the blue phase is due to a split in x and y between two planar molecules of DBDCS. Therefore, one can make the hypothesis, that II presents a structure with another minimum (x_{II} , y_{II}) while for I, it has been estimated around (2Å , 8Å) and (2.5Å , 3Å) for III (see figure 1.22).

Microfluidic production conditions of phase I, II and III gives the following comments:

- Phase I and phase III are obtained in each situation (condition 1: ($\rho_{3c} = 16 \text{ g/l}, Q_c = 148 \text{ nl/min}, \phi_{tp} = 30\%, Q_p = 1 \mu\text{l/min}$) or in water-1,4 dioxane or in water-1,4 dioxane (70 %), THF (30 %)) obtained spontaneously or *via* NPLIN, measured directly or deduced from a PCA analysis.
- Phase II is obtained in the same conditions than phase I excepted that the PCA analysis as not identified this phase.

Finally, observation of the whole Figure D.1 could call to mind on the wide range of values increasing almost continuously. That could be explained by different reasons depending of the crystal or the method: i) polymorphs are sensitive to the crystallisation methods; ii) lifetime decay is sensitive to the default at the molecular level (see figure 1.13) iii) the number of photons collected *per* crystal in our experiment were closed to the limit of detection; iv) the DBDCS structure (sheets of DBDCS molecule) could easily sleep (different values of (x, y)). At the birth of the crystal, there could be a wide range of values, leading to different lifetime decays.

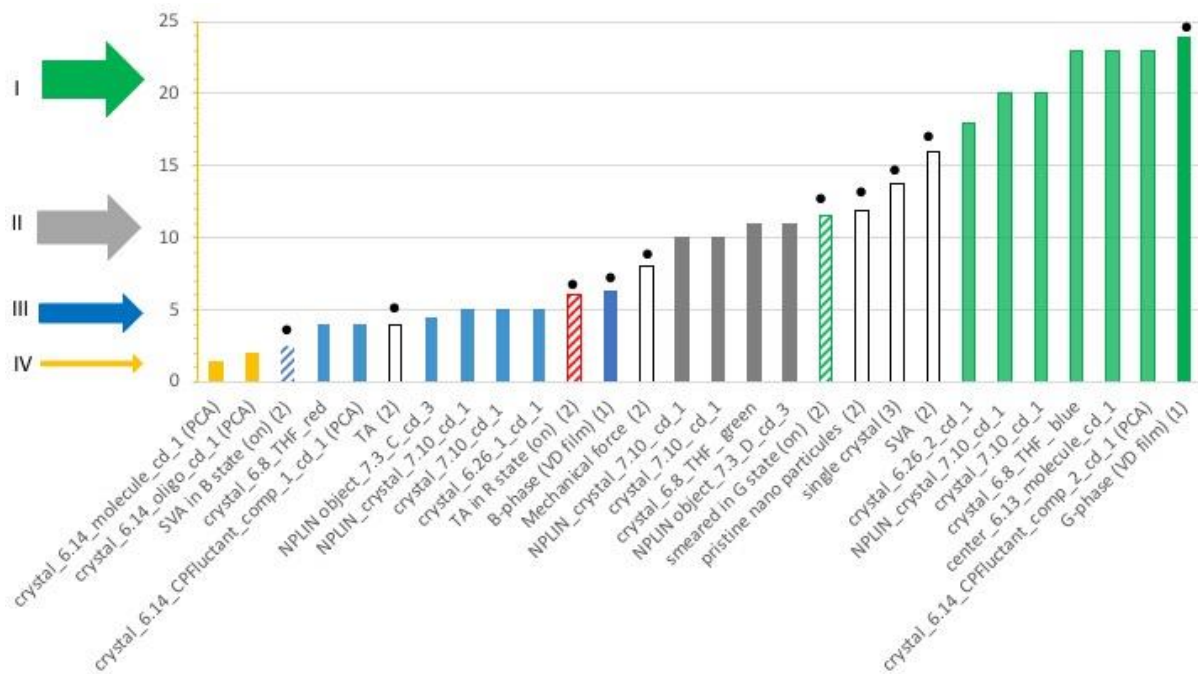


Figure D.1. Lifetime decay (ns) of “object” produced in the microfluidic device compared to the literature (black circle). (1) [Yoon, 2011], (2) [Kim, 2015], (3) [Shi, 2017b]. The colour

of the bar corresponds to the identification of the phase (green, blue, or red) when it has been indicated.

Characterisation by SAXS

X-ray diffraction on the flow on SWING@soleil has been measured with photons of 12 KeV, leading a wavelength of $\lambda = 1.0332 \text{ \AA}$. Three peaks have been observed at 0.28, 0.55 and 0.65 in q , leading to the following values in d :10.54 \AA 6.029 \AA and 0.14 \AA . Figure X.1 presents two spectra. The SAXS measurements have been performed at the end of the second capillary, i.e. after 25 mm from the nozzle. Due to this difference, the experimental conditions (the four parameters) cannot be strictly compared with the experiences performed in our Laboratory.

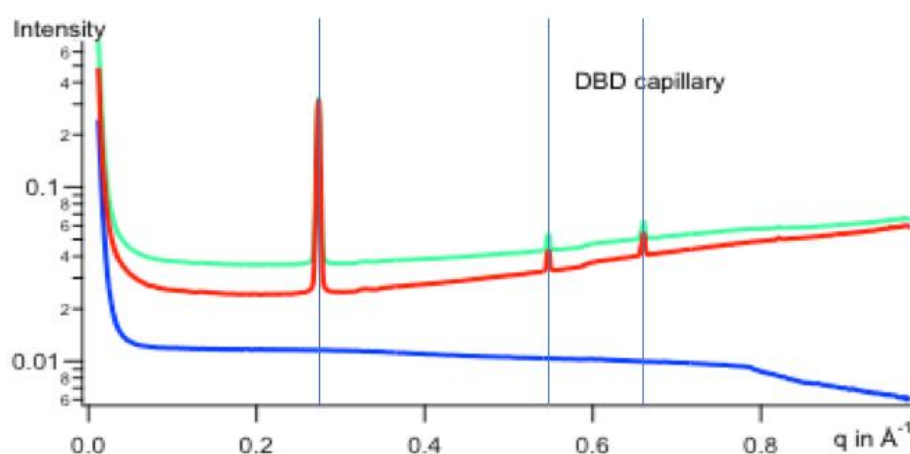


Figure D.2. Experimental SAXS spectra of DBDCS crystals in microfluidic device. Green and red observations have been measured at different distances on the tube. The blue line is the spectra of the capillary without DBDCS.

The calculation of the theoretical spectra based on the single crystal experiment of the green phase (refcode ANUYEO) is given in Figure D.2. The first peak is at 9.65 \AA .

No.	h	k	l	d (Å)	F(real)	F(imag)	F	2θ	I	M	λ	Phase
1	0	0	1	9.61598	36.2814	0.0691341	36.2814	9.1893	59.8876	2	1	1
2	0	0	1	9.61598	36.2819	0.0694732	36.282	9.2116	29.7988	2	2	1
3	0	1	0	8.83561	20.5688	0.0627748	20.5689	10.0029	16.2222	2	1	1
4	0	1	0	8.83561	20.5692	0.0630688	20.5693	10.0272	8.0718	2	2	1
5	1	0	0	7.50649	17.4463	0.0174662	17.4463	11.7798	8.3867	2	1	1
6	1	0	0	7.50649	17.4466	0.017565	17.4466	11.8084	4.1729	2	2	1
7	0	1	-1	6.97202	-6.96365	0.00288461	6.96365	12.6864	1.1498	2	1	1

Figure D.3. Theoretical powder X-ray diffraction spectra of DBDCS calculated by *reciprOgraph*

In order to discriminate with the two phases reported (the green and the blue phase) by [Yoon, 2010], we have reported a part of Table S2 of their supporting information in ground powder sate (Figure D.3). The (2 0 0) plane is at 10.96 Å for the green phase and at 14.82 Å for the green phase. Therefore, one can state that the objects produced where crystalline and that crystals which are mainly formed in our experimental setup were of the Green phase.

2theta (°)	D _{hkl} (Å)	(h k l)
3.02	29.23	(1 0 0)'
5.96	14.82	(2 0 0)'

29.23/14.82 = 1.972 Lamellar Structure

2theta (°)	D _{hkl} (Å)	(h k l)
4.03	21.91	(1 0 0)''
8.06	10.96	(2 0 0)''


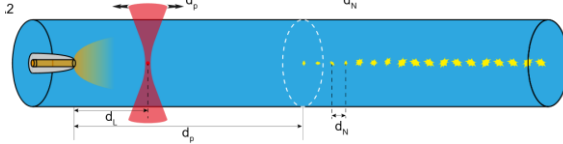
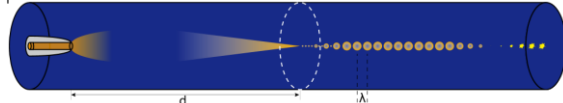
21.91/10.96 = 1.999 Lamellar Structure


Figure D.4. Extraction of Table S2 from [Yoon, 2010]. The Green and the Blue phases in ground powder sate are indicated with a coloured border.

On the different crystallisation techniques

This work has shown different methods to produce crystals. The goal of this work was to control spatially and temporally the crystal nucleation. Table D.10 summarises the different situation we have been able to observe.

Table D.10. Different conditions and nucleation methods to obtain crystals from our microfluidic device in the ternary mixture water (1)-1,4-dioxane (2)-DBDCS (3). Conditions and Figures are given as examples.

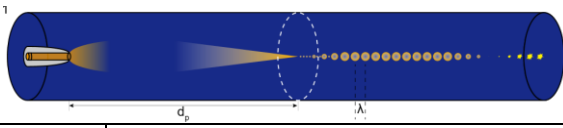
	Description	Spatial control	Temporal control	Conditions	Figure, Scheme
Spontaneous nucleation from solution	$d_P \approx 2$ mm, first crystal appears $d_P \approx 5$ mm, No more new crystal t_N at $x = 10$ mm = 2.05 s.	In a range of 3 mm	In a range of 2 s	$\rho_{3c} = 16$ g/l, $Q_c = 148$ nl/min, $\phi_{1p} = 30\%$, $Q_p = 1$ μ l/min	Fig. 6.27
				Roughly between $65\% < \phi_2 < 85\%$ and $0.6 < \rho_3 < 8$ g/l	yellow point (Fig.5.2)
					
NPLIN from solution	$d_P \approx 2$ mm, first crystal appears $d_P \approx 5$ mm, No more new crystal at $x = 10$ mm, $t_N = 0.05$ s.	In a range of 3 mm	In a range of 0.01 s	$\rho_{3c} = 16$ g/l, $Q_c = 148$ nl/min, $\phi_{1p} = 30\%$, $Q_p = 1$ μ l/min Fig. 7.8 $\lambda = 1030$ nm, $f_{rep} = 10$ MHz, $\tau = 400$ fs, $P_{avg} = 330$ mW, LPS, $d_L = 30$ μ m	
				Roughly between $65\% < \phi_2 < 85\%$ and $0.6 < \rho_3 < 8$ g/l	yellow point (Fig. 5.2)
					
Spontaneous TSN from droplet	Droplet appears at d_P disappeared at d_{P2} and crystals appeared at d_{P3}	Difficult to estimate	Impossible to estimate	Roughly between $0\% < \phi_2 < 58\%$ and $0.02 < \rho_3 < 2$ g/l	red point (Fig. 5.2)
					
Abnormal droplet trap	Droplet appears at d_P moved back to the nozzle and crystals appeared	At the nozzle	Impossible to estimate	Roughly between $0\% < \phi_2 < 50\%$ and $0.02 < \rho_3 < 8$ g/l	Rose point (Fig. 5.2)

	inside		Scheme E1
--	--------	---	-----------

On the different methods for producing droplets

This work has shown different methods to induce LLPS, i.e. to produce droplets. Table D.11 summarises the different situation we have been able to observe

Table D.11. Different conditions and nucleation methods to obtain droplets from our microfluidic device in the ternary mixture water (1)-1,4-dioxane (2)-DBDCS (3). Conditions and Figures are given as examples.

	Description	Spatial control	Temporal control	Conditions	Figure, Scheme
Spontaneous LLPS	$d_p \approx 200 \mu\text{m}$, first droplet appears $t_N \approx 15 \text{ ms}$	In a range of $20 \mu\text{m}$	In a range of 20 ms	$\rho_{3c} = 5 \text{ g/l}$, $Q_c = 30 \text{ nl/min}$, $\phi_{1p} = 50\%$, $Q_p = 1 \mu\text{l/min}$	Figure 5.2
	d_p and t_N could be calculated through equation (5.5) and (5.9)			Roughly between $0\% < \phi_2 < 60\%$ and $0.01 < \rho_3 < 8 \text{ g/l}$	red point (Figure 5.4)
					Scheme D1
NPLIN droplets formation	$d_p \approx 2 \text{ mm}$, first crystal appears $d_p \approx 5 \text{ mm}$, No more new crystal t_N at $x = 10 \text{ mm} = 0.25 \text{ s}$.	In a range of 0.05 mm	In a range of 0.05 s	$\rho_{3c} = 1 \text{ g/l}$, $Q_c = 148 \text{ nl/min}$, $\phi_{1p} = 90\%$, $Q_p = 2 \mu\text{l/min}$ $\lambda = 1030 \text{ nm}$, $f_{\text{rep}} = 10 \text{ MHz}$, $\tau = 400 \text{ fs}$, $P_{\text{avg}} = 357 \text{ mW}$, LPS, $d_L = 410 \mu\text{m}$	Fig. 7.22
				Roughly between $0\% < \phi_2 < 60\%$ and $0.01 < \rho_3 < 8 \text{ g/l}$	red point (Fig. 5.2)

					Scheme D2
Droplet appears at d_p disappeared at d_{p2} and crystals appeared at d_{p3}	Difficult to estimate	Impossible to estimate	Roughly between $0\% < \phi_2 < 58\%$ and $0.02 < \rho_3 < 2 \text{ g/l}$		Cyan point (Fig. 5.2)
					Scheme B4
Droplet appears at d_p moved back to the nozzle and crystals appeared inside	At the nozzle	Impossible to estimate	Roughly between $0\% < \phi_2 < 50\%$ and $0.02 < \rho_3 < 8 \text{ g/l}$		Rose point (Fig. 5.2)
					Scheme E2

On the NPLIN mechanism

In chapter 7 we have observed that the laser can concentrate molecules of higher refraction index. It can deviate 1,4-Dioxane flow, accelerate the DBDCS focussing and LLPT of DBDCS. Thus we suppose that laser will increase locally the concentration of DBDCS and the supersaturation. This explains the increase of the nucleation rate that we measure. This is a soft NPLIN mechanism. This will explain that we observe the same polymorph distribution, the same habit and growth rate with and without laser.

The mechanism of the NPLIN that is operative under our conditions is an optical tweezer effect. This is one of the mechanisms that have been proposed for NPLIN but it does not apply in the case of our second setup in CentraleSupélec where NPLIN is done with a collimated, not focused laser beam. [Clair, 2014] The results of these thesis suggest that using irradiation volume composed on thousands of focal points may produce different results about the control of the polymorph by the laser irradiation.

The FLIM measurement of figure 7.3 is an example of how our NPLIN device could contribute to the observation of the nucleation mechanism. FLIM shows that, at the focal point, a polymorph with a lifetime of 4.5 ns is present. This polymorph disappears in some μs when a minor, stable, polymorph survives and grows.

But the OM measurement of figure 7.27 shows another mechanism for the NPLIN. By gathering nano liquid droplets into bigger ones, the probability of nucleation of a droplet increases and crystals are formed. This is an example of how our NPLIN device could contribute to the observation of the two step nucleation mechanism.

On the crystallisation mechanism

The LLPS dominates the phase diagram of our device. We cannot generalise this observation to all crystallisations since we use a solvent shifting approach to provoke the crystallisation. Furthermore, the coaxial geometry creates a focusing of the solute towards very high supersaturation and the LLPS limit. This favours a liquid-liquid phase separation in competition with the crystallisation.

On the other side, during this work, we have observed the liquid-liquid phase separation. This

is an opportunity to study this potentially important step of the nucleation. We shall study the composition, the thermodynamic, the structure of the locally dense and disordered aggregates that are precursors of the nucleus.

On the potentiality of our method

Among the results we have presented in this manuscript, there is a methodological development we want to enhance in this section. Beyond the experimental methodology we have established a processing methodology also: which experiments? which data analysis? which simulation? This methodology is illustrated in Figure D.5. This consists in performing OM measurements along the nozzle at different positions for a given thermodynamic conditions (the four parameters fixed for given ternary mixture system). At the same place, for the same system, in the same conditions, FLIM experiments are conducted. Because the data collection zone is different from OM (125 μm in radius) and fluorescence (50 μm in radius), it is possible to record the lifetime decay in the central flow and in peripheral flow. The lifetime decay can be obtained directly from the measurements or deduced of a PCA analysis. The observation of the number of crystals crossing a fictive line, knowing the velocity of the flux, allow us to determine the size and the crystal birth rate at different distances. All the input and output parameters are summarised in Figure D.6. Parallely to these experiments *Comsol* simulation could be done according to the fact that a preliminary works has been done to parametrise correctly the simulation (see chapter 4). The *Comsol* simulation will allow us to do quantitative measurements on a sample with concentrations in space, through image analysis. Prior to that the determination of the solubility curve of the solute into the ternary mixture must be done. This methodology process opens the door to a large application field which will be discussed in the Perspectives section.

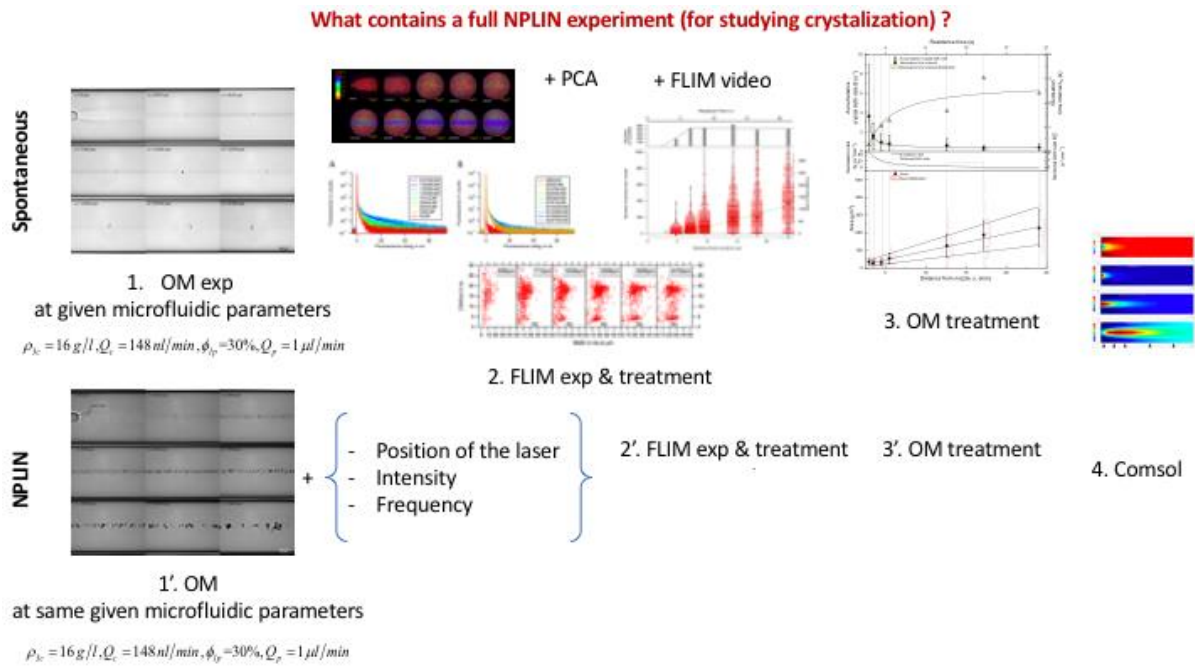


Figure D.5. Schematic illustration of a complete full NPLIN experiment in our microfluidic setup and its simulation.

- What are the parameters studied ? Input in red, observed or calculated in blue**
- Fluorescence lifetime **object_x.y_i** (ns)
 - Crystal habit
 - Position of the detection (OM, FLIM)
 - Average interval between 2 crystals d_w (μm)
 - Average nucleation time interval t_N (s)
 - Accumulative crystal birth rate B_x (s^{-1})
 - Nucleation rate N_S ($\text{s}^{-1} \text{mm}^{-3}$)
 - Sectional birth rate $B_{x1}x^2$ ($\text{s}^{-1} \text{mm}^{-1}$)
 - Average crystal area A_c (μm^2)
 - Area growth rate G_A ($\text{m}^2 \text{s}^{-1}$)
 - Average width of crystal L_c (μm)
 - Growth velocity G_L (ms^{-1})
 - Those parameters as a function of
 - The microfluidic parameters ρ_{3c} (g l^{-1}), Q_c (nl min^{-1}), ϕ_p (%), Q_r ($\mu\text{l min}^{-1}$)
 - The working diagram ρ_3 (g l^{-1}), ϕ_2 (%)
 - The observation distance from the nozzle x (mm)
 - The composition of the ternary mixture **1, 2, 3**
 - **1** = water **2** = 1,4 dioxane **3** = DBDCS
 - **1** = water **2** = THF(30%) + 1,4dioxane (70%) **3** = DBDCS
- Thermodynamic parameters**

 - Volume fraction of water ϕ_1 (μm)
 - Solubility ρ_3 (g l^{-1})
 - Mass concentration of DBDCS ρ (g l^{-1})
 - Supersturation ratio β (%)
 - Refractive index n_D
 - Refractive index gradient (m^{-1})
- Laser parameters**

 - Laser position d_L (μm)
 - Power energy P_{avr} (mW)
 - Frequency of the laser f_{rep} (Hz)
 - Polarisation **CP, LPS, LPP**
 - Wavelength λ (nm)
 - Pulse duration τ (fs)

Figure D.6. List of parameters used in a complete full NPLIN experiment in our microfluidic setup and its simulation

Perspectives

Different perspectives can be drawn covering all the aspects of this work. They will be presented in the following order: i) those concerning a better understanding of the DBDCS in ternary water (1)-1,4-dioxane (2)-DBDCS (3) or quaternary (DBDCS-water-1,4-dioxane-THF) mixture; ii) those concerning improvement in the experimental device; iii) those concerning the research methodology we have defined and finally iv) those concerning new insight in a better understanding nucleation mechanism.

On a better understanding of DBDCS

Despite the extremely large number of experiments, some additional experiments need to be done, to get a complete picture of DBDCS in solution. These experiments will not only contribute to the understanding of the molecule itself, but also will give additional information on the nucleation mechanism itself on the one side and on NPLIN mechanism on the other side. On Figure D.5 and Figure D.6, we have established what is a full experiment for a given condition. The idea is not to repeat systematically a full experiment at many new points without knowing what to do later with the data, but to perform some new experiment with a specific goal. These experiments have been summarised in the table D.12 (perspectives **P1** to **P7**). These experiments have been designed in this table with the actual microfluidic experimental setup.

Additionally, we have indicated when we have assigned the lifetime decay that we have not measured the emission light of the crystals produced in our microfluidic system. We should be tried to be perform such *post-mortem* characterisation (perspective **P8**). A feasibility study of an *in situ* characterisation would be also done (perspective **P9**).

Table P.1. Examples of experiment to be done on DBDCS solvent-antisolvent mixture.

	For which goals?	Which experiments?	With which conditions?
P1	To assign a polymorph to the rhombus or stars crystal habit observed	To measure the lifetime of stars, rhombus	Such as Figure 6.3 water -THF 20-30% dioxane 80-70 % -DBDCS system
P2	To visualise the effect of the THF on crystallisation	To do a full experiment (OM, FLIM, PCA for lifetime decay, crystal birth rate determination)	Chose a condition for with THF where crystals appear and for which it will be sufficiently slow to optimise fluorescence detection
P3	To better understand crystal nucleation of DBDCS in ternary mixture (water-1,4 dioxane)	At least full experiment (OM, FLIM, PCA for lifetime decay, crystal birth rate determination and NPLIN in LPS at a fixed power and a fixed rate) has been done in condition 1 (16 mg/l). For conditions 2 and 3 some experiments have been done but not fully exploited. Therefore, remaining treatments and experiments must be performed to have a complete table D9 and D10 for the 3 conditions.	water-1,4 dioxane, condition 2 and 3
P4	To increase the quality of the assignation of the different lifetime decay	To find a condition (close to the 1, 2 or 3) conditions) to have an analogue of Figure 7.10 with a larger number of photons.	Conditions 1, 2 or 3 with the slowest speed to optimise fluorescence detection
P5		Figure 6.4 has allowed us to “see” a crystal growth (inside abnormal droplet trap). To do FLIM on abnormal droplet trap to have good lifetime decay.	Such as Figure 6.4
P6	To have more statistic of the impact of polarisation on crystal birth rate	To get more points in Figure 7.19 with CP and LPP as (crystal birth rate as function of the energy power)	Such as Figure 7.19 To add on the plot the LPS results of Figure 7.17 and to measure new points with CP or LPP polarisation
P7	To study the composition of LLPS phase (droplet)	As for the crystal, to make FLIM on droplet and extract the lifetime decay.	Rose points of the working diagram, with a sufficiently low speed to optimise the FLIM measurement

The actual *post-mortem* characterisation was done by OM, FLIM and SEM. It would be very interesting to do micro Raman experiments on the product obtained on the glass (perspective **P10**). Technically, that could be done quite easily because such device is available at SPMS Laboratory with the help of the engineer Dr. Pascale Gemeiner. However, despite a precise IR spectra study of the DBDCS film on a ZnSe substrate before and after photoirradiation [Fujimori, 2016], there is no Raman study. Therefore, a preparation work on the different DBDCS state (solution, amorphous nano particles) with Raman would be done. (perspective **P11**).

Finally, we have already indicated the difficulties of assignment of the lifetime decay to a given phase due mainly to the small number of photons. Let imagine, that we will overcome these difficulties (**P4** and **P5** successful). Therefore, the next subject to tackle will be the correlation between the lifetime decays and the DBDCS structure at the molecular level. Based on the theoretical work done by Yoon *et al* [Yoon, 2010] the splitting of the DBDCS sheets seems to be a pertinent hypothesis to explain its polymorphism. If we could theoretically estimate a lifetime decay based on a structural description of the molecules packing, it would really help. Predicting lifetime remains a great challenge. Very few studies have been published on that domain. One can cite the work of Grieser team [Träbert, 2012] or the very recent study of Zhang *et al* [Xiao-he, 2018]. The ERC team of our Laboratory at ENS Paris-Saclay is working on that direction (calculation of spectra) and therefore would be able to de predict lifetime decays. We shall collaborate with them (perspective **P12**).

We have not had sufficient time to explore more systematically the relation in NPLIN with microfluidic parameters (working diagram) d_L and d_p apparition of objects (OM or FLIM). With the new experiments (P3 and P6) we should have sufficient material to draw new conclusions (perspective P13).

On the improvements of our experimental device

The heterogeneous nucleation on the wall of the device limits strongly the observation

time (by OM and by FLIM) and should be improved (perspective **P14**). Despite the huge work already done in this PhD on that subject, one should find new ideas.

Our microfluidic setup has proved its capacity to allow a great number of measurements. However, performing an experiment is highly human time demanding. Firstly, the platform is not motorised, and it is impossible to follow by OM or FLIM the same crystal in the flux (see Figure 2.15). We already have got the funds to motorise the platform. We are currently, searching the commercial solution, matching our requirements (perspective **P15**). Secondly, one can imagine building a version 2 of our device dedicated to high throughput experiments (motorisation of syringes, automatic image analysis) in the spirit of the high throughput crystallisation batches, the high throughput biological target determination for a drug or high throughput chemical synthesis for new drugs (perspective **P16**).

To add some new insight to the mechanism, it should be important to know the temperature (and the local increase of temperature) at the NPLIN laser focal spot. That should be done *via* nanothermometers (perspective **P17**). We are applying for a grant with Prof Marc Verelst de Chromalys, spin off de l'Université de Toulouse. Actually, all measurements are done at "room" temperature, without any possibility to control it. Replacing our syringes by temperature control syringe would be useful (perspective **P18**). Such syringes are commercially available (4 000 € *per* syringe).

Further studies are required to control the size and size dispersity of the nanodroplets. Therefore, another great breakthrough of our device would be to have an *in situ* monitoring of the size and size dispersion of the nanoparticle by monitoring the diffraction of laser light or X ray (perspective **P19**). That must be designed, for example in the framework of an ANR project.

Finally, we have already evoked the post-mortem characterisation of the object product (**P10**), if it gives interesting results (especially in term of resolution limit), we could install on our device an *in situ* micro Raman detection (perspective **P20**). Such super head exists, but has a significant cost (around 57 000 €, Spelec Raman from Metrohm).

On the improvements of methodologic developments

The initial goal of this manuscript, as written in the PhD proposal, was to implement NPLIN@PPSM, fluo@SPMS and to do it on the same compound. We have succeeded on the first point (NPLIN in microfluidic), but we have absolutely no time to work on the reverse fluorescence on the static NPLIN. The funds have been obtained (small equipment of Cristech project), the design is established, we need to buy and install it (perspective **P21**). Evidently, that has a sense if we can compare the results obtained by static and microfluidic NPLIN. To do that, we need to do on the same compound. We plane to do OM microfluidic NPLIN, on glycine (perspective **P22**), because there is a large number of results on glycine laser induce nucleation (12 papers in table Appen A.1 including the work done at SPMS laboratory). However, the characterisation of glycine polymorphism cannot be done using the crystal habit of glycine crystal (different crystal habit for the same polymorph). Additionally, glycine is not a fluorescence molecule.

Due to collaboration at ENS Paris-Saclay, we plane to perform an OM microfluidic experiment on a protein: albumin (perspective **P23**). As observed in Figure 1.6, 32 papers have shown that NPLIN could help to produce single crystal of protein. The case of albumin has not been treated.

At the beginning of this PhD, we have searched a compound which could be studied by the both experiments (static and microfluidic) and characterised *in situ* by fluorescence. Due to the large number of experiments needed to be performed with static experiments, a commercial product (not too expensive) must be chosen. This compound must be an AIE molecule. It would have some polymorphs with different fluorescence spectra. Therefore, we have chosen the tetraphenylethylene (TPE) (perspective **P24**). Bottle of this compound are already waiting in our chemical room.

We have undergone a new collaboration on metal halide perovskite with important applications in photovoltaics and electronic applications, in collaboration with Dr. Damien Garrot (GEMC) and Emmanuel Delaporte (LAC). This has been the subject of two unsuccessful

ANR application. We plan to re-apply next year (perspective **P25**).

Concerning the *Comsol* simulation and the thermodynamic development behind, we have opened large possibilities to use it in co-flow microfluidic experiments. We will use it for our next studies, these simulations are included in what we have called a full experiment (Figure D.6 and D.7). However, these simulations can only describe the situation before the phase transitions. Moreover, one has not simulated the impact of the laser on the solution. That is a point which we would already tackled for the static NPLIN, some years ago, but we have never succeeded. We have few months ago initiated a collaboration with Dr. Clément Lafarge from LPQM (UMR 8537, CNRS, ENS Paris-Saclay and CentraleSupélec) Laboratory on refractive index. Working on optical tweezer by *Comsol* could be a possible stimulating challenge for him (perspective **P26**).

In the work presented in this manuscript, we have planned to use the 3 types of *Comsol* results (i) time-dependent computation (ii) parametric sweep (iii) stationary simulation. Due to a lack of pages, we have not reported the time-dependent computation. It should be done on DBDCS system of for the other systems we plan to work with (**P22** or **P24**). Generally speaking, the link of our experimental results and the simulation would be intensified (perspective **P27**).

The nucleation efficiency is increased by the laser, but the photo-nucleation yield of one crystal *per* laser shot is not reached. The number of shots required to have a crystal with a probability of 10% will define the time resolution of the time resolved nucleation studies. We shall work on that (perspective **P28**).

Towards the understanding the mechanism of nucleation

It would be very challenging to apply the optical tweezer hypothesis to static NPLIN: how to create a high number of bright and dark points in the tube using Fresnel lens or an array of micro-lens that will resist to the high-power density of the laser? Our research engineer Dr Jean-François Audibert is already working on that (perspective **P29**).

In the text we have given some insight to the better understanding of the nucleation mechanism. However, we have the feeling that we could better correlate our observations to the hypothesis already stated in the NPLIN bibliography. This will be done shortly (perspective **P30**).

This section contains at least contains 30 “perspectives”. We will evidently have to rank them by their feasibility (easy or not), their time depending (short, long), their cost (funds available, or application to a project), their challenge interest.

As a (very) final conclusion...

Using microfluidic device, a focused fs IR laser and a FLIM setup, we have observed the first milliseconds of the birth of a crystal. The flow properties of microfluidic allows the observation of hundreds of nucleation events and the use of a laser allows the synchronisation of the spectroscopic tools with the nucleation. We have shown that the laser, by transiently squeezing the nucleation precursors, can induce the nucleation without changing its mechanism.

Several experimental constraints limit this approach.

- We have been probably lucky that the spontaneous nucleation rate and the growth rate have allowed us to detect crystal after 2s of residence time. To have the nucleation occurring in the observation window of our device, implied to have very low flow rate of a few tenth of nanolitre *per* minutes.

- Another limit is the precipitation of the amorphous phase. The use of a strong antisolvent can focus the solute up to the concentration where a fast LLPS of an amorphous phase will occur. We have shown that the focusing strength can be anticipated by measuring the difference of solubility of the solute between the two solvents, and the focusing strength can be reduced by mitigated the anti-solvent. This can be done in the limit of the heterogeneous nucleation on the wall of the device.

We think that by localizing in space and time the nucleation we have opened this research domain to by time and space resolved studies (video). It should have the same impact

than the flash photolysis had on chemical kinetics a few years ago^{1,2}.

The solvent focusing of the solute gathers molecules until the concentration reaches the LLPS threshold. We produce a cloud of nanodroplets. The remaining solvent gradient further gather the micro emulsion into a necklace of monodisperse micrometric drops. We had the chance to see, better than our predecessors, the details of a process that has been extensively used in laboratories and industry. Further studies are required to control the size and size dispersity of the nanodroplets. But our quantitative description of the process of production of nanoparticles will allow the calculation of the optimised mixing conditions and make a step in the direction of computer optimised, quickly reconfigurable production: industry 4.0.

¹ <https://www.nobelprize.org/prizes/chemistry/1967/summary/>

² <https://www.nobelprize.org/prizes/chemistry/1999/summary/>

References

- Abbott, M. M. & K. K. Nass. 1986. Equations of State and Classical Solution Thermodynamics. In *Equations of State*, 2-40. American Chemical Society. <https://doi.org/10.1021/bk-1986-0300.ch001>
- Abecassis, B., F. Testard, O. Spalla & P. Barboux (2007) Probing in situ the nucleation and growth of gold nanoparticles by small-angle X-ray scattering. *Nano Lett*, 7, 1723-7. <https://doi.org/10.1021/nl0707149>
- Abou-Hassan, A., O. Sandre, S. Neveu & V. Cabuil (2009) Synthesis of goethite by separation of the nucleation and growth processes of ferrihydrite nanoparticles using microfluidics. *Angew Chem Int Ed Engl*, 48, 2342-5. <https://doi.org/10.1002/anie.200805933>
- Abrams, D. S. & J. M. Prausnitz (1975) Statistical thermodynamics of liquid mixtures: A new expression for the excess Gibbs energy of partly or completely miscible systems. *AIChE Journal*, 21, 116-128. <https://doi.org/10.1002/aic.690210115>
- Acree, W. E. (1992) Mathematical representation of thermodynamic properties. *Thermochimica Acta*, 198, 71-79. [https://doi.org/10.1016/0040-6031\(92\)85059-5](https://doi.org/10.1016/0040-6031(92)85059-5)
- Acree, W. E., J. W. McCargar, A. I. Zvaigzne & I. L. Teng (1991a) Mathematical Representation of Thermodynamic Properties. Carbazole Solubilities in Binary Alkane + Dibutyl Ether and Alkane + Tetrahydropyran Solvent Mixtures. *Physics and Chemistry of Liquids*, 23, 27-35. <https://doi.org/10.1080/00319109108030630>
- Acree, W. E. & A. I. Zvaigzne (1991b) Thermodynamic properties of non-electrolyte solutions. *Thermochimica Acta*, 178, 151-167. [https://doi.org/10.1016/0040-6031\(91\)80307-5](https://doi.org/10.1016/0040-6031(91)80307-5)
- Adrianowicz, K., M. Paluch & R. Richert (2018) Formation of new polymorphs and control of crystallization in molecular glass-formers by electric field. *Phys Chem Chem Phys*, 20, 925-931. <https://doi.org/10.1039/c7cp07352f>
- Al-haq, M. I., E. Lebrasseur, H. Tsuchiya & T. Torii (2007) Protein crystallization under an electric field. *Crystallography Reviews*, 13, 29-64. <https://doi.org/10.1080/08893110701421463>
- Alantary, D. & S. H. Yalkowsky (2018) Estimating the Physicochemical Properties of Polysubstituted Aromatic Compounds Using UPPER. *J Pharm Sci*, 107, 297-306. <https://doi.org/10.1016/j.xphs.2017.10.018>
- Alexander, A. J. & P. J. Camp (2009) Single Pulse, Single Crystal Laser-Induced Nucleation of Potassium Chloride. *Crystal Growth & Design*, 9, 958-963. <https://doi.org/10.1021/cg8007415>
- Aminabhavi, T. M. & B. Gopalakrishna (1995) Density, Viscosity, Refractive Index, and Speed of Sound in Aqueous Mixtures of N,N-Dimethylformamide, Dimethyl Sulfoxide, N,N-Dimethylacetamide, Acetonitrile, Ethylene Glycol, Diethylene Glycol, 1,4-Dioxane, Tetrahydrofuran, 2-Methoxyethanol, and 2-Ethoxyethanol at 298.15 K. *Journal of Chemical & Engineering Data*, 40, 856-861. <https://doi.org/10.1021/jc00020a026>
- Andreetta, M. R. B. 2012. *Crystallization-Science and Technology*.
- Anna, S. L., N. Bontoux & H. A. Stone (2003) Formation of dispersions using “flow focusing” in microchannels. *Applied Physics Letters*, 82, 364-366. <https://doi.org/10.1063/1.1537519>

- Antolovic, I. M., S. Burri, R. A. Hoebe, Y. Maruyama, C. Bruschini & E. Charbon (2016) Photon-Counting Arrays for Time-Resolved Imaging. *Sensors (Basel)*, 16, 1005. <https://doi.org/10.3390/s16071005>
- Arellano, M. P., J. M. Aguilera & P. Bouchon (2004) Development of a digital video-microscopy technique to study lactose crystallisation kinetics in situ. *Carbohydr Res*, 339, 2721-30. <https://doi.org/10.1016/j.carres.2004.09.009>
- Aubry, J., F. Ganachaud, J. P. Cohen Addad & B. Cabane (2009) Nanoprecipitation of polymethylmethacrylate by solvent shifting: 1. Boundaries. *Langmuir*, 25, 1970-9. <https://doi.org/10.1021/la803000e>
- Balasubramaniam, R. & R. S. Subramanian (2000) The migration of a drop in a uniform temperature gradient at large Marangoni numbers. *Physics of Fluids*, 12, 733-743. <https://doi.org/10.1063/1.870330>
- Bartkiewicz, S. & A. Miniewicz (2015) Whirl-enhanced continuous wave laser trapping of particles. *Phys Chem Chem Phys*, 17, 1077-83. <https://doi.org/10.1039/c4cp04008b>
- Becker, W., V. Shcheslavkiy, S. Frere & I. Slutsky (2014) Spatially resolved recording of transient fluorescence-lifetime effects by line-scanning TCSPC. *Microsc Res Tech*, 77, 216-24. <https://doi.org/10.1002/jemt.22331>
- Becker, W., V. Shcheslavskiy & H. Studier. 2015. TCSPC FLIM with Different Optical Scanning Techniques. In *Advanced Time-Correlated Single Photon Counting Applications*, ed. W. Becker, 65-117. Cham: Springer International Publishing. https://doi.org/10.1007/978-3-319-14929-5_2
- Beer, N. R., E. K. Wheeler, L. Lee-Houghton, N. Watkins, S. Nasarabadi, N. Hebert, P. Leung, D. W. Arnold, C. G. Bailey & B. W. Colston (2008) On-chip single-copy real-time reverse-transcription PCR in isolated picoliter droplets. *Anal Chem*, 80, 1854-8. <https://doi.org/10.1021/ac800048k>
- Belloni, J., A. Spasojevic de-Biré, S. Sorgues, M. Mostafavi, P. Scoufflaire & N.-E. Ghermani (2014) Nucléation/croissance des cristaux déclenchée par impulsion. *L'Actualité Chimique*, 387-388-389, 77-84.
- Bergfors, T. M. 2009. *Protein crystallization*. Internat'l University Line.
- Besbes, R., N. Ouerfelli & H. Latrous (2009) Density, dynamic viscosity, and derived properties of binary mixtures of 1,4 dioxane with water at T=298.15 K. *Journal of Molecular Liquids*, 145, 1-4. <https://doi.org/10.1016/j.molliq.2008.09.009>
- Bhamidi, V., P. J. A. Kenis & C. F. Zukoski (2017) Probability of Nucleation in a Metastable Zone: Induction Supersaturation and Implications. *Crystal Growth & Design*, 17, 1132-1145. <https://doi.org/10.1021/acs.cgd.6b01529>
- BI, R. 2016. IUT intership.
- Bondi, A. A. (1968) Physical properties of molecular crystals liquids, and glasses.
- Brick, M. C., H. J. Palmer & T. H. Whitesides (2003) Formation of Colloidal Dispersions of Organic Materials in Aqueous Media by Solvent Shifting†. *Langmuir*, 19, 6367-6380. <https://doi.org/10.1021/la034173o>
- Carman, P. C. (1967) Self-diffusion and interdiffusion in complex-forming binary systems. *The Journal of Physical Chemistry*, 71, 2565-2572. <https://doi.org/10.1021/j100867a027>
- Casadevall i Solvas, X. & A. deMello (2011) Droplet microfluidics: recent developments and future applications. *Chem Commun (Camb)*, 47, 1936-42. <https://doi.org/10.1039/c0cc02474k>
- Chandrasekhar, S. 2013. *Hydrodynamic and hydromagnetic stability*. Courier Corporation.

- Chang, S. Y., Y. Gründer, S. G. Booth, L. B. Molleta, A. Uehara, J. F. W. Mosselmans, G. Cibin, V. T. Pham, L. Nataf, R. A. W. Dryfe & S. L. M. Schroeder (2016) Detection and characterisation of sub-critical nuclei during reactive Pd metal nucleation by X-ray absorption spectroscopy. *CrystEngComm*, 18, 674-682. <https://doi.org/10.1039/c5ce01883h>
- Charoenrein, S. & D. S. Reid (1989) The use of DSC to study the kinetics of heterogeneous and homogeneous nucleation of ice in aqueous systems. *Thermochimica Acta*, 156, 373-381. [https://doi.org/10.1016/0040-6031\(89\)87204-1](https://doi.org/10.1016/0040-6031(89)87204-1)
- Chaudhari, A., M. Naganathappa, M. N. Shinde & A. C. Kumbharkhane (2011) Theoretical investigation of molecular interactions in dioxane and water using hydrogen bonding model and density functional method. *International Journal of Quantum Chemistry*, 111, 2972-2979. <https://doi.org/10.1002/qua.22605>
- Chen, D. L. & R. F. Ismagilov (2006) Microfluidic cartridges preloaded with nanoliter plugs of reagents: an alternative to 96-well plates for screening. *Curr Opin Chem Biol*, 10, 226-31. <https://doi.org/10.1016/j.cbpa.2006.04.004>
- Chevreuril, M., D. Law-Hine, J. Chen, S. Bressanelli, S. Combet, D. Constantin, J. Degrouard, J. Moller, M. Zeghal & G. Tresset (2018) Nonequilibrium self-assembly dynamics of icosahedral viral capsids packaging genome or polyelectrolyte. *Nat Commun*, 9, 3071. <https://doi.org/10.1038/s41467-018-05426-8>
- Chickos, J. S., W. E. Acree & J. F. Liebman (1999) Estimating Solid–Liquid Phase Change Enthalpies and Entropies. *Journal of Physical and Chemical Reference Data*, 28, 1535-1673. <https://doi.org/10.1063/1.556045>
- Christensen, J. J., R. W. Hanks & R. M. Izatt. 1982. *Handbook of heats of mixing*. New York: Wiley.
- Clair, B., A. Ikni, W. Li, P. Scoufflaire, V. Quemener & A. Spasojević-de Biré (2014) A new experimental setup for high-throughput controlled non-photochemical laser-induced nucleation: application to glycine crystallization. *Journal of Applied Crystallography*, 47, 1252-1260. <https://doi.org/10.1107/s160057671401098x>
- Cöelfen, H. & M. Antonietti. 2008. *Mesocrystals and nonclassical crystallization*. John Wiley & Sons.
- Currey, J. D. (1997) Mechanical properties of mother of pearl in tension. *Proceedings of the Royal Society of London. Series B. Biological Sciences*, 196, 443-463. <https://doi.org/10.1098/rspb.1977.0050>
- D'Agostino, C., M. D. Mantle, L. F. Gladden & G. D. Moggridge (2011) Prediction of binary diffusion coefficients in non-ideal mixtures from NMR data: Hexane–nitrobenzene near its consolute point. *Chemical Engineering Science*, 66, 3898-3906. <https://doi.org/10.1016/j.ces.2011.05.014>
- (2012) Prediction of mutual diffusion coefficients in non-ideal mixtures from pulsed field gradient NMR data: Triethylamine–water near its consolute point. *Chemical Engineering Science*, 74, 105-113. <https://doi.org/10.1016/j.ces.2012.02.025>
- Dadmand, S., F. Kamari, W. E. Acree, Jr. & A. Jouyban (2018) Solubility Prediction of Drugs in Binary Solvent Mixtures at Various Temperatures Using a Minimum Number of Experimental Data Points. *AAPS PharmSciTech*, 20, 10. <https://doi.org/10.1208/s12249-018-1244-4>
- Dannenfelser, R.-M. & S. H. Yalkowsky (1996) Estimation of Entropy of Melting from Molecular Structure: A Non-Group Contribution Method. *Industrial &*

- Engineering Chemistry Research*, 35, 1483-1486.
<https://doi.org/10.1021/ie940581z>
- Dannenfelser, R. M., N. Surendran & S. H. Yalkowsky (1993) Molecular Symmetry and Related Properties. *SAR and QSAR in Environmental Research*, 1, 273-292. <https://doi.org/10.1080/10629369308029892>
- Darken, L. S. (1948) Diffusion, mobility and their interrelation through free energy in binary metallic systems. *Trans. Aime*, 175, 184-201.
- De Beer, T. R., P. Vercruysee, A. Burggraeve, T. Quinten, J. Ouyang, X. Zhang, C. Vervaet, J. P. Remon & W. R. Baeyens (2009) In-line and real-time process monitoring of a freeze drying process using Raman and NIR spectroscopy as complementary process analytical technology (PAT) tools. *J Pharm Sci*, 98, 3430-46. <https://doi.org/10.1002/jps.21633>
- Demond, A. H. & A. S. Lindner (2002) Estimation of interfacial tension between organic liquids and water. *Environmental Science & Technology*, 27, 2318-2331. <https://doi.org/10.1021/es00048a004>
- Donahue, D. J. & F. E. Bartell (1952) The Boundary Tension at Water-Organic Liquid Interfaces. *The Journal of Physical Chemistry*, 56, 480-484. <https://doi.org/10.1021/j150496a016>
- Dorozhkin, S. V. (2016) Calcium orthophosphates (CaPO₄): occurrence and properties. *Prog Biomater*, 5, 9-70. <https://doi.org/10.1007/s40204-015-0045-z>
- Douglas, P., H. D. Burrows & R. C. Evans. 2013. Foundations of Photochemistry: A Background on the Interaction Between Light and Molecules. In *Applied Photochemistry*, 1-88. Springer. https://doi.org/10.1007/978-90-481-3830-2_1
- Douroumis, D. & A. Nokhodchi (2017) Preface: Engineering of pharmaceutical cocrystals, salts and polymorphs: Advances and Challenges. *Adv Drug Deliv Rev*, 117, 1-2. <https://doi.org/10.1016/j.addr.2017.10.002>
- Duffus, C., P. J. Camp & A. J. Alexander (2009) Spatial control of crystal nucleation in agarose gel. *J Am Chem Soc*, 131, 11676-7. <https://doi.org/10.1021/ja905232m>
- Einstein, A. (1905) Über die von der molekularkinetischen Theorie der Wärme geforderte Bewegung von in ruhenden Flüssigkeiten suspendierten Teilchen. *Annalen der Physik*, 322, 549-560. <https://doi.org/10.1002/andp.19053220806>
- Erdemir, D., A. Y. Lee & A. S. Myerson (2009) Nucleation of crystals from solution: classical and two-step models. *Acc Chem Res*, 42, 621-9. <https://doi.org/10.1021/ar800217x>
- Fang, K., S. Arnold & B. A. Garetz (2014) Nonphotochemical Laser-Induced Nucleation in Levitated Supersaturated Aqueous Potassium Chloride Microdroplets. *Crystal Growth & Design*, 14, 2685-2688. <https://doi.org/10.1021/cg5004319>
- Fick, A. (1855) V. On liquid diffusion. *The London, Edinburgh, and Dublin Philosophical Magazine and Journal of Science*, 10, 30-39. <https://doi.org/10.1080/14786445508641925>
- Filobelo, L. F., O. Galkin & P. G. Vekilov (2005) Spinodal for the solution-to-crystal phase transformation. *J Chem Phys*, 123, 014904. <https://doi.org/10.1063/1.1943413>
- Fleming, G. (1986) Chemical applications of ultrafast spectroscopy.
- Fleury, B., M. A. Neouze, J. M. Guigner, N. Menguy, O. Spalla, T. Gacoin & D. Carriere (2014) Amorphous to crystal conversion as a mechanism governing the structure of luminescent YVO₄:Eu nanoparticles. *ACS Nano*, 8, 2602-8. <https://doi.org/10.1021/nn4062534>

- Fratzl, P., H. S. Gupta, E. P. Paschalis & P. Roschger (2004) Structure and mechanical quality of the collagen–mineral nano-composite in bone. *J. Mater. Chem.*, 14, 2115-2123. <https://doi.org/10.1039/b402005g>
- Frontana-Uribe, B. A. & A. Moreno (2008) On Electrochemically Assisted Protein Crystallization and Related Methods†. *Crystal Growth & Design*, 8, 4194-4199. <https://doi.org/10.1021/cg800731p>
- Fujimori, J.-i., A. Katsuki & F. Ito (2016) Fluorescence Enhancement of a Dicyanostilbene Derivative Film Casted from an Alcoholic Solution Triggered by UV-light Irradiation. *Chemistry Letters*, 45, 421-423. <https://doi.org/10.1246/cl.151195>
- Galkin, O., K. Chen, R. L. Nagel, R. E. Hirsch & P. G. Vekilov (2002) Liquid-liquid separation in solutions of normal and sickle cell hemoglobin. *Proc Natl Acad Sci U S A*, 99, 8479-83. <https://doi.org/10.1073/pnas.122055299>
- Gao, Z., S. Rohani, J. Gong & J. Wang (2017) Recent Developments in the Crystallization Process: Toward the Pharmaceutical Industry. *Engineering*, 3, 343-353. <https://doi.org/10.1016/j.Eng.2017.03.022>
- Garetz, B. A., J. E. Aber, N. L. Goddard, R. G. Young & A. S. Myerson (1996) Nonphotochemical, Polarization-Dependent, Laser-Induced Nucleation in Supersaturated Aqueous Urea Solutions. *Phys Rev Lett*, 77, 3475-3476. <https://doi.org/10.1103/PhysRevLett.77.3475>
- Garetz, B. A., J. Matic & A. S. Myerson (2002) Polarization switching of crystal structure in the nonphotochemical light-induced nucleation of supersaturated aqueous glycine solutions. *Phys Rev Lett*, 89, 175501. <https://doi.org/10.1103/PhysRevLett.89.175501>
- Garin, M., C. Jin, D. Cardador, T. Trifonov & R. Alcubilla (2017) Controlling Plateau-Rayleigh instabilities during the reorganization of silicon macropores in the Silicon Millefeuille process. *Sci Rep*, 7, 7233. <https://doi.org/10.1038/s41598-017-07393-4>
- Garside, J., A. Mersmann & J. Nývlt. 2002. *Measurement of crystal growth and nucleation rates*. IChemE.
- Gavezzotti, A. (1999) Molecular aggregation of acetic acid in a carbon tetrachloride solution: a molecular dynamics study with a view to crystal nucleation. *Chemistry—A European Journal*, 5, 567-576. [https://doi.org/10.1002/\(SICI\)1521-3765\(19990201\)5:2%3C567::AID-CHEM567%3E3.0.CO;2-6](https://doi.org/10.1002/(SICI)1521-3765(19990201)5:2%3C567::AID-CHEM567%3E3.0.CO;2-6)
- Gebauer, D. & H. Cölfen (2011) Prenucleation clusters and non-classical nucleation. *Nano Today*, 6, 564-584. <https://doi.org/10.1016/j.nantod.2011.10.005>
- Gebauer, D., H. Cölfen, A. Verch & M. Antonietti (2009) The Multiple Roles of Additives in CaCO₃Crystallization: A Quantitative Case Study. *Advanced Materials*, 21, 435-439. <https://doi.org/10.1002/adma.200801614>
- Gebauer, D., M. Kellermeier, J. D. Gale, L. Bergstrom & H. Colfen (2014) Prenucleation clusters as solute precursors in crystallisation. *Chem Soc Rev*, 43, 2348-71. <https://doi.org/10.1039/c3cs60451a>
- Gebauer, D., A. Volkel & H. Colfen (2008) Stable prenucleation calcium carbonate clusters. *Science*, 322, 1819-22. <https://doi.org/10.1126/science.1164271>
- Ghosh, G. (1999) Dispersion-equation coefficients for the refractive index and birefringence of calcite and quartz crystals. *Optics Communications*, 163, 95-102. [https://doi.org/10.1016/s0030-4018\(99\)00091-7](https://doi.org/10.1016/s0030-4018(99)00091-7)
- Gibbs, J. W. (1879) On the equilibrium of heterogeneous substances. ---. 1906. *The Scientific Papers of Josiah Willard Gibbs*. London: LONGMANS,

GREEN, AND CO.,

- Gierycz, P. (1986) Thermodynamics of mixtures of N-methylpyrrolidone with hydrocarbons and their hydroxyl derivatives. *Thermochimica Acta*, 108, 229-238. [https://doi.org/10.1016/0040-6031\(86\)85095-x](https://doi.org/10.1016/0040-6031(86)85095-x)
- Goates, J. R. & R. J. Sullivan (1958) Thermodynamic Properties of the System Water-p-Dioxane. *The Journal of Physical Chemistry*, 62, 188-190. <https://doi.org/10.1021/j150560a011>
- Grabowski, Z. R., K. Rotkiewicz & W. Rettig (2003) Structural changes accompanying intramolecular electron transfer: focus on twisted intramolecular charge-transfer states and structures. *Chem Rev*, 103, 3899-4032. <https://doi.org/10.1021/cr9407451>
- Grossier, R., Z. Hammadi, R. Morin & S. Veessler (2011) Predictive nucleation of crystals in small volumes and its consequences. *Phys Rev Lett*, 107, 025504. <https://doi.org/10.1103/PhysRevLett.107.025504>
- Guillot, P., A. Colin, A. S. Utada & A. Ajdari (2007) Stability of a jet in confined pressure-driven biphasic flows at low reynolds numbers. *Phys Rev Lett*, 99, 104502. <https://doi.org/10.1103/PhysRevLett.99.104502>
- Haas, C. (2000) The Interface between a Protein Crystal and an Aqueous Solution and Its Effects on Nucleation and Crystal Growth. *The Journal of Physical Chemistry B*, 104, 368-377. <https://doi.org/10.1021/jp993210a>
- Haeberle, S. & R. Zengerle (2007) Microfluidic platforms for lab-on-a-chip applications. *Lab Chip*, 7, 1094-110. <https://doi.org/10.1039/b706364b>
- Hajian, R. & S. Hardt (2015) Formation and lateral migration of nanodroplets via solvent shifting in a microfluidic device. *Microfluidics and Nanofluidics*, 19, 1281-1296. <https://doi.org/10.1007/s10404-015-1644-7>
- Hale, G. M. & M. R. Querry (1973) Optical Constants of Water in the 200-nm to 200-microm Wavelength Region. *Appl Opt*, 12, 555-63. <https://doi.org/10.1364/AO.12.000555>
- Hammadi, Z., J.-P. Astier, R. Morin & S. Veessler (2007) Protein Crystallization Induced by a Localized Voltage. *Crystal Growth & Design*, 7, 1472-1475. <https://doi.org/10.1021/cg070108r>
- Hammadi, Z., J.-P. Astier, R. Morin & S. p. Veessler (2009a) Spatial and Temporal Control of Nucleation by Localized DC Electric Field. *Crystal Growth & Design*, 9, 3346-3347. <https://doi.org/10.1021/cg900150n>
- Hammadi, Z., N. Candoni, R. Grossier, M. Ildefonso, R. Morin & S. Veessler (2013) Small-volume nucleation. *Comptes Rendus Physique*, 14, 192-198. <https://doi.org/10.1016/j.crhy.2012.12.004>
- Hammadi, Z., R. Grossier, S. Zhang, A. Ikni, N. Candoni, R. Morin & S. Veessler (2015) Localizing and inducing primary nucleation. *Faraday Discuss*, 179, 489-501. <https://doi.org/10.1039/c4fd00274a>
- Hammadi, Z. & S. Veessler (2009b) New approaches on crystallization under electric fields. *Prog Biophys Mol Biol*, 101, 38-44. <https://doi.org/10.1016/j.pbiomolbio.2009.12.005>
- Han, Z., W. Li, Y. Huang & B. Zheng (2009) Measuring rapid enzymatic kinetics by electrochemical method in droplet-based microfluidic devices with pneumatic valves. *Anal Chem*, 81, 5840-5. <https://doi.org/10.1021/ac900811y>
- Hansen, C. L., S. Classen, J. M. Berger & S. R. Quake (2006) A microfluidic device for kinetic optimization of protein crystallization and in situ structure determination. *J Am Chem Soc*, 128, 3142-3. <https://doi.org/10.1021/ja0576637>

- Hartmann, L., A. Kumar, M. Welker, A. Fiore, C. Julien-Rabant, M. Gromova, M. Bardet, P. Reiss, P. N. Baxter, F. Chandezon & R. B. Pansu (2012) Quenching dynamics in CdSe nanoparticles: surface-induced defects upon dilution. *ACS Nano*, 6, 9033-41. <https://doi.org/10.1021/nm303150j>
- Hatase, M., M. Hanaya & M. Oguni (2004) Studies of homogeneous-nucleation-based crystal growth: significant role of phenyl ring in the structure formation. *Journal of Non-Crystalline Solids*, 333, 129-136. <https://doi.org/10.1016/j.jnoncrysol.2003.10.010>
- He, M., J. S. Edgar, G. D. Jeffries, R. M. Lorenz, J. P. Shelby & D. T. Chiu (2005) Selective encapsulation of single cells and subcellular organelles into picoliter- and femtoliter-volume droplets. *Anal Chem*, 77, 1539-44. <https://doi.org/10.1021/ac0480850>
- Helliwell, J. R. (2017) New developments in crystallography: exploring its technology, methods and scope in the molecular biosciences. *Biosci Rep*, 37, BSR20170204. <https://doi.org/10.1042/BSR20170204>
- Hiroaki, A., T. Kazufumi, H. Youichiroh, I. Tsuyoshi, M. Yusuke, M. Hiroyoshi, Y. Masashi, T. Yasuo, M. Masaaki, K. Shigenori, M. Hiroshi, K. Yasushi & S. Takatomo (2003) Laser Irradiated Growth of Protein Crystal. *Japanese Journal of Applied Physics*, 42, L798. <https://doi.org/10.1143/JJAP.42.L798/meta>
- Holz, M., S. R. Heil & A. Sacco (2000) Temperature-dependent self-diffusion coefficients of water and six selected molecular liquids for calibration in accurate ¹H NMR PFG measurements. *Physical Chemistry Chemical Physics*, 2, 4740-4742. <https://doi.org/10.1039/b005319h>
- Hosokawa, Y., H. Adachi, M. Yoshimura, Y. Mori, T. Sasaki & H. Masuhara (2005) Femtosecond Laser-Induced Crystallization of 4-(Dimethylamino)-N-methyl-4-stilbazolium Tosylate. *Crystal Growth & Design*, 5, 861-863. <https://doi.org/10.1021/cg049709y>
- Hughes, C. E., S. Hamad, K. D. Harris, C. R. Catlow & P. C. Griffiths (2007) A multi-technique approach for probing the evolution of structural properties during crystallization of organic materials from solution. *Faraday Discuss*, 136, 71-89; discussion 107-23. <https://doi.org/10.1039/b616611c>
- Hwang, C.-A., J. C. Holste, K. R. Hall & G. Ali Mansoori (1991) A simple relation to predict or to correlate the excess functions of multicomponent mixtures. *Fluid Phase Equilibria*, 62, 173-189. [https://doi.org/10.1016/0378-3812\(91\)80009-k](https://doi.org/10.1016/0378-3812(91)80009-k)
- Iefuji, N., R. Murai, M. Maruyama, Y. Takahashi, S. Sugiyama, H. Adachi, H. Matsumura, S. Murakami, T. Inoue, Y. Mori, Y. Koga, K. Takano & S. Kanaya (2011) Laser-induced nucleation in protein crystallization: Local increase in protein concentration induced by femtosecond laser irradiation. *Journal of Crystal Growth*, 318, 741-744. <https://doi.org/10.1016/j.jcrysgro.2010.10.068>
- Ikeda, K., M. Maruyama, Y. Takahashi, Y. Mori, H. Y. Yoshikawa, S. Okada, H. Adachi, S. Sugiyama, K. Takano, S. Murakami, H. Matsumura, T. Inoue, M. Yoshimura & Y. Mori (2015) Selective crystallization of the metastable phase of indomethacin at the interface of liquid/air bubble induced by femtosecond laser irradiation. *Applied Physics Express*, 8, 045501. <https://doi.org/10.7567/apex.8.045501>
- Ikni, A., B. Clair, P. Scoufflaire, S. Veessler, J.-M. Gillet, N. El Hassan, F. Dumas & A. Spasojević-de Biré (2014) Experimental Demonstration of the Carbamazepine Crystallization from Non-photochemical Laser-Induced Nucleation in

- Acetonitrile and Methanol. *Crystal Growth & Design*, 14, 3286-3299.
<https://doi.org/10.1021/cg500163c>
- Incropera, F. P., A. S. Lavine, T. L. Bergman & D. P. DeWitt. 2007. *Fundamentals of heat and mass transfer*. Wiley.
- Jacob, J. A., S. Sorgues, A. Dazzi, M. Mostafavi & J. Belloni (2012) Homogeneous Nucleation-Growth Dynamics Induced by Single Laser Pulse in Supersaturated Solutions. *Crystal Growth & Design*, 12, 5980-5985.
<https://doi.org/10.1021/cg301024t>
- Jain, A., G. Yang & S. H. Yalkowsky (2004) Estimation of Melting Points of Organic Compounds. *Industrial & Engineering Chemistry Research*, 43, 7618-7621.
<https://doi.org/10.1021/ie049378m>
- Javid, N., T. Kendall, I. S. Burns & J. Sefcik (2016) Filtration Suppresses Laser-Induced Nucleation of Glycine in Aqueous Solutions. *Crystal Growth & Design*, 16, 4196-4202. <https://doi.org/10.1021/acs.cgd.6b00046>
- Jeon, S., J. P. Lee & J.-M. Kim (2015) In situ synthesis of stimulus-responsive luminescent organic materials using a reactive inkjet printing approach. *Journal of Materials Chemistry C*, 3, 2732-2736.
<https://doi.org/10.1039/c5tc00334b>
- Jouyban, A. (2007) In silico prediction of drug solubility in water-dioxane mixtures using the Jouyban-Acree model. *Die Pharmazie - An International Journal of Pharmaceutical Sciences*, 62, 46-50. <https://doi.org/10.1691/ph2007.1.6057>
- Jouyban, A. & W. E. Acree, Jr. (2006) In silico prediction of drug solubility in water-ethanol mixtures using Jouyban-Acree model. *J Pharm Pharm Sci*, 9, 262-9.
- Kacker, R., S. Dhingra, D. Irimia, M. K. Ghatkesar, A. Stankiewicz, H. J. M. Kramer & H. B. Eral (2017) Multiparameter Investigation of Laser-Induced Nucleation of Supersaturated Aqueous KCl Solutions. *Crystal Growth & Design*, 18, 312-317. <https://doi.org/10.1021/acs.cgd.7b01277>
- Karthika, S., T. K. Radhakrishnan & P. Kalaichelvi (2016) A Review of Classical and Nonclassical Nucleation Theories. *Crystal Growth & Design*, 16, 6663-6681.
<https://doi.org/10.1021/acs.cgd.6b00794>
- Kashchiev, D. 2000. *Nucleation*. Elsevier.
- Kathmann, S. M. (2005) Understanding the chemical physics of nucleation. *Theoretical Chemistry Accounts*, 116, 169-182.
<https://doi.org/10.1007/s00214-005-0018-8>
- Katsura, S., K. Hirano, Y. Matsuzawa, K. Yoshikawa & A. Mizuno (1998) Direct laser trapping of single DNA molecules in the globular state. *Nucleic Acids Res*, 26, 4943-5. <https://doi.org/10.1093/nar/26.21.4943>
- Kim, H. J., D. R. Whang, J. Gierschner, C. H. Lee & S. Y. Park (2015) High-contrast red-green-blue tricolor fluorescence switching in bicomponent molecular film. *Angew Chem Int Ed Engl*, 54, 4330-3. <https://doi.org/10.1002/anie.201411568>
- Knott, B. C., M. F. Doherty & B. Peters (2011a) A simulation test of the optical Kerr mechanism for laser-induced nucleation. *J Chem Phys*, 134, 154501.
<https://doi.org/10.1063/1.3574010>
- Knott, B. C., J. L. LaRue, A. M. Wodtke, M. F. Doherty & B. Peters (2011b) Communication: Bubbles, crystals, and laser-induced nucleation. *J Chem Phys*, 134, 171102. <https://doi.org/10.1063/1.3582897>
- Koizumi, H., S. Uda, K. Fujiwara, M. Tachibana, K. Kojima & J. Nozawa (2016) Technique for High-Quality Protein Crystal Growth by Control of Subgrain Formation under an External Electric Field. *Crystals*, 6, 95.
<https://doi.org/10.3390/cryst6080095>

- Krishna, R. (2015) Serpentine diffusion trajectories and the Ouzo effect in partially miscible ternary liquid mixtures. *Phys Chem Chem Phys*, 17, 27428-36. <https://doi.org/10.1039/c5cp04520g>
- Larkin, J. A. (1975) Thermodynamic properties of aqueous non-electrolyte mixtures I. Excess enthalpy for water + ethanol at 298.15 to 383.15 K. *The Journal of Chemical Thermodynamics*, 7, 137-148. [https://doi.org/10.1016/0021-9614\(75\)90261-x](https://doi.org/10.1016/0021-9614(75)90261-x)
- Leaist, D. G., K. MacEwan, A. Stefan & M. Zamari (2000) Binary Mutual Diffusion Coefficients of Aqueous Cyclic Ethers at 25 °C. Tetrahydrofuran, 1,3-Dioxolane, 1,4-Dioxane, 1,3-Dioxane, Tetrahydropyran, and Trioxane. *Journal of Chemical & Engineering Data*, 45, 815-818. <https://doi.org/10.1021/je000079n>
- Lee, G.-B., C.-I. Hung, B.-J. Ke, G.-R. Huang, B.-H. Hwei & H.-F. Lai (2001) Hydrodynamic Focusing for a Micromachined Flow Cytometer. *Journal of Fluids Engineering*, 123, 672-679. <https://doi.org/10.1115/1.1385514>
- Lee, S., H. S. Wi, W. Jo, Y. C. Cho, H. H. Lee, S. Y. Jeong, Y. I. Kim & G. W. Lee (2016) Multiple pathways of crystal nucleation in an extremely supersaturated aqueous potassium dihydrogen phosphate (KDP) solution droplet. *Proc Natl Acad Sci U S A*, 113, 13618-13623. <https://doi.org/10.1073/pnas.1604938113>
- Lemaistre, J. P. (2004) Intraband relaxation and dephasing of Frenkel exciton states in one-dimensional J-aggregates. *Journal of Luminescence*, 107, 332-338. <https://doi.org/10.1016/j.jlumin.2003.12.016>
- Leng, J. & J. B. Salmon (2009) Microfluidic crystallization. *Lab Chip*, 9, 24-34. <https://doi.org/10.1039/b807653g>
- Lewis, A., M. Seckler, H. Kramer & G. Van Rosmalen. 2015. *Industrial crystallization: fundamentals and applications*. Cambridge University Press.
- Li, L. & R. F. Ismagilov (2010) Protein crystallization using microfluidic technologies based on valves, droplets, and SlipChip. *Annu Rev Biophys*, 39, 139-58. <https://doi.org/10.1146/annurev.biophys.050708.133630>
- Li, W. 2016a. Nucléation non-photochimique induite par laser (NPLIN) : Contribution au mécanisme de nucléation à travers des études expérimentales sur le sulfathiazole, L-acide glutamique et la glycine et la modélisation de quelques petites molécules. In *aaa, ddd*. Châtenay-Malabry, France: CentraleSupélec.
- Li, W., A. Ikni, P. Scouflaire, X. Shi, N. El Hassan, P. Gémeiner, J.-M. Gillet & A. Spasojević-de Biré (2016b) Non-Photochemical Laser-Induced Nucleation of Sulfathiazole in a Water/Ethanol Mixture. *Crystal Growth & Design*, 16, 2514-2526. <https://doi.org/10.1021/acs.cgd.5b01526>
- Liao, Y.-Y., S. T. A. G. Melissen, J.-F. Audibert, T.-T. Vu, G. Clavier, R. Méallet-Renault, P. Retailleau, J.-P. Lemaistre, V. Génot & R. Pansu (2018) Fluorescence Spectroscopy of AdamBODIPY Single Crystals. *ChemPhotoChem*, 2, 72-80. <https://doi.org/10.1002/cptc.201700173>
- Liao, Y. 2013. Crystals and nanoparticles of a BODIPY derivative : spectroscopy and microfluidic precipitation. École normale supérieure de Cachan - ENS Cachan.
- Lignos, I., S. Stavrakis, G. Nedelcu, L. Protesescu, A. J. deMello & M. V. Kovalenko (2016) Synthesis of Cesium Lead Halide Perovskite Nanocrystals in a Droplet-Based Microfluidic Platform: Fast Parametric Space Mapping. *Nano Lett*, 16, 1869-77. <https://doi.org/10.1021/acs.nanolett.5b04981>
- Liu, J., H. Xia, D. Xue & L. Lu (2009) Double-shelled nanocapsules of V2O5-based

- composites as high-performance anode and cathode materials for Li ion batteries. *J Am Chem Soc*, 131, 12086-7. <https://doi.org/10.1021/ja9053256>
- Liu, T.-H., T. Uwada, T. Sugiyama, A. Usman, Y. Hosokawa, H. Masuhara, T.-W. Chiang & C.-J. Chen (2013) Single femtosecond laser pulse-single crystal formation of glycine at the solution surface. *Journal of Crystal Growth*, 366, 101-106. <https://doi.org/10.1016/j.jcrysgro.2012.11.018>
- Liu, Y., M. H. van den Berg & A. J. Alexander (2017a) Supersaturation dependence of glycine polymorphism using laser-induced nucleation, sonocrystallization and nucleation by mechanical shock. *Phys Chem Chem Phys*, 19, 19386-19392. <https://doi.org/10.1039/c7cp03146g>
- Liu, Y., M. R. Ward & A. J. Alexander (2017b) Polarization independence of laser-induced nucleation in supersaturated aqueous urea solutions. *Phys Chem Chem Phys*, 19, 3464-3467. <https://doi.org/10.1039/c6cp07997k>
- Lutsko, J. F. & G. Nicolis (2006) Theoretical evidence for a dense fluid precursor to crystallization. *Phys Rev Lett*, 96, 046102. <https://doi.org/10.1103/PhysRevLett.96.046102>
- Lyman, W., W. Reehl & D. Rosenblatt. 1982. Chemical property estimation methods. McGraw-Hill, New York.
- Ma, J., S. M. Lee, C. Yi & C. W. Li (2017) Controllable synthesis of functional nanoparticles by microfluidic platforms for biomedical applications - a review. *Lab Chip*, 17, 209-226. <https://doi.org/10.1039/c6lc01049k>
- Maeki, M., H. Yamaguchi, K. Yamashita, H. Nakamura, M. Miyazaki & H. Maeda (2012) A method for generating single crystals that rely on internal fluid dynamics of microdroplets. *Chem Commun (Camb)*, 48, 5037-9. <https://doi.org/10.1039/c2cc30637a>
- Malitson, I. H. (1965) Interspecimen Comparison of the Refractive Index of Fused Silica*,†. *Journal of the Optical Society of America*, 55, 1205-1209. <https://doi.org/10.1364/josa.55.001205>
- Masuhara, H., T. Sugiyama, T. Rungsimanon, K.-i. Yuyama, A. Miura & J.-R. Tu. 2011. Laser-trapping assembling dynamics of molecules and proteins at surface and interface. In *Pure and Applied Chemistry*, 869. <https://doi.org/10.1351/PAC-CON-10-09-32>
- Masuhara, H., T. Sugiyama, K.-i. Yuyama & A. Usman (2015) Optical trapping assembling of clusters and nanoparticles in solution by CW and femtosecond lasers. *Optical Review*, 22, 143-148. <https://doi.org/10.1007/s10043-015-0029-1>
- Matic, J., X. Sun, B. A. Garetz & A. S. Myerson (2005) Intensity, Wavelength, and Polarization Dependence of Nonphotochemical Laser-Induced Nucleation in Supersaturated Aqueous Urea Solutions. *Crystal Growth & Design*, 5, 1565-1567. <https://doi.org/10.1021/cg050041c>
- McRae, E. G. & M. Kasha (1958) Enhancement of Phosphorescence Ability upon Aggregation of Dye Molecules. *The Journal of Chemical Physics*, 28, 721-722. <https://doi.org/10.1063/1.1744225>
- Meijering, J. (1950) Segregation in regular ternary solutions. *Philips research reports*, 5, 333-356.
- Millar, D. P., R. J. Robbins & A. H. Zewail (1981) Picosecond dynamics of electronic energy transfer in condensed phases. *The Journal of Chemical Physics*, 75, 3649-3659. <https://doi.org/10.1063/1.442529>
- Mirkin, N., B. A. Frontana-Urbe, A. Rodriguez-Romero, A. Hernandez-Santoyo & A. Moreno (2003) The influence of an internal electric field upon protein

- crystallization using the gel-acupuncture method. *Acta Crystallogr D Biol Crystallogr*, 59, 1533-8. <https://doi.org/10.1107/s0907444903013027>
- Mirsaleh-Kohan, N., A. Fischer, B. Graves, M. Bolorizadeh, D. Kondepudi & R. N. Compton (2017) Laser Shock Wave Induced Crystallization. *Crystal Growth & Design*, 17, 576-581. <https://doi.org/10.1021/acs.cgd.6b01437>
- Miura, A., Y.-H. Huang & H. Masuhara (2013) Single crystal formation of amino acid with high temporal controllability by combining femtosecond and continuous wave laser trapping. *Applied Physics B*, 112, 473-477. <https://doi.org/10.1007/s00340-013-5595-y>
- Moggridge, G. D. (2012) Prediction of the mutual diffusivity in binary liquid mixtures containing one dimerising species, from the tracer diffusion coefficients. *Chemical Engineering Science*, 76, 199-205. <https://doi.org/10.1016/j.ces.2012.04.014>
- Moreno, A. 2017. Advanced methods of protein crystallization. In *Protein Crystallography*, 51-76. Springer. https://doi.org/10.1007%2F978-1-4939-7000-1_3
- Moutzouris, K., M. Papamichael, S. C. Betsis, I. Stavrakas, G. Hloupis & D. Triantis (2013) Refractive, dispersive and thermo-optic properties of twelve organic solvents in the visible and near-infrared. *Applied Physics B*, 116, 617-622. <https://doi.org/10.1007/s00340-013-5744-3>
- Mullin, J. W. 2001. *Crystallization*. Elsevier.
- Murai, R., H. Y. Yoshikawa, H. Hasenaka, Y. Takahashi, M. Maruyama, S. Sugiyama, H. Adachi, K. Takano, H. Matsumura, S. Murakami, T. Inoue & Y. Mori (2011) Influence of energy and wavelength on femtosecond laser-induced nucleation of protein. *Chemical Physics Letters*, 510, 139-142. <https://doi.org/10.1016/j.cplett.2011.05.016>
- Murai, R., H. Y. Yoshikawa, Y. Takahashi, M. Maruyama, S. Sugiyama, G. Sasaki, H. Adachi, K. Takano, H. Matsumura, S. Murakami, T. Inoue & Y. Mori (2010) Enhancement of femtosecond laser-induced nucleation of protein in a gel solution. *Applied Physics Letters*, 96, 043702. <https://doi.org/10.1063/1.3294622>
- Myerson, A. 2002. *Handbook of industrial crystallization*. Butterworth-Heinemann.
- Nakamura, K., Y. Hosokawa & H. Masuhara (2007) Anthracene Crystallization Induced by Single-Shot Femtosecond Laser Irradiation: Experimental Evidence for the Important Role of Bubbles. *Crystal Growth & Design*, 7, 885-889. <https://doi.org/10.1021/cg060631q>
- Nakayama, S., H. Y. Yoshikawa, R. Murai, M. Kurata, M. Maruyama, S. Sugiyama, Y. Aoki, Y. Takahashi, M. Yoshimura, S. Nakabayashi, H. Adachi, H. Matsumura, T. Inoue, K. Takano, S. Murakami & Y. Mori (2013) Effect of Gel-Solution Interface on Femtosecond Laser-Induced Nucleation of Protein. *Crystal Growth & Design*, 13, 1491-1496. <https://doi.org/10.1021/cg301618h>
- Nanev, C. (2017a) Recent Insights into the Crystallization Process; Protein Crystal Nucleation and Growth Peculiarities; Processes in the Presence of Electric Fields. *Crystals*, 7, 310. <https://doi.org/10.3390/cryst7100310>
- Nanev, C. N. (2017b) On some aspects of crystallization process energetics, logistic new phase nucleation kinetics, crystal size distribution and Ostwald ripening. *Journal of Applied Crystallography*, 50, 1021-1027. <https://doi.org/10.1107/s1600576717007105>
- Nardone, M. & V. G. Karpov (2012a) Nucleation of metals by strong electric fields. *Applied Physics Letters*, 100, 151912. <https://doi.org/10.1063/1.3703611>

- (2012b) A phenomenological theory of nonphotochemical laser induced nucleation. *Phys Chem Chem Phys*, 14, 13601-11. <https://doi.org/10.1039/c2cp41880k>
- Nernst, W. 1888. Zur Kinetik der in Lösung befindlichen Körper. In *Zeitschrift für Physikalische Chemie*, 613. <https://doi.org/10.1515/zpch-1888-0274>
- Nicolis, G. & C. Nicolis (2003) Enhancement of the nucleation of protein crystals by the presence of an intermediate phase: a kinetic model. *Physica A: Statistical Mechanics and its Applications*, 323, 139-154. [https://doi.org/10.1016/s0378-4371\(03\)00060-8](https://doi.org/10.1016/s0378-4371(03)00060-8)
- Nielsen, M. H., S. Aloni & J. J. De Yoreo (2014) In situ TEM imaging of CaCO₃ nucleation reveals coexistence of direct and indirect pathways. *Science*, 345, 1158-62. <https://doi.org/10.1126/science.1254051>
- Ohno, K., K. Tachikawa & A. Manz (2008) Microfluidics: applications for analytical purposes in chemistry and biochemistry. *Electrophoresis*, 29, 4443-53. <https://doi.org/10.1002/elps.200800121>
- Pan, W., A. B. Kolomeisky & P. G. Vekilov (2005) Nucleation of ordered solid phases of proteins via a disordered high-density state: phenomenological approach. *J Chem Phys*, 122, 174905. <https://doi.org/10.1063/1.1887168>
- Pandalaneni, K. & J. K. Amamcharla (2016) Focused beam reflectance measurement as a tool for in situ monitoring of the lactose crystallization process. *J Dairy Sci*, 99, 5244-5253. <https://doi.org/10.3168/jds.2015-10643>
- Pareja-Rivera, C., M. Cuéllar-Cruz, N. Esturau-Escofet, N. Demitri, M. Polentarutti, V. Stojanoff & A. Moreno (2016) Recent Advances in the Understanding of the Influence of Electric and Magnetic Fields on Protein Crystal Growth. *Crystal Growth & Design*, 17, 135-145. <https://doi.org/10.1021/acs.cgd.6b01362>
- Pekker, L. (2017) Plateau-Rayleigh Instability of a Cylinder of Viscous Liquid (Rayleigh vs. Chandrasekhar). *arXiv preprint arXiv:1712.07069*.
- Plateau, J. 1873. *Statique expérimentale et théorique des liquides soumis aux seules forces moléculaires*. Gauthier-Villars.
- Price, S., B. Rimez, W. Sun, B. Peters, H. Christenson, C. Hughes, C. C. Sun, S. Veessler, H. Pan, C. Brandel, B. Biscans, H. Meekes, I. Rosbottom, W. J. Roth, L. Seton, F. Taulelle, S. Black, T. Threlfall, P. Vekilov, S. Poornachary, J. Diemand, D. Toroz, M. Salvalaglio, P. Tipduangta, J. Sefcik, S. Booth, A. Rasmuson, S. Janbon, J. Ter Horst, E. Simone, R. Hammond, C. A. Bertran, T. Vetter, R. Sear, J. De Yoreo, K. Harris, R. Ristic, A. Kavanagh, K. Roberts, E. Breynaert, A. Myerson, G. Coquerel, D. Wu, H. Colfen, H. Cuppen, M. Smets & D. T. Wu (2015a) Nucleation in complex multi-component and multi-phase systems: general discussion. *Faraday Discuss*, 179, 503-42. <https://doi.org/10.1039/c5fd90039e>
- Price, S., S. Veessler, H. Pan, K. Lewtas, M. Smets, B. Rimez, A. Myerson, C. Hughes, A. Hare, F. Zhang, H. Meekes, M. Mazzotti, I. Rosbottom, D. Khamar, J. van den Ende, L. Fabian, S. Black, F. Taulelle, M. Gich, P. Vekilov, D. Toroz, C. A. Bertran, J. Sefcik, S. Schroeder, S. Booth, A. Rasmuson, E. Breynaert, E. Simone, R. Hammond, R. Sear, J. de Yoreo, R. Davey, J. Anwar, R. Ristic, D. M. Camacho Corzo, K. Roberts, K. Harris, H. Colfen & T. Turner (2015b) Molecular self-assembly and clustering in nucleation processes: general discussion. *Faraday Discuss*, 179, 155-97. <https://doi.org/10.1039/c5fd90036k>
- Qu, G., J. J. Kwok & Y. Diao (2016) Flow-Directed Crystallization for Printed

- Electronics. *Acc Chem Res*, 49, 2756-2764.
<https://doi.org/10.1021/acs.accounts.6b00445>
- Rayleigh, L. (1997) VI. On the capillary phenomena of jets. *Proceedings of the Royal Society of London*, 29, 71-97. <https://doi.org/10.1098/rspl.1879.0015>
- (2010) XVI. On the instability of a cylinder of viscous liquid under capillary force. *The London, Edinburgh, and Dublin Philosophical Magazine and Journal of Science*, 34, 145-154. <https://doi.org/10.1080/14786449208620301>
- Redlich, O. & A. T. Kister (1948) Algebraic Representation of Thermodynamic Properties and the Classification of Solutions. *Industrial & Engineering Chemistry*, 40, 345-348. <https://doi.org/10.1021/ie50458a036>
- Rehm, D. & A. Weller (1970) Kinetics of Fluorescence Quenching by Electron and H-Atom Transfer. *Israel Journal of Chemistry*, 8, 259-271.
<https://doi.org/10.1002/ijch.197000029>
- Reisch, A., D. Heimburger, P. Ernst, A. Runser, P. Didier, D. Dujardin & A. S. Klymchenko (2018) Protein-Sized Dye-Loaded Polymer Nanoparticles for Free Particle Diffusion in Cytosol. *Advanced Functional Materials*, 28, 1805157. <https://doi.org/10.1002/adfm.201805157>
- Renon, H. & J. M. Prausnitz (1968) Local compositions in thermodynamic excess functions for liquid mixtures. *AIChE Journal*, 14, 135-144.
<https://doi.org/10.1002/aic.690140124>
- Richards, J. W. (1897) Relations between the melting points and the latent heats of fusion of the metals. *Journal of the Franklin Institute*, 143, 379.
- Rinnenthal, J. L., C. Bornchen, H. Radbruch, V. Andresen, A. Mossakowski, V. Siffrin, T. Seelemann, H. Spiecker, I. Moll, J. Herz, A. E. Hauser, F. Zipp, M. J. Behne & R. Niesner (2013) Parallelized TCSPC for dynamic intravital fluorescence lifetime imaging: quantifying neuronal dysfunction in neuroinflammation. *PLoS One*, 8, e60100.
<https://doi.org/10.1371/journal.pone.0060100>
- Roach, L. S., H. Song & R. F. Ismagilov (2005) Controlling nonspecific protein adsorption in a plug-based microfluidic system by controlling interfacial chemistry using fluorinated-phase surfactants. *Anal Chem*, 77, 785-96.
<https://doi.org/10.1021/ac049061w>
- Rodriguez-Ruiz, I., Z. Hammadi, R. Grossier, J. Gomez-Morales & S. Veessler (2013) Monitoring picoliter sessile microdroplet dynamics shows that size does not matter. *Langmuir*, 29, 12628-32. <https://doi.org/10.1021/la402735k>
- Rungsimanon, T., K.-i. Yuyama, T. Sugiyama & H. Masuhara (2010) Crystallization in Unsaturated Glycine/D2O Solution Achieved by Irradiating a Focused Continuous Wave Near Infrared Laser. *Crystal Growth & Design*, 10, 4686-4688. <https://doi.org/10.1021/cg100830x>
- Sauter, A., F. Roosen-Runge, F. Zhang, G. Lotze, A. Feoktystov, R. M. Jacobs & F. Schreiber (2015) On the question of two-step nucleation in protein crystallization. *Faraday Discuss*, 179, 41-58.
<https://doi.org/10.1039/c4fd00225c>
- Schaerli, Y., R. C. Wootton, T. Robinson, V. Stein, C. Dunsby, M. A. Neil, P. M. French, A. J. Demello, C. Abell & F. Hollfelder (2009) Continuous-flow polymerase chain reaction of single-copy DNA in microfluidic microdroplets. *Anal Chem*, 81, 302-6. <https://doi.org/10.1021/ac802038c>
- Schöll, J., D. Bonalumi, L. Vicum, M. Mazzotti & M. Müller (2006) In Situ Monitoring and Modeling of the Solvent-Mediated Polymorphic Transformation of L-Glutamic Acid. *Crystal Growth & Design*, 6, 881-891.

- <https://doi.org/10.1021/cg0503402>
- Schott, H. (1961) Densities, Refractive Indices, and Molar Refractions of the System Water-Dioxane at 25° C. *Journal of Chemical & Engineering Data*, 6, 19-20. <https://doi.org/10.1021/je60009a006>
- Schreiner, E. (1922) Om anvendelsen av bjerrums elektrolitiske teori paa elektrolytdiffusjonen og diffusjonpotensialet. *Tidsskrift for Kemi og Bergvaesen*, 2, 151.
- Schubert, R., A. Meyer, D. Baitan, K. Dierks, M. Perbandt & C. Betzel (2017) Real-Time Observation of Protein Dense Liquid Cluster Evolution during Nucleation in Protein Crystallization. *Crystal Growth & Design*, 17, 954-958. <https://doi.org/10.1021/acs.cgd.6b01826>
- SegrÉ, G. & A. Silberberg (1961) Radial Particle Displacements in Poiseuille Flow of Suspensions. *Nature*, 189, 209-210. <https://doi.org/10.1038/189209a0>
- Shang, L., Y. Cheng & Y. Zhao (2017) Emerging Droplet Microfluidics. *Chem Rev*, 117, 7964-8040. <https://doi.org/10.1021/acs.chemrev.6b00848>
- Shi, H. H., Y. Xiao, S. Ferguson, X. Huang, N. Wang & H. X. Hao (2017a) Progress of crystallization in microfluidic devices. *Lab Chip*, 17, 2167-2185. <https://doi.org/10.1039/c6lc01225f>
- Shi, J., L. E. Aguilar Suarez, S.-J. Yoon, S. Varghese, C. Serpa, S. Y. Park, L. Lüer, D. Roca-Sanjuán, B. Milián-Medina & J. Gierschner (2017b) Solid State Luminescence Enhancement in π -Conjugated Materials: Unraveling the Mechanism beyond the Framework of AIE/AIEE. *The Journal of Physical Chemistry C*, 121, 23166-23183. <https://doi.org/10.1021/acs.jpcc.7b08060>
- Shilpa, T. (2015) Small and Macromolecules Crystallization Induced by Focused Ultrafast Laser. *Proceedings of the Indian National Science Academy*, 81, 517-523. <https://doi.org/10.16943/ptinsa/2015/v81i2/48104>
- Shore, J. D., D. Perchak & Y. Shnidman (2000) Simulations of the nucleation of AgBr from solution. *The Journal of Chemical Physics*, 113, 6276-6284. <https://doi.org/10.1063/1.1308517>
- Sindt, J. O., A. J. Alexander & P. J. Camp (2014) Structure and dynamics of potassium chloride in aqueous solution. *J Phys Chem B*, 118, 9404-13. <https://doi.org/10.1021/jp5049937>
- (2017) Effects of nanoparticle heating on the structure of a concentrated aqueous salt solution. *J Chem Phys*, 147, 214506. <https://doi.org/10.1063/1.5002002>
- Sitnikova, N. L., R. Sprik, G. Wegdam & E. Eiser (2005) Spontaneously formed trans-anethol/water/alcohol emulsions: mechanism of formation and stability. *Langmuir*, 21, 7083-9. <https://doi.org/10.1021/la046816l>
- Sleutel, M. & A. E. Van Driessche (2014) Role of clusters in nonclassical nucleation and growth of protein crystals. *Proc Natl Acad Sci U S A*, 111, E546-53. <https://doi.org/10.1073/pnas.1309320111>
- Smeets, P. J. M., A. R. Finney, W. Habraken, F. Nudelman, H. Friedrich, J. Laven, J. J. De Yoreo, P. M. Rodger & N. Sommerdijk (2017) A classical view on nonclassical nucleation. *Proc Natl Acad Sci U S A*, 114, E7882-E7890. <https://doi.org/10.1073/pnas.1700342114>
- Soare, A., R. Dijkink, M. R. Pascual, C. Sun, P. W. Cains, D. Lohse, A. I. Stankiewicz & H. J. M. Kramer (2011) Crystal Nucleation by Laser-Induced Cavitation. *Crystal Growth & Design*, 11, 2311-2316. <https://doi.org/10.1021/cg2000014>
- Soga, K. G., J. R. Melrose & R. C. Ball (1999) Metastable states and the kinetics of colloid phase separation. *The Journal of Chemical Physics*, 110, 2280-2288.

- <https://doi.org/10.1063/1.477881>
- Song, H., D. L. Chen & R. F. Ismagilov (2006) Reactions in droplets in microfluidic channels. *Angew Chem Int Ed Engl*, 45, 7336-56.
<https://doi.org/10.1002/anie.200601554>
- Soraruf, D., F. Roosen-Runge, M. Grimaldo, F. Zanini, R. Schweins, T. Seydel, F. Zhang, R. Roth, M. Oettel & F. Schreiber (2014) Protein cluster formation in aqueous solution in the presence of multivalent metal ions--a light scattering study. *Soft Matter*, 10, 894-902. <https://doi.org/10.1039/c3sm52447g>
- Sosso, G. C., J. Chen, S. J. Cox, M. Fitzner, P. Pedevilla, A. Zen & A. Michaelides (2016) Crystal Nucleation in Liquids: Open Questions and Future Challenges in Molecular Dynamics Simulations. *Chem Rev*, 116, 7078-116.
<https://doi.org/10.1021/acs.chemrev.5b00744>
- Stokes, G. G. 1851. *On the effect of the internal friction of fluids on the motion of pendulums*. Pitt Press Cambridge.
- Suarez, J. T., C. Torres-Marchal & P. Rasmussen (1989) Prediction of surface tensions of nonelectrolyte solutions. *Chemical Engineering Science*, 44, 782-785. [https://doi.org/10.1016/0009-2509\(89\)85055-9](https://doi.org/10.1016/0009-2509(89)85055-9)
- Sugiyama, T., T. Adachi & H. Masuhara (2007) Crystallization of Glycine by Photon Pressure of a Focused CW Laser Beam. *Chemistry Letters*, 36, 1480-1481.
<https://doi.org/10.1246/cl.2007.1480>
- Sugiyama, T. & H. Masuhara (2011) Laser-induced crystallization and crystal growth. *Chem Asian J*, 6, 2878-89. <https://doi.org/10.1002/asia.201100105>
- Sugiyama, T., K. Yuyama & H. Masuhara (2012) Laser trapping chemistry: from polymer assembly to amino acid crystallization. *Acc Chem Res*, 45, 1946-54.
<https://doi.org/10.1021/ar300161g>
- Sun, C. & D. Xue (2013) In situ ATR-IR observation of nucleation and crystal growth of KH₂PO₄ in aqueous solution. *CrystEngComm*, 15, 10445-10450.
<https://doi.org/10.1039/c3ce41628c>
- Sun, X., B. A. Garetz, M. F. Moreira & P. Palfy-Muhoray (2009) Nonphotochemical laser-induced nucleation of nematic phase and alignment of nematic director from a supercooled thermotropic liquid crystal. *Phys Rev E Stat Nonlin Soft Matter Phys*, 79, 021701. <https://doi.org/10.1103/PhysRevE.79.021701>
- Sun, X., B. A. Garetz & A. S. Myerson (2006) Supersaturation and Polarization Dependence of Polymorph Control in the Nonphotochemical Laser-Induced Nucleation (NPLIN) of Aqueous Glycine Solutions. *Crystal Growth & Design*, 6, 684-689. <https://doi.org/10.1021/cg050460+>
- (2008) Polarization Switching of Crystal Structure in the Nonphotochemical Laser-Induced Nucleation of Supersaturated Aqueousl-Histidine†. *Crystal Growth & Design*, 8, 1720-1722. <https://doi.org/10.1021/cg800028v>
- Sutherland, W. (1905) LXXV. A dynamical theory of diffusion for non-electrolytes and the molecular mass of albumin. *The London, Edinburgh, and Dublin Philosophical Magazine and Journal of Science*, 9, 781-785.
<https://doi.org/10.1080/14786440509463331>
- Suzuki, T., M. Fujisawa, S. Takagi & T. Kimura (2006) Excess enthalpies of water+1,4-dioxane at 278.15, 298.15, 318.15 and 338.15 K. *Journal of Thermal Analysis and Calorimetry*, 85, 545-550.
<https://doi.org/10.1007/s10973-006-7658-3>
- Taleb, M., C. Didierjean, C. Jelsch, J. P. Mangeot & A. Aubry (2001) Equilibrium kinetics of lysozyme crystallization under an external electric field. *Journal of Crystal Growth*, 232, 250-255. [https://doi.org/10.1016/s0022-0248\(01\)01167-](https://doi.org/10.1016/s0022-0248(01)01167-)

- Taleb, M., C. Didierjean, C. Jelsch, J. P. Mangeot, B. Capelle & A. Aubry (1999) Crystallization of proteins under an external electric field. *Journal of Crystal Growth*, 200, 575-582. [https://doi.org/10.1016/s0022-0248\(98\)01409-2](https://doi.org/10.1016/s0022-0248(98)01409-2)
- Talreja, S., S. L. Perry, S. Guha, V. Bhamidi, C. F. Zukoski & P. J. Kenis (2010) Determination of the phase diagram for soluble and membrane proteins. *J Phys Chem B*, 114, 4432-41. <https://doi.org/10.1021/jp911780z>
- Tao, J., S. F. Chow & Y. Zheng (2019) Application of flash nanoprecipitation to fabricate poorly water-soluble drug nanoparticles. *Acta Pharm Sin B*, 9, 4-18. <https://doi.org/10.1016/j.apsb.2018.11.001>
- ten Wolde, P. R. & D. Frenkel (1997) Enhancement of protein crystal nucleation by critical density fluctuations. *Science*, 277, 1975-8. <https://doi.org/10.1126/science.277.5334.1975>
- Theberge, A. B., F. Courtois, Y. Schaerli, M. Fischlechner, C. Abell, F. Hollfelder & W. T. Huck (2010) Microdroplets in microfluidics: an evolving platform for discoveries in chemistry and biology. *Angew Chem Int Ed Engl*, 49, 5846-68. <https://doi.org/10.1002/anie.200906653>
- Träbert, E., M. Grieser, C. Krantz, R. Repnow, A. Wolf, F. J. Diaz, Y. Ishikawa & J. A. Santana (2012) Isoelectronic trends of the E1-forbidden decay rates of Al-, Si-, P-, and S-like ions of Cl, Ti, Mn, Cu, and Ge. *Journal of Physics B: Atomic, Molecular and Optical Physics*, 45, 215003. <https://doi.org/10.1088/0953-4075/45/21/215003>
- Tran, V. L., V. Génot, J.-F. Audibert, Y. Prokazov, E. Turbin, W. Zuschratter, H.-J. Kim, J. Jung, S. Y. Park & R. B. Pansu (2016) Nucleation and growth during a fluorogenic precipitation in a micro-flow mapped by fluorescence lifetime microscopy. *New Journal of Chemistry*, 40, 4601-4605. <https://doi.org/10.1039/c5nj03400k>
- Tsuboi, Y., T. Shoji & N. Kitamura (2007) Crystallization of Lysozyme Based on Molecular Assembling by Photon Pressure. *Japanese Journal of Applied Physics*, 46, L1234-L1236. <https://doi.org/10.1143/jjap.46.L1234>
- Tsunesada, F., T. Iwai, T. Watanabe, H. Adachi, M. Yoshimura, Y. Mori & T. Sasaki (2002) High-quality crystal growth of organic nonlinear optical crystal DAST. *Journal of Crystal Growth*, 237-239, 2104-2106. [https://doi.org/10.1016/s0022-0248\(01\)02266-7](https://doi.org/10.1016/s0022-0248(01)02266-7)
- Tung, H.-H., E. L. Paul, M. Midler & J. A. McCauley. 2009. *Crystallization of organic compounds: an industrial perspective*. John Wiley & Sons.
- Usman, A., W. Y. Chiang & H. Masuhara (2013) Optical trapping of nanoparticles by ultrashort laser pulses. *Sci Prog*, 96, 1-18. <https://doi.org/10.3184/003685013X13592844053451>
- Usman, A., T. Uwada & H. Masuhara (2011) Optical Reorientation and Trapping of Nematic Liquid Crystals Leading to the Formation of Micrometer-Sized Domain. *The Journal of Physical Chemistry C*, 115, 11906-11913. <https://doi.org/10.1021/jp200721f>
- Utada, A. S., E. Lorraineau, D. R. Link, P. D. Kaplan, H. A. Stone & D. A. Weitz (2005) Monodisperse double emulsions generated from a microcapillary device. *Science*, 308, 537-41. <https://doi.org/10.1126/science.1109164>
- Vekilov, P. G. (2004) Dense Liquid Precursor for the Nucleation of Ordered Solid Phases from Solution. *Crystal Growth & Design*, 4, 671-685. <https://doi.org/10.1021/cg049977w>
- Vekilov, P. G. (2010) The two-step mechanism of nucleation of crystals in solution.

- Nanoscale*, 2, 2346-57. <https://doi.org/10.1039/c0nr00628a>
- Vekilov, P. G. (2011) Nucleation of protein condensed phases. *Reviews in Chemical Engineering*, 27, 1-13. <https://doi.org/10.1515/revce.2011.003>
- Vekilov, P. G., M. Ataka & T. Katsura (1995) Growth process of protein crystals revealed by laser Michelson interferometry investigation. *Acta Crystallogr D Biol Crystallogr*, 51, 207-19. <https://doi.org/10.1107/S09074444994007146>
- Vierk, A.-L. (1950) Experimentelle Untersuchungen an den Zweistoffsystemen: Wasser-Acetonitril, Wasser-Dioxan, Äthanol-Acetonitril und Cyclohexan-Dioxan. *Zeitschrift für anorganische Chemie*, 261, 283-296. <https://doi.org/10.1002/zaac.19502610504>
- Vitale, S. A. & J. L. Katz (2003) Liquid Droplet Dispersions Formed by Homogeneous Liquid-Liquid Nucleation: “The Ouzo Effect”. *Langmuir*, 19, 4105-4110. <https://doi.org/10.1021/la026842o>
- Vorontsova, M. A., D. Maes & P. G. Vekilov (2015) Recent advances in the understanding of two-step nucleation of protein crystals. *Faraday Discuss*, 179, 27-40. <https://doi.org/10.1039/c4fd00217b>
- Vu, T. T., M. Dvorko, E. Y. Schmidt, J.-F. Audibert, P. Retailleau, B. A. Trofimov, R. B. Pansu, G. Clavier & R. Méallet-Renault (2013) Understanding the Spectroscopic Properties and Aggregation Process of a New Emitting Boron Dipyrromethene (BODIPY). *The Journal of Physical Chemistry C*, 117, 5373-5385. <https://doi.org/10.1021/jp3097555>
- Walden, P. (1908) Über die Schmelzwärme, spezifische Kohäsion und Molekulargröße bei der Schmelztemperatur. *Zeitschrift für Elektrotechnik und Elektrochemie*, 14, 713-724. <https://doi.org/10.1002/bbpc.19080144302>
- Walton, F. & K. Wynne (2018) Control over phase separation and nucleation using a laser-tweezing potential. *Nat Chem*, 10, 506-510. <https://doi.org/10.1038/s41557-018-0009-8>
- Wang, Y., J. He, C. Liu, W. H. Chong & H. Chen (2015) Thermodynamics versus kinetics in nanosynthesis. *Angew Chem Int Ed Engl*, 54, 2022-51. <https://doi.org/10.1002/anie.201402986>
- Ward, M. R. & A. J. Alexander (2012a) Nonphotochemical Laser-Induced Nucleation of Potassium Halides: Effects of Wavelength and Temperature. *Crystal Growth & Design*, 12, 4554-4561. <https://doi.org/10.1021/cg300750c>
- Ward, M. R., I. Ballingall, M. L. Costen, K. G. McKendrick & A. J. Alexander (2009) Nanosecond pulse width dependence of nonphotochemical laser-induced nucleation of potassium chloride. *Chemical Physics Letters*, 481, 25-28. <https://doi.org/10.1016/j.cplett.2009.09.049>
- Ward, M. R., G. W. Copeland & A. J. Alexander (2011) Chiral hide-and-seek: retention of enantiomorphism in laser-induced nucleation of molten sodium chlorate. *J Chem Phys*, 135, 114508. <https://doi.org/10.1063/1.3637946>
- Ward, M. R., A. M. Mackenzie & A. J. Alexander (2016) Role of Impurity Nanoparticles in Laser-Induced Nucleation of Ammonium Chloride. *Crystal Growth & Design*, 16, 6790-6796. <https://doi.org/10.1021/acs.cgd.6b00882>
- Ward, M. R., S. McHugh & A. J. Alexander (2012b) Non-photochemical laser-induced nucleation of supercooled glacial acetic acid. *Phys Chem Chem Phys*, 14, 90-3. <https://doi.org/10.1039/c1cp22774b>
- Ward, M. R., A. Rae & A. J. Alexander (2015) Nonphotochemical Laser-Induced Crystal Nucleation by an Evanescent Wave. *Crystal Growth & Design*, 15, 4600-4605. <https://doi.org/10.1021/acs.cgd.5b00854>
- Warzecha, M., R. Guo, R. M. Bhardwaj, S. M. Reutzel-Edens, S. L. Price, D. A.

- Lamprou & A. J. Florence (2017) Direct Observation of Templated Two-Step Nucleation Mechanism during Olanzapine Hydrate Formation. *Crystal Growth & Design*, 17, 6382-6393. <https://doi.org/10.1021/acs.cgd.7b01060>
- Wilbraham, L., M. Louis, D. Alberga, A. Brosseau, R. Guillot, F. Ito, F. Labat, R. Metivier, C. Allain & I. Ciofini (2018) Revealing the Origins of Mechanically Induced Fluorescence Changes in Organic Molecular Crystals. *Adv Mater*, 30, e1800817. <https://doi.org/10.1002/adma.201800817>
- Wohlfarth, C. 2008. Surface tension of the mixture (1) water; (2) 1,4-dioxane. In *Supplement to IV/16*, ed. M. D. Lechner, 319-319. Berlin, Heidelberg: Springer Berlin Heidelberg. https://doi.org/10.1007/978-3-540-75508-1_225
- Wurthner, F., T. E. Kaiser & C. R. Saha-Moller (2011) J-aggregates: from serendipitous discovery to supramolecular engineering of functional dye materials. *Angew Chem Int Ed Engl*, 50, 3376-410. <https://doi.org/10.1002/anie.201002307>
- Xiao-he, Z., M. Chao-qun, C. Guo-qing, L. Huai-bo, Z. Chun, S. Xin-shu & Z. Cong-hai (2018) The Fluorescence Lifetime and Quantum Chemistry Calculation of Ethyl Caproate and Ethyl Acetate. *SPECTROSCOPY AND SPECTRAL ANALYSIS*, 38, 502-505.
- Xu, J., S. Zhang, A. Machado, S. Lecommandoux, O. Sandre, F. Gu & A. Colin (2017) Controllable Microfluidic Production of Drug-Loaded PLGA Nanoparticles Using Partially Water-Miscible Mixed Solvent Microdroplets as a Precursor. *Sci Rep*, 7, 4794. <https://doi.org/10.1038/s41598-017-05184-5>
- Xue, D., F. Liu & C. Sun. 2010. Observation and simulation of crystallization behaviors of inorganic materials. In *AIP Conference Proceedings*, 324-339. AIP. <https://doi.org/10.1063/1.3476235>
- Yalkowsky, S. H. (1979) Estimation of Entropies of Fusion of Organic Compounds. *Industrial & Engineering Chemistry Fundamentals*, 18, 108-111. <https://doi.org/10.1021/i160070a003>
- Yalkowsky, S. H. & D. Alantary (2018) Estimation of Melting Points of Organics. *J Pharm Sci*, 107, 1211-1227. <https://doi.org/10.1016/j.xphs.2017.12.013>
- Yalkowsky, S. H., G. L. Flynn & G. L. Amidon (1972) Solubility of nonelectrolytes in polar solvents. *J Pharm Sci*, 61, 983-4. <https://doi.org/10.1002/jps.2600610643>
- Yalkowsky, S. H., J. F. Krzyzaniak & P. B. Myrdal (1994) Relationships between Melting Point and Boiling Point of Organic Compounds. *Industrial & Engineering Chemistry Research*, 33, 1872-1877. <https://doi.org/10.1021/ie00031a030>
- Yamaguchi, H., M. Maeki, K. Yamashita, H. Nakamura, M. Miyazaki & H. Maeda (2013) Controlling one protein crystal growth by droplet-based microfluidic system. *J Biochem*, 153, 339-46. <https://doi.org/10.1093/jb/mvt001>
- Yamazaki, T., Y. Kimura, P. G. Vekilov, E. Furukawa, M. Shirai, H. Matsumoto, A. E. Van Driessche & K. Tsukamoto (2017) Two types of amorphous protein particles facilitate crystal nucleation. *Proc Natl Acad Sci U S A*, 114, 2154-2159. <https://doi.org/10.1073/pnas.1606948114>
- Yang, X., X. Wang & C. B. Ching (2008) Solubility of Form α and Form γ of Glycine in Aqueous Solutions. *Journal of Chemical & Engineering Data*, 53, 1133-1137. <https://doi.org/10.1021/jc7006988>
- Yau, S. T. & P. G. Vekilov (2001) Direct observation of nucleus structure and nucleation pathways in apoferritin crystallization. *J Am Chem Soc*, 123, 1080-9. <https://doi.org/10.1021/ja003039c>

- Ye, X., Y. Liu, Y. Lv, G. Liu, X. Zheng, Q. Han, K. A. Jackson & X. Tao (2015) In Situ Microscopic Observation of the Crystallization Process of Molecular Microparticles by Fluorescence Switching. *Angew Chem Int Ed Engl*, 54, 7976-80. <https://doi.org/10.1002/anie.201503052>
- Yennawar, N., S. Denev, V. Gopalan & H. Yennawar (2010) Laser-improved protein crystallization screening. *Acta Crystallogr Sect F Struct Biol Cryst Commun*, 66, 969-72. <https://doi.org/10.1107/S1744309110023857>
- Yoon, S.-J. & S. Park (2011) Polymorphic and mechanochromic luminescence modulation in the highly emissive dicyanodistyrylbenzene crystal: secondary bonding interaction in molecular stacking assembly. *Journal of Materials Chemistry*, 21, 8338-8346. <https://doi.org/10.1039/c0jm03711g>
- Yoon, S. J., J. W. Chung, J. Gierschner, K. S. Kim, M. G. Choi, D. Kim & S. Y. Park (2010) Multistimuli two-color luminescence switching via different slip-stacking of highly fluorescent molecular sheets. *J Am Chem Soc*, 132, 13675-83. <https://doi.org/10.1021/ja1044665>
- Yoshikawa, H. Y., Y. Hosokawa & H. Masuhara (2006) Explosive Crystallization of Urea Triggered by Focused Femtosecond Laser Irradiation. *Japanese Journal of Applied Physics*, 45, L23-L26. <https://doi.org/10.1143/jjap.45.L23>
- Yoshikawa, H. Y., R. Murai, H. Adachi, S. Sugiyama, M. Maruyama, Y. Takahashi, K. Takano, H. Matsumura, T. Inoue, S. Murakami, H. Masuhara & Y. Mori (2014) Laser ablation for protein crystal nucleation and seeding. *Chem Soc Rev*, 43, 2147-58. <https://doi.org/10.1039/c3cs60226e>
- Yoshikawa, H. Y., R. Murai, S. Maki, T. Kitatani, S. Sugiyama, G. Sazaki, H. Adachi, T. Inoue, H. Matsumura, K. Takano, S. Murakami, T. Sasaki & Y. Mori (2008) Laser energy dependence on femtosecond laser-induced nucleation of protein. *Applied Physics A*, 93, 911-915. <https://doi.org/10.1007/s00339-008-4790-x>
- Yoshikawa, H. Y., R. Murai, S. Sugiyama, G. Sazaki, T. Kitatani, Y. Takahashi, H. Adachi, H. Matsumura, S. Murakami, T. Inoue, K. Takano & Y. Mori (2009) Femtosecond laser-induced nucleation of protein in agarose gel. *Journal of Crystal Growth*, 311, 956-959. <https://doi.org/10.1016/j.jcrysgro.2008.09.137>
- Yuyama, K.-i., J. George, K. G. Thomas, T. Sugiyama & H. Masuhara (2016) Two-Dimensional Growth Rate Control of l-Phenylalanine Crystal by Laser Trapping in Unsaturated Aqueous Solution. *Crystal Growth & Design*, 16, 953-960. <https://doi.org/10.1021/acs.cgd.5b01505>
- Yuyama, K.-i., T. Rungsimanon, T. Sugiyama & H. Masuhara (2012) Selective Fabrication of α - and γ -Polymorphs of Glycine by Intense Polarized Continuous Wave Laser Beams. *Crystal Growth & Design*, 12, 2427-2434. <https://doi.org/10.1021/cg300065x>
- Yuyama, K., C. S. Wu, T. Sugiyama & H. Masuhara (2014) Laser trapping-induced crystallization of L-phenylalanine through its high-concentration domain formation. *Photochem Photobiol Sci*, 13, 254-60. <https://doi.org/10.1039/c3pp50276g>
- Yuyama, K. I., K. D. Chang, J. R. Tu, H. Masuhara & T. Sugiyama (2018) Rapid localized crystallization of lysozyme by laser trapping. *Phys Chem Chem Phys*, 20, 6034-6039. <https://doi.org/10.1039/c7cp06990a>
- Zaccaro, J., J. Matic, A. S. Myerson & B. A. Garetz (2001) Nonphotochemical, Laser-Induced Nucleation of Supersaturated Aqueous Glycine Produces Unexpected γ -Polymorph. *Crystal Growth & Design*, 1, 5-8. <https://doi.org/10.1021/cg0055171>

- Zanni, M., D. J. E. S. Aravamudhan, A. Pallipurath, E. Arunan, C. Schnedermann, A. K. Mishra, M. Warren, J. D. Hirst, F. John, R. Pal, J. R. Helliwell, K. Moirangthem, S. Chakraborty, A. G. Dijkstra, P. Roy Chowdhury, K. Ghiggino, R. J. Miller, S. Meech, H. Medhi, M. Hariharan, F. Ariese, A. Edwards, A. R. Mallia, S. Umapathy, M. Meedom Nielsen, N. Hunt, Z. Y. Tian, J. Skelton, G. Sankar & D. Goswami (2015) Time and Space resolved Methods: general discussion. *Faraday Discuss*, 177, 263-92.
<https://doi.org/10.1039/c5fd90017d>
- Zhang, F. (2017a) Nonclassical nucleation pathways in protein crystallization. *J Phys Condens Matter*, 29, 443002. <https://doi.org/10.1088/1361-648X/aa8253>
- Zhang, S., C. J. J. Gerard, A. Ikni, G. Ferry, L. M. Vuillard, J. A. Boutin, N. Ferte, R. Grossier, N. Candoni & S. Veessler (2017b) Microfluidic platform for optimization of crystallization conditions. *Journal of Crystal Growth*, 472, 18-28. <https://doi.org/10.1016/j.jcrysgro.2017.01.026>
- Zhao, L. & S. H. Yalkowsky (1999) A Combined Group Contribution and Molecular Geometry Approach for Predicting Melting Points of Aliphatic Compounds. *Industrial & Engineering Chemistry Research*, 38, 3581-3584.
<https://doi.org/10.1021/ie990281n>

Appendix A

A.i. Thermodynamic versus kinetic aspect of nucleation

It is well known that the crystallisation process is composed of crystal nucleation and growth. In this context, a crystal nucleus is first formed in a supercooled liquid as a small region in which molecules are arranged in the same ordered way as in a crystalline phase, and then each molecule on the interface between the crystal and liquid rearranges to grow the nucleus to a large crystal. Since the former process requires the stabilisation of the ordered aggregate composed of many molecules, it is expected that, the lower the temperature, the more the process is enhanced. In reality, the kinetic aspect of how fast the molecules can rearrange becomes an important factor for the nucleation rate at low temperatures. Therefore, the maximum rate has been considered to appear around the glass transition temperature T_g below which the molecular rearrangement is frozen in. On the other hand, the crystal growth proceeds under the condition in which a stable crystal is already present, and the maximum rate is considered to be observed in the middle between the T_g and fusion temperature T_{fus} because the rate of molecular rearrangements is larger at higher temperatures. Based on the above considerations, it is ordinarily expected that the maximum rate of the crystal nucleation is located at a lower temperature than that of the crystal growth. [Hatase, 2004]

After crystals nucleate, they start growing immediately. In this second crystallisation stage, the crystals grow until solution depletion reaches a level which corresponds to zero supersaturation with respect to the smallest crystal in the system; this point marks the beginning of the so-called Ostwald ripening. [Nanev, 2017b]

A.ii. Bibliography description of NPLIN experiment

The bibliographic review of the NPLIN experiments has led to attribute to our NPLIN definition (those stated in Figure 1.4) to 54 experimental papers. The characterisation of the experience led in these papers is summarised in Table Appen.A.1 and Table Appen.A.2. A list of NPLIN modelling papers is given in Table Appen.A.3 while the list of review papers is given in Table Appen.A.4.

Table Appen.A.1. NPLIN papers, compounds, and solvent

N.	Reference	Compound				Solvent
		Organic	protein	Inorganic	Other	
P1	[Garetz, 1996]	Urea				water
P2	[Zaccaro, 2001]	Glycine				water
P3	[Garetz, 2002]	Glycine / urea / <i>L-alanine</i> / <i>adipic acid</i> / <i>L-glutamic acid</i> / <i>succinic acid</i>				water / ethanol / water / water / water / water
P4	[Tsunesada, 2002]	4-dimethylamino-N-methyl-4-stilbazolium tosylate = DAST				nr
P5	[Hiroaki, 2003]		lysozyme / Glucose isomerase / Ribonuclease H / Trypanosoma brucei prostaglandin			2.5% sodium chloride, 0.1M sodium acetate buffer / 0.2M ammonium sulphate and 15% PEG 6000 / 5mg/ml in 0.05M Tris-HCl pH 9, outer solution; 0.2M Tris-HCl
P6	[Hosokawa, 2005]	4-dimethylamino-N-methyl-4-stilbazolium tosylate = DAST				methanol
P7	[Matic, 2005]	Urea				water

P8	[Sun, 2006]	Glycine				water
P9	[Yoshikawa, 2006]	Urea				water
P10	[Yoshikawa, 2008]	Anthracene				cyclohexane
P11	[Yoshikawa, 2009]		lysozyme			gel = polyethylene glycol
P12	[Sugiyama, 2007]	Glycine				D ₂ O
P13	[Tsuboi, 2007]		lysozyme			50mM of sodium acetate and 3.0 wt% of NaCl in D ₂ O
P14	Lee, 2008 [Sun, 2008]		lysozyme / Bovine Pancreas Trypsin			0.1 M acetate aqueous buffer / 10 mM calcium chloride, 10 mg/mL benzamidine hydrochloride, and 25 mM Hepes
P15	[Sun, 2008]	l-Histidine				water
P16	[Yoshikawa, 2008]8		lysozyme			100 mM sodium acetate buffer
P17	[Alexander, 2009]			KCl		water
P18	[Duffus, 2009]			KCl		water + agarose gel
P19	[Sun, 2009]	4'-pentyl-4-cyanobiphenyl			nematic liquid (5CB)	no solvent
P20	[Ward, 2009]			KCl		water
P21	[Yoshikawa, 2009]		Thaumatococcus / F-lysozyme			0.1M N-[2-acetamido]-2-iminodiacetic acid (ADA) / 50 mM sodium acetate buffer
P22	[Murai, 2010]		lysozyme			0.1 M NaAc buffer
P23	[Rungsimanon, 2010]	Glycine				D ₂ O
P24	[Yennawar, 2010]		Ribonuclease B / sheep liver sorbitol dehydrogenase / Glucose dehydrogenase / Lysozyme / Fructose dehydrogenase			different Hampton Research Index conditions
P25	[Iefuji, 2011]		glucose isomerase			50 mM Tris-HCl buffer (pH 4.5) and 0.1M CaCl ₂ / water or PEG
P26	[Knott, 2011b]	glycine			CO ₂	water / water + Ar
P27	[Murai, 2011]		lysozyme / glucose isomerase			0.1 M sodium acetate buffer at pH 4.5 including 3.0 wt% sodium chloride / in

						0.1 M HEPES buffer (pH 7.0), 15% PEG6000)
P28	[Soare, 2011]			(NH ₄) ₂ SO ₄ / KMnO ₄		water
P29	[Usman, 2011]	4'-pentyl-4-cyanobiphenyl			nematic liquid (5CB)	no solvent
P30	[Ward, 2011]			NaClO ₃		no solvent
P31	[Jacob, 2012]			KNO ₃		water
P32	[Ward, 2012a]			KCl / KBr		water / water
P33	[Ward, 2012b]	glacial acetic acid				no solvent
P34	[Yuyama, 2012]	Glycine				D ₂ O
P35	[Liu, 2013]	Glycine				water
P36	[Miura, 2013]	Glycine				water
P37	[Nakayama, 2013]	paracetamol	lysozyme / AcrB			water / NaCl in 0.1 M NaAc buffer + agarose
P38	[Yuyama, 2014]	L-phenylalanine				water / D ₂ O
P39	[Clair, 2014]	Glycine				water
P40	[Fang, 2014]			KCl		water
P41	[Ikni, 2014]	carbamazepine				acetone / methanol
P42	[Bartkiewicz, 2015]	p-nitroaniline				1,4-dioxane
P43	[Ikeda, 2015]	indomethacin				acetonitrile
P44	[Shilpa, 2015]	urea / 3-(4-hydroxyphenyl)-1-(2-methoxyphenyl) propan-1-one / 3-(4-hydroxyphenyl)-1-(4-methoxy phenyl) propan-1-one / 1-(5-acetamido-2-hydroxy-4-fluoro phenyl)-3-phenyl propen-2-one / 1-(5-acetamido-2-hydroxy	lysozyme	NaCl		water / methanol / methanol /methanol /methanol /methanol /100 mM sodium acetate / water

		phenyl)-3-(2,3,5-trimethoxy phenyl)- propen-2-one / 1-(5-acetamido-2-hydroxy phenyl)-3-(3,4-methoxylylene dioxy phenyl) - propen-2-one						
P45	[Ward, 2015]				KCl			water
P46	[Javid, 2016]	Glycine						water
P47	[Li, 2016b]	sulfathiazole						ethanol - water
P48	[Ward, 2016]				NH ₄ Cl			water
P49	[Yuyama, 2016]	L-Phenylalanine						water
P50	[Liu, 2017a]	Glycine						water
P51	[Liu, 2017b]	urea						water
P52	[Mirsaleh-Kohan, 2017]	Tartaric acid			NaBr			nr / nr
P53	[Kacker, 2017]				KCl			water
P54	[Yuyama, 2018]		lysozyme					D ₂ O, NaCl

Table Appen.A.2. NPLIN papers, experimental conditions. Laser type: P: pulsed; CW: continuous waves; D: laser diode; fs: femtosecond; ns: nanosecond pulse; The sample-holder numbers refer to Figure 1.8.

N.	Reference	Laser type	Wavelength (nm)	Frequency (Hz)	Pulse	Energy	Energy density	Beam surface (mm ²)	Sample holder
P1	[Garetz, 1996]	P - ns - nfoc	1064		20 ns	0.1 J	250 MW/cm ²	2 mm ²	8
P2	[Zaccaro, 2001]	P - ns - nfoc	1064				0,7 (±10%) GW/cm ²		8
P3	[Garetz, 2002]	P - ns -	1064	10	9 ns	0,065	0,7 (±10%) GW/cm ²		8

		nfoc				J/pulse			
P4	[Tsunesada, 2002]	P - ns - foc	1064	23				$1.67 \cdot 10^{-4}$ cm ²	nr
P5	[Hiroaki, 2003]	P - fs - foc	800 (sample holder 2) / 780 (sample holder 2-m)	50 - 100 / 1000	120 fs / 200 fs	1,95 nJ/pulse			3 - m
P6	[Hosokawa, 2005]	P - fs - foc	800	20 / 1000	120 fs	300 μJ/pulse			9 - c - m
P7	[Matic, 2005]	P - ns - nfoc	1064 / 532		7 ns / 9 ns		0,02- 0,06 GW/cm ²	2,688	8
P8	[Sun, 2006]	P - ns - nfoc	1064 / 532		7 ns / 9 ns		0,24 GW/cm ² / 0,46 GW/cm ²	2,688	8
P9	[Yoshikawa, 2006]	P - fs - foc	800	1000	120 fs	50 - 340 μJ/pulse			14
P10	[Yoshikawa, 2008]	P - fs - foc	800	125	120 fs	0 to 20,6 μJ/pulse			6
P11	[Yoshikawa, 2009]	P - fs - foc	800	1000	120 fs	1,8 to 30 μJ/pulse			3 - m
P12	[Sugiyama, 2007]	CW - foc	1064			1,1 W	0,4 GW/cm ²		3
P13	[Tsuboi, 2007]	CW - foc	1064			0,3W			3
P14	Lee, 2008 [Sun, 2008]	P - ns - nfoc / P - ps - nfoc	1064 / 532 / 355	20 / 20 / 30	5 ns / 4 ns / 100 ps		0.125 / 0.026 to 0.0032 / 0.257 to 0.058 GW/cm ²	9,621	4 - m
P15	[Sun, 2008]	P - ns - nfoc	532		7 ns		0,24 GW/cm ²	2,688	8
P16	[Yoshikawa, 2008]8	P - fs - foc	780	1000	67 - 200 - 1800 fs	0 to 8 μJ/pulse			3
P17	[Alexander, 2009]	P - ns - nfoc	1064		7 ns		4 - 40 MW/cm ²		8
P18	[Duffus, 2009]	P - ns - nfoc	1064		6 ns		5 - 60 MW/cm ²		8

P19	[Sun, 2009]	P - ns - nfoc	532	1000	45 ps		3,9 MW/cm ²		10
P20	[Ward, 2009]	P - ns - nfoc	1064		6 ns / 200 ns		2,14 - 2,30 MW/cm ²		8
P21	[Yoshikawa, 2009]	P - fs - foc	780	1000					6
P22	[Murai, 2010]	P - fs - foc	780		200 fs	5.5 μJ/pulse			3
P23	[Rungsimanon, 2010]	CW - foc	1064			1 W	0,4 GW/cm ²		6
P24	[Yennawar, 2010]	P - fs - nr	532			6 mW			nr
P25	[Iefuji, 2011]	P - fs - foc	780	1000	200 fs	10 μJ/pulse			2
P26	[Knott, 2011b]	P - ns - nfoc	1064 / 532 / 355		9 ns			7,068	7
P27	[Murai, 2011]	P - fs - foc	780 / 260	1000	200 fs	0,7 - 10 μJ/pulse			3 - m
P28	[Soare, 2011]	P - ns - foc	532		6 ns	0,05 0,5 mJ			3
P29	[Usman, 2011]	CW - foc	1064			0,4 - 1,4 W			6
P30	[Ward, 2011]	P - ns - nfoc	1064		7 ns	100 mJ/pulse	0,14 GW/cm ²		8
P31	[Jacob, 2012]	P - ns - foc	532		7 ns		15 GW/cm ²		10
P32	[Ward, 2012a]	P - ns - nfoc	1064 / 532				5 - 42 MW/cm ² / 9 - 20 MW/cm ²	23,758	8
P33	[Ward, 2012b]	P - ns - nfoc	1064	10	7 ns		5,85 MW/cm ²		8
P34	[Yuyama, 2012]	CW - foc	1064			0,8 to 1,4 W			6
P35	[Liu, 2013]	P - fs - foc	800	1 - 1000	160 fs	3 mJ / pulse			14
P36	[Miura, 2013]	P - fs - foc / CW - foc	800 / 1064	80000 / -	120 fs / -	600 - 1000 mW			6
P37	[Nakayama, 2013]	P - fs - foc	780 / 800		200 fs	10 - 20 μJ / pulse			6

P38	[Yuyama, 2014]	CW - foc	1064 / 532			1,1 W			6
P39	[Clair, 2014]	P - ns - nfoc	532	10	7 ns		0 - 0,46 GW/cm ²		11
P40	[Fang, 2014]	P - ns - nfoc	532	11000	1 ns	5 mW	55 MW/cm ²		1
P41	[Ikni, 2014]	P - ns - nfoc	532	10	7 ns		0 - 0,46 GW/cm ²		11
P42	[Bartkiewicz, 2015]	D - nfoc	405				64–640 W/cm ²		4
P43	[Ikeda, 2015]	P - fs - foc	800	1000	200 fs	30 mJ / pulse			14
P44	[Shilpa, 2015]	P - fs - foc	800	5200	60 fs		970 mJ/cm ² (NaCl, urea)/ 70 mJ/cm ² (chalcone) / 160 mJ/cm ² (lysozyme)		13 - m / 8 - m ?
P45	[Ward, 2015]	P - ns - ev	532		5 ns		33 MW/cm ²	4,908 +	5
P46	[Javid, 2016]	P - fs - nfoc	1064	1000	6 ns		0,47 GW/cm ²		8 - c
P47	[Li, 2016b]	P - ns - nfoc	532	10	7 ns		0 - 0,46 GW/cm ²		11
P48	[Ward, 2016]	P - ns - nfoc	1064		5,5 ns		12 MW/cm ²	7,068	8
P49	[Yuyama, 2016]	CW - foc	1064				0,39 GW/cm ²		6
P50	[Liu, 2017a]	P - ns - nfoc	1064	10	5,6 ns		0,5 GW/cm ²		8
P51	[Liu, 2017b]	P - ns - nfoc	1064 / 532	10	5 ns / 5,6 ns		200 MW/cm ² / 270 MW/cm ²	18,095 / 4,908	8
P52	[Mirsaleh-Kohan, 2017]	P - ns - foc	1064		8-12 ns	800 mW	1.9 TW/cm ²		12
P53	[Kacker, 2017]	P - ns - nfoc	1064 / 532 / 355		7 ns		0,42 to 55 MW/cm ²		8
P54	[Yuyama, 2018]	CW - foc	1064			0,5 - 1,1 W			6

Table Appen.A.3. List of NPLIN modelling papers.

N.	Reference
M1	[Ward, 2011]
M2	[Knott, 2011a]
M3	[Nardone, 2012b]
M4	[Nardone, 2012a]
M5	[Usman, 2013]
M6	[Sindt, 2014]
M7	[Sindt, 2017]

Table Appen.A.4. List of NPLIN review papers.

N.	Reference
R1	[Masuhara, 2011]
R2	[Sugiyama, 2011]
R3	[Sugiyama, 2012]
R4	Spasojevic-de Biré, 2013
R5	[Yoshikawa, 2014]
R6	[Belloni, 2014]
R7	[Masuhara, 2015]

A.iii. Experimental techniques for crystallisation observation

A.iii.i. Classical techniques for crystallisation observation

Classical methods for crystallisation from solid-state as well as solution state are summarised in Figure Appen.A.1.

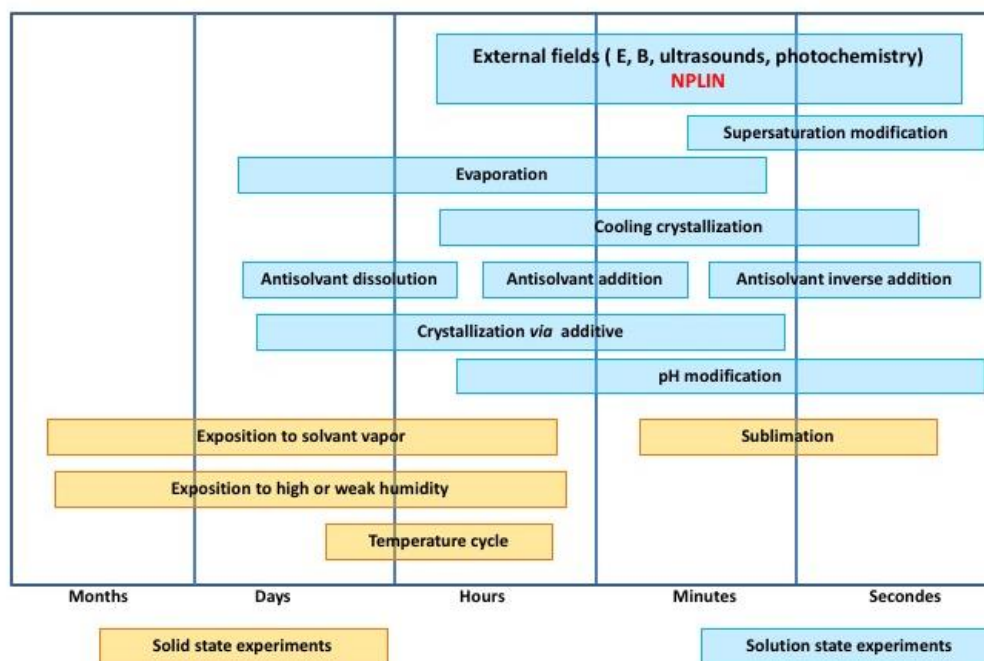


Figure Appen.A.1. Schematic representation of different crystallisation techniques. X axis represents the time necessary for inducing crystallisation.

Crystallisation *via* external physical factors, such as magnetic and electric fields (EFs); proper crystallisation conditions can be fine-tuned using variation of both direct current (dc) and alternating current (ac) EFs. Pioneered by Aubry's group [Taleb, 1999, Taleb, 2001] some 20 years ago, protein crystallisation under EF attracts an increasing attention, becoming a mature scientific branch today. Major contributions in this research field have been made by the teams of Moreno [Mirkin, 2003, Pareja-Rivera, 2016], Koizumi [Koizumi, 2016], Veessler [Hammadi, 2007, Hammadi, 2009a, Hammadi, 2015, Zhang, 2017b], etc. (the list is not exhaustive). Traditionally, most of the experimental studies were performed with hen-egg white lysozyme (HEWL). Three reviews [Al-haq, 2007, Frontana-Urbe, 2008, Hammadi, 2009b], and a book chapter [Moreno, 2017] have already been published.

A.iii.ii. Techniques for pre-nucleation clusters observation

Traditional offline techniques, such as X-ray diffraction (XRD), solid-state nuclear magnetic resonance (ssNMR) [Hughes, 2007], differential scanning calorimetry (DSC) and scanning electron microscopy (SEM), usually cannot provide real-time information on the crystallisation process because they require invasive sample preparation before the measurement, which might change the polymorph and morphology of the crystals. Therefore, researchers attempt to use the available *in situ* techniques, such as focused beam reflectance measurement (FBRM), Raman spectroscopy [Schöll, 2006], attenuated total reflectance Fourier-transform infrared spectroscopy (ATR-FTIR) [Yang, 2008], near-infrared (NIR) spectroscopy and particle vision and measurement (PVM), to study the polymorphic crystallisation and transformation process. Among them, *in situ* Raman spectroscopy is attracting particular interest because of its capability for rapid and accurate determination of the composition and properties of the solid phase during the crystallisation process, especially in an aqueous slurry. Table Appen.A.5 summarises different observation techniques which have already been used for studying nucleation while Figure Appen.A.2 indicates schematically the spatial and resolution limit.

Crystallisation could occur *via* external physical factors, such as magnetic and electric fields (EFs); proper crystallisation conditions can be fine-tuned using variation of both direct current (dc) [Adrjanowicz, 2018] and alternating current (ac) EFs. Three reviews [Al-haq, 2007, Frontana-Urbe, 2008, Hammadi, 2009b], and a book chapter [Moreno, 2017] have already been published on that subject.

Zhang establish in [Price, 2015b] that: “The combination of ultra-centrifugation, dynamic light scattering (DLS), optical microscopy (OM) and real-time SAXS can provide deeper understanding on the early stage of nucleation. It is important to note the difference in their application conditions. Optical microscopy has a relatively low spatial resolution. While it is not easy to distinguish the exact nucleation sites on the intermediate, it provides direct and solid information on the number and the shape and size of the crystals with time. SAXS on the

other hand provides the internal structure changes before nucleation, which is crucial to establish the relationship between the intermediate and the crystal nucleation. DLS is a very convenient technique to monitor the protein clusters as presented by Vorontsova *et al* [Vorontsova, 2015]. DLS has also employed to study the cluster formation in protein solutions in the presence of multivalent metal ions [Soraruf, 2014]. Importantly, in DLS studies, the clusters normally have a low volume fraction to avoid the problem of multiple-scattering.” Unfortunately, however, dynamic light scattering is unable to discern structured (crystalline) from amorphous (or liquid) clusters.[Nanev, 2017a]

Table Appen.A.5. Selection of experimental approaches that have been employed to study nucleation phenomena, along with some examples of systems examined (adapted and completed from [Sosso, 2016]). The references for which *in situ* experiments were performed, have been indicated. The colour refers to those used in Figure Appen.A.2.

Abbreviation	Name	<i>In situ</i>	Typical results	Examples of references for which the method has been used for studying nucleation
AUC	Analytical Ultra Centrifugation		spectra	CaCO ₃ [Gebauer, 2008]
AFM	Atomic Force Microscope		photography	Olanzapine Hydrate [Warzecha, 2017], Mg ₅ (CO ₃) ₄ (OH) ₂ [Xue, 2010], Apoferritin [Yau, 2001]
ATR-FTIR	Attenuated Total Reflectance Fourier-Transform Infrared Spectroscopy	•	spectra	glycine [Yang, 2008]
ATR-IR	Attenuated Total Reflectance-Infrared		spectra	KH ₂ PO ₄ [Sun, 2013]
BM	Brownian Microscopy	•	photography	[Sleutel, 2014]
	Concentration change	•	number	Lactose [Garside, 2002]
CLSM	Confocal Laser Scanning Microscopy or Confocal Fluorescence Microscopy	•	photography	Membrane protein [Borodgoskiy_2015]
	Digital video-microscopy technique	•	photography	Lactose [Arellano, 2004]
DSC	Differential Scanning Calorimetry		heat of reaction	Ice [Charoenrein, 1989]
DLS	Dynamic Light Scattering/ Static–Dynamic Light Scattering/ Light Transmittance Through Solution/ Particle Vision and Measurement	•	Spectra, turbidity	Protein [Schubert, 2017], Paracetamol [Bhamidi, 2017], KNO ₃ [Jacob, 2012]
ESL	Electrostatic Levitation + X-Ray Synchrotron Scattering + Raman	•	Device	KDP [Lee, 2016]
FLIM	Fluorescence lifetime imaging microscopy/ Fluorescence	•	Photography, spectra	BBFT [Ye, 2015], DBDCS [Tran, 2016]
FBRM	Focused Beam Reflectance Measurement	•	spectra	lactose [Pandalaneni, 2016]
ISEs	Ion-Selective Electrodes	•	spectra	CaCO ₃ [Gebauer, 2009]
LCM-DIM	Laser Confocal Microscopy Enhanced by Differential	•	photography	protein [Sleutel, 2014]

	Interference Contrast			
LC-TEM, TEM	Liquid Cell Transmission Electron Microscopy / Transmission Electron Microscopy	•	Device + photography	Gold particles [Tan_2017], protein [Yamazaki, 2017]
MI	Michelson Interferometry		spectra	lysozyme [Vekilov, 1995]
NIR	Near-Infrared Spectroscopy		spectra	mannitol [De Beer, 2009]
NMR + X ray + neutron scattering	Neutron Magnetic Resonance + X-ray + neutron scattering	•	spectra	Glycine [Hughes, 2007]
OM	Optical Microscope / High Speed Camera	•	photography	
	Raman Spectroscopy	•	spectra	l-Glutamic Acid [Schöll, 2006]
SAXS, XAFS	Real-Time SAXS, XAFS	•	spectra	[Abecassis, 2007, Fleury, 2014, Chang, 2016]

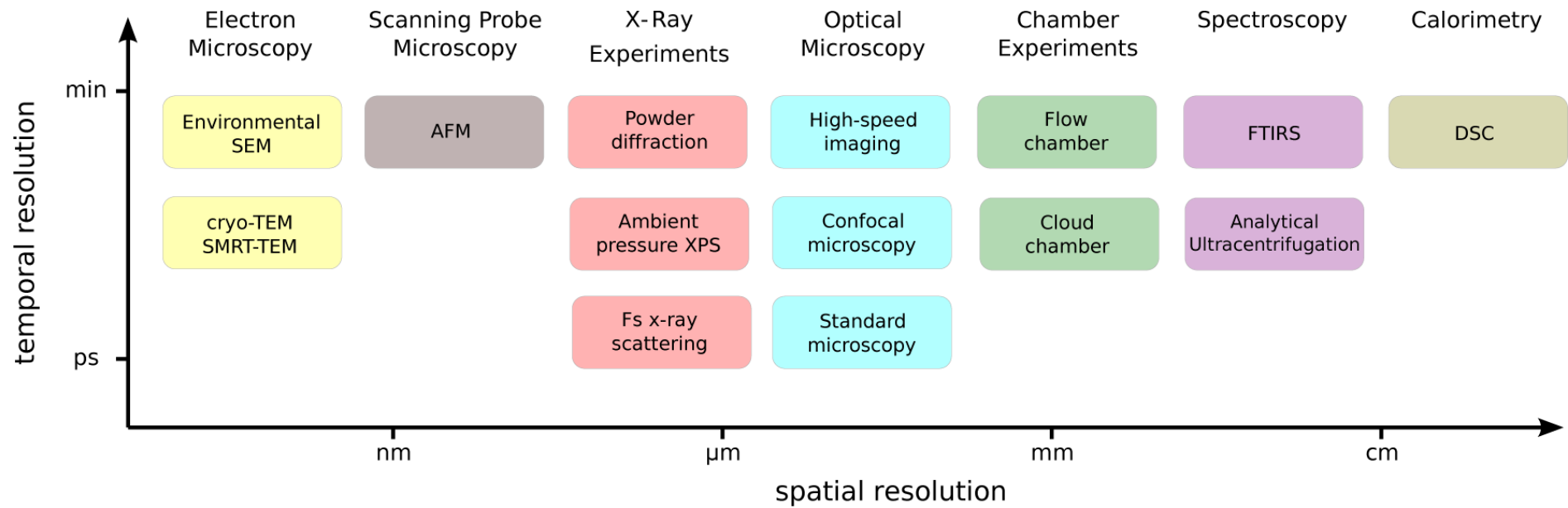


Figure Appen.A.2. Overview of some of some experimental methods that have been applied to characterise nucleation. Ranges of the spatial and temporal resolutions typical of each approach are reported on the x and y axes, respectively. (Adapted from [Sosso, 2016]).

A.iv. Bibliography of DBDCS characterisation

Table Appen.A.6. Experimental characterisation of DBDCS according to the different synthesis methods (TA = Thermal annealing, SVA = Solvent Vapor Assisted); 1 [Yoon, 2010]; 2 [Kim, 2015]; 3 [Shi, 2017b]

Ref	1				2								3	
type	G-phase			B-phase						G state	R state	B state		
Space group	P-1													
Unit cell (Å, °)	a = 7.6944(19) b = 8.914(2) c = 9.926(3) α = 96.945(4) β = 102.309(4) γ = 91.532(4) V = 659.3(3)													
morphology	Needle ?				powder	Nano part	In solution							Single crystal
Production		Figure 5d	G-phase (VD film)	Figure 5c	B-phase (VD film)	pristine	pristine	TA	SVA	pure	pure	pure	Mech.force	
Lifetime			23,9 ns		6,1 ns	11,9 ns	4,2 ps	4 ns	16 ns	11,5 ns	6 ns	2,5 ns	8 ns	13,7 ns
fluorescence quantum yield			0,45		0,31									
λ_{ex}			365		365	365	365	377	377				377	

λ_{em}			538 / 533		457 / 458	507	-	460	500				500	
x-slip y-slip angle	(8 ; 2) 26,6°				(3,5 ; 3) 62,8°									
CSD code, refcode	778284, ANUYEO													
d spacing (Å)	0 0 1 20.3008513 0 0 2. 10.1504257 0 1 0. 8.83560792 1 0 0 7.5064851 0 0 3. 6.76695044	23,5 11,5 7,7 5,7 4,58	21,91 10,96	28 14 9,28 7 5,6	28,03 14,03 29,23 14,82 28,03 14,04 27,94 13,97 27,3									

A.v. Preliminary test materials

Three other compounds have been tested in the preliminary experiments: Calix-Cousulf- Cs^{+2} complex, caesium acetate and CsCl , with water as the good solvent and THF the anti-solvent. The structure of Calix-Cousulf- Cs^{+2} complex (synthesised by Director Isabelle Leray's team) and caesium acetate are shown in Figure Appen.A.3.

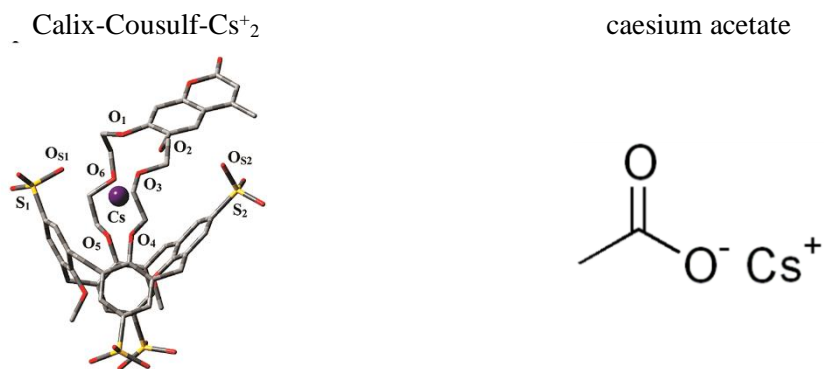


Figure Appen.A.3. Structure of Calix-Cousulf- Cs^{+2} complex and caesium acetate.

Appendix B

B.i. Technical details of the microfluidics

B.i.i. The microfluidic system holder

One of those sample holders is made in ABS as a prototype device, others are made in Dural. It is a homemade design in collaboration with LPS (Sandrine MARIOT) and PPSM (J-P LEFEVRE, J-F AUDIBERT). CAD and assembly are built under SketchUp or SolidWorks, printing are made with an HP Design Jet 3D printer and machining is made by a local company (*STIM*, Cachan) or in LPS facilities.

This mixing device can be used horizontally with an inverted microscope or vertically as on the synchrotron beam line SWING.

B.i.ii. Microfluidic capillaries, connectors, and chambers

- Glass tubing used:

The small capillary for the central jet is made of Clear fused Quartz:

<https://www.vitrocom.com/products/view/CV8010>

The intermediate capillary for the peripheral flow is made of Borosilicate:

<https://www.vitrocom.com/products/view/CV2033>

The big capillary for flow expansion is made of fused Silica:

https://www.molex.com/molex/products/datasheet.jsp?part=active/1068150381_CAPILLAR_Y_TUBING.xml

- Connectors and chambers are purchased from *IDEX Health & Science*: <https://www.idex-hs.com/catalog/>
- Tubing are purchased from *IDEX Health & Science*: <https://www.idex-hs.com/catalog/>

B.i.iii. Pumps system, Harvard Apparatus

Table Appen.B.1. Characteristics of the pumps

Specifications	Pico Plus Elite	PHD2000	11 Plus	11 pico Plus
Accuracy	± 0.35%	± 0.35%	±0.5%	±0.5%
Reproducibility	± 0.05%	± 0.05%	±0.1%	±0.1%
Syringes (Min./Max.)	0.5 µl / 10 ml	0.5 µl / 140 ml	(single syringe) 0.5 µl/50-60 ml (dual syringe) 0.5 µl /10 ml	0.5 µl / 10 ml
Flow Rate:				
Minimum (0.5 µl syringe)	0.54 pl/min	0.0001 µl/hr	(dual syringe) 0.0014 µl/hr (single syringe) 0.0014 µl/hr	1.3 pl/min
Maximum (10 ml syringe)	11.70 ml/min		(dual syringe) 7.91 ml/min	0.8788 ml/min (using 2 x 10 ml syringes combined output)
Maximum (60 ml syringe)	N/A		(single syringe) 26.56 ml/min	N/A
Maximum (140 ml syringe)	N/A	220.82 ml/min	N/A	N/A

B.ii. Structure of the coaxial microflow

B.ii.i. Central jet radius

The maximum central jet radius was measured from OM images (Figure 2.7) by taking the maximum gradient of the grey scale profile along the radius, $r_{c,max} = \frac{r_{up} - r_{down}}{2}$. The values are listed in Table Appen.B.2, as well as the predicted value by equation (2.14) and *Comsol* simulation.

Table Appen.B.2. Maximum central flow jet radius under different flow rates.

Q_c (nl/min)	Q_p (μ l/min)	Q_c/Q_p	r_{down} / μ m	r_{up} / μ m	$r_{c,max} = \frac{r_{up} - r_{down}}{2}$ / μ m	$R \cdot \sqrt{1 - \sqrt{1 - \frac{Q_c}{Q_c + Q_p}}}$ / μ m	Comsol simulation
37	1	0.037	62.38	91.37	14.495	14.10776815	12.42
37	2	0.0185	64.95	88.8	11.925	10.0369258	9.85
37	4	0.00925	67.88	86.6	9.36	7.11900458	7.78
37	8	0.004625	69.72	84.76	7.52	5.041607235	6.27
37	10	0.0037	70.08	84.76	7.34	4.510727454	6.09
74	1	0.074	57.24	94.67	18.715	19.71361113	17.17
74	2	0.037	62.75	91	14.125	14.10776815	13.01
74	4	0.0185	65.68	88.06	11.19	10.0369258	10.05
74	8	0.00925	67.88	86.96	9.54	7.11900458	7.97
74	10	0.0074	68.25	86.23	8.99	6.371335331	7.29
148	1	0.148	51.74	100.17	24.215	27.24532049	24.7
148	2	0.074	57.98	94.67	18.345	19.71361113	18.46
148	4	0.037	62.38	91	14.31	14.10776815	13.34
148	8	0.0185	65.31	88.8	11.745	10.0369258	10.31
148	10	0.0148	66.05	88.06	11.005	8.988336632	9.37
296	1	0.296	38.53	108.61	35.04	36.90625917	35.55
296	2	0.148	49.54	100.54	25.5	27.24532049	25.01
296	4	0.074	55.77	95.4	19.815	19.71361113	18.97
296	8	0.037	61.64	91	14.68	14.10776815	13.88
296	10	0.0296	63.11	90.27	13.58	12.64919977	12.56
370	1	0.37	35.96	113.38	38.71	40.43461946	39.3
370	2	0.185	45.5	102.74	28.62	30.12480374	29.36
370	4	0.0925	55.77	96.5	20.365	21.91165825	21.62
370	8	0.04625	61.28	92.1	15.41	15.72521932	15.33
370	10	0.037	63.11	90.63	13.76	14.10776815	14.11

B.ii.ii. Flow entrance length

The concentration entrance length and hydrodynamic entrance length were estimated using equation (2.21) and equation (2.16), respectively. The values are listed in Table Appen.B.3.

Table Appen.B.3. Calculated flow entrance length, Péclet number and Reynolds number

Q_c /(nl/min)	Q_c /(μ l/min)	$v_{effective}$ /(mm/s)	Pe	l_c /mm	Re	l_p / μ m
37	1	0.499251364	104.8427864	1.100849257	0.104842786	1.431104034
37	2	0.980689516	205.9447983	2.162420382	0.205944798	2.811146497
37	4	1.94356582	408.1488222	4.285562633	0.408148822	5.571231423

37	8	3.869318428	812.5568699	8.531847134	0.81255687	11.09140127
37	10	4.832194732	1014.760894	10.65498938	1.014760894	13.8514862
74	1	0.517064575	108.5835608	1.140127389	0.108583561	1.482165605
74	2	0.998502727	209.6855727	2.201698514	0.209685573	2.862208068
74	4	1.961379031	411.8895966	4.324840764	0.411889597	5.622292994
74	8	3.88713164	816.2976443	8.571125265	0.816297644	11.14246285
74	10	4.850007944	1018.501668	10.69426752	1.018501668	13.90254777
148	1	0.552690999	116.0651097	1.218683652	0.11606511	1.584288747
148	2	1.034129151	217.1671216	2.280254777	0.217167122	2.96433121
148	4	1.997005455	419.3711455	4.403397028	0.419371145	5.724416136
148	8	3.922758063	823.7791932	8.649681529	0.823779193	11.24458599
148	10	4.885634367	1025.983217	10.77282378	1.025983217	14.00467091
296	1	0.623943845	131.0282075	1.375796178	0.131028207	1.788535032
296	2	1.105381997	232.1302194	2.437367304	0.232130219	3.168577495
296	4	2.068258301	434.3342433	4.560509554	0.434334243	5.92866242
296	8	3.994010909	838.742291	8.806794055	0.838742291	11.44883227
296	10	4.956887213	1040.946315	10.92993631	1.040946315	14.2089172
370	1	0.659570268	138.5097563	1.454352442	0.138509756	1.890658174
370	2	1.14100842	239.6117683	2.515923567	0.239611768	3.270700637
370	4	2.103884724	441.8157921	4.639065817	0.441815792	6.030785563
370	8	4.029637333	846.2238399	8.885350318	0.84622384	11.55095541
370	10	4.992513637	1048.427864	11.00849257	1.048427864	14.31104034

B.iii. Assembling the microfluidic system

B.iii.i. Assembling procedures

Before assembling the system, a coaxial aligner - a pinch ($ID = 80\mu m$) - on the borosilicate capillary for the silica capillary was made by a 2 mm pulling step with a PC-10 puller (*NARISHIGE*) at its heater level 55, procedures shown in Figure Appen.B.1. The coaxiality of capillary on two sides of the pinch was checked to make sure it was not bending.

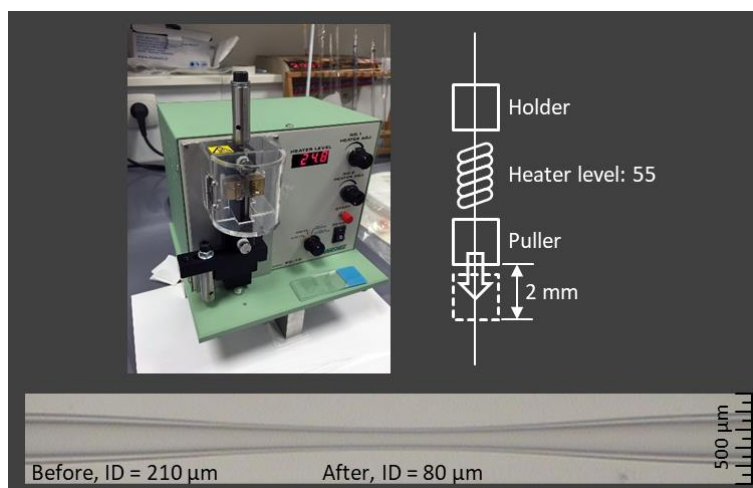


Figure Appen.B.1. Procedures to make the coaxial aligning pinch on the borosilicate capillary for the central flow injection nozzle.

To mitigate heterogeneous nucleation on the microfluidic channel, before assembling the system, a hydrophobic surface treatment by POTS was performed on the inner surface of the borosilicate capillary. About 350 nl 1H,1H,2H,2H-perfluorooctyltriethoxysilane was sucked into each borosilicate tube and baked in oven at 150C° for 2 hours with both ends sealed by fusing. Then, both ends of the capillary were cut open and washed with acetone to remove the excess agent. The contact angle before and after the treatment is shown in Figure Appen.B.2.

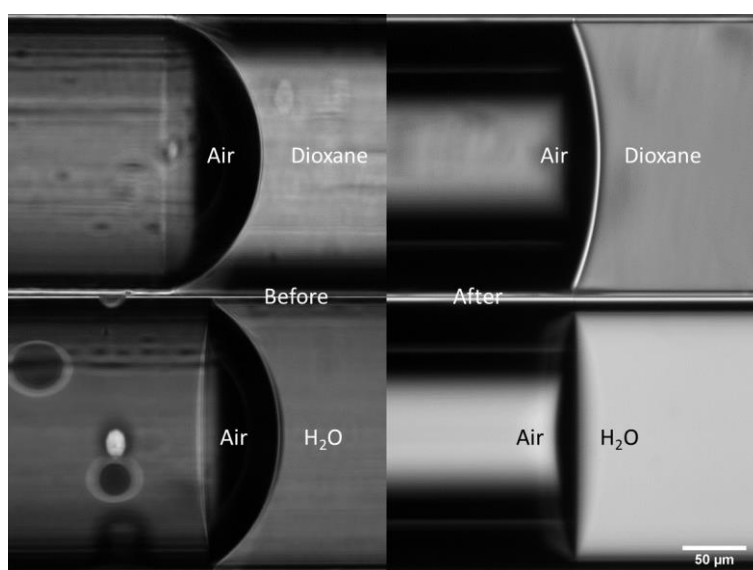


Figure Appen.B.2. Contact angle of H₂O and 1,4-dioxane in the borosilicate capillary

before and after hydrophobic surface treatment.

Two polydimethylsiloxane (PDMS) droplets were made on the intermediate capillary for its coaxial alignment in the big capillary, procedures shown in Figure Appen.B.3.

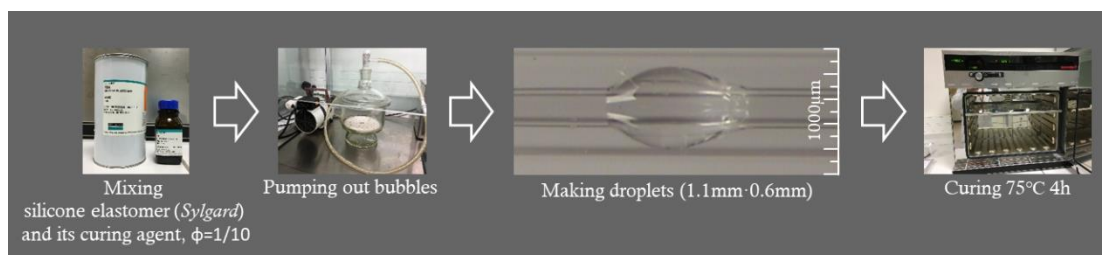


Figure Appen.B.3. Procedures to make PDMS droplets on the borosilicate capillary to align it coaxially in the big quartz tube.

After all the treatment, the intermediate borosilicate capillary entered the two high-pressure PEEK 7-port manifold (*IDEX*) from the back ports (on the observation window's side), stopped at the middle of the top port of 7-port manifold 1 and was fixed by two F-333N PEEK nuts (*IDEX*) paired with F-142N ferrules and F-241x fluorinated ethylene propylene (FEP) sleeves (*IDEX*) at the front port of manifold 2 and back port of manifold 1. The pinch aligner would be at the beginning of the observation window.

Syringes of $Q_I \sim Q_{IV}$ were paired with luer adapters (P-659, *Delrin*) connected to fluorinated ethylene propylene (FEP) tubes (ID = 200 μm , OD = 1.6mm, *IDEX*) by F-330N polyether ether ketone (PEEK) nuts (*IDEX*) with F-142N ethylene tetrafluoroethylene (ETFE) ferrules (*IDEX*). Polytetrafluoroethylene (PTFE) filters (pore size 0.22 μm , *Millipore*) were cut into circular slices, 5 mm in diameter, and fitted between the syringe luer lock tip and adapter so that impurities larger than 200 nm were removed. The FEP tubing of Q_I and Q_{II} were connected to a high-pressure PEEK mixing tee (*IDEX*) by F-331N PEEK nuts (*IDEX*) paired with F-142N ferrules. Q_I and Q_{II} were mixed inside the tee and came out from the third thru-hole, as Q_c , into the small silica capillary connected by a F-330N nut paired with a F-142N

ferrule and a F-237x FEP tubing sleeve (*IDEX*). Then this smallest capillary was fixed in a “positioner” (Figure 2.3) before inserting coaxially into the intermediate borosilicate capillary. The positioner was a PEEK zero-dead-volume union (*IDEX*) paired with a F-331N nut, a F-142N ferrule and a F-237x FEP sleeve.

The injection nozzle of the small capillary was made 10 μm in diameter by fusing and then pulling manually. It was slid into the intermediate capillary, from the front thru-hole of 7-port manifold 1 through a F-333N nut (*IDEX*) paired with a F-142N ferrule and a F-237x sleeve, until it bottomed out the aligner on the intermediate capillary at the beginning of the observation window. The exact alignment of the injection nozzle of the central flow was adjusted by both the positioner and the aligner. The aligner held the nozzle approximately at a coaxial position with respect to the intermediate capillary. The positioner adjusted precisely the angle and position of the small capillary in the coaxial aligner from outside. When a good coaxial alignment was found, the positioner was maintained on the microfluidic device with a piece of plasticine.

The two FEP tubes of solvent 1 and 2 of Q_{III} were connected to port 6 and port 2 (Figure 2.9) of the switching valve respectively by 6000-282 PEEK *RheFlex* fittings (*IDEX*). Port 1 was the exit. The output from port 1 was solvent 1 on position 1 and solvent 2 on position 2, as shown in Figure Appen.B.4. Out from port 1 was a FEP tube ($\text{ID} = 200\mu\text{m}$, $\text{OD} = 1.6\text{mm}$, *IDEX*) linked to a second high-pressure mixing tee. Connected by the same type fittings than Q_{I} and Q_{II} , Q_{III} and Q_{IV} were mixed in the tee, becoming Q_{p} . Thus, Q_{p} was switched between a mixture of solvent 1 and 2 and pure solvent 2 by the actuated valve. Q_{p} came out from the third thru-hole of the tee into a FEP tube ($\text{ID} = 200\mu\text{m}$, $\text{OD} = 1.6\text{mm}$, *IDEX*) and was injected into the intermediate capillary through the top port of 7-port manifold 1 by a F-330N nut paired with a F-142N ferrule. The four rest side ports of manifold 1 were sealed by P-550 PEEK plugs (*IDEX*).

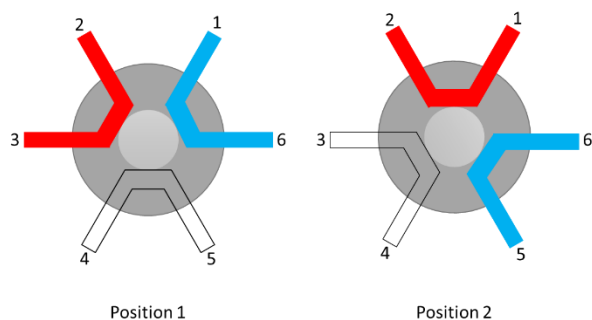


Figure Appen.B.4. Flow path in the switching valve.

The big capillary was coaxially slid outside the intermediate capillary, with the small capillary inside, and then reached the centre of manifold 2 by the front port through a F-333N nut paired with a F-142N ferrule and a F-252x sleeve (*IDEX*). The alignment of the intermediate capillary inside the big capillary was maintained by the two PDMS droplets. Syringes of Q_V were connected to FEP tubes (ID = 500 μ m, OD = 1.6mm, *IDEX*) by same fittings as Q_I to Q_{IV} and then through 2 side ports of manifold 2 into the big capillary by a F-330N nut paired with a F-142N ferrule. The rest 3 ports of manifold 2 were sealed by P-550 plugs.

The original observation window on the microfluidic device was designed 48.5 mm long, but because its frame interfered with the objective (20 \times /0.45, WD 7.4, *Nikon Plan Fluo*) for microscopic observation, the actual observable distance was limited down to 25 mm after the injection nozzle inside the borosilicate capillary. The observation window was covered by 2 borosilicate glass slides (0.17 mm thick, *VWR*). Refractive index matching liquid, immersion oil (*Nikon NF*) or pure water, was filled between the slides to correct the image distortion by the cylindrical tubes. The refractive indices of the materials in the observation window are listed in Table Appen.B.4. For matching refractive indices with the capillary tubes, the immersion oil should have served better than water. But it had autofluorescence under the excitation UV laser ($\lambda = 343\text{nm}$), therefore, pure water was used as the index matching material for fluorescence experiment. For a short experiment, index matching water was added into the observation window manually with a syringe, and for a parametric sweep, a *Pico Plus* syringe pump

(*Harvard Apparatus*) was used to feed pure water through a FEP tube (ID = 500 μ m , OD = 1.6mm, *IDEX*) at a constant flow rate, 3 μ l/min, to compensate evaporation.

Table Appen.B.4. Refractive indices (589 nm) of the materials in the microfluidic system

Fused silica	Borosilicate glass	Quartz	<i>Nikon NF oil</i>	Water	1-4-dioxane
1.4584 [Malitson, 1965]	1.5100	1.5442 [Ghosh, 1999]	1.515	1.3324 [Hale, 1973]	1.4202 [Moutzouris, 2013]

All air bubbles in syringes and fittings were carefully removed before connecting. All fittings and plugs were screwed by toothed tweezers to avoid leakage. Tubes were cleaned by acetone with optic papers and checked under microscope after assembling. One by one, any remaining impurity on the capillary was evaporated by focusing the maximum power of the pulsed IR laser at it. The clarity of the capillaries was crucial for microfluidic NPLIN experiment, as the absorption of the focused IR laser by the impurities was able to evaporate the impurity or even cause explosion or ablation, creating bubbles in the microfluidic system, by which the experiment had to be stopped. In the worst scenarios, the capillary could be burnt. When necessary, remote control of the syringe pumps was deployed by homemade *Labview* routines, and the switching valve by *Rheodyne TitanMX* software.

B.iv. Problems related with the microfluidic device

B.iv.i. Cleanness of the capillaries

Liquid in all syringes must be filtered to remove impurities at the syringe luer tip before entering the microfluidic system. Not only will the impurities increase the probability of heterogeneous nucleation and interfere with OM observation, they might clog the capillaries. Especially for the 10 μ m diameter injection nozzle, any impurity in the small capillary must either be removed through the other end or be carefully evaporated by the IR laser in water with a risk of fusing the silica.

Both the inside and outside of the borosilicate capillary must be cleaned with acetone

and checked under microscope with the whole system mounted. Any impurity must be carefully evaporated by the focused IR laser before experiment started, otherwise bubbles would be created on the surface of the impurity if the IR laser happened to shine on an absorbing impurity.

B.iv.ii. Temperature control

In the co-microflow antisolvent mixer, temperature was not actively controlled, but relied on the room temperature. A change in the phase transition behaviour was observed even by adjusting the light source of the microscope. To capture the objects in the microflow at a velocity ranging from 1 mm/s to 10 mm/s, the exposure time of the camera was set to the minimum, 0.01 ms and the brightness of the halogen lamp was dialled to the maximum. Once we tried to increase the signal by pushing the field diagram lever also to the maximum and this had stopped spontaneous crystallisation immediately. Temperature influences solubility, viscosity, diffusion coefficient and molecule mobility.

In Figure 2.13, 10 g/l and 16 g/l were made by supersaturated mother solutions dissolved at 60 °C and then kept at room temperature in Q_1 syringe. To prevent crystallisation of the supersaturation solution in syringe, active temperature control of Q_1 syringe should be deployed.

B.iv.iii. Deformation and degradation of the device

The two prototypes of the microfluidic device were 3D-printed of ABS. ABS was dissolved by 1,4-dioxane or THF when there was a leakage. Then the device started to degrade and deform. To keep the coaxiality of the capillaries, the device had to be strongly pressed on the microscope stage by slide clips. After some time, it cracked and broke into pieces. For that, all fittings must be strongly screwed by toothed tweezers, instead of fingers, to avoid any leakage of organic solvent.

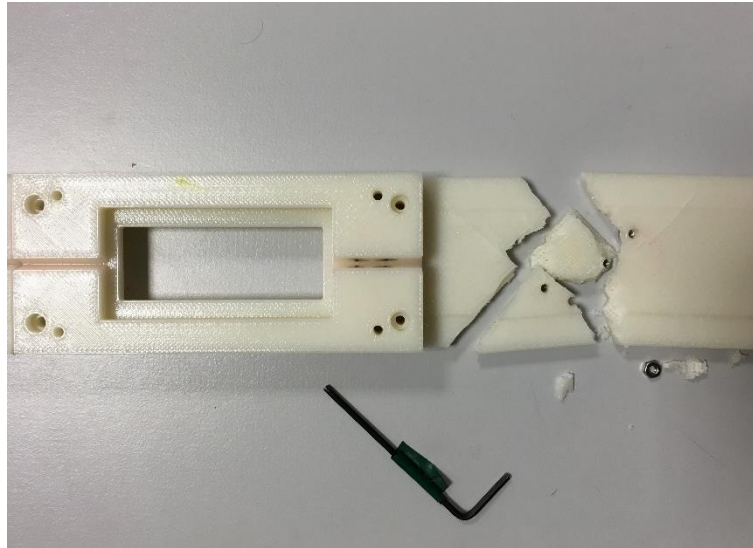


Figure Appen.B.5. Degradation of the 3D-printed ABS microfluidic device

If active temperature control will be added in the observation window, the device will start to bend because of the thermal stress caused by local heating. For these reasons, material for the device should have a high resistance to organic solvents, a low thermal expansion rate, and be suitable for rapid prototyping.

B.iv.iv. Precipitation on the injection nozzle of the central flow

Heterogeneous precipitation on the injection nozzle was seen in our previous work and *Comsol* simulation has suggested a hydrodynamic dead zone after the nozzle [Liao, 2013]. To reduce the thickness of the wall of the injection nozzle, we tried to etch the injection nozzle with HF. The problem persisted. Then we made the nozzle of 10 μm diameter with a streamline outside profile. This has changed the behaviour of the co-flows from hydrodynamic focusing to jetting. The average velocity of the central flow at the nozzle was 40~400 times as high as that of the peripheral flow, depending on the flow ratio. Precipitation on the injection nozzle was alleviated yet still existed when ϕ_p was high. Should precipitation on central flow injection nozzle occur, a system clean procedure needs to be performed by actuate the switching valve from position 1 to position 2.

B.iv.v. Working distance of the objective

Although an ultra-long working distance objective ($20\times/0.45$, WD 7.4, *Nikon Plan Fluo*) was selected, it interfered with the frame of the observation window of the microfluidic device, rendering the designed length reduced from 48.5 mm to 25 mm. Either the thickness of the device needs to be reduced or an objective with an even longer working distance should be selected.

B.iv.vi. Leakage and bubble

All fittings must be screwed with toothed tweezers to prevent solvent leakage. All syringes must be degassed to remove bubbles. After Q_{III} and Q_{IV} were mixed in the tee, gas bubbles were generated from time to time.

B.iv.vii. Influence of gravity

In the preliminary experiment, it was found that gravity started to play a role. For that, THF and 1,4-dioxane was mixed to match the density of water. But this was meaningless since the density of the precipitates were not controllable and the mixing properties (solubility, viscosity, density...) among 3 solvents was difficult to predict. For the microfluidic SAXS, the device was installed vertically on a motorised stage with the flow direction upwards, whereas it could have been placed horizontally.

B.iv.viii. Flow expansion by the big capillary

The third capillary is to expand the flow for SAXS. But this introduces a new central/peripheral flow system at the end of the intermediate capillary. Different microfluidic behaviour could occur depending on the parameters. Adding one more coaxial flow or solvent will greatly increase the complexity of the microfluidics and difficulties in understanding the mixing properties.

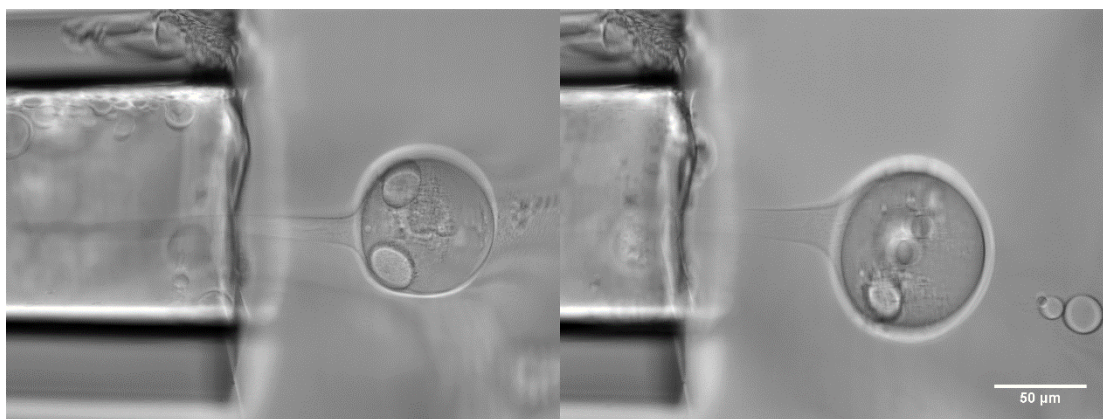


Figure Appen.B.6. Abnormally large droplets trapped by the antisolvent gradient at the outlet of the intermediate capillary to the big flow expansion capillary for the

SAXS experiment. Microfluidic parameters:

$$\rho_{3c} = ? \text{ g/l}, Q_c = 1000 \text{ nl/min}, \phi_{\text{THF20+dioxane80,p}} = 100\%, Q_p = 10 \mu\text{l/min}, Q_{\text{water,external}} = 30 \text{ ul/min}$$

B.v. Technical details of the laser sources and illumination type

B.v.i. Diascopic illumination for bright field (BF) imaging, KhÖler illumination type:

- Tungsten halogen bulb EVA64623HLX 12V 40/CS 1/SKU 100 W. *Osram*
- TE-C ELWD 65mm (Condenser Extra Long Working Distance) NA=0.05-0.3. *Nikon*
- BF in combination with crossed Polariser–Analyzer is used to look randomly at the birefringence of the produced objects inside the flow. They are crossed at 90° to have a dark background. The polariser in excitation is a standard multi-coated glass polariser, type *Nikon C-SP 754097*. The analyser is cut in a *TECHSPEC®* visible linear polarizing laminated film made of cellulose triacetate (CTA), *Edmund Optics*.

B.v.ii. Episcopic illumination for wide-field fluorescence (ep-fl) imaging and IR focusing:

The IR (1030nm) laser is from a T-pulse 200 ytterbium-doped tungstate mode locked femtosecond oscillator, 400fs-FWHM, repetition rate 10MHz and average power about 2.7 W,

Amplitude System. The IR beam is extended by a factor 1.5 and slightly divergent. The polarisation can be controlled. The illumination type is confocal (CF) at the sample plane.

- The UV (343nm) laser is from third-harmonic generation. The UV beam is collimated and extended by 2, the polarisation filtered by a laser-Glan's prism to be pure s-polarised respect to the dichroic, and a 300mm focal lens tube used in infinite conjugation with the rear focal plane of the objective to achieve a wide-field (WF) illumination.

B.vi. Technical details of the microscope and optics

B.vi.i. Microscope

The microscope is a two turrets stage inverted microscope, TE2000-U (*Nikon*) for epifluorescence.

B.vi.ii. Objective and filters arrangement

- Objective: CFI S Plan Fluor ELWD, WD 8.2 – 6.9mm, magnification 20X, NA= 0.45, infinite corrected, correction ring range 0–2.6mm, *Nikon*:
[https://www.nikoninstruments.com/fr_FR/Product-Selectors/Objective-Comparison/\(items\)/i114](https://www.nikoninstruments.com/fr_FR/Product-Selectors/Objective-Comparison/(items)/i114)

It is used with a parfocal length extender ring of 5 mm thickness to match the right traveling distance of the focusing at the sample plane.

- Half-waveplate and quarter-waveplates are 1030 nm zero-order waveplates. They are used alone or in cascade to control the CF excitation polarisation (p-polarised, s-polarised or circular (R or L)) at the sample plane:

<https://www.thorlabs.com/thorproduct.cfm?partnumber=WPH05M-1030> and

<https://www.thorlabs.com/thorproduct.cfm?partnumber=WPQ05M-1030>

- Dichroic and emission filters:
- Dichroic filter @ 343nm: cutoff at 350 nm, Reflection band (R > 95 %) 330-340

- Dichroic filter @ 1030nm : DM1000R, cutoff at 1000nm, Reflection band (R > 90%)1020 - 1550 nm: <https://www.thorlabs.com/thorproduct.cfm?partnumber=DMSP1000R>
- Emission filters: notch filters @515nm (stop line, bandwidth 16nm, OD@515nm # 6, OD@343nm # 5) and SP785 (Short wave pass 785nm, band width 430nm, OD@1030nm # 7, OD@343nm # 5), *Semrock*

B.vii. Technical details of the sensor and detector

B.vii.i. CCD camera Retiga R1, *QImaging*

It is a standard interline transfer scientific CCD camera. The CCD is run under the μ Manager open source software.

Table Appen.B.5. Characteristics of the Camera

Sensor Type	Sony ICX-825 Scientific Interline CCD (Monochrome)
CCD Array	1360 x 1024
Full Well Capacity	>16,000e ⁻ single pixel (>22,000e ⁻ with on-chip binning)
Digital Output	14 bits
Digitisation Rate USB3	50MHz high frame rate
Read Noise (typical)	<7e ⁻ (RMS)
Peak Quantum Efficiency	75% at 600nm
Pixel Size	6.45 μ m x 6.45 μ m
Frame Rate	12 fps at full resolution ,40 fps binned 2x2
Exposure Time Range	25 μ s - 60min

B.vii.ii. QA–Fluorescence Life time Imaging (FLIM)

It is a single photon counting camera Quadrant Anode MCP-PM based photodetector operating in TCSPC mode. Each photon is digitalised in a 12 bits array in position and Time–Tagged–Time–Resolved (TTTR) with a time resolution of 10 ns and 50 ps, respectively. [doi:10.1088/1748-0221/9/12/C12015](https://doi.org/10.1088/1748-0221/9/12/C12015) . Hardware, electronic interface, and GUI are maintained by *Photonscore*, Germany; coupling optical setup, calibration, post processing and analysis tools software are managed in our team (Dr. Robert PANSU, J-F AUDIBERT, PPSM).

Table Appen.B.6. Characteristics of the detector

General	
Active area	∅ 25mm
Time resolution	< 49ps FWHM
Positional resolution	40um FWHM
Maximal count rate	> 300kHz
Dead time	<400ns
Arrival Time Resolution	10ns
Time to digital Conversion	
Dead time	< 300ns
Minimum bin width	< 1.25ps
Electrical resolution	< 6ps FWHM
Number of time bins	4095
Time Windows	50/100ns

B.viii. Laser power, repetition rate, and laser focal spot intensity profile

The average power of the laser was adjusted by turning the half-wave plate. The average power of the laser at the exit of the pulse picker was measured for different half-plate angles, values listed in Table Appen.B.7 and plotted in Figure Appen.B.7.

Table Appen.B.7. Half-wave plate angle and average power of IR laser after the pulse picker at 10MHz

$\theta/^\circ$	0	5	10	15	20	25	30	35	40	45
P_r/mW	1100	1090	1020	900	720	500	320	160	0	0

P_r was plotted against θ in Figure Appen.B.7 and fitted with equation

$$P_r = A \cdot P_o \cdot \cos^2 2\theta \quad (\text{B.1})$$

where P_o is the average power of the laser source, 2.8 W, A the transmission coefficient of the pulse picker, fitted to be 0.41, which means 60% of the power was lost inside the pulse picker.

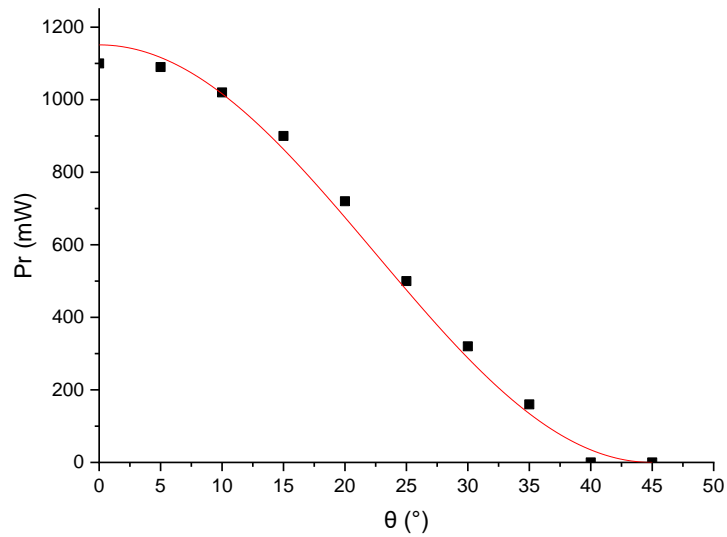


Figure Appen.B.7. The average power of the IR laser after the pulse picker as a function of half-wave plate angle.

Table Appen.B.8. Repetition rate and average power of IR laser after the pulse picker with halfwave plate at 11°

$f_{\text{rep}}/\text{MHz}$	1	2	3.3	5	10
P_r/mW	70	150	260	400	1050

P_r was plotted against f_{rep} in Figure Appen.B.8. The dependence was not strictly linear.

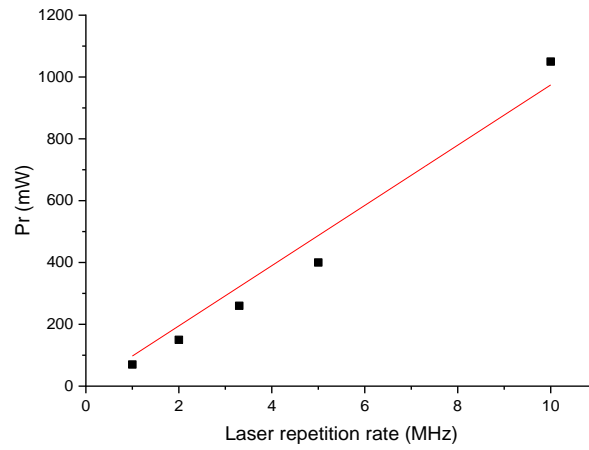


Figure Appen.B.8. The average power of the IR laser after the pulse picker as a function of the repetition rate.

The intensity profile of the IR laser focal spot at the microscope sample plane is shown on Figure Appen.B.9. The full width at half maximum (FWHM) was measured to be $2.365 \mu\text{m}$. For a Gaussian beam, $2\omega = FWHM \cdot 1.69 = 4 \mu\text{m}$. The optical intensity of the focal spot of the IR laser was estimated as

$$I = \frac{P_{\text{avg}}}{\pi\omega^2/2} . \quad (\text{B.2})$$

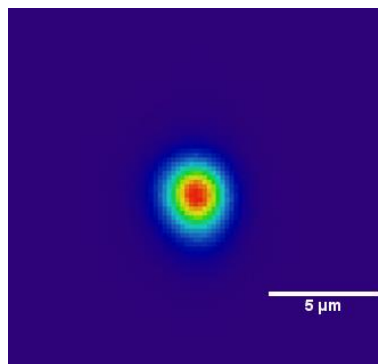


Figure Appen.B.9. Profile of the IR laser (1030nm) focal spot ($\times 20 \times 1.5$, NA 0.45, WD 6.7 mm) at the microscope sample plane.

Appendix C

C.i. Thermodynamic activity of water (1)-1,4-dioxane (2) system

Thermodynamic activity of water (1)-1,4-dioxane (2) system measured by [Vierk, 1950] are listed in Table Appen.C.1.

Table Appen.C.1. Thermodynamic activity of water (1)-1,4-dioxane (2) system[Vierk, 1950]

x_2	0.04	0.11	0.23	0.28	0.55	0.76	0.9	0.95
a_1	0.971	0.882	0.812	0.774	0.702	0.618	0.456	0.278
a_2	0.187	0.447	0.666	0.734	0.84	0.888	0.931	0.978
γ_1	1.01146	0.99101	1.05455	1.075	1.56	2.575	4.56	5.56
γ_2	4.675	4.06364	2.89565	2.62143	1.52727	1.16842	1.03444	1.02947

C.ii. Limitation of H³M model and Acree-Jouyban equation

Although H³M model has been up to now satisfactory in predicting vapor-liquid equilibria and ΔG_m of ternary aqueous-organic ternary mixtures, it has purposely avoided the difficulties in the structure of liquid by assuming an ideal mixing entropy. This assumption is far from the fact with the presence of hydrogen bonds between water molecules.

The excess enthalpy of water (1)-1,4-dioxane (2) at 298.15 K [Goates, 1958, Christensen, 1982, Suzuki, 2006] is plotted in Figure Appen.C.1. The red dashed line is $\Delta H_m = x_1 x_2 (\Omega_{12} + a_1^{12} x_1^3 + a_2^{12} x_2^3)$ (H³M model, equation (3.22)), with Ω_{12} , a_1^{12} and a_2^{12} values fitted from water (1)-1,4-dioxane (2) activity measured by [Vierk, 1950]. We can see in Figure Appen.C.1 ΔH_m calculated by H³M model is far away from the real measurement. [Suzuki, 2006] fitted their measurement of ΔH_m with Redlich-Kister equation to a 5 order polynomial expansion expansion, and got a good description. Whereas we tried to use H3M model to fit the measured ΔH_m (the thin red line). It shows that the interaction in water (1)-1,4-dioxane (2) binary system is too complex to be described by H³M model, which is essentially a Redlich-Kister kind equation with 3 order polynomial expansion with fitting

parameters correlated to two-body-three-body interaction and three-body self-association assuming a fully random mixing. This is because in real aqueous-organic mixtures, not only the interaction energy is not regular, but the mixing is far from random. $-T\Delta S_m = \Delta G_m - \Delta H_m$ calculated with the measured values is also plotted in Figure Appen.C.1 (black dots). The mixing entropy is much smaller than the ideal (red dots in Figure Appen.C.1) represented by Raoult's law. This suggests the arrangement of water molecules and 1,4-dioxane molecules is not random but highly organised. From the $-T\Delta S_m$ curve, we can tell that the configuration of water and 1,4-dioxane molecules in the binary mixture can be divided into three parts: (1) $x_2 \in (0, 0.2)$, the mixing entropy is negative in this range, the presence of small amount of 1,4-dioxane molecules have strengthened the order in the structure; (2) $x_2 \in (0.2, 0.8)$, the configuration of molecules is still far from ideal, but the entropy start to be positive, at least the randomness is higher than the pure solvents; (3) $x_2 \in (0.8, 1)$, when small amount of water molecules is added into 1,4-dioxane, the entropy is nearly ideal, which means the molecules configuration is very close to random.

Table Appen.C.2. Excess enthalpies of water (1)-1,4-dioxane (2)[Suzuki, 2006]

x_2	$H_m^E / (\text{J} \cdot \text{mol}^{-1})$	x_2	$H_m^E / (\text{J} \cdot \text{mol}^{-1})$	x_2	$H_m^E / (\text{J} \cdot \text{mol}^{-1})$
8.8E-4	-9.12	0.21895	-456.8	0.67064	575.1
0.00543	-53.6	0.30865	-264.2	0.68685	578.6
0.01093	-104.2	0.3992	-52.54	0.76755	551.2
0.01465	-135.4	0.47668	117.6	0.78396	504.6
0.02594	-225.9	0.47961	118.7	0.83241	350.4
0.03071	-261.5	0.54208	254.4	0.86937	274.5
0.04753	-355.7	0.59731	361.8	0.92833	229.3
0.06306	-434.3	0.62234	399.3	0.95079	575.1
0.0814	-491.9	0.62697	408.5	0.95881	578.6
0.13076	-556.7	0.65285	442.8		
0.1772	-525.5	0.65937	465.1		

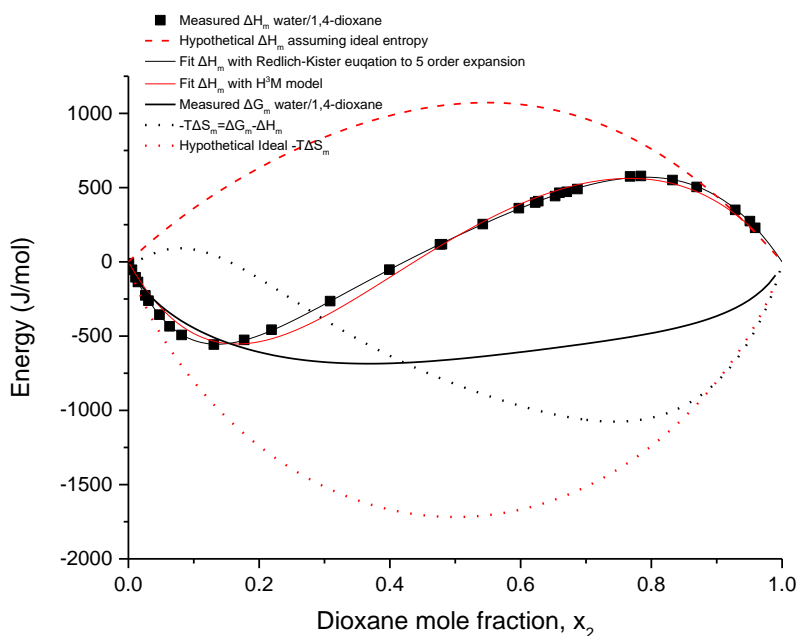
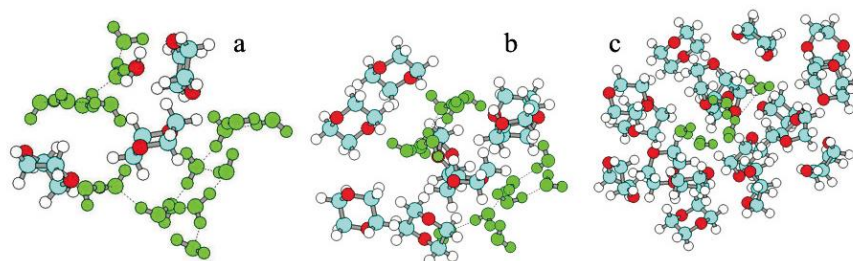


Figure Appen.C.1. Measured mixing ΔH_m , ΔG_m , and hypothetical values assuming ideal mixing entropy using H^3M model.

This observation is similar to [Suzuki, 2006]'s work on the partial enthalpies and the lowest energy conformation of aqueous solutions of 1,4-dioxane by means of ab initio molecular orbital calculations, as shown in Figure Appen.C.2. They proposed the mixing of water (1)-1,4-dioxane (2) can be categorised into three parts: $x_2 < 0.3$, $0.3 < x_2 < 0.8$ and $0.8 < x_2$. When $x_2 < 0.3$, there were no hydrogen-bonding between water and 1,4-dioxane. The network structures in those concentrations of water were increased by so-called hydrophobic hydration. When $0.3 < x_2 < 0.8$, the network structure of water was weaker, and water and 1,4-dioxane might be constructing different clusters each other. When $0.8 < x_2$, water molecules seem to be in the cage of 1,4-dioxane with less hydrogen-bonding water. And these behaviours are very similar to water-ethanol binary mixture reported by [Larkin, 1975].



*Figure Appen.C.2. Lowest energy conformation of aqueous solutions of 1,4-dioxane by means of *ab initio* molecular orbital calculations: (a) $x_2=0.14$, (b) $x_2=0.59$ and (c) $x_2=0.81$ [Suzuki, 2006] Here hydrogen-bonding showed by dotted lines.*

[Chaudhari, 2011] investigated molecular interactions in water (1)-1,4-dioxane (2) using hydrogen bonding model. They reported that for $0.17 < x_2 < 1$, 1,4-dioxane molecules interact with surrounding water molecules by hydrogen bonding, and these molecules form cooperative domain of water-dioxane. At $x_2=0.17$, the average size of cooperative domain of water–dioxane as well as the average number of hydrogen bonds between water and 1,4-dioxane molecules is the maximum. This can be correlated with the maximum of our calculation of $-T\Delta S_m$ curve in Figure Appen.C.1. They also plotted the average number of hydrogen bonds between water-water and between water-1,4-dioxane molecules as a function of water amount fraction (Figure Appen.C.3). Figure Appen.C.3 indicates that the water cluster are broken step by step by adding 1,4-dioxane, and these water molecules form clusters with 1,4-dioxane molecules. From that we can see, not only the configuration, but also the nature of the interaction between molecules is a function of concentration. The reality is much more complex than the H³M model.

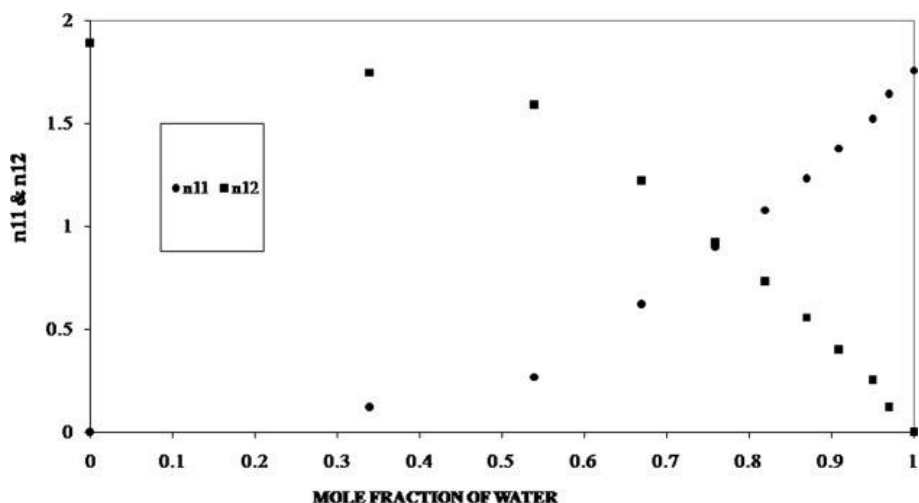


Figure Appen.C.3. The average number of hydrogen bonds between water–water molecules (n_{11} pair) and that between water–dioxane molecules (n_{12} pair) against amount fraction of water [Chaudhari, 2011].

Indeed, H³M model only considers enthalpy. They pretend their equation stand for ΔG_m , actually they have been using equation of ΔH_m to fit and predict ΔG_m . However, it was successful in predicting some aqueous-organic ternary liquid-vapor equilibria. This is because with a correction term of 3 order polynomial expansion, you can almost fit everything, including the sum of entropy and enthalpy (the molar excess free energy), both in binary and ternary system, though the values of the “interaction parameters” fitted by this equation will be very wrong.

Acree-Jouyban equation is successful in predicting drug solubility in aqueous-organic mixtures and correlating the curve fitting parameters with two-body-three-body interaction energies, the approximation Acree used in his extension of the H³M was only appropriate when the solute solubility is miniscule. In addition, Jouyban have been using solvent volume fraction instead of amount fraction. The solubility of DBDCS was plotted over amount fraction and volume fraction of 1,4-dioxane in Figure 3.6. Surprisingly, $x_{3s1}^{\phi_1} x_{3s2}^{\phi_2}$ (as Jouyban did) gives closer approximation of the real solubility measurements than $x_{3s1}^{x_1} x_{3s2}^{x_2}$ (as in the original Acree’s paper and in the regular solution model), before multiplied by the correction factor.

This means not only is the Jouyban-Acree model's prediction of solubility more convenient in practice by using solvent volume fractions, but it is also more accurate. Indeed, this is only by coincidence. By coincidence, most organic co-solvent molecules are far larger than H₂O. The molar volume of water (1)-1,4-dioxane (2) mixture, calculated by equation (2.10) is plotted over 1,4-dioxane volume fraction and amount fraction respectively in Figure 3.6. The molar volume of the mixture decreases linearly with the amount fraction of 1,4-dioxane but drops dramatically with its volume fraction. Thus, by predicting the solubility by solvent volume fraction, the points will be dragged to the right, which looks more, linear only by coincidence. For example, if we use, instead of water, another solvent that is much larger than water or, instead of most organic solvents, another solvent that is even smaller than water, to predict the solubility by solvent volume fraction will not make the nonideality more linear. Furthermore, the curve fitting parameters given by Jouyban cannot be used in our thermodynamic calculation.

C.iii. Estimation of the melting point, the solid-liquid phase change

enthalpy and entropy of DBDCS

The difference between the molar free energy of the liquid and solid state solute is given by Equation (3.8)

$$\begin{aligned}\mu_3^* &= \mu_3^{\text{solid}} + \Delta_{\text{fus}} H_{\text{m},3} \left(1 - \frac{T}{T_{\text{melt},3}^*} \right) \\ &= \mu_3^{\text{solid}} + T_{\text{melt},3}^* \Delta_{\text{fus}} S_{\text{m},3} \left(\frac{\Delta T}{T_{\text{melt},3}^*} \right) \\ &= \mu_3^{\text{solid}} + \Delta_{\text{fus}} S_{\text{m},3} \Delta T\end{aligned}$$

Neither the fusing entropy $\Delta_{\text{fus}} H_{\text{m},3}$ nor the melting point of DBDCS $T_{\text{melt},3}^*$ has been published yet. The fusion enthalpy of an organic molecule is dependent upon the interactions between its molecular fragments and therefore can be calculated by the summation of its constituent group values [Zhao, 1999, Jain, 2004]:

$$\Delta_{\text{fus}} H_{\text{m}} = \sum n_i m_i \quad (\text{C.1})$$

with n_i the number of times a group i appears in a compound and m_i the contribution of group i to the enthalpy of melting. We took values from Yalkowsky's analysis of 3000 organic compounds [Alantary, 2018] to estimate the molar fusion enthalpy of DBDCS

$$\begin{aligned}\Delta_{\text{fus}}H_{\text{m},3} &= 2(XCH_3 -) + 4(X - CH_2 -) + 2(X - CH_2 -*) + 2(Y - O -) \\ &\quad + 6(C_{\text{ar}}) + 12(CH_{\text{ar}}) + 2(YY - CH =) + 2(YY > C =) + 2(YCN -) \\ &= 2 \cdot 0.701 + 4 \cdot 1.408 + 2 \cdot 3.807 + 2 \cdot 3.162 + 6 \cdot 1.777 + 12 \cdot 1.235 \\ &\quad + 2 \cdot 1.689 + 2 \cdot 0.655 + 2 \cdot 6.558 \\ &= 64.258 \text{ kJ/mol}\end{aligned}$$

where X, Y and YY represents the attachment of a group to sp^3 , sp^2 , and two sp^2 atoms, respectively; $_{\text{ar}}$ represents the group is in an aromatic ring; $-CH_2-*$ is a methylene group bonded to two unbranched CH_2 atoms.

Bondi [Bondi, 1968] and Yalkowsky [Yalkowsky, 1972, Yalkowsky, 1979, Yalkowsky, 1994] proposed the total fusion entropy is the sum of its positional, rotational, and conformational components

$$\Delta_{\text{fus}}S_{\text{m}} = \Delta_{\text{fus}}S_{\text{m}}^{\text{pos}} + \Delta_{\text{fus}}S_{\text{m}}^{\text{rot}} + \Delta_{\text{fus}}S_{\text{m}}^{\text{conf}} \quad (\text{C.2})$$

Richards' rule shows that the molar fusion entropy for small spherical molecules $\Delta_{\text{fus}}S_{\text{m}}^{\text{pos}}$ is about $10.5\text{J} \cdot \text{mol}^{-1} \cdot \text{K}^{-1}$ [Richards, 1897]. This is the positional term of fusion entropy, because the rotational term is not applicable to the spherical molecules. Walden suggested an empirical rule that, for many aromatic hydrocarbons with little flexibility, the fusion entropy is about $56.5\text{J} \cdot \text{mol}^{-1} \cdot \text{K}^{-1}$ [Walden, 1908]. Therefore, the rotational term of fusion entropy is $46\text{J} \cdot \text{mol}^{-1} \cdot \text{K}^{-1}$. Fusion entropy for flexible molecules is generally greater than Walden's $56.5\text{J} \cdot \text{mol}^{-1} \cdot \text{K}^{-1}$. Chickos and Acree [Chickos, 1999] analysed the solid-liquid phase change enthalpies and entropies of 1858 compounds using a group additivity method and then tested their group values on 260 additional compounds. From that, Dannenfelser and Yalkowsky [Dannenfelser, 1996] proposed a semiempirical equation

$$\Delta_{\text{fus}}S_{\text{m}} = 50 - R \ln \sigma + R \ln \Phi \quad (\text{C.3})$$

with the molecular rotational symmetry number σ , a , is the number of indistinguishable positions that can be obtained by rigidly rotating the molecule about its centre of mass, which representing the number of positions into which a molecule can be rotated that are identical with a reference position [Dannenfelser, 1993]; and the molecular flexibility number Φ as a measure of the probability of the molecule having the proper conformation for incorporation into the crystal. The molecular flexibility number Φ is an exponential function of the chain length and can be calculated by [Jain, 2004]

$$\Phi = 2.435^{SP3+0.5SP2+0.5RING-1} \quad (C.4)$$

where $SP3$ is the number of nonring, nonterminal sp^3 atoms, $SP2$ the number of nonring, nonterminal sp^2 atoms, and $RING$ the number of single or fused aromatic ring systems. Although more sophisticated estimations have been proposed recently [Alantary, 2018, Yalkowsky, 2018], we need a simple equation to get a reasonably close estimation. Therefore, we will use equation (C.3) to estimate the fusion entropy of DBDCS $\Delta_{fus}S_{m,3}$ at its melting point and assume the same value for the ambient temperature:

$$\begin{aligned} \sigma &= 1 \\ \Phi &= 2.435^{8+0.5 \cdot 4+0.5 \cdot 3-1} = 2.435^{10.5} \\ \Delta_{fus}S_{m,3} &= 50 - 8.314 \ln(1) + 8.314 \ln(2.435^{10.5}) \\ &= 127.7 J \cdot mol^{-1} \cdot K^{-1} \end{aligned}$$

At equilibrium, the free energy change of phase transition $\Delta_{fus}G = \Delta_{fus}H - T_{melt} \Delta_{fus}S$ is zero. Therefore, the melting point of DBDCS can be predicted using equation (C.1) and (C.3):

$$T_{melt,3}^* = \frac{\Delta_{fus}H_{m,3}}{\Delta_{fus}S_{m,3}} = 503K \quad (C.5)$$

and the difference between the chemical potential of the solid and liquid DBDCS using equation (3.8):

$$\begin{aligned}\mu_3^* &= \mu_3^{\text{solid}} + \Delta_{\text{fus}} S_{m,3} (T_{\text{melt},3}^* - T) \\ &= \mu_3^{\text{solid}} + 26187 \text{ J/mol} \\ &= \mu_3^{\text{solid}} + 10.6RT\end{aligned}$$

Table Appen.C.3. Group contribution coefficients (kJ/mol) for calculating the enthalpy of melting and boiling [Alantary, 2018]

Environmental descriptor	Contribution coefficient (kJ/mol)		Environmental descriptor	Contribution coefficient (kJ/mol)	
	bi	mi		bi	mi
XCH ₃ -	1.707	0.701	YBr	-	2.911
YCH ₃	2.020	1.221	XI	-	4.034
ZCH ₃	-	0.331	YI	8.793	4.334
XCH ₂	2.520	1.408	XO	2.447	2.921
XCH ₂ *	2.163	3.807	YO	5.331	3.162
YCH ₂	1.967	0.331	YYO	-	-6.918
YYCH ₂	0.769	-2.524	Ar-O	-	-0.922
YZCH ₂	-	1.644	XOH	16.185	4.953
XCH	2.446	1.875	YOH	10.770	6.699
YCH	1.314	-0.916	YSH	8.993	2.635
XC	1.829	1.177	YS	-	5.313
YC	1.424	-1.076	YSO ₂ NH ₂	-	10.642
CH ₂ =	1.557	0.454	Y-SO ₂ N-X	-	6.739
YCH=	2.452	1.691	XNH ₂	9.595	6.884
YYCH=	2.457	1.689	XNH	-	1.181
YC=	2.679	2.250	YNH ₂	11.948	5.681
YYC=	1.506	0.655	YNH	8.091	3.799
CH≡	1.169	2.357	YN	5.579	2.013
ZC≡	5.332	3.853	YNO ₂	14.786	4.584
YZC≡	4.524	-1.732	YNHCO	24.063	8.167
Callenic	2.309	2.033	XCN	-	5.714
Car	3.031	1.777	YCN	10.223	6.558
CHar	2.591	1.235	XCOO	8.286	9.488
CBIP	2.604	2.602	YCOO	9.216	6.208
CBR1	3.053	1.329	XCOOH	-	14.287
CBR2	1.853	-0.564	YCOOH	20.606	11.785
CHfus	2.523	1.695	YCHO	10.844	5.470
Cfus	2.558	1.332	XCO	10.193	8.037
CH ₂ RING	2.221	1.054	YCO	11.718	3.332
CHRING	2.287	1.046	YOCO	-	7.568
CRING	1.261	0.757	YOCOO	-	5.335
=CHRING	2.598	0.883	YCONH ₂	-	12.814
=CRING	2.316	1.362	YCONH	-	9.083
XF	-0.641	-0.087	YNHCOO	-	6.929
YF	-0.518	0.409	YNHCONH ₂	-	14.865
XCl	3.917	1.889	YNHCON	-	16.721

YCl	3.070	1.581	XCONH ₂	–	13.418
XBr	7.103	4.674	Ortho	–0.194	–0.282
2&6	–	–2.954	IHB	–11.065	–3.495
Constant	16.319	0.883	–	–	–

CH₂* = methylene group bonded to two unbranched CH₂ atoms.

The experimental value of the melting temperature and the melting enthalpy has been measured using DSC [Kim, 2015]. $T_{\text{melt}} = 446.85\text{K}$, $\Delta_{\text{fus}} H_{\text{m}} = 27833.44\text{J/mol}$. Therefore,

the melting entropy $\Delta_{\text{fus}} S_{\text{m},3} = \frac{\Delta_{\text{fus}} H_{\text{m},3}}{T_{\text{melt},3}^*} = 62\text{J} \cdot \text{mol}^{-1} \cdot \text{K}^{-1}$. This means that DBDCS is

basically a rigid molecule.

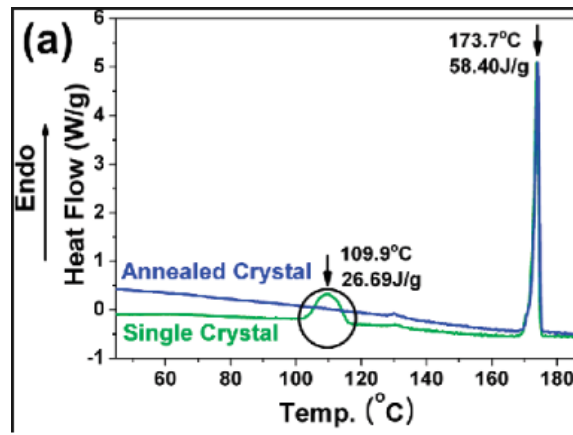


Figure Appen.C.4. DSC curve of DBDCS. (Adapted from [Kim, 2015])

C.iv. Recent development on the mutual diffusion coefficient of self-associating species

Self-diffusion coefficient can be estimated as

$$D_i^* = \frac{1}{6\pi r_i \dot{\mu}_i} k_B T, \quad (\text{C.6})$$

Equation (C.6) and (3.38) gives a simple relation between D_i^* and D_i^∞ :

$$\frac{D_i^\infty}{D_i^*} = \frac{\dot{\mu}_i}{\dot{\mu}_j} \quad (\text{C.7})$$

If this is true, the intrinsic diffusion coefficient without estimating the size of the

diffusing molecule (similarly to equation (3.39))

$$D_i^F = D_i^* \frac{\ddot{\mu}_i}{\ddot{\mu}} \left(1 + \frac{d \ln \gamma_i}{d \ln x_i} \right). \quad (\text{C.8})$$

Then, besides equation (3.41), the mutual diffusion coefficients of binary systems can be calculated using Darken equation [Darken, 1948] as:

$$D_{12}^F = \frac{1}{\ddot{\mu}} (x_2 \ddot{\mu}_1 D_1^* + x_1 \ddot{\mu}_2 D_2^*) \left(1 + \frac{d \ln \gamma_1}{d \ln x_1} \right) \quad (\text{C.9})$$

or

$$D_{12}^F = \frac{1}{\ddot{\mu}} (x_2 \ddot{\mu}_2 D_1^\infty + x_1 \ddot{\mu}_1 D_2^\infty) \left(1 + \frac{d \ln \gamma_1}{d \ln x_1} \right), \quad (\text{3.41})$$

or

$$\begin{aligned} D_{12}^F &= \frac{\ddot{\mu}_1}{\ddot{\mu}} (x_2 D_1^* + x_1 D_2^\infty) \left(1 + \frac{d \ln \gamma_1}{d \ln x_1} \right) \\ &= \frac{\ddot{\mu}_2}{\ddot{\mu}} (x_2 D_1^\infty + x_1 D_2^*) \left(1 + \frac{d \ln \gamma_1}{d \ln x_1} \right). \end{aligned} \quad (\text{C.10})$$

Recently, [D'Agostino, 2011] proposed a correction of the thermodynamic correction factor in cases with no strong correlation between the motion of different molecules:

$$D_{12}^F = \frac{1}{\ddot{\mu}} (x_2 \ddot{\mu}_1 D_1^* + x_1 \ddot{\mu}_2 D_2^*) \left(1 + \frac{d \ln \gamma_1}{d \ln x_1} \right)^\alpha \quad (\text{3.42})$$

with $\alpha \approx 0.64$ and got effective prediction with 14 non-ideal liquid mixtures. They further proposed [D'Agostino, 2012], for systems with one strongly self-associated species, when the self-associated species is diluted, equation (3.42) is applicable; when species 1 is strongly dimerised,

$$D_{12}^F = \frac{1}{\ddot{\mu}} (2x_2 \ddot{\mu}_1 D_1^* + x_1 \ddot{\mu}_2 D_2^*) \left(1 + \frac{d \ln \gamma_1}{d \ln x_1} \right)^\alpha. \quad (\text{C.11})$$

This is because with the presence of strong association between molecules, the estimation of molecules mobility fails. Instead of monomers, the associated molecules or clusters will migrate together. To make their equation cover the full range of composition, they proposed [Moggridge, 2012]

$$\chi = \frac{-\frac{1}{2} + \sqrt{\frac{1}{4} + 2cKx_1}}{2cKx_1}$$

$$f(\chi) = \frac{1.41 - 0.41\chi}{0.71 + 0.29\chi} \quad (\text{C.12})$$

$$D_{12}^F = \frac{1}{\ddot{\mu}} \left(f(\chi) x_2 \ddot{\mu}_1 D_1^* + x_1 \ddot{\mu}_2 D_2^* \right) \left(1 + \frac{d \ln \gamma_1}{d \ln x_1} \right)^\alpha$$

with species 1 the self-association component, K its dimerisation constant.

Strong interaction between species might even cause correlated movement of molecules of different species. This is more complex. We will use the simplest but effective model.

Appendix D

D.i. Global parameters, global variables, and local variables for *Comsol* simulation

To make the simulation model versatile and user friendly, we have defined global parameters (Table Appen.D.1), global variables (Table Appen.D.2) and local variables (Table Appen.D.3). To adapt this simulation model for other systems, one just need to input the corresponding parameters.

Table Appen.D.1. Global parameters for Comsol simulation

Name	Expression	Description
T	298.15[K]	Experimental temperature
Qcnomi	800[nl/min]	Nominal central flow rate
Qp	2[ul/min]	Peri flow rate
Qc	Qcnomi*0.37	Central flow rate
phi1p	100[%]	Peri flow antisolvent volume fraction
rho3c	1[g/l]	Inner flow concentration
M1	18.015[g/mol]	Molar mass of antisolvent
M2	88.11[g/mol]	Molar mass of good solvent
M3	476.6[g/mol]	Molar mass of dye
rho1	997.3[g/l]	Density of antisolvent
rho2	1028.6[g/l]	Density of good solvent
rho3	M3/Vm3	Density of dye
Vm1	M1/rho1	Molar volume of antisolvent
Vm2	M2/rho2	Molar volume of good solvent
r3	$(V3/4*3/pi)^{(1/3)}$	Solute molecule radius
V3	635E-30[m^3]	Solute molecule volume
Vm3	V3*N_A_const	Molar volume of liquid DBDCS
mu1	0.891E-3[Pa*s]	Dynamic viscosity of antisolvent
mu2	1.172E-3[Pa*s]	Dynamic viscosity of good solvent
x3s1	8.14111E-12	Amount fraction solubility in antisolvent
x3s2	0.001456632	Amount fraction solubility in good solvent
S1	$x3s1*M3/(x3s1*Vm3+(1-x3s1)*Vm1)$	Solubility of dye in antisolvent
S2	$x3s2*M3/(x3s2*Vm3+(1-x3s2)*Vm2)$	Solubility of dye in good solvent
nD1	1.3324	Refractive index of antisolvent
nD2	1.4167	Refractive index of good solvent
D1limit	2.53E-9[m^2/s]	diffusion coefficient of water in 1,4-dioxane
D2limit	1.13E-9[m^2/s]	diffusion coefficient of 1,4-dioxane in water

Table Appen.D.2. Global variables for Comsol simulation

Name	Expression	Description
Knc	$2.2[s^{-1}]/4.8119E-8[kg^2/m^3]$	Factor in nucleation rate
rhoc	$(\rho_{3c}+\rho_{2c}) * 1[l]/(1[l]+\rho_{3c} * 1[l]/\rho_{3c})$	Central flow density
rhop	$(x_{1p} * M_1 + x_{2p} * M_2) / (V_{m1} * x_{1p} + V_{m2} * x_{2p} + x_{1p} * x_{2p} * (-2.496E-3[l/mol] + 1.756E-3[l/mol] * (x_{2p} - x_{1p}) - 0.703E-3[l/mol] * (x_{2p} - x_{1p})^2 + 0.204E-3[l/mol] * (x_{2p} - x_{1p})^3 - 0.462E-3[l/mol] * (x_{2p} - x_{1p})^4))$	Peripheral flow density
rhomix	$(x_{1t} * M_1 + x_{2t} * M_2 + x_{3t} * M_3) / (V_{m1} * x_{1ta} + V_{m2} * x_{2ta} + (x_{1t} + x_{2t}) * x_{1ta} * x_{2ta} * (-2.496E-3[l/mol] + 1.756E-3[l/mol] * (x_{2ta} - x_{1ta}) - 0.703E-3[l/mol] * (x_{2ta} - x_{1ta})^2 + 0.204E-3[l/mol] * (x_{2ta} - x_{1ta})^3 - 0.462E-3[l/mol] * (x_{2ta} - x_{1ta})^4) + x_{3t} * V_{m3})$	Mixture flow density
x1p	$\phi_{1p} * V_{m2} / (\phi_{1p} * V_{m2} + (1 - \phi_{1p}) * V_{m1})$	Amount fraction of antisolvent in peri flow
x2p	$1 - x_{1p}$	Amount fraction of good solvent in peri flow
x1t	$(\phi_{1p} * Q_p / V_{m1}) / (\phi_{1p} * Q_p / V_{m1} + (Q_c - \rho_{3c} / \rho_{3c} * Q_c + (1 - \phi_{1p}) * Q_p) / V_{m2} + \rho_{3c} * Q_c / M_3)$	Total amount fraction of antisolvent
x2t	$((Q_c - \rho_{3c} / \rho_{3c} * Q_c + (1 - \phi_{1p}) * Q_p) / V_{m2}) / (\phi_{1p} * Q_p / V_{m1} + (Q_c - \rho_{3c} / \rho_{3c} * Q_c + (1 - \phi_{1p}) * Q_p) / V_{m2} + \rho_{3c} * Q_c / M_3)$	Total amount fraction of good solvent
x3t	$(\rho_{3c} * Q_c / M_3) / (\phi_{1p} * Q_p / V_{m1} + (Q_c - \rho_{3c} / \rho_{3c} * Q_c + (1 - \phi_{1p}) * Q_p) / V_{m2} + \rho_{3c} * Q_c / M_3)$	Dye amount fraction full mixture
x1ta	$(\phi_{1p} * Q_p / V_{m1}) / (\phi_{1p} * Q_p / V_{m1} + (Q_c - \rho_{3c} / \rho_{3c} * Q_c + (1 - \phi_{1p}) * Q_p) / V_{m2})$	Water amount fraction without DBDCS full mix
x2ta	$((Q_c - \rho_{3c} / \rho_{3c} * Q_c + (1 - \phi_{1p}) * Q_p) / V_{m2}) / (\phi_{1p} * Q_p / V_{m1} + (Q_c - \rho_{3c} / \rho_{3c} * Q_c + (1 - \phi_{1p}) * Q_p) / V_{m2})$	1,4-Dioxane amount fraction without DBDCS full mix
mup	$\mu_1 * x_{1p} + \mu_2 * x_{2p} + x_{1p} * x_{2p} * (2.339E-3[Pa*s] - 3.769E-3[Pa*s] * (x_{2p} - x_{1p}) + 3.583E-3[Pa*s] * (x_{2p} - x_{1p})^2 - 0.732E-3[Pa*s] * (x_{2p} - x_{1p})^3 - 1.471E-3[Pa*s] * (x_{2p} - x_{1p})^4)$	Dynamic viscosity of peri flow
mumix	$\mu_1 * x_{1ta} + \mu_2 * x_{2ta} + x_{1ta} * x_{2ta} * (2.339E-3[Pa*s] - 3.769E-3[Pa*s] * (x_{2ta} - x_{1ta}) + 3.583E-3[Pa*s] * (x_{2ta} - x_{1ta})^2 - 0.732E-3[Pa*s] * (x_{2ta} - x_{1ta})^3 - 1.471E-3[Pa*s] * (x_{2ta} - x_{1ta})^4)$	Dynamic viscosity after full mixing
phi1ta	$(\phi_{1p} * Q_p) / (\phi_{1p} * Q_p + (Q_c - \rho_{3c} / \rho_{3c} * Q_c + (1 - \phi_{1p}) * Q_p))$	Total volume fraction of the antisolvent neglecting solute
phi2ta	$(Q_c - \rho_{3c} / \rho_{3c} * Q_c + (1 - \phi_{1p}) * Q_p) / (\phi_{1p} * Q_p + (Q_c - \rho_{3c} / \rho_{3c} * Q_c + (1 - \phi_{1p}) * Q_p))$	Total volume fraction of the good solvent neglecting solute
x3smix	$x_{3s1}^{\phi_{1ta}} * x_{3s2}^{\phi_{2ta}} * \exp(2206.9[K]/T + 1173.1[K] * (\phi_{2ta} - \phi_{1ta}) / T + 1197.4[K] * (\phi_{2ta} - \phi_{1ta})^2 / T)$	Mole solubility in mixture
rho3smix	$x_{3smix} * M_3 / (V_{m1} * x_{1ta} + V_{m2} * x_{2ta} + (x_{1t} + x_{2t}) * x_{1ta} * x_{2ta} * (-2.496E-3[l/mol] + 1.756E-3[l/mol] * (x_{2ta} - x_{1ta}) - 0.703E-3[l/mol] * (x_{2ta} - x_{1ta})^2 + 0.204E-3[l/mol] * (x_{2ta} - x_{1ta})^3 - 0.462E-3[l/mol] * (x_{2ta} - x_{1ta})^4) + x_{3t} * V_{m3})$	Mass concentration solubility in mixture

	$x1ta)-0.703E-3[l/mol]*(x2ta-x1ta)^2+0.204E-3[l/mol]*(x2ta-x1ta)^3-0.462E-3[l/mol]*(x2ta-x1ta)^4)+x3smix*Vm3)$	
ve	$(Qc+Qp)/(pi*(105[um])^2)$	Total effective velocity
R1	$(nD1^2-1)/(nD1^2+2)*Vm1$	Mole refractivity of antisolvent
R2	$(nD2^2-1)/(nD2^2+2)*Vm2$	Mole refractivity of good solvent

Table Appen.D.3. Local variables for Comsol simulation

Name	Expression	Description
phi1o	$(w1/rho1)/(w1/rho1+w2/rho2)$	local volume fraction of antisolvent with no solute
phi2o	$(w2/rho2)/(w1/rho1+w2/rho2)$	local volume fraction of good solvent with no solute
phi1	$(w1/rho1)/(w1/rho1+w2/rho2+w3/rho3)$	local volume fraction of antisolvent
phi2	$(w2/rho2)/(w1/rho1+w2/rho2+w3/rho3)$	local volume fraction of good solvent
phi3	$(w3/rho3)/(w1/rho1+w2/rho2+w3/rho3)$	local volume fraction of solute
localmu	$mu1*x1o+mu2*x2o+x1o*x2o*(2.339E-3[Pa*s]-3.769E-3[Pa*s]*(x2o-x1o)+3.583E-3[Pa*s]*(x2o-x1o)^2-0.732E-3[Pa*s]*(x2o-x1o)^3-1.471E-3[Pa*s]*(x2o-x1o)^4)$	local dynamic viscosity
localrho	$(tcs.x_w1*M1+tcs.x_w2*M2+tcs.x_w3*M3)/(Vm1*tcs.x_w1+Vm2*tcs.x_w2+Vm3*tcs.x_w3+(tcs.x_w1+tcs.x_w2)*x1o*x2o*(-2.496E-3[l/mol]+1.756E-3[l/mol]*(x2o-x1o)-0.703E-3[l/mol]*(x2o-x1o)^2+0.204E-3[l/mol]*(x2o-x1o)^3-0.462E-3[l/mol]*(x2o-x1o)^4))$	local density
x1o	$tcs.x_w1/(tcs.x_w1+tcs.x_w2)$	amount fraction of antisolvent without solute
x2o	$tcs.x_w2/(tcs.x_w1+tcs.x_w2)$	amount fraction of good solvent without solute
x3s	$x3s1^{(phi1o)}*x3s2^{(phi2o)}*exp((phi1o)*(phi2o)*(2206.9[K]+1173.1[K]*(phi2o-phi1o)+1997.4[K]*(phi2o-phi1o)^2)/T)$	local solubility amount fraction
c3s	$x3s*M3/(x3s1*Vm3+x1o*Vm1+x2o*Vm2)$	local solubility mass concentration
localnD	$((tcs.Mn+2*localR*tcs.rho)/(tcs.Mn-localR*tcs.rho))^0.5$	local refractivity index
localR	$R1*phi1o+R2*phi2o$	molar refractivity
betam	$tcs.x_w2/x3s$	local supersaturation ratio amount fraction
beta	$tcs.cmass_w3/c3s$	local supersaturation ratio mass concentration
ita1	$D1limit*mu2/spf.mu$	mobility of antisolvent
ita2	$D2limit*mu1/spf.mu$	mobility of good solvent
ita3	$1/(6*pi*spf.mu*r3)$	mobility of solute

D.ii. Justification of separation of the concentration- and composition-driven diffusion by using the migration in electric field model in *Comsol*

To illustrate the uphill and downhill diffusion separately, the downhill term of the diffusion driving force was computed in *Comsol* Fick's Law Model and uphill term in *Comsol* Migration in Electric Field model.

In Fick's Law model for the downhill diffusion, downhill diffusion coefficient

$$D_{\text{down}}^{\text{F}} = \frac{k_{\text{B}}T}{6\pi\left(\frac{3}{4\pi}V_{\text{DBD}}\right)^{\frac{1}{3}}\dot{\mu}}, \quad (\text{D.1})$$

and the downhill diffusive flux

$$\begin{aligned} \mathbf{j}_{\text{down}} &= -D_{\text{down}}^{\text{F}}(\nabla\rho_3) \\ &= -\frac{k_{\text{B}}T\nabla\rho_3}{6\pi\left(\frac{3}{4\pi}V_{\text{DBD}}\right)^{\frac{1}{3}}\dot{\mu}} \end{aligned} \quad (\text{D.2})$$

In the Migration in Electric Field model, we pretended every DBDCS molecule had been carrying one virtual elementary charge. Then the uphill chemical potential gradient was converted into a virtual electric field:

$$\begin{aligned} U &= -\frac{\mu_{\text{up}}}{F} \\ &= -\frac{k_{\text{B}}T \ln \frac{\rho_{3\text{s}}}{1\text{g/l}}}{e} \end{aligned} \quad (\text{D.3})$$

with μ_{up} the uphill term of the chemical potential, F the Faraday constant and e the elementary charge. The virtual electric field

$$\begin{aligned} \mathbf{E} &= -\nabla U \\ &= \frac{k_{\text{B}}T\nabla \ln \frac{\rho_{3\text{s}}}{1\text{g/l}}}{e}. \end{aligned} \quad (\text{D.4})$$

The virtual electrical mobility of DBDCS molecules was defined by Nernst-Einstein relation:

$$\begin{aligned}
\eta_e &= \frac{qD_{\text{down}}^F}{k_B T} \\
&= \frac{e}{6\pi \left(\frac{3}{4\pi} V_{\text{DBD}}\right)^{\frac{1}{3}} \ddot{\mu}} \\
&= e\eta
\end{aligned} \tag{D.5}$$

Then the virtual electrical migration flux

$$\begin{aligned}
\mathbf{j}_e &= \rho_3 v_e \\
&= \rho_3 \eta_e \mathbf{E} \\
&= \rho_3 \frac{e}{6\pi \left(\frac{3}{4\pi} V_{\text{DBD}}\right)^{\frac{1}{3}} \ddot{\mu}} \frac{k_B T \nabla \ln \frac{\rho_{3s}}{1g/l}}{e} \\
&= \frac{\rho_3 k_B T \nabla \ln \frac{\rho_{3s}}{1g/l}}{6\pi \left(\frac{3}{4\pi} V_{\text{DBD}}\right)^{\frac{1}{3}} \ddot{\mu}}
\end{aligned} \tag{D.6}$$

The sum of the diffusive flux and electrical migration flux

$$\begin{aligned}
\mathbf{j}_{\text{down}} + \mathbf{j}_e &= -\frac{k_B T \nabla \frac{\rho_3}{1g/l}}{6\pi \left(\frac{3}{4\pi} V_{\text{DBD}}\right)^{\frac{1}{3}} \ddot{\mu}} + \frac{\rho_3 k_B T \nabla \ln \frac{\rho_{3s}}{1g/l}}{6\pi \left(\frac{3}{4\pi} V_{\text{DBD}}\right)^{\frac{1}{3}} \ddot{\mu}} \\
&= \rho_3 \frac{k_B T}{6\pi \left(\frac{3}{4\pi} V_{\text{DBD}}\right)^{\frac{1}{3}} \ddot{\mu}} (-\nabla \ln \rho_3 + \nabla \ln \rho_{3s}) .
\end{aligned} \tag{D.7}$$

This is equivalent to equation (3.49). In this second way, the uphill term and downhill terms in the diffusion driving force of DBDCS in a mixture of H₂O and 1,4-dioxane were independently computed and then summed.

Thus, in the simulation domain, the local solubility of DBDCS was estimated as

$$x_{3s} = x_{3s1}^{\frac{\phi_1}{\phi_1 + \phi_2}} \cdot x_{3s2}^{\frac{\phi_2}{\phi_1 + \phi_2}} \exp \left(\phi_1 \phi_2 \sum_{n=0}^2 \frac{A_n \left(\frac{\phi_2 - \phi_1}{\phi_1 + \phi_2} \right)^n}{T} \right) \tag{D.8}$$

with ϕ_1 and ϕ_2 the local volume fraction of species 1 and 2.

Appendix E

E.i. FLIM measurement of spontaneous precipitation of Calix-Cousulf- Cs^{+2} nano-particles

An experiment of precipitation of Calix-Cousulf- Cs^{+2} nano-particles is shown in Figure Appen.E.1. Its FLIM map and PCA results are shown in Figure Appen.E.2.

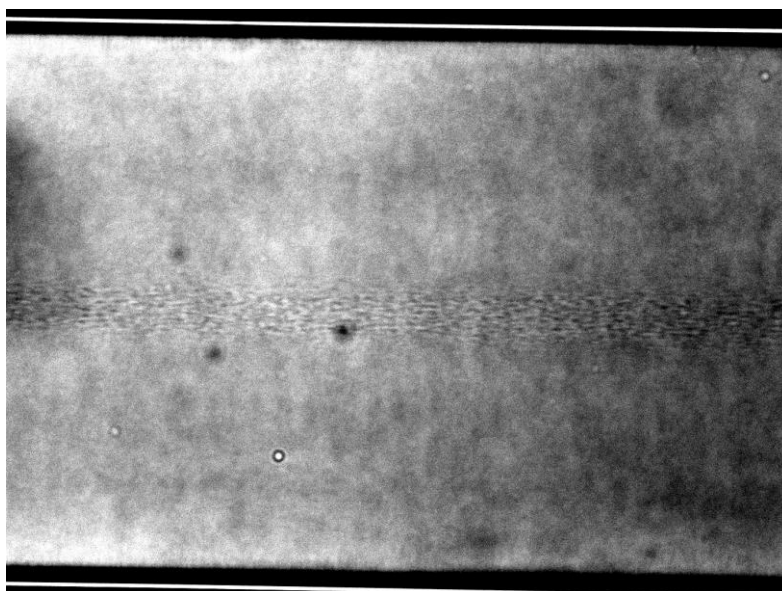


Figure Appen.E.1. Precipitation of Calix-Cousulf- Cs^{+2} nano-particles from a mixture of THF-water-Calix-Cousulf- Cs^{+2} in the coaxial microfluidic mixer.

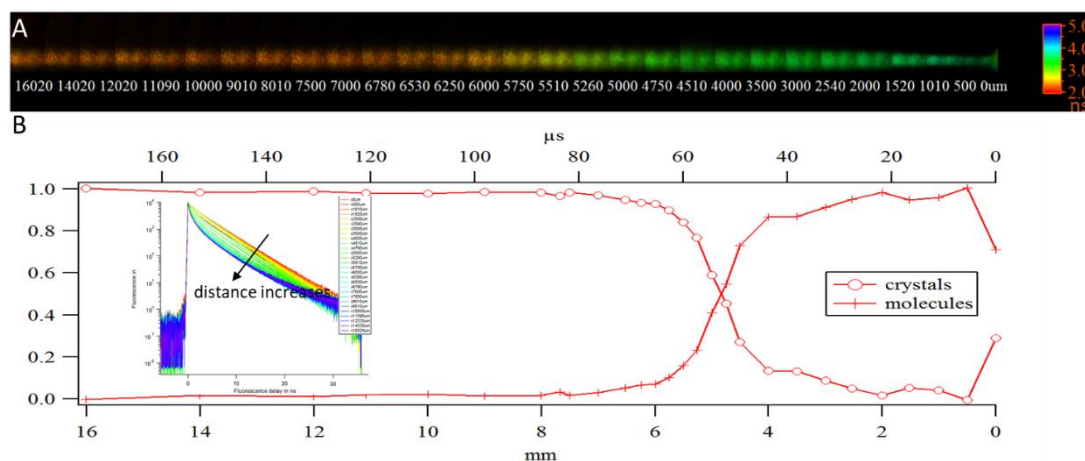


Figure Appen.E.2. FLIM map of Precipitation of Calix-Cousulf- Cs^{+2} nano-particles from a mixture of THF-water-Calix-Cousulf- Cs^{+2} in the coaxial microfluidic mixer.

The flow is from right to left. A: the FLIM map. B: PCA shows the fluorescence decays collected along the flow consists of two species. Their contribution is plotted against the distance from the injection nozzle.

Appendix F

F.i. SAXS study with swing@soleil experiment

EXPERIMENTAL REPORT FOR PROPOSAL 20151103 Probing the Kinetics of Dye Crystallization and DNA Compaction by Rapid Mixing and Defocusing in Microfluidic Capillaries

Guillaume Tresset,¹ Brigitte Pansu,¹ Mehdi Zeghal,¹ Sandrine Mariot,¹ Robert Pansu,² Valérie Génot,² Jean-Frédéric Audibert,² Zhengyu Zhang,^{2,3} Anne Spasojevic³

¹Laboratoire de Physique des Solides, Orsay

²Ecole Normale Supérieure de Cachan, Cachan

³Ecole Centrale de Paris, Châtenay-Malabry

1/ Initial goal

The experiment aimed at elucidating the early stage of the crystallization of two organic dyes and to relate the fluorescence properties extensively studied via inhouse measurements to the structure inferred from scattering data. The organic dyes were DBDCS ($C_{32}H_{32}N_2O_2$) and CalixCs. DBDCS is soluble in THF and CalixCs in a mixture of THF and dioxane. Upon mixing with pure water, both dyes self-assemble into a crystal structure. We devised a microfluidic device based on the hydrodynamic flow focusing of a highly concentrated dye solution by a stream of pure water. In principle, our setup could thus capture the crystal growth in a continuous flow in such a way that the signal-to-noise ratio could be arbitrarily increased via long exposure time, the only limitation being the amount of materials.

2/ Experimental results

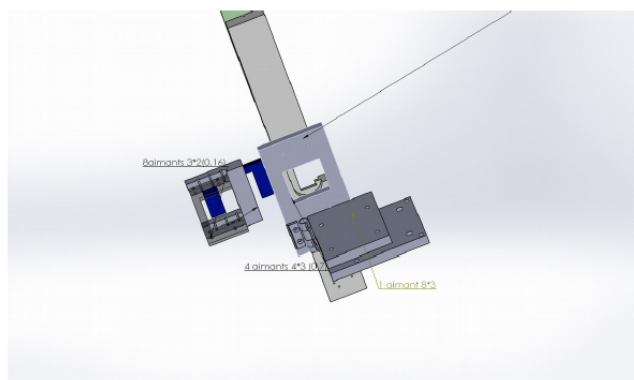


Figure 1: Holder for the microfluidic device. It was mounted on the XY stage of the SWING beamline.

We designed and fabricated in dural a holder that could be mounted on the XY stage of the SWING beamline (Figure 1). The microfluidic device consisted of three concentric quartz capillaries with inner diameters of 20 μm , 200 μm and 800 μm , respectively. The flow rates were controlled by three syringe pumps operated individually from the control room using a LabView interface. An endoscopic camera was mounted on the holder to monitor in real time the flows inside the

capillaries. Moreover, a removable holder for sealed capillaries was devised for control experiments with standard samples.

The first experiments were performed with cubosomes in pure water. The purpose was to verify that cubosomes could be readily diluted by tuning the flow rates in the three capillaries. We chose cubosomes because they exhibit an internal liquid-crystal structure, which produces Bragg peaks at high q -values, and they can be washed away easily by flowing pure water. Figure 2 shows the effects of

dilution on cubosomes when the flow rate of the large capillary containing pure water was varied from 1 $\mu\text{L}/\text{min}$ to 4 $\mu\text{L}/\text{min}$. The black curve on Figure 2 was obtained for a threefold lower flow rate of cubosomes and a water flow rate of 1 $\mu\text{L}/\text{min}$. After analysis, the peak intensities were consistent with the dilution factors, which gave us confidence on the quality of the mixing occurring inside the capillaries.

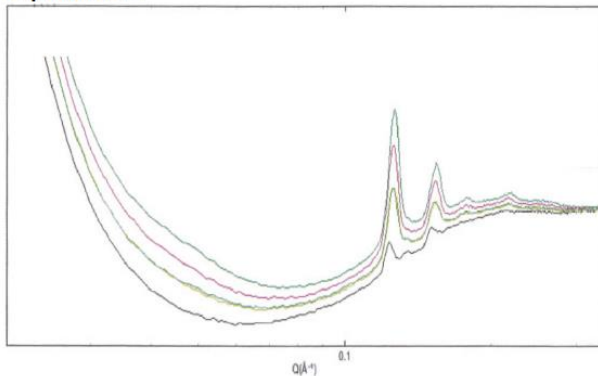


Figure 2: Dilution effects on cubosomes. The scattering intensities were collected at a fixed position in the large capillary and for different flow rates.

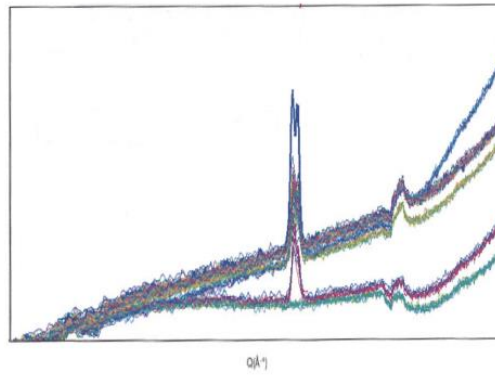


Figure 3: Scattering intensities of crystallized DBDCS collected at different positions along the large capillary.

In the second series of experiments, we investigated the crystallization of DBDCS. Initially in THF at 10 g/L, DBDCS was mixed with different ratios of THF and water. Above 32% of water (Figure 3), crystallization occurred very rapidly and macroscopic crystals appeared at the tip of the medium capillary. After a few seconds, the large capillary was clogged and the whole system had to be washed thoroughly with THF. Quite interestingly, the Bragg peaks were slightly shifted in comparison with those obtained with DBDCS crystals in powder form. This means that the presence of solvent has an effect on the crystal structure and on the lattice parameters. Below 32% of water, no scattering intensity coming from DBDCS crystals was detected, even at long distances from the tip of the medium capillary, where the crystal growth was expected to be nearly completed. It was therefore very difficult to capture the early events along the crystallization pathway.

Since DBDCS has a low electron density, we tested the crystallization of CalixCs, which has a better contrast than DBDCS due to the presence of cesium. Unfortunately, we faced up difficulties with the change of microfluidic device and we broke several capillaries. We finally did not have enough time for a single test with CalixCs.

3/ Conclusion

The microfluidic device turned out to be robust and easy to use partly thanks to the new holder. The leakage problems that hampered the previous experiment (n°20140859) have been mostly solved. We still have to find a suitable molecule, which can crystallize slowly in mild conditions. This molecule must also contain heavy elements in such a way that it produces a strong scattering intensity.

Thèse de doctorat

Titre : Nucléation induite par laser en Mélangeur Microfluidique Coaxial

Mots clés : nucléation induite par laser, droplet, Simulation *Comsol*, microfluidique, fluorescence.

Résumé : Nous avons développé un dispositif microfluidique cylindrique pour observer la précipitation par déplacement de solvant. Le soluté est introduit au centre dans un bon solvant (le 1,4-dioxane) avec l'anti solvant (l'eau) à la périphérie. Le DBDCS (le soluté) est une molécule dont les nombreux polymorphes fluorescent différemment à l'état cristallin. Nous montrons que le soluté est repoussé au centre (focalisation) par la diffusion de l'eau, jusqu'à l'apparition d'une phase liquide presque pure. Cette phase liquide s'organise en gouttes de mêmes tailles. Nous avons déterminé le diagramme de fonctionnement du dispositif et nous montrons que la distance focalisation et la taille des gouttes sont contrôlés par le rapport des flux et la composition de la solution d'anti solvant.

En présence d'un anti-solvant doux, on observe la nucléation et la croissance d'une mélange de

polymorphes. La vitesse de nucléation et de croissance et, pour chaque cristal, son habitus et son polymorphe sont déterminés. Mais la nucléation reste un phénomène rare, dispersé sur 2 mm et non synchronisé.

En focalisant un laser infra rouge sur le dispositif, nous observons des effets de pinces optiques puissants sur les flux de solvants, les flux de gouttelettes et la multiplication d'un à deux ordres de grandeur de la vitesse de nucléation. La vitesse de croissance, l'habitus des cristaux et la distribution des polymorphes sont inchangés par l'induction laser.

La nucléation est localisée au point de focalisation et synchronisée par le laser. Nous montrons que le polymorphe présent majoritairement au point de focalisation disparaît en quelques millisecondes alors qu'un polymorphe minoritaire croît à partir du point de focalisation.

Title: Laser-induced Nucleation in a Coaxial Microfluidic Mixer

Keywords: crystallisation, laser-induced nucleation, *Comsol* simulation, microfluidics, fluorescence.

Abstract: We have developed a cylindrical microfluidic device to observe precipitation by solvent displacement. The solute is focused into the centre in a good solvent (1,4-dioxane) with the anti-solvent (water) on the periphery. DBDCS (solute) is a molecule whose many polymorphs fluoresce differently in the crystalline state. We show that solute is pushed back to the centre (focusing) by the diffusion of water, until an almost pure liquid phase appears. This liquid phase is organised into drops of the same size. We have determined the operating diagram of the device and show that the focusing distance and drop size are controlled by the flow ratio and the composition of the anti-solvent solution.

In the presence of a mild anti-solvent, the mixture undergoes crystal nucleation and

growth. The rate of nucleation and growth, crystal habits and polymorphs are determined for each crystal. But nucleation remains a rare phenomenon, scattered over 2 mm and not synchronised.

By focusing an infrared laser on the device, we observe powerful optical tweezing effect on solvent flows, droplet flows, and the multiplication of the nucleation rate by one to two orders of magnitude. The growth rate, crystal habitus, and polymorph distribution are unchanged by laser induction.

The nucleation is located at the point of focus and synchronised by the laser. We show that the polymorph present mainly at the focus point disappears in a few milliseconds while a minority polymorph grows from the focus point.

